UNIVERSIDAD DE LEÓN

DEPARTAMENTO DE QUÍMICA Y FÍSICA APLICADAS

ÁREA DE FÍSICA APLICADA

TESIS DOCTORAL

INFLUENCIA DE LA MICROESTRUCTURA DE LA PRECIPITACIÓN EN LAS CARACTERÍSTICAS DEL AEROSOL ATMOSFÉRICO

INFLUENCE OF PRECIPITATION MICROSTRUCTURE ON THE CHARACTERISTICS OF ATMOSPHERIC AEROSOL

Carlos del Blanco Alegre

Directores: Roberto Fraile Laiz, Ana Isabel Calvo Gordaliza y Amaya Castro Izquierdo

Doctorado en Ciencia y Tecnología del Medio Ambiente

León, 2021

AGRADECIMIENTOS

Esta tesis está dedicada a mi abuelo Antonio Alegre, al cual el apellido le describía perfectamente. Aunque no lo haya podido ver, seguro que estaría orgulloso de su nieto (espero). Empezó siendo como un padre y acabó siendo como un hijo, pero haber estado a su lado todo el tiempo posible es mil veces superior a cualquier tesis. Aunque sean un montón de letras, que sirva como homenaje a la mejor persona que he conocido. Además, esta tesis está dedicada a muchas personas, por lo que trataré de no ser muy pesado. Pido perdón de antemano ya que seguro que se me olvida alguien.

En primer lugar, quisiera agradecer el apoyo y enseñanza durante estos años a mis directores de tesis, Roberto, Ana y Amaya, que me han apoyado desde el primer día en todos los sentidos. Sé lo complicado que ha sido compaginar clases, trabajos fin de grado, dos tesis en curso, problemas de salud… solo faltaba una pandemia… ¡ah, no! que también la ha habido. Aún con todo, siempre han tenido tiempo (donde no lo había) para resolver dudas o problemas.

Quisiera agradecer a Fernanda, compañera de tesis durante gran parte del doctorado y con la cual ha sido un placer trabajar codo a codo. Igualmente, al resto del personal del Departamento de Química y Física Aplicadas, destacando especialmente a Ángel, Toyi y Camino, quienes siempre trataron de ayudarme. A todos los componentes del Departamento, profesores y personal. Quisiera destacar por su cercanía hacia mí a Javier, a Roberto y a Rosa, la cual era el pegamento del Departamento y siempre nos juntaba para tomar el café. Agradecer al grupo de Botánica su apoyo para resolver cualquier duda relacionada con datos de bioaerosoles, especialmente a Delia, Rosa y Alberto. Quisiera acordarme también de todos aquellos que trataron algún dato que luego utilicé: Bea, Sergio, Víctor…

A lo largo de estos cuatro años he tenido la suerte de conocer a muchas personas relacionadas con el estudio de la contaminación atmosférica, las cuales me han transmitido parte de su conocimiento. Quisiera destacar especialmente a dos personas: Eli, sin cuya ayuda y ánimo

hubiese sido imposible avanzar al comienzo de la tesis, y a Paulo Fialho, quien no solo me enseñó el tratamiento de datos de carbono negro si no que en la estancia en las islas Azores me trató de la mejor de las maneras. Agradecer a Véro su trato excelente en las dos estancias en Toulouse, aparte de su gran conocimiento y ayuda. A todos los miembros del grupo de investigación de Aveiro, especialmente Célia, Teresa, Margarita y Cátia por su apoyo en los análisis y estancias. A los componentes del instituto de investigación de El Arenosillo (Huelva) en donde me permitieron aprender de forma veloz el funcionamiento del SMPS. En definitiva, a todo aquel que ha invertido un tiempo en transmitir conocimientos hacia mí.

En cuanto a familia, esta tesis no podría haberla escrito sin la educación prestada por mis padres y por su continuo apoyo. Ángel y Pilar, Geli y Pili. No negaré que a lo largo de la tesis me han dado muchos disgustos… Pero siempre están ahí y siempre estaré a su lado. Os quiero. Al igual que a mis padres, quisiera dedicar la tesis a mis tíos César y Gelines, quienes siempre han sido como unos segundos padres, estando siempre en los peores momentos y ayudándome cuando lo necesitaba. A mi doble primo Dani, con el cual no hablo todo lo que debería… pero siempre está presente.

¿Y qué voy a decir de Noelia? Probablemente la persona que más se ha sacrificado por mi culpa, viniendo a León ("Invernalia" para ella), aguantándome las frikadas sobre aerosoles o gotas de lluvia, aguantándome en definitiva… A lo largo de una tesis hay momentos de tristeza, de pensar que no se avanza (2020 por ejemplo), de pensar qué estoy haciendo… Yo me callo todo porque no soy capaz de contarlo. Sin embargo, Noelia lograba que se me pasara. Desde que la conocí siempre hemos estado juntos y solo puedo decir que es la mejor del mundo. Te quiero.

Agradecer el apoyo a los amigos y todo aquel que en algún momento se ha preocupado por mí. Quisiera agradecer especialmente a Víctor, quien desde el primer día me ha ayudado y aconsejado, incluso entrando en el mundillo del aerosol.

En agradecimientos random, aunque pueda parecer extraño, quisiera agradecer el entretenimiento durante la tesis. Sí, porque tratar miles y miles de datos sin escuchar nada, es un martirio. Y la radio ha sido la mejor aliada. Así pues, un trocito de la tesis es debida a programas como *La Vida Moderna*, *La resistencia* o *Aquí hay dragones*. Aunque sus creadores nunca lo leerán, para mí ha sido un gran apoyo.

Por último, quisiera agradecer a la educación pública española haberme permitido estudiar el grado, el máster y realizar la tesis gratuitamente. Es algo para sentirse orgulloso y que no en todos los países del mundo ocurre, por lo que creo que entre todos debemos cuidar y mejorar la educación pública

FINANCIACIÓN

La presente tesis se ha realizado gracias a una beca predoctoral concedida por el Ministerio de Educación, Cultura y Deporte, dentro del *Programa de Formación de Profesorado Universitario (FPU16/05764)*. Además, la campaña de muestreo y posterior tratamiento de los datos fue posible gracias al proyecto AERORAIN, financiado por el Ministerio de Economía y Competitividad (CGL2014-52556-R, cofinanciado con fondos FEDER).

PREMIOS

Una parte de la tesis ha sido galardonada con el Premio "Mariano Rodríguez" para jóvenes investigadores de la Fundación "Carolina Rodríguez" de León.

En el Congreso Asociación Meteorológica Española celebrado en marzo de 2018 se ha recibido el galardón "Premio en calidad de joven investigador por el interés de su contribución al Congreso".

El póster titulado "Air pollution in León during a set of forest fires in the NW of the Iberian Peninsula: a post-fires rain event" presentado en el congreso "6th Iberian Meeting on Aerosol Science and Technology – RICTA 2018", celebrado en junio de 2018 ha recibido el premio "Best Poster Award".

ÍNDICE DE CONTENIDOS

CAPÍTULO 1. INTRODUCCIÓN *1*

1.1. Aerosol atmosférico **1**

1.1.1. Formación y origen 2

1.1.2. Sumideros: deposición seca y húmeda 6

1.1.3. Distribución de tamaño 6

1.1.4. Carbono negro 10

1.1.5. Normativa 12

1.2. Precipitación **14**

1.2.1. Características de los hidrometeoros 14

1.2.2. Distribución de tamaños de gota 15

1.3. Interacción aerosol-precipitación **17**

1.3.1. Mecanismos de barrido debajo de la nube 17

1.3.2. Coeficientes de lavado 19

1.4. Estructura de la memoria **20**

1.5. Referencias **21**

CAPÍTULO 2. HIPÓTESIS Y OBJETIVOS *27*

CAPÍTULO 3. MATERIAL Y MÉTODOS *37*

3.1. Zona de estudio **37**

3.2. Contexto del muestreo **41**

3.3. Muestreo: equipos de medida **41**

3.3.1. Etalómetro 42

3.3.2. Contador de partículas basado en movilidad eléctrica 46

3.3.3. Contador de partículas óptico 48
3.3.4. Disdrómetro láser 50
3.3.5. Colector de lluvia 52
3.3.6. Captadores de PM_{10} y polen 53
3.3.7. Medidores de gases 55
3.3.8. Variables meteorológicas 56

3.4. Análisis post-muestreo 57
3.4.1. Carbono orgánico y elemental 57
3.4.2. Iones y azúcares: Cromatografía iónica 59
3.4.3. Elementos traza 59
3.4.4. Morfología y composición: Microscopía 60

3.5. Modelos y herramientas 61
3.5.1. Forzamiento radiativo: Modelo GAME 61
3.5.2. Herramientas estadísticas 63
3.5.3. Herramientas adicionales 64
3.5.4. Fracciones inhalable, torácica y respirable 67

3.6. Referencias 68

CHAPTER 4. Scavenging of submicron aerosol particles in a suburban atmosphere 73

4.1. Introduction 73

4.2. Measurements 76
4.2.1. Sampling site 76
4.2.2. Rain event selection 76
4.2.3. Aerosol particle characterization 77
4.2.4. Respirable fraction 78
4.2.5. Raindrop characterization and meteorological data 79
4.2.6. Air mass origin 80
4.2.7. Scavenging efficiency and coefficient 80
4.2.8. Statistical analysis 81

4.3. Results and discussion 82
4.3.1. Events characterization 82
4.3.2. Scavenging efficiency 83
4.3.3. Scavenging coefficient 85
4.3.4. Raindrop size effect 86
4.3.5. Impact of aerosol scavenging by rain on the respirable fraction 88

4.4. Conclusions 89

4.5. References 89

Supplementary material **94**
S.4.1. Figures 95
S.4.2. Tables 100

CHAPTER 5. Below-cloud scavenging of fine and coarse aerosol particles by rain *103*

5.1. Introduction **103**

5.2. Study zone **105**

5.3. Methodology **106**
5.3.1. Aerosol characterization 107
5.3.2. Raindrop characterization 109

5.4. Results and discussion **110**
5.4.1. Meteorological and precipitation study 110
5.4.2. Daily pattern in particle concentration 111
5.4.3. Study of the scavenging effect 112
5.4.4. Study of scavenging effect in one rain event 119

5.5. Conclusions **121**

5.6. References **122**

CHAPTER 6. Evolution of size-segregated aerosol concentration in NW Spain *125*

6.1. Introduction **125**

6.2. Methodology **127**
6.2.1. Sampling site 127
6.2.2. Aerosol particles characterization 128
6.2.3. New particle formation events 128
6.2.4. Statistical analyses 130

6.3. Results and discussion **131**
6.3.1. Evolution of particle concentration 131
6.3.2. Weekly evolution 134
6.3.3. Meteorological parameters 135
6.3.4. New particle formation events 137
6.3.5. Model for the identification of new particle formation events 140

6.4. Conclusions **141**

6.5. References **142**

Supplementary material **147**
S.6.1. New particle formation parameters 147
S.6.2. Verification indexes 149

S.6.3. Figures 150
S.6.4. Tables 155

CHAPTER 7. Searching the contribution of coal combustion to black carbon 159

7.1. Introduction 159

7.2. Material and methods 161

7.2.1. Sampling site 161
7.2.2. Methodology 162
7.2.3. Statistical analyses 164

7.3. Results and discussion 165

7.3.1. Aethalometer model application 165
7.3.2. Coal combustion contribution 171

7.4. Conclusions 175

7.5. References 176

Supplementary material 183

S.7.1. Figures 183
S.7.2. Tables 187
S.7.3. Method using the median value to estimate the coal combustion contribution 190

CHAPTER 8. Aethalometer measurements in a road tunnel 193

8.1. Introduction 193

8.2. Experimental 195

8.2.1. Sampling site and measurements 195
8.2.2. Black carbon data 196
8.2.3. Statistical analyses 197
8.2.4. Emission factors 197

8.3. Results and discussion 198

8.3.1. Equivalent Black Carbon values 198
8.3.2. Absorption Ångström Exponent 201
8.3.3. Vehicles-BC relationship 202
8.3.4. Gaseous emissions-BC relationship 203
8.3.5. Emission factors 204

8.4. Conclusions 206

8.5. References 207

Supplementary material 211

CHAPTER 9. Quantification of source specific black carbon scavenging 215

9.1. Introduction 215

9.2. Material and methods 218

9.2.1. Sampling site and measurements 218

9.2.2. Black carbon data 218

9.2.3. Disdrometer and meteorological data 219

9.2.4. Air mass trajectories 220

9.2.5. Selecting data criteria 221

9.2.6. Diurnal pattern normalization 222

9.3. Results and discussion 223

9.3.1. Rain effect on eBC concentration 224

9.3.2. Air masses origin and weather types 226

9.3.3. Scavenging coefficients 227

9.3.4. Relation between lambda and meteorological parameters 228

9.3.5. Model for ΔeBC 229

9.4. Conclusions 231

9.5. References 232

Supplementary material 238

S.9.1. Aethalometer model 238

S.9.2. Tables 238

S.9.3. Figures 241

CHAPTER 10. Towards a model of wet deposition of bioaerosols 247

10.1. Introduction 247

10.2. Material and methods 250

10.2.1. Sampling site 250

10.2.2. Pollen concentration characterization 250

10.2.3. Rain characterization 251

10.2.4. Rain events selection 252

10.2.5. Scavenging efficiency and coefficient 253

10.2.6. Linear model 254

10.3. Results and discussion 254

10.3.1. Meteorological and precipitation analysis 254

10.3.2. Pollen concentration analysis 256

10.3.3. Study of the scavenging effect 257

10.3.4. Raindrop size effect 261

10.3.5. Modelling the variation of pollen concentration 262

10.4. Conclusions 264

10.5. References 265

Supplementary material 270

CHAPTER 11. Links between aerosol radiative forcing and rainwater 271

11.1. Introduction 271

11.2. Methods 273

11.2.1. Sampling site 273

11.2.2. Aerosol particle size distribution 273

11.2.3. Density and refractive index 274

11.2.4. Raindrop characterization and meteorological data 275

11.2.5. Radiative forcing model 276

11.2.6. Criteria for rain event selection 278

11.2.7. Air mass origin 279

11.3. Results and discussion 279

11.3.1. Raindrop analysis 279

11.3.2. Stratiform rain events 281

11.3.3. Convective rain events 290

11.4. Conclusions 292

11.5. References 294

Supplementary material 299

CAPÍTULO 12. CONCLUSIONES Y PERSPECTIVAS 303

12.1. Conclusiones 303

12.2. Perspectivas de futuro 306

12.3. Conclusions 309

12.4. Future prospects 312

ANEXO A 315

A1. Eficiencia de colisión 315

A2. Referencias 320

ANEXO B 321

B1. Preparación pre-muestreo 321

B1.1. Equipos de medida 321

B1.2. Filtros de muestreo 322

B1.3. Material para muestras de lluvia 323

B2. Muestreo: equipos de medida 324

B2.1. Funcionamiento del SMPS 324

B2.2. Correcciones del contador de partículas óptico PCASP-X 327

B3. Referencias 328

RESUMEN

La contaminación atmosférica es uno de los principales problemas que afectan a la población mundial en el siglo XXI. Es provocada por gases [destacando el monóxido de carbono (CO), el ozono (O_3), y los óxidos de nitrógeno (NOx)] y material particulado (PM). Este material particulado o aerosol atmosférico se define como el conjunto de partículas sólidas y/o líquidas (excepto los hidrometeoros) que están suspendidas en el aire, cuyo tamaño se encuentra en un intervalo entre 0.001 y 100 μm. Los aerosoles pueden ser partículas biogénicas (polen, esporas, virus o bacterias) y no biogénicas (polvo mineral, sales marinas, carbono negro…) que interactúan entre sí, pudiendo provocar graves efectos sobre la población, el medio ambiente y el clima.

Los aerosoles atmosféricos son polidispersos, es decir, presentan un amplio rango de tamaños que puede variar desde nanómetros hasta decenas de micras. El material particulado se clasifica en función de su tamaño en PM_{10}, $PM_{2.5}$ y PM_1 que son aquellas partículas con un diámetro aerodinámico inferior a 10 μm, 2.5 μm y 1 μm, respectivamente. El tamaño de las partículas de aerosol depende de sus fuentes, sumideros y su transporte a través de la atmósfera. También los procesos meteorológicos contribuyen a la variabilidad espacial y temporal de su composición, concentración y distribución de tamaños.

Uno de los componentes del material particulado con mayor efecto sobre el clima y la salud es el carbono negro o *Black Carbon* (BC). Se trata de un contaminante de corta vida media, cuya principal característica es que absorbe fuertemente la luz visible. El BC es emitido por la combustión incompleta de combustibles fósiles y biomasa, por lo que sus fuentes principales son los motores diésel utilizados para el transporte y los combustibles sólidos utilizados en instalaciones domésticas e industriales. Cabe resaltar que el BC es el segundo contribuyente al calentamiento global, después del CO_2, con un forzamiento radiativo medio global estimado de 0.4 a 1.2 W m^{-2}.

Dada la importancia del material particulado atmosférico, es vital el estudio de sus principales sumideros: la deposición seca y húmeda. Esta última, en la que nos centraremos en la presente tesis doctoral, es el proceso por el que los aerosoles son barridos (*scavenging*) por hidrometeoros en la atmósfera, depositándolos sobre la superficie terrestre. Existen dos tipos de *scavenging* en función de dónde ocurre el proceso: dentro de la nube o ICS (*In-Cloud Scavenging*) o bien debajo de la nube o BCS (*Below-Cloud Scavenging*), a través de los procesos de precipitación, que pueden tomar diversas formas: lluvia, tormenta, granizo, nieve, etc.

El BCS tiene lugar mediante diferentes mecanismos de barrido (difusión browniana, interceptación, impacto inercial, termoforesis, difusioforesis y efectos electrostáticos) que actúan entre los hidrometeoros y las partículas de aerosol. El peso específico de cada mecanismo dependerá de las condiciones de la atmósfera y de las características de la precipitación y los aerosoles. Cabe destacar que el proceso de interacción aerosol-gota de lluvia es complejo debido a que su diferencia de tamaño es de varios órdenes de magnitud. La interacción gota-aerosol se modela a partir de la *eficiencia de colisión,* que se define como la fracción de las partículas de aerosol con diámetro d_p, contenidas en el volumen de colisión, que se recogen por la caída de gotas de lluvia de diámetro D_r. Para estimar la eficiencia de lavado de los aerosoles en la atmósfera real se utiliza el *coeficiente λ de lavado de aerosoles* por la precipitación, que expresa el cambio temporal en la concentración de partículas de aerosol. Otro parámetro útil para evaluar el efecto de lavado es el *porcentaje de variación de la concentración de partículas de aerosol* (*%ΔC*), para determinar el cambio en la concentración entre dos instantes dados.

La presente Memoria está dividida en **12** Capítulos: el ***Capítulo 1*** presenta una breve introducción teórica tanto de la contaminación atmosférica y sus características como de la precipitación. El ***Capítulo 2*** detalla los objetivos generales y específicos de la tesis doctoral y una presentación de la estructura de esta Memoria. El ***Capítulo 3*** incluye una descripción detallada del material y métodos utilizados en el estudio, especificando los procedimientos llevados a cabo durante la campaña de muestreo y el tratamiento de datos. En los ***Capítulos 4 al 11*** se muestran los resultados obtenidos con un formato similar al de los artículos científicos. Finalmente, en el ***Capítulo 12*** se establecen las principales conclusiones, aplicaciones y perspectivas futuras de la investigación.

El ***Capítulo 4*** constituye un estudio del lavado de las partículas ultrafinas (UFP; <100 nm) y de acumulación, así como su dependencia con los diferentes tamaños de las gotas de lluvia en un entorno urbano. Se utilizó un espectrómetro de movilidad eléctrica (SMPS) para medir las partículas de aerosol y un disdrómetro láser (LPM) para analizar las variables físicas de las gotas de lluvia (intensidad de precipitación, precipitación acumulada, número de gotas en los 22 canales, volumen barrido y tamaño medio de las gotas de lluvia). Se realizó un análisis de la

eficiencia de barrido y del coeficiente de lavado (λ) según las intensidades de la lluvia, en los distintos rangos de tamaño del aerosol. Además, se determinó el impacto en la salud humana a través de la fracción de partículas que alcanza las distintas zonas del tracto respiratorio (fracción respirable). Los principales resultados observados fueron: i) las modas de nucleación (entre 14-30 nm), Aitken (entre 30-100 nm), acumulación 1 (entre 100-300) y acumulación 2 (entre 300-1000 nm) presentaron una eficiencia (y un coeficiente) de lavado del 15% ($3.9 \cdot 10^{-5}$), 4% ($3.1 \cdot 10^{-5}$), 22% ($4.8 \cdot 10^{-5}$) y 21% ($5.2 \cdot 10^{-5}$ s^{-1}), respectivamente; ii) los eventos con intensidades de lluvia entre 1 y 3 mm h^{-1} causaron menor lavado en todas las modas; y iii) los tamaños de gota de lluvia entre 1.25 y 3.5 mm lavaron principalmente los tamaños de partículas entre 70 y 250 nm. Se observó un menor lavado en las partículas de tamaño superior a 300 nm, y las partículas mayores de 600 nm sólo fueron lavadas por las gotas de lluvia mayores de 4.75 mm; iv) la fracción respirable antes y después de los eventos de lluvia presentó una disminución significativa del -35%.

A partir de los datos de la precipitación registrados cada minuto y del tamaño de las partículas de aerosol atmosférico, se incluye en el ***Capítulo 5*** un estudio sobre el lavado de partículas de aerosol finas y gruesas y sobre su relación con el tamaño de las gotas de lluvia. Como resultado de una campaña de muestreo de 6 meses en León, se calcularon los coeficientes de barrido en 54 eventos de lluvia, con un valor medio de $2.6 \cdot 10^{-5} \pm 6.0 \cdot 10^{-5}$ s^{-1} para la moda fina y $5.8 \cdot 10^{-5} \pm 9.6 \cdot 10^{-5}$ s^{-1} para la moda gruesa. Asimismo, la concentración de partículas disminuyó durante la lluvia en un 10% y tras la lluvia en un 18%. En el *intervalo de Greenfield* (tamaños entre 0.3 y 1 μm), el lavado es menos eficaz que en aerosoles de otros tamaños. El número de gotas entre 0.75 y 3 mm muestra correlaciones negativas estadísticamente significativas ($p<0.05$) con el número de partículas entre 0.16 y 1.76 μm, sugiriendo así el posible papel de esas gotas de lluvia en el lavado de partículas de este tamaño. Además, se encontraron correlaciones negativas significativas entre el volumen total barrido por la caída de gotas (mm^3 m^{-3}) y la variación del número de partículas con diámetros de entre 0.12 y 0.19 μm.

Con el fin de identificar una de las principales fuentes de partículas ultrafinas, en el ***Capítulo 6*** se incluye un estudio de las partículas de tamaños entre 15 y 736 nm. También se ha caracterizado la evolución de sus concentraciones y los eventos de formación de nuevas partículas (NPF). Las concentraciones de partículas de Aitken (N_{Ait}) y de acumulación (N_{acc}) registraron sus máximos en los meses fríos durante las horas punta, por la mañana (0600-0900 UTC) y por la tarde (1700-2000 UTC), mientras que los máximos para la concentración de partículas de nucleación (N_{nuc}) se alcanzaron en los meses cálidos durante las horas del mediodía. N_{Ait}, N_{acc} y N_{total} mostraron una correlación negativa significativa con la velocidad del viento y una relación con la altura de la capa límite planetaria (ABL) por períodos. En el periodo cálido se registró una correlación significativa positiva entre ABL y N_{nuc}, lo que indica que la mayor dispersión con una

ABL alta provoca condiciones favorables para la aparición de eventos NPF. Tras una clasificación visual, se identificaron y analizaron 96 eventos NPF, que se produjeron principalmente entre las 1100 y las 1500 UTC, en primavera y verano. Además, se desarrolló un modelo estadístico en dos pasos para identificar los eventos NPF: un análisis cluster seguido de un análisis discriminante. La aplicación del análisis discriminante a uno de los clusters, que agrupaba 93 días, permitió identificar 55 de los 56 días de eventos NPF incluidos en el cluster. Por lo tanto, este método es una herramienta valiosa para identificar tales eventos de forma rápida y eficaz.

En el ***Capítulo 7*** se presenta el estudio de la concentración de carbono negro (BC) desde enero de 2016 hasta marzo de 2017, en los alrededores de una ciudad (León) donde el carbón se utiliza habitualmente como combustible en instalaciones domésticas de calefacción. La concentración anual media de BC equivalente (eBC) fue de 0.9±0.9 μg m^{-3}, que puede dividirse a su vez en valores anuales medios de eBC_{ff} (eBC procedente de combustibles fósiles líquidos) y eBC_{bb+cc} (eBC procedente de la quema de biomasa más la combustión de carbón) de 0.6±0.7 y 0.3±0.4 μg m^{-3}, respectivamente. El eBC obtenido a partir del etalómetro AE-31 y el carbono elemental (EC) cuantificado mediante un método de Transmitancia Óptica Térmica presentaron una correlación positiva fuerte y significativa ($r=0.84$; $p<0.01$). Se estableció un modelo de regresión multilineal para desacoplar el eBC_{bb} del eBC_{cc} ($r^2=0.85$) basado en dos trazadores: arsénico para la combustión de carbón y potasio para la quema de biomasa. La aplicación del modelo permitió determinar las contribuciones al eBC_{bb+cc} durante el periodo frío: 74% de la quema de biomasa y 26% de la combustión de carbón. La mayor concentración de eBC_{cc} se estimó para diciembre de 2016 y enero de 2017 (0.18 μg m^{-3}). Este resultado está en consonancia con el Exponente Ångström de Absorción (AAE), que mostró el valor máximo en enero de 2017 (1.43±0.37) debido a las altas contribuciones de la quema de biomasa y la combustión de carbón.

Con el objetivo de caracterizar una de las principales fuentes de carbono negro, el tráfico, en el ***Capítulo 8*** se presenta un trabajo sobre las emisiones de BC procedente del tráfico medidas con un etalómetro en un túnel. Se realizó una campaña de muestreo en el túnel de la Avenida Liberdade (Braga, Portugal) durante una semana (con 56,000 vehículos) para medir la concentración de eBC, mediante un etalómetro AE-31, y de varios contaminantes gaseosos (CO_2, CO y NOx). En el interior del túnel, la concentración másica media de eBC fue de 21±10 μg m^{-3}, con un valor máximo horario de 49.0 μg m^{-3}. Se realizó un estudio horario y semanal, distinguiendo entre días laborables y fines de semana. En cuanto al Exponente Ångström de Absorción (AAE), se obtuvo un valor medio de 0.97±0.10, para una fuente de tráfico prácticamente pura. Hubo una correlación positiva significativa entre la concentración de eBC y el número de vehículos ligeros ($r^2=0.22$; $p<0.01$) y entre la concentración de eBC y las emisiones gaseosas: CO ($r^2=0.45$; $p<0.01$), CO_2 ($r^2=0.50$; $p<0.01$), NO ($r^2=0.40$; $p<0.01$) y NO_2 ($r^2= 0.49$; $p<0.01$). Los factores de emisión medios de carbono negro (EF_{BC}) dentro del túnel fueron

0.31±0.08 g (kg combustible)$^{-1}$ y 0.11±0.08 mg veh^{-1} km^{-1}, similares a los encontrados en otros estudios para vehículos de gasolina y diésel en túneles de tráfico.

Una vez analizada la principal fuente de BC, en el ***Capítulo 9*** se analiza la relación del BC con su principal sumidero, la precipitación acuosa. Para ello se incluye un estudio centrado en el lavado del carbono negro, usando un etalómetro y un disdrómetro, a lo largo de una campaña de muestreo continuo de 15 meses en León (España). Se estudiaron un total de setenta y cinco eventos de lluvia y en el 73% de ellos hubo un barrido efectivo ($eBC_{inicial} > eBC_{final}$), con una disminución media de 48±37% en eventos de lluvia largos (>8 h) y 39±38% en eventos de lluvia cortos. El lavado de BC está fuertemente relacionado con su origen. Por lo tanto, el valor medio del coeficiente de barrido (λ) del BC procedente de la quema de combustibles fósiles (eBC_{ff}) para eventos de lluvia cortos y largos fue de $5.1 \cdot 10^{-5}$ y $1.3 \cdot 10^{-5}$ s^{-1}, respectivamente. Sin embargo, para el BC procedente de la quema de biomasa (eBC_{bb}), los valores de λ fueron $1.6 \cdot 10^{-4}$ y $2.8 \cdot 10^{-5}$ s^{-1} en eventos cortos y largos, respectivamente. Hubo una correlación positiva significativa entre λ y el número de gotas con diámetros entre 0.375 y 2.5 mm. El lavado provocado por la lluvia también se analizó en función del origen de la masa de aire, obteniendo un barrido eficaz en las masas de aire procedentes del Atlántico, Ártico y África. Se construyó un modelo lineal (r^2=0.72) para estimar los valores de ΔeBC con variables del etalómetro, del disdrómetro y de una estación meteorológica: la concentración de eBC antes de la lluvia, el volumen barrido y la precipitación acumulada. La prueba estadística de Kolmogorov-Smirnov confirmó la bondad de ajuste del modelo a los datos medidos.

El lavado provocado por la lluvia sobre otro tipo de material particulado totalmente diferente, un aerosol de tipo biogénico como es el polen, es el argumento central del ***Capítulo 10***. El análisis se basa en un muestreo realizado en León entre 2015 y 2018. Las variables de precipitación y la concentración de 9 tipos de polen se han obtenido con un disdrómetro y un captador volumétrico de tipo *Hirst*, respectivamente. Para evaluar el barrido, hemos calculado 3 parámetros: la eficiencia de barrido promedio ponderada por la concentración (*%ΔC*), el coeficiente de barrido (λ) y el porcentaje de eventos con un lavado efectivo (*%ES*). El 71% de los eventos de lluvia presentaron un lavado efectivo en la concentración total de polen. El valor medio de *%ΔC* para la concentración total de polen fue 24±18% (los valores positivos indican un lavado efectivo) y los tipos de polen con los valores más altos fueron *Castanea* y Cupressaceae (71 y 40%, respectivamente). Se construyó un modelo lineal (r^2=0.94) para estimar la concentración de polen después de la lluvia a partir de variables como la concentración de polen antes de la lluvia y otras variables procedentes de una estación meteorológica y un disdrómetro. Además, hemos mostrado la posibilidad de conocer en tiempo real la concentración probable de polen de Cupressaceae, a partir de la concentración inicial de polen y los parámetros físicos de la lluvia, como el tamaño de la gota, la intensidad de la lluvia o el volumen barrido por las gotas en su caída.

El estudio del efecto de lavado provocado por la lluvia sobre el forzamiento radiativo, fundamental para la modelización climática, se incluye en el ***Capítulo 11.*** Entre febrero de 2016 y marzo de 2017 se calcularon los flujos de forzamiento radiativo utilizando el modelo GAME. Tras la aplicación de un conjunto de criterios de selección, se identificaron 16 eventos de lluvia estratiformes, concentrados en invierno y primavera, y 15 eventos de lluvia convectiva en primavera y verano. Los eventos de lluvia se agruparon según el forzamiento atmosférico (ΔF_{ATM}) antes de la lluvia en *bajo* (inferior a 30 W m^{-2}) o *alto* (superior a 30 W m^{-2}). Hubo diferencias significativas entre los eventos estratiformes y convectivos en cuanto a la duración de la lluvia, el diámetro medio de las gotas de lluvia y los parámetros *a* y *b* de la relación entre la intensidad de la lluvia *R* y la reflectividad del radar $Z = a \cdot R^b$. Al comparar los grupos *bajo* y *alto*, el diámetro de la gota de lluvia fue similar para los eventos estratiformes (0.51±0.08 vs 0.48±0.12 mm) y convectivos (0.96±0.98 vs 0.83±0.63 mm), registrando valores más altos para estos últimos. Este hecho puede estar relacionado con el efecto semidirecto del aerosol. En los eventos estratiformes, el efecto de barrido de las partículas de aerosol se observa claramente en el grupo *alto* con una disminución del forzamiento radiativo de -27.0±25.3%, y en menor medida, en el grupo *bajo*, probablemente causado por la menor carga de aerosol en la atmósfera. En los eventos estratiformes, la moda de la distribución gamma del tamaño de las gotas de lluvia presentó diferencias significativas entre los grupos *bajo* (0.25±0.13 mm) y *alto* (0.35±0.05 mm). Esto apunta a una relación entre el forzamiento radiativo antes de la lluvia y las características específicas de las precipitaciones medidas a nivel del suelo.

ABSTRACT

Air pollution is one of the main concerns affecting the world's population in the 21st century. It is caused by gases [such as carbon monoxide (CO), ozone (O_3) or nitrogen oxides (NOx)] and particulate matter (PM). Particulate matter or atmospheric aerosol is defined as the set of solid and/or liquid airborne particles (except hydrometeors), with sizes between 0.001 and 100 μm. Aerosols can be biogenic (pollen, spores, viruses or bacteria) or non-biogenic (mineral dust, sea salts, black carbon, etc.) and interact with each other causing serious effects on the population, the environment and climate.

Atmospheric aerosols are polydisperse, i.e. they have a wide range of sizes, from nanometres to tens of microns. Particulate matter is classified according to its size into PM_{10}, $PM_{2.5}$ and PM_1, which are particles with an aerodynamic diameter smaller than 10 μm, 2.5 μm and 1 μm, respectively. The size of aerosol particles depends on their sources, sinks and transport through the atmosphere. Also, meteorological processes contribute to the spatial and temporal variability of their composition, concentration and size distribution.

One of the PM pollutants with the greatest effect on climate and health is *Black Carbon* (BC). It is a short-lived pollutant whose main characteristic is that it strongly absorbs visible light. BC is emitted by the incomplete combustion of fossil fuels and biomass. The main sources are diesel engines used for transport and solid fuels used in domestic and industrial installations. It is worth noting that BC is the second largest contributor to global warming after CO_2, with an estimated global mean radiative forcing of 0.4 to 1.2 W m^{-2}.

Given the importance of atmospheric particulate matter, it is vital to study its main sinks: dry and wet deposition. The latter, the focus of this PhD dissertation, is the process by which aerosols are scavenged by hydrometeors in the atmosphere. There are two types of scavenging depending on where the process occurs: within the cloud or ICS (*In-Cloud Scavenging*) or below the cloud

or BCS (*Below-Cloud Scavenging*), through precipitation processes, which can take different forms: rain, storm, hail, snow, etc.

BCS is caused by different scavenging mechanisms (Brownian diffusion, interception, inertial impact, thermophoresis, diffusiophoresis and electrostatic effects) that occur between hydrometeors and aerosol particles. The importance of each mechanism will depend on the atmospheric conditions and the characteristics of the type of precipitation and the aerosols. It should be noted that the aerosol-raindrop interaction process is complex because of the difference in size, which is of several orders of magnitude. The raindrop-aerosol interaction is based on the *collision efficiency*, defined as the fraction of aerosol particles with diameter d_p contained in the collision volume which are collected by falling raindrops of diameter D_r. To estimate the aerosol scavenging efficiency in real atmosphere, the *coefficient λ of aerosol scavenging by precipitation* is used, expressing the temporal change in the aerosol particle concentration. Another useful parameter for assessing the scavenging effect is the *percentage of change in aerosol particle concentration* (*%ΔC*), to determine the change in concentration between two given instants.

This dissertation is divided into **12** chapters: ***Chapter 1*** presents a brief theoretical introduction of both air pollution and precipitation. ***Chapter 2*** lists the general and specific aims of the PhD Thesis and describes of the structure of this dissertation. ***Chapter 3*** includes a detailed description of the material and methods used in the study, specifying the procedures carried out during the sampling campaign and data processing. ***Chapters 4 to 11*** present the results obtained in a format similar to that of scientific articles. Finally, ***Chapter 12*** sets out the main conclusions, applications and future prospects of the research.

Chapter 4 is a study about the scavenging of ultrafine (UFP; < 100 nm) and accumulation particles and its dependence on raindrop sizes in an urban environment. An electrical mobility spectrometer (SMPS) measured aerosol sizes and a laser disdrometer (LPM) was used to analyze the physical variables of raindrops (precipitation intensity, accumulated precipitation, number of raindrops in 22 channels, swept volume and raindrop sizes). An analysis of the scavenging efficiency and the scavenging coefficient (λ) according to rainfall intensities was performed for the different aerosol size ranges. In addition, the impact on human health was determined through the fraction of particles reaching different areas of the respiratory tract (respirable fraction). The main results observed were: i) nucleation (between 14-30 nm), Aitken (between 30-100 nm), accumulation 1 (between 100-300) and accumulation 2 (between 300-1000 nm) modes presented a scavenging efficiency (and coefficient) of 15% ($3.9 \cdot 10^{-5}$), 4% ($3.1 \cdot 10^{-5}$), 22% ($4.8 \cdot 10^{-5}$) and 21% ($5.2 \cdot 10^{-5}$ s^{-1}), respectively; ii) events with rainfall intensities between 1 and 3 mm h^{-1} caused less scavenging in all modes; and iii) raindrop sizes between 1.25 and 3.5 mm scavenged mainly particles of sizes between 70 and 250 nm. Lower scavenging was observed on particle sizes >300

nm, and particle sizes >600 nm were only scavenged by raindrop sizes >4.75 mm; iv) the respirable fraction before and after the rain events presented a significant decrease of -35%.

From precipitation data recorded every minute and atmospheric aerosol particle size, a study of fine and coarse aerosol particle scavenging and its relation to raindrop size is included in ***Chapter 5***. As a result of a 6-month sampling campaign in León, Spain, scavenging coefficients were calculated for 54 rainfall events, with a mean value of $2.6 \cdot 10^{-5} \pm 6.0 \cdot 10^{-5}$ s^{-1} for the fine mode and $5.8 \cdot 10^{-5} \pm 9.6 \cdot 10^{-5}$ s^{-1} for the coarse mode. Also, the particle concentration decreased during rainfall by 10% and after rainfall by 18%. In the *Greenfield range* (sizes between 0.3 and 1 μm), scavenging is less effective than for other aerosol sizes. The number of drops between 0.75 and 3 mm shows significant negative correlations ($p<0.05$) with the number of particles between 0.16 and 1.76 μm, suggesting a possible role of these raindrops in the scavenging of particles of this size. In addition, significant negative correlations were found between the total volume swept by the falling raindrops (mm^3 m^{-3}) and the variation of the number of particles with diameters between 0.12 and 0.19 μm.

In order to identify one of the main sources of ultrafine particles, a study of particles with sizes between 15 and 736 nm is included in ***Chapter 6***. The evolution of their concentrations and new particle formation (NPF) events has also been characterised. Aitken (N_{Ait}) and accumulation (N_{acc}) particle concentrations registered their maximums in the cold months during the peak hours, in the morning (0600-0900 UTC) and in the afternoon (1700-2000 UTC), while the peaks for nucleation (N_{nuc}) particle concentrations were reached in the warm months during the midday hours. N_{Ait}, N_{acc} and N_{total} showed a significant negative correlation with wind speed and a relationship with atmospheric boundary layer (ABL) height by periods. In the warm period, a significant positive correlation between ABL and N_{nuc} was recorded, indicating that higher dispersion with high ABL leads to favourable conditions for the occurrence of NPF events. After visual classification, 96 NPF events were identified and analyzed, occurring mainly between 1100 and 1500 UTC, in spring and summer. In addition, a two-step statistical model was developed to identify NPF events: a cluster analysis followed by a discriminant analysis. The application of the discriminant analysis to one of the clusters, which grouped 93 days, allowed the identification of 55 of the 56 days of NPF events included in the cluster. This method is therefore a valuable tool to identify such events quickly and efficiently.

Chapter 7 presents the study of black carbon (BC) concentration from January 2016 to March 2017, in the surroundings of the city of León, Spain, where coal is commonly used as fuel in domestic heating devices. The mean annual equivalent BC concentration (eBC) was 0.9±0.9 μg m^{-3}, which can be further divided into mean annual values of eBC_{ff} (eBC from liquid fossil fuel) and eBC_{bb+cc} (eBC from biomass burning plus coal combustion) of 0.6±0.7 and 0.3±0.4 μg m^{-3},

respectively. The eBC measured by the AE-31 aethalometer and the elemental carbon (EC) quantified by a Thermal Optical Transmittance method showed a strong and significant positive correlation (r=0.84; p<0.01). A multi-linear regression model was established to decouple eBC_{bb} from eBC_{cc} (r^2=0.85) based on two tracers: arsenic for coal combustion and potassium for biomass burning. The application of the model allowed us to determine the contributions to eBC_{bb+cc} during the cold period: 74% from biomass burning and 26% from coal combustion. The highest eBC_{bb+cc} concentration was estimated for December 2016 and January 2017 (0.18 μg m^{-3}). This result is in line with the Ångström Absorption Exponent (AAE), which showed the maximum value in January 2017 (1.43±0.37) due to high contributions from biomass burning and coal combustion.

In order to characterize one of the main sources of BC, traffic, ***Chapter 8*** presents a study on BC emissions from traffic measured with an aethalometer inside a tunnel. A sampling campaign was carried out in the Avenida Liberdade tunnel (Braga, Portugal) during one week (with 56,000 vehicles) to measure the concentration of eBC, using an AE-31 aethalometer, and of several gaseous pollutants (CO_2, CO and NOx). Inside the tunnel, the mean mass concentration of eBC was 21±10 μg m^{-3}, with a maximum hourly value of 49.0 μg m^{-3}. An hourly and weekly study was carried out, distinguishing between workdays and weekends. As for the Ångström Absorption Exponent (AAE), a mean value of 0.97±0.10 was obtained, for a practically pure traffic source. There was a positive significant correlation between eBC concentration and the number of light vehicles (r^2=0.22; p<0.001) and between eBC concentration and the gaseous emissions: CO (r^2=0.45; p<0.001), CO_2 (r^2=0.50; p<0.001), NO (r^2=0.40; p<0.001) and NO_2 (r^2=0.49; p<0.001). The mean emission factors for black carbon (EF_{BC}) inside the tunnel were 0.31±0.08 g (kg fuel)$^{-1}$ and 0.11±0.08 mg veh^{-1} km^{-1}, similar to those found in other studies for gasoline and diesel vehicles in traffic tunnels.

After analysing the main source of BC, ***Chapter 9*** discusses the relationship of BC with its main sink, liquid precipitation. For this purpose, a study focused on black carbon scavenging is included, using an aethalometer and a disdrometer, throughout a continuous 15-month sampling campaign carried out in León, Spain. A total of 75 rain events were studied and in 73% of them there was an effective scavenging ($eBC_{initial} > eBC_{final}$), with a mean decrease of 48±37% in long rain events (>8 h) and 39±38% in short rain events. The scavenging is strongly related to the BC origin. Therefore, the mean value of the scavenging coefficient (λ) of BC from fossil fuel burning (eBC_{ff}) for short and long rainfall events was $5.1 \cdot 10^{-5}$ and $1.3 \cdot 10^{-5}$ s^{-1}, respectively. However, for BC from biomass burning (eBC_{bb}), the λ values were $1.6 \cdot 10^{-4}$ and $2.8 \cdot 10^{-5}$ s^{-1} in short and long events, respectively. There was a significant positive correlation between λ and the number of drops with diameters between 0.375 and 2.5 mm. Rain scavenging of eBC was analysed depending on the air mass origin, obtaining an effective scavenging for air masses from the Atlantic, Arctic and Africa. A linear model (r^2=0.72) was built to estimate the ΔeBC values with

variables from the aethalometer, the disdrometer and a meteorological station: the eBC concentration before rain, the swept volume and the accumulated precipitation. A Kolmogorov-Smirnov statistical test confirmed the goodness of fit of the model to the measured data.

The scavenging caused by rain on a completely different type of particulate matter, a biogenic type of aerosol such as pollen, is the central topic in ***Chapter 10***. The analysis is based on a sampling campaign carried out in León between 2015 and 2018. Precipitation variables and the concentration of 9 pollen types were obtained by a disdrometer and a *Hirst*-type volumetric sampler, respectively. To evaluate the scavenging, we calculated 3 parameters: scavenging efficiency with the concentration-weighted average ($\%\Delta C$), the scavenging coefficient (λ) and the percentage of events with a decrease in pollen concentration ($\%ES$), also called events with *effective* scavenging. An effective scavenging in total pollen concentration occurred in 71% of rain events. The mean value of $\%\Delta C$ for total pollen concentration was 24±18% (positive values indicate an effective washout) and the pollen types with the highest values were *Castanea* and Cupressaceae (71 and 40%, respectively). A linear model (r^2=0.94) was built to estimate pollen concentration after rainfall from variables such as pollen concentration before rainfall and other variables from a weather station and a disdrometer. In addition, we have shown the possibility of knowing in real time the probable concentration of Cupressaceae pollen, based on the initial pollen concentration and the physical parameters of the rain, such as the drop size, the intensity of the rain or the volume swept by raindrops in their falling path.

The study of the scavenging of rainwater on radiative forcing, crucial for climate modelling, is included in ***Chapter 11***. Between February 2016 and March 2017, radiative forcing fluxes were calculated using the GAME model. After applying a set of selection criteria, 16 stratiform rainfall events were identified, concentrated in winter and spring, and 15 convective rainfall events in spring and summer. Rainfall events were grouped according to the atmospheric forcing (ΔF_{ATM}) before rain: *low* (lower than 30 W m^{-2}) or *high* (higher than 30 W m^{-2}). There were significant differences between stratiform and convective events in terms of rain duration, mean raindrop diameter and parameters *a* and *b* of the relationship between rain intensity R and radar reflectivity $Z = a \cdot R^b$. When comparing the *low* and *high* groups, the raindrop diameters were similar in the stratiform (0.51±0.08 vs 0.48±0.12 mm) and convective (0.96±0.98 vs 0.83±0.63 mm) events, registering higher values for the latter. This fact may be related to the semi-direct effect of aerosols. In the stratiform events, the scavenging effect of aerosol particles is clearly observed in the *high* group with a decrease in radiative forcing of -27.0±25.3%, and to a lesser extent, in the *low* group, probably caused by the lower aerosol loading in the atmosphere. In the stratiform events, the mode of the gamma raindrop size distribution showed significant differences between the *low* (0.25±0.13 mm) and *high* (0.35±0.05 mm) groups. This points towards a relationship

between radiative forcing before rain and the specific characteristics of rainfall measured at ground level.

LISTADO DE ABREVIATURAS

λ (d_p)	Coeficiente de scavenging (S*cavenging coefficient*)
λ_w	Longitud de onda (*Wavelentgh*)
%ES	Porcentaje de eventos con un lavado efectivo (*Percentage of events with effective scavenging*)
%ΔC	Eficiencia de lavado (*Scavenging efficiency*)
Δ*eBC%*	Eficiencia de lavado del carbono negro equivalente (*Scavenging efficiency of equivalent black carbon*)
Δ*F%*	% de variación de los flujos radiativos (*% of variation of radiative fluxes*)
ΔF_{ATM}	Forzamiento radiativo directo del aerosol (*Atmospheric aerosol direct forcing*)
ΔF_{BOA}	Forzamiento radiativo directo en la base de la atmósfera (*Aerosol direct forcing at the bottom of the atmosphere*)
ΔF_{TOA}	Forzamiento radiativo directo en el techo de la atmósfera (*Aerosol direct forcing at the top of the atmosphere*)
AAE	Exponente Ångström de absorción (*Absorption Ångström Exponent*)
ABL	Capa límite atmosférica (*Atmospheric Boundary Layer*)
ACTRIS	*European Research Infrastructure for the observation of Aerosol, Clouds and Trace Gases*
ADRF	Forzamiento radiativo directo del aerosol (*Aerosol Direct Radiative Forcing*)
AE	Aetalómetro modelo AE-31 (*Aethalometer model AE-31*)
AEMET	Agencia Estatal de Meteorología (*Spanish Meteorological Agency*)
AERONET	*AErosol RObotic NETwork*
AIRF	Forzamiento radiativo indirecto del aerosol (*Aerosol Indirect Radiative Forcing*)
AOT	Espesor óptico del aerosol (*Aerosol Optical Thickness*)
ATN	Atenuación (*Attenuation)*
b_{abs} (λ_w)	Coeficiente de absorción a una λ_w (*Absorption coefficient at wavelength* λ_w)
BB(%)	Porcentaje eBC generado por la quema de biomasa (*eBC percentage generated by biomass burning*)

BC	Carbono negro (*Black Carbon*)
BCS	Lavado debajo de la nube (*Below-Cloud Scavenging*)
CAPE	*Convective Available Potential Energy*
CAV	Captador de Alto Volumen (*High Volume Collector*)
CC(%)	Porcentaje eBC generado por la quema de carbón (*eBC percentage generated by coal combustion*)
CI/IC	Cromatografía iónica (*Ionic Chromatography*)
CNN	Núcleos de condensación (*Cloud Condensation Nuclei*)
CPC	Contador de partículas (*Condensation Particle Counter*)
CS	Sumidero de condensación (*Condensation Sink*)
CSI	*Critical Success Index*
CWTs	Tipos de tiempo *(Circulation Weather Types)*
DGT	Dirección General de Tráfico (*Spanish General Direction of Traffic*)
DMA	Analizador diferencial de movilidad (*Differential Mobility Analyser*)
D_{mode}	Diámetro modal de las partículas (*Particle mode diameter*)
DOC	Carbono Orgánico Disuelto *(Dissolved Organic Carbon)*
d_p	Diámetro de partículas de aerosol *(Aerosol particle diameter)*
D_r	Diámetro de gota de lluvia *(Raindrop diameter)*
DSD	Distribución de gotas de agua por tamaños (*Drop Size Distribution*)
$E\ (d_p, D_r)$	Eficiencia de colisión (*Collision efficiency*)
eBC	Carbono negro equivalente (*Equivalent Black Carbon*)
eBC_{bb}	Carbono negro generado por la quema de biomasa (*Black Carbon generated from biomass burning*)
eBC_{cc}	Carbono negro generado por la quema de carbón (*Black Carbon generated from coal combustion*)
eBC_{ff}	Carbono negro generado por la quema de combustibles fósiles (*Black Carbon generated from fossil fuel*)
EC	Carbono Elemental *(Elemental Carbon)*
EF	Factor de emisión (*Emission Factor*)
EPA	Agencia Protección Ambiental de EEUU *(United States Environmental Protection Agency)*
F_{coag}	Flujo de partículas perdidas por coagulación (*Flux of of particles losses due to coagulation*)
F_{growth}	Flujo de partículas fuera del rango de tamaño de la moda de nucleación (*Flux of particles out from the nucleation mode size range*)
g	Parámetro de asimetría (*Asymmetry parameter)*
GAME	*Global Atmospheric ModEL*
GDAS	*Global Data Assimilation System*
GR	Ratio de crecimiento (*Growth rate*)
GTP	Conversión gas-partícula (*Gas To Particle*)

HSS	*Heidke Skill Score*
HYSPLIT	*Hybrid Single Particle Lagrangian Integrated Trajectory*
ICS	Lavado dentro de la nube (*In-Cloud Scavenging*)
IN	Núcleo de congelación *(Ice Nuclei)*
$J_{15\text{-}30}$	Flujo de partículas formadas en la moda de nucleación (*Flux of particles nucleated in the nucleation mode interval*)
LPM	Disdrómetro *Laser Precipitation Monitor*
m	Índice de refracción (*Refractive index*)
MEB	Microscopía Electrónica de Barrido (*Scanning Electron Microscopy*)
N_{acc}	Concentración modal de partículas de acumulación (*Particle concentration in accumulation mode*)
N_{Ait}	Concentración modal de partículas de Aitken (*Particle concentration in Aitken mode*)
NCAR	*National Center for Atmospheric Research*
$Ndrops_x$	Número de gotas por m^2 de un tamaño x (*Number of drops per m^2 in the size channel of x mm*)
N_{nuc}	Concentración modal de partículas de nucleación (*Particle concentration in nucleation mode*)
NOAA	*National Oceanic and Atmospheric Administration*
NOx	Óxidos de nitrógeno (*Nitrogen Oxides*)
NPF	Eventos de formación de partículas (*New Particle Formation*)
N_{total}	Concentración total de partículas (*Total particle concentration*)
OC	Carbono Orgánico (*Organic Carbon*)
OMS/WHO	Organización Mundial de la Salud (*World Health Organization*)
PBA	Aerosoles biológicos primarios (*Primary Biological Aerosols*)
PCASP-X	*Passive Cavity Aerosol Spectrometer Probe*
PIXE	*Particle-Induced X-ray Emission*
PM	Material particulado (*Particulate Matter*)
PM_1	Material particulado con diámetro aerodinámico inferior a 1 µm
PM_{10}	Material particulado con diámetro aerodinámico inferior a 10 µm
$PM_{2.5}$	Material particulado con diámetro aerodinámico inferior a 2.5 µm
PNC	Concentración del número de partículas (*Particle Number Concentration*)
PNSD	Distribución de número de partículas por tamaños (*Particle Number Size Distribution*)
PSD	Distribución de partículas por tamaños (*Particle Size Distribution*)
PTFE	Politetrafluoroetileno (*Polytetrafluoroethylene*)
Q	Ratio de vapor condensable (*Condensable vapor source rate*)
R	Intensidad de la lluvia (*Rainfall intensity*)
RH	Humedad relativa (*Relative Humidity*)
RTM	Modelo de transferencia radiativa (*Radiative Transfer Model*)
$S(D_r)$	Sección de una gota (*Section of the raindrop*)

SMPS	*Scanning Mobility Particle Sizer*
SOx	Óxidos de azufre (*Sulphur Oxides*)
SSA	*Single Scattering Albedo*
S_{total}	Distribución total de superficie de partículas (*Total particle surface distribution*)
$S_V(D_r)$	Volumen barrido (*Swept volume*)
TC	Carbono Total (*Total Carbon*)
TOT	Transmitancia Termo-Óptica (*Thermo-Optical Transmittance*)
TSS	*True Skill Statistic*
UFP	Partículas ultrafinas (*UltraFine Particles*)
$U_t(D_r)$	Velocidad terminal de una gota de tamaño D_r (*Raindrop terminal velocity*)
UTC	Tiempo Universal Coordinado (*Coordinated Universal Time*)
VOCs	Compuestos orgánicos volátiles (*Volatile Organic Compounds*)
V_{total}	Distribución total de volumen de partículas (*Total particle volume distribution*)
WMO/GAW	*World Meteorological Organization/ Global Atmosphere Watch Programme*
WS	Velocidad del viento (*Wind Speed*)
Z	Reflectividad del radar (*Radar reflectivity*)
α	Parámetro alfa de una DSD gamma (*Alpha parameter*)
β	Parámetro beta de una DSD gamma (*Beta parameter*)
μ	Tamaño medio de las gotas de lluvia (*Mean of raindrop sizes*)
ρ_a	Densidad del aire (*Air density*)
ρ_p	Densidad de las partículas de aerosol (*Aerosol particles density*)
σ^2	Varianza (*Variance*)
σ_g	Desviación estándar geométrica (*Geometric standard deviation*)

CAPÍTULO 1. INTRODUCCIÓN

La introducción de la memoria de la tesis doctoral se ha dividido en tres bloques principales, donde en el primero analizaremos las propiedades del aerosol atmosférico, en el segundo las características de la precipitación y por último abordaremos la interacción aerosol-precipitación.

1.1. AEROSOL ATMOSFÉRICO

En los últimos 70 años ha existido un aumento de la contaminación de la atmósfera provocada por el desarrollo industrial y económico, principalmente en las áreas urbanas. La Directiva 2008/50/CE define un contaminante atmosférico como "toda sustancia presente en el aire ambiente que pueda tener efectos nocivos para la salud humana y el medio ambiente en su conjunto". Los graves efectos que producen los contaminantes atmosféricos han provocado un creciente interés científico por su estudio.

La contaminación atmosférica procedente de fuentes naturales o antropogénicas está provocada por gases (p.ej. óxidos de nitrógeno NOx, óxidos de azufre SOx, monóxido de carbono CO o los compuestos orgánicos volátiles VOCs) y material particulado (PM; *Particulate Matter*) o aerosol atmosférico. Se define este aerosol como "el conjunto de partículas líquidas (excepto los hidrometeoros) o sólidas que están suspendidas en el aire, cuyo tamaño se encuentra en un intervalo entre 0.001[1] y 100 μm" (Kulnarni et al., 2011). Los aerosoles incluyen partículas biogénicas (polen, esporas, virus o bacterias) y no biogénicas (polvo mineral, sales marinas,

[1] A lo largo de la tesis se utiliza el punto como separador decimal con el fin de unificar criterios entre la lengua castellana y la inglesa, ya que parte de la tesis está escrita en inglés.

carbono negro…) que interactúan entre sí, pudiendo provocar graves efectos sobre la población y el medio ambiente.

La exposición continuada de la población a altas concentraciones de aerosoles atmosféricos está relacionada con enfermedades cardiovasculares, respiratorias y numerosos tipos de cáncer, especialmente el de pulmón (Dockery et al., 2007; Lelieveld et al., 2015; Tang et al., 2017), que afecta principalmente a los pacientes de enfermedades respiratorias y niños (UNICEF, 2016). Como muestra de ello, en 2019 la Organización Mundial de la Salud (OMS) consideró la contaminación del aire como el principal riesgo ambiental para la salud humana. Según sus datos, unos 4.2 millones de muertes son provocadas cada año por la contaminación del aire y el 80% de la población respira niveles de contaminación superiores a los límites recomendados para la salud humana por las diferentes normativas. Además, se ha estimado que la contaminación del aire ha provocado un aumento del 15% de las muertes causadas por la pandemia COVID-19 en el mundo (Pozzer et al., 2020).

Las partículas de aerosol y los gases provocan graves efectos en el clima global actual y futuro. Los efectos más directos del cambio climático son el aumento del nivel del mar, el deshielo de los polos o una mayor frecuencia de eventos meteorológicos extremos (ICCP, 2014). Su impacto se puede cuantificar mediante el estudio del forzamiento radiativo. El aerosol es la principal fuente de incertidumbre en la cuantificación del forzamiento radiativo, debido al corto tiempo de residencia de los aerosoles en la atmósfera y a su heterogeneidad espacial (Höller et al., 2003).

Por otra parte, el análisis de la contaminación del aire, principalmente en sitios urbanos, es crucial debido a sus efectos en múltiples objetivos de políticas esenciales como la calidad del aire, la actividad económica o las restricciones de tráfico (EEA, 2016; Kinney, 2008; Tong et al., 2017, 2016; Viard and Fu, 2015).

1.1.1. FORMACIÓN Y ORIGEN

El origen de los aerosoles atmosféricos es variado y existen varias clasificaciones en función de su origen: antrópico o natural, primario o secundario (Alonso-Blanco, 2019; Calvo, 2009; Escudero, 2006). Los aerosoles de origen primario son aquellos emitidos directamente a la atmósfera y los secundarios son los que se forman en la atmósfera, por ejemplo por procesos de nucleación de gas a partícula (GTP) (Kulmala et al., 2017; Seinfeld and Pandis, 2016). Este proceso de nucleación tiene lugar en los denominados eventos de nucleación (NPF: *New Particle Formation*) e incluye dos pasos principales: la nucleación de un grupo inicial de partículas

(diámetro <1 nm) y el posterior crecimiento de las mismas (Kulmala et al., 2005). El aerosol atmosférico de origen secundario incrementa su diámetro por procesos de **condensación** (el material en fase gaseosa se condensa en las partículas existentes) o de **coagulación** (dos partículas de aerosol se unen formando una sola). Durante el proceso de nucleación, en la superficie de las partículas existe una expulsión y/o retención de átomos o moléculas, denominándose procesos de **adsorción** y **desorción**, que modifican la masa del material particulado (Colbeck and Lazaridis, 2014). La nucleación (Seinfeld and Pandis, 2016) puede ser:

- *Homogénea*: cuando se forman partículas por condensación de gases sin partículas preexistentes. Los principales vapores condensables en la atmósfera son el H_2SO_4 y el NH_3.
- *Heterogénea* o **condensación**: cuando las moléculas de gas condensan sobre partículas insolubles, siendo el proceso inverso la **evaporación**.

A continuación, se describen brevemente las principales fuentes de aerosol en la atmósfera. Una descripción más detallada puede encontrarse en Calvo (2009) y Hewitt and Jackson (2003):

a) **Fuentes naturales de origen primario**:
   - Polvo mineral: incluye las partículas de la fracción mineral o *crustal* generadas por la acción del viento sobre la superficie terrestre en regiones áridas, y que son transportadas cientos o miles de kilómetros (Choobari et al., 2014). En la Península Ibérica, la principal fuente de polvo mineral es el desierto del Sáhara (F. Oduber et al., 2019b), con unos tamaños de partícula que oscilan entre 0.1 y 2 µm.
   - Aerosol marino: son aquellas procedentes de la ruptura de burbujas en la superficie de océanos y mares, por acción del viento y las olas. El tamaño de las partículas emitidas oscila entre 0.1 y 8 µm y están compuestas principalmente de sales marinas como NaCl o KCl.
   - Origen biogénico: hace referencia a los bioaerosoles o aerosoles biogénicos primarios (PBA; *Primary Biological Aerosols*). Incluye bacterias, virus, emisiones de materia orgánica en descomposición y polen, esporas u hongos. El tamaño de los bioaerosoles es muy variable, desde unos pocos nm (virus o bacterias) hasta más de 100 µm (polen) (Fröhlich-Nowoisky et al., 2016).
   - Incendios forestales de origen natural: son responsables de la emisión de grandes cantidades de material particulado, CO_2, CO, CH_4 y VOCs (Viana et al., 2014). Se estima que un 5% de todos los incendios forestales son de origen natural.
   - Actividad volcánica: a pesar de ser eventos discretos en el tiempo, los volcanes lanzan anualmente entre un 10 y un 20% del total de azufre emitido a la atmósfera. Además,

emiten gran cantidad de material particulado con importantes efectos sobre el forzamiento radiativo (Hirtl et al., 2019).

b) **Fuentes naturales de origen secundario**:

- Rayos y bacterias: emisión de gases precursores de procesos GTP, principalmente la formación de óxidos de nitrógeno (NOx).
- Actividad metabólica del fitoplancton en los océanos: emisión de sulfuro de dimetilo
- Vegetación, océanos y suelo: emisión de terpenos y otros VOCs a partir de los que se forman aerosoles orgánicos secundarios por oxidación (Colbeck, 2008).

c) **Fuentes antrópicas de origen primario**:

- Tráfico: es la principal fuente de contaminantes atmosféricos en las zonas urbanas. Las emisiones se dividen en:
  - Emisiones a través del tubo de escape *(exhaust)*. La combustión relacionada con el tráfico es la fuente principal de partículas ultrafinas (UFP; *UltraFine Particles*) en las áreas urbanas, sobre todo durante las horas punta (Alam et al., 2003; Jones and Harrison, 2006). Estas partículas presentan una distribución de tamaño bimodal, con una moda de nucleación (partículas cuyo diámetro es inferior a 30 nm) formada por procesos GTP cuando la relación de saturación de las mezclas gaseosas de baja volatilidad alcanza un máximo (Arnold et al., 2006; Burtscher, 2005) y una segunda moda formada por partículas carbonosas (50-200 nm), que incluye el carbono negro (Casati et al., 2007; Rose et al., 2006).
  - Emisiones no procedentes del tubo de escape *(non-exhaust)*: proceden de otras fuentes relacionadas con el tráfico como, por ejemplo, el desgaste del pavimento, la abrasión de los frenos o la resuspensión del polvo (Alves et al., 2015b). Presentan una importante contribución de partículas contenidas en la moda gruesa (>1 μm), principalmente procedente del desgaste de los frenos (55%) y del polvo en resuspensión (38%) (Harrison et al., 2012).
- Actividad industrial: los contaminantes emitidos son muy variados en función del tipo de producción y materia prima utilizada. Incluye, entre otros, procesos de minería, quema de combustibles fósiles o fundición de metales (Hewitt and Jackson, 2003). Los tamaños de aerosol emitido también son muy variables según el proceso industrial, pero Vu et al. (2015) señalan que la principal contribución son partículas con tamaños entre 40 y 50 nm.
- Quema de biomasa: incluye los incendios forestales relacionados con la actividad humana, así como la quema de rastrojos y el uso de chimeneas como sistema de

calefacción doméstica. La principal emisión de la quema de biomasa es el material carbonoso, principalmente carbono orgánico (OC) (>80%) junto a la emisión de gases como el CO_2, CH_4, VOCs y CO (Alves et al., 2011). Cabe destacar su importante contribución al BC, debido a la combustión incompleta. Los tamaños de aerosol emitidos dependen del tipo de combustible pero, en general, son superiores a 0.1 µm (Elisabeth Alonso-Blanco et al., 2018; Castro et al., 2018).

- Quema de carbón: el uso de carbón es habitual para la generación de energía eléctrica y para los sistemas de calefacción domésticos, siendo común su uso en la ciudad de León. Es responsable de la emisión de As, Se, SOx, VOCs y NOx (Chen et al., 2013). El material particulado emitido presenta rangos de tamaño entre 50 y 100 nm (Bond et al., 2002). En China, la generación de energía eléctrica mediante quema de carbón es responsable del 23, 45 y 64% de las emisiones totales nacionales de PM_{10}, SOx y NOx (Yuan et al., 2018). En España, en 2017 el 14.2% de la generación eléctrica procedía de la quema de carbón, mientras que en 2019 el porcentaje no llegó al 5%. Esto contribuyó a una disminución en la emisión de CO_2 equivalente procedente de la generación de electricidad de 74.5 millones de toneladas en 2017 a 43.1 millones de toneladas en 2019 (REE, 2020).

d) **Fuentes antrópicas de origen secundario**: la quema de combustibles fósiles provoca la emisión de VOCs, NOx y SOx que actúan, al oxidarse, como precursores gaseosos de partículas secundarias (Querol et al., 2004). Los VOCs y NOx son, además, precursores del ozono troposférico (Atkinson, 2000).

En España, según datos del Ministerio para la Transición Ecológica y el Reto Demográfico (2020) incluidos en el Inventario Nacional de gases de efecto invernadero (1990-2018), se emitieron 334255 kt de CO_2 equivalente. El sector con mayor nivel de emisiones fue el transporte (27.0%), seguido de las actividades industriales (19.9%), la generación de electricidad (17.8%) y la agricultura (11.9%). Se estima que anualmente las actividades industriales son responsables de las emisiones de 492 kt de CO, 74 kt de SOx y 120 kt de NO_2 y el transporte de las emisiones de 172 kt de CO, 0.4 kt de SOx y 237 kt de NO_2.

Cabe destacar la existencia de otras múltiples fuentes de aerosol con un importante peso específico en ciertos puntos del planeta, destacando las emisiones agrícolas y la quema de residuos principalmente en zonas rurales (Zhang et al., 2017).

1.1.2. SUMIDEROS: DEPOSICIÓN SECA Y HÚMEDA

Una vez los contaminantes son emitidos hacia la atmósfera, los principales mecanismos de eliminación de aerosoles en la atmósfera son la deposición seca y la deposición húmeda.

La deposición seca es el proceso de sedimentación de las partículas/gases sobre superficies. Este proceso tiene lugar por acción de la gravedad sobre las partículas gruesas y por acción del movimiento Browniano en las partículas finas (Seinfeld and Pandis, 2016). Se trata de un proceso dependiente de la turbulencia atmosférica, el tamaño y la composición química de las sustancias. Seinfeld and Pandis (2016) describen el proceso en tres etapas: i) transporte aerodinámico de la partícula hasta una capa muy delgada de aire estancada adyacente a la superficie; ii) transporte molecular en los gases o Browniano en las partículas a través de la capa de aire estancada; iii) captación de la partícula/gas por la superficie.

La deposición húmeda es el proceso por el cual los aerosoles son barridos (*scavenging*) por hidrometeoros (gotas de lluvia, neblina, nubes, copos de nieve, granizo) en la atmósfera depositándolos sobre la superficie terrestre. Existen dos tipos de scavenging en función de dónde ocurre el proceso: dentro de la nube o ICS (*In-Cloud Scavenging*) o bien debajo de la nube o BCS (*Below-Cloud Scavenging*). El BCS es menos eficiente que el ICS, aunque existen varias condiciones ambientales para las que este proceso es importante, sobre todo en los casos donde partículas grandes de origen mecánico están presentes cerca de la superficie terrestre (Andronache, 2003). El proceso ICS ocurre por nucleación, o sea, cuando el aerosol actúa como núcleo de condensación (CCN; *Cloud Condensation Nuclei*) o como núcleo de congelación (IN; *Ice Nuclei*), se activa y por difusión del vapor crece (Levin, 2009). En esta tesis se analizará el barrido bajo la nube (BCS) sobre diferentes tamaños de aerosol y se describirá detalladamente en el apartado 1.3.

1.1.3. DISTRIBUCIÓN DE TAMAÑO

Los aerosoles atmosféricos son polidispersos, presentan un amplio rango de tamaños que pueden variar desde nanómetros hasta decenas de micras (Rose et al., 2006). El material particulado se clasifica en PM_{10}, $PM_{2.5}$ y PM_1, que son aquellas partículas que atraviesan un cabezal de tamaño selectivo, para un diámetro aerodinámico de 10 µm, 2.5 µm y 1 µm

respectivamente, con una eficiencia de corte del 50%. El *diámetro aerodinámico* se define como el diámetro de una determinada partícula esférica de densidad 1 g cm^{-3} con la misma velocidad de sedimentación que la partícula a la que se hace referencia, siendo este diámetro menor de 10, 2.5 y 1 µm, para el PM_{10}, $PM_{2.5}$ y PM_1, respectivamente (Calvo, 2009).

El tamaño de las partículas de aerosol depende de sus fuentes, así como de los procesos que sufren durante su existencia (Ito, 1993; Suzuki and Tsunogai, 1988), está relacionado con su composición química y condiciona sus propiedades ópticas. La Figura 1.1 muestra los rangos de tamaño típicos para algunos tipos de aerosoles.

Los aerosoles atmosféricos muestran un amplio rango de tamaños (*polidisperso*). Analizaremos las modas o máximos relativos de la distribución de tamaños de las partículas, que están relacionadas, en su mayoría, con sus mecanismos de formación (Colbeck and Lazaridis, 2014). En una distribución de tamaños de partículas de aerosol pueden observarse las siguientes modas (Figura 1.2):

- **Moda de nucleación** (tamaño de partícula d_p <30 nm): su origen es la nucleación a partir de precursores gaseosos como el H_2SO_4 y el NH_3, o sea, la formación de partículas por la conversión gas-partícula (GTP-*Gas To Particle*) (Kulmala et al., 2017). El proceso de nucleación depende principalmente de la humedad relativa, la temperatura, la insolación y la concentración del gas precursor. La mayor concentración en número de partículas se encuentra entre 5 y 15 nm. Estas partículas tienen una vida media de dos horas, puesto que coagulan rápidamente con otras partículas o incrementan su tamaño por condensación (Salma et al., 2011). Debido a su pequeño tamaño, su contribución a la masa total es mínima.

- **Moda de Aitken** (30 nm <d_p <100 nm): las partículas pueden tener un origen primario o secundario. Las de origen primario presentan su principal fuente en el tráfico rodado. Las de origen secundario se forman por procesos de coagulación a partir de la moda de nucleación, por condensación y/o por reacciones en fase líquida. Junto con la moda de nucleación conforman las denominadas *partículas ultrafinas* (UFP), aquellas cuyo diámetro es inferior a 100 nm (Colbeck and Lazaridis, 2014).

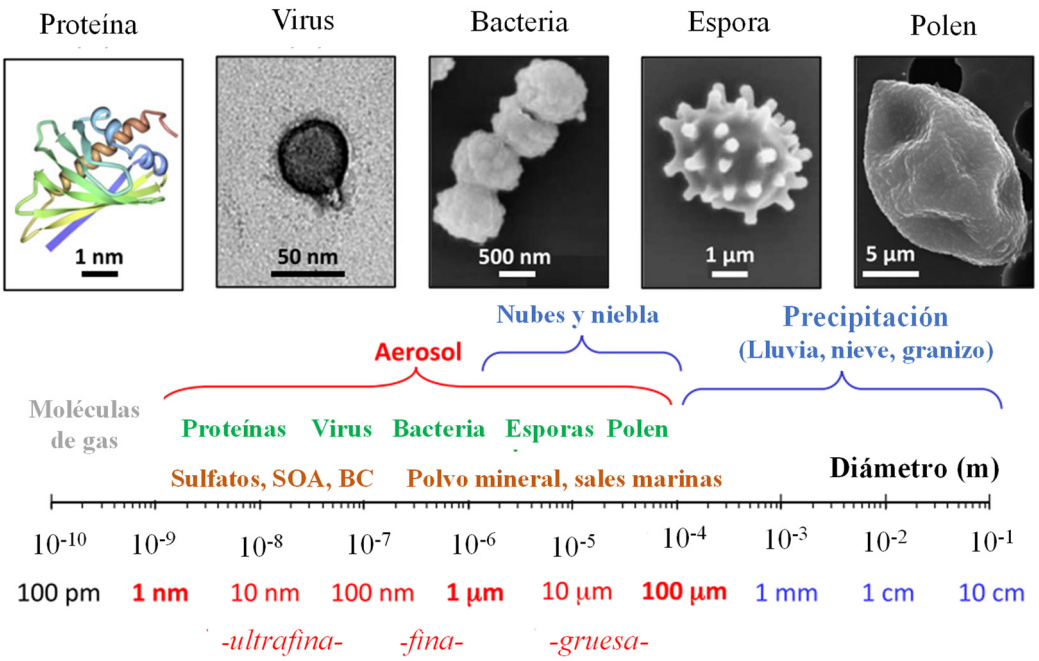

Figura 1.1. Rangos de tamaño de diferentes tipos de aerosol. Imagen adaptada de Fröhlich-Nowoisky et al. (2016).

- **Moda de acumulación** (100 nm< d_p <1000 nm): su origen es primario o secundario. Las partículas primarias tienen un origen, principalmente, desértico o marino y son generadas también por la resuspensión de polvo. Las partículas de origen secundario, se forman a partir de las partículas de la moda Aitken, que crecen en la atmósfera por medio de reacciones hasta formar parte de la moda de acumulación en condiciones de alta humedad relativa (Colbeck and Lazaridis, 2014; Seinfeld and Pandis, 2016). Junto con la moda de nucleación y Aitken, conforman las denominadas *partículas finas*, aquellas cuyo diámetro es inferior a 1000 nm. Cabe destacar que las *partículas finas* incluyen metales, compuestos orgánicos primarios y secundarios, y carbono negro o BC (*Black Carbon*). El BC es uno de los principales contaminantes que se estudian en la presente tesis, por lo que se analizará en profundidad en el apartado 1.1.4.

- **Moda gruesa** (d_p >1000 nm): se caracteriza por presentar un reducido número de partículas, pero con una elevada masa. Aunque las partículas de origen primario dominan en esta moda, también es posible encontrar partículas de origen secundario. El origen de la mayor parte de las partículas primarias se encuentra en procesos mecánicos como la erosión de la superficie terrestre (materia mineral) o de otros materiales y en la explosión de burbujas en la superficie de mares y océanos (aerosoles marinos). Tales procesos mecánicos no pueden normalmente producir partículas de diámetro inferior a 1 µm, excepto parte del aerosol marino, como indican Mårtensson et al. (2003).

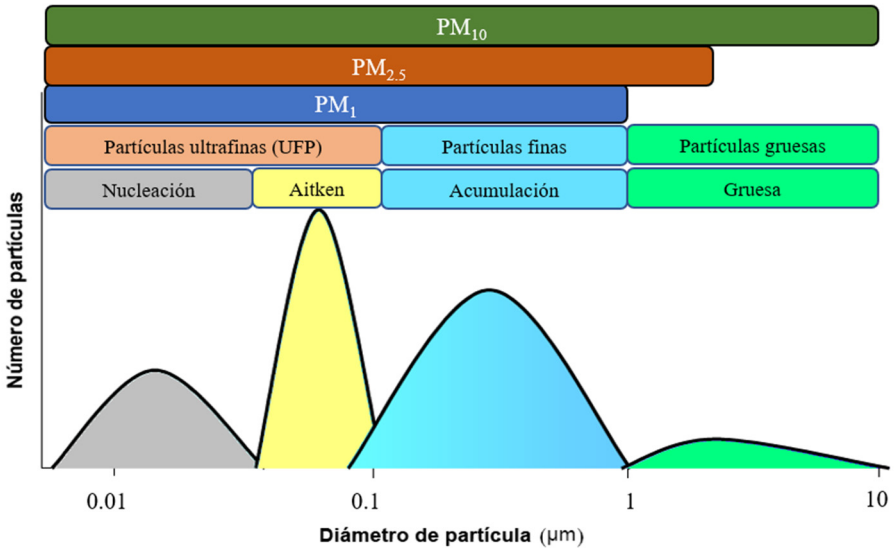

Figura 1.2. Distribución del número de partículas en función del tamaño, identificación de las modas y diferentes clasificaciones por tamaños. Imagen modificada de EPA (2004).

Para analizar cuantitativamente las distribuciones de tamaños de los aerosoles es necesario obtener una descripción matemática de las mismas, ajustando los datos a una función que caracterice la distribución mediante pocos parámetros. Aunque se han utilizado distribuciones como la gamma modificada o la de Weibull (Duhanyan and Roustan, 2011; Seinfeld and Pandis, 2016), la función más empleada es la log-normal, al presentar un buen ajuste para una gran variedad de datos empíricos.

Las distribuciones de tamaños de las partículas se describen mediante funciones log-normales (Kulnarni et al., 2011), siendo generalmente la suma de *m* distribuciones log-normales (Whitby, 2007; Mäkelä et al., 2000; Hussein et al., 2003), definidas por la Eq. 1.1. La distribución multi log-normal para la moda *j* depende de tres parámetros: la concentración numérica o el número total de partículas N_j (cm^{-3}), el diámetro geométrico medio $d_{g,j}$ (nm) y de la desviación geométrica media ($\sigma_{g,j}$).

$$\frac{dN}{d\ logd} = \sum_{j=1}^{m} \frac{N_j}{\sqrt{2\pi}\ \log \sigma_{g,j}} exp\left[-\frac{(\log d_{g,j} - \log d_j)^2}{2(\log \sigma_{g,j})^2}\right] \qquad \textit{Eq. 1.1}$$

Siendo $d_{g,j}$ y $\sigma_{g,j}$ los valores resultantes de la Eq. 1.2 y la Eq. 1.3.

$$d_{g,j} = \exp\left[\frac{\sum_i (N_i log d_i)}{N_j}\right] \qquad \textit{Eq. 1.2}$$

$$\sigma_{g,j} = \exp\left[\frac{\sum_i N_i (log d_{g,j} - log d_i)^2}{N_j - 1}\right]^{0.5} \qquad \textit{Eq. 1.3}$$

donde N_i es el número de partículas del tamaño d_i.

Si la distribución del número de partículas es multi log-normal, suponiendo que las partículas son esféricas, las distribuciones de superficie y volumen también lo son (John, 2001). Estas distribuciones vienen dadas por la Eq. 1.1 sustituyendo el número de partículas N_j, por la superficie S_j y el volumen V_j, respectivamente, y el diámetro geométrico medio de m distribuciones log-normales $d_{g,j}$ por el diámetro de la mediana de la superficie y del volumen, respectivamente.

1.1.4. CARBONO NEGRO

El BC es un contaminante atmosférico de vida corta, emitido por la combustión incompleta de combustibles fósiles y biomasa. Tiene algunas propiedades físicas distintivas como que absorbe fuertemente la luz visible, es refractario e insoluble en agua y en múltiples solventes orgánicos, y existe como un agregado de pequeñas esferas (Figura 1.3) (Bond et al., 2013a).

Las principales fuentes de BC son los: i) motores diésel utilizados para el transporte, ii) combustibles sólidos utilizados en viviendas (madera y carbón), iii) incendios forestales y iv) procesos industriales (Bond et al., 2013a). El periodo de estancia en la atmósfera del BC varía de días a semanas (Begam et al., 2016). Los principales sumideros del BC son la deposición húmeda, mediante la precipitación en forma de lluvia o nieve (Blanco-Alegre et al., 2019), y la deposición seca, que provoca efectos en la superficie terrestre cubierta por nieve en latitudes medias (Bond et al., 2013a). Un resumen de estas fuentes y sumideros del BC se muestra en la Figura 1.4. La concentración de BC depende, por una parte, de las contribuciones de las fuentes y, por otra, de las condiciones atmosféricas. Un factor importante es la altura de la capa límite atmosférica (ABL; *Atmospheric Boundary Layer*), que controla la concentración de BC a nivel de superficie (Joshi et al., 2016).

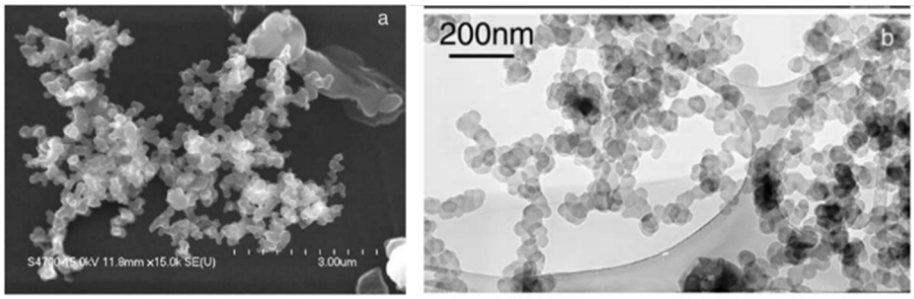

Figura 1.3. Imágenes de agregados de BC obtenidas de Li et al. (2003) en humo del incendio de: a) Madikwe Game Reserve, Sudáfrica, mediante microscopía electrónica de barrido. b) Dambo, Zambia, mediante microscopía electrónica de transmisión.

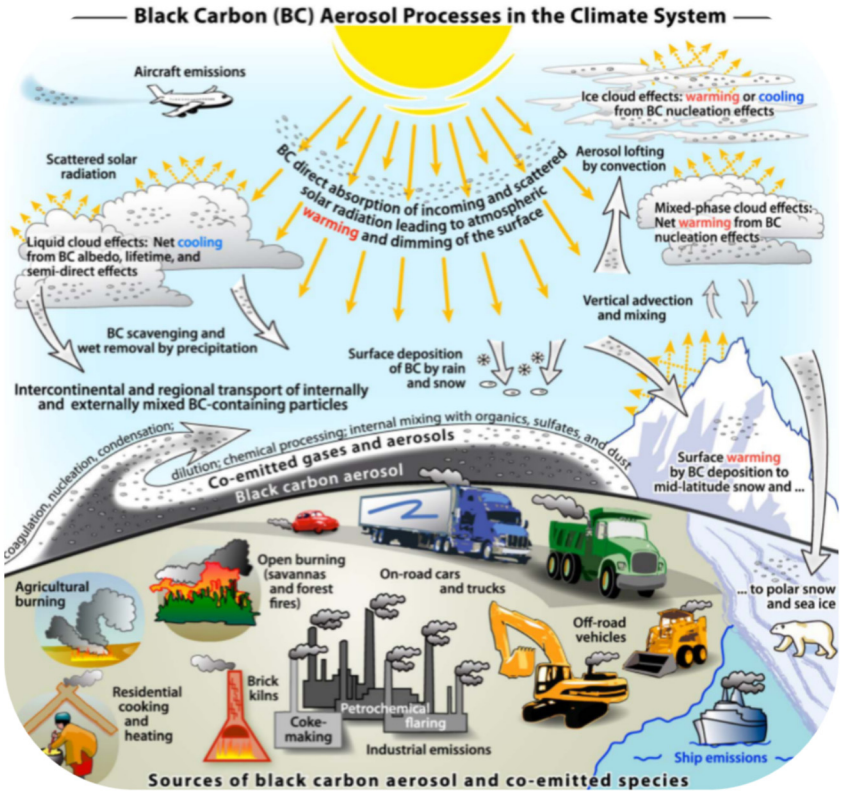

Figura 1.4. Esquema de las principales fuentes y sumideros de carbono negro y de los procesos que controlan su distribución en la atmósfera y que determinan su papel en el sistema climático. Imagen de Bond et al. (2013).

Estudios recientes sobre los riesgos para la salud del BC indican que el conjunto OC-BC puede producir anualmente alrededor de 3 millones de muertes prematuras (Apte et al., 2015; Bond et al., 2013a; Lelieveld et al., 2015; WHO, 2012). Por otra parte, el otro gran impacto del BC es su efecto sobre el clima, en la medida en que el BC absorbe fuertemente la radiación solar. Cabe resaltar que el BC es el segundo contribuyente al calentamiento global, después del CO_2, con un forzamiento radiativo medio global estimado de 0.4 a 1.2 W m^{-2} (ICCP, 2014). Otros efectos de menor calado son la reducción de la visibilidad atmosférica y el retraso en el crecimiento de las plantas (Auffhammer et al., 2006; Chameides et al., 1999). Por todo ello, el estudio del BC es crítico debido a sus múltiples efectos sobre el clima, la salud pública y la calidad del aire (EEA, 2016; Kinney, 2008; Tong et al., 2017, 2016). En esta tesis se incluyen **3** artículos sobre fuentes y sumideros de BC (***Capítulos 7,8 y 9***).

Para la medición del BC, el equipo más utilizado en los últimos años es el etalómetro (Hansen et al., 1984), que mide la atenuación de la luz visible y parte del ultravioleta e infrarrojo cercanos para estimar el denominado *BC equivalente* (eBC) (Andreae and Gelencsér, 2006; Petzold et al., 2013), que es la masa de carbono derivada del coeficiente de absorción de la luz. Mediante modelos (Sandradewi et al., 2008a) se pueden discernir las fuentes del eBC, destacando

principalmente el procedente de la quema de combustibles fósiles (eBC_{ff}) y de la quema de biomasa (eBC_{bb}). El eBC_{ff} suele estar relacionado con el tráfico, pero en ciertas zonas la combustión de carbón puede ser una importante fuente, como en numerosos municipios de la provincia de León (España), que fue una importante zona minera de carbón. La dificultad para discernir la fuente de carbón es que el humo procedente de la quema de carbón absorbe la misma longitud de onda λ_w (a 370 nm) que el humo procedente de la quema de biomasa (Bond et al., 2002; Harrison et al., 2013). Así pues, en regiones donde la combustión de carbón es una práctica común, el modelo de Sandradewi et al. (2008a) necesitaría otro tipo de mediciones, tal y como señala Herich et al. (2011). Existen otros modelos para discernir fuentes de eBC como el propuesto por Fialho et al. (2014), que permite diferenciar las fracciones de eBC_{ff} y eBC_{dust} (carbono negro procedente del polvo desértico) cuando se producen intrusiones de polvo desértico y se puede despreciar la contribución de la quema de biomasa. Una descripción detallada del equipo y el tratamiento de datos se encuentra en el apartado 3.3.1.

1.1.5. NORMATIVA

La normativa europea vigente relativa a la calidad del aire en exteriores se recoge en:

- La Directiva 2008/50/EC del Parlamento Europeo y del Consejo, de 21 de mayo de 2008, *relativa a la calidad del aire ambiente y a una atmósfera más limpia en Europa*. En España ha sido transpuesta mediante el Real Decreto 102/2011, de 28 de enero, relativo a la mejora de la calidad del aire. Este Real Decreto junto con la Ley 34/2007 del 15 de noviembre de 2007, referente a la Protección de la Calidad del Aire y de la Atmósfera, recogen la legislación española vigente.
- La Directiva 2004/107/CE del Parlamento Europeo y del Consejo, de 15 de diciembre de 2004, *relativa al arsénico, el cadmio, el mercurio, el níquel y los hidrocarburos aromáticos policíclicos en el aire ambiente*.
- La Directiva 2015/1480/CE, de la Comisión, de 28 de agosto de 2015 en la que se establecen las normas relativas a los métodos de referencia, la validación de datos y la ubicación de los puntos de muestreo para la evaluación de la calidad del aire ambiente.

La normativa anteriormente mencionada establece los *valores límite* permitidos para diferentes contaminantes atmosféricos (NOx, SO_2, PM_{10}, $PM_{2.5}$, CO y O_3), con el objetivo de proteger la salud humana. Los valores límite recogidos en la Directiva 2008/50/EC y en el Real Decreto 102/2011 se incluyen en la Tabla 1.1.

Tabla 1.1. Valores límite y máximo número de superaciones por año civil para el NO_x, SO_2, PM_{10}, $PM_{2.5}$, CO y O_3, para la protección de la salud humana indicados en la Directiva 2008/50/EC.

Contaminante	Valor medio horario	Valor diario	Valor medio anual
NOx	200 µg m^{-3}. 18 veces/año		40 µg m^{-3}
SO_2	350 µg m^{-3}. 24 veces/año	Media: 125 µg m^{-3}. 3 veces/año	
PM_{10}		Media: 50 µg m^{-3}. 35 veces/año	40 µg m^{-3}
CO		Máximo de las medias móviles de 8 h: 10 mg m^{-3}	
O_3		Máximo de las medias móviles de 8 h: 120 µg m^{-3}. 25 días/año, en promedio de 3 años	

Dado que la tesis se desarrolla en la ciudad de León, se debe tener en cuenta la normativa de la Comunidad Autónoma de Castilla y León. En el acuerdo del 22 de agosto de 2002, de la Junta de Castilla y León, se aprobó la *Estrategia de Control de la Calidad del Aire de Castilla y León 2001-2010* para prevenir y reducir la concentración de contaminantes atmosféricos nocivos, con el objetivo de proteger el medio ambiente y la salud humana. A nivel local, en 2012 en León se aprobó la *Ordenanza Municipal de Protección de la Atmósfera*, con el objetivo de regular todas las actividades e instalaciones que puedan producir humo, polvo, gases, vapores y olores en el ámbito municipal, a fin de evitar la contaminación del aire.

Para cumplir con la evaluación de los contaminantes, según el Anexo VII del RD102/2011, la ciudad de León cuenta actualmente con dos estaciones de control de calidad del aire fijas y las mediciones son realizadas por la Red de Calidad del Aire de la Junta de Castilla y León.

Cabe destacar que la calidad del aire en interiores está regulada a nivel europeo por la Norma UNE 171330. A nivel nacional está regulada por el Código Técnico de la Edificación a través de la Sección 3 del Documento Básico de Salubridad, pero solo para ciertos usos como: la calidad del aire interior en viviendas y trasteros, en almacenes de residuos y en aparcamientos y garajes en edificios de cualquier uso. Para el resto de usos se debe consultar el Reglamento de Instalaciones Térmicas en Edificios.

1.2. PRECIPITACIÓN

La precipitación es el principal mecanismo para transportar el agua desde la atmósfera a la superficie terrestre. Es un proceso físico clave que vincula aspectos del clima, la meteorología y el ciclo hidrológico global. El proceso de precipitación se ve afectado principalmente por la dinámica atmosférica; sin embargo, también está influenciado por los procesos microfísicos de la nube asociados con las propiedades de los aerosoles, que son los principales responsables de formación de gotas de nube y cristales de hielo (Levin, 2009). La precipitación está constituida por un conjunto de hidrometeoros de diferentes tamaños que caen sobre la superficie terrestre, pudiendo ocurrir de diversas formas, como lluvia, granizo o nieve. En esta tesis nos centraremos en la lluvia.

1.2.1. CARACTERÍSTICAS DE LOS HIDROMETEOROS

El tamaño de un hidrometeoro varía en función del momento del proceso de precipitación. En la nube, las gotitas esféricas suelen presentar un diámetro (D_r) en torno a 50 µm (Pujol, 2006) y no son consideradas gotas precipitables hasta alcanzar un radio de 100 µm, proceso que ocurre al superarse el radio y saturación críticos (Molina-Sanchez, 2009). El proceso de precipitación se inicia cuando las corrientes ascendentes no soportan a las gotas en suspensión, que caen por la acción de la gravedad. La velocidad de caída es constante y se denomina *velocidad límite o terminal*, y ocurre cuando se alcanza un equilibrio entre el peso de la gota, la fuerza de empuje y la fuerza de rozamiento causada por el aire.

La forma de las gotas de agua es esférica si su diámetro equivalente (diámetro de una esfera hipotética que tuviera el mismo volumen que la que cae) es inferior a 1 mm. Sin embargo, para tamaños entre 1 y 10 mm, la forma será pseudoelíptica (Beard et al., 2010), tal y como se muestra en la Figura 1.5.

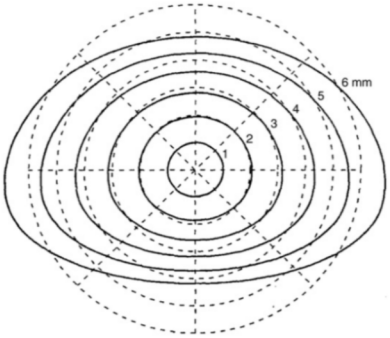

Figura 1.5. Ilustración de la forma de una gota de lluvia en función de su diámetro equivalente (Beard et al., 2010).

1.2.2. DISTRIBUCIÓN DE TAMAÑOS DE GOTA

Para analizar cuantitativamente la distribución de tamaño de las gotas de agua es necesario obtener una representación matemática de las mismas, denominada de forma genérica distribución de gotas de agua por tamaños (DSD; *Drop Size Distribution*), y se utiliza para modelar procesos como el lavado bajo la nube (BCS). Para ello, resulta conveniente ajustar los datos a una función que permita caracterizar la distribución mediante unos pocos parámetros.

La DSD representa el número de gotas por unidad de intervalo dimensional (generalmente el diámetro) por unidad de volumen espacial. Otra opción es definirla como $N(D_r)$, que es la concentración de número de gotas (número de gotas m^{-3} mm^{-1}), donde D_r es el diámetro de cada gota (en mm). Tales distribuciones varían en función del momento y la localización, pero las precipitaciones de lluvia se caracterizan por presentar una rápida disminución del número de gotas al crecer el tamaño de las mismas, sobre todo en diámetros superiores a 1 mm. La DSD también está ligada a la intensidad de precipitación, con mayor concentración de gotas grandes a mayor intensidad de precipitación (Fernández-Raga et al., 2010).

Existen múltiples estudios experimentales en donde se utilizan varias funciones DSD con éxito, siendo de cuatro clases principalmente: exponencial, gamma, log-normal y Weibull. Marshall and Palmer (1948) propusieron una distribución exponencial, generalizada por Sekhon and Srivastava (1971). Más tarde se observó que la distribución exponencial sobreestimaba la cantidad de gotas pequeñas registradas, por lo que Ulbrich (1983) y Willis (1984) introdujeron la distribución gamma. Actualmente, las más difundidas son la distribución exponencial y la gamma. El uso y, por lo tanto, los beneficios de una u otra dependen de las incertidumbres observacionales (Smith, 2003) y de la intensidad de la lluvia (Harikumar et al., 2010). Un detallado análisis de la evolución del ajuste de las DSDs puede encontrarse en Rosenfeld and Ulbrich (2003).

A continuación, se describirá brevemente la distribución gamma, que es la distribución que habitualmente mejor se ajusta y la utilizada en la presente tesis. En general, se utiliza para modelar el comportamiento de variables aleatorias continuas con asimetría positiva. La función de densidad de probabilidad gamma se define en la Eq. 1.4, donde Γ es la función gamma de Euler (Eq. 1.5):

$$f(x) = \frac{\beta^{\alpha} x^{\alpha-1} e^{(-\beta x)}}{\Gamma(\alpha)} \qquad \textit{Eq. 1.4}$$

$$\Gamma(x) = \int_0^{\infty} t^{s-1} e^{(-t)} dt \qquad \textit{Eq. 1.5}$$

La función está definida para valores positivos de x y, como se observa en la Eq. 1.4, depende de dos parámetros, que deben ser reales positivos:

- α (parámetro de forma): se reduce a la función exponencial al tomar un valor de 1.
- β (parámetro de escala): representa la rapidez de caída de la curva a 0.

Para la función gamma, el tamaño medio del diámetro de gota de lluvia es $\mu = \alpha / \beta$. Asimismo, el valor de la varianza es $\sigma^2 = \alpha / \beta^2$. En ocasiones se utiliza un diámetro representativo de los valores centrales de la distribución, siendo los más frecuentes:

- $D_{r,mediana}$: mediana de los diámetros.
- $D_{r,moda}$: moda, o sea, el diámetro de gota más frecuente.
- $D_{r,medio}$: media aritmética de los diámetros definida por la Eq. 1.6.

$$D_{r,medio} = \int_0^{\infty} N(D_r)\, D_r\, dD_r \qquad \textit{Eq. 1.6}$$

donde D_r es el diámetro de la gota y $N(D_r)$ es la cantidad de gotas de tamaño D_r por unidad de volumen.

La intensidad de precipitación (mm h^{-1}) se calcula mediante la Eq. 1.7, donde $v_t(D_r)$ es la velocidad terminal de la gota (m s^{-1})

$$R = \frac{6\pi}{1000} \int_0^{\infty} N(D_r) {D_r}^3 v_t(D_r) dD_r \qquad \textit{Eq. 1.7}$$

En este trabajo se ha supuesto que la velocidad terminal v_t (m s^{-1}) de las gotas es función del tamaño, siguiendo la Eq. 1.8 (Fernández-Raga et al., 2010), basada en estudios de Gunn and Kinzer (1949).

$$v_t = -9.748\, 10^{-4} {D_r}^4 + 0.0573\, {D_r}^3 - 0.8393\, {D_r}^2 + 4.7120\, D_r \qquad \textit{Eq. 1.8}$$

Los dispositivos para la medición de la DSD más utilizados son: i) el radar Doppler de incidencia vertical, que permite estudiar el aire desde el suelo hasta miles de metros y; ii) el disdrómetro mecánico u óptico que solo proporciona información de la precipitación en la superficie terrestre. Estos aparatos permiten medir el tamaño de las gotas de agua y su velocidad. En la presente tesis se ha utilizado un disdrómetro láser para obtener la DSD a nivel de superficie. Una descripción detallada del equipo puede encontrarse en el apartado 3.3.4.

1.3. INTERACCIÓN AEROSOL-PRECIPITACIÓN

La interacción entre el aerosol atmosférico y la precipitación es la base del estudio del lavado o *scavenging* debajo de la nube (BCS). A continuación, se describirán los parámetros para la estimación de la eficiencia de colisión entre el hidrometeoro y el aerosol, los principales mecanismos de barrido de los aerosoles en la atmósfera, y por último se describirán los coeficientes más utilizados para evaluar el efecto lavado que tiene la precipitación sobre los contaminantes atmosféricos.

1.3.1. MECANISMOS DE BARRIDO DEBAJO DE LA NUBE

Como se ha observado en el anterior apartado, el BCS es provocado por diferentes mecanismos. El peso específico de cada mecanismo dependerá de las condiciones de la atmósfera y de las características de la precipitación y de los aerosoles (Chate et al., 2011; Seinfeld and Pandis, 2016). Cabe destacar que el proceso de interacción aerosol-gota de lluvia es muy complejo debido a la diferencia de tamaño (varios ordenes de magnitud) entre ambos. Además, el mayor tamaño de las gotas de lluvia crea patrones de flujo complicados: oscilaciones de las gotas, estelas, remolinos, etc. Una representación del flujo alrededor de una gota cayendo e interceptando partículas y/o gotas más pequeñas se muestra en la Figura 1.6.

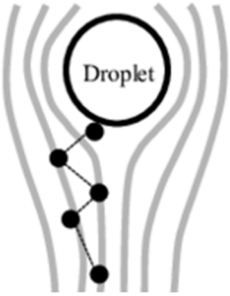

Figura 1.6. Representación del flujo alrededor de una gota de lluvia que cae y partículas de aerosol dentro del flujo. Fuente: Imagen modificada de Ladino (2011).

Los principales mecanismos de BSC son:

- **Difusión browniana**

Los aerosoles en la atmósfera sufren el choque continuo de moléculas de aire debido al "movimiento browniano". Es un proceso de difusión microscópica, provocado por el movimiento aleatorio y sin interacciones mutuas de un gran número de partículas. Así, cuando una fracción de partículas, que se mueven aleatoriamente, entra en contacto con un hidrometeoro, aumenta la eficiencia (Anexo A) de captura de la gota de lluvia debido a la difusión browniana.

- **Interceptación e impacto inercial**

La interceptación se produce cuando una partícula de aerosol, debido a su ligero peso, entra en contacto con la gota de lluvia. Esto ocurre cuando la partícula se sitúa dentro de las líneas del flujo de corriente alrededor de la gota de lluvia.

El barrido por impacto inercial ocurre cuando una partícula no puede seguir las líneas del flujo de corriente de la gota de lluvia y finalmente es capturada por la gota de lluvia. Por lo tanto, el impacto inercial se produce debido a la masa del aerosol, independientemente de su tamaño estructural. Las partículas superiores a 1 µm con densidades mayores a 1 g cm^{-3} tienen una mayor probabilidad (Anexo A) de ser capturadas por las gotas de agua debido a su inercia, mientras que en partículas inferiores a 1 µm el impacto inercial es insignificante.

- **Termoforesis y difusioforesis**

La termoforesis y la difusioforesis se refieren al movimiento de las partículas inducido por los gradientes de temperatura (calentamiento no uniforme de la superficie de la partícula) y por la concentración de las partículas, respectivamente. La termoforesis aumenta la eficiencia de colisión (Anexo A) de las gotas de lluvia con los aerosoles de tamaño inferior a 1 µm. La fuerza de la termoforesis aumenta con el gradiente de temperatura y la curvatura de la superficie de las partículas. Las moléculas de aire chocan por el lado más caliente de la partícula ejerciendo una

fuerza mayor que en el lado más frío. Como resultado, las partículas más pequeñas se mueven lejos de las áreas de mayor temperatura.

- **Efectos electrostáticos**

Debajo de una nube débilmente electrificada (sin tormenta), la fuerza eléctrica favorece el barrido de los aerosoles por las gotas de lluvia, por lo que la influencia eléctrica afecta significativamente a la colisión aerosol-gota (Tinsey et al., 2001). Los aerosoles cargados eléctricamente son atraídos hacia la gota de lluvia debido a la inducción provocada por la carga opuesta. La probabilidad con la que las partículas son barridas por las gotas de agua aumenta bajo un ambiente electrificado (tormenta) debido a la presencia de cargas eléctricas en las gotas y en las partículas que chocan (Pruppacher and Klett, 1998).

En el Anexo A se ha incluido una descripción sobre la eficiencia de colisión, su definición, ecuaciones y representación gráfica.

1.3.2. COEFICIENTES DE LAVADO

Varios estudios han estimado un valor para el coeficiente de lavado de aerosoles. Para ello, han realizado mediciones directas de los cambios en la distribución del tamaño de aerosol durante gran variedad de eventos de lluvia (Davenport and Peters, 1978; Laakso et al., 2003; Maria and Russell, 2005; Zikova and Zdimal, 2016). Cabe recordar que los coeficientes obtenidos en mediciones de campo son preferibles a los obtenidos a partir de experimentos de laboratorio ya que tienen en cuenta las variables atmosféricas.

El *coeficiente de lavado de aerosoles* por la precipitación (λ), dado por Eq. 1.9, expresa el cambio temporal en la concentración de partículas de aerosol $C(d_p)$.

$$\frac{dC(d_p)}{dt} = -\lambda\, C(d_p) \qquad \textit{Eq. 1.9}$$

donde d_p es el diámetro de la partícula de aerosol. Al integrar la Eq. 1.9 de t_0 a t_1, con sus correspondientes concentraciones $C_0(d_p)$ y $C_1(d_p)$, se obtiene:

$$\lambda(d_p) = -\frac{1}{t_1 - t_0} ln \frac{C_1(d_p)}{C_0(d_p)} \qquad \textit{Eq. 1.10}$$

Así, obteniendo mediante medidas experimentales las concentraciones $C_0(d_p)$ y $C_1(d_p)$ en los tiempos t_1 y t_0, es posible calcular λ para un intervalo discreto de diámetros d_p de aerosol o para

el total de partículas de aerosol. Un valor positivo de λ es indicativo de un efecto de lavado efectivo, con un descenso de la concentración de partículas de aerosol.

Otro parámetro para evaluar el efecto de lavado es el *porcentaje de variación de la concentración de partículas* (*%ΔC*), definido en la Eq. 1.11, para determinar el cambio en la concentración entre los momentos t_0 a t_1. Se ha introducido un signo menos previo a los paréntesis para que el lavado efectivo presente valores positivos, al igual que el parámetro λ. Los intervalos de tiempo antes y después de la precipitación para determinar el cambio en la concentración oscilan entre 30 y 60 minutos, tal y como indican Laakso et al. (2003).

$$\%\Delta C = -\left(\frac{C_1(d_p) - C_0(d_p)}{C_0(d_p)}\right) \cdot 100 \qquad \textit{Eq. 1.11}$$

1.4. ESTRUCTURA DE LA MEMORIA

La presente tesis doctoral se estructura de la siguiente forma:

- El ***Capítulo 1*** presenta una introducción sobre conceptos clave sobre la formación, fuentes y sumideros del aerosol atmosférico, el carbono negro y la normativa aplicable sobre la contaminación atmosférica, las características de la precipitación y los mecanismos que influyen en la interacción aerosol-precipitación.
- El ***Capítulo 2*** incluye las hipótesis y los objetivos generales y específicos de esta Memoria, así como la relevancia de la investigación. Además, se muestra, para cada uno de los objetivos, en qué capítulo se desarrolla.
- El ***Capítulo 3*** incluye una descripción de la zona de estudio, el contexto del mismo, la caracterización de los equipos de muestreo (incluyendo aerosol, precipitación y meteorología) y la descripción de los métodos analíticos físicos, químicos o estadísticos utilizados.
- En los ***Capítulos 4 al 11*** se presentan los resultados derivados de esta tesis doctoral.
- Por último, las principales conclusiones obtenidas del estudio se presentan en castellano e inglés en el ***Capítulo 12.***

1.5. REFERENCIAS

Alam, A., Shi, J.P., Harrison, R.M., 2003. Observations of new particle formation in urban air. J. Geophys. Res. Atmos. 108, n/a--n/a. doi:10.1029/2001jd001417

Alonso-Blanco, E., 2019. Caracterización de la distribución de tamaños y propiedades higroscópicas del aerosol atmosférico en España mediante Analizadores de Movilidad Diferencial (DMA). Álcala de Henares.

Alonso-Blanco, E., Castro, A., Calvo, A.I., Pont, V., Mallet, M., Fraile, R., 2018. Wildfire smoke plumes transport under a subsidence inversion: Climate and health implications in a distant urban area. Sci. Total Environ. 619–620, 988–1002. doi:10.1016/j.scitotenv.2017.11.142

Alves, C., Gonçalves, C., Fernandes, A.P., Tarelho, L., Pio, C., 2011. Fireplace and woodstove fine particle emissions from combustion of western Mediterranean wood types. Atmos. Res. 101, 692–700. doi:10.1016/j.atmosres.2011.04.015

Alves, C.A., Gomes, J., Nunes, T., Duarte, M., Calvo, A., Custódio, D., Pio, C., Karanasiou, A., Querol, X., 2015. Size-segregated particulate matter and gaseous emissions from motor vehicles in a road tunnel. Atmos. Res. 153, 134–144. doi:10.1016/j.atmosres.2014.08.002

Andreae, M.O., Gelencsér, A., 2006. Black carbon or brown carbon? the nature of light-absorbing carbonaceous aerosols. Atmos. Chem. Phys. 6, 3131–3148. doi:10.5194/acp-6-3131-2006

Andronache, C., 2003. Estimated variability of below-cloud aerosol removal by rainfall for observed aerosol size distributions. Atmos. Chem. Phys. 3, 131–143. doi:10.5194/acp-3-131-2003

Apte, J.S., Marshall, J.D., Cohen, A.J., Brauer, M., 2015. Addressing Global Mortality from Ambient PM2.5. Environ. Sci. Technol. 49, 8057–8066. doi:10.1021/acs.est.5b01236

Arnold, F., Pirjola, L., Aufmhoff, H., Schuck, T., Lahde, T., Hameri, K., 2006. First gaseous sulfuric acid measurements in automobile exhaust: Implications for volatile nanoparticle formation. Atmos. Environ. 40, 7097–7105. doi:10.1016/j.atmosenv.2006.06.038

Atkinson, R., 2000. Atmospheric chemistry of VOCs and NOx. Atmos. Environ. 34, 2063–2101. doi:10.1016/S1352-2310(99)00460-4

Auffhammer, M., Ramanathan, V., Vincent, J.R., 2006. Integrated model shows that atmospheric brown clouds and greenhouse gases have reduced rice harvests in India. Proc. Natl. Acad. Sci. 103, 19668–19672. doi:10.1073/pnas.0609584104

Barros, V.R., C.B. Field, D.J. Dokken, M.D. Mastrandrea, K.J. Mach, T.E. Bilir, M. Chatterjee, K.L. Ebi, Y.O. Estrada, R.C. Genova, B. Girma, E.S. Kissel, A.N. Levy, S. MacCracken, P.R.M., (eds.), L.L.W., ICCP, 2014. Climate Change 2014 Impacts, Adaptation, and Vulnerability Part B: Regional Aspects, Igarss 2014. doi:10.1007/s13398-014-0173-7.2

Beard, K. V., Bringi, V.N., Thurai, M., 2010. A new understanding of raindrop shape. Atmos. Res. 97, 396–415. doi:10.1016/j.atmosres.2010.02.001

Begam, G.R., Vachaspati, C.V., Ahammed, Y.N., Kumar, K.R., Babu, S.S., Reddy, R.R., 2016. Measurement and analysis of black carbon aerosols over a tropical semi-arid station in Kadapa, India. Atmos. Res. 171, 77–91. doi:10.1016/j.atmosres.2015.12.014

Blanco-Alegre, C., Calvo, A.I., Coz, E., Castro, A., Oduber, F., Prévôt, A.S.H.H., Močnik, G., Fraile, R., 2019. Quantification of source specific black carbon scavenging using an aethalometer and a disdrometer. Environ. Pollut. 246, 336–345. doi:10.1016/j.envpol.2018.11.102

Bond, T.C., Covert, D.S., Kramlich, J.C., Larson, T. V, Charlson, R.J., 2002. Primary particle emissions from residential coal burning: Optical properties and size distributions. J. Geophys. Res. Atmos. 107. doi:10.1029/2001JD000571

Bond, T.C., Doherty, S.J., Fahey, D.W., Forster, P.M., Berntsen, T., Deangelo, B.J., Flanner, M.G., Ghan, S., Kärcher, B., Koch, D., Kinne, S., Kondo, Y., Quinn, P.K., Sarofim, M.C., Schultz, M.G., Schulz, M., Venkataraman, C., Zhang, H., Zhang, S., Bellouin, N., Guttikunda, S.K., Hopke, P.K., Jacobson, M.Z., Kaiser, J.W., Klimont, Z., Lohmann, U., Schwarz, J.P., Shindell, D., Storelvmo, T., Warren, S.G., Zender, C.S., 2013. Bounding the role of black carbon in the climate system: A scientific assessment. J. Geophys. Res. Atmos. 118, 5380–5552. doi:10.1002/jgrd.50171

Burtscher, H., 2005. Physical characterization of particulate emissions from diesel engines: A review. J. Aerosol Sci. 36, 896–932. doi:10.1016/j.jaerosci.2004.12.001

Calvo, A.I., 2009. Caracterización y transporte del aerosol atmosférico: medio urbano, rural y quema de biomasa 137–177.

Casati, R., Scheer, V., Vogt, R., Benter, T., 2007. Measurement of nucleation and soot mode particle emission from a diesel passenger car in real world and laboratory in situ dilution. Atmos. Environ. 41, 2125–2135. doi:10.1016/j.atmosenv.2006.10.078

Castro, A., Calvo, A.I., Blanco-Alegre, C., Oduber, F., Alves, C., Coz, E., Amato, F., Querol, X., Fraile, R., 2018. Impact of the wood combustion in an open fireplace on the air quality of a living room: Estimation of the respirable fraction. Sci. Total Environ. 628–629, 169–176. doi:10.1016/j.scitotenv.2018.02.001

Chameides, W., Yu, H., Liu, S., Bergin, M., Xhou, X., Mearns, L., Wang, G., Kiang, C., Saylor, R.D., Luo, C., Huang, Y., Steiner, A., Giorgi, F., 1999. Study of the effects of atmospheric regional haze on agriculture: enhance crop yields in China through emission controls? Proc. Natl. Acad. Sci. 96, 13626–13633.

Chate, D.M., Murugavel, P., Ali, K., Tiwari, S., Beig, G., 2011. Below-cloud rain scavenging of atmospheric aerosols for aerosol deposition models. Atmos. Res. 99, 528–536. doi:10.1016/j.atmosres.2010.12.010

Chen, J., Liu, G., Kang, Y., Wu, B., Sun, R., Zhou, C., Wu, D., 2013. Atmospheric emissions of F, As, Se, Hg, and Sb from coal-fired power and heat generation in China. Chemosphere 90, 1925–1932. doi:10.1016/j.chemosphere.2012.10.032

Choobari, O.A., Zawar-Reza, P., Sturman, A., 2014. The global distribution of mineral dust and its impacts on the climate system: A review. Atmos. Res. 138, 152–165. doi:10.1016/j.atmosres.2013.11.007

Colbeck, I., 2008. Environmental Chemistry of Aerosols. Blackwell Publishing Ltd., Oxford, UK. doi:10.1002/9781444305388

Colbeck, I., Lazaridis, M., 2014. Aerosol Science: Technology and Applications. John Wiley & Sons Ltd.

Davenport, H.M., Peters, L.K., 1978. Field studies of atmospheric particulate concentration changes during precipitation. Atmos. Environ. 12, 997–1008.

Diario Oficial de la Unión Europea, 2008. Parlamento Europeo y del Consejo, 2008. Directiva 2008/50/CE: relativa a la calidad del aire ambiente y a una atmósfera más limpia en Europa.

Dockery, D.W., Sc, D., Stone, P.H., 2007. Cardiovascular risks from fine particulate air pollution. N. Engl. J. Med. 336, 511–513. doi:10.1056/NEJMe068274

Duhanyan, N., Roustan, Y., 2011. Below-cloud scavenging by rain of atmospheric gases and particulates. Atmos. Environ. 45, 7201–7217. doi:10.1016/j.atmosenv.2011.09.002

EEA, 2016. Air quality in Europe - 2016 Report. Copenhagen, Denmark. doi:10.2800/413142

EPA, 2004. Particulate Matter (PM) Air Quality Standards.

Escudero, M., 2006. Suspended particulate matter and wet deposition fluxes in regional background stations of the Iberian Peninsula : a detailed study of african dust outbreaks.

Fernández-Raga, M., Fraile, R., Keizer, J.J., Varela Teijeiro, M.E., Castro, A., Palencia, C., Calvo, A.I., Koenders, J., Da Costa Marques, R.L., 2010. The kinetic energy of rain measured with an optical disdrometer: An application to splash erosion. Atmos. Res. 96, 225–240. doi:10.1016/j.atmosres.2009.07.013

Fialho, P., Cerqueira, M., Pio, C., Cardoso, J., Nunes, T., Custódio, D., Alves, C., Almeida, S.M., Almeida-Silva, M., Reis, M., Rocha, F., 2014. The application of a multi-wavelength aethalometer to estimate iron dust and black carbon concentrations in the marine boundary layer of Cape Verde. Atmos. Environ. 97, 136–143. doi:10.1016/j.atmosenv.2014.08.008

Fröhlich-Nowoisky, J., Kampf, C.J., Weber, B., Huffman, J.A., Pöhlker, C., Andreae, M.O., Lang-Yona, N., Burrows, S.M., Gunthe, S.S., Elbert, W., Su, H., Hoor, P., Thines, E., Hoffmann, T., Després, V.R., Pöschl, U., 2016. Bioaerosols in the Earth system: Climate, health, and ecosystem interactions. Atmos. Res. 182, 346–376. doi:10.1016/j.atmosres.2016.07.018

Gunn, R., Kinzer, G., 1949. The terminal velocity of fall for water droplets in stagnant air. J. Meteorol. 6, 243–248.

Hansen, A.D.A., Rosen, H., Novakov, T., 1984. The aethalometer - An instrument for the real-time measurement of optical absorption by aerosol particles. Sci. Total Environ. 36, 191–196. doi:10.1016/0048-9697(84)90265-1

Harikumar, R., Sampath, S., Sasi Kumar, V., 2010. Validation of rain drop size distribution with rain rate at a few coastal and high altitude stations in southern peninsular India. Adv. Sp. Res. 45, 576–586.

Harrison, R.M., Beddows, D.C.S., Jones, A.M., Calvo, A., Alves, C., Pio, C., 2013. An evaluation of some issues regarding the use of aethalometers to measure woodsmoke concentrations. Atmos. Environ. 80, 540–548. doi:10.1016/j.atmosenv.2013.08.026

Harrison, R.M., Jones, A.M., Gietl, J., Yin, J., Green, D.C., 2012. Estimation of the Contributions of Brake Dust, Tire Wear, and Resuspension to Nonexhaust Traffic Particles Derived from Atmospheric Measurements. Environ. Sci. Technol. 46, 6523–6529. doi:10.1021/es300894r

Herich, H., Hueglin, C., Buchmann, B., 2011. A 2.5 year's source apportionment study of black carbon from wood burning and fossil fuel combustion at urban and rural sites in Switzerland. Atmos. Meas. Tech. 4, 1409–1420. doi:10.5194/amt-4-1409-2011

Hewitt, C.N., Jackson, A. V., 2003. Handbook of Atmospheric Science. Blackwell Science Ltd, Malden, MA, USA. doi:10.1002/9780470999318

Hirtl, M., Stuefer, M., Arnold, D., Grell, G., Maurer, C., Natali, S., Scherllin-Pirscher, B., Webley, P., 2019. The effects of simulating volcanic aerosol radiative feedbacks with WRF-Chem during the EyjafjallajÖkull eruption, April and May 2010. Atmos. Environ. 198, 194–206. doi:10.1016/j.atmosenv.2018.10.058

Höller, R., Ito, K., Tohno, S., Kasahara, M., 2003. Wavelength-dependent aerosol single-scattering albedo: Measurements and model calculations for a coastal site near the Sea of Japan during ACE-Asia. J. Geophys. Res. D Atmos. 108, 1–15. doi:10.1029/2002jd003250

Hussein, T., Puustinen, A., Aalto, P.P., Mäkelä, J.M., Hämeri, K., Kulmala, M., 2003. Urban aerosol number size distributions. Atmos. Chem. Phys. Discuss. 3, 5139–5184. doi:10.5194/acpd-3-5139-2003

ICCP, 2014. Climate change 2014: Impacts, adaptation, and vulnerability. Part A: Global and sectoral aspects. Contribution of working group II to the fifth assessment report of the intergovernmental panel on climate change.

Ito, T., 1993. Size distribution of Antarctic submicron aerosols. Tellus, Ser. B. doi:10.1034/j.1600-0889.1993.t01-1-00007.x

John, W., 2001. Aerosols Measurements: Principles, Techniques, and Applications, 2nd ed. New York.

Jones, A.M., Harrison, R.M., 2006. Estimation of the emission factors of particle number and mass fractions from traffic at a site where mean vehicle speeds vary over short distances. Atmos. Environ. 40, 7125–7137. doi:10.1016/j.apcatb.2007.04.020

Joshi, H., Naja, M., Singh, K.P., Kumar, R., Bhardwaj, P., Babu, S.S., Satheesh, S.K., Moorthy, K.K., Chandola, H.C., 2016. Investigations of aerosol black carbon from a semi-urban site in the Indo-Gangetic Plain region. Atmos. Environ. 125, 346–359. doi:10.1016/j.atmosenv.2015.04.007

Kinney, P.L., 2008. Climate change, air quality, and human health. Am. J. Prev. Med. 35, 459–467. doi:10.1016/j.amepre.2008.08.025

Kulmala, M., Kerminen, V.M., Petäjä, T., Ding, A.J., Wang, L., 2017. Atmospheric gas-to-particle conversion: Why NPF events are observed in megacities? Faraday Discuss. 200, 271–288. doi:10.1039/c6fd00257a

Kulmala, M., Petäjä, T., Mönkkönen, P., Koponen, I.K., Dal Maso, M., Aalto, P., Lehtinen, K.E.J., Kerminen, V.-M., 2005. On the growth of nucleation mode particles: source rates of condensable vapor in polluted and clean environments. Atmos. Chem. Phys. 5, 409–416. doi:10.5194/acp-5-409-2005

Kulnarni, P., Baron, P.A.., Willeke, K., 2011. Aerosol Measurement. John Wiley & Sons, Inc., Hoboken, NJ, USA. doi:10.1002/9781118001684

Laakso, L., Grönholm, T., Rannik, Ü., Kosmale, M., Fiedler, V., Vehkamäki, H., Kulmala, M., 2003. Ultrafine particle scavenging coefficients calculated from 6 years field measurements. Atmos. Environ. 37, 3605–3613. doi:10.1016/S1352-2310(03)00326-1

Lelieveld, J., Evans, J.S., Fnais, M., Giannadaki, D., Pozzer, A., 2015. The contribution of outdoor air pollution sources to premature mortality on a global scale. Nature 525, 367–371. doi:10.1038/nature15371

Levin, Z., 2009. Aerosol Pollution Impact on Precipitation, Aerosol Pollution Impact on Precipitation. doi:10.1007/978-1-4020-8690-8

Li, J., Pósfai, M., Hobbs, P. V., Buseck, P.R., 2003. Individual aerosol particles from biomass burning in southern Africa: 2. Compositions and aging of inorganic particles. J. Geophys. Res. D Atmos. 108, 1–12. doi:10.1029/2002jd002310

Mäkelä, J.M., Koponen, I.K., Aalto, P., Kulmala, M., 2000. One-year data of submicron size modes of tropospheric background aerosol in Southern Finland. J. Aerosol Sci. 31, 595–611. doi:10.1016/S0021-8502(99)00545-5

Maria, S.F., Russell, L.M., 2005. Organic and inorganic aerosol below-cloud scavenging by suburban New Jersey precipitation. Environ. Sci. Technol. 39, 4793–4800. doi:10.1021/es0491679

Marshall, J.S., Palmer, W.M.K., 1948. The distribution of raindrops with size. J. Meteorol. 165–166.

Ministerio para la Transición Ecológica y el Reto Demográfico, 2020. Informe de Inventario Nacional de Gases de Efecto Invernadero (1990-2018).

Molina-Sanchez, A., 2009. Acondicionamiento e implementación de un laboratorio para el estudio del crecimiento de gotas de lluvia en nubes cálidas. Universidad Carlos III, Madrid (España).

Oduber, F., Calvo, A.I., Blanco-Alegre, C., Castro, A., Nunes, T., Alves, C., Sorribas, M., Fernández-González, D., Vega-Maray, A.M., Valencia-Barrera, R.M., Lucarelli, F., Nava, S., Calzolai, G., Alonso-Blanco, E., Fraile, B., Fialho, P., Coz, E., Prevot, A.S.H.H., Pont, V., Fraile, R., 2019. Unusual winter Saharan dust intrusions at Northwest Spain: Air quality, radiative and health impacts. Sci. Total Environ. 669, 213–228. doi:10.1016/j.scitotenv.2019.02.305

Petzold, A., Ogren, J.A., Fiebig, M., Laj, P., Li, S.M., Baltensperger, U., Holzer-Popp, T., Kinne, S., Pappalardo, G., Sugimoto, N., Wehrli, C., Wiedensohler, A., Zhang, X.Y., 2013. Recommendations for reporting black carbon measurements. Atmos. Chem. Phys. 13, 8365–8379. doi:10.5194/acp-13-8365-2013

Pozzer, A., Dominici, F., Haines, A., Witt, C., Münzel, T., Lelieveld, J., 2020. Regional and global contributions of air pollution to risk of death from COVID-19. Cardiovasc. Res. 116, 2247–2253. doi:10.1093/cvr/cvaa288

Pruppacher, H. R. & Klett, J.D., 1998. Microphysics of Clouds and Precipitation, Second Revised and Enlarged Edition with an Introduction to Cloud Chemistry and Cloud Electricity. Clim. Change 38, 1664–1669. doi:10.1023/A:1005304329379

Pujol, O., 2006. Étude mocrophyique des nuages et des précipitations par radar polarimétrique et simulation numérique. Influence du milieu de propagation sur la mesure de la réflectivité. Université Toulouse III - Paul Sabatier (France).

Querol, X., Alastuey, A., Ruiz, C.R., Artiñano, B., Hansson, H.C., Harrison, R.M., Buringh, E., ten Brink, H.M., Lutz, M., Bruckmann, P., Straehl, P., Schneider, J., 2004. Speciation and origin of PM10 and PM2.5 in selected European cities. Atmos. Environ. 38, 6547–6555. doi:10.1016/j.atmosenv.2004.08.037

REE, 2020. Red Eléctrica Española [WWW Document]. URL 2020 (accessed 1.19.21).

Rose, D., Wehner, B., Ketzel, M., Engler, C., Voigtländer, J., Tuch, T., Wiedensohler, A., 2006. Atmospheric number size distributions of soot particles and estimation of emission factors. Atmos. Chem. Phys. 6, 1021–1031. doi:10.5194/acp-6-1021-2006

Rosenfeld, D., Ulbrich, C.W., 2003. Cloud Microphysical Properties, Processes, and Rainfall Estimation Opportunities. Meteorol. Monogr. 30, 237–237. doi:10.1175/0065-9401(2003)030<0237:CMPPAR>2.0.CO;2

Salma, I., Borsòs, T., Weidinger, T., Aalto, P., Hussein, T., Dal Maso, M., Kulmala, M., 2011. Production, growth and properties of ultrafine atmospheric aerosol particles in an urban environment. Atmos. Chem. Phys. 11, 1339–1353. doi:10.5194/acp-11-1339-2011

Sandradewi, J., Prévôt, A.S.H., Szidat, S., Perron, N., Alfarra, M.R., Lanz, V.A., Weingartner, E., Baltensperger, U.R.S., 2008. Using aerosol light absorption measurements for the quantitative determination of wood burning and traffic emission contribution to particulate matter. Environ. Sci. Technol. 42, 3316–3323. doi:10.1021/es702253m

Seinfeld, J.H., Pandis, S., 2006. Atmospheric from air pollution to climate change, Atmospheric Chemistry and Physics. Wiley. doi:10.1016/0016-7037(87)90252-3

Seinfeld, J.H., Pandis, S.N., 2016. Atmospheric Chemistry and Physics: From Air Pollution to Climate Change, Atmospheric Chemistry and Physics. Wiley. doi:10.1016/0016-7037(87)90252-3

Sekhon, R.S., Srivastava, R.C., 1971. Doppler Radar Observations of Drop-Size Distributions in a Thunderstorm. J. Atmos. Sci. 28, 983–994. doi:10.1175/1520-0469(1971)028<0983:DROODS>2.0.CO;2

Smith, P.L., 2003. Raindrop Size Distributions: Exponential or Gamma—Does the Difference Matter? J. Appl. Meteorol. 42, 1031–1034. doi:10.1175/1520-0450(2003)042<1031:RSDEOG>2.0.CO;2

Suzuki, T., Tsunogai, S., 1988. Daily variation of aerosols of marine and continental origin in the surface air over a small island, Okushiri, in the Japan Sea. Tellus 40B, 42–49.

Tang, G., Zhao, P., Wang, Yinghong, Gao, W., Cheng, M., Xin, J., Li, X., Wang, Yuesi, 2017. Mortality and air pollution in Beijing: The long-term relationship. Atmos. Environ. 150, 238–243. doi:10.1016/j.atmosenv.2016.11.045

Tinsey, B.A., Rohrbaugh, R.P., Hei, M., 2001. Electroscavenging in clouds with broad droplet size distributions and weak electrification. Atmos. Res. 59–60, 115–135.

Tong, Z., Chen, Y., Malkawi, A., Adamkiewicz, G., Spengler, J.D., 2016. Quantifying the impact of traffic-related air pollution on the indoor air quality of a naturally ventilated building. Environ. Int. 89–90, 138–146. doi:10.1016/j.envint.2016.01.016

Tong, Z., Yang, B., Hopke, P.K., Zhang, K.M., 2017. Microenvironmental air quality impact of a commercial-scale biomass heating system. Environ. Pollut. 220, 1112–1120. doi:10.1016/j.envpol.2016.11.025

Ulbrich, C.W., 1983. Natural Variations in the Analytical Form of the Raindrop Size Distribution. J. Clim. Appl. Meteorol. 22, 1764–1775. doi:10.1175/1520-0450(1983)022<1764:NVITAF>2.0.CO;2

UNICEF, 2016. Clear the air for children. The impact of air pollution on children.

Viana, M., Pey, J., Querol, X., Alastuey, A., de Leeuw, F., Lükewille, A., 2014. Natural sources of atmospheric aerosols influencing air quality across Europe. Sci. Total Environ. 472, 825–833. doi:10.1016/j.scitotenv.2013.11.140

Viard, V.B., Fu, S., 2015. The effect of Beijing's driving restrictions on pollution and economic activity. J. Public Econ. 125, 98–115. doi:10.1016/j.jpubeco.2015.02.003

Vu, T. V., Delgado-Saborit, J.M., Harrison, R.M., 2015. Review: Particle number size distributions from seven major sources and implications for source apportionment studies. Atmos. Environ. 122, 114–132. doi:10.1016/j.atmosenv.2015.09.027

Whitby, K.T., 2007. The physical characteristics of sulfur aerosols. Atmos. Environ. 41, 25–49. doi:10.1016/j.atmosenv.2007.10.057

WHO, 2012. Health effects of Black carbon. Copenhagen, Denmark.

Willis, P.T., 1984. Functional fits to some observed drop size distributions and parameterization of rain. J. Atmos. Sci. doi:10.1175/1520-0469(1984)041<1648:FFTSOD>2.0.CO;2

Yuan, J., Na, C., Lei, Q., Xiong, M., Guo, J., Hu, Z., 2018. Coal use for power generation in China. Resour. Conserv. Recycl. 129, 443–453. doi:10.1016/j.resconrec.2016.03.021

Zhang, H., Hu, J., Qi, Y., Li, C., Chen, J., Wang, X., He, J., Wang, Shuxiao, Hao, J., Zhang, Linlin, Zhang, Lijia, Zhang, Y., Li, R., Wang, Shulan, Chai, F., 2017. Emission characterization, environmental impact, and control measure of PM2.5 emitted from agricultural crop residue burning in China. J. Clean. Prod. 149, 629–635. doi:10.1016/j.jclepro.2017.02.092

Zikova, N., Zdimal, V., 2016. Precipitation scavenging of aerosol particles at a rural site in the Czech Republic. Tellus B 68, 1–14. doi:10.3402/tellusb.v68.27343

CAPÍTULO 2. HIPÓTESIS Y OBJETIVOS

Debido a los importantes impactos del aerosol atmosférico y al papel esencial de la lluvia como mecanismo de eliminación de estas partículas, resulta de especial relevancia la cuantificación del efecto de lavado del aerosol por parte de la precipitación (deposición húmeda). La hipótesis de partida fue la posibilidad de parametrizar este efecto de lavado en función de ciertas variables físicas, tanto de las gotas de lluvia como del aerosol atmosférico.

Por lo tanto, el *objetivo general* de la presente tesis es evaluar, en condiciones de campo, el efecto de la precipitación sobre la concentración del aerosol atmosférico en función del tamaño de las gotas y de las partículas.

Partiendo de este objetivo general, se han definido los siguientes *objetivos específicos*:

1. Estudiar las características físicas del aerosol y cuantificar el efecto de lavado que tiene la precipitación sobre el aerosol atmosférico en función del espectro de tamaños de las gotas de lluvia.

2. Discernir entre la contribución de carbono negro por procesos de quema de combustibles fósiles y de biomasa, y evaluar el efecto de la precipitación sobre la concentración de carbono negro emitido por diferentes fuentes.

3. Estudiar el impacto de la precipitación en dos variables con consecuencias importantes para la vida humana: la concentración de bioaerosoles y el forzamiento radiativo.

El ***Objetivo 1***, relacionado con el efecto de lavado y el tamaño de la gota de lluvia, se desarrolla en los ***Capítulos 4, 5 y 6***. El ***Objetivo 2***, relativo al carbono negro, se aborda en los ***Capítulos 7, 8 y 9.*** El ***Objetivo 3***, relacionado con las consecuencias de la precipitación en el material polínico y en el forzamiento radiativo se trata en los ***Capítulos 10 y 11.***

Los resultados de la presente tesis doctoral se exponen en ocho capítulos (4 al 11). Cinco de ellos están publicados en formato de artículo científico y los otros tres se encuentran enviados y/o aceptados en revistas indexadas en el *Journal Citation Reports (**JCR**)*.

A continuación, se describe brevemente cada publicación incluida, las cuales serán expuestas en sucesivos apartados, señalando la implicación de la misma en cada objetivo de forma más específica y señalando la contribución de los autores a la publicación.

ARTÍCULO I (Capítulo 4)

Environmental Pollution 285 (2021) 117371

Contents lists available at ScienceDirect

Environmental Pollution

journal homepage: www.elsevier.com/locate/envpol

Scavenging of submicron aerosol particles in a suburban atmosphere: The raindrop size factor☆

C. Blanco-Alegre [a], A.I. Calvo [a,*], A. Castro [a], F. Oduber [a], E. Alonso-Blanco [b], R. Fraile [a]

[a] Department of Physics, IMARENAB University of León, 24071, León, Spain
[b] Centre for Energy, Environment and Technology Research (CIEMAT), Environment Department, Madrid, Spain

ARTICLE INFO

Keywords:
Aerosol size distributions
Disdrometer
Rain scavenging
SMPS
Ultrafine particles

ABSTRACT

This paper studies the below-cloud scavenging caused by precipitation on ultrafine and accumulation modes, as well as the role of the different raindrop sizes in an urban environment. The equipment used to measure aerosol particles and raindrop variables includes a scanning mobility particle sizer spectrometer-SMPS and a Laser Precipitation Monitor (LPM), respectively. An analysis of the scavenging efficiency and the scavenging coefficient (λ) by modes and rain intensities was carried out. The main results observed have been: i) the nucleation (between 14 and 30 nm), Aitken (between 30 and 100 nm), accumulation 1 (between 100 and 300) and accumulation 2 (between 300 and 1000 nm) modes presented a scavenging efficiency of 15, 4, 22 and 21%, respectively; ii) events with rain intensities between 1 and 3 mm h^{-1} caused less scavenging in all modes; iii) raindrop sizes between 1.25 and 3.5 mm scavenged mainly particle sizes between 70 and 250 nm. Lower scavenging was observed on particle sizes >300 nm, and particle sizes >600 nm were only scavenged by raindrop sizes >4.75 mm; iv) the respirable fraction before and after the rain events presented a statically significant decrease of −35%. The combination in this study of SMPS and disdrometer measurements has resulted in a more detailed characterization of the influence of this process on the submicrometer aerosol fraction, noting that below-cloud scavenging is one of the main removal pathways for submicrometer aerosol particles. This study thus contributes to improving the current state of knowledge of *below-cloud scavenging*.

Factor de impacto JCR: 8.071 (D1) **Factor SJR (***Scimago Journal Rank***)**: 2.136 (D1)

DOI: 10.1016/j.envpol.2021.117371

Objetivo tratado: 1.

Contribución del doctorando:

- Participación en la campaña de muestreo, de 13 meses, con verificaciones periódicas de los equipos de medida y toma de datos diaria.
- Descarga, organización y tratamiento de datos del TSI- SMPS y del disdrómetro LPM.
- Selección de eventos de precipitación y análisis estadístico de los datos.
- Ajuste de distribuciones de tamaño del aerosol antes, durante y después de la lluvia.
- Determinación de las fracciones respirable e inhalable.
- Cálculo de las variables físicas de la precipitación para cada día de lluvia.
- Determinación de la procedencia de las masas de aire mediante el modelo HYSPLIT y clasificación en diferentes sectores.
- Determinación del coeficiente de scavenging y eficiencia.
- Redacción del borrador original del artículo y sucesivas versiones.

ARTÍCULO II (Capítulo 5)

RESEARCH ARTICLE

Quarterly Journal of the Royal Meteorological Society RMetS

Below-cloud scavenging of fine and coarse aerosol particles by rain: The role of raindrop size

Carlos Blanco-Alegre[1] | Amaya Castro[1] | Ana I. Calvo[1] | Fernanda Oduber[1] | Elisabeth Alonso-Blanco[2] | Delia Fernández-González[3,4] | Rosa M. Valencia-Barrera[3] | Ana M. Vega-Maray[3] | Roberto Fraile[1]

[1]Department of Physics (IMARENAB), University of León, León, Spain
[2]Department of Environment, Centre for Energy, Environment and Technology Research (CIEMAT), Madrid, Spain
[3]Department of Biodiversity and Environmental Management, University of León, León, Spain
[4]Institute of Atmospheric Sciences and Climate, National Research Council, Bologna, Italy

Correspondence
Roberto Fraile, Department of Physics (IMARENAB), University of Leon, 24071 Leon, Spain.
Email: rfral@unileon.es

Funding information
Ministerio de Economía y Competitividad, BES-2015-074473; CGL2014-52556-R; TEC2014-57821-R. Ministerio de Educación, Cultura y Deporte, FPU16/05764. Universidad de León, Programa Propio 2015/00054/001.

Below-cloud aerosol scavenging is an important process to remove particles from the atmosphere. In this study, both precipitation (measured with a laser disdrometer registering drops between 0.125 and 8 mm) and atmospheric aerosol particles (measured with a Passive Cavity Aerosol Spectrometer Probe registering aerosol sizes between 0.1 and 24 μm) have been sampled on a 1 min basis. Based on 6 months of outdoor measurements in León (northwest Iberian Peninsula), the scavenging coefficients were calculated for the aerosol particles measured, with a mean value of $2.6\times10^{-5}\pm6.0\times10^{-5}$ s^{-1} for the fine mode and $5.8\times10^{-5}\pm9.6\times10^{-5}$ s^{-1} for the coarse mode in 54 rain events. Likewise, the particle concentration decreased during rain by 10%, and by 18% between the time before and after the rain. In the Greenfield Gap (sizes between 0.3 and 1 μm) the scavenging is less effective, mainly between 0.6 and 1 μm, than with smaller particles. The number of drops between 0.75 and 3 mm shows statistically significant ($p<0.05$) negative correlations with the number of particles between 0.16 and 1.76 μm, thus illustrating the potential of those raindrops to favour the scavenging of particles of that size. In addition, there were statistically significant negative correlations between the total volume removed by falling drops (mm^3/m^3) and the variation of the number of particles in channels with diameters between 0.12 and 0.19 μm.

KEYWORDS
aerosols, below-cloud scavenging, disdrometer, Greenfield Gap, hydrometeors, size distributions

Factor de impacto JCR: 3.198 (Q2) **Factor SJR**: 2.607 (D1)

DOI: 10.1002/qj.3399

Objetivo tratado: 1.

Contribución del doctorando:

- Participación en la campaña de muestreo, de 13 meses, con verificaciones periódicas de los equipos de medida y toma de datos diaria.
- Descarga, organización y tratamiento de datos de la PCASP, del disdrómetro LPM y estación meteorológica Davis.
- Selección de eventos de precipitación y análisis estadístico de los datos.
- Ajuste de distribuciones de tamaño del aerosol antes, durante y después de la lluvia.
- Cálculo de las variables físicas de la precipitación para cada día de lluvia.
- Determinación del coeficiente de scavenging y eficiencia.
- Redacción del borrador original del artículo y sucesivas versiones.

ARTÍCULO III (Capítulo 6)

Título*:* **Evolution of size-segregated aerosol concentration in NW Spain: a two-step classification to identify new particle formation events**

Autores: Blanco-Alegre, C., A.I. Calvo, E. Blanco-Alonso, A. Castro, F. Oduber, R. Fraile

Enviado para publicación

Objetivo tratado: 1

Contribución del doctorando:

- Participación en la campaña de muestreo, de 13 meses, con verificaciones periódicas de los equipos de medida y toma de datos diaria.
- Descarga, organización y tratamiento de datos del TSI- SMPS.
- Descarga y tratamiento de los datos de las estaciones de calidad del aire.
- Selección de eventos de formación de nuevas partículas.
- Ajuste de distribuciones de tamaño del aerosol.
- Análisis estadístico de los datos.
- Cálculo de los parámetros asociados a los eventos de nucleación.
- Redacción del borrador original del artículo y sucesivas versiones.

Investigación: En este trabajo se estudió la evolución de las partículas de tamaños entre 15 y 736 nm en la ciudad de León, con el fin de identificar los eventos de nucleación de nuevas partículas. Para ello, se muestrearon las partículas de aerosol atmosférico medidas con un espectrómetro de movilidad de eléctrica (SMPS). Mediante un método visual se identificaron y caracterizaron dichos eventos. Además, se estudió la relación de las concentraciones de aerosoles con la altura de la capa límite atmosférica. Por último, se creó un modelo de dos etapas (un análisis cluster seguido de un análisis discriminante) con el fin de identificar los eventos de nucleación.

ARTÍCULO IV (Capítulo 7)

Título*:* **Searching the contribution of coal combustion to black carbon: coupling tracers with the aethalometer model**

Autores: C. Blanco-Alegre, P. Fialho, A.I. Calvo, A. Castro, E. Coz, F. Oduber, A.S.H. Prévôt, G. Močnik, C. Alves, F. Giardi, G. Pazzi, R. Fraile

Enviado para publicación

Objetivo tratado: 2

Contribución del doctorando:

- Participación en la campaña de muestreo, de 13 meses, con verificaciones periódicas de los equipos de medida y toma de datos diaria.
- Descarga, organización y tratamiento de datos del etalómetro AE-31.
- Selección de días con quema de carbón y biomasa.
- Análisis estadístico de los datos.
- Participación en la toma de muestras mediante la recogida diaria de filtros y en los análisis químicos de los filtros.
- Realización de polar plots para la determinación del origen del carbono negro.
- Redacción del borrador original del artículo y sucesivas versiones.

Investigación: En este estudio se presenta el análisis de la concentración de carbono negro (BC) desde enero de 2016 hasta marzo de 2017, en los alrededores de la ciudad de León donde el carbón se utiliza habitualmente como combustible. La concentración anual media de BC fue de 0.9±0.9 μg m^{-3}. El BC obtenido a partir del etalómetro AE-31 y el carbono elemental cuantificado mediante un método de Transmitancia Óptica Térmica presentaron una correlación positiva significativa. Además, se estableció un modelo de regresión multilineal para desacoplar el BC procedente de la quema de biomasa y de carbón, usando dos trazadores: arsénico para la combustión de carbón y potasio para la quema de biomasa. La aplicación del modelo permitió determinar las contribuciones durante el periodo frío: 74% de la quema de biomasa y 26% de la combustión de carbón.

ARTÍCULO V (Capítulo 8)

Science of the Total Environment 703 (2020) 135483

Contents lists available at ScienceDirect

Science of the Total Environment

journal homepage: www.elsevier.com/locate/scitotenv

Aethalometer measurements in a road tunnel: A step forward in the characterization of black carbon emissions from traffic

C. Blanco-Alegre [a], A.I. Calvo [a], C. Alves [b], P. Fialho [c], T. Nunes [b], J. Gomes [b], A. Castro [a], F. Oduber [a], E. Coz [d], R. Fraile [a,*]

[a] Department of Physics, IMARENAB University of León, 24071 León, Spain
[b] Centre for Environment and Marine Studies, Department of Physics, University of Aveiro, 3810-193 Aveiro, Portugal
[c] Research Institute of Volcanology and Evaluation – IVAR, Rua da Mãe de Deus, 9500-321 Ponta Delgada, Portugal
[d] Centre for Energy, Environment and Technology Research (CIEMAT), Department of the Environment, Madrid, Spain

HIGHLIGHTS

- Black carbon and gaseous pollutants were measured in a tunnel during a week.
- The mean eBC concentration (21 μg m^{-3}) was close to the daily $PM_{2.5}$ limit set by WHO.
- A mean $AAE_{470-950}$ of 0.97 ± 0.10 was obtained for a source of almost pure traffic.
- A positive correlation between eBC, traffic flow and gaseous pollutants was found.
- The mean eBC emission factor inside the tunnel was 0.11 ± 0.08 mg $vehicle^{-1}$ km^{-1}.

GRAPHICAL ABSTRACT

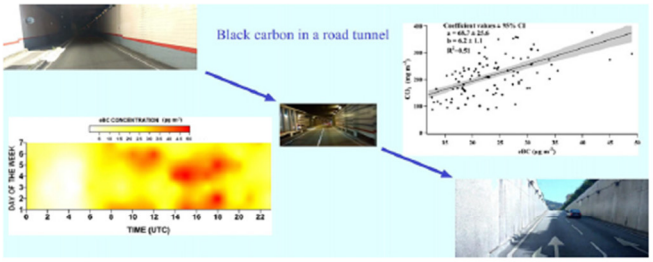

ARTICLE INFO

Article history:
Received 6 August 2019
Received in revised form 20 October 2019
Accepted 10 November 2019
Available online 12 November 2019

Editor: Pavlos Kassomenos

Keywords:
Absorption Ångström exponent
Aethalometer
Black carbon
Emission factors

ABSTRACT

A sampling campaign was conducted in the Liberdade Avenue tunnel (Braga, Portugal) during a week (with 56,000 vehicles) to monitor black carbon (eBC-equivalent black carbon) by means of an Aethalometer AE-31, and gaseous pollutants (CO_2, CO, NO_x). Inside the tunnel, the mean eBC mass concentration was 21 ± 10 μg m^{-3}, reaching a maximum hourly value of 49.0 μg m^{-3}. An hourly and weekday-weekend study was carried out. Regarding the Absorption Ångström exponent (AAE), a mean value of 0.97 ± 0.10 was obtained, for a source of practically pure traffic. There was a positive significant correlation between eBC and the number of light vehicles ($r = 0.47$; $p < 0.001$) and between eBC and the gaseous emissions: CO ($r = 0.67$; $p < 0.001$), CO_2 ($r = 0.71$; $p < 0.001$), NO ($r = 0.63$; $p < 0.001$) and NO_2 ($r = 0.70$; $p < 0.001$). The mean black carbon emission factors (EF_{BC}) inside the tunnel were 0.31 ± 0.08 g (kg fuel)$^{-1}$ and 0.11 ± 0.08 mg veh^{-1} km^{-1}, similar to those found in other studies for gasoline and diesel vehicles in road tunnels.

Factor de impacto JCR: 7.963 (D1) **Factor SJR**: 1.795 (D1)

DOI: 10.1016/j.scitotenv.2019.135483

Objetivo tratado: 2

Contribución del doctorando:

- Organización y tratamiento de datos del etalómetro AE-31 y de gases.
- Análisis estadístico de los datos.
- Determinación del Exponente Ångström de Absorción para una fuente pura de tráfico.
- Cálculo de los factores de emisión de carbono negro.
- Redacción del borrador original del artículo y sucesivas versiones.

ARTÍCULO VI (Capítulo 9)

Environmental Pollution 246 (2019) 336–345

Contents lists available at ScienceDirect

Environmental Pollution

journal homepage: www.elsevier.com/locate/envpol

Quantification of source specific black carbon scavenging using an aethalometer and a disdrometer☆

C. Blanco-Alegre [a], A.I. Calvo [a], E. Coz [b], A. Castro [a], F. Oduber [a], A.S.H. Prévôt [c], G. Močnik [d], R. Fraile [a, *]

[a] Department of Physics, IMARENAB University of León, 24071, León, Spain
[b] Centre for Energy, Environment and Technology Research (CIEMAT), Department of the Environment, Madrid, Spain
[c] Laboratory of Atmospheric Chemistry, Paul Scherrer Institute, 5232, Villigen, Switzerland
[d] Condensed Matter Physics Dept., Jožef Stefan Institute, 1000, Ljubljana, Slovenia

ARTICLE INFO

Article history:
Received 27 July 2018
Received in revised form
22 October 2018
Accepted 29 November 2018
Available online 30 November 2018

Keywords:
Black carbon
BC scavenging estimation model
Raindrop diameter
Rainfall
Scavenging coefficient
Wet deposition

ABSTRACT

Aerosol black carbon (BC) is the second strongest contributor to global warming, after CO_2, and it is linked to many adverse health effects. A sampling campaign of 15 months was carried out in León (Spain) in order to evaluate the scavenging of BC with an ensemble aethalometer-disdrometer. The aethalometer provides the concentration of equivalent black carbon (eBC), and the disdrometer, the raindrop size distribution. A total of seventy-five rain events were studied and in 73% of them there was an effective ($eBC_{initial} > eBC_{final}$) scavenging, with a mean decrease of 48 ± 37% in long rain events (>8 h) and 39 ± 38% in short rain events. The scavenging of BC is strongly related to its source. Thus, the scavenging coefficient (*SC*) mean value of the BC from fossil fuel (eBC_{ff}) for short and long rain events was 5.1 10^{-5} and 1.3 10^{-5} s^{-1}, respectively. For the BC from biomass burning (eBC_{bb}), the *SC* values were 1.6 10^{-4} and 2.8 10^{-5} s^{-1} in short and long events, respectively. There was a significant positive correlation between the *SC* and the number of drops with diameters between 0.375 and 2.5 mm. Rain scavenging of eBC was analyzed depending on the air mass origin obtaining an effective scavenging for air masses from Atlantic, Arctic and Africa. A linear model ($R^2 = 0.72$) was built to estimate the *ΔeBC* values with variables from an aethalometer, a disdrometer and a weather station: eBC concentration before rain, swept volume and precipitation accumulated. A Kolmogorov-Smirnov statistical test confirmed the goodness of fit of the model to the measured data.

Factor de impacto JCR: 6.791 (D1) **Factor SJR**: 1.968 (D1)

DOI: 10.1016/j.envpol.2018.11.102

Objetivo tratado: 2

Contribución del doctorando:

- Participación en la campaña de muestreo, de 13 meses, con verificaciones periódicas de los equipos de medida y toma de datos diaria.
- Descarga y tratamiento de datos del etalómetro AE-31 y del disdrómetro LPM.
- Selección de eventos de precipitación y análisis estadístico de los datos.
- Cálculo de las variables físicas de la precipitación para cada día de lluvia.
- Determinación de la procedencia de las masas de aire mediante el modelo HYSPLIT y clasificación en diferentes sectores.
- Determinación del coeficiente de scavenging y eficiencia.
- Redacción del borrador original del artículo y sucesivas versiones.

ARTÍCULO VII (Capítulo 10)

Science of the Total Environment 767 (2021) 145426

Contents lists available at ScienceDirect

Science of the Total Environment

journal homepage: www.elsevier.com/locate/scitotenv

Towards a model of wet deposition of bioaerosols: The raindrop size role

Carlos Blanco-Alegre [a], Amaya Castro [a], Ana I. Calvo [a,*], Fernanda Oduber [a], Delia Fernández-González [b,c], Rosa María Valencia-Barrera [b], Ana María Vega-Maray [b], Tibor Molnár [d], Roberto Fraile [a]

[a] Department of Physics (IMARENAB), University of León, Spain
[b] Department of Biodiversity and Environmental Management, University of León, Spain
[c] Institute of Atmospheric Sciences and Climate, National Research Council, Bologna, Italy
[d] Szent Istvan University, Institute of Agricultural Sciences and Rural Development, Hungary

HIGHLIGHTS

- Hourly variables of rain and 9 types of pollen were measured during 4 years in León.
- An effective scavenging was observed for all types of pollen in 71% of rain events.
- The swept volume was mainly caused by raindrops of sizes between 0.25 and 3 mm.
- Using meteorological and pollen variables, a linear model predicts pollen after rain.

GRAPHICAL ABSTRACT

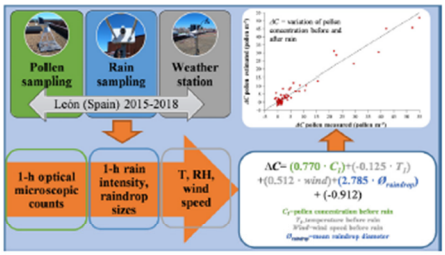

ARTICLE INFO

Article history:
Received 2 December 2020
Received in revised form 16 January 2021
Accepted 21 January 2021
Available online 27 January 2021

Editor: Pavlos Kassomenos

Keywords:
Allergies
Disdrometer
Meteorological parameters
Rainfall
Scavenging

ABSTRACT

Bioaerosols play a major role in the plant life of ecosystems. In addition, they have a profound impact on human health, since they may cause lung diseases or allergies. The key objective of this study is to assess the below cloud scavenging effect of rainfall on pollen concentration. The analysis is based on a sampling carried out in León, Spain, between 2015 and 2018. The rainfall variables and the pollen concentrations have been obtained with a disdrometer and a volumetric Hirst type spore-trap, respectively. In order to evaluate the scavenging, three parameters have been calculated: scavenging efficiency (through the concentration-weighted average (%ΔC)), the scavenging coefficient (λ) and the percentage of events with a decrease in pollen concentration (%*ES*) also called events with *effective* scavenging. 71% of rain events presented an effective scavenging that affected all types of pollen. The %ΔC mean value of total pollen was 24 ± 18% (positive values indicate an effective scavenging) and the types of pollen with the highest values were *Castanea* and Cupressaceae (71 and 40%, respectively). A linear model ($R^2 = 0.94$) to estimate the pollen concentration after rain was built with variables such as pollen concentration before rain and other variables from a weather station and a disdrometer. Furthermore, we have shown the possibility of knowing in real time the probable Cupressaceae pollen concentration, from the initial pollen concentration and the physical parameters of rain (such as raindrop size, rain intensity or volume swept by raindrops in their falling path).

Factor de impacto JCR: 7.963 (D1) (2020) **Factor SJR**: 1.795 (D1)

DOI: 10.1016/j.scitotenv.2021.145426

Objetivo tratado: 3

Contribución del doctorando:

- Participación en la campaña de muestreo, de 13 meses, con verificaciones periódicas de los equipos de medida y toma de datos diaria.
- Descarga y tratamiento de datos de la concentración de polen y del disdrómetro LPM.
- Selección de eventos de precipitación y análisis estadístico de los datos.
- Cálculo de las variables físicas de la precipitación para cada día de lluvia.
- Determinación del coeficiente de scavenging y eficiencia.
- Redacción del borrador original del artículo y sucesivas versiones.

ARTÍCULO VIII (Capítulo 11)

Título*:* **Links between aerosol radiative forcing and rainwater: stratiform and convective precipitation**

Autores: C. Blanco-Alegre, V. Pont, A.I. Calvo, A. Castro, F. Oduber, D. Pimienta-del-Valle, R. Fraile

Enviado para publicación

Objetivo tratado: 3

Contribución del doctorando:

- Participación en la campaña de muestreo, de 13 meses, con verificaciones periódicas de los equipos de medida y toma de datos diaria.
- Descarga, organización y tratamiento de datos del TSI- SMPS, de la PCASP y del disdrómetro LPM.
- Determinación de la densidad y del índice de refracción de las partículas.
- Selección de eventos de precipitación y clasificación en función de sus características.
- Ajuste de distribuciones de tamaño del aerosol antes y después de la lluvia.
- Cálculo de las variables físicas de la precipitación para cada evento de lluvia.
- Determinación de la procedencia de las masas de aire mediante el modelo HYSPLIT y clasificación en diferentes sectores.
- Descarga y tratamiento diario de radiosondeos y datos AERONET, y aplicación del modelo GAME de forzamiento radiativo.
- Redacción del borrador original del artículo y sucesivas versiones.

Investigación: Esta publicación se centra en el estudio del efecto de lavado del aerosol sobre el forzamiento radiativo**.** Entre febrero de 2016 y marzo de 2017 se calcularon los flujos de forzamiento radiativo utilizando el modelo GAME (*Global Atmospheric ModEL*). Durante la campaña de medida, y tras la aplicación de un conjunto de criterios de selección, se identificaron 16 eventos de lluvia estratiforme y 15 eventos de lluvia convectiva. Estos eventos se clasificaron según su forzamiento atmosférico *bajo* (inferior a 30 W m^{-2}) o *alto* (superior a 30 W m^{-2}) en la situación previa a la precipitación. En los eventos estratiformes, se ajustó el tamaño de las gotas de lluvia a una distribución gamma y se observó que la moda presentaba diferencias significativas entre los grupos *bajo* y *alto*.

CAPÍTULO 3. MATERIAL Y MÉTODOS

Este capítulo se centra en la descripción de la zona de estudio, de los equipos de medida y de las metodologías usadas, tanto en la preparación de la campaña de muestreo como en la propia campaña y en los análisis posteriores al muestreo. Los análisis de las muestras obtenidas durante la campaña son tanto físicos como químicos, por lo que señalaremos el fundamento básico de cada análisis, así como la bibliografía en donde se encuentra detallada cada técnica.

3.1. ZONA DE ESTUDIO

A excepción del trabajo presentado en el ***Capítulo 8,*** desarrollado en la ciudad de Braga (Portugal), toda la investigación se ha realizado en la ciudad de León. León se localiza al noroeste de la Península Ibérica (42º 60' N, 5º 37' O) a una altitud de 837 m sobre el nivel del mar. El punto de muestreo de todos los equipos involucrados en el estudio fue la terraza de Facultad de Veterinaria en la Universidad de León (Figura 3.1). Según el Instituto Nacional de Estadística (INE), la población total de la ciudad y su alfoz (municipios de Onzonilla, San Andrés del Rabanedo, Villaquilambre y Valverde de la Virgen) ha aumentado ligeramente en los últimos 15 años, pasando de 180644 habitantes en 2004 a 182719 habitantes en 2019. Sin embargo, la tendencia de la ciudad de León es a la baja con una disminución de -11486 habitantes mientras que en su alfoz es al alza con +13560 habitantes.

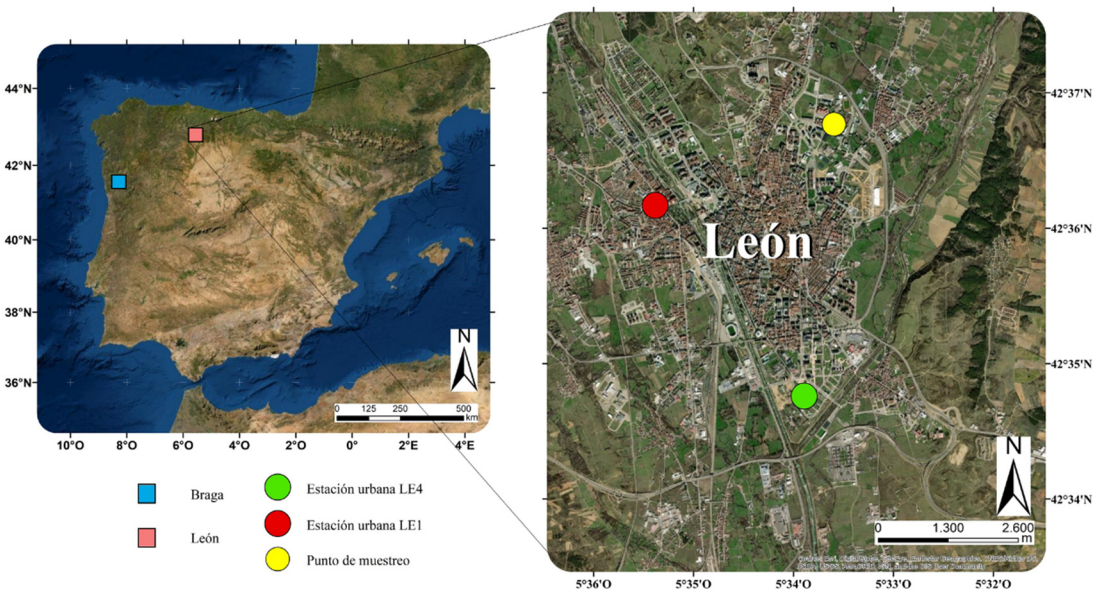

Figura 3.1. Mapa de la Península Ibérica señalando la ciudad de León (España) y Braga (Portugal). Con mayor detalle, mapa de la ciudad de León y localización del punto de muestreo en la Universidad de León, así como las estaciones de control de la calidad del aire LE1 y LE4.

La ciudad de León, situada en una cuenca minera, presenta unas características particulares desde el punto de vista de la calidad del aire, ya que es de las pocas ciudades del sur de Europa en donde el uso de carbón para calefacciones es todavía común. Así pues, las principales fuentes de material particulado en la ciudad son el tráfico y las calefacciones, ya que la industria en la ciudad presenta un bajo impacto (Oduber et al., 2018, 2021). Además, en los meses veraniegos son frecuentes las intrusiones de polvo procedentes del desierto del Sáhara (Oduber et al., 2019; Russo et al., 2020).

El tráfico está concentrado principalmente en las carreteras de circunvalación alrededor de la ciudad; una de ellas, a 200 m del punto de muestreo. La intensidad media de vehículos es de 25000 vehículos día^{-1}. El parque vehicular en 2017 estaba compuesto por 116415 vehículos en la ciudad de León y su alfoz. Según datos de la Dirección General de Tráfico (DGT, 2016) la distribución de vehículos por tipos es: camiones (8.2%), furgonetas (6.7%), autobuses (0.1%), turismos (71.7%), motocicletas (8.1%), tractores industriales (1.4%), remolques (2.5%) y otros vehículos (1.4%). En cuanto al combustible utilizado, el 41.5% utilizan gasolina, el 58.4% usan gasoil, mientras que solo el 0.1% son vehículos eléctricos. Los turismos y motocicletas clasificados en función del distintivo medioambiental presentan los siguientes porcentajes: CERO (0.03%), B (30.6%), C (18.4%), ECO (0.5%), "Sin distintivo" (42.3%) y "Se desconoce" (8.2%).

Las fuentes de energía en calefacciones domésticas utilizadas en el año 2008 (año del último informe de la Junta de Castilla y León) fueron los combustibles de gasoil (29%), gas (28%), energía eléctrica (11%), quema de biomasa (6%) y quema de carbón (6%). Este último dato es

destacable porque el carbón es utilizado principalmente en viviendas antiguas del centro de la ciudad y alrededores, cuyo uso es todavía habitual (Junta de Castilla y León, 2008). Los depósitos de carbón de las cuencas mineras de la provincia de León son de antracita y hulla, y tienen un gran contenido de carbono (>75%) (Junta de Castilla y León, 2009). Sin embargo, en torno al 85% del carbón utilizado en la ciudad es de importación. Relacionado con las fuentes de energía, en 2016 la demanda total de calor fue $1.6 \cdot 10^6$ MWh año^{-1} (IDAE, 2017) y 476 toneladas de carbono negro fueron emitidas en la provincia de León, principalmente por plantas de combustión no industriales (55%), tratamiento y eliminación de residuos (15%) y el transporte rodado (14%). En León durante el año 2016, según datos de la Consejería de Medio Ambiente de la Junta de Castilla y León (2018), se emitieron un total de 2493 t de $PM_{2.5}$, 4050 t de PM_{10}, 21996 t de SOx, 29273 t de NOx y 476 t de carbono negro (BC). Las plantas de combustión no industrial formaron parte del sector más contaminante (Tabla 3.1).

El clima en León es mediterráneo continentalizado, muy influido por la presencia de la Cordillera Cantábrica, situada 30 km al norte de la ciudad (Castro et al., 2010). Los valores climatológicos normales en León, obtenidos a partir de los registros de la Agencia Estatal de Meteorología (AEMET) entre 1981 y 2010, en la estación de la Virgen del Camino (situada a 6 km de León) se muestran en la Tabla 3.2. La temperatura media anual es de 11.1 °C, la media anual de la temperatura máxima diaria es 16.7 °C y la media anual de la temperatura mínima diaria es 5.5 °C. La precipitación media anual es 515 mm, concentrada principalmente entre octubre y enero. Hay una media de 74.9 días de precipitación acuosa superior a 1 mm y 13 de precipitación en forma de nieve. Las tormentas se concentran en los meses de primavera y verano, con una media de 16.1 días al año. Las nieblas y heladas, características de la ciudad de León en los meses invernales, presentan una media de 27.8 y 71.6 días respectivamente (AEMET, 2020). El número de horas de insolación promedio mensual es superior a las 300 h en los meses de verano, lo que facilita la aparición de eventos de formación de partículas (NPF).

La vegetación en León, fuente de bioaerosoles, está influida por la cercanía de la cordillera Cantábrica (características en el *Capítulo 10*). La vegetación de las áreas verdes más cercanas al punto de muestreo (campus universitario y parques) está además caracterizada por árboles de la familia Pinaceae, *Platanus hispanica*, *Fraxinus excelsior*, *Fraxinus angustifolia*, *Betula pubescens*, *Acer negundo*, *Tilia platyphylus*, así como por árboles de polinización entomófila. Las praderas están principalmente constituidas por césped y *Plantago sp.*, que se cortan generalmente antes de florecer.

Tabla 3.1. Emisiones por sectores en la provincia de León (España) en 2016. Fuente: Consejería de Medio Ambiente de la Junta de Castilla y León (2018).

Sector	SOx (t)	NOx (t)	$PM_{2.5}$ (t)	PM_{10} (t)	BC (t)
Combustión en la producción y transformación de energía	20764	16798	305	564	11
Plantas de combustión no industrial	436	1217	1617	1661	263
Plantas de combustión industrial	675	3435	74	101	19
Procesos industriales sin combustión			61	212	0
Extracción y distribución de combustibles fósiles y energía geotérmica			1	5	
Uso de disolventes y otros productos	0	0	2	4	0
Transporte por carretera	6	3826	161	216	66
Otros modos de transporte y maquinaria móvil	3	1681	72	72	46
Tratamiento y eliminación de residuos	5	138	140	147	70
Agricultura		1646	61	1066	
Otras fuentes y sumideros (naturaleza)	106	531			

Tabla 3.2. Valores climatológicos normales medios, por meses y anual, en la ciudad de León en el periodo de 1981-2010: T-temperatura media (°C), $T_{máx}$- temperatura máxima media (°C), $T_{mín}$- temperatura mínima media (°C), R-precipitación media (mm), HR-humedad relativa media (%), I-número medio de horas de sol, y número medio de días de: DR-precipitación superior a 1 mm, DN-nieve, DT-tormenta, DF-niebla, DH-helada, DD-cielos despejados. Fuente: Agencia Estatal de Meteorología (AEMET).

Mes	T	$T_{máx}$	$T_{mín}$	R	HR	I	DR	DN	DT	DF	DH	DD
E	3.2	7.1	-0.7	50	82	130	7.6	4.1	0	8.1	18.6	5.8
F	4.7	9.5	0.0	34	74	161	6.0	3.1	0.1	2.8	15	5.8
M	7.6	13.3	1.9	32	66	214	5.6	1.6	0.3	1	9.4	6.9
A	9.0	14.8	3.3	45	65	228	7.7	0.9	1.2	0.3	5.2	4.1
M	12.6	18.6	6.6	56	62	259	8.8	0.1	3.9	0.6	0.7	3.6
J	17.1	24	10.2	31	56	314	4.6	0	2.9	0.2	0	7.3
J	19.8	27.4	12.2	19	52	358	2.8	0	3	0.1	0	12.3
A	19.6	26.9	12.3	23	54	327	2.7	0	2.6	0.1	0	11.8
S	16.5	22.9	10.1	39	62	246	4.5	0	1.5	0.2	0	9
O	11.7	16.7	6.7	61	74	178	8.2	0	0.4	1.7	0.7	4.9
N	7.0	11.2	2.8	59	80	137	7.5	0.8	0	4.8	7.3	5.4
D	4.2	8.0	0.4	66	83	120	8.7	2.2	0.1	7.9	14.6	6.3
Anual	11.1	16.7	5.5	515	67	2673	74.9	13	16.1	27.8	71.6	83

La Red de Calidad del Aire de la Junta de Castilla y León lleva a cabo las medidas en dos estaciones de control fijas (Figura 3.1) y son:

- León 1 (LE1): situada en la Avenida San Ignacio de Loyola, es de tipo *tráfico* y registra, desde 1997, las concentraciones de NOx, SO_2, PM_{10}, CO y O_3.
- León 4 (LE4): situada en el Coto Escolar, es una estación *de fondo*, situada en una zona suburbana, y registra, desde 2010, las concentraciones de NOx, SO_2, PM_{10} y O_3.

3.2. CONTEXTO DEL MUESTREO

Los resultados de esta tesis doctoral se basan principalmente en el periodo de estudio del proyecto AERORAIN, financiado por el Ministerio de Economía y Competitividad (MINECO-CGL2014-52556-R). La campaña de muestreo de múltiples contaminantes y de la precipitación se llevó a cabo de manera ininterrumpida entre el 9 de marzo del 2016 y el 14 de marzo del 2017 en la terraza de Facultad de Veterinaria de la Universidad de León (Figura 3.1).

Durante el periodo se muestreó diariamente, de manera continua, el contenido de material particulado (PM_{10}), mediante colectores con filtros de cuarzo (354 muestras) y teflón (354 muestras), la distribución de tamaños de partículas mediante contadores, la precipitación mediante colectores (74 muestras) y un disdrómetro láser, y la concentración de carbono negro mediante un etalómetro. En el mismo punto, se muestreó diariamente el contenido de polen y alérgenos del aerosol atmosférico mediante diversos colectores.

La preparación pre-muestreo se incluye en el Anexo B en donde se describe la preparación del material para el muestreo de material particulado y lluvia.

3.3. MUESTREO: EQUIPOS DE MEDIDA

Durante el periodo de estudio (9 marzo 2016 - 14 marzo 2017) los equipos de medida se colocaron en la terraza de la Facultad de Veterinaria de la Universidad de León, con un cambio de filtros diario a las 1000 UTC. En la Figura 3.2 se muestra la ubicación de parte de los equipos de muestreo. El resto de equipos que necesitaban estar a cubierto se situaron en una caseta y las sondas de captación de aerosoles, carbono negro y polen se sacaron al exterior. A continuación, se describirán los equipos de medida utilizados a lo largo del periodo de estudio. Mi participación fue diaria a lo largo de todo el muestro realizado para el proyecto.

Figura 3.2. Situación de los equipos de medida en la terraza de la Facultad de Veterinaria de la Universidad de León.

3.3.1. ETALÓMETRO

El etalómetro es el instrumento utilizado para la medida del carbono negro equivalente (eBC). La atenuación de la luz provocada por el aerosol atmosférico se midió continuamente a siete longitudes de onda λ_w (370, 470, 520, 590, 660, 880 y 950 nm) durante el periodo de estudio con un etalómetro modelo AE-31 (Magee Scientific, USA) equipado con una cámara "Extended Range", que presenta un área de "spot" de 167±1 mm^2 y una atenuación (ATN) máxima de 75. El esquema general del equipo se muestra en la Figura 3.3, donde se observa la cinta de cuarzo utilizada para la deposición del aerosol atmosférico. La entrada de aerosol es un tubo vertical con un cabezal PM_{10} conectado al equipo con un flujo de muestreo de 4 L min^{-1}, verificado cada 15 días con el kit de diagnóstico Gilian Gilibrator 2. Aunque cada 2 minutos se disponía de una medida, se calcularon medias horarias para reducir el ruido de los datos.

Figura 3.3. a) Etalómetro AE-31 utilizado durante la campaña de muestreo; b) Cinta de cuarzo; c) "Spot" con aerosol atmosférico muestreado.

El equipo consta de dos fotodetectores: uno mide la intensidad de la luz que atraviesa un punto de la cinta de cuarzo sin muestra (referencia) y el otro mide la intensidad en un punto del filtro de cuarzo con muestra de aerosol (spot) que se acumula hasta alcanzar una ATN de 75, momento en cual el "spot" avanza, por lo que el equipo realiza un blanco de 10 minutos sin medida. Una descripción técnica detallada del equipo aparece en Fialho et al. (2005) y Hansen (2005).

El tratamiento de los datos proporcionados por el equipo es complejo. Los datos que proporciona el etalómetro directamente son: la concentración de carbono negro (ng m^{-3}) para las 7 λ_w, el flujo de muestreo (L min^{-1}), la atenuación óptica para las 7 λ_w y los diferentes parámetros del láser del equipo (intensidad de la señal y referencia cero). Sin embargo, los datos de concentración deben ser corregidos posteriormente por los denominados "efecto carga" y "efecto *multiscattering*" (Sandradewi et al., 2008). El "efecto carga", lineal a la atenuación de la luz en el AE-31, está provocado por la acumulación gradual de partículas absorbentes en el filtro cargado causando una no linealidad entre la transmisión de la luz a través del filtro cargado de muestra y la cantidad de muestra que absorbe la luz en el filtro, mientras que el "efecto *muliscattering*" está provocado por la dispersión múltiple del haz de luz por las fibras del filtro de cuarzo.

La Eq. 3.1 expresa, para cada instante *t*, el cálculo del parámetro $\sigma_{ATN-AE}(t, \lambda_w)$ para una atenuación dada (ATN) por el etalómetro (AE) según la λ_w y que es medido en Mm^{-1}, en donde C_{AE} es la concentración de carbono negro en ng m^{-3} para cada λ_w en condiciones estándar, λ_w es la longitud de onda correspondiente en nm y K_{BC} es el valor del coeficiente (14.625 µm m^2 g^{-1}) proporcionado por el fabricante del equipo para el cálculo del eBC (Fialho et al., 2005).

$$\sigma_{ATN-AE}(t;\lambda_w) = \frac{C_{AE}(t;\lambda_w) \times K_{BC}}{\lambda_w} \qquad \textit{Eq. 3.1}$$

A continuación, este valor σ_{ATN-AE} debe ser corregido por el "efecto carga" y el "efecto *multiscattering*", obteniendo $\sigma_{abs}(t;\lambda_w)$. En la Eq. 3.2, $C_W(\lambda_w)$ hace referencia al valor para compensar el "efecto *multiscattering*" que depende del material de la fibra del filtro. Durante la campaña de muestreo se utilizó una cinta de cuarzo con un valor de $C_W(\lambda)$ de 3.5±0.9 siguiendo las indicaciones de la WMO/GAW Aerosol Measurement Procedures, Guidelines and Recommendations (WMO, 2016). En esta tesis se presentan puntualmente valores de absorción, centrándose en valores de concentración. El "efecto carga" fue corregido utilizando el método sugerido por Weingartner et al. (2003) mediante el parámetro R_W, cuyo cálculo se basa en la expresión Eq. 3.3. Por último, en la Eq. 3.2 se utilizaron los $f(\lambda_w)$ de la época cálida y fría propuestos por Sandradewi et al. (2008b) (Tabla 3.3). Tal y como se observa en la Eq. 3.3, la corrección de los valores se realiza con atenuaciones de entre 10 y 50, por lo que entre 50 y 75 se llevó a cabo una interpolación lineal.

$$\sigma_{abs}(t;\lambda_w) = \frac{\sigma_{atn}(t;\lambda_w)}{C_W(\lambda_w) \times R_W\big(f(\lambda_w); ATN(\lambda_w)\big)} \qquad \textit{Eq. 3.2}$$

$$R\big(f(\lambda_w); ATN(\lambda_w)\big)_w = \left(\frac{1}{f(\lambda_w)} - 1\right) \times \frac{ln\big(ATN(\lambda_w)\big) - ln(10)}{ln(50) - ln(10)} + 1 \qquad \textit{Eq. 3.3}$$

La concentración de carbono negro equivalente (eBC) se determina a partir de la *ATN* a una λ_w de 880 nm (Eq. 3.4), ya que otras partículas carbonosas o minerales del aerosol absorben significativamente menos que el carbono negro en esa λ_w (Fialho et al., 2005; Sandradewi et al., 2008b). Depende de la concentración C_0 de carbono negro dada por el equipo en condiciones estándar a una λ_w de 880 nm y del coeficiente K_{BC}.

$$C_{eBC}(880nm;t) = \sigma_{abs}(880nm;t) \times C_0 \times \frac{0.880}{K_{BC}} \qquad \textit{Eq. 3.4}$$

Mediante la aplicación de modelos utilizando diferentes λ_w, se puede discernir entre fuentes de BC. En nuestro caso, aplicamos el modelo de Sandradewi et al. (2008b) que utiliza las λ_w a 470 nm (α_1) y 950 nm (α_2) para estimar, por un lado, la contribución de la quema de los combustibles fósiles (eBC_{ff}) y, por otro, la contribución de la quema de biomasa (eBC_{bb}) al valor del eBC total. Se utiliza la λ_w más corta de 470 nm en lugar de la de 370 nm, porque esta última está influenciada por la presencia de aerosoles orgánicos secundarios (SOA) con propiedades ópticas muy variables (Zotter et al., 2017).

Tabla 3.3. Parámetros $f(\lambda_w)$ para la compensación del "efecto carga" de cada λ_w en función de la época fría o cálida del año (Sandradewi et al., 2008b).

λ_w (nm)	370	470	520	590	660	880	950
$f(\lambda_w)$ Época fría	1.155	1.137	1.128	1.116	1.103	1.064	1.051
$f(\lambda_w)$ Época cálida	1.141	1.132	1.127	1.120	1.114	1.093	1.086

Los Exponentes de Absorción de Ångström (AAE) utilizados para discriminar entre la quema de combustibles fósiles y la quema de biomasa fueron AAE_{ff} =1.0 y AAE_{bb} =1.68 (Zotter et al., 2017). El valor de 1.0 utilizado para la quema de combustible fósil (principalmente tráfico) fue obtenido a través de medidas realizadas en el centro de León, en dos zonas con mucho tráfico en dos días calurosos sin influencia de calefacciones (Figura 3.4). Cabe destacar que los datos anómalos registrados de AAE (aquellos menores de 0.7 y superiores a 5), a lo largo de la campaña de medida, fueron eliminados, ya que estas mediciones no son indicativas del eBC real (constituyeron menos del 1% durante todo el periodo de muestreo).

Así pues, la concentración de eBC por fuentes (eBC_{ff} y eBC_{bb}) se determina a través de las Eqs. 3.5, 3.6, 3.7, 3.8 y 3.9. El valor de $\sigma_{abs}(t)$ puede considerarse como el sumatorio de dos fuentes: quema de combustibles fósiles $\sigma_{BC;ff}(t)$ y quema de biomasa $\sigma_{BC;bb}(t)$, asumiendo que solo existen esas dos fuentes de eBC.

$$\sigma_{abs}(470nm;t) = \sigma_{BC;ff}(470nm;t) + \sigma_{BC;bb}(470nm;t) \qquad \textit{Eq. 3.5}$$

$$\sigma_{BC;ff}(470-950;t) = \frac{\sigma_{abs}(470nm;t) - \sigma_{abs}(950nm;t) \times \left(\frac{470}{950}\right)^{-AAE_{bb}}}{\left(\frac{470}{950}\right)^{-AAE_{ff}} - \left(\frac{470}{950}\right)^{-AAE_{bb}}} \qquad \textit{Eq. 3.6}$$

$$w_{bb}(470-950;t) = \frac{\sigma_{abs}(950nm;t) - \sigma_{BC;ff}(470-950;t)}{\sigma_{abs}(950nm;t)} \qquad \textit{Eq. 3.7}$$

$$\text{y} \begin{cases} si\ w_{bb}(470-950;t) < 0 \Longrightarrow w_{bb}(470-950;t) = 0 \\ si\ w_{bb}(470-950;t) > 1 \Longrightarrow w_{bb}(470-950;t) = 1 \end{cases}$$

$$eBC_{bb}(470-950nm;t) = w_{bb}(470-950;t) \times C_{eBC}(880nm;t) \qquad \textit{Eq. 3.8}$$

$$eBC_{ff}(470-950nm;t) = C_{eBC}(880nm;t) - C_{eBC;bb}(470-950;t) \qquad \textit{Eq. 3.9}$$

Figura 3.4. Equipamiento para la determinación del Exponente Ångström de Absorción correspondiente a una fuente "pura" de tráfico en el centro de la ciudad de León.

La localización geográfica de la zona de estudio (León) presenta una importante fuente extra de eBC durante los meses fríos: la quema de carbón. Por ello, se llevó a cabo una modificación del modelo anteriormente mencionado para discernir entre la contribución de quema de biomasa y la quema de carbón, a partir del uso de trazadores de quema de biomasa y de quema de carbón. En el ***Capítulo 7*** se incluye el artículo "Searching the contribution of coal combustion to black carbon: coupling tracers with the aethalometer model" donde se desarrolla tal modelo.

3.3.2. CONTADOR DE PARTÍCULAS BASADO EN MOVILIDAD ELÉCTRICA

La distribución de tamaños de partículas de aerosol con un diámetro aerodinámico inferior a 1 µm se midió continuamente con un espectrómetro de partículas submicrométricas (SMPS, *Scanning Mobility Particle Sizer*). El modelo utilizado fue el TSI-3938, con un analizador de movilidad diferencial modelo 3081 (DMA, *Differential Mobility Analyser*) y un contador de partículas modelo 3772 (CPC, *Condensation Particle Counter*). Las mediciones del SMPS se basan en la técnica de detección de la movilidad eléctrica, donde el voltaje varía de forma exponencial en el rango de movilidad eléctrica de las partículas a medir. En la Figura 3.5 se muestran los diferentes componentes del SMPS utilizado.

La configuración utilizada para el muestreo fue la siguiente: la relación de flujo de aerosol y flujo de arrastre "sheath" o envolvente fue de 1:10 (0.3 y 3 L min^{-1}, respectivamente). Cada 15 días se limpió el impactador y se verificaron los flujos con un medidor de flujo Gilian Gilibrator 2

para asegurar la calidad de los datos. La distribución de tamaño fue obtenida entre 14.3 y 1000 nm en 110 canales con una resolución temporal de 6 minutos. La resolución de los canales de partículas fue de 64 canales por década. Se aplicaron las correcciones de carga múltiple y de difusión en la línea y en el sistema de acuerdo con los estándares ACTRIS SMPS (Wiedensohler et al., 2012):

- Corrección por múltiple carga: las partículas superiores a 100 nm pueden tener múltiples cargas provocando que aumente su movilidad eléctrica y si se considera una única carga, se infravaloraría su diámetro. Por ello, el software TSI aplica la corrección automáticamente basada en la teoría de aproximación de distribución bipolar de carga (Wiedensohler, 1988).

- Corrección por difusión de las partículas: se trata de corregir la deposición de las partículas por difusión browniana a lo largo de la sonda de medida. La corrección depende enormemente del caudal y el tamaño de partícula (a mayor caudal y diámetro, menores pérdidas). Por ello, el factor de corrección en tamaños inferiores a 100 nm es muy importante y para la corrección se sigue el protocolo indicado en Wiedensohler et al. (2012) que depende de: i) las condiciones de muestreo (longitud equivalente de sonda, caudal, presión y temperatura); ii) las propiedades del gas (*gas mean free path* y *dynamic gas viscosity*) ambos proporcionados por el equipo; iii) las propiedades de las partículas (*Cunningham slip correction*).

A partir de los datos proporcionados se calculó la concentración total del número de partículas (PNC) (# cm^{-3}), la distribución del tamaño del área de la superficie de la partícula (nm^2 cm^{-3}), la distribución del volumen de partículas (nm^3 cm^{-3}) y el diámetro geométrico medio (nm). Una descripción detallada del funcionamiento del equipo y un esquema de cada componente se muestra en el Anexo B.

Figura 3.5. Espectrómetro de partículas submicrométricas (SMPS) utilizado en el periodo de estudio.

3.3.3. CONTADOR DE PARTÍCULAS ÓPTICO

La distribución de tamaño de partículas de aerosol con un diámetro óptico entre 0.1 y 10 µm se muestreó con un espectrómetro láser óptico denominado *Passive Cavity Aerosol Spectrometer Probe*, PMS, Modelo PCASP-X, fabricado por Particle Measuring Systems, Inc. (PMS) (Figura 3.6). El flujo de muestreo fue de 0.12 L min^{-1}. La sonda PCASP-X determina el tamaño de las partículas según el grado en que dispersan la luz de manera individual a una longitud de onda (λ_w) de 632.8 nm entre ángulos de dispersión de 45° y 135°. La calibración del instrumento se realizó mediante esferas de látex de diámetro conocido, con un índice de refracción de 1.58-0i. La sonda presenta 31 canales discretos y un canal extra donde incluyen las partículas de tamaño superior a 10 µm. En la Tabla 3.4 se muestran los intervalos de diámetro de partículas para los 32 canales.

a) b)

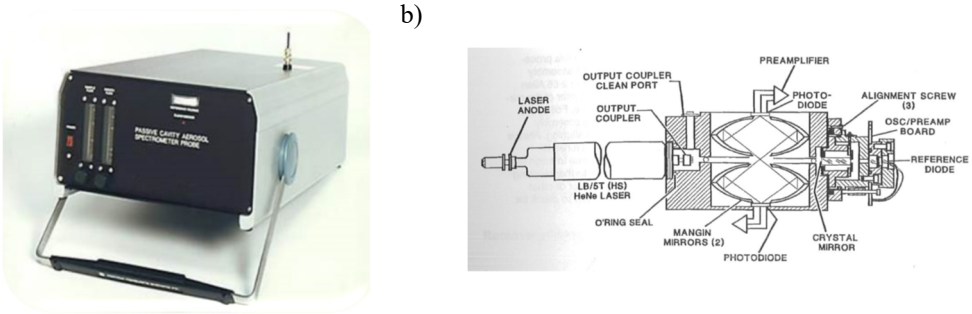

c)

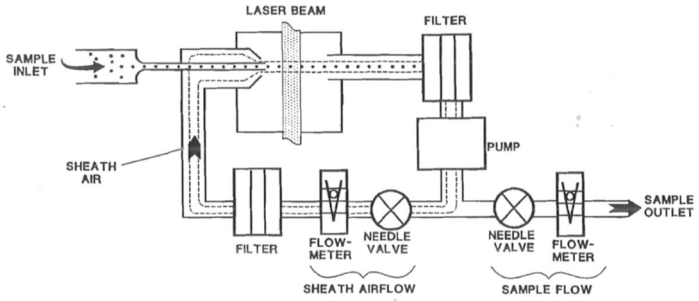

Figura 3.6. a) Espectrómetro láser PCASP-X utilizado en el periodo de estudio; b) Esquema óptico general del equipo; c) Esquema de flujos general del equipo.

Tabla 3.4. Intervalos de diámetro de partículas medidos con la sonda PCASP-X, comprendidos entre 0.1 y 10 µm para un índice de refracción de esferas de látex de 1.58-0i.

Canal	Tamaño (µm)	Intervalo (µm)	Canal	Tamaño (µm)	Intervalo (µm)
1	0.10 - 0.12	0.02	17	0.90 - 1.00	0.10
2	0.12 - 0.14	0.02	18	1.00 - 1.20	0.20
3	0.14 - 0.16	0.02	19	1.20 - 1.40	0.20
4	0.16 - 0.18	0.02	20	1.40 - 1.60	0.20
5	0.18 - 0.20	0.02	21	1.60 - 1.80	0.20
6	0.20 - 0.23	0.03	22	1.80 - 2.00	0.20
7	0.23 - 0.26	0.03	23	2.00 - 2.30	0.30
8	0.26 - 0.30	0.04	24	2.30 - 2.60	0.30
9	0.30 - 0.35	0.05	25	2.60 - 3.00	0.40
10	0.35 - 0.40	0.05	26	3.00 - 3.50	0.50
11	0.40 - 0.45	0.05	27	3.50 - 4.00	0.50
12	0.45 - 0.50	0.05	28	4.00 - 5.00	1.00
13	0.50 - 0.60	0.10	29	5.00 - 6.50	1.50
14	0.60 - 0.70	0.10	30	6.50 - 8.00	1.50
15	0.70 - 0.80	0.10	31	8.00 - 10.00	2.00
16	0.80 - 0.90	0.10	32	>10.00	

Para determinar la concentración de partículas en cada canal se deben realizar diferentes correcciones (Figura 3.7) sobre el número de partículas que indica el espectrómetro directamente, que se pueden encontrar en el Anexo B.

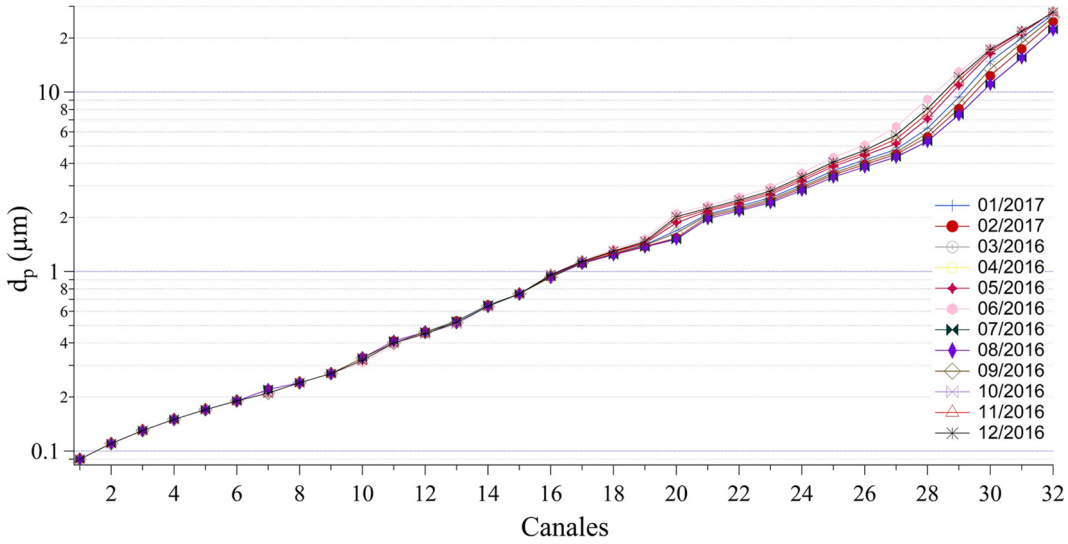

Figura 3.7. Diámetros de los canales del espectrómetro láser PCASP-X corregidos por el índice de refracción mensual.

Una descripción más detallada del equipo, así como de las correcciones necesarias e incertidumbre de las medidas puede encontrarse en Calvo (2009).

3.3.4. DISDRÓMETRO LÁSER

El espectro de tamaños de gotas de lluvia se muestreó mediante un disdrómetro óptico *Laser Precipitation Monitor* (LPM) de *Thies Clima* (Figura 3.8). El equipo determina la velocidad de caída y el volumen de los hidrometeoros a partir de la duración y cantidad de pérdida de la señal láser emitida y detectada en un área de muestreo de 228 x 20 mm^2. La fuente del rayo láser produce un rayo paralelo de luz infrarroja de 780 nm. Un fotodiodo con una lente se sitúa en el lado del receptor que mide la intensidad óptica transformándola en señal eléctrica. Cuando un hidrometeoro cae a través del rayo de luz, la señal que se recibe permanentemente se ve reducida, y el diámetro de los hidrometeoros es calculado a partir de la amplitud de tal reducción. La velocidad de la partícula se calcula al relacionar esa amplitud con la duración de esa disminución de la señal y los valores de medida son recogidos por un procesador de señal.

a) b)

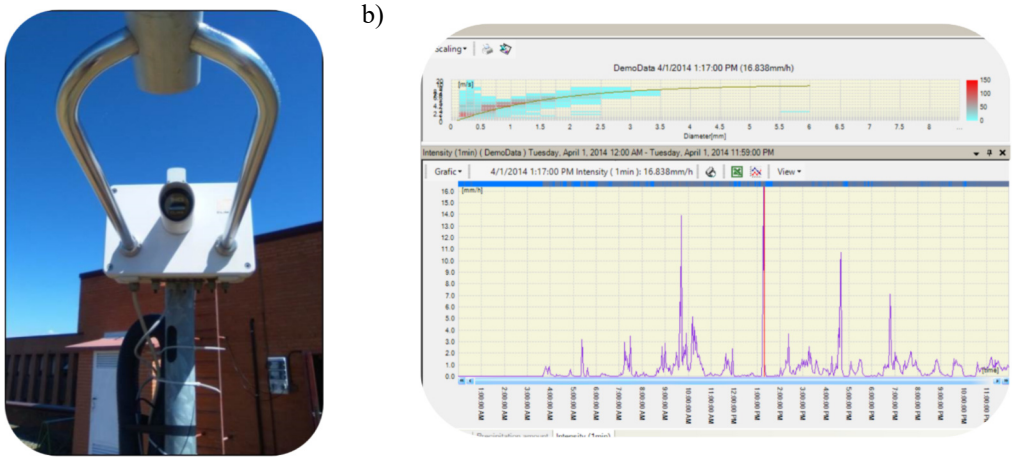

Figura 3.8. a) Disdrómetro *Laser Precipitation Monitor* (LPM) de *Thies Clima*; b) Software de visualización y descarga de los datos.

Los tamaños de las gotas medidas se agrupan en 21 clases, entre 0.125 mm y 8 mm de diámetro, y una clase extra 22 para las gotas de un diámetro superior a 8 mm (Tabla 3.5). Los datos se integraron en intervalos de 1 min.

Para evitar errores de sobreestimación en la distribución de tamaños de gotas, debido a la propia naturaleza de la gota, se utilizó la metodología mixta creada por Fernández-Raga et al. (2010) en la cual, a partir de los diámetros recogidos por el disdrómetro, los tamaños de las gotas se calculan de la siguiente forma:

- para gotas inferiores a 1 mm, se consideran gotas esféricas.
- para gotas mayores de 1 mm, se calculó un radio horizontal teórico equivalente basándose en Brandes et al. (2002).

Tabla 3.5. Diámetros de gota medidos por los canales del disdrómetro *LPM*: tamaño D_r (mm) e intervalo (mm).

Canal	D_r (mm)	Intervalo (μm)	Canal	D_r (mm)	Intervalo (μm)
1	≥ 0.125	0.125	12	≥ 3	0.5
2	≥ 0.25	0.125	13	≥ 3.5	0.5
3	≥ 0.375	0.125	14	≥ 4	0.5
4	≥ 0.5	0.25	15	≥ 4.5	0.5
5	≥ 0.75	0.25	16	≥ 5	0.5
6	≥ 1	0.25	17	≥ 5.5	0.5
7	≥ 1.25	0.25	18	≥ 6	0.5
8	≥ 1.5	0.25	19	≥ 6.5	0.5
9	≥ 1.75	0.25	20	≥ 7	0.5
10	≥ 2	0.5	21	≥ 7.5	0.5
11	≥ 2.5	0.5	22	≥ 8	∞

Las variables obtenidas/calculadas a partir del disdrómetro fueron: intensidad de precipitación (mm min^{-1}), precipitación acumulada (mm min^{-1}), número de gotas en los 22 canales (# min^{-1}), volumen barrido por las gotas (mm^3 m^{-3}), media y desviación estándar del tamaño de las gotas de lluvia (mm). Además, la distribución de tamaños de gota de lluvia (DSD) se ajustó a una función de densidad de probabilidad gamma (explicada en la Introducción, apartado 1.2.2) para la cual se calcularon los parámetros α y β por el método de los momentos (Marques et al., 2014b).

Además, con el objetivo de discernir entre eventos de precipitación convectiva y estratiforme se obtuvieron los parámetros característicos (a y b) de la distribución Z-R en donde a partir de la intensidad de precipitación (R; mm h^{-1}) y de la reflectancia (Z; mm^6 mm^{-3}) se calculan dichos parámetros ($Z=a \cdot R^b$). El ajuste Marshall-Palmer entre ambas variables es proporcionado por el disdrómetro directamente.

3.3.5. COLECTOR DE LLUVIA

La precipitación acuosa se recogió mediante el uso de un colector automático *Eigenbrodt UNS 130/E* (Figura 3.9), con un sensor que detecta el inicio de la precipitación y abre la cubierta. Igualmente, al finalizar la precipitación, la cubierta se cierra. En su interior se colocó una botella de cristal de 3.5 L (Anexo B1.3) que se cambiaba diariamente a las 1000 UTC, simultáneamente al cambio de filtros de material particulado.

Figura 3.9. Colector automático Eigenbrodt UNS 130/E de deposición húmeda.

3.3.6. CAPTADORES DE PM_{10} Y POLEN

Los captadores de material particulado (PM_{10}) fueron dos de bajo volumen (TECORA y GENT) y uno de alto volumen (CAV). El funcionamiento de todos los captadores PM_{10} se basa en la circulación de un caudal controlado a través de un cabezal selector de los tamaños de las partículas. Para ello, el colector dispone de una bomba de vacío (interior o exterior al equipo) que provoca la aspiración de un caudal de aire. Además, se utilizaron dos captadores de polen: un captador volumétrico de tipo *Hirst* y un captador ciclónico de bajo volumen. Todos los captadores fueron colocados en la terraza de la Facultad de Veterinaria de la Universidad de León. A continuación, se describen individualmente:

- El captador de bajo volumen TECORA ECHOPM (Figura 3.10a) con un cabezal selector de tamaño PM_{10} se equipó con filtros de teflón (47 mm de diámetro) para tomar muestras de los aerosoles contenidos en el flujo de aire circulante. Cada filtro se colocaba a las 1000 UTC y el muestreo duraba 23.5 h (≈1 día). La media hora restante se dedicó al cambio de los filtros. El volumen de muestreo configurado fue de 2.3 m^3 h^{-1}. Los filtros retirados cada día se almacenaron en placas Petri en un congelador a -18 °C para su posterior pesaje (determinación de la concentración de PM_{10}) y análisis químicos.
- Se utilizó otro captador de bajo volumen denominado GENT (Figura 3.10b) con un volumen de muestreo de 1.2 m^3 h^{-1}. Se equipó con filtros de policarbonato (47 mm de diámetro) para tomar muestras de aerosoles en eventos de especial interés, como intrusiones de polvo sahariano o quema de carbón. Por lo tanto, la duración del muestreo no estaba preestablecida, yendo de horas a días de muestreo. Los filtros muestreados se almacenaron sobre una capa de papel de aluminio calcinado en el interior de placas Petri, en un refrigerador a 5 °C, hasta su posterior análisis por microscopía.
- El captador de alto volumen CAV- modelo A/Mb (Figura 3.10c) se utilizó con un cabezal selector de tamaño PM_{10} y se equipó con filtros de cuarzo (150 mm de diámetro) para tomar muestras de la masa de aerosoles contenida en el flujo de aire circulante. Al igual que con el TECORA, cada filtro se colocaba a las 1000 UTC y el muestreo duraba 23.5 h (≈1 día). La media hora restante se dedicó al cambio de los filtros. El volumen de muestreo configurado fue de 30 m^3 h^{-1}. Los filtros retirados cada día se almacenaron en el congelador a -18 °C hasta su posterior pesaje y análisis químico del contenido de carbono orgánico y elemental.

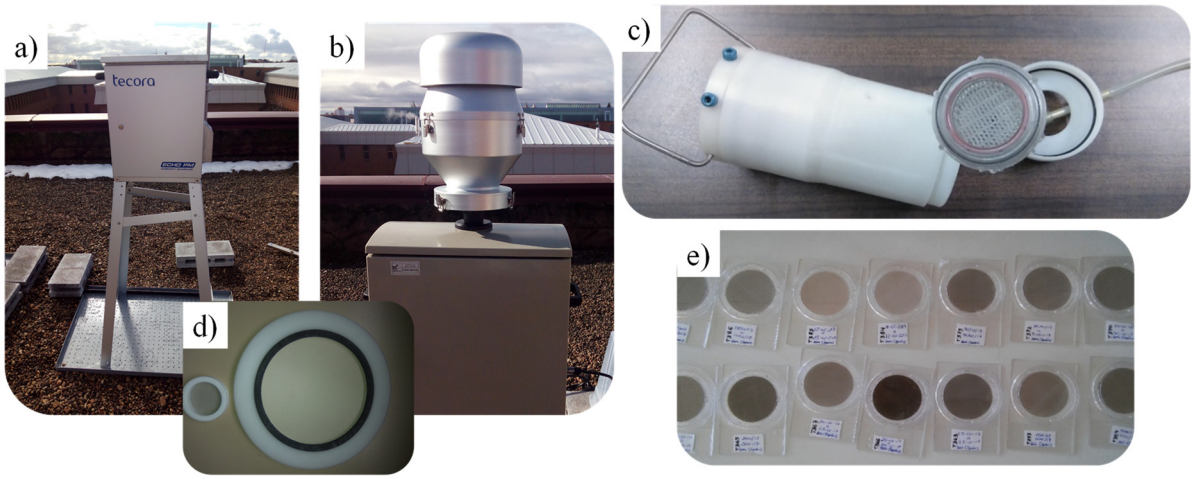

Figura 3.10. a) Colector de bajo volumen TECORA; b) colector de alto volumen CAV; c) colector de bajo volumen GENT; d) filtro muestreado de cuarzo (CAV) y de teflón (TECORA); e) muestras diarias de filtros de teflón recogidas mediante el colector TECORA.

En cuanto a los bioaerosoles, se utilizaron dos captadores que se describen a continuación:

- Un captador volumétrico de tipo *Hirst* (Hirst, 1952) (Figura 3.11a) con un flujo volumétrico de 0.06 m^3 h^{-1}. En las muestras recogidas en una cinta Melinex se realizaron conteos horarios y diarios mediante microscopio óptico, siguiendo la metodología recomendada por la Red Española de Aerobiología (Soldevilla et al., 2007), que cumple el Estándar Europeo 2018 CEN FprEN 16868:2018 E. Los análisis se realizaron con un microscopio óptico de 40x (400 aumentos). Se analizaron cuatro bandas longitudinales de 48 x 12 mm^2 de área y el análisis supone el 12% de esa superficie. A partir de estos análisis se determinó la concentración de 54 tipos de polen: *Acer*, *Aesculus*, *Ailanthus*, *Alnus*, Apiaceae, *Artemisia*, Asteraceae, *Betula*, Brassicaceae, Campanulaceae, *Carpinus*, *Castanea*, *Cedrus*, *Corylus*, Cupresaceae, Cyperaceae, Chenopodiaceae, *Echium*, Ericaceae, Fabaceae, *Fagus*, *Fraxinus*, *Galium*, *Helianthus*, *Juglans*, Juncaceae, Lamiaceae, *Ligustrum*, *Mercurialis*, *Morus*, Myrtaceae, *Olea*, Oleaceae, *Papaver*, *Pinus*, *Plantago*, *Platanus*, Poaceae, Polygonaceae, *Populus*, *Quercus*, *Quercus pyrenaica*, *Quercus rotundifolia*, Rosaceae, *Rumex*, *Salix*, *Sambucus*, Scrophulariaceae, *Sedum*, *Taraxacum*, *Tilia*, *Ulmus*, Urticaceae y *Typha*.
- Un captador ciclónico de bajo volumen Burkard Multi-Vial Cyclone (Burkard Manufacturing Co. Ltd.) (Figura 3.11b) con un flujo volumétrico de 0.99 m^3 h^{-1}. Las muestras se recogieron en seco cada 24 horas en un vial Eppendorf de 1.5 ml. Posteriormente se almacenaron a -20 ºC hasta el posterior análisis de la fracción alergénica del aerosol atmosférico.

a) b)

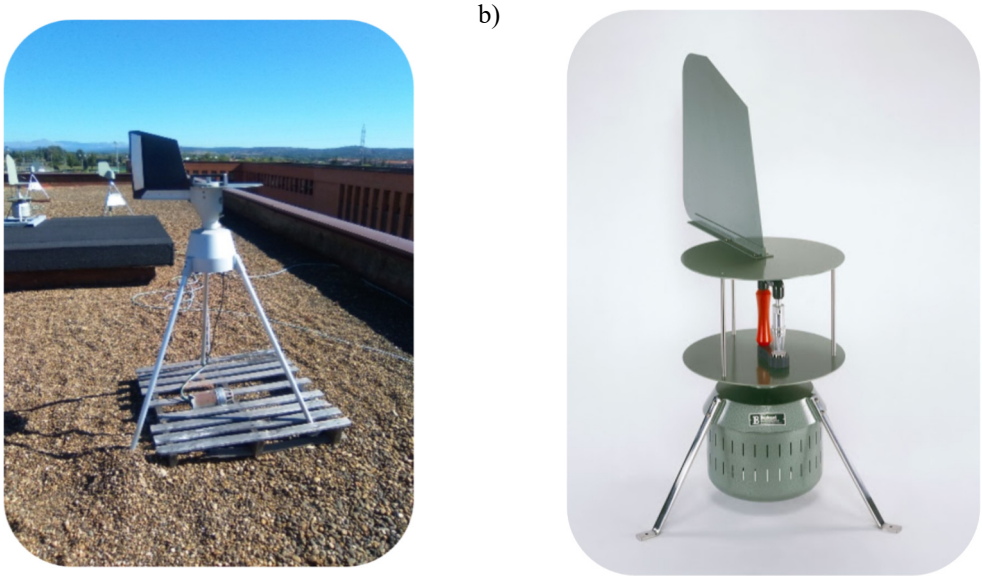

Figura 3.11. a) Captador volumétrico de tipo *Hirst*; b) colector de bajo volumen de la fracción alergénica.

3.3.7. MEDIDORES DE GASES

Para medir la concentración de determinados gases contaminantes se utilizaron dos equipos diferentes:

- Un monitor automático de infrarrojos Gray Wolf (WolfSense IQ-610) (Figura 3.12a) fue utilizado para medir continuamente la concentración de CO, CO_2, NO y compuestos orgánicos volátiles (VOCs). También proporciona otras variables ambientales como la temperatura y la humedad relativa. El equipo fue calibrado y comparado con un equipo de medición de calidad del aire de TSI modelo 7525.
- Tres monitores portátiles Aeroqual Serie 500 fueron utilizados para medir la concentración de O_3, NO_2 y SO_2 (Figura 3.12b). Este equipo funciona mediante sensores electroquímicos en el rango de 0-1 ppm para el NO_2, entre 0-500 ppm para el O_3 y entre 0-100 ppm para el SO_2, siendo calibrados por comparación con un analizador UV fluorescente certificado. Más información acerca de su funcionamiento puede encontrarse en Masey et al. (2018).

a) b)

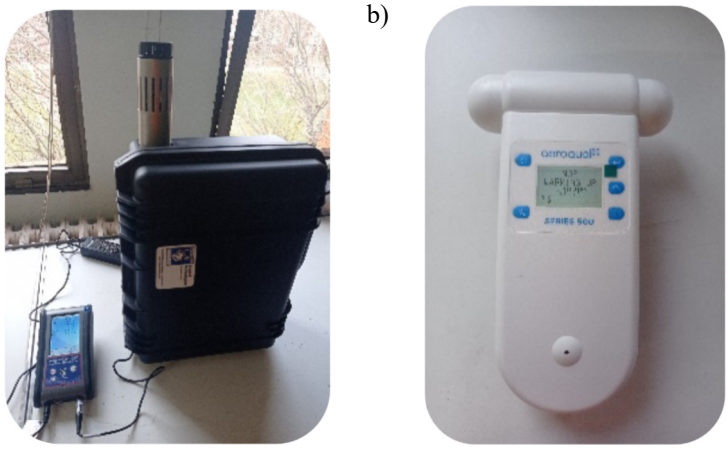

Figura 3.12. a) Monitor automático de infrarrojos de Gray Wolf (WolfSense IQ-610); b) Monitor Aeroqual serie 500.

Cabe destacar que estos equipos no estuvieron en funcionamiento durante la campaña principal de medida. Sin embargo, sí se han utilizado en muestreos puntuales en el desarrollo de la tesis, como en el artículo incluido en el ***Capítulo 8*** "Aethalometer measurements in a road tunnel: A step forward in the characterization of black carbon emissions from traffic".

3.3.8. VARIABLES METEOROLÓGICAS

Las variables meteorológicas en superficie se registraron cada minuto a través de una estación meteorológica Davis (Figura 3.13). Las principales variables fueron: temperatura (°C), humedad relativa (%), presión (hPa), velocidad (m s^{-1}) y dirección del viento. Otros datos fueron suministrados por la Agencia Estatal de Meteorología, como la radiación solar diaria (kJ m^{-2}) registrada en la estación situada en La Virgen del Camino, a 7 km del punto de muestreo.

Figura 3.13. Estación meteorológica Davis situada en la terraza de la Facultad de Veterinaria.

Las variables meteorológicas en altura se obtuvieron de los radiosondeos suministrados por el modelo READY (https://www.ready.noaa.gov/READYamet.php) de la *National Oceanic and Atmospheric Administration* (NOAA) sobre la ciudad de León cada 3 horas. A partir de tales radiosondeos se obtuvo la evolución de la altura de la capa límite (ABL).

3.4. ANÁLISIS POST-MUESTREO

Tras la campaña de muestreo se llevaron a cabo los análisis químicos de las muestras de aerosol y precipitación recolectadas. Su caracterización química estuvo conformada por los análisis de:

- Filtros de cuarzo de PM_{10}: análisis de carbono orgánico y elemental mediante un método termo-óptico (apartado 3.5.1) y análisis de azúcares solubles en agua por cromatografía iónica (apartado 3.5.4).
- Filtros de teflón de PM_{10}: análisis de iones inorgánicos solubles en agua por cromatografía iónica (apartado 3.5.2) y análisis de metales traza por el método PIXE (apartado 3.5.3).
- Filtros de policarbonato de PM_{10}: análisis de la composición elemental y la morfología de las partículas por Microscopía Electrónica de Barrido por Emisión de Campo (apartado 3.5.5).
- Filtros de cuarzo de PM contenido en la lluvia: análisis de carbono orgánico y elemental mediante un método termo-óptico del carbono insoluble en el agua de lluvia (apartado 3.5.1)
- Muestras de lluvia: determinación del carbono orgánico disuelto (DOC) mediante un método termo-óptico (apartado 3.5.1) y análisis de los iones solubles en agua por cromatografía iónica (apartado 3.5.2).

Además, durante el muestreo y tras él, se realizó el tratamiento de datos de los equipos de medición continua y su aplicación en diferentes modelos. A continuación, se describen detalladamente los análisis químicos y los modelos llevados a cabo.

3.4.1. CARBONO ORGÁNICO Y ELEMENTAL

El Carbono Orgánico (OC) y el Carbono Elemental (EC) presente en los filtros de cuarzo de PM_{10} muestreados y en los filtros de cuarzo de precipitación (fracción insoluble del carbono) se analizaron mediante los equipos ubicados en el Departamento de Medio Ambiente de la Universidad de Aveiro (Portugal). La masa de Carbono Total (TC) fue obtenida aplicando un método de Transmitancia Termo-Óptica (TOT) que permite la separación del OC y del EC.

El equipo de análisis está formado por un tubo de cuarzo con dos zonas de calentamiento, un láser analizador de CO_2 por infrarrojo no dispersivo (Figura 3.14) y que fue calibrado con corrientes de CO_2 a 45.81 y 349.5 ppm. Para el análisis de los filtros se tomaron muestras de 9 mm de diámetro. Tanto la técnica como el equipo utilizado están descritos en Pio et al. (2011), Castro et al. (1999) y Oduber (2020).

También se analizó el Carbono Orgánico Disuelto (DOC) contenido en las muestras de precipitación mediante un analizador de carbono orgánico total Shimadzu (TOC-V CPH) basado en la combustión y detección infrarroja. El equipo se encuentra en el Departamento de Química de la Universidad de Aveiro (Portugal). Además, una alícuota del agua recolectada se utilizó para medir su pH y conductividad durante la hora siguiente a su recogida mediante un equipo Hach, HQ 40d multi.

La preparación de las muestras de agua consistió en la adición de HCl disuelto, a la vez que se burbujeaba con N_2 para acidificar la muestra. Así, el carbono inorgánico se convierte en CO_2 y la concentración de carbono total que se analizará en el equipo corresponde con el DOC. Una descripción detallada del funcionamiento del equipo puede encontrarse en Oduber (2020).

a)

b)

c)

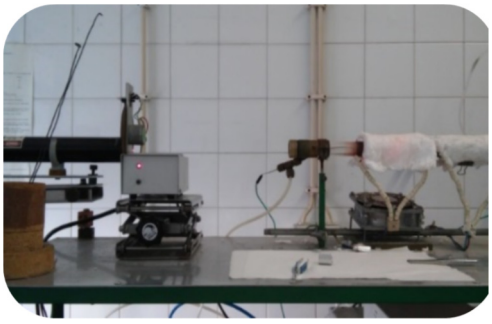

Figura 3.14. Equipo de análisis de carbono. a) Analizador-detector de CO_2/H_2O; b) Controlador de temperatura; c) Láser (He Ne) y ventilador (BOCHEM DON 12897).

3.4.2. IONES Y AZÚCARES: CROMATOGRAFÍA IÓNICA

Los iones inorgánicos solubles en agua presentes en los filtros de teflón y en las muestras de lluvia fueron analizados por cromatografía iónica (CI). Los iones inorgánicos fueron extraídos de los filtros de teflón mediante dos agitaciones ultrasónicas de 15 minutos cada una en 6 ml de agua milli-Q. Tanto estos extractos como las muestras de lluvia se filtraron con jeringas de PTFE (Politetrafluoroetileno) con filtros de poro de 0.2 µm y transferidos a viales de vidrio. El equipo utilizado para el análisis fue un cromatógrafo Thermo Scientific DionexTM ICS-5000 con una columna analítica de intercambio iónico CarboPac® PA-1, situado en el Centro de Estudios Ambientales y Marinos de la Universidad de Aveiro (Portugal).

La concentración de los cationes Li^+, Na^+, K^+, NH_4^+, Mg^{2+} y Ca^{2+} se determinó usando una columna IonPac® CS16 y el eluyente fue una solución de 30 mM de ácido metanosulfónico (0.36 ml min^{-1}). La concentración de los aniones Br^-, Cl^-, F^-, SO_4^{2-}, PO_4^{2-}, NO_2^- y NO_3^- fue determinada con una columna IonPac® AS11 y el eluyente fue una solución de 30 mM de Hidróxido de Potasio (0.20 ml min^{-1}). La concentración iónica se calculó mediante curvas de calibración obtenidas a partir de las concentraciones de las soluciones patrón.

La misma metodología, pero utilizando una columna analítica de intercambio iónico CarboPac® PA-1, se utilizó para el análisis de 17 azúcares presentes en los filtros de cuarzo de PM_{10}. Para ello, se llevó a cabo la extracción de los azúcares solubles en agua de un área de 14.14 cm^2 de filtro, mediante agitación ultrasónica (2·15 minutos) y se extrajeron en 3 ml de agua milli-Q. La técnica y la metodología utilizada detallada aparece en Oduber (2020) y Creatchman y Landsberger (1999).

3.4.3. ELEMENTOS TRAZA

La determinación de los elementos traza con número atómico mayor a 10 (desde Na a U) se realizó mediante la técnica de emisión de rayos X inducida por partículas, denominada PIXE (*Particle-Induced X-ray Emission*), siguiendo la metodología descrita por Lucarelli et al. (2015). Esta técnica es no destructiva y no requiere ningún tratamiento previo sobre la muestra, en este caso la mitad del filtro de teflón. Los análisis se realizaron en el acelerador Tandetron 3MV situado en el Instituto Nacional de Física Nuclear (INFN-LABEC) de Florencia (Italia) (Figura 3.15).

Figura 3.15. Acelerador Tandetron 3MV situado en el Instituto Nacional de Física Nuclear (INFN-LABEC) de Florencia (Italia). Fuente: INFN/L.

El análisis se basa en la excitación de los electrones de las capas internas de los átomos provocado por el choque de protones energéticos causando vacantes. Ello provoca una emisión de rayos X proporcional a la masa del elemento contenido en la muestra. Una descripción más detallada del análisis y del equipo puede encontrarse en Lucarelli et al. (2014, 2015) y Oduber (2020).

3.4.4. MORFOLOGÍA Y COMPOSICIÓN: MICROSCOPÍA

La morfología y la composición de partículas individuales recogidas en filtros de policarbonato se analizó mediante la técnica de Microscopía Electrónica de Barrido (MEB). Los análisis se realizaron en la Universidad de Alcalá, en Alcalá de Henares (España), con un Microscopio Electrónico Hitachi TM-100 (composición) y un Microscopio Electrónico de Barrido DSM950 (obtención de imágenes) (Figura 3.16).

El Microscopio Electrónico Hitachi TM-100 permitió la obtención de la composición química (desde C a U) de partículas individuales presentes en la muestra. Su funcionamiento está basado en la excitación de los átomos de la muestra por los electrones incidentes, provocando una emisión de rayos X a una longitud de onda característica de los elementos presentes. Esta emisión es analizada mediante un software que permite finalmente identificar el elemento y su concentración en la muestra.

El Microscopio Electrónico de Barrido DSM950 permitió la obtención de imágenes de las partículas contenidas en la muestra, al ser recorrida por un haz concentrado de electrones, que son dispersados por la muestra, creando así una imagen ampliada de la misma. Las muestras fueron previamente colocadas en un portamuestras de grafito y recubierto de oro.

a) b)

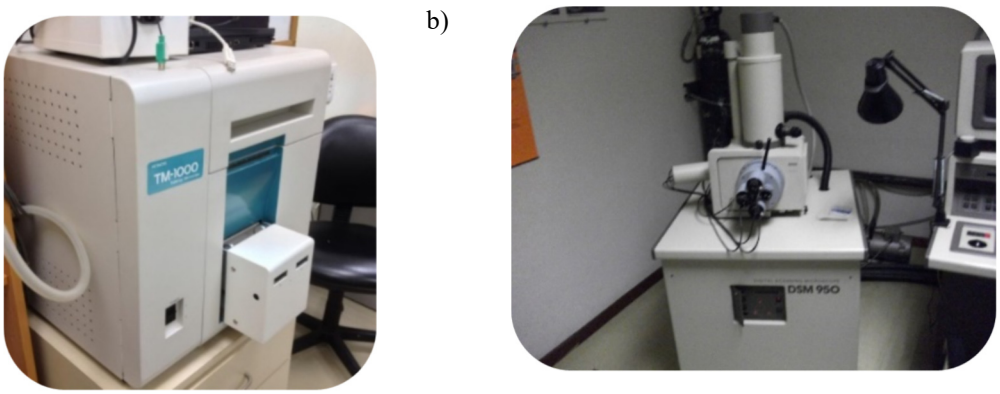

Figura 3.16. a) Microscopio Electrónico Hitachi TM-100; b) Microscopio Electrónico de Barrido DSM950.

3.5. MODELOS Y HERRAMIENTAS

Varias herramientas estadísticas y diferentes modelos han sido aplicados para el análisis de los datos. El forzamiento radiativo causado por el aerosol atmosférico fue estimado mediante el modelo GAME (apartado 3.5.1), cuya descripción detallada se encuentra en el ***Capítulo 11***, donde se incluye el artículo titulado " Links between aerosol radiative forcing and rainwater: stratiform and convective precipitation". Para establecer diferencias estadísticamente significativas entre grupos de datos se aplicaron diferentes análisis estadísticos (apartado 3.5.2). Además, diferentes herramientas y modelos se han utilizado para la determinación del origen de las masas de aire (apartado 3.5.3). Por último, se incluye el modelo para el cálculo de la fracción de aerosol atmosférico respirable por el ser humano (apartado 3.5.4).

3.5.1. FORZAMIENTO RADIATIVO: MODELO GAME

El efecto de las partículas de aerosol atmosférico y los gases en el clima se cuantifica mediante la evaluación del forzamiento radiativo, que puede ser: i) forzamiento radiativo directo del aerosol, mediante la dispersión y absorción de la radiación solar y terrestre dependiendo de su composición química y física (Charlson et al., 1992); ii) forzamiento radiativo indirecto del aerosol, actuando como CCN o IN, provocando un cambio en las propiedades microfísicas de las nubes o por ejemplo el efecto de calentamiento causado en el hielo y la nieve por la deposición del BC en su superficie; iii) efecto semidirecto, que es la cuantificación del efecto de calentamiento o enfriamiento que tiene el efecto directo sobre la termodinámica de la atmósfera,

lo cual modula la abundancia de núcleos de condensación en las nubes, la distribución del tamaño de las gotas y las propiedades de las nubes (albedo, reflectividad, etc.) (Bond et al., 2013a; Rosenfeld et al., 2014). Este efecto modifica la lluvia y la temperatura en la superficie terrestre (Bollasina et al., 2011; Menon et al., 2002).

El modelo de transferencia radiativa GAME (*Global Atmospheric ModEL*) fue aplicado a los datos del periodo de muestreo en la ciudad de León y permite estimar el forzamiento radiativo directo instantáneo de onda corta provocado por el aerosol en cielo despejado. Se utilizaron las propiedades ópticas del aerosol atmosférico junto con los perfiles verticales de temperatura, ozono y humedad relativa. Una descripción detallada del modelo puede encontrarse en Dubuisson et al. (2004) y Roger et al. (2006). A continuación, se describe brevemente el procedimiento llevado a cabo para la aplicación del modelo.

GAME tiene en cuenta la capacidad de dispersión y absorción de partículas y gases. Los cálculos de transferencia radiativa dependen de los parámetros ópticos del aerosol, como el espesor óptico del aerosol (AOT), el albedo de dispersión simple (*single scattering albedo*, SSA) y el parámetro de asimetría (g). En este estudio, las estimaciones de estos parámetros ópticos se basaron en la teoría de Mie, considerando la distribución del tamaño del aerosol junto con el índice de refracción. Así pues, se calcularon los perfiles de SSA, g y del coeficiente de extinción a las siete longitudes de onda utilizadas (0.48, 0.55, 0.65, 0.87, 1.24, 1.65 y 2.13 µm).

Los perfiles verticales de las propiedades atmosféricas se obtuvieron cada 3 horas a través de los radiosondeos disponibles en la NOAA. Para obtener las propiedades ópticas, se estimó un índice de refracción mensual a partir de la composición química del aerosol conocida mediante el análisis de los filtros de cuarzo y teflón muestreados. El espesor óptico del aerosol y el albedo de la superficie se obtuvieron de los fotómetros AERONET (*AErosol RObotic NETwork*) en Palencia (41° 9' N, 4° 7' W) y Valladolid (41° 7' N, 4° 7' W), lugares situados a unos 120 km de León. AERONET es una base óptica basada en una red de monitoreo de aerosoles y un archivo de datos respaldado por el Sistema de Observación de la Tierra de la NASA y ampliado por federación con muchas instituciones que no son de la NASA (http://aeronet.gfsc.nasa.gov).

Los flujos radiativos netos hacia arriba y hacia abajo, en el espectro solar desde 2500 a 50000 cm^{-1}, con una resolución espectral de 100 cm^{-1}, se calcularon sobre toda la región de onda corta y se realizaron cada 3 h (0600, 0900, 1200, 1500 y 1800 UTC). A partir de estos flujos, se calculó el forzamiento directo en la base de la atmósfera (ΔF_{BOA}) y en la parte superior de la atmósfera (ΔF_{TOA}) (Eqs. 3.10 y 3.11).

$$\Delta F_{BOA} = F_{BOA}(w)\downarrow - F_{BOA}(o)\downarrow \qquad \textit{Eq. 3.10}$$

$$\Delta F_{TOA} = -(F_{TOA}(w)\uparrow - F_{TOA}(o)\uparrow) \qquad \textit{Eq. 3.11}$$

donde $F_{BOA}(w)\downarrow$ y $F_{BOA}(o)\downarrow$ son los flujos radiativos netos descendentes simulados en la superficie con *(w)* y sin *(o)* aerosoles, respectivamente. Igualmente, $F_{TOA}(w)\uparrow$ y $F_{TOA}(o)\uparrow$ son los flujos radiativos netos ascendentes simulados en la parte superior de la atmósfera con (*w*) y sin (*o*) aerosoles, respectivamente. Por lo tanto, un signo positivo de ΔF implica un efecto de calentamiento. El forzamiento atmosférico, ΔF_{ATM}, se calculó utilizando la Eq. 3.12 y representa la absorción de la radiación solar debido a las propiedades de absorción de partículas dentro de la capa atmosférica (desde la superficie hasta 20 km). Además, se estimó el calentamiento asociado (K día^{-1}) provocado por estos aerosoles para cuantificar el calentamiento potencial en toda la columna atmosférica.

$$\Delta F_{ATM} = \Delta F_{TOA} - \Delta F_{BOA} \qquad \textit{Eq. 3.12}$$

3.5.2. HERRAMIENTAS ESTADÍSTICAS

Los análisis estadísticos se llevaron a cabo mediante dos programas: el software SPSS Statistics versión 24 (IBM) y el software R versión 3.5.3. (The R Project for Statistical Computing). Los principales análisis llevados a cabo fueron:

- El test no-paramétrico de Kruskal-Wallis para la evaluación de las diferencias estadísticamente significativas entre *k* muestras independientes de datos analizando si provienen o no de la misma población.
- La prueba U de Mann-Whitney para la determinación de diferencias estadísticamente significativas entre *k* grupos de datos de diferentes poblaciones.
- El coeficiente de correlación lineal de Pearson para la determinación de una posible relación lineal significativa entre dos variables continuas.
- La regresión lineal múltiple para la generación de un modelo lineal, donde el valor de la variable dependiente (y_i) se determina a partir de dos o más variables (x_{1i}, x_{2i}, x_{3i}…) independientes entre sí (Eq. 3.13). Las condiciones para llevar a cabo la regresión lineal múltiple son la no colinealidad entre las variables independientes, la homocedasticidad y la normalidad de los residuos.

$$y_i = (\beta_0 + \beta_1 x_{1i} + \beta_2 x_{2i} + \beta_3 x_{3i} + \cdots + \beta_n x_{ni}) + e_i \qquad \textit{Eq. 3.13}$$

siendo β_0 la ordenada en el origen, β_i el coeficiente parcial de la regresión para cada variable independiente sobre la variable dependiente y e_i el residuo, o sea, la diferencia entre el valor estimado por el modelo y el valor real observado.

- La realización de *Polar plots* a través del paquete Openair en el *software* R que permiten la visualización de un parámetro (p.ej., la concentración de un contaminante en un punto concreto) en función de la dirección y velocidad del viento y, como resultado, el modelo matemático proporciona una superficie continua de concentración del parámetro seleccionado, permitiendo conocer la dirección de procedencia del mismo.

3.5.3. HERRAMIENTAS ADICIONALES

Para la determinación del origen de las masas de aire, los tipos de tiempo y el estado de la atmósfera fueron utilizados diferentes modelos, así como imágenes de satélites meteorológicos, que a continuación se describen brevemente.

HYSPLIT-Retrotrayectorias de masas de aire

Se calcularon las retrotrayectorias de las masas de aire, cuatro días atrás, a diferentes alturas (500, 1000, 1500 y 3000 m sobre el nivel del mar) mediante la aplicación del modelo HYSPLIT (*Hybrid Single Particle Lagrangian Integrated Trajectory*) (Draxler and Rolph, 2012) de la NOAA que posibilita llevar a cabo simulaciones del transporte, dispersión y depósito de contaminantes a gran escala. Posteriormente se analizaron las retrotrayectorias para determinar el origen de las masas de aire presentes en León. El modelo se ejecutó con datos meteorológicos de los archivos del *Global Data Assimilation System* (GDAS) (http://ready.arl.noaa.gov/HYSPLIT_traj.php). Las retrotrayectorias fueron descargadas diariamente como archivos *shapefile* y mediante el software ArcMap 10.4.1 fueron agrupadas. Basado en las retrotrayectorias a 1000 m (representativa de la capa de mezcla en la ciudad de León) se realizó una clasificación de seis grupos en función del origen de la masa de aire predominante. El grupo asignado fue aquel en el que la retrotrayectoria pasó la mayor parte del tiempo. Los seis grupos se muestran en la Figura 3.17 y son: Grupo I-Región Ártica, Grupo II-Océano Atlántico, Grupo III-Continental europeo, Grupo IV-América del Norte, Grupo V-Océano Atlántico Norte y Grupo VI-Desierto del Sáhara.

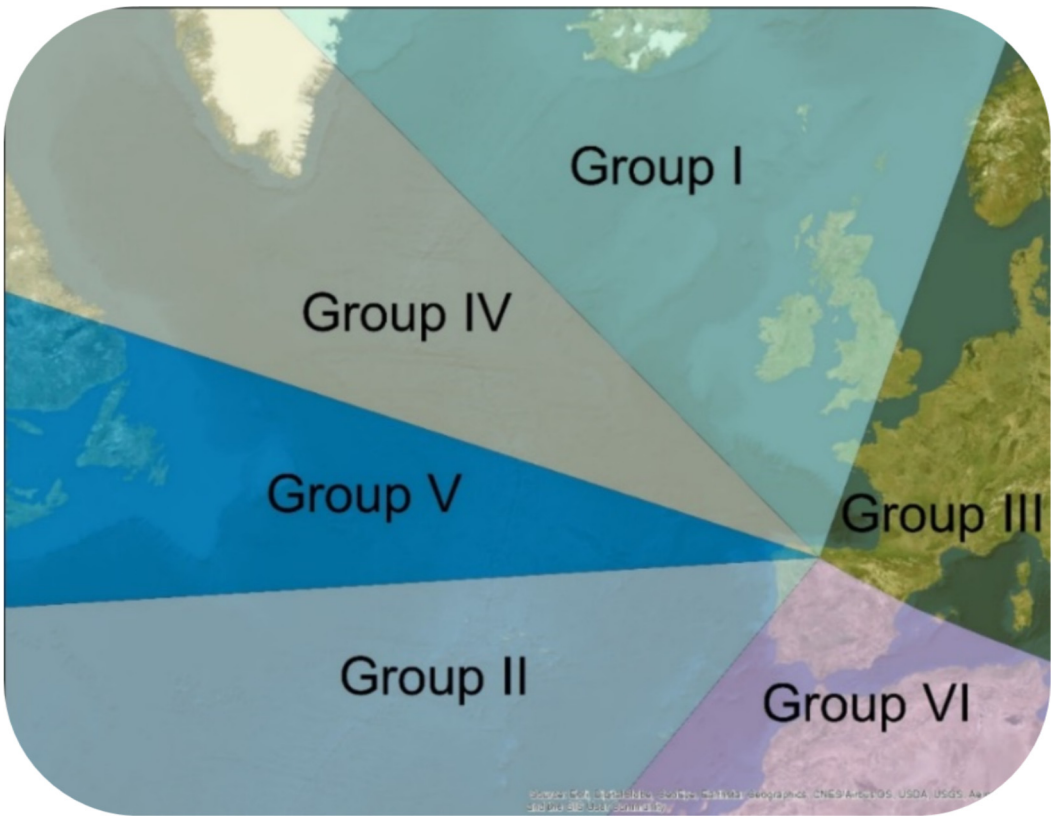

Figura 3.17. Delimitación de regiones para la determinación del origen de las masas de aire: I-Región Ártica, II-Océano Atlántico, III Continental europeo, IV-América del Norte, V-Océano Atlántico Norte y VI-Desierto del Sáhara.

Tipos de tiempo de Lamb

Los tipos de tiempo o *Circulation Weather Types* (CWTs) se clasificaron de acuerdo con Lamb (1972), para identificar un tipo de tiempo con una situación sinóptica determinada. Se aplicó el mismo método que el utilizado en Calvo et al. (2012) y Russo et al. (2014). El modelo está basado en una serie de índices sobre la dirección y vorticidad del flujo geostrófico, obtenidos para 16 puntos de una red distribuidos en torno a la Península Ibérica (Trigo and DaCamara, 2000) (Figura 3.18). Los valores de presión se descargaron del *National Center for Atmospheric Research* (NCAR) que posibilita la descarga de datos en intervalos de 5° de latitud y 5° de longitud en el hemisferio norte. Los índices son: flujo del sur (SF), flujo del oeste (WF), flujo total (F), vorticidad de corte del sur (ZS), vorticidad de corte del oeste (ZW) y vorticidad de corte total (Z). A partir de ellos se establecen 26 CWTs (Tabla 3.6) de los cuales 8 son *Puros Direccionales*, 2 son *Puros No direccionales* y 16 son *Híbridos* entre los tipos direccionales y no direccionales. Una explicación detallada de esta clasificación puede encontrarse en Trigo y DaCamara (2000).

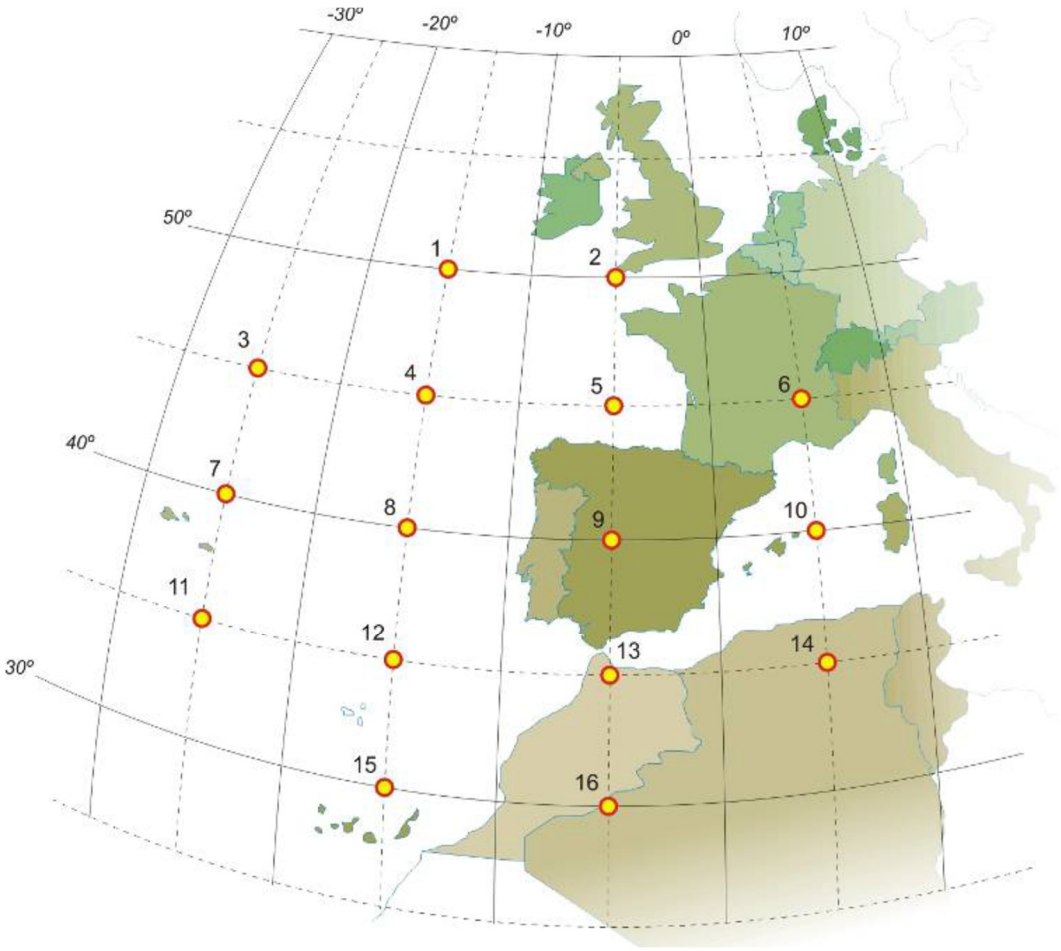

Figure 3.18. Red de puntos de presión sobre la Península Ibérica (Fernández-Raga, 2009).

Tabla 3.6. Clasificación de tipos de tiempo (CWTs) de acuerdo a Trigo y DaCamara (2000).

Puros No Direccionales	Puros Direccionales	Híbridos	
		Anticiclónicos	Ciclónicos
A (Anticiclónico)	N (Norte)	AN	CN
C (Ciclónico)	NE (Nordeste)	ANE	CNE
	E (Este)	AE	CE
	SE (Sureste)	ASE	CSE
	S (Sur)	AS	CS
	SW (Suroeste)	ASW	CSW
	W (Oeste)	AW	CW
	NW (Noroeste)	ANW	CNW

3.5.4. FRACCIONES INHALABLE, TORÁCICA Y RESPIRABLE

Las fracciones de aerosol que alcanzan cada parte del aparato respiratorio se estimaron siguiendo la metodología reflejada en la Norma UNE 77213: *Calidad del aire. Definiciones de las fracciones de los tamaños de partículas para el muestreo asociado a problemas de salud*, equivalente a la Norma ISO 7708:1995 *Air quality: particle size fractions definitions for health-related sampling.* Cabe destacar que se estima la masa de partículas de aerosol que alcanza cada zona del aparato respiratorio, pero no la cantidad depositada. La masa de partículas de aerosol fue calculada mediante las distribuciones de tamaño del número de partículas obtenidas a través de los espectrómetros SMPS y/o PCASP-X, teniendo en cuenta sus diámetros aerodinámicos y ópticos, respectivamente, y usando la densidad estimada a partir de los análisis químicos diarios de los filtros de teflón y cuarzo.

En la Norma ISO 7708:1995 se definen las diferentes regiones del tracto respiratorio alcanzadas por las fracciones de masa de partículas de aerosol atmosférico en función de su tamaño (Figura 3.19):

- Fracción inhalable: aquellas que se inhalan por la nariz y la boca.
- Fracción extratorácica: aquellas que se retienen en la región respiratoria anterior a la laringe.
- Fracción torácica: aquellas inhaladas capaces de penetrar más allá de la laringe. Son aquellas equivalentes al porcentaje de la fracción inhalable de una distribución log-normal acumulativa con una mediana de 11.64 µm y una desviación estándar geométrica de 1.5.
- Fracción traqueobronquial: aquellas inhaladas que pueden atravesar la laringe, pero no pueden atravesar las vías respiratorias no ciliadas.
- Fracción respirable: aquellas inhaladas que penetran en las vías respiratorias no ciliadas llegando a la fracción alveolar (bronquiolos y alveolos). Son aquellas equivalentes al porcentaje de la fracción inhalable de una distribución log-normal acumulativa con una mediana de 4.25 y 2.5 µm y una desviación estándar geométrica de 1.5, para individuos sanos y de alto riesgo, respectivamente.

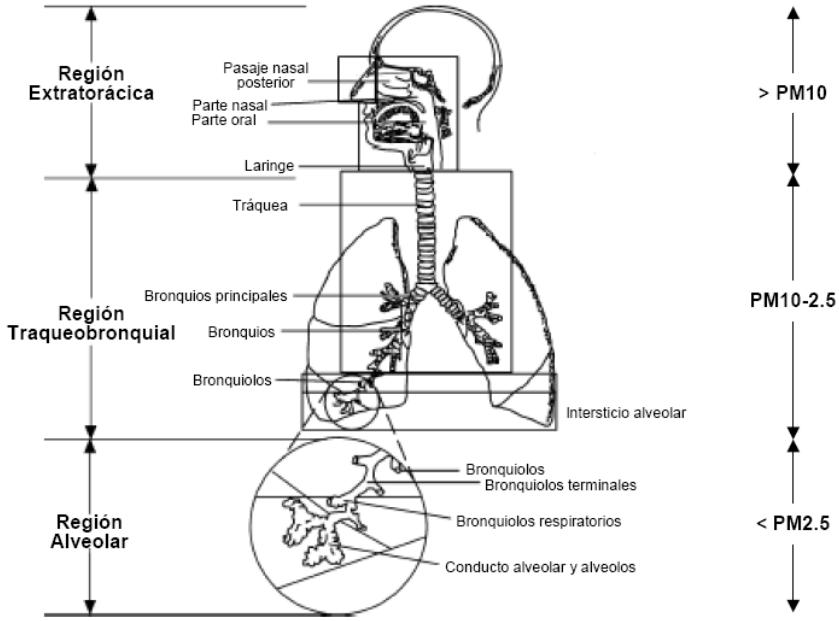

Figura 3.19. Regiones del aparato respiratorio humano en función de la llegada de material particulado según su tamaño. Imagen adaptada de EPA (2004).

3.6. REFERENCIAS

AEMET, 2020. Agencia Estatal de Meteorología Española [WWW Document]. URL http://www.aemet.es/es/portada (accessed 6.29.20).

Blanco-Alegre, C., Calvo, A.I., Coz, E., Castro, A., Oduber, F., Prévôt, A.S.H.H., Močnik, G., Fraile, R., 2019. Quantification of source specific black carbon scavenging using an aethalometer and a disdrometer. Environ. Pollut. 246, 336–345. doi:10.1016/j.envpol.2018.11.102

Bollasina, M.A., Ming, Y., Ramaswamy, V., 2011. Anthropogenic aerosols and the weakening of the south asian summer monsoon. Science (80-.). 334, 502–505. doi:10.1126/science.1204994

Bond, T.C., Doherty, S.J., Fahey, D.W., Forster, P.M., Berntsen, T., Deangelo, B.J., Flanner, M.G., Ghan, S., Kärcher, B., Koch, D., Kinne, S., Kondo, Y., Quinn, P.K., Sarofim, M.C., Schultz, M.G., Schulz, M., Venkataraman, C., Zhang, H., Zhang, S., Bellouin, N., Guttikunda, S.K., Hopke, P.K., Jacobson, M.Z., Kaiser, J.W., Klimont, Z., Lohmann, U., Schwarz, J.P., Shindell, D., Storelvmo, T., Warren, S.G., Zender, C.S., 2013. Bounding the role of black carbon in the climate system: A scientific assessment. J. Geophys. Res. Atmos. 118, 5380–5552. doi:10.1002/jgrd.50171

Brandes, E.A., Zhang, G., Vivekanandan, J., 2002. Experiments in Rainfall Estimation with a Polarimetric Radar in a Subtropical Environment. J. Appl. Meteorol. 41, 674–685. doi:10.1175/1520-0450(2002)041<0674:EIREWA>2.0.CO;2

Calvo, A.I., 2009. Caracterización y transporte del aerosol atmosférico: medio urbano, rural y quema de biomasa 137–177.

Calvo, A.I., Pont, V., Olmo, F.J., Castro, A., Alados-Arboledas, L., Vicente, A.M., Fernández-Raga, M., Fraile, R., 2012. Air masses and weather types: A useful tool for characterizing precipitation chemistry and wet deposition. Aerosol Air Qual. Res. 12, 856–878. doi:10.4209/aaqr.2012.03.0068

Castro, A., Alonso-Blanco, E., González-Colino, M., Calvo, A.I., Fernández-Raga, M., Fraile, R., 2010. Aerosol size distribution in precipitation events in León, Spain. Atmos. Res. 96, 421–435. doi:10.1016/j.atmosres.2010.01.014

Castro, L.M., Pio, C.A., Harrison, R.M., Smith, D.J.T., 1999. Carbonaceous aerosol in urban and rural European atmospheres: estimation of secondary organic carbon concentrations. Atmos. Environ. 33, 2771–2781. doi:10.1016/S1352-2310(98)00331-8

Charlson, R.J., Schwartz, S.E., Hales, J.M., Cess, R.D., Coakley, J.A., Hansen, J.E., Hofmann, D.J., 1992. Climate forcing by anthropogenic aerosols. Science (80-.). 255, 423–430. doi:10.1126/science.255.5043.423

Creatchman, M., Landsberger, S., 1999. Elemental Analysis of Airborne Particles, Advances in environmental, industrial, and process control technologies. Gordon and Breach Science Publishers, Amsterdan (Netherlands).

DGT, 2016. Informe anual-Parque vehicular por provincias en España.

Draxler, R., Rolph, G., 2012. Hysplit (Hybrid Single-Particle Lagrangian Integrated Trajectory). Silver Spring. NOAA Air Resour. Lab.

Dubuisson, P., Dessailly, D., Vesperini, M., Frouin, R., 2004. Water vapor retrieval over ocean using near-infrared radiometry. J. Geophys. Res. D Atmos. 109, 1–14. doi:10.1029/2004JD004516

EPA, 2004. Particulate Matter (PM) Air Quality Standards.

Fernández-Raga, M., Fraile, R., Keizer, J.J., Varela Teijeiro, M.E., Castro, A., Palencia, C., Calvo, A.I., Koenders, J., Da Costa Marques, R.L., 2010. The kinetic energy of rain measured with an optical disdrometer: An application to splash erosion. Atmos. Res. 96, 225–240. doi:10.1016/j.atmosres.2009.07.013

Fialho, P., Hansen, A.D.A., Honrath, R.E., 2005. Absorption coefficients by aerosols in remote areas: A new approach to decouple dust and black carbon absorption coefficients using seven-wavelength Aethalometer data. J. Aerosol Sci. 36, 267–282. doi:10.1016/j.jaerosci.2004.09.004

Hansen, A.D.A., 2005. The Aethalometer, Magee Scientific Corporation. Magee Scientific, Berkeley, CA, USA.

Hirst, J.M., 1952. An automatic volumetric spore trap. Ann. Appl. Biol. 39, 257–265. doi:10.1111/j.1744-7348.1952.tb00904.x

IDAE, 2017. Spanish Institute for Energy Diversification and Saving.

Junta de Castilla y León, 2018. Consejería de Fomento y Medio Ambiente.

Junta de Castilla y León, 2009. El carbón en Castilla y León. Junta de Castilla y León. Consejería de Economía y Empleo - Dirección General de Energía y Minas.

Junta de Castilla y León, 2008. Encuesta de hogares y medio ambiente. Castilla y León 2008. URL: http://www.jcyl.es/estadistica.

Lamb, H.H., 1972. British Isles Weather Types and a Register of the Daily Sequence of Circulation Patterns 1861-1971, Geophysical memoirs. H.M. Stationery Office.

Lucarelli, F., Calzolai, G., Chiari, M., Giannoni, M., Mochi, D., Nava, S., Carraresi, L., 2014. The upgraded external-beam PIXE/PIGE set-up at LABEC for very fast measurements on aerosol samples. Nucl. Instruments Methods Phys. Res. Sect. B Beam Interact. with Mater. Atoms 318, 55–59. doi:10.1016/j.nimb.2013.05.099

Lucarelli, F., Chiari, M., Calzolai, G., Giannoni, M., Nava, S., Udisti, R., Severi, M., Querol, X., Amato, F., Alves, C., Eleftheriadis, K., 2015. The role of PIXE in the AIRUSE project "testing and development of air quality mitigation measures in Southern Europe." Nucl. Instruments Methods Phys. Res. Sect. B Beam Interact. with Mater. Atoms 363, 92–98. doi:10.1016/j.nimb.2015.08.023

Marques, R.F. de P.V., Mello, C.R. de, Silva, A.M. da, Franco, C.S., Oliveira, A.S. de, 2014. Performance of the probability distribution models applied to heavy rainfall daily events. Ciência e Agrotecnologia 38, 335–342. doi:10.1590/s1413-70542014000400003

Masey, N., Gillespie, J., Ezani, E., Lin, C., Wu, H., Ferguson, N.S., Hamilton, S., Heal, M.R., Beverland, I.J., 2018. Temporal changes in field calibration relationships for Aeroqual S500 O3 and NO2 sensor-based monitors. Sensors Actuators, B Chem. 273, 1800–1806. doi:10.1016/j.snb.2018.07.087

Menon, S., Hansen, J., Nazarenko, L., Luo, U., 2002. Climate effects of black carbon aerosols in China and India. Science (80-.). 297, 2250–2253. doi:10.1126/science.1075159

NOAA, 2017. National Oceanic and Atmospheric Administration.

Oduber, F., 2020. Calidad del aire en León: fuentes y deposición húmeda de contaminantes biogénicos y no biogénicos. León.

Oduber, F., Calvo, A.I., Blanco-Alegre, C., Castro, A., Nunes, T., Alves, C., Sorribas, M., Fernández-González, D., Vega-Maray, A.M., Valencia-Barrera, R.M., Lucarelli, F., Nava, S., Calzolai, G., Alonso-Blanco, E., Fraile, B., Fialho, P., Coz, E., Prevot, A.S.H.H., Pont, V., Fraile, R., 2019. Unusual winter Saharan dust intrusions at Northwest Spain: Air quality, radiative and health impacts. Sci. Total Environ. 669, 213–228. doi:10.1016/j.scitotenv.2019.02.305

Oduber, F., Calvo, A.I., Castro, A., Blanco-Alegre, C., Alves, C., Calzolai, G., Nava, S., Lucarelli, F., Nunes, T., Barata, J., Fraile, R., 2021. Characterization of aerosol sources in León (Spain) using Positive Matrix Factorization and weather types. Sci. Total Environ. 754, 142045. doi:10.1016/j.scitotenv.2020.142045

Oduber, F., Castro, A., Calvo, A.I., Blanco-Alegre, C., Alonso-Blanco, E., Belmonte, P., Fraile, R., 2018. Summer-autumn air pollution in León, Spain: changes in aerosol size distribution and expected effects on the respiratory tract. Air Qual. Atmos. Heal. 5, 1–16. doi:10.1007/s11869-018-0556-6

Pio, C., Cerqueira, M., Harrison, R.M., Nunes, T., Mirante, F., Alves, C., Oliveira, C., Sanchez, A., Campa, D., Artíñano, B., Matos, M., 2011. OC / EC ratio observations in Europe : Re-thinking the approach for apportionment between primary and secondary organic carbon. Atmos. Environ. 45, 6121–6132. doi:10.1016/j.atmosenv.2011.08.045

Roger, J.C., Mallet, M., Dubuisson, P., Cachier, H., Vermote, E., Dubovik, O., Despiau, S., 2006. A synergetic approach for estimating the local direct aerosol forcing: Application to an urban zone during the Expérience sur Site pour Contraindre les Modèles de Pollution et de Transport d'Emission (ESCOMPTE) experiment. J. Geophys. Res. Atmos. 111. doi:10.1029/2005JD006361

Russo, A., Sousa, P.M., Durão, R.M., Ramos, A.M., Salvador, P., Linares, C., Díaz, J., Trigo, R.M., 2020. Saharan dust intrusions in the Iberian Peninsula: Predominant synoptic conditions. Sci. Total Environ. 717, 137041. doi:10.1016/j.scitotenv.2020.137041

Rosenfeld, D., Andreae, M.O., Asmi, A., Chin, M., de Leeuw, G., Donovan, D.P., Kahn, R., Kinne, S., Kivekäs, N., Kulmala, M., Lau, W., Schmidt, K.S., Suni, T., Wagner, T., Wild, M., Quaas, J., 2014. Global observations of aerosol-cloud-precipitation-climate interactions. Rev. Geophys. 52, 750–808. doi:10.1002/2013RG000441

Russo, A., Trigo, R.M., Martins, H., Mendes, M.T., 2014. NO2, PM10 and O3 urban concentrations and its association with circulation weather types in Portugal. Atmos. Environ. 89, 768–785. doi:10.1016/j.atmosenv.2014.02.010

Sandradewi, J, Prévôt, A.S.H., Szidat, S., Perron, N., Alfarra, M.R., Lanz, V.A., Weingartner, E., Baltensperger, U.R.S., 2008a. Using aerosol light absorption measurements for the quantitative determination of wood burning and traffic emission contribution to particulate matter. Environ. Sci. Technol. 42, 3316–3323. doi:10.1021/es702253m

Sandradewi, J., Prévôt, A.S.H., Weingartner, E., Schmidhauser, R., Gysel, M., Baltensperger, U., 2008. A study of wood burning and traffic aerosols in an Alpine valley using a multi-wavelength Aethalometer. Atmos. Environ. 42, 101–112. doi:10.1016/j.atmosenv.2007.09.034

Sandradewi, J, Prévôt, A.S.H., Weingartner, E., Schmidhauser, R., Gysel, M., Baltensperger, U., 2008b. A study of wood burning and traffic aerosols in an Alpine valley using a multi-wavelength Aethalometer. Atmos. Environ. 42, 101–112. doi:10.1016/j.atmosenv.2007.09.034

Soldevilla, C.G., González, P.C., Teno, P.A., Vilches, E.D., Rodríguez, C.A., Jesús, M., Sánchez, A., Soler, B., 2007. Manual de calidad y gestion de la red española de aerobiologia, rea 1.

Trigo, R.M., DaCamara, C.C., 2000. Circulation weather types y their influence on the precipitation regime in Portugal. Int. J. Clim. 20, 1559–1581. doi:10.1002/1097-0088(20001115)20

Weingartner, E., Saathoff, H., Schnaiter, M., Streit, N., Bitnar, B., Baltensperger, U., 2003. Absorption of light by soot particles: Determination of the absorption coefficient by means of aethalometers. J. Aerosol Sci. 34, 1445–1463. doi:10.1016/S0021-8502(03)00359-8

Wiedensohler, A., 1988. An approximation of the bipolar charge distribution for particles in the submicron size range. J. Aerosol Sci. 19, 387–389. doi:10.1016/0021-8502(88)90278-9

Wiedensohler, A., Birmili, W., Nowak, A., Sonntag, A., Weinhold, K., Merkel, M., Wehner, B., Tuch, T., Pfeifer, S., Fiebig, M., Fjäraa, A.M., Asmi, E., Sellegri, K., Depuy, R., Venzac, H., Villani, P., Laj, P., Aalto, P., Ogren, J.A., Swietlicki, E., Williams, P., Roldin, P., Quincey, P., Hüglin, C., Fierz-Schmidhauser, R., Gysel, M., Weingartner, E., Riccobono, F., Santos, S., Grüning, C., Faloon, K., Beddows, D., Harrison, R., Monahan, C., Jennings, S.G., O'Dowd, C.D., Marinoni, A., Horn, H.G., Keck, L., Jiang, J., Scheckman, J., McMurry, P.H., Deng, Z., Zhao, C.S., Moerman, M., Henzing, B., De Leeuw, G., Löschau, G., Bastian, S., 2012. Mobility particle size spectrometers: Harmonization of technical standards and data structure to facilitate high quality long-term observations of atmospheric particle number size distributions. Atmos. Meas. Tech. 5, 657–685. doi:10.5194/amt-5-657-2012

WMO, 2016. WMO/GAW Aerosol Measurement procedures guidelines and recommendations, GAW Report. Geneva, Switzerland.

Zotter, P., Herich, H., Gysel, M., El-Haddad, I., Zhang, Y., Močnik, G., Hüglin, C., Baltensperger, U., Szidat, S., Prévôt, A.S.H., 2017. Evaluation of the absorption Ångström exponents for traffic and wood burning in the Aethalometer based source apportionment using radiocarbon measurements of ambient aerosol. Atmos. Chem. Phys. 17, 4229–4249. doi:10.5194/acp-17-4229-2017

CHAPTER 4. Scavenging of submicron aerosol particles in a suburban atmosphere

Full title: Scavenging of submicron aerosol particles in a suburban atmosphere: the raindrop size factor

Published in: Environmental Pollution, 2021,281, 117271
DOI: *10.1016/j.envpol.2021.117371*

4.1. INTRODUCTION

Today air pollution is one of the main threats to human health and climate change (Fuzzi et al., 2015; Pöschl, 2005) due to anthropogenic emissions and aerosols formed via gas-to-particle conversion in the atmosphere. In this regard, atmospheric aerosols are related to respiratory and cardiovascular diseases (Dockery et al., 2007; Tang et al., 2017), mainly affecting children's health (UNICEF, 2016), and also to climate change (Seinfeld and Pandis, 2016). As a result, in 2019 air pollution was considered by the WHO the main environmental risk to human health, and it has recently been demonstrated that it is an important factor in the transmission of viruses, e.g. SARS-CoV-2 (Seminara et al., 2020). Besides, the study of air pollution, mainly in urban sites, is crucial because of its effects on many essential policies such as those related to air quality, economic activity or traffic restrictions (EEA, 2016; Kinney, 2008; Tong et al., 2017, 2016; Viard and Fu, 2015).

The analysis of the main aerosol sinks has thus become a major goal in recent years. Wet deposition, the main mechanism to remove atmospheric pollutants (Textor et al., 2006), has been studied from various standpoints, including air quality modelling (Chate, 2005; Ladino et al.,

2011; Pryor et al., 2016; Tost et al., 2006; Zhang et al., 2013), the estimation of chemical compounds deposition (Chate et al., 2011) or the estimation of aerosol particles scavenging (Andronache et al., 2006; Kulshrestha et al., 2009; Laakso et al., 2003; Paramonov et al., 2011; Zikova and Zdimal, 2016). There are two types of wet scavenging depending on where the aerosol particles are in the atmosphere: in-cloud scavenging (ICS) and below-cloud scavenging (BCS) (Ladino et al., 2011). In ICS the aerosol particles serve as cloud condensation nuclei, while in BCS (also called 'impaction scavenging' or washout) the aerosol particles are washed out by hydrometeors.

The aerosol removal process by raindrops has been widely discussed in the literature (Loosmore and Cederwall, 2004; Pilat, 1975; Rasch et al., 2000; Wang et al., 1978). The study of this relationship comprises several processes, but the three most important ones involved in BCS are: i) Brownian diffusion (for particles with diameter (d_p) <10 nm), ii) interception (for particles with d_p between 10-1000 nm) and iii) inertial impaction (for particles with d_p >1000 nm). Other mechanisms that may affect the efficiency of aerosol scavenging are thermophoresis, diffusiophoresis, electro scavenging and electrical charge effects during thunderstorms (Andronache et al., 2006; Lemaitre et al., 2020).

Several field studies and laboratory experiments of the processes listed above have determined that BCS is lower in the range of particle diameters between 0.3 and 2 μm. This interval is generally referred to as *Greenfield Gap* (Greenfield, 1957; Ladino et al., 2011; Loosmore and Cederwall, 2004; Paramonov et al., 2011; Pruppacher et al., 1983; Zikova and Zdimal, 2016). It must be emphasised that in the delimitation of this interval there is great variability between studies due to the numerous factors that influence BCS, such as aerosol particle concentration, composition, the presence of electric charges (Ladino et al., 2011) or raindrop size distribution and rainfall intensity (Zikova and Zdimal, 2016).

Generally, BCS has been estimated using two parameters: the "scavenging efficiency" *(%ΔC)*, defined as the percentage of aerosols collected by raindrops relative to initial number concentrations of aerosols in its path; and the "scavenging coefficient", λ (s^{-1}), as a "rate of aerosols washout by precipitation which varies with collection efficiency, particles and raindrop size distributions and their terminal velocities, for different particle sizes", both defined by Seinfeld and Pandis (2016).

Numerous studies have estimated these values under different meteorological conditions and for different particle sizes (Chate, 2011; Laakso et al., 2003; Mircea et al., 2000; Pryor et al., 2016; Zikova and Zdimal, 2016). Based on a sampling campaign in a boreal forest in Finland, Laakso et al. (2003) obtained a median scavenging coefficient between $7 \cdot 10^{-6}$ and $4 \cdot 10^{-5}$ s^{-1} for particle sizes between 10 and 510 nm, and found a relationship between rain intensity and λ. In

the Czech Republic, Zikova and Zdimal (2016) obtained mean values of $\%\Delta C$ during rain events between 0 and -10% in particle sizes between 10 and 800 nm.

In addition, it should be noted that there are large differences in λ estimations between laboratory and field studies, of one to two orders of magnitude smaller for particles lower than 3 μm in laboratory studies (Berthet et al., 2010; Chate, 2011). Various authors advocate the results obtained in field measurements, because they take into account uncontrollable real-world situations (Blanco-Alegre et al., 2018; Chate, 2011; Maria and Russell, 2005).

In spite of the great number of studies about BCS, there is a noticeable lack of information about the scavenging caused by different raindrop sizes on the different particle sizes, as indicated by Zhao et al. (2015), who focused on the effect of the terminal velocity of raindrops on scavenging in Lanzhou (north western China).

Nevertheless, this study focuses on BCS including the raindrop size effect. The innovative approach of this study lies in the evaluation of the effect caused by different raindrop diameters on different particle sizes, a type of information scarcely found in the scientific literature. It should be noted that our results derive from field measurements, and not from laboratory simulations. Besides, the results could be valuable to use in air quality models in the northwest of the Iberian Peninsula, an area with scarce information available about BCS.

The main aim of this study is the evaluation of BCS through the scavenging efficiency and the scavenging coefficient for nucleation (d_p <30 nm), Aitken (30 nm <d_p <100 nm) and accumulation (100 nm <d_p <1000 nm) mode particles, caused by different rainfall intensities in an urban background station. The simultaneous sampling carried out with a disdrometer (for raindrop size distribution) and a scanning mobility particle sizer spectrometer-SMPS (for aerosol size distribution) has allowed us to establish the scavenging effect caused by different raindrop sizes on the different particle sizes. Furthermore, a useful application for human health is the influence of rainfall on ultrafine and accumulation modes in the respiratory tract. It has been analysed through the study of the inhalable, thoracic, respirable and tracheobronchial fractions of aerosols that would be deposited in these regions.

4.2. MEASUREMENTS

4.2.1. SAMPLING SITE

León (42°36′N, 05°35′W) is a Spanish city located in the NW of the Iberian Peninsula (838 m a.s.l) (Figure S4.1) with a population of about 200,000 inhabitants. The area has a Mediterranean climate with continental features, but it is tempered by the Cantabrian mountain range located at 40 km from the city. León presents an annual average temperature of 11.1 °C, 13 snow days and 75 rain days, with a total mean precipitation of 515 mm concentrated in winter and spring, based on data from the past 35 years (data provided by Spanish Meteorological Agency (http://www.aemet.es)). In the city, the major sources of particulate emissions are traffic, heating devices, especially in winter, and wildfires and Saharan dust intrusions in summer (Blanco-Alegre et al., 2019; Oduber et al., 2021). The sampling was carried out between February 12, 2016 and March 14, 2017 (13 months).

The instruments were installed in the Faculty of Veterinary Sciences of the University of León, located in the NE of the city (Figure S4.1). Close to the sampling area, the main activities are commercial and residential, with no large emitting industries. Thus, it can be considered an urban background site.

4.2.2. RAIN EVENT SELECTION

The data selection was carried out in several steps:

1) Events with missing data were not considered.
2) Events were only considered when an accumulated precipitation higher than 0.4 mm was registered, the mean event precipitation intensity (total rain h^{-1}) exceeded 0.2 mm h^{-1}, similar than proposed by Laakso et al. (2003), and when there was a minimum of 60 rain-free minutes between events.
3) The events in days with New Particle Formation (NPF) bursts were discarded to avoid their influence on the scavenging caused by rain.
4) To avoid changes caused by meteorological factors other than precipitation (Hussein et al., 2006), we only considered events with variations in temperature (T), relative humidity (RH)

and wind speed (WS) below ±3.5°C, ±25% and 2 m s^{-1}, respectively, between 30-minutes before and after the rain event. These meteorological conditions, more restrictive for an extended period before and after the rain event, have been considered by other authors to avoid the influence of hygroscopic aerosol growth and meteorology on scavenging (Kyrö et al., 2009; Zhao et al., 2015).

5) The events selected should have a previous particle concentration of 200, 300 and 100 particles cm^{-3} for nucleation, Aitken and accumulation modes, respectively, to avoid events without pollution burden. These limits were selected to be 6 times lower than the annual average of each mode. In the sampling, the mean values of nucleation, Aitken and accumulation modes were, respectively, 940±950, 2000±1200 and 760±460 particles cm^{-3} during cold months (October to March) and 1600±1000, 2600±1200 and 750±400 particles cm^{-3} during warm months (April to September).
6) The selected events were classified in three groups according to precipitation intensity: <1, 1-3 and >3 mm h^{-1}.

That is the same procedure as in Blanco-Alegre et al. (2018) with the addition of the criteria of NPF events, meteorological conditions and minimum particle concentration. These factors have been added due to their eventual influence on scavenging process (Cugerone et al., 2018; Hussein et al., 2006; Kyrö et al., 2009).

Considering the general requirements mentioned above 1), 2) and 3), a total of 108 potential events were selected to conduct the study. Out of these 108 rain events, only 51 complied with the rest of the criteria 4), 5) and 6).

4.2.3. AEROSOL PARTICLE CHARACTERIZATION

A continuous monitoring of size distributions of ultrafine particles (UFP) and accumulation aerosol particles has been obtained by a scanning mobility particle sizer spectrometer (TSI-SMPS Model 3938). The SMPS system consists of a long differential mobility analyser (DMA model 3081) connected to a condensation particle counter (CPC model 3772). Before entering the SMPS, the aerosol sample flow passes through a Nafion dryer incorporated at the inlet that dries aerosol to or below 40% RH (Wiedensohler et al., 2012).

The SMPS measurements employ an electrical mobility detection technique. The dry aerosol sample passes through a bipolar charger (TSI X-Ray neutralizer). Subsequently, these particles

are classified in the DMA according to their mobility in an electrical field. Finally, the CPC counts the classified particles after growing due to the effect of butanol, generating a size distribution. The set flow ratio has been 0.3 and 3 LPM for aerosol and sheath flow, respectively. This configuration provided a complete size distribution between 14.3 and 1000 nm in 110 channels with a temporal resolution of 6 minutes. Multiple charge and diffusion corrections in the line and system were applied according to the ACTRIS SMPS standards (Wiedensohler et al., 2012). The total particle number concentration (PNC) (cm^{-3}) and the count median geometric diameter (CMGD) have been computed using AIM software.

During the sampling campaign, every 15 days the impactor of SMPS was cleaned and the SMPS flows were checked with a Gilian Gilibrator bubble flowmeter to insure the SMPS data quality.

In order to mitigate the effect of variations of PNCs in different size ranges on the scavenging role of precipitation, data were corrected following the methodology described in Blanco-Alegre et al. (2018b) based on the diurnal pattern of particle number concentration for no-rainy days.

The particle number size distribution (PNSD) of each rain event has been obtained before, during and after rainfall. The PNSD was fitted to a lognormal distribution through the sum of two or three lognormal distributions.

4.2.4. RESPIRABLE FRACTION

The inhalable, thoracic, tracheobronchial and respirable fractions were estimated using the methodology described in ISO 7708:1995 and previously applied in other studies (Alonso-Blanco et al., 2017; Castro et al., 2018, 2015; Oduber et al., 2018). The mass fractions of aerosols, estimated using a monthly density of the particles measured in León, were calculated from the diameter midpoint of each channel and the number of particles measured.

4.2.5. RAINDROP CHARACTERIZATION AND METEOROLOGICAL DATA

A Laser Precipitation Monitor (LPM) manufactured by *Thies Clima* has been used to register raindrops between 0.125-8 mm in 22 channels. The equipment measures the size of hydrometeors and the falling speed by computing the loss of the laser signal emitted (a parallel beam of 780 nm infrared light) and detected in a sampling area of 228 x 20 mm^2. A detailed description of this equipment can be found in Fernández-Raga et al. (2009). The following precipitation variables were obtained on a one-minute basis: precipitation intensity (mm h^{-1}), accumulated precipitation (mm), number of drops in every channel, drop concentration (m^{-3}), water content (total volume of drops per cubic metre (mm^3 m^{-3})), total drop section (mm^2 m^{-2}), swept volume by falling drops in every channel (mm^3 m^{-3}) and mean and standard deviation of raindrop sizes. Next to the disdrometer, a Davis weather station continuously registered T, RH, WS and wind direction (WD).

The volume $S_V(D_r)$ swept by a raindrop of size D_r is defined in Eq. 4.1 and the terminal velocity of hydrometeors was computed according to Fernandez-Raga (2011), based on Gunn and Kinzer (1949):

$$S_V(D_r) = S(D_r) \cdot U_t(D_r) \cdot t \qquad Eq.\ 4.1$$

where $S(D_r)$ is the section of raindrop (mm^2 m^{-3}), $U_t(D_r)$ is the terminal velocity of raindrops (m s^{-1}) and t is the time of sampling (60 s).

In the present study, the terminal velocity (U_t) of raindrops is considered a function of size, calculated following Eq. 4.2 proposed by Fernández-Raga et al. (2010) based on Gunn and Kinzer (1949):

$$U_t = -9.748 \cdot 10^{-4} \cdot {D_r}^4 + 0.0573 \cdot {D_r}^3 - 0.8393 \cdot {D_r}^2 + 4.7120 \cdot D_r \qquad Eq.\ 4.2$$

In order to characterize the raindrop size distribution, the gamma distribution has been used, defined as follows:

$$f(x) = \frac{\beta^{\alpha} x^{\alpha-1} e^{-\beta x}}{\Gamma(\alpha)} \qquad Eq.\ 4.3$$

where Γ is the gamma function as described in Eq. 4.4 below:

$$\Gamma(\alpha) = \int_0^\infty t^{\alpha-1} e^{-t} dt \qquad \textit{Eq. 4.4}$$

The gamma distribution relies upon two parameters: α and β, computed from the relations $\mu = \alpha / \beta$ and $\sigma^2 = \alpha / \beta^2$, where μ is the mean size of hydrometeors and σ^2 is the variance (Duhanyan and Roustan, 2011). Besides, if α>1, the mode of the gamma distribution through (α-1)/β can be calculated (Tokay et al., 2001).

4.2.6. AIR MASS ORIGIN

The NOAA HYSPLIT 4 (Hybrid Single Particle Lagrangian Integrated Trajectory) model (R Draxler and Rolph, 2012) was used to determine the air mass origin. Based on four-day back trajectories at 1000 m a.g.l. (prevailing air mass origin and transport pathway) over the sampling point, the days were classified into six categories (Arctic, Atlantic, Continental, North America, North Atlantic and Saharan) following the methodology described in Blanco-Alegre et al. (2019), where the category assigned coincides with the sector on which the air mass spent most of the time. The model was run with meteorological data from the Global Data Assimilation System (GDAS) archives (http://ready.arl.noaa.gov/HYSPLIT_traj.php).

4.2.7. SCAVENGING EFFICIENCY AND COEFFICIENT

Once the rain events were selected, the particle concentration was analysed 30 minutes before rain (t_1), as proposed by Laakso et al. (2003), during rain and 30 minutes after rain (t_2). The $\%\Delta C$ was calculated by Eq. 4.5, to evaluate the change in particle concentration (C_1 and C_2) during the period between the initial t_1 and final t_2 times moments:

$$\%\Delta C = -\left(\frac{C_2 - C_1}{C_1}\right) \cdot 100 \qquad \textit{Eq. 4.5}$$

In terms of scavenging coefficient (Eq. 4.6), the basic equation for the change of aerosol particle number concentration proposed by Seinfeld and Pandis, (2016) was used. It is common to calculate the scavenging coefficient (λ) caused by precipitation from the change in concentration of aerosol particles $C(d_p)$, which depends on aerosol size:

$$\frac{dC\,(d_p)}{dt} = -\lambda \cdot C(d_p) \qquad \textit{Eq. 4.6}$$

where d_p is the aerosol particle diameter and λ is the scavenging coefficient.

Inasmuch as aerosol particles may be scavenged by different raindrop sizes, λ can be expressed as:

$$\lambda(d_p) = \int_0^\infty \frac{\pi}{4} {D_p}^2 U_t(D_p) E(D_p, d_p) N(D_p) dD_p \qquad Eq.\ 4.7$$

where D_r is the raindrop diameter, $U_t\ (D_r)$ is the terminal velocity of the falling drop, $E(D_r,d_p)$ is the collision efficiency between the falling raindrops and aerosol particles (see Supplementary material, paragraph 6.1.) and $N(D_r)$ is the concentration of hydrometeors as a function of its size (Seinfeld and Pandis, 2016). All symbols and acronyms are listed in Table S4.1.

In this study, λ for rain is calculated using Eq. 4.8, a semi-empirical approach described in Laakso et al. (2003) and Mircea and Stefan (1998). Thus, positive values of $\%\Delta C$ and λ are indicative of effective scavenging. Eq. 4.8 is the integration of Eq. 4.6 between the instants t_1 and t_2 with aerosol particle concentrations of $C(d_p)_1$ and $C(d_p)_2$:

$$\lambda\ (d_p) = -\frac{1}{t_2 - t_1} \cdot ln\left(\frac{C(d_p)_2}{C(d_p)_1}\right) \qquad Eq.\ 4.8$$

Due to the selection criteria employed, the processes of nucleation, condensation, coagulation and hygroscopic growth of aerosols can be considered negligible during the rain events (Chate, 2005; Laakso et al., 2003). An example of $E\ (d_p, D_r)$ with a raindrop diameter of 1.125 mm is shown in Figure S4.2.

Scavenging coefficient λ (s^{-1}) was estimated for nucleation mode (λ_{nuc}), particle sizes <30 nm; for Aitken mode (λ_{Ait}), particle sizes between 30-100 nm; accumulation mode (λ_{acc}) in two groups (λ_{acc1} between 100-300 and λ_{acc2} between 300-1000 nm) and a global coefficient (λ_{global}) for the total aerosol particle distribution.

4.2.8. STATISTICAL ANALYSIS

For the statistical treatment, SPSS software (IBM Statistics Software v.24) was used. The Kruskal-Wallis (Kruskal and Wallis, 1952) one-way analysis of variance was used as a non-parametric method to test the changes in the mass respirable fraction between before and after rain of the three rainfall intensities considered in this study. Also, the Pearson's correlation coefficients between the number of raindrops of different sizes and the percentage of variation of

the number of particles per channel during rain have been calculated to analyse the influence of different raindrop sizes on different aerosol sizes.

4.3. RESULTS AND DISCUSSION

4.3.1. EVENTS CHARACTERIZATION

During the sampling campaign 103 precipitation-days were registered, with 108 potential events to analyze. From these 108 events, only 51 rain events (Figure S4.2) complied with all the selection criteria described in section 2.2. These rain events had a mean duration of 287±282 minutes (median: 195 minutes), a mean accumulated rain of 3.73±5.25 mm (median: 1.91 mm) and a mean rainfall intensity of 0.97±1.14 mm h^{-1} (median: 0.61 mm h^{-1}). These mean values are lower than those reported by other studies such as Laakso et al. (2003) or Pryor et al. (2016), but in the same order of magnitude. The month with the highest number of events (13) and the highest accumulated rainfall (81.2 mm) was February 2017. However, the month with the highest mean rain intensity (1.87 mm h^{-1}) was October 2016 and the month with the highest mean rain duration (867 min) was December 2016. In regard to meteorological conditions during rainfall, there was a mean temperature of 7.3 °C, a mean wind speed of 2.0 m s^{-1} and a mean relative humidity of 82.3%. Similar mean values were observed before rain (7.6 °C, 1.8 m s^{-1} and 78.6%) and after rain (7.4 °C, 1.8 m s^{-1} and 81.9%)

From the selected events, there was a prevalence of air masses coming from the Atlantic (41%) and the North Atlantic (25%) areas (Figure S4.3). The highest accumulated rain was registered for Arctic air masses (29.9 mm) and the highest rainfall intensity (7.2 mm h^{-1}) for North American air masses.

To check the absence of extreme meteorological conditions before rain, a comparison between the meteorological variables before rain and the monthly mean values of the same hours of those days without recorded rainfall, in a log-log plot, is shown in Figure S4.4. Wind speed is the most problematic parameter, because during rain events it varies, as observed Zhao et al. (2015). Although the fitting is not good, the influence of wind on the scavenging process is null after the selection process, as the wind values in the rain events were lower than the monthly means. In addition, events with wide variations of wind speed were discarded. The fitting of T and RH was better. Therefore, it can be deduced that the data selection carried out (with data 30 minutes before

and after rain) was appropriate to eliminate the meteorological influence on the scavenging process.

A general characterization of PNC by modes before rain is shown in Table S4.1. Before rain, the nucleation mode showed a mean concentration of 891±772 cm^{-3} with low rain intensity, 445±238 cm^{-3} with medium rain intensity and 1282±992 cm^{-3} with high rain intensity. In all rain intensities, the Aitken mode registered the highest PNC, with a maximum of 3587 cm^{-3}. The accumulation mode acc_1 (100-300 nm) presented mean concentrations ranging between 300 and 400 cm^{-3}, with a maximum of 3032 cm^{-3}. In the accumulation mode acc_2, between 300 and 1000 nm, the mean concentration did not exceed in any category 30 cm^{-3}, with a maximum in low rain intensity of 239 cm^{-3}.

4.3.2. SCAVENGING EFFICIENCY

The scavenging efficiency (*%ΔC*) was calculated for each aerosol mode (Table S4.2). The nucleation mode (28.4% of total aerosol concentration before rain) presented a mean *%ΔC* decrease of 15%. In the case of the Aitken mode (51.2% of total aerosol concentration before rain) a decrease of 4% was found. The highest values were obtained in the accumulation mode: acc_1 (19.4% of total aerosol concentration before rain) showed a *%ΔC* decrease of 22% and in acc_2, including the *Greenfield Gap*, (0.9% of total aerosol concentration before rain) decreased a 21%. In the Czech Republic, Zikova and Zdimal (2016) found in the Aitken mode a *%ΔC* similar to the one found in this study, but a low value of *%ΔC* in the accumulation mode. This fact could be related to the different range of particle sizes corresponding to the Aitken (20 to 50 nm) and accumulation (50 to 800 nm) modes used in their study.

With regard to *%ΔC* under different precipitation intensities (Figure 4.1), the rain intensities <1 mm h^{-1} caused an effective scavenging in all aerosol size fractions considered in this study. *%ΔC* was higher for nucleation-mode particles (17%) than in the Aitken mode (4%) and the two ranges considered in the accumulation mode acc_1 and acc_2 were 17 and 11 %, respectively. Regarding the intensities between 1-3 mm h^{-1}, the highest *%ΔC* occurred on acc_1 (21%) and, Aitken and nucleation modes did not show an effective scavenging. The highest *%ΔC* values were obtained when intensities >3 mm h^{-1} occurred, with mean *%ΔC* values of 62, 62, 62 and 52% in nucleation, Aitken, acc_1 and acc_2 modes, respectively. Thus, the effect of rainfall was different according to aerosol particle sizes and rain intensity.

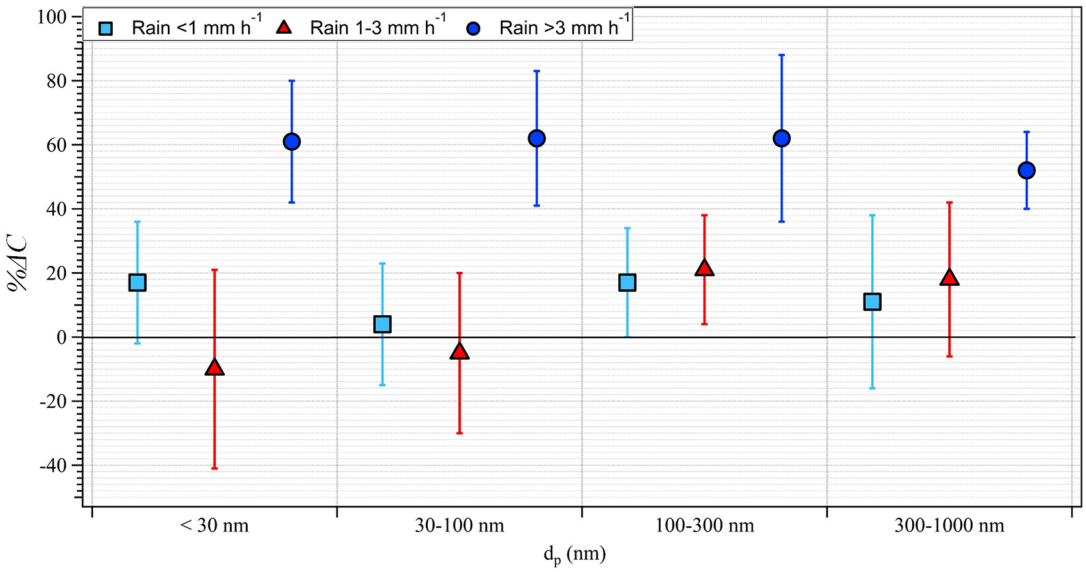

Figure 4.1. The mean *%ΔC* values in aerosol concentrations between before and after rain (markers), and the standard deviation (bars). Positive values are indicative of an effective scavenging.

Changes in PNSD between before, during and after rain have also been analysed. Without rain, along the year, the aerosol size distribution is bimodal, with the peaks in 20.1 and 73.5 nm. Peaks obtained from log-normal fitting of the PNSD for different rain intensities have been compiled in Table S4.3. During rain (Figure 4.2), a bimodal aerosol size distribution was observed for all rainfall intensities, and most of aerosol sizes presented a lower number of particles after rain than before rain. It must be emphasised that with rainfall intensities <3 mm h^{-1}, there was a slight increase in the concentration of aerosols of sizes between 40 and 60 nm. With intensities >3 mm h^{-1}, the aerosol concentration before rain was higher in the Aitken mode, with a clear scavenging in all particle sizes >20 nm, related with the higher terminal velocities of drops (Paramonov et al., 2011). The modal peaks between before and after rain decreased with rain intensities <1 mm h^{-1}.

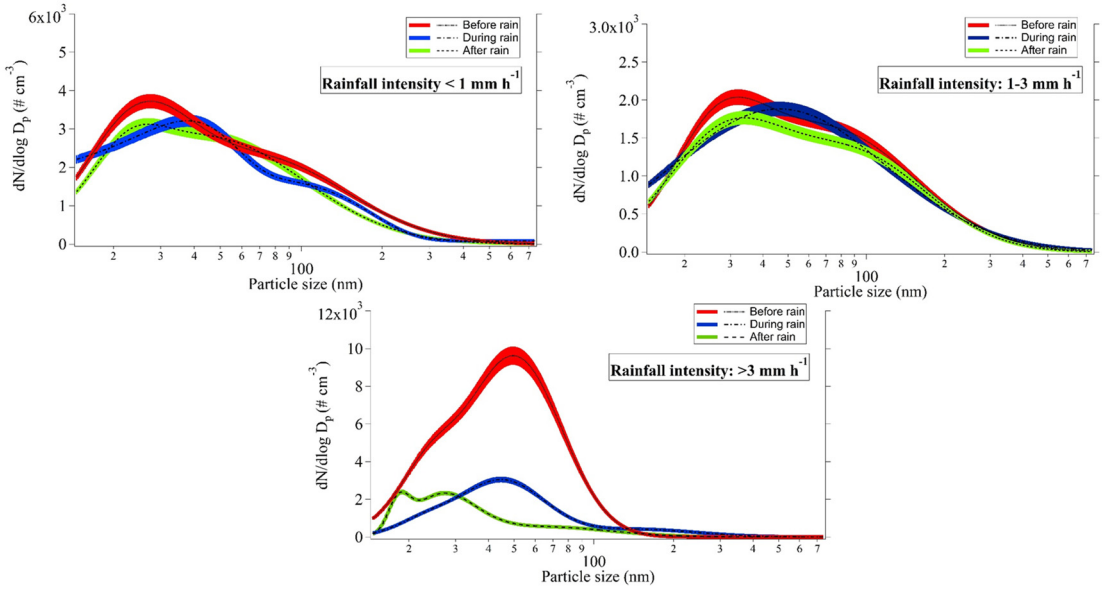

Figure 4.2. Lines shows log-normal fit of the PNSD before, during and after rain events according to rainfall intensity groups.

4.3.3. SCAVENGING COEFFICIENT

The mean scavenging coefficient (λ) values obtained by modes, regardless of the intensity of rain, were: $3.9 \cdot 10^{-5}$, $3.1 \cdot 10^{-5}$, $4.8 \cdot 10^{-5}$ and $5.2 \cdot 10^{-5}$ s^{-1} for nucleation, Aitken, acc_1 and acc_2 modes, respectively, in line with those found by other authors (Kyrö et al., 2009; Zhao et al., 2015; Zikova and Zdimal, 2016). The low values of scavenging parameters ($\%\Delta C$ and λ) observed in the Aitken mode may be related to the high number of events with low rain intensity and low rain amount (Figures S4.5 and S4.6), rainfall conditions with the lowest scavenging observed in the Aitken mode. Table 4.1 shows λ values for aerosol size fractions considered in this study as a function of rain intensities. The intensities >3 mm h^{-1} caused an effective scavenging in all size ranges studied (particle sizes <1000 nm). By modes, the nucleation-mode particles presented an effective scavenging with rainfall intensities <1 mm h^{-1} ($1.9 \cdot 10^{-5}$ s^{-1}) and >3 mm h^{-1} ($8.3 \cdot 10^{-4}$ s^{-1}). For the accumulation-mode particles, the higher λ values were found for the same intensities (<1 and >3 mm h^{-1}). The rain intensities between 1 and 3 mm did not produce positive values of λ, thus, these rain intensities do not produce an effective scavenging for any mode.

Table 4.1. Mean ($\bar{x}$), median, percentiles 5 and 95 ($P_{0.05}$, $P_{0.95}$), quartiles 1 and 3 (Q_1, Q_3) values and standard deviation (SD) of scavenging coefficients ($10^{-5}\cdot\lambda$), for selected events grouped by rainfall intensities and modal concentration: nucleation (14-30 nm), Aitken (30-100 nm), acc_1(100-300 nm) and acc_2 (300-1000 nm).

PNC (cm^{-3})	<1 mm h^{-1} (*10^{-5} s^{-1})							1-3 mm h^{-1} (*10^{-5} s^{-1})						
	$P_{0.05}$	Q_1	Median	Q_3	$P_{0.95}$	$\bar{x}$	SD	$P_{0.05}$	Q_1	Median	Q_3	$P_{0.95}$	$\bar{x}$	SD
14-30 nm	-10.0	-1.9	1.8	4.6	15.1	1.9	8.2	-28.8	-6.9	-1.1	4.5	16.8	-2.9	16.4
30-100 nm	-6.7	-2.1	0.4	2.9	5.4	0.1	3.8	-22.3	-5.8	0.0	2.2	13.3	-2.0	12.7
100-300 nm	-4.0	-0.1	1.3	3.6	6.8	2.1	5.5	-10.1	-2.0	1.2	3.6	5.5	-0.2	5.7
300-1000 nm	-6.1	-1.3	1.4	3.8	11.0	1.6	5.6	-21.1	0.2	1.5	3.2	8.1	-1.6	10.7

PNC (cm^{-3})	>3 mm h^{-1} (*10^{-5} s^{-1})						
	$P_{0.05}$	Q_1	Median	Q_3	$P_{0.95}$	$\bar{x}$	SD
14-30 nm	54.0	66.9	83.1	99.2	112.1	83.1	45.7
30-100 nm	51.8	68.2	88.8	109.3	125.8	88.8	58.1
100-300 nm	74.0	75.8	78.0	80.2	82.0	78.0	80.0
300-1000 nm	29.9	52.2	80.0	107.8	130.1	80.0	78.7

For each SMPS channel, a global λ coefficient of all rain events has been calculated (Figure S4.7). Events with intensities <1 mm h^{-1} presented the gap with the lowest scavenging effect between 140-190 nm. A similar pattern was observed for events with intensities between 1-3 mm h^{-1}, being the gap with lower scavenging between 160-180 nm. However, the events with intensities >3 mm h^{-1} presented the gap with lower scavenging between 220-500 nm. These results are in concordance with those observed by Laakso et al., (2003), with a minimum observed at 200 nm. The λ coefficients obtained for intensities >3 mm h^{-1} (10^{-3}-10^{-4} s^{-1}) were higher than those obtained for intensities <3 mm h^{-1} (10^{-4}-10^{-5} s^{-1}). This last finding should be interpreted with caution, since the number of events with high rain intensity is low.

4.3.4. RAINDROP SIZE EFFECT

The scavenging effect caused by different raindrop sizes on the different aerosol particle sizes was analysed. For that purpose, Pearson's correlation coefficients between the number of raindrops of different sizes and the percentage of variation of the number of particles per channel during rain (in 10-minute periods) have been calculated (Figure 4.3). The raindrops with

sizes >1.25 mm scavenged mainly the particles with sizes between 70-300 nm, coinciding with statistically significant correlations. At this point, it must be highlighted that the lowest scavenging was caused, by raindrops of all sizes, on particles with sizes above 250 nm (*Greenfield Gap*), mainly with raindrop sizes >0.5 mm. In addition, particle sizes >600 nm were not scavenged by raindrop sizes <4.75 mm, but they are eliminated by larger raindrops. In the same way, raindrops with sizes <0.25 mm caused a clear scavenging on particles with sizes between 650-750 nm. This fact occurred mainly in events with low rain intensity but a high concentration of raindrops with size <0.25 mm.

The volume swept by different raindrop sizes is depicted in Figure S4.8. With rain intensities <3 mm h^{-1}, raindrop sizes between 0.5 and 1 mm showed the highest swept volume ($8.7 \cdot 10^8$ mm^3 m^{-3}). However, with intensities >3 mm h^{-1}, raindrops between 0.75 and 1.175 mm clearly caused the highest swept volume ($3.1 \cdot 10^8$ mm^3 m^{-3}). Regardless of rainfall intensity, the main swept volume was caused by raindrops ranging between 0.125 and 4 mm.

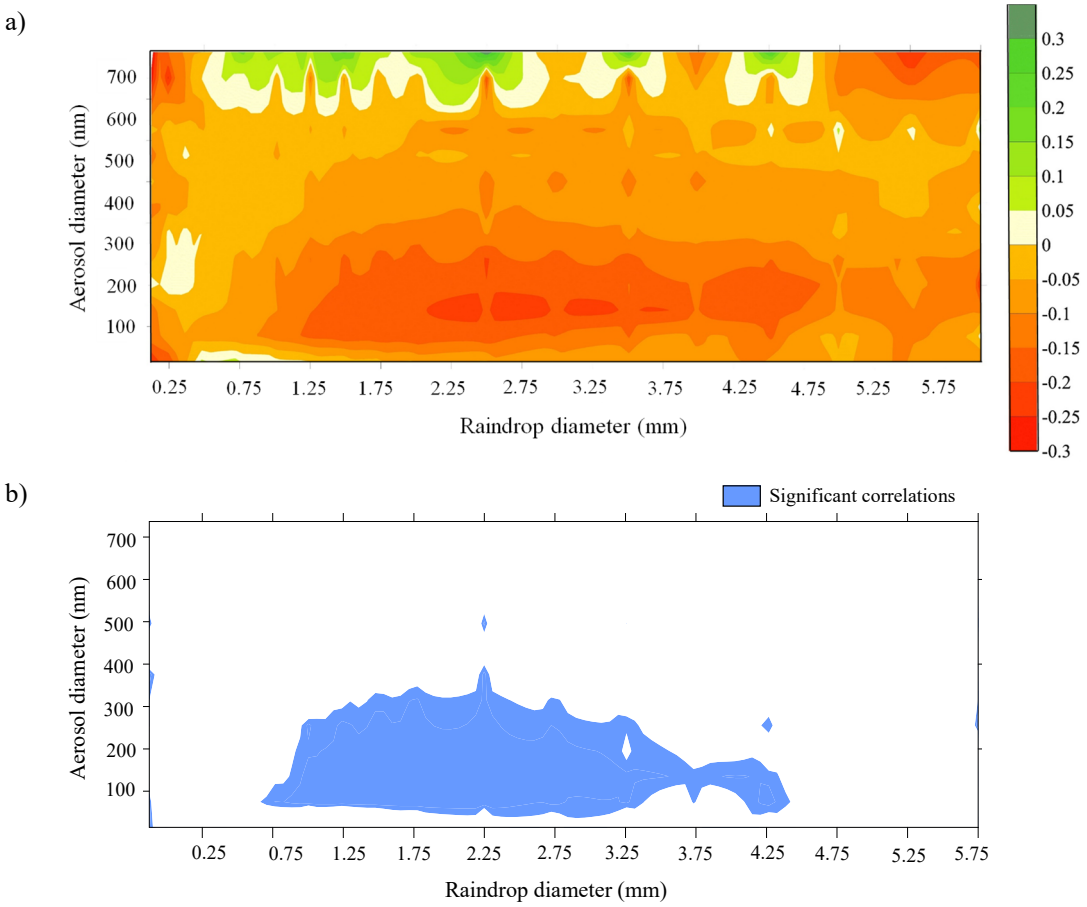

Figure 4.3. a) Pearson correlation coefficients between the number of raindrop sizes and the variation of PNC (%) in 10-minute intervals during the rain events; b) significative correlations ($p<0.05$).

Based on the results observed in Figure 4.3 and Figure S4.8, the influence of the different raindrop sizes on the scavenging effect is clear. But does the raindrop size distribution influence scavenging? To answer this question, the gamma distribution parameters (α and β) have been calculated to characterize the raindrop size distribution. Rain events have been classified according to their mean $\%\Delta C$ value into: <-20% (no scavenging), between -20 and 0% (no scavenging) and >0% (effective scavenging). It must be emphasised that, in all modes, low α and β values cause a higher scavenging efficiency. Modal raindrop diameter and β did not present significant differences, and there were significant differences only in acc_2 in α between $\%\Delta C$ groups (Figure S4.9).

4.3.5. IMPACT OF AEROSOL SCAVENGING BY RAIN ON THE RESPIRABLE FRACTION

As seen in the previous sections, the elimination of aerosols by rain contributes clearly to the washing of the atmosphere and, therefore, could reduce their impact on human health. For this reason, the study of the effect of rain washing on the respirable aerosol fraction has been considered. The ISO 7708: 1995 standard establishes the definitions of inhalable, thoracic, extrathoracic and respirable fractions. Numerically, the respirable fraction is equivalent to the percentage of the inhalable convention given by a cumulative log-normal distribution with a median of 4.25 and 2.5 µm, for healthy and high-risk individuals, respectively. Thus, the particles analysed in this study affect the respirable fraction, since the maximum size is 1 µm. More details about values for different activities and breathing habits can be found in Brown et al. (2013) and Morawska and Salthammer (2004). The contribution of fine particles to the respirable tract fraction is lower than 2%, so inhalable and respirable fractions presented similar values. The respirable fraction, calculated between before and after rain, presented a clear decrease of 38, 28 and 30% in rain intensities <1, between 1-3 and >3 mm h^{-1}, respectively (Figure S4.10). Thus, the respirable fraction decreased during rainfall, but the effect was similar for healthy adults and high-risk adults. The decreases of aerosol concentration in the respirable fraction are higher than those shown by García Nieto et al. (2006), who also differ in the fact that low rain intensity causes a higher decrease in the respirable fraction. In the three rainfall intensity classes, the changes are statistically significant ($p<0.05$).

4.4. CONCLUSIONS

This study has analysed below-cloud scavenging caused by precipitation on ultrafine and accumulation modes, as well as the role of the different raindrop sizes during rain events in an urban environment. The Aitken mode showed the lowest scavenging effect with a scavenging efficiency of 4% and λ scavenging coefficient of $3.1 \cdot 10^{-5}$ s^{-1}, while the accumulation mode presented the highest values (22%; $5.0 \cdot 10^{-5}$ s^{-1}). This aerosol scavenging depends on the intensity of precipitation. Events with rain intensities between 1-3 mm h^{-1} did not cause an effective scavenging in the accumulation mode, and a lower scavenging than other intensities in the nucleation and Aitken modes. In rainfall intensities <1 and >3 mm h^{-1}, there was a decrease of modal peaks in the bimodal lognormal aerosol concentration distribution. The raindrop sizes between 1.25 and 3.5 mm scavenged mainly the particles sizes between 70 and 300 nm. These results are empirical, and to further investigate the causes a larger number of events with different rainfall characteristics (intensity, total amount) and aerosol size spectra are needed.

A high resolution SMPS distribution, especially for the ultrafine fraction, in combination with disdrometer measurements have made it possible to carry out a detailed study of aerosol scavenging by raindrops in the Northwest of Spain. This type of information is scarce in the literature but very important, as this process plays an important role in clearing air. Thus, these findings could contribute to improve our understanding of the effect of scavenging caused by different raindrop sizes on different aerosol particle sizes, and can be applied in the field of artificial scavenging of indoor or outdoor polluted air. From the point of view of human health, these findings are relevant due to the important decrease of the respirable fraction of particles after rain. Evidence of this are the decreases registered between -38 and -28% depending on rain intensity. Furthermore, the estimation of the scavenging coefficients caused by rain provide useful information on aerosol sinks to use as input to climate models.

4.5. REFERENCES

Alonso-Blanco, E., Gómez-Moreno, F.J., Núñez, L., Pujadas, M., Cusack, M., Artíñano, B., 2017. Aerosol particle shrinkage event phenomenology in a South European suburban area during 2009–2015. Atmos. Environ. 160, 154–164. doi:10.1016/j.atmosenv.2017.04.013

Andronache, C., Grönholm, T., Laakso, L., Phillips, V., Venalainen, A., Phillips, Y., Venäläinen, A., 2006. Scavenging of ultrafine particles by rainfall at a boreal site: observations and model estimations. Atmos. Chem. Phys. 6, 4739–4754. doi:10.5194/acp-6-4739-2006

Berthet, S., Leriche, M., Pinty, J.P., Cuesta, J., Pigeon, G., 2010. Scavenging of aerosol particles by rain in a cloud resolving model. Atmos. Res. 96, 325–336. doi:10.1016/j.atmosres.2009.09.015

Blanco-Alegre, C., Calvo, A.I., Coz, E., Castro, A., Oduber, F., Prévôt, A.S.H.H., Močnik, G., Fraile, R., 2019. Quantification of source specific black carbon scavenging using an aethalometer and a disdrometer. Environ. Pollut. 246, 336–345. doi:10.1016/j.envpol.2018.11.102

Blanco-Alegre, C., Castro, A., Calvo, A.I., Oduber, F., Alonso-Blanco, E., Fernández-González, D., Valencia-Barrera, R.M., Vega-Maray, A.M., Fraile, R., 2018. Below-cloud scavenging of fine and coarse aerosol particles by rain: The role of raindrop size. Q. J. R. Meteorol. Soc. 144, 2715–2726. doi:10.1002/qj.3399

Brown, J., Gordon, T., Price, O., Asgharian, B., 2013. Thoracic and respirable particle definitions for human health risk assessment. Part. Fibre Toxicol. 10, 1–12.

Castro, A., Calvo, A.I., Alves, C., Alonso-Blanco, E., Coz, E., Marques, L., Nunes, T., Fernández-Guisuraga, J.M., Fraile, R., 2015. Indoor aerosol size distributions in a gymnasium. Sci. Total Environ. 524–525, 178–186. doi:10.1016/j.scitotenv.2015.03.118

Castro, A., Calvo, A.I., Blanco-Alegre, C., Oduber, F., Alves, C., Coz, E., Amato, F., Querol, X., Fraile, R., 2018. Impact of the wood combustion in an open fireplace on the air quality of a living room: Estimation of the respirable fraction. Sci. Total Environ. 628–629, 169–176. doi:10.1016/j.scitotenv.2018.02.001

Chate, D.M., 2011. Below-thunderstorm rain scavenging of urban aerosols in the health hazardous modes. Nat. Hazards 56, 81–91. doi:10.1007/s11069-010-9550-5

Chate, D.M., 2005. Study of scavenging of submicron-sized aerosol particles by thunderstorm rain events. Atmos. Environ. 39, 6608–6619. doi:10.1016/j.atmosenv.2005.07.063

Chate, D.M., Murugavel, P., Ali, K., Tiwari, S., Beig, G., 2011. Below-cloud rain scavenging of atmospheric aerosols for aerosol deposition models. Atmos. Res. 99, 528–536. doi:10.1016/j.atmosres.2010.12.010

Dockery, D.W., Sc, D., Stone, P.H., 2007. Cardiovascular risks from fine particulate air pollution. N. Engl. J. Med. 336, 511–513. doi:10.1056/NEJMe068274

Draxler, R., Rolph, G., 2012. Hysplit (Hybrid Single-Particle Lagrangian Integrated Trajectory). Silver Spring. NOAA Air Resour. Lab.

Duhanyan, N., Roustan, Y., 2011. Below-cloud scavenging by rain of atmospheric gases and particulates. Atmos. Environ. 45, 7201–7217. doi:10.1016/j.atmosenv.2011.09.002

EEA, 2016. Air quality in Europe - 2016 Report. Copenhagen, Denmark. doi:10.2800/413142

Fernandez-Raga, M., 2011. Estudio de la precipitación mediante disdrómetros. Una aplicación particular : erosión por salpicadura. University of León (Spain).

Fernández-Raga, M., Castro, A., Palencia, C., Calvo, A.I., Fraile, R., 2009. Rain events on 22 October 2006 in León (Spain): Drop size spectra. Atmos. Res. 93, 619–635. doi:10.1016/j.atmosres.2008.09.035

Fernández-Raga, M., Fraile, R., Keizer, J.J., Varela Teijeiro, M.E., Castro, A., Palencia, C., Calvo, A.I., Koenders, J., Da Costa Marques, R.L., 2010. The kinetic energy of rain measured with an optical disdrometer: An application to splash erosion. Atmos. Res. 96, 225–240. doi:10.1016/j.atmosres.2009.07.013

Fuzzi, S., Baltensperger, U., Carslaw, K., Decesari, S., Denier van der Gon, H., Facchini, M.C., Fowler, D., Koren, I., Langford, B., Lohmann, U., Nemitz, E., Pandis, S., Riipinen, I., Rudich, Y., Schaap, M., Slowik, J.G., Spracklen, D. V, Vignati, E., Wild, M., Williams, M., Gilardoni, S., 2015. Particulate matter,

air quality and climate: lessons learned and future needs. Atmos. Chem. Phys. 15, 8217–8299. doi:10.5194/acp-15-8217-2015

García Nieto, P.J., Del Coz Díaz, J.J., Ordóñez Galán, C., Taboada Castro, J., 2006. A mathematical approach to selective scavenging of the different classes of typical atmospheric aerosols by rainout and health impact. Environ. Technol. 27, 337–348. doi:10.1080/09593332708618648

Greenfield, S.M., 1957. Rain scavenging of radioactive particulate matter from the atmosphere. J. Meteorol. doi:10.1175/1520-0469(1957)014<0115:RSORPM>2.0.CO;2

Gunn, R., Kinzer, G.D., 1949. The terminal velocity of fall for water droplets in stagnant Air. J. Meteorol. doi:10.1175/1520-0469(1949)006<0243:TTVOFF>2.0.CO;2

Hussein, T., Karppinen, A., Kukkonen, J., Härkönen, J., Aalto, P., Hämeri, K., Kerminen, V.M., Kulmala, M., 2006. Meteorological dependence of size-fractionated number concentrations of urban aerosol particles. Atmos. Environ. 40, 1427–1440. doi:10.1016/j.atmosenv.2005.10.061

Kinney, P.L., 2008. Climate change, air quality, and human health. Am. J. Prev. Med. 35, 459–467. doi:10.1016/j.amepre.2008.08.025

Kruskal, W.H., Wallis, W.A., 1952. Use of ranks in one-criterion variance analysis. J. Am. Stat. Assoc. 47, 583–621.

Kulshrestha, U.C., Reddy, L.A.K., Satyanarayana, J., Kulshrestha, M.J., 2009. Real-time wet scavenging of major chemical constituents of aerosols and role of rain intensity in Indian region. Atmos. Environ. 43, 5123–5127. doi:10.1016/j.atmosenv.2009.07.025

Kyrö, E.M., Grönholm, T., Vuollekoski, H., Virkkula, A., Kulmala, M., Laakso, L., 2009. Snow scavenging of ultrafine particles: Field measurements and parameterization. Boreal Environ. Res. 14, 527–538.

Laakso, L., Grönholm, T., Rannik, Ü., Kosmale, M., Fiedler, V., Vehkamäki, H., Kulmala, M., 2003. Ultrafine particle scavenging coefficients calculated from 6 years field measurements. Atmos. Environ. 37, 3605–3613. doi:10.1016/S1352-2310(03)00326-1

Ladino, L., Stetzer, O., Hattendorf, B., Günther, D., Croft, B., Lohmann, U., 2011. Experimental study of collection efficiencies between submicron aerosols and cloud droplets. J. Atmos. Sci. 68, 1853–1864. doi:10.1175/JAS-D-11-012.1

Lemaitre, P., Sow, M., Quérel, A., Dépée, A., Monier, M., Menard, T., Flossmann, A., 2020. Contribution of phoretic and electrostatic effects to the collection efficiency of submicron aerosol particles by raindrops. Atmosphere (Basel). 11. doi:10.3390/atmos11101028

Loosmore, G.A., Cederwall, R.T., 2004. Precipitation scavenging of atmospheric aerosols for emergency response applications: Testing an updated model with new real-time data. Atmos. Environ. 38, 993–1003. doi:10.1016/j.atmosenv.2003.10.055

Maria, S.F., Russell, L.M., 2005. Organic and inorganic aerosol below-cloud scavenging by suburban New Jersey precipitation. Environ. Sci. Technol. 39, 4793–4800. doi:10.1021/es0491679

Mircea, M., Stefan, S., 1998. A theoretical study of the microphysical parameterization of the scavenging coefficient as a function of precipitation type and rate. Atmos. Environ. 32, 2931–2938. doi:10.1016/S1352-2310(98)00018-1

Mircea, M., Stefan, S., Fuzzi, S., 2000. Precipitation scavenging coefficient: Influence of measured aerosol and raindrop size distributions. Atmos. Environ. 34, 5161–5167. doi:10.1016/S1352-2310(00)00349-6

Morawska, L., Salthammer, T., 2004. Indoor environment: Airborne particles and settled dust, Indoor Environment: Airborne Particles and Settled Dust. doi:10.1002/9783527610013

Oduber, F., Castro, A., Calvo, A.I., Blanco-Alegre, C., Alonso-Blanco, E., Belmonte, P., Fraile, R., 2018. Summer-autumn air pollution in León, Spain: changes in aerosol size distribution and expected effects on the respiratory tract. Air Qual. Atmos. Heal. 5, 1–16. doi:10.1007/s11869-018-0556-6

Oduber, F., Isabel, A., Castro, A., Blanco-alegre, C., Alves, C., Calzolai, G., Nava, S., Lucarelli, F., Nunes, T., Barata, J., Fraile, R., 2021. Characterization of aerosol sources in León (Spain) using Positive Matrix Factorization and weather types. Sci. Total Environ. 754, 142045. doi:10.1016/j.scitotenv.2020.142045

Paramonov, M., Grönholm, T., Virkkula, A., 2011. Below-cloud scavenging of aerosol particles by snow at an urban site in Finland. Boreal Environ. Res. 16, 304–320. doi:10.1017/CBO9781107415324.004

Pilat, M.J., 1975. Collection of aerosol particles by electrostatic droplet spray scrubbers. J. Air Pollut. Control Assoc. 25, 176–178. doi:10.1080/00022470.1975.10470070

Pöschl, U., 2005. Atmospheric aerosols: Composition, transformation, climate and health effects. Angew. Chemie - Int. Ed. 44, 7520–7540. doi:10.1002/anie.200501122

Pruppacher, H.R., Semonin, R.G., Slinn, W.G.N., 1983. Precipitation scavenging, dry deposition and resuspension, vol 1., chap. Precipitation scavenging.

Pryor, S.C., Joerger, V.M., Sullivan, R.C., 2016. Empirical estimates of size-resolved precipitation scavenging coefficients for ultrafine particles. Atmos. Environ. 143, 133–138. doi:10.1016/j.atmosenv.2016.08.036

Rasch, P.J., Feichter, J., Law, K., Mahowald, N., Penner, J., Benkovitz, C., Genthon, C., Giannakopoulos, C., Kasibhatla, P., Koch, D., Levy, H., Maki, T., Prather, M., Roberts, D.L., Roelofs, G.J., Stevenson, D., Stockwell, Z., Taguchi, S., Kritz, M., Chipperfield, M., Baldocchi, D., McMurry, P., Barrie, L., Balkanski, Y., Chatfield, R., Kjellstrom, E., Lawrence, M., Lee, H.N., Lelieveld, J., Noone, K.J., Seinfeld, J., Stenchikov, G., Schwartz, S., Walcek, C., Williamson, D., 2000. A comparison of scavenging and deposition processes in global models: Results from the WCRP Cambridge workshop of 1995, Tellus, Series B: Chemical and Physical Meteorology. doi:10.3402/tellusb.v52i4.17091

Santachiara, G., Prodi, F., Belosi, F., 2013. Atmospheric aerosol scavenging processes and the role of thermo- and diffusio-phoretic forces. Atmos. Res. 128, 46–56. doi:10.1016/j.atmosres.2013.03.004

Seinfeld, J.H., Pandis, S., 2006. Atmospheric from air pollution to climate change, Atmospheric Chemistry and Physics. Wiley. doi:10.1016/0016-7037(87)90252-3

Seinfeld, J.H., Pandis, S.N., 2016. Atmospheric Chemistry and Physics: From Air Pollution to Climate Change, Atmospheric Chemistry and Physics. Wiley. doi:10.1016/0016-7037(87)90252-3

Seminara, G., Carli, B., Forni, G., Fuzzi, S., Mazzino, A., Rinaldo, A., 2020. Biological fluid dynamics of airborne COVID-19 infection. Rend. Lincei 31, 505–537. doi:10.1007/s12210-020-00938-2

Slinn, W.G.N., 1983. Precipitation scavenging. Division of Biomedical Environmental Research, US Department of Energy, Washington DC.

Tang, G., Zhao, P., Wang, Yinghong, Gao, W., Cheng, M., Xin, J., Li, X., Wang, Yuesi, 2017. Mortality and air pollution in Beijing: The long-term relationship. Atmos. Environ. 150, 238–243. doi:10.1016/j.atmosenv.2016.11.045

Textor, C., Schulz, M., Guibert, S., Kinne, S., Balkanski, Y., Bauer, S., Berntsen, T., Berglen, T., Boucher, O., Chin, M., Dentener, F., Diehl, T., Easter, R., Feichter, H., Fillmore, D., Ghan, S., Ginoux, P., Gong, S., Grini, A., Hendricks, J., Horowitz, L., Huang, P., Isaksen, I., Iversen, T., Kloster, S., Koch, D., Kirkevåg, A., Kristjansson, J.E., Krol, M., Lauer, A., Lamarque, J.F., Liu, X., Montanaro, V., Myhre, G., Penner, J., Pitari, G., Lamarque, J.F., Liu, X., Montanaro, V., Myhre, G., Penner, J., Pitari, G., Reddy, S., Seland, Ø., Stier, P., Takemura, T., Tie, X., 2006. Analysis and quantification of the diversities of aerosol life cycles within AeroCom. Atmos. Chem. Phys. 6, 1777–1813. doi:10.5194/acpd-5-8331-2005

Tokay, A., Kruger, A., Krajewski, W.F., 2001. Comparison of Drop Size Distribution Measurements by Impact and Optical Disdrometers. J. Appl. Meteorol. 40, 2083–2097. doi:10.1175/1520-0450(2001)040<2083:CODSDM>2.0.CO;2

Tong, Z., Chen, Y., Malkawi, A., Adamkiewicz, G., Spengler, J.D., 2016. Quantifying the impact of traffic-related air pollution on the indoor air quality of a naturally ventilated building. Environ. Int. 89–90, 138–146. doi:10.1016/j.envint.2016.01.016

Tong, Z., Yang, B., Hopke, P.K., Zhang, K.M., 2017. Microenvironmental air quality impact of a commercial-scale biomass heating system. Environ. Pollut. 220, 1112–1120. doi:10.1016/j.envpol.2016.11.025

Tost, H., Jöckel, P., Kerkweg, A., Sander, R., Lelieveld, J., 2006. Technical note: A new comprehensive scavenging submodel for global atmospheric chemistry modelling. Atmos. Chem. Phys. Discuss. 5, 11157–11181. doi:10.5194/acpd-5-11157-2005

UNICEF, 2016. Clear the air for children. The impact of air pollution on children.

Viard, V.B., Fu, S., 2015. The effect of Beijing's driving restrictions on pollution and economic activity. J. Public Econ. 125, 98–115. doi:10.1016/j.jpubeco.2015.02.003

Wang, P.K., Grover, S.N., Pruppacher, H.R., 1978. On the effect of electric charges on the scavenging of aerosol particles by clouds and small raindrops. J. Atmos. Sci. doi:10.1175/1520-0469(1978)035<1735:OTEOEC>2.0.CO;2

Wang, P.K., Pruppacher, H.R., 1977. An experimental determination of the efficiency with which aerosol particles are collected by water drops in subsaturated air. J. Atmos. Sci. 34, 1664–1669. doi:10.1175/1520-0469(1977)034<1664:AEDOTE>2.0.CO;2

Wang, X., Zhang, L., Moran, M.D., 2010. Uncertainty assessment of current size-resolved parameterizations for below-cloud particle scavenging by rain. Atmos. Chem. Phys. 10, 5685–5705. doi:10.5194/acp-10-5685-2010

Wiedensohler, A., Birmili, W., Nowak, A., Sonntag, A., Weinhold, K., Merkel, M., Wehner, B., Tuch, T., Pfeifer, S., Fiebig, M., Fjäraa, A.M., Asmi, E., Sellegri, K., Depuy, R., Venzac, H., Villani, P., Laj, P., Aalto, P., Ogren, J.A., Swietlicki, E., Williams, P., Roldin, P., Quincey, P., Hüglin, C., Fierz-Schmidhauser, R., Gysel, M., Weingartner, E., Riccobono, F., Santos, S., Grüning, C., Faloon, K., Beddows, D., Harrison, R., Monahan, C., Jennings, S.G., O'Dowd, C.D., Marinoni, A., Horn, H.G., Keck, L., Jiang, J., Scheckman, J., McMurry, P.H., Deng, Z., Zhao, C.S., Moerman, M., Henzing, B., De Leeuw, G., Löschau, G., Bastian, S., 2012. Mobility particle size spectrometers: Harmonization of technical standards and data structure to facilitate high quality long-term observations of atmospheric particle number size distributions. Atmos. Meas. Tech. 5, 657–685. doi:10.5194/amt-5-657-2012

Zhang, L., Wang, X., Moran, M.D., Feng, J., 2013. Review and uncertainty assessment of size-resolved scavenging coefficient formulations for below-cloud snow scavenging of atmospheric aerosols. Atmos. Chem. Phys. 13, 10005–10025. doi:10.5194/acp-13-10005-2013

Zhao, S., Yu, Y., He, J., Yin, D., Wang, B., 2015. Below-cloud scavenging of aerosol particles by precipitation in a typical valley city, northwestern China. Atmos. Environ. 102, 70–78. doi:10.1016/j.atmosenv.2014.11.051

Zikova, N., Zdimal, V., 2016. Precipitation scavenging of aerosol particles at a rural site in the Czech Republic. Tellus B 68, 1–14. doi:10.3402/tellusb.v68.27343

SUPPLEMENTARY MATERIAL

In order to evaluate the scavenging effect caused by different raindrop sizes on different aerosol particle sizes, the efficiency collision $E\ (d_p, D_r)$ and theoretical $\lambda\ (d_p, D_r)$ values for each aerosol particle size has been calculated. To estimate the collision efficiency $E\ (d_p, D_r)$ between raindrops and aerosol particles, Eq. S4.1 has been used, an expression presented in Seinfeld and Pandis (2016; see Eq. 20.56), based on Slinn (1983) and Andronache et al. (2006). The same methodology has been used in several laboratory studies (Andronache et al., 2006; Mircea et al., 2000; Santachiara et al., 2013; Slinn, 1983; Wang and Pruppacher, 1977; Wang et al., 2010).

$$E(d_p, D_r) = \overbrace{\frac{4}{R_e S_c}\left[1 + 0.4 {R_e}^{1/2} {S_c}^{1/3} + 0.16 {R_e}^{1/2} {S_c}^{1/2}\right]}^{Brownian\ diffusion} + \overbrace{4\frac{d_p}{D_r}\left[\frac{\eta_a}{\eta_w} + \left(1 + 2{R_e}^{1/2}\right)\frac{d_p}{D_r}\right]}^{Interception} + \overbrace{\left[\left(\frac{St - St_t}{St - St_t + \frac{2}{3}}\right)^{3/2}\left(\frac{\rho_p}{\rho_w}\right)^{1/2}\right]}^{Inertial\ impaction} + \overbrace{\left[\frac{4\alpha_{th}\left(2 + 0.6 {R_e}^{1/2} {P_r}^{1/3}\right)(T_a - T_s)}{U_t\,(D_r)\,D_r}\right]}^{Thermophoretic} + \overbrace{\left[\frac{4\gamma_{dph}\left(2 + 0.6 {R_e}^{1/2} {S_{cw}}^{1/3}\right)\left(\frac{{P_s}^0}{T_s} - \frac{{P_a}^0 RH}{T_a}\right)}{U_t\,(D_r)\,D_r}\right]}^{Diffusiophoretic} + \overbrace{\left[\frac{16 k C_c Q_r q_p}{3\pi\eta_a U_t\,(D_r)\,{D_r}^2 d_p}\right]}^{Electrostatic} \qquad Eq.\ \text{S4.1}$$

where

$$S_c = \frac{\eta_a}{\rho_a D_{diff}} \quad ; \quad D_{diff} = \frac{k_b T_a C_c}{3\pi\,\eta_a\,d_p} \quad ; \quad R_e = \frac{D_p\,U_t\,(D_r)\,\rho_a}{2\,\eta_a} \quad ; \quad St = \frac{2\tau\left[U_t\,(D_r) - u_t\,(d_p)\right]}{D_r} \quad ;$$

$$\tau = \frac{(\rho_p - \rho_a){d_p}^2 C_c}{18\,\eta_a} \quad ; \quad C_c = 1 + \frac{2\delta}{d_p}\left(1.257 + 0.4 e^{\left(-0.55\frac{d_p}{\delta}\right)}\right) \quad ; \quad St_t = \frac{1.2 + \frac{1}{12} ln(1 + R_e)}{1 + ln(1 + R_e)} \quad ;$$

$$u_t(d_p) = \frac{\rho_p {d_p}^2 g\,C_c}{18\,\eta_a} \quad ; \quad \alpha_{th} = \frac{2C_c\left(k_a + \frac{5\delta}{D_r k_p}\right)k_a}{5P\left(1 + \frac{5\delta}{D_r}\right)\left(2k_a + k_p + \frac{10\delta}{D_r k_p}\right)} \quad ; \quad P_r = \frac{c_p \eta_a}{k_a} \quad ; \quad \gamma_{dph} = \frac{T_a D_{diffw}}{P}\sqrt{\frac{M_w}{M_a}}$$

$$Sc_w = \frac{\eta_a}{\rho_a D_{diffw}} \quad ; \quad Q_r = a\alpha {D_r}^2 \quad ; \quad q_p = a\alpha {d_p}^2$$

All symbols of Eq. S4.1 are listed in Table S4.4. In Eq. S4.1, the first term represents Brownian diffusion, the second represents interception, the third represents the inertial impaction, the fourth represents the thermophoretic effect, the fifth represents the diffusiophoretic effect and the sixth represents the electrostatic effect. The third term is only valid when the Particle Stokes number

St is higher than the critical particle Stokes number St_t, and it is scaled by $(\rho_p/\rho_w)^{1/2}$ due to particle density ρ_p being different from 1 g cm^{-3} (Seinfeld and Pandis, 2016; Slinn, 1983). Eq. S4.1 has been used in several articles to estimate $E(D_r,d_p)$ (Andronache et al., 2006; Chate, 2005; Loosmore and Cederwall, 2004; Mircea et al., 2000; Tost et al., 2006; Wang et al., 2010).

In this study, several mechanisms influenced the scavenging process: Brownian diffusion, interception and thermophoretic, diffusiophoretic and electrostatic effects. Aerosol particles with diameters larger than 100 nm and raindrops with diameters smaller than 0.5 mm presented the highest values of $E\ (d_p, D_r)$ caused by interception mechanisms. An example of $E\ (d_p, D_r)$ with a raindrop diameter of 1.125 mm is shown in Figure S4.11. Regarding the effect of the different physical processes, Brownian diffusion is the main mechanism in aerosol particles smaller than 65 nm. Interception is the main mechanism in aerosol particle sizes larger than 65 nm and diffusiophoresis is the second mechanism in particles between 10 and 1000 nm. The electrostatic effect and the thermophoretic effect were both very low and could be considered negligible. Thus, the scavenging effect caused by rain in this study was mainly caused by Brownian diffusion, interception and diffusiophoretic mechanisms.

S.4.1. FIGURES

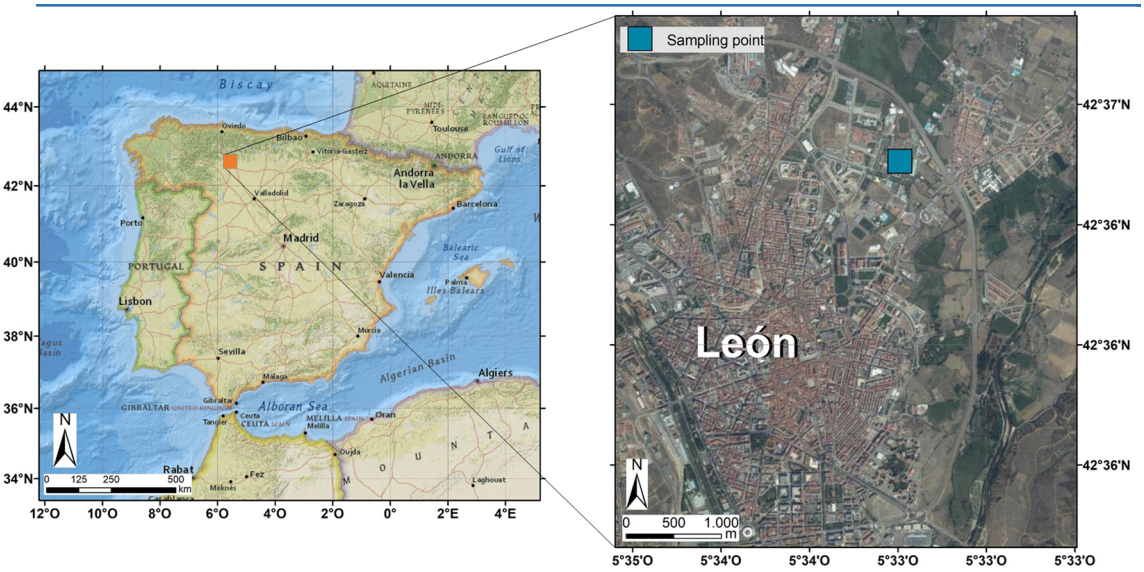

Figure S4.1. Geographic location of the city of León in Spain and sampling site.

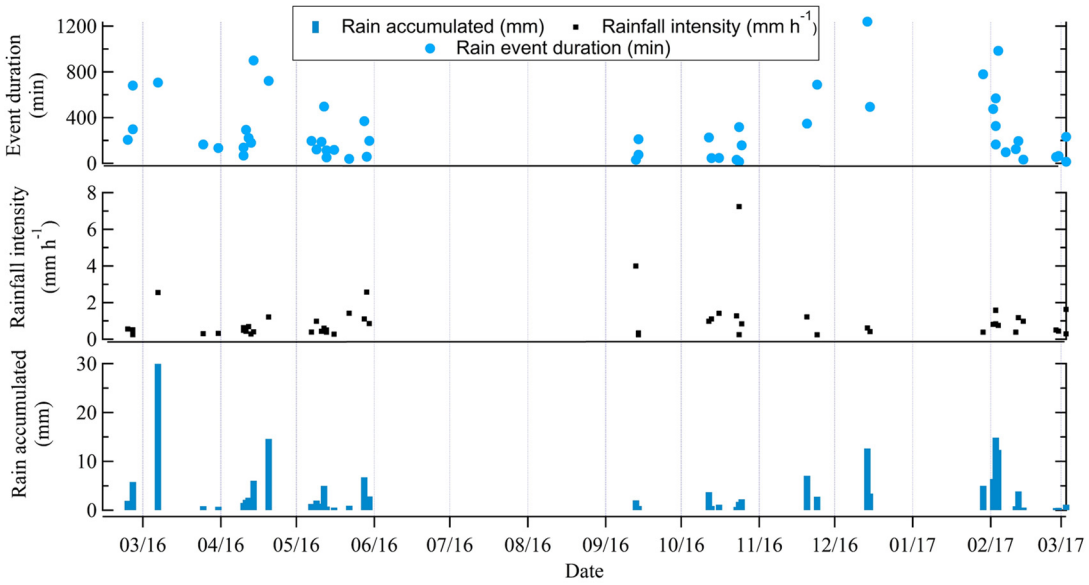

Figure S4.2. Event duration, rainfall intensity and accumulated rain of the selected events during the sampling campaign.

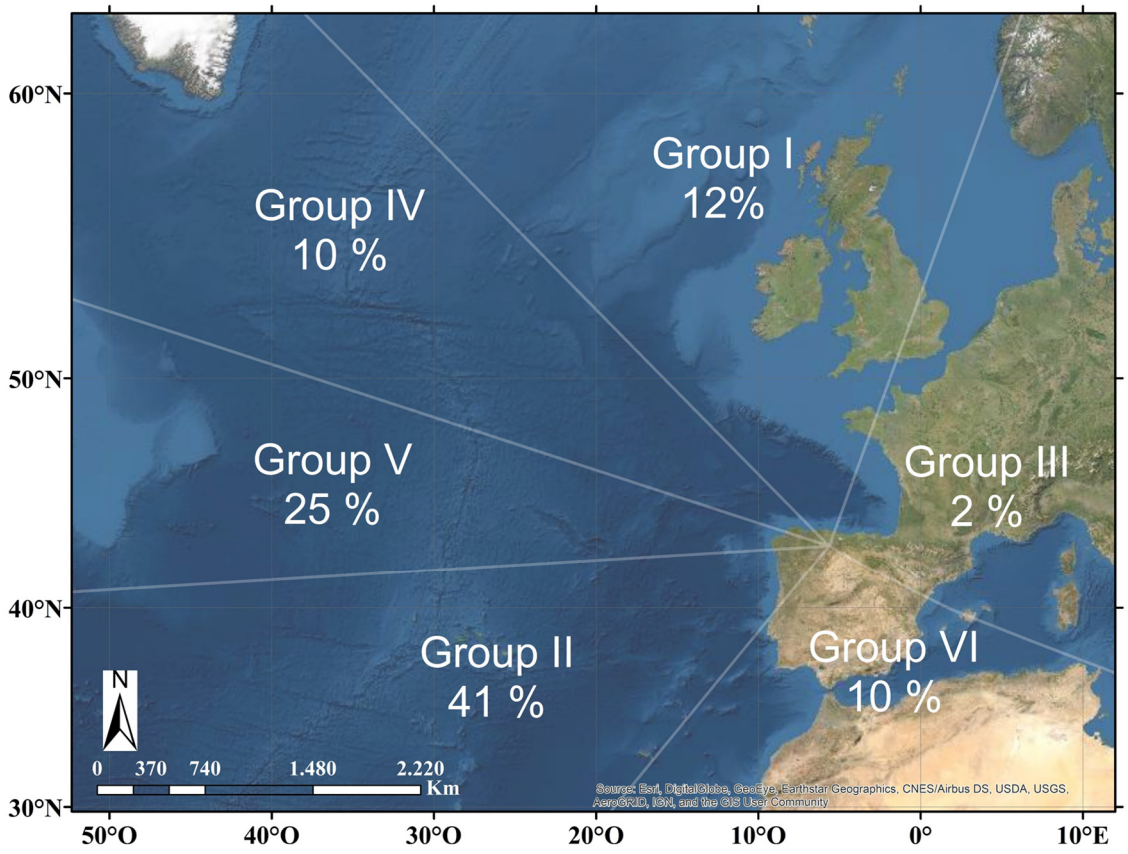

Figure S4.3. Percentages of four-days back trajectories arriving in León at 1000 m a.g.l during rain events (% of each category). Group I: Arctic, Group II: Atlantic, Group III: Continental, Group IV: North America, Group V: North Atlantic and Group VI: Saharan

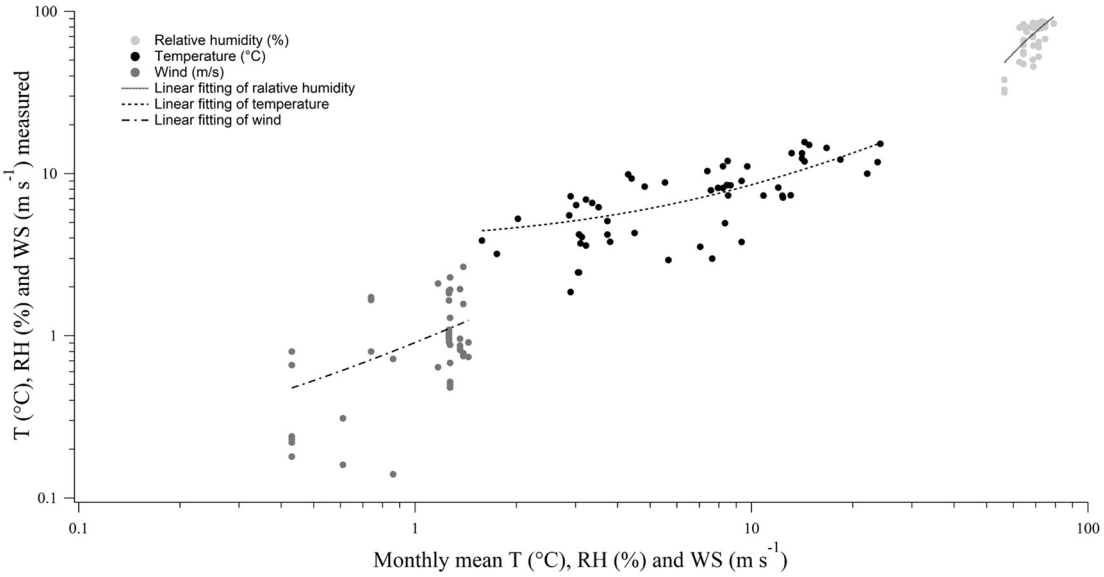

Figure S4.4. Mean temperature (T), relative humidity (RH) and wind speed (WS) comparison between 30 minutes measured before rain and the corresponding interval of the remaining days of the month (excluding rainy days).

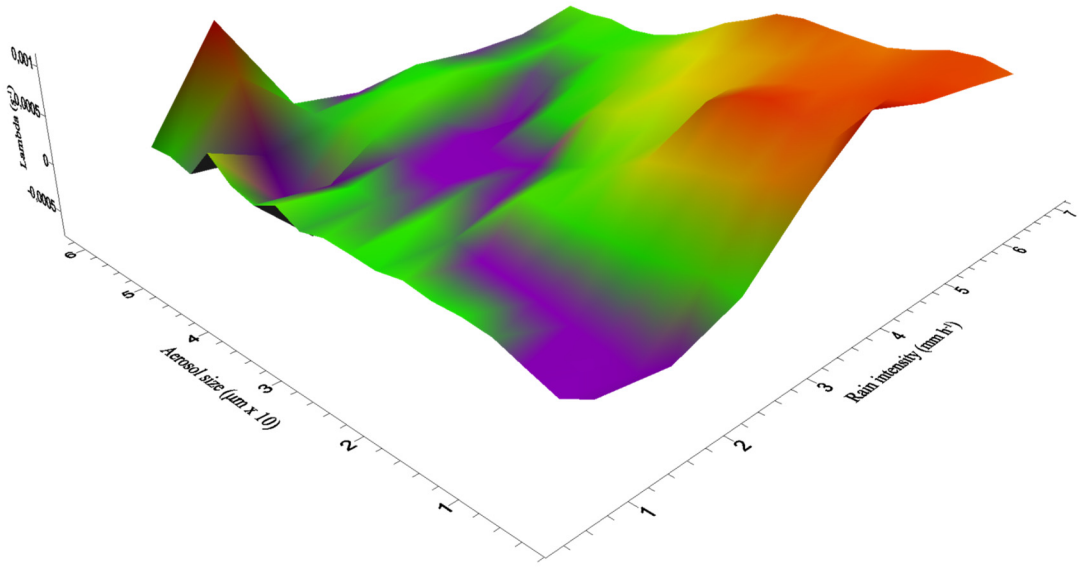

Figure S4.5. Scavenging coefficient variation according to aerosol sizes and rain intensity.

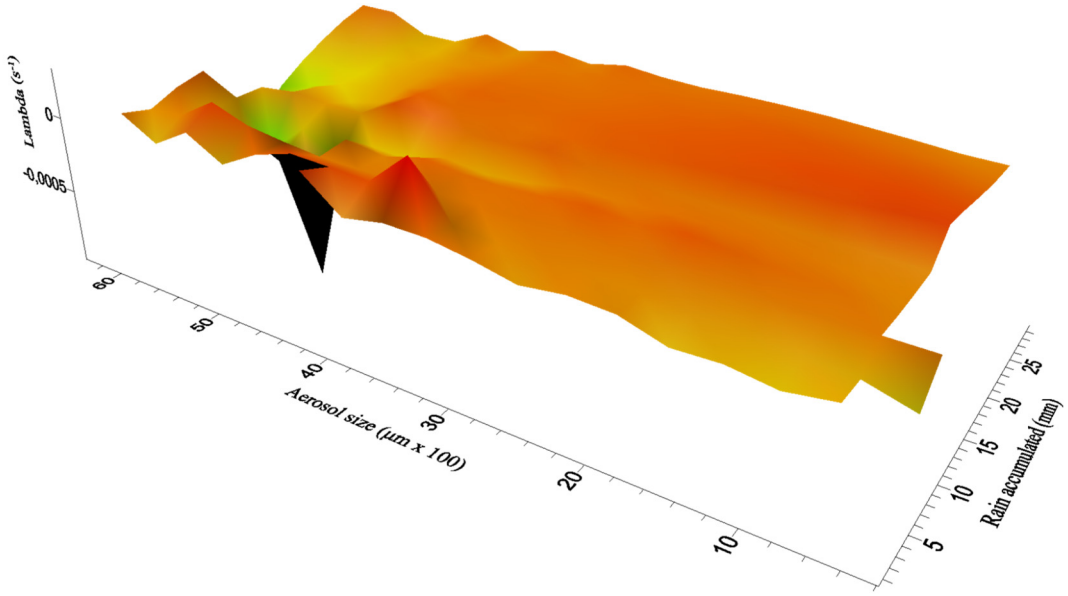

Figure S4.6. Scavenging coefficient variation according to aerosol sizes and accumulated rain.

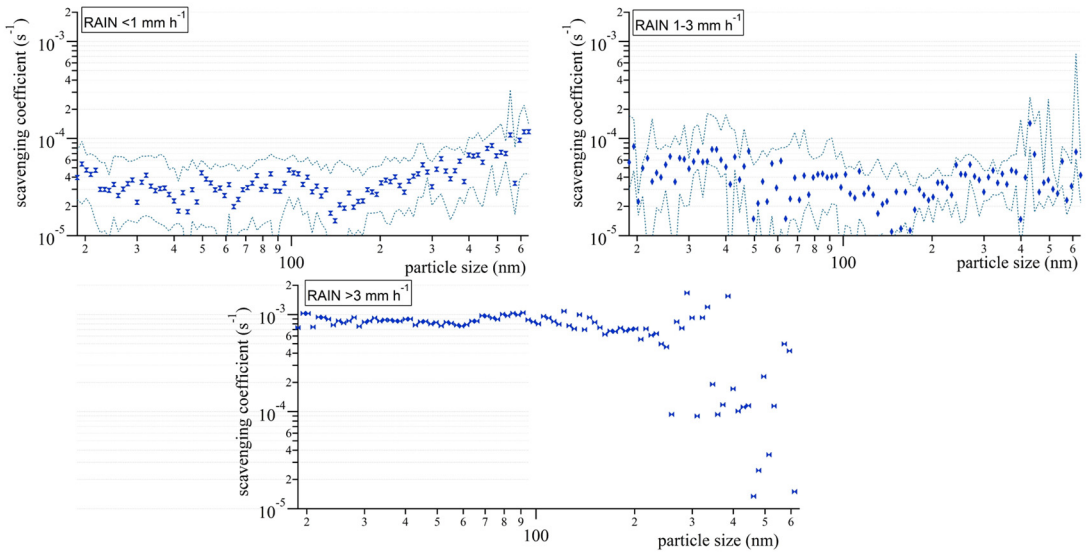

Figure S4.7. Mean scavenging coefficient (λ) obtained for each SMPS channel. Dotted lines represent the confidence interval with a significance level of 0.05.

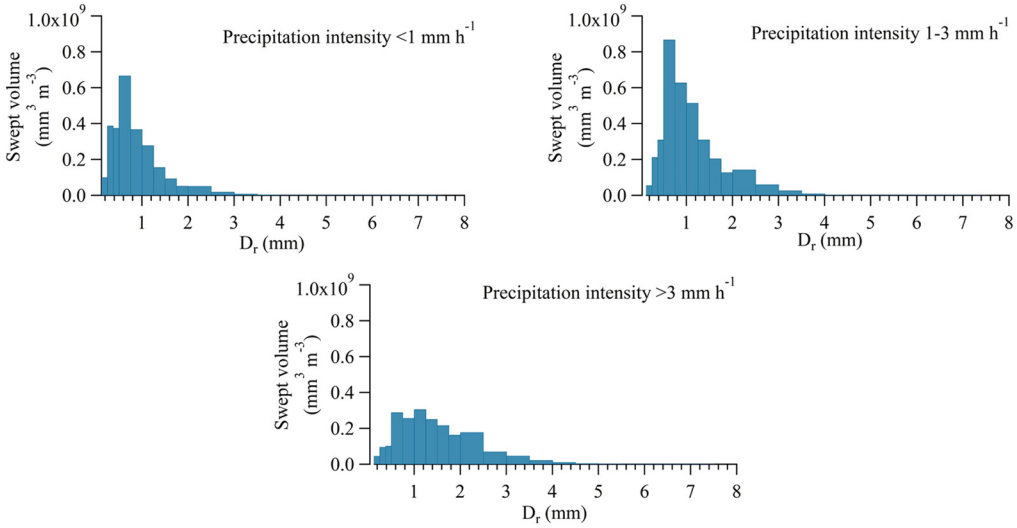

Figure S4.8. Mean volume swept caused by different raindrop sizes classified by rain precipitation intensities.

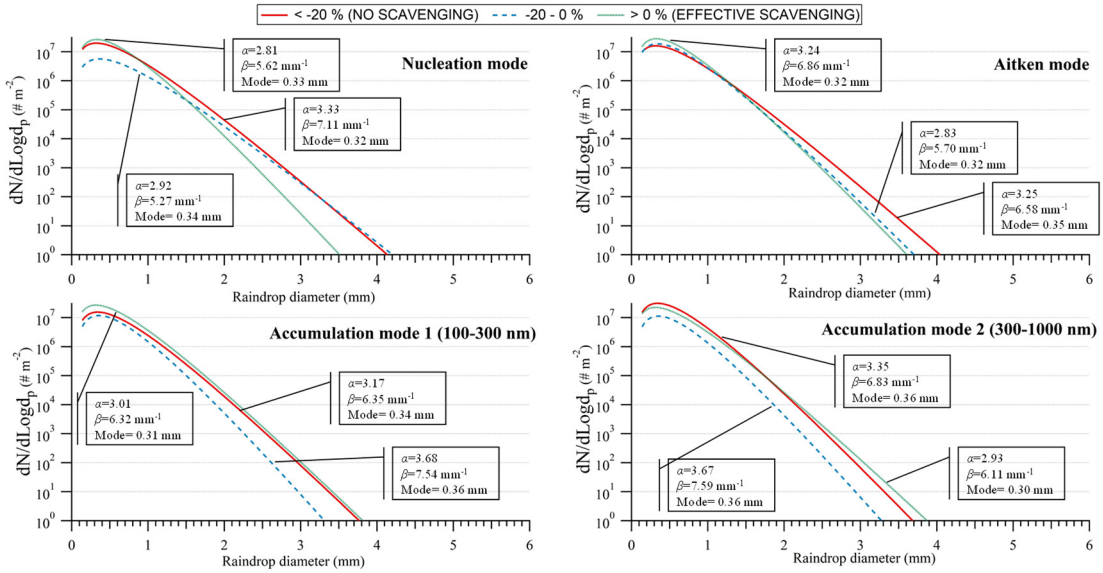

Figure S4.9. Raindrop size distributions representative of the three *%ΔC* groups by aerosol particle modes. The parameters of gamma distribution (α, β and modal raindrop diameter) are shown in boxes.

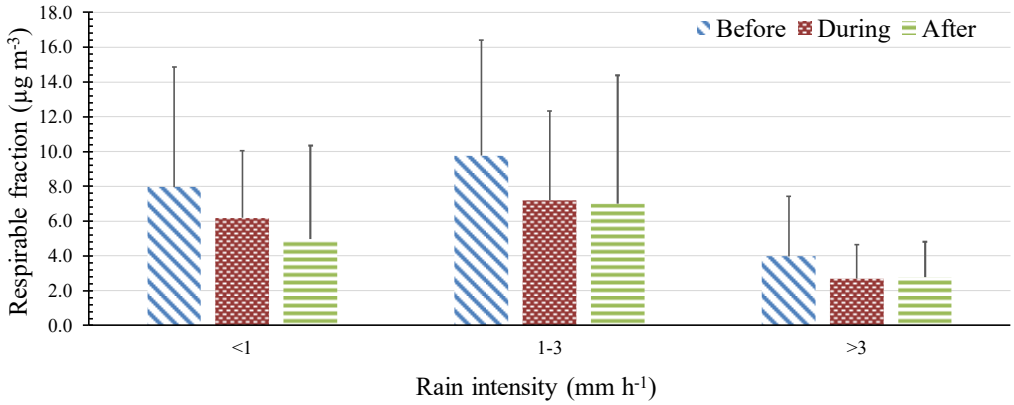

Figure S4.10. Respirable fraction (µg m^{-3}) by rain intensity classes between before, during and after rainfall.

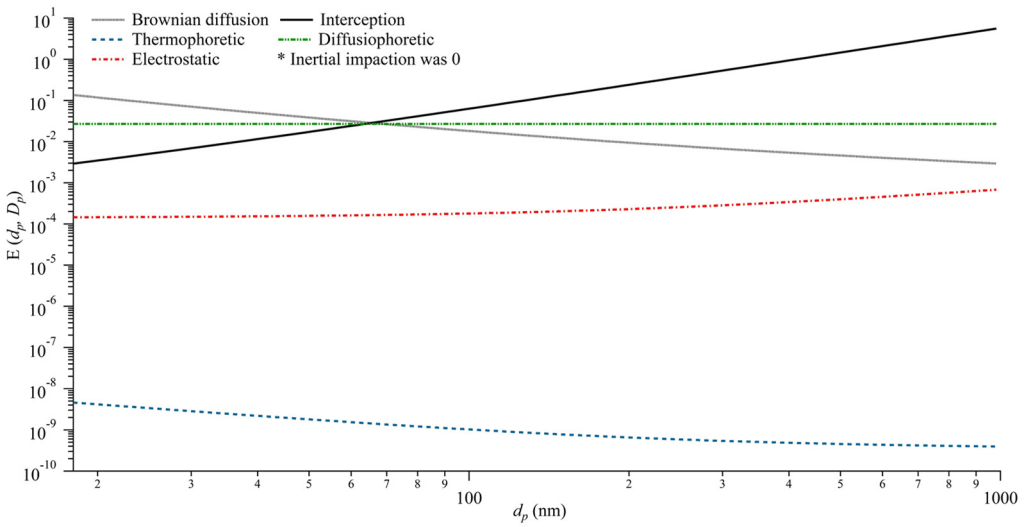

Figure S4.11. Contribution of several collection mechanisms to the collision efficiency *E (d_p, D_r)* for raindrops with a diameter of 1.125 mm as a function of aerosol particle diameter in this study.

S.4.2. TABLES

Table S4.1. Mean, standard deviation and maximum (in brackets) particle number concentration (cm^{-3}) for rainfall intensities classification considered in this study, before, during and after rain events. N is the number of events of each category.

	Nucleation 14-30 nm	Aitken 30-100 nm	Accumulation 1 100-300 nm	Accumulation 2 300-1000 nm
Intensity ($mm\ h^{-1}$)	Before	Before	Before	Before
Low (<1) (N=36)	891±772 (2779)	1392±887 (3587)	509±525 (3032)	26±40 (239)
Medium (1-3) (N=13)	445±238 (779)	892±347 (1375)	361±178 (738)	16±13 (49)
High (>3) (N=2)	1282±992 (1983)	2488±1216 (3348)	313±44 (344)	9±8 (15)

Table S4.2. Mean ($\bar{x}$), median, percentiles 5 and 95 ($P_{0.05}$, $P_{0.95}$) and quartiles 1 and 3 (Q_1, Q_3) values and standard deviation (SD) of scavenging efficiency (*%ΔC*) are shown, obtained for nucleation (14-30 nm), Aitken (30-100 nm) and accumulation (100-300 and 300-1000 nm) modes.

Modal Concentration (cm^{-3}) (N=51)	$P_{0.05}$	Q_1	Median	Q_3	$P_{0.95}$	$\bar{x}$	SD
Nucleation	84	37	19	0	-71	15	43
Aitken	57	31	6	-13	-82	4	42
Accumulation 1 (100-300 nm)	17	44	17	4	-19	22	29
Accumulation 2 (300-1000 nm)	24	52	24	-6	-46	21	43

Table S4.3. Modal peaks (nm) obtained from PNSD log-normal fitting for rainfall intensities classification considered in this study, before, during and after rain. N is the number of events of each category.

Rainfall intensity	<1 mm h^{-1} (N=36)		1-3 mm h^{-1} (N=13)		>3 mm h^{-1} (N=2)	
Modal Peaks (nm)	Peak 1	Peak 2	Peak 1	Peak 2	Peak 1	Peak 2
Before	24.0	64.9	26.6	66.4	33.8	99.9
During	23.3	43.3	27.1	70.0	36.27	136.8
After	23.8	46.5	25.8	69.5	36.8	139.2

Table S4.4. List of symbols and acronyms used in Supplementary material.

τ	Relaxation time of particle (s)	S_c	Particle Schmidt number
C_c	Cunningham slip correction factor	St	Particle Stokes number
D_{diff}	Particle Brownian diffusivity coefficient (m^2 s^{-1})	St_t	Critical Stokes number of particles
$E(D_r,d_p)$	Collision efficiency	T_a	Air temperature (°C)
k_b	Boltzmann constant (J K^{-1})	δ	Mean free path of air molecules (m)
η_a	Air viscosity (kg m^{-1} s^{-1})	μ	Mean size of raindrops (mm)
η_w	Water viscosity(kg m^{-1} s^{-1})	ρ_a	Air density (kg m^{-3})
Q_r	mean charge of a raindrop (C)	ρ_p	Aerosol particle density (kg m^{-3})
q_p	mean charge of a particle (C)	P_r	Prandtl number for air
k_a	thermal conductivity of air (J m^{-1} s^{-1} K^{-1})	T_s	temperature of the raindrop surface (K)
k_p	thermal conductivity of particle (J m^{-1} s^{-1} K^{-1})	S_{cw}	Schmidt number for water in air
a	cte = 0.83 10^{-6}	P_a^0	vapour pressure of water at temperature T_a (Pa)
α	Electrified parameter	P_s^0	vapour pressure of water at temperature T_s (Pa)
R_e	Raindrop Reynolds number	K	cte = 9 10^9 N m^2 C^{-2}

CHAPTER 5. Below-cloud scavenging of fine and coarse aerosol particles by rain

Full title: Below-cloud scavenging of fine and coarse aerosol particles by rain: The role of raindrop size

Published in: Quarterly Journal Royal Meteorology Society, 2018, 2715–2726.
DOI: 10.1002/qj.3399

5.1. INTRODUCTION

Air pollution poses a major threat to human health. It is linked to respiratory infections and cardiovascular diseases, and causes an increase in population morbidity and mortality, mainly affecting the health of children (UNICEF, 2016). One of the main pollutants linked to health concerns is the atmospheric aerosol (Calvo et al., 2013a; Fröhlich-Nowoisky et al., 2016). The characterization of atmospheric particulate matter has become a key issue for the scientific community because of the important implications it has not only in public health, but also in the climate, in ecosystems, in visibility, etc. (Andronache, 2003).

The characterization of aerosol sources and sinks plays a crucial role in the study of atmospheric pollution. More specifically, the mechanisms involved in the removal of atmospheric aerosols should be studied in detail in order to propose measures for mitigating air pollution. Textor et al. (2006) showed that rainfall is responsible for the removal of most atmospheric aerosols.

Below-cloud scavenging (BCS) (also called impaction scavenging or washout), linked to wet deposition, consti- tutes an important sink of aerosol particles (Chate et al., 2011; Pilon, et al.,

2015; Sportisse, 2007; Tost et al., 2006; Zhao et al., 2015). However, the study of aerosol-rain interaction is not an easy task. The complexity in the characterization of BCS lies in its dependence on several parameters: concentration, size distribution and composition of atmospheric aerosol (Peter et al., 2006), the presence of an electric charge, (Ladino et al., 2011), raindrop size distribution and rainfall intensity (Zikova and Zdimal, 2016).

Different parametrizations have been tested to model the removal processes by rain (Fournier et al. 2005). Nevertheless, it is common to calculate the scavenging coefficient (λ) by precipitation from the change in concentration of aerosol particles C (Seinfeld and Pandis, 2016), which depends on aerosol size. The processes of nucleation, condensation, coagulation and hygroscopic growth of aerosols can change the particle concentration, but during rain events its effects are modest (Laakso et al., 2003) and can be considered negligible, as in Chate (2005).

$$\frac{dC}{dt} = -\lambda \cdot C \qquad \textit{Eq. 5.1}$$

The integration of this differential equation between the instants t_0 and t_1 with concentrations C_0 and C_1, gives:

$$\lambda = -\frac{1}{t_1 - t_0} ln \frac{C_1}{C_0} \qquad \textit{Eq. 5.2}$$

A close connection between λ and particle size has been observed in previous works (Glantz et al., 2003; Peter et al., 2006; Zikova and Zdimal, 2016). BCS is less efficient with particles of sizes between 0.3 and 1–2 μm, which is called the *Greenfield Gap* (Greenfield, 1957; Loosmore and Cederwall, 2004; Zikova and Zdimal, 2016). Chate et al. (2011) discuss processes involved in BCS (Brownian diffusion, directional interception, inertial impaction, thermo-phoresis,diffusion-phoresis, electro-scavenging and electrical effects during thunderstorm rain) and describe uncertainties in λ from field and laboratory studies. These authors emphasise the importance of carrying out field studies, as laboratory experiments do not represent natural aerosol scavenging. In fact, λ values determined in field studies are higher than those measured in the laboratory and/or estimated by theoretical studies (with no electrical and phoretic effects). These differences are one to two orders of magnitude smaller for particlessmaller than 3 μm in laboratory and/or theoretical studies (Berthet et al., 2010; Chate et al., 2011; Ladino et al., 2011; Wang et al., 2010). The ratios obtained in field measurements are preferred over the ratios obtained from laboratory experiments because in the first case real atmospheric variables are considered. The differences in the λ values between field measurements, experimental and theoretical formulations are caused by many factors, mainly the uncontrollable real-world situations and others caused by experimental errors or theoretical formulations (Maria and Russell, 2005; Wang and Pruppacher, 1977).

Despite the existence of several theoretical and experimental studies devoted to BCS (Andronache et al., 2006; Chate et al., 2011), a complete understanding of this process remains a challenge because of its extreme complexity. For a deeper understanding of BCS, field research is essential, bringing together the instrumentation needed to characterize simultaneously the sizes of aerosol and raindrops.

Most studies estimate BCS from rain intensity and duration. Nevertheless, Kulshrestha et al. (2009) have found that "the maximum fall in aerosol levels was observed during continuous and low intensity rain events that did not allow building up of aerosol concentrations."

This study aims at evaluating the effect of precipitationon aerosol concentration depending on the size of the drops and particles under field conditions. The study, carried out in the northwest of the Iberian Peninsula, focuses mainly on the accumulation (0.1–1 μm) and coarse (>1 μm) modes. For these sizes, Wang et al. (2010) have observed a certain absence of agreement on the scavenging coefficient values.

In the present study, changes in the aerosol size distribution before, during and after rain events with different precipitation intensities have also been estimated. In order to carry out a more detailed research, one particular rain event was studied in depth. The relevance of this study lies in the fact that our results derive from field measurements, instead of laboratory simulations. The effect of raindrop size on aerosol scavenging is also analysed here, a type of study scarcely found in the scientific literature. This study represents a step forward towards a better characterization of aerosol–rain interaction, providing valuable information for air-quality models. Besides, the results could be useful for designing mitigation measures in polluted places indoors by the generation of an artificial cloud with drops of selected sizes.

5.2. STUDY ZONE

The study site is at the campus of the University of León, a city located in the Northwest of the Iberian Peninsula (42° 36′ N, 05° 35′ W and 838 m above sea level), shown in Figure 5.1. León has a population of about 200,000 people (population density ~3300 inhab. km^{-2}), including the metropolitan area. The main source of particulate matter in the city is road traffic, because there are no large emitting industries (Castro et al., 2010).

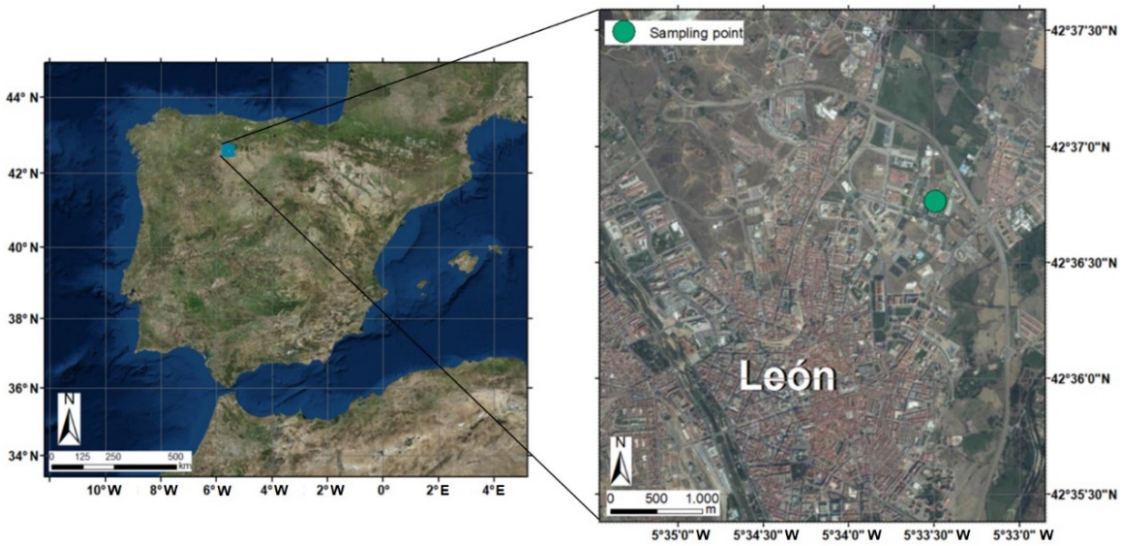

Figure 5.1. Geographic location of the city of León, Spain, and sampling point.

Following AEMET, the Spanish Meteorological Agency (http://www.aemet.es/en/), the city of León is characterised by rain events irregularly scattered over the year, with mini- mum precipitation values in the summer and peaks in spring and autumn. The main normalised values in the past 35 years are the following: annual mean precipitation is 556 mm and the temperatures are cool, with an annual mean of 10.9 ºC. The winter is cold with frequent frosts (74 frost days per year, on average). The summer is tempered by the altitude of the city, with maximum temperatures around 27 ºC. There are 2,624 sunshine hours per year, 78 rain days, 16 storm days and 16 snow days. Thus, León presents a Mediterranean climate with continental features, tempered by the proximity of the Cantabrian Mountain Range.

5.3. METHODOLOGY

From July 2015 until the end of January 2016 a sampling campaign was carried out at the Campus of the University of León, Spain. Both precipitation [measured with a laser disdrometer, Laser Precipitation Monitor (LPM)], and atmospheric aerosol particles [measured with a Passive Cavity Aerosol Spectrometer Probe (PCASP-X)] were sampled on a 1 min basis. A weather station was installed next to the aerosol probe PCASP-X and the LPM. The weather station provided information on temperature, wind and relative humidity. Rain events were considered only when the following three conditions were fulfilled:

- an accumulated precipitation higher than 0.4 mm was registered,

- the global precipitation intensity (total rain h^{-1}) in the event exceeded 0.2 mm h^{-1}, as proposed by Laakso et al. (2003).
- there was a minimum of 30 rain-free minutes between events (minimum needed to enable the λ calculation using the criteria described below).

For each rain event, the number and mass of aerosol particles before, during (time period in which it was raining) and after precipitation have been analysed. In other words, three stage pairs have been compared:

- 30 minutes before rain [as proposed by Laakso et al. (2003)] and during rain;
- while it was raining and 30 minutes after rain;
- 30 minutes before and 30 minutes after rain.

The ratio used to determine the change in particle concentration during the period between the times t_1 and t_2, was $\%\Delta C$, defined as:

$$\%\Delta C = \left(\frac{C_2 - C_1}{C_1}\right) \cdot 100 \qquad \textit{Eq. 5.3}$$

Besides, we estimated the scavenging coefficient λ (s^{-1}) for fine mode (λ_{fine}), coarse mode (λ_{coarse}) and global (λ). Equations 5.1 and 5.2 were used to estimate λ. A global analysis of all the events that meet the previously cited requirements was carried out. In addition, one particular precipitation event was studied in greater detail.

5.3.1. AEROSOL CHARACTERIZATION

Particle size distributions were measured every minute using an optical spectrometer PCASP-X, manufactured by Particle Measuring Systems, Inc. (PMS). This instrument measures aerosol optical diameters ranging between 0.1 and 10 µm in 31 channels on the basis of the light-scattering properties of particles at a wavelength of 633 nm between angles 35° and 135°. The probe was calibrated by the manufacturer using polystyrene latex particles of a known size. The refractive index of latex beads ($1.588 - 0i$) is different from that of atmospheric particles, resulting in an aerosol size distribution that is *latex equivalent* (Calvo et al., 2010). In this paper we are presenting PCASP-X size distributions corrected using Mie theory and implemented with a computer code developed by Bohren and Huffman (1984) for an average refractive index of $m = 1.549\text{-}0.025i$

which was estimated in the city of León by Castro et al. (2015). The variability in the estimated refractive index can affect the values of the estimated particle diameters. This slight influence can be assessed from Figure 5.2. These same authors have obtained a particle mean density of 1.36 g cm^{-3}, also used in the present paper. This value is typical of urban aerosols (Lide, 1993). After correction, the particle size range changed from 0.1–10 μm to 0.1–24.32 μm.

For each rain event, the aerosol size distributions were analysed, as well as the mean geometric diameter and the geometric standard deviation. The features of the accumulation and coarse modes were also studied for the particle distribution in three different stages: before, during, and after the rain event.

From the data provided by the PCASP-X, we obtained the following 66 variables relating to aerosol particles: total number and mass concentration of aerosol particles, number and mass of aerosol particles in 31 channels between 0.1 and 24.32 μm, geometric mean and geometric standard deviation of aerosol particles.

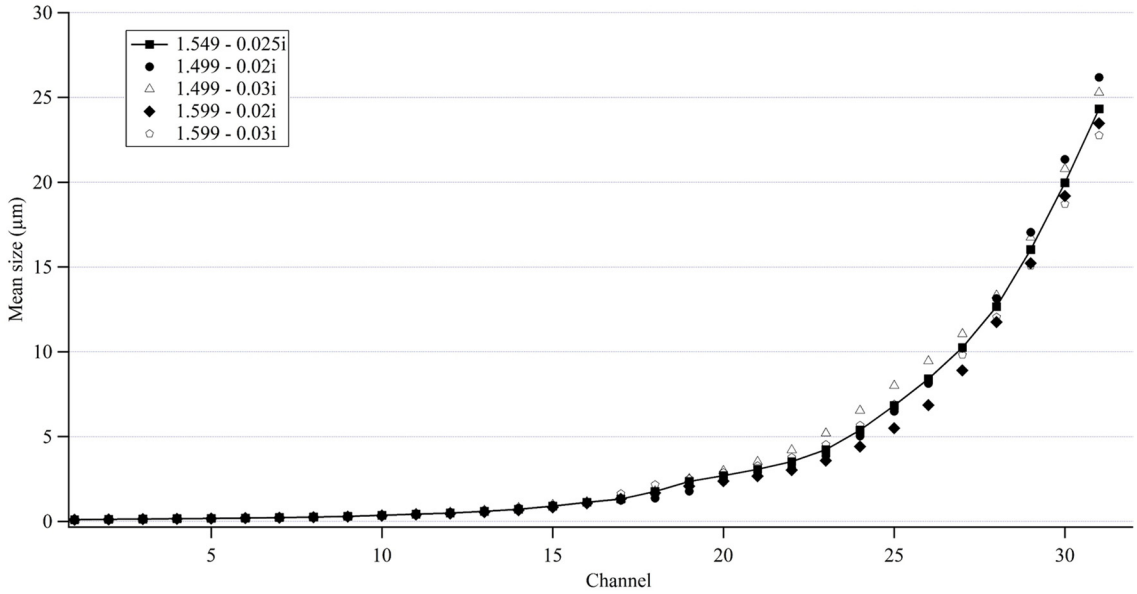

Figure 5.2. Mean diameters (μm) corresponding to the different channels of the PCASP-X using different refractive indices [1.549±0.050-i (0.025±0.005)].

5.3.2. RAINDROP CHARACTERIZATION

The raindrop spectrum was obtained using a disdrometer, Laser Precipitation Monitor (LPM) of *Thies Clima*, which registered drops between 0.125-8 mm in 22 channels (Fernández-Raga et al., 2010). It determines the falling speed and volume of hydrometeors obtained from the duration and amount of loss of the laser signal emitted and detected in a sampling area of 228 × 20 mm². In the data analysis, we have taken into account the possible wind effect on the disdrometer measurement (Montero-Martínez and García-García, 2016). This measuring equipment has been widely used before (Fernández-Raga et al., 2009; Tapiador et al., 2010).

In order to characterize the raindrop size distribution, we have used the gamma distribution defined as:

$$f(x) = \frac{\beta^{\alpha} x^{\alpha-1} e^{-\beta x}}{\Gamma(\alpha)} \qquad \textit{Eq. 5.4}$$

where Γ is the gamma function, defined as:

$$\Gamma(s) = \int_0^{\infty} t^{s-1} e^{-t} dt \qquad \textit{Eq. 5.5}$$

The gamma distribution is defined for all positive real numbers and depends on two parameters: α and β (Fernandez-Raga et al., 2017), which may be computed following the method of moments, from the relations $\mu = \alpha / \beta$ and $\sigma^2 = \alpha / \beta^2$, where μ and σ^2 are, respectively, the mean size of raindrops and the variance (Duhanyan & Roustan, 2011; Johnson, et al., 2014). Besides, when α>1, we determined the mode of the gamma distribution through (α-1)/β (Fernandez-Raga et al., 2017).

From the data provided by the LPM we obtained for every minute the following 32 rainfall variables: precipitation intensity, accumulated precipitation, number of drops in 22 channels between 0.125 mm and 8 mm, total number of recorded drops (# min^{-1} m^{-2}), drop concentration (# m^{-3}), water content [total volume of drops per m^3 (mm^3 m^{-3})], total drop section (mm^2 m^{-2}), volume removed by falling drops (mm^3 m^{-3}), mean and standard deviation (mm) of raindrop sizes and drop size mode.

5.4. RESULTS AND DISCUSSION

5.4.1. METEOROLOGICAL AND PRECIPITATION STUDY

Fifty-four rain events were recorded during the study period. The average wind speed was also registered (mean of wind speed during event); the peak was measured on 09/16/2015 with 5.3 m s^{-1}, although most of the events showed speeds between 0.1 and 2 m s^{-1}. The average temperature during the events was between 15 and 25 °C in summer, between 8 and 15 °C in autumn, and between -2 and 11 °C in winter. Finally, low pressures were recorded in all rain events, with values between 986 and 1027 hPa. The maximum, minimum and mean meteorological data are shown in Table 5.1. A particular time series of full processed data can be seen in section 4.4.

The accumulated rainfall ranged between 0.4 mm (event occurred on 13 September 2015) and 32.7 mm (on 15 September 2015) and precipitation intensities ranged between 0.2 mm h^{-1} (26 October 2015) and 5.8 mm h^{-1} (30 August 2015). The mean accumulated rainfall was 4.3 mm per event, and the mean precipitation intensity was 1.1 mm h^{-1}. The shortest event lasted for 28 minutes (30 August) and the longest 20 hours and 32 minutes (between 5 and 6 November), with an average of 286 minutes. October was the month with more rain events (20), with a total of 71.5 mm of accumulated precipitation.

Table 5.1. Meteorological study of rain events with data of maximum, minimum and mean temperature, relative humidity, wind intensity and pressure.

	T (°C)	Relative Humidity (%)	Wind Speed (m s^{-1})	Pressure (hPa)
Min	-1.6	31	0.0	986
Max	24.4	96	5.3	1027
Mean	11.0	84	1.4	1005

5.4.2. DAILY PATTERN IN PARTICLE CONCENTRATION

For no-rain days the daily pattern of aerosol concentration on a 1 min basis was obtained, aiming at eliminating the daily evolution of aerosol concentration effects on the rain events. To do this, we have used the particle concentration of all days without rain between July 2015 and January 2016, distinguishing between weekdays and weekend days. We have first determined, for each day, the ratio between the concentration every minute and the average particle concentration of that day. With the daily ratio series, the average daily pattern was computed. We calculated the minute ratio ($R_{i,j}$) of the daily pattern for the minute i of the day j with the following formula: $R_{i,j} = \frac{N_{i,j}}{\overline{N}_j}$ where $N_{i,j}$ is the particle concentration during the minute i of the day j, $\overline{N}_j = \frac{\sum_i N_{i,j}}{n}$, and n is the number of minutes in one day (1440). With the data from the whole sampling period, we subsequently determined the 1 min average R_i for each minute of the day: $R_i = \frac{\sum_j R_{i,j}}{d}$ where d being the number of days without rain (106) during the sampling campaign. Obviously, this value represents the daily concentration pattern on a 1 min basis, in relation to the daily mean concentration. During the sampling campaign, the daily mean concentration was 165 # cm^{-3}.

In the daily pattern (Figure 5.3), the highest values - regardless of weather conditions on days without rain - were recorded before 1000 UTC and after 1800 UTC, coinciding with the entrance and exit times to college, schools and work, with the resulting increase in traffic. The minimum number of particles was registered between 1400 and 1600 UTC. Therefore, this daily pattern seems to respond to traffic emissions and domestic heating devices.

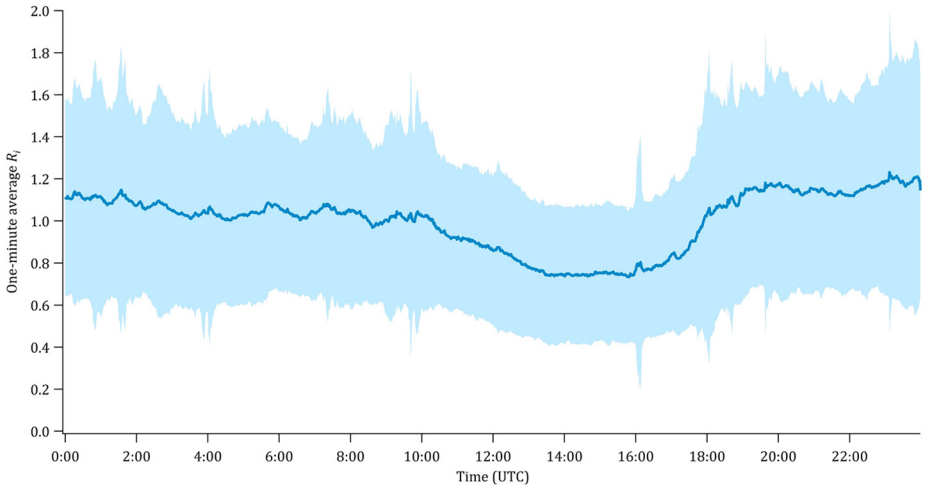

Figure 5.3. Daily pattern on weekdays of the number of particles per cubic metre (line) minute by minute regarding the daily mean between July 2015 and January 2016 at the University of Leon. The shaded area represents the standard deviation.

As the relative humidity may significantly affect aerosol size, one might wonder how this variable influences the daily pattern. As the daily pattern has been defined regardless of aerosol size, it only represents the evolution of the particle number. So, the relative humidity has no relevance to the pattern shown in Figure 5.3. As a consequence, the calculation of the scavenging (analysed in the next section on the basis of the daily pattern), is only related to the total number of particles, with no reference to their size.

This daily pattern was used to correct the data in order to remove the influence of the daily pattern on aerosol concentration, thus preserving the main effect of the rainfall. This correction was done by dividing the number of particles in each minute by R_i as shown in Figure 5.3.

5.4.3. STUDY OF THE SCAVENGING EFFECT

4.4.3.1. Change in aerosol concentration

For each episode the number and mass of particles has been analysed before, during and after rainfall. We observed an average decrease in the number of particles of 10% when comparing the aerosol concentration before and during rain, and of 19% when comparing before and after rain. Due to the effect caused by precipitation there was a mean decrease of 14% in the aerosol concentration registered after rain with respect to the moment of the shower. These results indicate that precipitation has a global scavenging effect on aerosol particles in the atmosphere (Table 5.2).

Table 5.2. Summary of evolution of number of particles, before, during and after rain events. Data for episodes of maximum and minimum concentrations are shown, together with the mean values for all rain episodes.

	Concentration (part. cm^{-3})			Variation (%)		
	Before	During	After	Before-During	During-After	Before-After
Min	49±9	25±6	20±2	73	50	75
Max	1192±62	1174±96	1011±52	-62	-62	-78
Mean	276±26	266±67	243±37	-10	-14	-19

The mean geometric diameter of the aerosol particles was evaluated in each event, minute by minute, before, during and after rainfall (Table 5.3). There was a decrease in the mean particle size between before and during precipitation of about 0.5%, while between before and after rain there was a decrease of 1.6%. Therefore, BCS caused by rain in León leads to a decrease in the concentration of particles, mainly in the coarse mode concentration (which represents 13.8% of total aerosol mass), but due to the low number of large particles, it has little influence on the geometric mean of particle size. Figure 5.4 shows the concentration of particles before, during and after rainfall in two events: one with a low pre-rain particle concentration and one with a high concentration (which will be described in detail later).

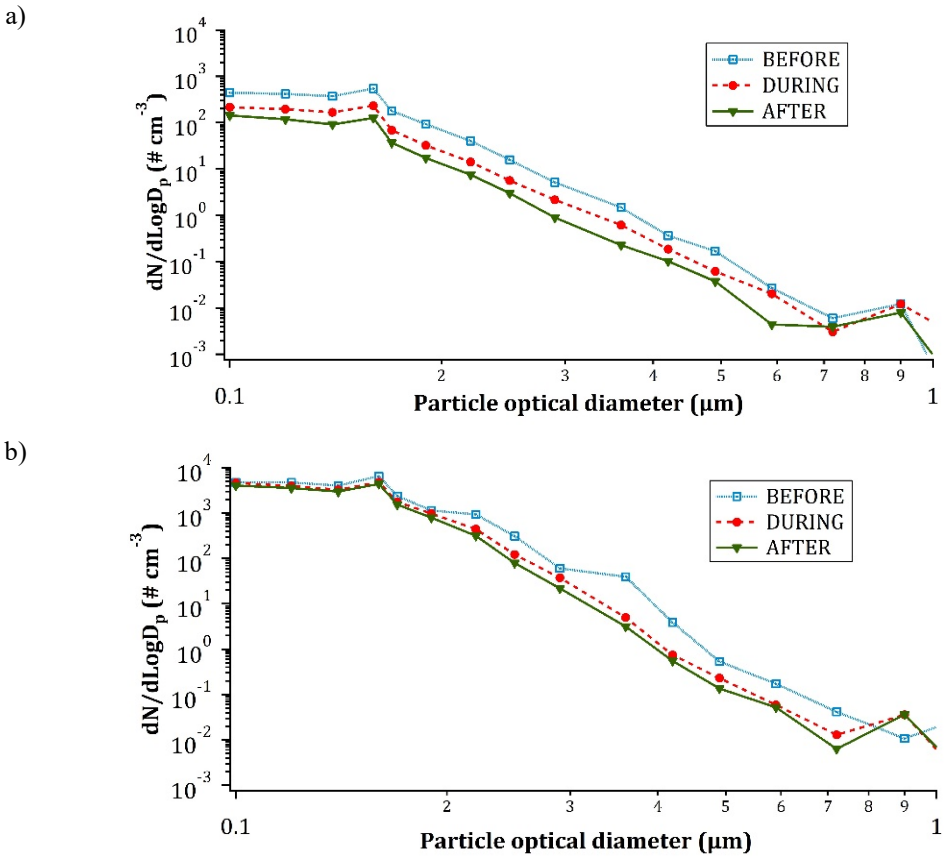

Figure 5.4. Concentration of particles before (squares), during (circles) and after (triangles) rainfall in the rain events of a) 13 September 2015 and b) 26 October 2015.

Table 5.3. Summary of evolution of geometric mean particle size before, during and after rain events. Data for episodes of maximum and minimum aerosol diameters are shown, together with the mean values for all rain episodes.

	Diameter (d_p, µm) and geometric deviation (σ_g)						Variation (%)		
	Before		During		After		Before-During	During-After	Before-After
	d_p	(σ_g)	d_p	(σ_g)	d_p	(σ_g)			
Min	0.122	1.253	0.123	1.256	0.123	1.244	8.4	6.9	8.2
Max	0.171	1.452	0.137	1.425	0.174	1.425	-7.3	-10.8	-13.1
Mean	0.138	1.301	0.137	1.307	0.136	1.303	-0.5	-1.1	-1.6

These percentages are significantly higher than those found by Radke et al. (1980), who conducted field measurements on natural, anthropogenic and volcanic aerosols, where the concentration of aerosol decreased with BCS by 6% (in number) and 21% (in volume) for an average precipitation intensity of 0.85 mm h^{-1} (similar intensity to our study) and a duration of 170 min. Other studies, such as Loosmore and Cederwall (2004), are based on models and obtained a 70% decrease in the number of particles caused by wet deposition. More recent studies show decreases of 25% in the number of particles between 0.2 and 0.8 μm in rainfall events (Zikova and Zdimal, 2016).

5.4.3.2. Estimation of the scavenging coefficient

In order to evaluate the scavenging caused by rain, the λ parameter was also used, from aerosol mass data in 10 min intervals, as in Chate et al. (2011) and Olszowski (2015). Scavenging coefficients over an ensemble of 54 rain events (with a mean intensity of 1.1 mm h^{-1}) and 31 aerosol particle diameter (d_p) classes (from 0.1 to 24.32 μm) for the fine mode (0.1-1 μm) indicate a mean value of $2.6 \cdot 10^{-5}$ s^{-1} (with a standard deviation of $6.0 \cdot 10^{-5}$ s^{-1}) and a median of $1.7 \cdot 10^{-5}$ s^{-1} (interquartile range: $1.4 \cdot 10^{-6}$ to $3.4 \cdot 10^{-5}$ s^{-1}), a value lower than the one found by Laakso et al. (2003) and Zikova and Zdimal (2016), although in the same order of magnitude. Scavenging coefficients for the coarse mode (>1 μm) indicate a mean value of $5.8 \cdot 10^{-5}$ s^{-1} (with a standard deviation of $9.6 \cdot 10^{-5}$ s^{-1}) and a median of $4.0 \cdot 10^{-5}$ s^{-1} (interquartile range: $3.5 \cdot 10^{-6}$ to $7.6 \cdot 10^{-5}$ s^{-1}). The values obtained are comparable to those obtained by Cugerone et al. (2018) in Italy (between $2 \cdot 10^{-5}$ and $5 \cdot 10^{-5}$ s^{-1}) and lower than scavenging coefficients during thunderstorm rain events (Chate, 2005). This result indicated that collection of aerosol particles by raindrops was more efficient in a highly electrified thunderstorm, mainly in the fine mode (Zhao et al., 2015).

The λ coefficient in each rain event was computed and related to the wind speed to observe the influence of this meteorological variable on particle concentration. Figure 5.5a shows that in the fine mode there was less variability in the λ coefficient than in the coarse mode. Regardless of the precipitation intensity, a positive λ value can be found. There was no clear influence of the wind, although for negative values of λ low wind speeds dominate. In Figure 5.5b, there are four events with low wind speed with negative λ values, whereas the rest of the events with low wind speed have positive values very close to 0.

Scavenging in the coarse mode is more effective than with fine particles. With rain intensities greater than 1.5 mm h^{-1}, both in the fine and the coarse modes, there were no events with λ negative values, so scavenging was always effective with such rain intensity.

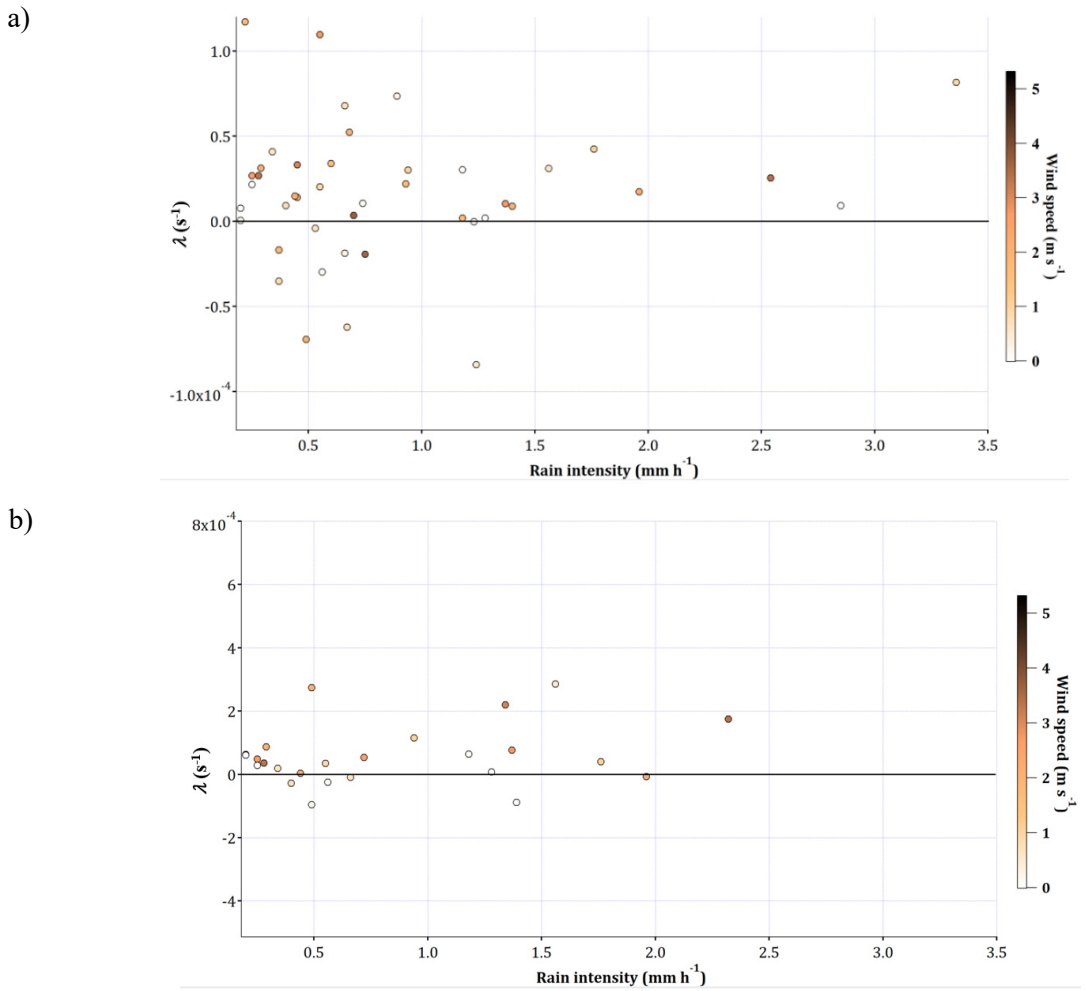

Figure 5.5. Scavenging coefficients in fine (a) and coarse (b) mode in relation with rain intensity and wind speed (colour points).

In all the events analysed globally, positive values of λ were obtained in the fine and coarse modes, indicating an effective scavenging of atmospheric aerosol, which is higherin the coarse mode. In addition, the evolution of λ depends on the timing of the rain event where the rainfall intensityis increasing. In most episodes the trend of the scavenging coefficient over the event was negative. Many other studies (Davenport and Peters, 1978; Laakso et al. 2003; Maria and Russell, 2005) have estimated the scavenging efficiency of aerosols in the real atmosphere by means of various physical mechanisms.

Other studies have determined a smaller λ in the coarse mode with a diameter range between 3.5 and 10 μm (Volken and Schumann, 1993) and around $1 \cdot 10^{-5}$ s^{-1} on average for particles in the 0.1–1 μm size (Laakso et al. 2003). Why is there so much variability among the λ values? We agree with Zhang et al. (2013), who suggested several possible explanations for the differences in the data from the different studies: errors caused by the instruments and processes, chemical processes, microphysical processes (nucleation, condensation, hygroscopic growth and coagulation) and physical processes (turbulent diffusion, e.g.).

5.4.3.3. *Greenfield Gap* analysis

The so-called Greenfield Gap, an interval where the particles suffer less from the BCS effect, comprises sizes between 0.3 and 1 µm (Greenfield, 1957). In the present article, there are not enough samples to establish significance levels to make comparisons with particle sizes larger than 1 µm because of a very low particle concentration. The scavenging was analysed in this study, represented as *%ΔC*, the percentage of change in particle concentration as a function of the rainfall intensity over the particle size spectrum. As can be seen in Figure 5.6, in the Greenfield Gap (0.3–1 µm) scavenging was less effective than in the rest of the spectrum, although less scavenging was observed mainly for particles of sizes between 0.6 and 1.0 µm. This pattern occurred with low and high precipitation intensities. With high rainfall intensities, the Greenfield Gap fits perfectly to the size spectrum with less scavenging. Particles with diameters smaller than 0.6 µm presented a 20% decrease between after and before rain with low (0.2–1 mm h^{-1}) and medium (1–3 mm h^{-1}) intensities. However, with high rainfall intensities (>3 mm h^{-1}) the decrease was around 10% in the particles smaller than 0.25 µm, but effective scavenging did not occur in the rest of the spectrum until exceeding a size of 1 µm. This fact may be due to the resuspension from evaporated raindrops in the coarse mode after the beginning of the rain event (Wang et al., 2015) or caused by the resuspension of particles coming from soil splash (Bullard et al., 2018; Josserand and Thoroddsen, 2016; Pruppacher et al., 1983), producing an increase in coarse aerosol concentration. To sum up, particles with sizes between 0.6 and 1 µm suffer less scavenging than particles smaller than 0.6 µm.

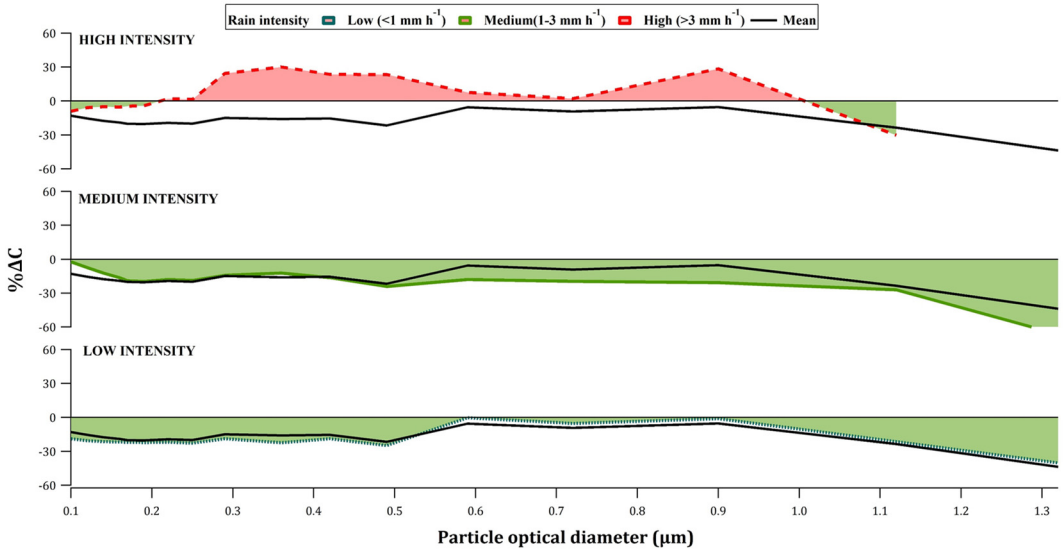

Figure 5.6. Percentage of particle concentration variation in particle spectrum with low (dotted line), medium (thin continuous line) and high rainfall intensities (dashed line), and mean of the 54 events studied (thick continuous line).

In the section 5.3.4 the correlations between the number of drops and the number of particles have been calculated, including Greenfield Gap.

The results of this study are, at least partially, in accordance with those obtained by Greenfield (1957). The scavenging of large particles at the beginning of a rain event is very effective and a low concentration of aerosol particles is registered. During rain events there are nearly no particles larger than 1 μm in diameter. The processes that explain this low coarse mode concentration are Brownian diffusion, which justifies a greater scavenging for small particles (with diameters close to 0.1 μm), and the effect of inertia, which accounts for a great scavenging of particles larger than 2 μm diameter (Quérel et al., 2014; Sportisse, 2007).

5.4.3.4. Pearson correlations

The 64 variables studied in the present paper are shown in Table 5.4. The Pearson correlations between all pairs of meteorological and aerosol-related variables were computed. The following statistically significant correlations, for all the rain events, might be highlighted, with a 0.05 significance level:

- Between the precipitation intensity and the total number of particles ($r=-0.53$; $p<0.001$).
- There were significant negative correlations between the four variables that give the number of aerosol particles with diameters between 0.10 and 0.16 μm and the nine variables that give the number of drops with sizes between 0.5 and 3 mm.
- There were significant negative correlations between the 15 variables that give the number of aerosol particles with diameters between 0.16 and 1.76 μm and the eight variables that give the number of drops with sizes between 0.75 and 3 mm.
- Between the total mass of aerosol particles and precipitation intensity ($r=-0.53$; $p<0.001$).

Table 5.4. Variables studied for Pearson correlations: 38 aerosol variables, 3 meteorological variables and 23 precipitation variables.

Aerosol variables
Total number of particles and mass
Number of particles in 17 channels between 0.1 µm and 1.76 µm
Mass of particles in 17 channels between 0.1 µm and 1.76 µm
Geometric mean diameter and standard deviation of aerosol
Meteorological variables
Temperature
Humidity
Wind intensity
Precipitation variables
Precipitation intensity
Accumulated precipitation
Number of drops in 13* channels between 0.125 mm and 3.5 mm
Total number of recorded drops
Raindrop concentration
Water content
Section drops
Total volume removed by falling drops
Mean and standard deviation of drop size
Mode of drop size

* Only the first 13 channels registered some raindrops.

The Pearson correlation coefficients between the drop channels and the percentage variation in 10 min periods in the particle channels were plotted (Figure 5.7) in order to observe the BCS effect of the different drop sizes on the different particle sizes. The main scavenging effect in the fine mode occurred between drop sizes ranging from 0.3 to 1 mm and the particle sizes between 0.2 and 0.4 µm. Drop sizes between 0.5 and 2 mm affected only marginally the particles between 0.7 and 0.9 µm (included in the "Greenfield Gap"). The coarse mode suffered a clear scavenging by all drop sizes, mainly drops larger than 1.5 mm. Finally, the scavenging caused by raindrops larger than 2 mm is unclear for particles smaller than 0.6 µm.

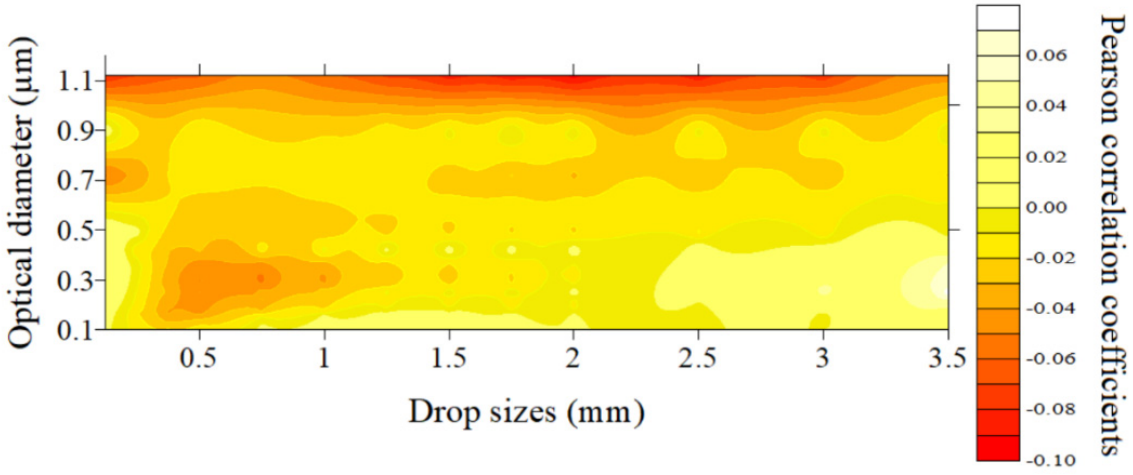

Figure 5.7. Pearson correlation coefficients between the raindrop channels and the variation of particle concentration in 10-minute periods.

Regarding the parameters obtained from the laser disdrometer, there were statistically significant negative Pearson correlations ($p<0.05$) between the water content [total volume of drops per m^3 (mm^3 m^{-3})], total drop section (mm^2 m^{-2}) and total volume removed by falling drops (mm^3 m^{-3}) and the variation of the number of particles of channels with diameters between 0.12 and 0.19 μm, which indicates that a higher volume removed by drops caused a higher scavenging on particles between 0.12 and 0.19 μm.

5.4.4. STUDY OF SCAVENGING EFFECT IN ONE RAIN EVENT

One rain event was analysed in detail. The main reason for choosing this event is that both the concentration and the variations registered were close to the average values recorded throughout the sampling period. The drop size distribution, the particle size distribution and the scavenging effect were analysed. This rain event occurred on 26 October 2015 between 0619 and 0840 UTC, lasting 2 h 21 min. Accumulated rainfall was 3.66 mm, with a maximum precipitation intensity of 0.94 mm in 10 min. The maximum intensity in 1 h was 2.89 mm h^{-1}.

Figure 5.8 shows the evolution of the number of particles per unit volume of air and of the precipitation on a 1 min basis, corrected using the daily pattern from Figure 5.3. During the half hour before the precipitation, the particle number remained constant, with no change in the air mass, because no change in wind direction or speed was observed. With the beginning of precipitation, a slight increase in the number of particles was recorded first, and then, a slow but steady decline. As stated above, the slight increase in the number of particles may be caused by

resuspension (Bullard et al., 2018; Josserand and Thoroddsen, 2016; Pruppacher et al., 1983; Wang et al., 2015). The peaks in the number of particles occurred when the rain almost completely reduced its intensity. Table 5.5 shows a brief characterization of the event on the basis of data compiled by the LPM.

Comparing the average number of particles 30 min before the start of the precipitation and 30 min after, there is a decrease of 26%. Compared before rain and during precipitation, there is a decrease of 5%. The aerosol mass concentration evolution is similar to the number of particles, with a decreasing percentage of 30%, between before and after rain.

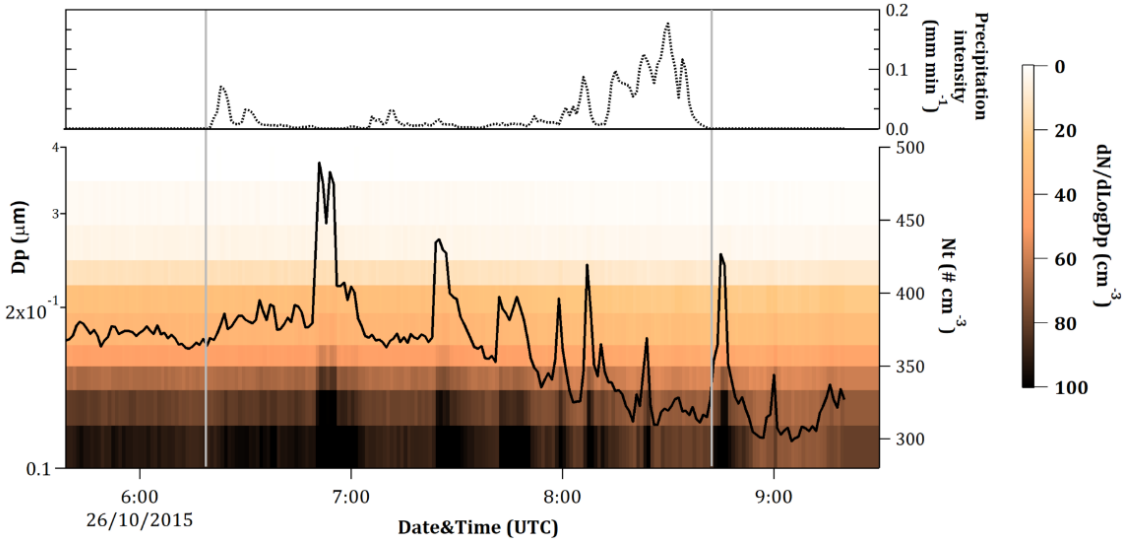

Figure 5.8. Time evolution of the aerosol size distribution (colour-coded), total number of particles (continuous black line) and precipitation intensity (dotted grey line) on 1 min basis, in rain event of 26 October 2015. White vertical lines separate 30 min before and after rain.

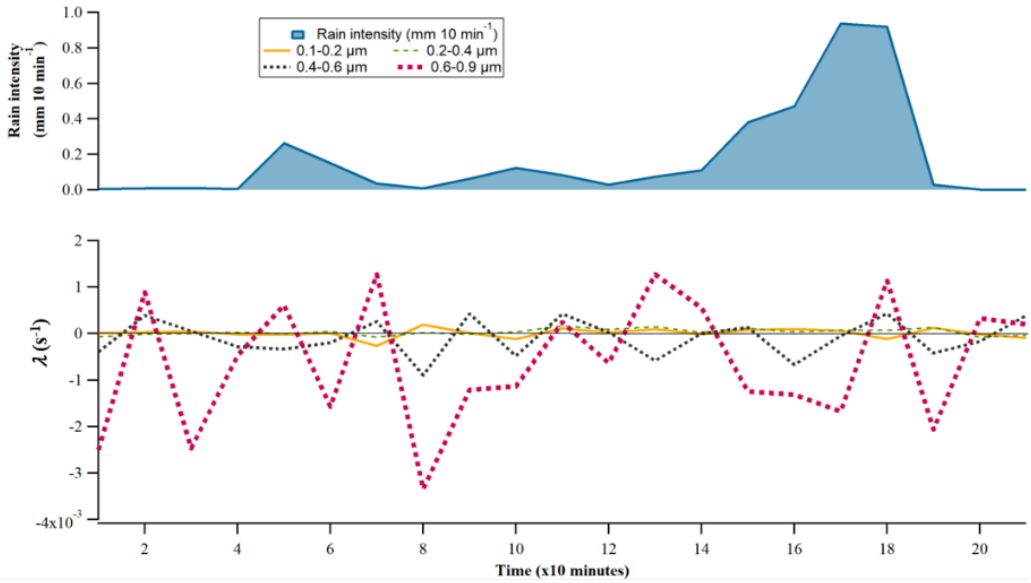

Figure 5.9. Time evolution of the scavenging factor and precipitation intensity on a 10 min basis, in the rain event of 26 October 2015.

Table 5.5. Characterization of the event on 26 October 2015 with data compiled by the laser precipitation monitor.

Total precipitation (mm)	3.72
Total number of drops recorded per m^2	$1.58 \cdot 10^7$
Mean drop size (mm)	0.56
Variance of mean size (mm)	0.12
α	2.62
β (mm^{-1})	4.65
Mode (mm)	0.35

5.5. CONCLUSIONS

In this study the main conclusions are the following:

- Scavenging is less effective in the Greenfield Gap (0.3 to 1 μm), mainly between 0.6 and 1 μm, than in particles smaller than 0.3 μm.
- In the whole sample, on average, the number of atmospheric particles decreased during rain by 10%, and between before and after rain by 18%.
- While raining, the number of raindrops between 0.5 and 3 mm showed statistically significant ($p<0.05$) negative correlations with the number of particles between 0.1 and 0.16 μm. Besides, the number of drops between 0.75 and 3 mm showed statistically significant ($p<0.05$) negative correlations with the number of particles between 0.16 and 1.76 μm, thus demonstrating the potential of those raindrop sizes to favour the scavenging of particles of these particular sizes.
- In the events studied, rain caused a significant scavenging effect on aerosol particles in the atmosphere: the scavenging coefficient mean value, over an ensemble of 54 rain events, was $2.6 \cdot 10^{-5}$ s^{-1} (with a standard deviation of $6.0 \cdot 10^{-5}$ s^{-1}) for the fine mode and $5.8 \cdot 10^{-5}$ s^{-1} (with a standard deviation of $9.6 \cdot 10^{-5}$ s^{-1}) for the coarse mode, of the same order of magnitude as the results from other authors.
- After rain, the geometric mean diameter of aerosols remained stable (at around 0.13 μm) due to the low number of large particles, which are more effectively scavenged.

The joint study of both aerosol particles sizes and raindrop diameters proved to be a useful tool for the quantification of BCS, enabling us to estimate the raindrop sizes that produce effective scavenging. Future studies will focus on raindrop size distributions in order to analyse the scavenging effect on ultrafine, fine and coarse aerosol particles.

5.6. REFERENCES

Andronache C. 2003. Estimated variability of below-cloud aerosol removal by rainfall for observed aerosol size distributions. Atmos. Chem. Phys. 3: 131 – 143. DOI: 10.5194/acp-3-131-2003

Andronache C, Grönholm T, Laakso L, Phillips V, Venalainen A. 2006. Scavenging of ultrafine particles by rainfall at a boreal site: observations and model estimations. Atmos. Chem. Phys. 6: 4739 – 4754. DOI: 10.5194/acp-6-4739-2006

Berthet S, Leriche M, Pinty JP, Cuesta J, Pigeon G. 2010. Scavenging of aerosol particles by rain in a cloud resolving model. Atmos. Res. 96, 325–336. DOI: 10.1016/j.atmosres.2009.09.015

Bohren CF, Huffman DR. 1984. Absorption and Scattering of Light by Small Particles. Wiley. ed. New York.

Bullard JE, Ockelford A, Strong CL, Aubault H. 2018. Impact of multi-day rainfall events on surface roughness and physical crusting of very fine soils. Geoderma. 313: 181–192. DOI: 10.1016/j.geoderma.2017.10.038

Calvo AI, Alves, C, Castro A, Pont V, Vicente AM, Fraile R. 2013. Research on aerosol sources and chemical composition: Past, current and emerging issues. Atmos. Res. 120–121: 1–28. DOI: 10.1016/j.atmosres.2012.09.021

Calvo AI, Pont V, Castro A, Mallet M, Palencia C, Roger JC, Dubuisson P, Fraile R. 2010. Radiative forcing of haze during a forest fire in Spain. J. Geophys. Res. Atmos. 115: 1 – 10. DOI: 10.1029/2009JD012172

Castro A, Alonso-Blanco E, González-Colino M, Calvo AI, Fernández-Raga M, Fraile R. 2010. Aerosol size distribution in precipitation events in León, Spain. Atmos. Res. 96: 421 – 435. DOI: 10.1016/j.atmosres.2010.01.014

Castro A, Calvo AI, Alves C, Alonso-Blanco E, Coz E, Marques L, Nunes T, Fernández-Guisuraga JM, Fraile R. 2015. Indoor aerosol size distributions in a gymnasium. Sci. Total Environ. 524–525: 178 – 186. DOI: 10.1016/j.scitotenv.2015.03.118

Chate, DM 2005. Study of scavenging of submicron-sized aerosol particles by thunderstorm rain events. Atmos. Environ. 39: 6608–6619. doi:10.1016/j.atmosenv.2005.07.063

Chate DM, Murugavel P, Ali K, Tiwari S, Beig G. 2011. Below-cloud rain scavenging of atmospheric aerosols for aerosol deposition models. Atmos. Res. 99: 528 – 536. DOI: 10.1016/j.atmosres.2010.12.010

Cugerone K, De Michele C, Ghezzi A, Gianelle V. 2018. Aerosol removal due to precipitation and wind forcings in Milan urban area. J. Hydrol. 556: 1256–1262. doi:10.1016/j.jhydrol.2017.06.033

Davenport HM, Peters LK. 1978. Field studies of atmospheric particulate concentration changes during precipitation. Atmos. Environ. 12: 997–1008.

Duhanyan N, Roustan Y. 2011. Below-cloud scavenging by rain of atmospheric gases and particulates. Atmos. Environ. 45: 7201 – 7217. DOI: 10.1016/j.atmosenv.2011.09.002

Fernandez-Raga M, Castro A, Marcos E, Palencia C, Fraile R. 2017. Weather types and rainfall microstructure in Leon, Spain. Int. J. Climatol. 37: 1834 – 1842. DOI: 10.1002/joc.4816

Fernández-Raga M, Castro A, Palencia C, Calvo AI, Fraile R. 2009. Rain events on 22 October 2006 in León (Spain): Drop size spectra. Atmos. Res. 93: 619 – 635. DOI: 10.1016/j.atmosres.2008.09.035

Fernández-Raga M, Fraile R, Keizer JJ, Varela Teijeiro ME, Castro A, Palencia C, Calvo AI, Koenders J, Da Costa Marques RL. 2010. The kinetic energy of rain measured with an optical disdrometer: An application to splash erosion. Atmos. Res. 96: 225 – 240. DOI: 10.1016/j.atmosres.2009.07.013

Fournier N, Westo KJ, Dore, AJ, Sutton MA. 2005. Modelling the wet deposition of reduced nitrogen over the British Isles using a Lagrangian multi-layer atmospheric transport model. Q. J. R. Meteorol. Soc. 131: 703–722. doi: 10.1256/qj.04.76

Fröhlich-Nowoisky J, Kampf CJ, Weber B, Huffman JA, Pöhlker C, Andreae MO, Lang-Yona N, Burrows SM, Gunthe SS, Elbert W, Su H, Hoor P, Thines E, Hoffmann T, Després VR, Pöschl U. 2016. Bioaerosols in the Earth system: Climate, health, and ecosystem interactions. Atmos. Res. 182: 346–376. DOI: 10.1016/j.atmosres.2016.07.018

Glantz P, Noone KJ, Osborne SR. 2003. Scavenging efficiencies of aerosol particles in marine stratocumulus and cumulus clouds. Q. J. R. Meteorol. Soc. 129: 1329–1350. doi: 10.1256/qj.02.73

Greenfield SM. 1957. Rain scavenging of radioactive particulate matter from the atmosphere. J. Meteorol. DOI: 10.1175/1520-0469(1957)014<0115:RSORPM>2.0.CO;2

Johnson RW, Kliche DV, Smith PL. 2014. Maximum likelihood estimation of gamma parameters for coarsely binned and truncated raindrop size data. Q. J. R. Meteorol. Soc. 140: 1245 – 1256. DOI: 10.1002/qj.2209

Josserand C, Thoroddsen S. 2016. Drop Impact on a Solid Surface. Annual Review of Fluid Mechanics. Annual Reviews. 48: 365 - 391. DOI: 10.1146/annurev-fluid-122414-034401

Kulshrestha UC, Reddy LAK, Satyanarayana J, Kulshrestha MJ. 2009. Real-time wet scavenging of major chemical constituents of aerosols and role of rain intensity in Indian region. Atmos. Environ. 43: 5123 – 5127. DOI: 10.1016/j.atmosenv.2009.07.025

Laakso L, Grönholm T, Rannik Ü, Kosmale M, Fiedler V, Vehkamäki H, Kulmala M. 2003. Ultrafine particle scavenging coefficients calculated from 6 years field measurements. Atmos. Environ. 37: 3605 – 3613. DOI: 10.1016/S1352-2310(03)00326-1

Ladino L, Stetzer O, Hattendorf B, Günther D, Croft B, Lohmann U. 2011. Experimental Study of Collection Efficiencies between Submicron Aerosols and Cloud Droplets. J. Atmos. Sci. 68: 1853 – 1864. DOI: 10.1175/JAS-D-11-012.1

Lide DR. 1993. Handbook of Chemistry and Physics. 74.a ed. ed. Boca ratón.

Loosmore GA, Cederwall RT. 2004. Precipitation scavenging of atmospheric aerosols for emergency response applications: Testing an updated model with new real-time data. Atmos. Environ. 38: 993 – 1003. DOI: 10.1016/j.atmosenv.2003.10.055

Maria SF, Russell LM. 2005. Organic and inorganic aerosol below-cloud scavenging by suburban New Jersey precipitation. Environ. Sci. Technol. 39: 4793 – 4800. DOI: 10.1021/es0491679

Montero-Martínez G, García-García F. 2016. On the behaviour of raindrop fall speed due to wind. Q. J. R. Meteorol. Soc. 142: 2013 – 2020. DOI: 10.1002/qj.2794

Olszowski T. 2015. `The efficiency of PM 10 scavenging from troposphere as a function of type and duration of wet deposition`. In Proceedings of 1st International Conference on Atmospheric Dust. Castellaneta Marina, Italy. 1June-4June 2014. DOI: 10.14644/dust.2014.064

Peter JR, Siems ST, Jensen JB, Gras JL, Ishizaka Y, Hacker JM. 2006. Prediction and observation of cloud processing of the aerosol size distribution by a band of cumulus. Q. J. R. Meteorol. Soc. 132: 845–863. doi: 10.1256/qj.05.106

Pilon R, Grandpeix JY, Heinrich P. 2015. Representation of transport and scavenging of trace particlesin the Emanuel moist convection scheme. Q. J. R. Meteorol. Soc. 141: 1244–1258. doi: 10.1002/qj.2431

Pruppacher HR, Semonin RG, Slinn WGN. 1983. Precipitation scavenging, dry deposition and resuspension, vol 1., chap. Precipitation scavenging.

Quérel A, Lemaitre P, Monier M, Porcheron E, Flossmann AI, Hervo M. 2014. An experiment to measure raindrop collection efficiencies: Influence of rear capture. Atmos. Meas. Tech. 7: 1321 – 1330. DOI: 10.5194/amt-7-1321-2014

Radke LF, Hobbs PV, Eltgroth MW. 1980. Scavenging of Aerosol Particles by Precipitation. J. Appl. Meteorol. DOI: 10.1175/1520-0450(1980)019<0715:SOAPBP>2.0.CO;2

Seinfeld JH, Pandis S. 2006. Atmospheric from Air Pollution to Climate Change. Atmos. Chem. Phys. 51: 1248. DOI: 10.1016/0016-7037(87)90252-3

Sportisse B. 2007. A review of parameterizations for modelling dry deposition and scavenging of radionuclides. Atmos. Environ. 41: 2683 – 2698. DOI: 10.1016/j.atmosenv.2006.11.057

Tapiador FJ, Checa R, De Castro M. 2010. An experiment to measure the spatial variability of rain drop size distribution using sixteen laser disdrometers. Geophys. Res. Lett. 37: 1 – 6. DOI: 10.1029/2010GL044120

Textor C, Schulz M, Guibert S, Kinne S, Balkanski Y, Bauer S, Berntsen T, Berglen T, Boucher O, Chin M, Dentener F, Diehl T, Easter R, Feichter H, Fillmore D, Ghan S, Ginoux P, Gong S, Grini A, Hendricks J, Horowitz L, Huang P, Isaksen I, Iversen T, Kloster S, Koch D, Kirkevåg A, Kristjansson JE, Krol M, Lauer A, Lamarque JF, Liu X, Montanaro V, Myhre G, Penner J, Pitari G, Reddy S, Seland Ø, Stier P, Takemura T, Tie X. 2006. Analysis and quantification of the diversities of aerosol life cycles within AeroCom. Atmos. Chem. Phys. 6: 1777 – 1813. DOI: 10.5194/acp-6-1777-2006

Tost H, Jöckel P, Kerkweg A, Sander R, Lelieveld J. 2006. Technical note: A new comprehensive scavenging submodel for global atmospheric chemistry modelling. Atmos. Chem. Phys. 6: 565 – 574. DOI: 10.5194/acp-6-565-2006

UNICEF. 2016. Clear the air for children. The impact of air pollution on children. https://www.unicef.org/publications/index_92957.html (accessed 20/02/2018).

Volken M, Schumann T. 1993. A Critical review of below-cloud aerosol scavenging results on Mt. Rigi. Water, Air, Soil Pollut. 68: 15 – 28. DOI: 10.1007/BF00479390

Wang H. Easter RC, Ganguly D, Singh B, Rasch PJ. 2015. `Resuspension of Aerosol Particles from Evaporated Rain Drops to the Coarse Mode`. In Fall Meeting 2015, abstract id. A51W-04. American Geophysical Union.

Wang PK, Pruppacher HR. 1977. An Experimental Determination of the Efficiency with Which Aerosol Particles are Collected by Water Drops in Subsaturated Air. J. Atmos. Sci. 34: 1664 – 1669. DOI: 10.1175/1520-0469(1977)034<1664:AEDOTE>2.0.CO;2

Wang X, Zhang L, Moran MD. 2010. Uncertainty assessment of current size-resolved parameterizations for below-cloud particle scavenging by rain. Atmos. Chem. Phys. 10: 5685 – 5705. DOI: 10.5194/acp-10-5685-2010

Zhao S, Yu Y, He J, Yin D, Wang B. 2015. Below-cloud scavenging of aerosol particles by precipitation in a typical valley city, northwestern China. Atmos. Environ. 102: 70 – 78. DOI: 10.1016/j.atmosenv.2014.11.051

Zikova N, Zdimal V. 2016. Precipitation scavenging of aerosol particles at a rural site in the Czech Republic. Tellus B. 68: 1 – 14. DOI: 10.3402/tellusb.v68.27343

CHAPTER 6. Evolution of size-segregated aerosol concentration in NW Spain

Full title: *Evolution of size-segregated aerosol concentration in NW Spain: a two-step classification to identify new particle formation events*

Submitted for publication

6.1. INTRODUCTION

Atmospheric aerosol particles are ubiquitous and widely recognised as important contributors to global climate change (Feichter and Stier, 2012; Lohmann and Feichter, 2005) and in recent times, aerosols have been proved as vectors of virus transmission, e.g. SARS-CoV-2 (Seminara et al., 2020). Their impact is dependent on the composition and the number size distribution (Dusek et al., 2006; Fuzzi et al., 2015). Airborne particles have negative impacts on human health, mainly in urban areas. An important number of epidemiological studies have revealed a relationship between fine particles (smaller than 1 μm) concentration and respiratory-cardiovascular diseases (Pope, 2000; Pope and Dockery, 2006). Currently air quality standards are based on particle mass concentrations ($PM_{2.5}$ and PM_{10}). Nevertheless, numerous studies have reported a stronger correlation of the adverse health effects with the number concentration of ultrafine particles (UFP, sizes < 100 nm) than with the mass concentration (HEI Review Panel, 2013). What is the issue? The UFP have a minimum contribution to the total mass concentration of airborne particles in urban areas, although their number concentration is very high (Morawska

et al., 2008). Thus, UFP are more toxic, due to associated compounds, compared to larger particles of the same composition (Nel, 2005; Pekkanen et al., 2007). All this leads to the role of UFPs in urban air quality is being of great interest (Alonso-Blanco et al., 2017; Buonanno et al., 2012; Rahman et al., 2017).

Three types of particle sources are usually predominant in the urban areas (de Jesus et al., 2019):

i) Primary emissions (vehicle exhausts emissions): the combustion related with traffic is the major source in urban areas, as shown in several studies that reveal a strong correlation between UFP concentration and traffic activity, in particular, during rush hours (Alam et al., 2003; Jones and Harrison, 2006). These particles present a bimodal size distribution, with a nucleation mode (<30 nm) due to gas-to-particle conversion when the saturation ratio of gaseous mixtures of low volatility reaches a maximum (Arnold et al., 2006; Burtscher, 2005), and a second mode (50-200 nm) formed by carbonaceous particles (Casati et al., 2007; Rose et al., 2006).
ii) Local non-vehicular sources, such as coal-fired power plants, gas-fired facilities or biomass burning, mainly in winter (de Jesus et al., 2019).
iii) New Particle Formation (NPF) processes in ambient air: they are caused by photochemical reactions of naturally emitted gaseous precursors in ambient air by "in-situ nucleation" after emission. This mechanism includes two main steps: nucleation of an initial cluster (<1 nm) and subsequent particle growth (Kulmala et al., 2005). These processes are frequently observed in the warm period, when the following ambient conditions are favourable for NPF: i) low relative humidity (Hamed et al., 2011; Wu et al., 2008), ii) high temperature and solar radiation which promotes a high photochemical activity (Ma and Birmili, 2015), iii) clean conditions with low pre-existing aerosol concentration, iv) availability of condensable vapours in the atmosphere capable of promoting NPF events and; v) the phenological stage of the vegetation with the consequent contribution of biogenic precursors (Hakola et al., 2003).

The evaluation of the influence of the aerosol sources on ultrafine and fine particles is vital for knowing their contribution to the particle size distribution (PSD) in urban areas and, also, for understanding their effects on human, such as health problems or traffic restrictions (EEA, 2016; Kinney, 2008; Tong et al., 2017, 2016; Viard and Fu, 2015).

The NPF events are typically identified by using visual-based methods (Dal Maso et al., 2005). For it, PSD data are plotted throughout the hours of the day and analysed day by day in search of the banana shape, making it a tedious, somewhat subjective and time-consuming method. Some approaches have been proposed in order to simplify and automatize this process. Thus, Hyvönen

et al. (2005) and Mikkonen et al. (2006) applied a discriminant analysis to classify nucleation events and non-events, using different predictor variables. Joutsensaari et al. (2018) tried to automatize the identification of NPF events using deep learning through a transfer learning of a convolutional neural network applied to PSD images. Therefore, there is a need to develop a method to identify NPF events quickly and effectively.

Information about PSD in urban areas of the northwest of Iberian Peninsula is scarce. This area is only covered by two sites, an urban background coastal site in A Coruña (Iglesias-Samitier et al., 2014) and an urban background site in León (Blanco-Alegre et al., 2021). This latter is providing observations of aerosol number size distribution since a few years ago, complementing existing measurements in Spain (Alonso-Blanco et al., 2018). In this regard, this work presents for the first time an extensive overview of a 13-months field study of ground-level measurements of aerosol number size distributions in northwest Iberian Peninsula. The temporal variations of fine and ultrafine particle size distributions and their concentrations were analysed. Furthermore, their relationships with meteorological parameters at different temporal scales were investigated. A detailed study of NPF events (intensity, timing and growth rates) during the campaign was conducted, evaluating their impact on the suburban atmosphere of León. Finally, a statistical methodology, quick and easy, was proposed in order to identify the days with NPF events.

6.2. METHODOLOGY

6.2.1. SAMPLING SITE

León (42°36′N, 05°35′W, 838 m a.s.l.) is a Spanish city located at NW of the Iberian Peninsula with about 200,000 inhabitants (Figure S6.1). It has a Mediterranean climate with continental features. Traffic and heating devices, especially in winter, and wildfires and Saharan intrusions in summer are the major sources of aerosol particles (Blanco-Alegre et al., 2019; Oduber et al., 2021).

The sampling campaign covered the period from 12 February 2016 to 14 March at an urban background site. The instruments were installed at the University of León, situated in the NE border of the city. In order to analyse the evolution of the data over the year, the seasons have been defined, as in as in other paper of the same sampling campaign (Blanco-Alegre et al., 2019),

as follows: winter (cold period) from 15 December to 14 March, spring (warm period) from 15 March to 14 June, summer (warm period) from 15 June to 14 September and autumn (cold period) from 15 September to 14 December.

6.2.2. AEROSOL PARTICLES CHARACTERIZATION

Ultrafine and fine aerosol particles have been measured through a high-resolution nanoparticle sizer (TSI-SMPS Model 3938). A complete size distribution between 15 and 736.5 nm in 110 channels with a temporal resolution of 6 minutes was obtained. A description of the equipment and the measurement procedure is presented in Blanco-Alegre et al. (2021).

The total particle concentration (N_{total}) (# cm^{-3}), the total particle surface distribution (S_{total}, nm^2 cm^{-3}) and the total particle volume distribution (V_{total}, nm^3 cm^{-3}) were estimated using the AIM software, considering the aerosol particles spherical. Hourly average of PSDs have been fitted to lognormal distributions to parameterize the different particle modes: nucleation mode concentration (N_{nuc}) is the number of particles between 15 and 30 nm per unit volume; Aitken mode concentration (N_{Ait}) between 30 and 100 nm, and the accumulation mode concentration (N_{acc}) from 100 to 736.5 nm.

SMPS together with an optical spectrometer, a Passive Cavity Aerosol Spectrometer Probe (PCASP-X), have been used to obtain the particle size distributions between 15 nm and 17.42 µm, assuming particle sphericity and using a monthly density obtained from the chemical analysis of daily quartz filters sampled during the study period (Blanco-Alegre et al., 2021 RF). Finally, PM_{10} mass concentration was calculated from the aerosol size distribution.

6.2.3. NEW PARTICLE FORMATION EVENTS

The new particle formation (NPF) events selection was carried out in several steps:

1) Exclusion of hourly measurements with missing data.
2) Application of the visual method (day to day) proposed by Dal Maso et al. (2005) to carry out a first visual identification of the NPF events. For this purpose, daily (24-h) surface plots of aerosol size distributions have been plotted and subsequently inspected in search of the "banana shape" caused by the growth of particles from nucleation to Aitken mode. The new mode of particles must start in the nucleation mode, then growth and prevail for hours.

3) Classification of NPF events into three types following Dal Maso et al. (2005) method:
    a. Type *Ia*: days when growth and formation rate could be determined with a high degree of confidence, which is to say very clear and strong NPF events, with no particles initially in the nucleation mode.
    b. Type *Ib*: the rest of events with a high degree of confidence, but with pre-existing particles in the nucleation mode.
    c. Type *II*: unclear events, where the accuracy of the results is questionable.

After an exhaustive analysis of the database (13 months of sampling campaign), 45 events of type *Ia,* 36 of type *Ib* and 15 of type *II* were identified. In NPF days, the evolution of the aerosol size distribution was studied through the analysis of several parameters. The particle mode diameter (D_{mode}) was calculated for 6-min average PSDs using log-normal fits. The growth rate (*GR*, nm h^{-1}) was estimate using D_{mode}. The flux of particles out from the nucleation mode size range (F_{growth}, # cm^{-3} s^{-1}), the loss of particles due to coagulation (F_{coag}, # cm^{-3} s^{-1}) and the flux of particles nucleated in the nucleation mode interval ($J_{15\text{-}30}$, # cm^{-3} s^{-1}) (Eq. 6.1), were calculated as in Dal Maso et al. (2005) and compiled in the Supplementary material.

$$J_{15-30} = \frac{dN_{15-30}}{dt} + F_{coag} + F_{growth} \qquad Eq.\ 6.1$$

where N_{15-30} is the concentration of particles in nucleation mode.

Besides, the aerosol Condensation Sink (*CS*, s^{-1}) parameter that measures the scavenging speed of atmospheric molecules by condensation onto pre-existing aerosol particle, was calculated as shown in Eq. 6.2 (Lehtinen et al., 2008):

$$CS = 2\pi \cdot D \cdot \sum_i \beta_{Mi} \cdot d_{p,i} \cdot N_i \qquad Eq.\ 6.2$$

where *D* is the diffusion coefficient of the condensing vapor in the gas phase (in this study *D* is the H_2SO_4 diffusion coefficient, 0.104 cm^2 s^{-1}) (Lyman et al., 1990), β_{Mi} is the transitional correction factor using an accommodation coefficient of 1 (Fuchs and Sutugin, 1971), $d_{p,i}$ (nm) is the particle diameter and N_i (# cm^{-3}) is the PNC for each particle size discrete interval *i*.

The *Q* (cm^{-3} s^{-1}) is the condensable vapor source rate calculated as the product of *CS* and *C* (condensable vapor concentration). Low values of *CS* (lower than 0.014 s^{-1}) indicate a clean ambient. Conversely, a *CS* value higher than 0.038 s^{-1} indicates a high pre-existence of aerosol particles in the atmosphere (Kerminen et al., 2019).

It is considered that the nucleation of sulfuric acid, ammonium and highly oxidised organic molecules plays a significant role in the formation of such stable clusters, and may also contribute to particle growth by condensation (Ehn et al., 2014; Kirkby et al., 2011; Kulmala et al., 2006).

Besides, H_2SO_4 concentration in gas phase (Riipinen et al., 2007) and volatile organic compounds (VOCs) (Bianchi et al., 2016; Tröstl et al., 2016), especially biogenic, may play a relevant role in the NPF occurrence. Unfortunately, information on these species was not available in this study. Thus, complementary measurements of different pollutants such as NOx, O_3 and SO_2, provided by an air quality station from located 2.4 km far from the sampling point (belongs to from the Air Quality Network Castilla y León), were considered.

6.2.4. STATISTICAL ANALYSES

A univariate (i.e. mean, median, quartiles and standard deviation) and a bivariate analysis (Pearson correlations with 95% confidence intervals) were performed. Furthermore, a *k*-means cluster classification was performed using IBM SPSS Statistics 24 in order to discern between pollutant and non-pollutant days and to search a cluster that groups together days with NPF events. The variables used were: N_{nuc}, N_{Ait}, N_{acc}, N_{total}, NOx and O_3 concentration, total particle surface (S_{total}), atmospheric boundary layer (ABL), temperature (T), relative humidity (RH) and wind speed (WS). T, RH and WS were obtained from a weather station located at the sampling point while the ABL data was acquired from radiosoundings available in National Oceanic and Atmospheric Administration (NOAA) (http://www.ready.noaa.gov/READYamet.php).

Subsequently, in order to identify the NPF events days included in the cluster, a quadratic discriminant analysis was carried out using the aforementioned variables and comparing the results with those from the visual method. Several methods have been proposed for classifying quantitative variables. Amongst the many methods to classify quantitative variables, the discriminant function in Eq. 6.3 has been frequently applied to build a predictive model based on predictor variables (Wang et al., 2018). After testing several time windows, the best classification was obtained with 24 h averages as used by Mikkonen et al. (2006). In Eq. 3, k is the predicted class, x is the set of measurements, μ_c is the mean vector, Σ_c is the covariance matrix, and $\pi(k)$ is the prior probability.

$$d_k(x) = log\pi(k) - \frac{1}{2}log|\Sigma_c| - \frac{1}{2}(x-\mu_c)^T \sum_c^{-1}(x-\mu_c) \qquad Eq.\ 6.3$$

To verify the discriminant model, three indexes used for common events will be used: True Skill Statistic (TSS), Heidke Skill Score (HSS) and Critical Success Index (CSI) (Doswell et al., 1990). The first two indexes range between -1 and 1 (perfect prediction) and the last one between 0 and 1 (perfect prediction). Besides, an "error" index (Hyvönen et al., 2005) has been calculated

in order to compare our results with those from other studies. See supplementary material for further details about these indexes.

6.3. RESULTS AND DISCUSSION

6.3.1. EVOLUTION OF PARTICLE CONCENTRATION

A different daily and seasonal evolution of the modal particle number concentrations (Figure 6.1) were registered during the sampling period.

During the warm period, N_{nuc} presented high values during midday sun hours, clearly related to the occurrence of NPF events (Figure 6.1a). The maximum N_{nuc} value was found on 5 May 2016 with 111,000 # cm^{-3} (Table 6.1). Likewise, the higher N_{Ait} values were registered during the same time slot (Figure 6.1b), probably associated with the growth of the newly-formed particles during the NPF events (evaluated subsequently with F_{growth}). However, these new particles did not reach particle sizes into the accumulation mode, as observed in Figure 6.1c. During the cold period, the N_{Ait} value presented two rush-hour peaks: during the morning (0600-0900 UTC) and the afternoon (1700-2000 UTC). The highest peak, registered during the afternoon, is probably caused by the wind direction (from the city centre to the sampling point) during these hours and the high wind speed registered (mean values of 0.76±0.97 m s^{-1} during the afternoon vs 0.60±0.94 m s^{-1} during the morning) (Figure S6.2). The maximum N_{Ait} value was registered on 30 December 2016 with 33,700 # cm^{-3}. N_{acc} presented a similar pattern, with clear peaks during rush hours (Figure 6.1c). The maximum N_{acc} value was registered on 20 January 2017, with 25,800 # cm^{-3}. However, N_{nuc} presented a smoothed pattern during the cold period, with a slight increase of concentration during rush hours (these peaks are not visible in Figure 6.1a due to the high values involved in warm period because of the influence of NPF bursts). Similar patterns were observed in the urban Spanish sites analysed by Alonso-Blanco et al. (2018).

In short, N_{Ait} and N_{acc} registered their maximums in cold months during rush hours, while N_{nuc} in warm months during midday hours. This is directly related to NPF bursts and the evolution of ABL, given that the impact of traffic emissions in the warm period is lower than in the cold one around the sampling point (Oduber et al., 2021).

a) Nucleation mode

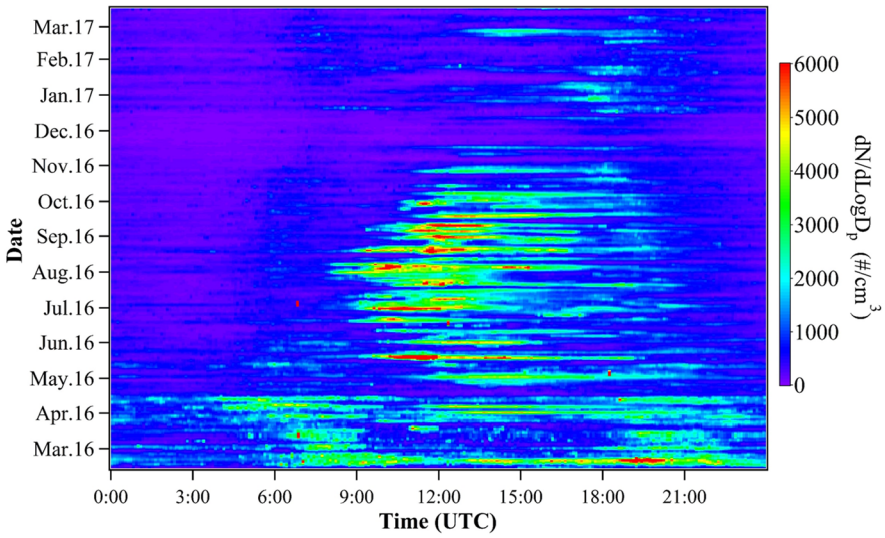

b) Aitken mode

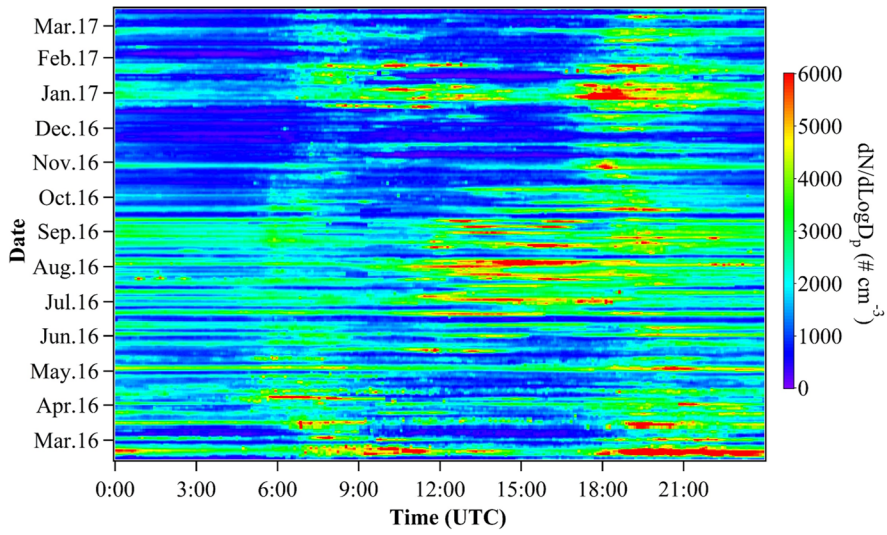

c) Accumulation mode

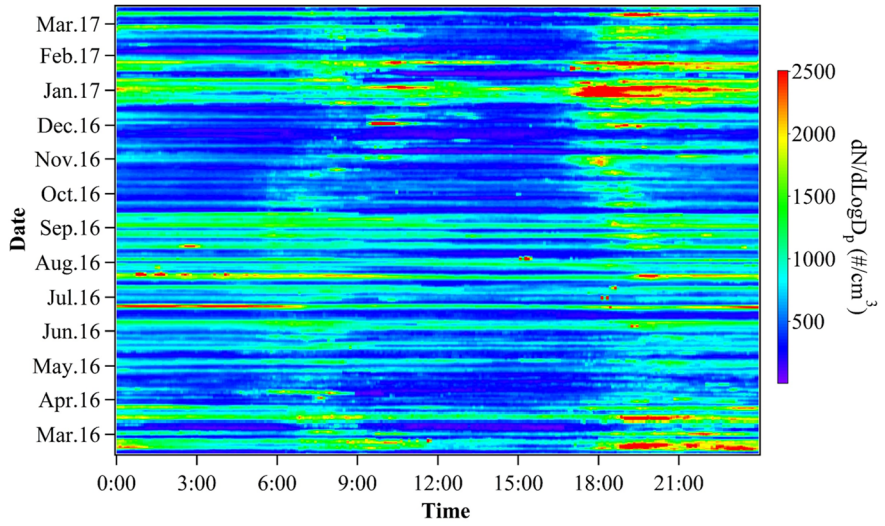

Figure 6.1. Hourly evolution along the study period of the modal particle number concentrations: a) nucleation (N_{nuc}); b) Aitken (N_{Ait}) and c) accumulation (N_{acc}) modes.

Table 6.1 shows the statistical parameters for the modal particle number concentrations and N_{total}, S_{total} and V_{total} for each season. The mean concentration was higher in N_{Ait} than in the other modes (e.g. in summer with 3,000 # cm^{-3}, two times higher than N_{nuc} and three than N_{acc}). This fact can be explained by the strong influence of traffic emissions on N_{Ait} in urban areas during the cold period (Hussein et al., 2004; Tuch et al., 2003; Wehner and Wiedensohler, 2003) and the aged of the newly-formed and pre-existing particles in warm period (Alonso-Blanco et al., 2018; Wang et al., 2013). N_{nuc} and N_{Ait} had a low contribution to PM_{10} mass, despite the high particle number concentration reached in both modes. The contribution of nucleation mode aerosols to the total PNC along the year ranged between 22% (autumn) and 33% (spring), lower values than those registered by Casquero-Vera et al. (2020) in Granada (Spain) who reported contributions of 47% and 48% in an urban and a remote site, respectively. This result raises questions about the suitability of the currently used air quality indices (e.g. Directive 2008/50/EC), based on mass particle, given the low mass contribution of ultrafine particles and their great health effects (de Jesus et al., 2019).

Table 6.1. Summary statistics (quartiles, maximum, mean and standard deviation) of total particle number (N_{total}) and modal (N_{nuc}, N_{Ait} and N_{acc}) concentration, total particle surface (S_{total}) and volume (V_{total}) concentration for each season (Wi: winter, Sp: spring, Su: summer, Au: autumn). The contribution of the modal concentration to PM_{10} (in %) and to PNC (in %) has been included in the table.

	Season	Q_1	Q_2	Q_3	Max	Mean	SD	PM_{10} (%)	PNC (%)
	Wi	1530	3000	5300	51,000	4200	4200	-	-
N_{total}	Sp	2400	3700	6000	116,000	4800	3800	-	-
(cm^{-3})	Su	2800	4300	6600	213,000	5400	4300	-	-
	Au	1400	2200	3500	23,700	2900	2400	-	-
	Wi	211	453	1100	29,700	1000	1600	0.3	24.7
N_{nuc}	Sp	494	949	1900	111,900	1600	2200	0.4	33.0
(cm^{-3})	Su	334	692	1600	202,100	1600	2700	0.4	30.0
	Au	146	302	697	18,500	691	1200	0.2	22.3
	Wi	796	1600	3000	33,700	2300	2300	9	53.6
N_{Ait}	Sp	1200	1900	3100	19,600	2500	1900	9	49.8
(cm^{-3})	Su	1400	2400	3900	29,300	3000	2300	13	52.5
	Au	768	1300	2000	11,500	1600	1300	8	55.6
	Wi	311	642	1200	25,800	871	801	89	21.6
N_{acc}	Sp	370	596	935	6500	711	484	75	16.7
(cm^{-3})	Su	415	736	1100	13,000	869	651	82	17.5
	Au	294	47	700	14,000	562	458	74	22.0
	Wi	42	85	153	2600	112	100	-	-
S_{total}	Sp	52	82	123	819	96	63	-	-
(μm^2 cm^{-3})	Su	64	103	143	1300	112	69	-	-
	Au	41	63	90	1200	72	52	-	-
	Wi	2	3	7	1300	22	64	-	-
V_{total}	Sp	1	2	4	29	3	2	-	-
(μm^3 cm^{-3})	Su	2	4	65	1100	38	60	-	-
	Au	1	2	3	36	2	2	-	-

6.3.2. WEEKLY EVOLUTION

The particle size and surface distributions have been analysed during workdays (Monday-Friday) and weekends (Sunday and Saturday), and clear differences have been observed (Figure 6.2). In general, the particles smaller than 300 nm presented a lower concentration on weekends than on workdays. The higher differences were observed in the range 20 - 40 nm (particle concentration 23% higher on workdays than on weekends). However, the particles larger than 300 nm did not show remarkable differences. This fact suggest that these particles might be associated to the background aerosol of the suburban atmosphere of León. Similar results were obtained by other authors in urban areas (Hama et al., 2017; Hussein et al., 2004; Morawska et al., 2002). The surface distribution presented differences between workdays and weekends in all sizes, with a mean decrease of -23.4% during weekend, mainly in sizes smaller than 30 nm (-31%), due to the reduced traffic and activity in the city and the absence of university activity on weekends. In order to analyse this pattern, the weekly evolution of the concentration by modes (N_{nuc}, N_{Ait} and N_{acc}) and surface concentration in each season was depicted in Figure 6.3.

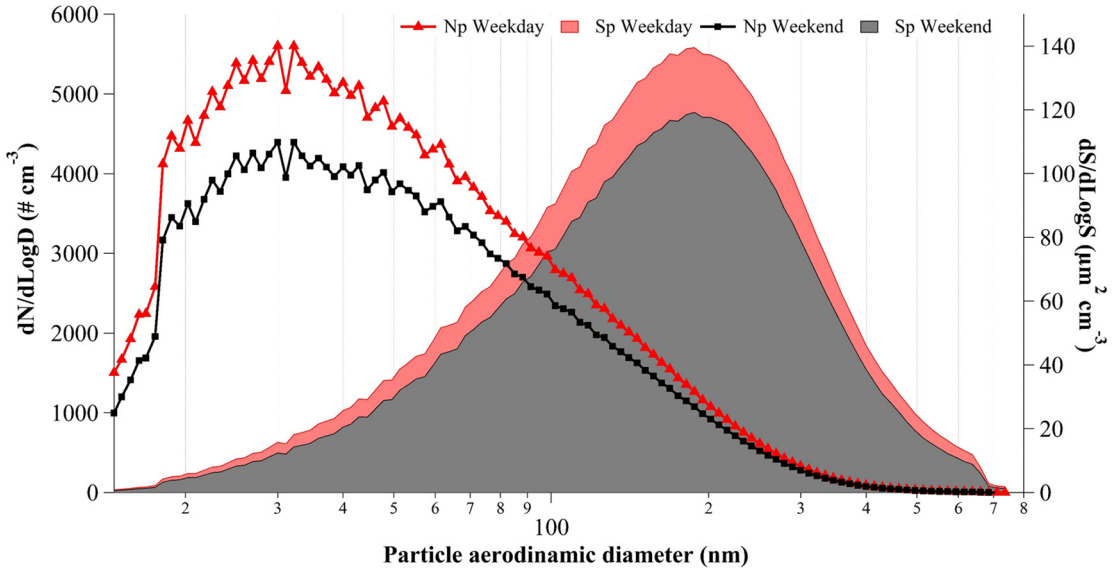

Figure 6.2. Particle number and surface size distributions during workdays and weekends.

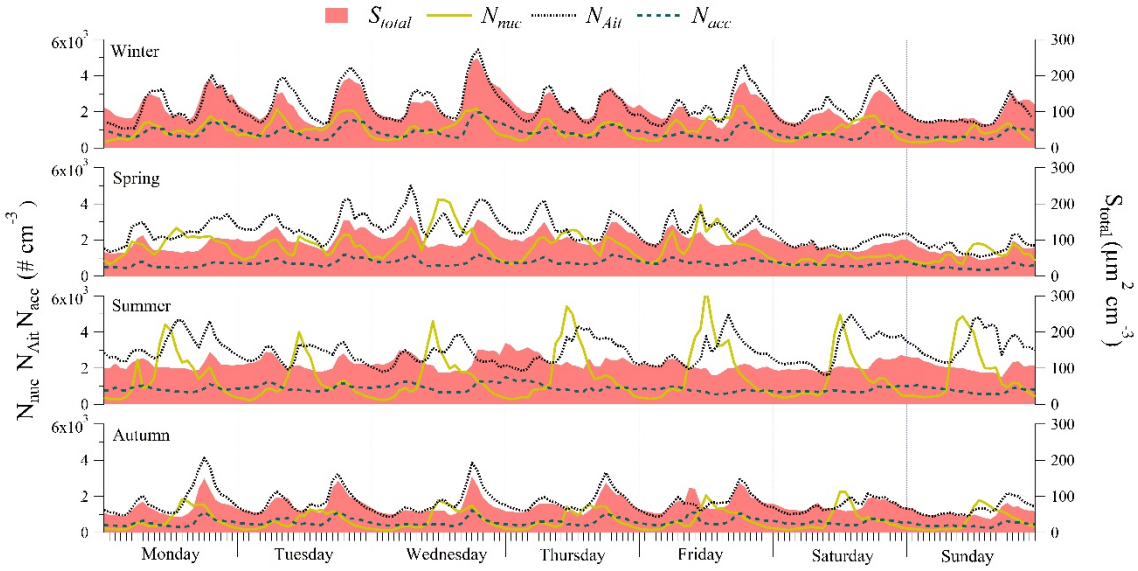

Figure 6.3. Weekly evolution of the modal concentration (N_{nuc}, N_{Ait} and N_{acc}) and surface concentration (S_{total}) in each season of the study period.

Except in summer, there was a decrease in the PNC in all modes during the weekends in comparison with workdays. In summer, there was a clear increment of N_{nuc} during midday caused by NPF events, favoured by a low polluted atmosphere during weekends. Following this increment, N_{Ait} presented an increase probably caused by the growth of the newly-formed particles to the Aitken mode. Except in summer, S_{total} presented a pattern similar to N_{Ait}, with lower values during weekends. During the warm period, the differences in S_{total} between weekdays and weekends were smoothed, probably due to the increase in the ABL as observed by Alonso-Blanco et al. (2018).

6.3.3. METEOROLOGICAL PARAMETERS

A clear relationship between some meteorological parameters and PNC was observed. Thus, temperature showed a significant positive correlation with N_{nuc} (r=0.251), N_{Ait} (r=0.165) and N_{total} (r=0.206). This fact might be related to the high particle concentrations associated to NPF events in summer. N_{acc} presented a negative correlation with temperature in the cold period (r=-0.225), since the main sources were traffic and heating devices (Oduber et al., 2021). In relation to relative humidity, it showed a significant negative correlation with N_{nuc} (r=-0.32), N_{Ait} (r=-0.194), N_{acc} (r=-0.022) and N_{total} (r=-0.255), as observed by Hussein et al. (2006). This fact was expected due to relative humidity counteract an increase of PNC through its influence on the processes of

condensation, nucleation or evaporation (Hussein et al., 2006). Wind speed (WS) presented significant negative correlations with N_{Ait} (r=-0.233), N_{acc} (r=-0.339) and N_{total} (r=-0.176), in line with He et al. (2017). It should be noted that high concentrations of N_{Ait}, N_{acc} and N_{total} were registered at wind speed lower than 1 m s^{-1}. These results might be related to the dilution effect, since wind speed control horizontal dilution (low wind speed causes longer transport times, promoting a higher accumulation of particles) (Hama et al., 2017).

Given the relationship between N_{total} and wind speed, two different techniques have been applied in order to identify and locate the main sources of air pollution: i) Conditional Probability Function (CPF) (Carslaw, 2015; Uria-Tellaetxe and Carslaw, 2014) and ii) bivariate polar plots (Carslaw, 2015; Carslaw and Ropkins, 2012). In order to know the origin of the aerosol particles during the rush-hour peaks, the hours with N_{total} higher than 90th percentile (8806.2 # cm^{-3}) were selected (Uria-Tellaetxe and Carslaw, 2014). Figure S6.3a shows that air samples with high N_{total} have a higher probability of coming from the south-west and south-east, i.e. from the city centre. In addition, the higher N_{total} occurred at low wind speed (< 2 m s^{-1}) from the same wind directions (Figure S6.3b). Focusing on seasons (Figures S6.4 and S6.5), it should be emphasised that: i) in summer, the total PNC was very high due to the occurrence of NFP events regardless of wind speed (Figures S6.5a and S6.5b); ii) in winter and autumn the south and west directions showed the higher PNC in the three modes (with wind speeds < 3 m s^{-1}), corresponding to the directions where León city is located; iii) in winter, west and north directions (that include the main roadway of León) registered higher N_{total} than the rest of the year. Thus, in the León urban background site, the higher N_{total} occurred under stable atmospheric conditions.

Besides, the relationship between ABL and N_{nuc}, N_{Ait} and N_{acc} is different by periods. In the cold period, there was a significant negative correlation between ABL and N_{Ait} (r=-0.287) and N_{acc} (r=-0.400), while ABL and N_{nuc} showed a significant positive correlation (r=0.090). Globally, N_{total} and ABL presented a significant negative correlation (r=-0.197), in accordance with He et al. (2017). These results reveal the low importance of NPF events during the cold period. However, in the warm period, a significant positive correlation between ABL and N_{nuc} (r=0.284) and N_{total} (r=0.136) was found -probably due to the influence of NPF burst- and a non-significative correlation with N_{Ait} (r=0.022). This may indicate that a higher ABL creates favourable conditions for the occurrence of NPF events (a low pollutant atmosphere), since it causes a more effective vertical mixing (higher dispersion) (Olofson et al., 2009). Otherwise, N_{acc} and ABL presented a significant negative correlation (r=-0.208) also in the warm period, stating that N_{acc} was not clearly affected by NPF events.

Similar relationships between other pollutants - such as black carbon (Blanco-Alegre et al., 2019), bioaerosols (Blanco-Alegre et al., 2021) or trace gases (SO_2, NO_x and O_3) (F. Oduber et al., 2019c) - and wind speed or ABL have been found in León.

6.3.4. NEW PARTICLE FORMATION EVENTS

The analysis and visual classification of NPF events resulted in the identification of 45 events of type *Ia,* 36 of type *Ib,* and 15 of type *II*. NPF events occurred primarily between 1100 and 1500 UTC, mainly between June and August (Figure 6.4), and were rarely identified between November and March, the coldest months in León. The events of type *Ia* occurred only in June, July, August and September. This is in line with the higher N_{nuc} observed in summer (Figure 6.1a) with the following conditions: i) low relative humidity (Hamed et al., 2011; Wu et al., 2008), ii) high temperature and solar radiation (Ma and Birmili, 2015), iii) clean conditions with low pre-existing aerosol concentration, iv) availability of condensable vapours in the atmosphere capable of promoting NPF events and; v) abundance of biogenic precursors (Hakola et al., 2003). The events that took place in autumn and winter months were doubtful (types *Ib* and *II*) and occurred prior to high concentration of particles in N_{nuc} derived from traffic emissions.

Given that NPF events of type *Ia* are the most frequent and clear, especially in warm seasons, the further analysis will be focused on them.

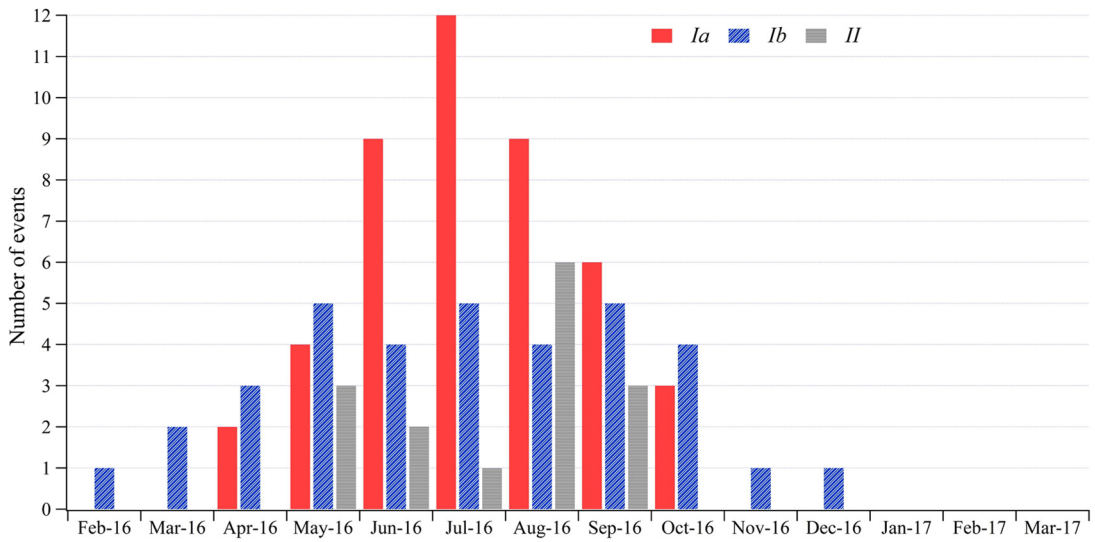

Figure 6.4. Number of NPF events based on visual classification according to Dal Maso et al. (2005).

During the events of type *Ia*, the O_3 mean concentration presented high values (82.1±19.3 μg m^{-3}; annual mean of 55.7±30.8 μg m^{-3}), indicating a strong photochemical activity promoting the NPF bursts. However, NOx concentration, traffic trace gases, was low (6.5±3.4 μg m^{-3}; annual mean of 17.0±21.6 μg m^{-3}) due to a reduction in traffic emissions and possibly a higher dilution of pollutants, especially during the warm period (Table S6.1).

All NPF *Ia* events presented *CS* values lower than 0.014 s^{-1}, indicating a clean atmosphere before the start of the events (Casquero-Vera et al., 2020; Kulmala et al., 2017) (Table S6.1). This is a usual situation prior to NPF bursts (Kulmala et al., 2017). The *CS* values ($9.12 \cdot 10^{-4} \pm 4.26 \cdot 10^{-4}$ s^{-1}) were lower in León than in other European cities such as Helsinki (Hussein et al., 2008), Marseille and Athens (Kulmala et al., 2005), Granada (Casquero-Vera et al., 2020) or Budapest (Salma et al., 2011) and two orders of magnitude lower than in polluted cities like New Delhi (Kulmala et al., 2005). These low *CS* values, associated to the low particle load in León, favoured the occurrence of NPF events. Due to the lack of information about hygroscopic properties of aerosol particles, *CS* values obtained in León can be considered as lower estimates for real condensation sinks. Similarly, *Q* values ($2.58 \cdot 10^{4} \pm 1.93 \cdot 10^{4}$ cm^{-3} s^{-1}) were lower than in polluted cities of India or China (Kulmala et al., 2005; Wang et al., 2013) and lower than in other European background sites ($2.6 \cdot 10^{5}$–$1.6 \cdot 10^{6}$ cm^{-3} s^{-1}) (Kulmala et al., 2005).

Globally, a mean *GR* value of 2.08±0.90 nm h^{-1} was obtained, that is within the typical range of growth rate of 1-20 nm h^{-1} estimated by Kulmala et al. (2005). The variations could be related with the production and availability of condensable vapours, according to different ambient conditions of temperature and relative humidity (Yli-Juuti et al., 2011). As expected, and as a result of the NPF bursts, a high mean of N_{total} ($9.2 \cdot 10^{3} \pm 4.2 \cdot 10^{3}$ # cm^{-3}) was observed, being N_{nuc} ($6.4 \cdot 10^{3} \pm 3.4 \cdot 10^{3}$ # cm^{-3}) the main contributor. The J_{15-30} values in León (1.84±0.98 cm^{-3} s^{-1}) were higher than in remote stations like Hyytiälä (Dal Maso et al., 2005), and generally lower than in other European cities like Helsinki or Budapest (urbans) (Hussein et al., 2008; Salma et al., 2011). However, in Leicester (urban station) (Hama et al., 2017) the values were lower than in León, which may be explained by the pre-existing particles in Leicester from traffic emissions that avoid coagulation. In summary, the main limiting factors for the occurrence of NPF-*Ia* events were O_3 concentration (>55 μg m^{-3}) and CS (< $2 \cdot 10^{-3}$ s^{-1}).

An example of an NPF event of type *Ia* occurred on 24 July 2016 is shown in Figure 6.5 and explained below. Other examples of NPF events of types *Ib* and *II* (doubtful) are showed in Figures S6.6 and S6.7, with a nucleation process but with pre-existing particles (*Ib*).

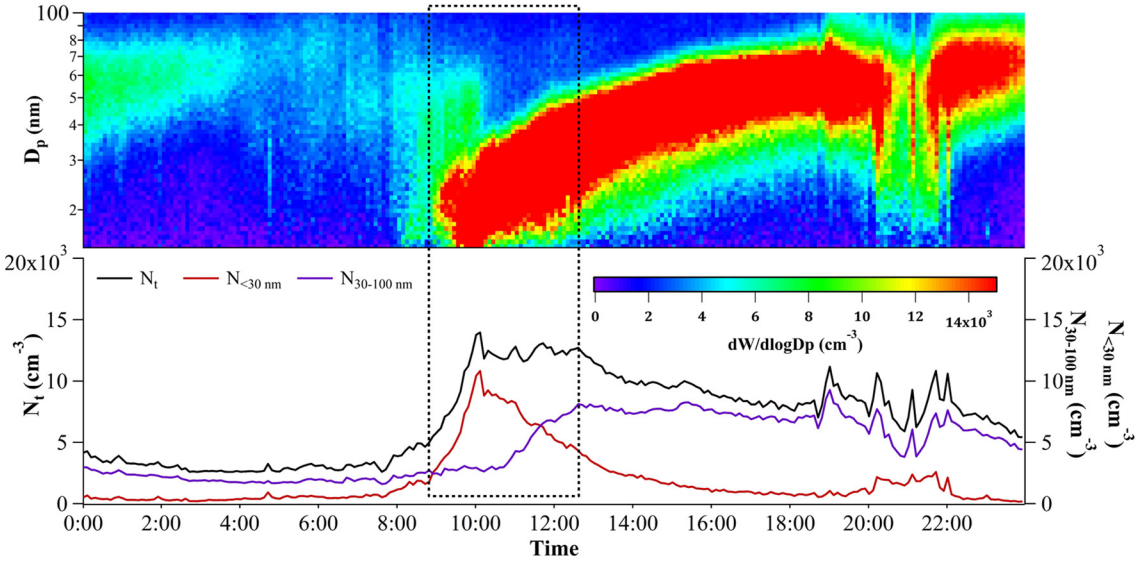

Figure 6.5. Example of a NPF event of type *Ia*. Evolution of the aerosol size distributions (surface plot) and total (N_{total}), nucleation (N_{nuc}) and Aitken (N_{Ait}) particle number concentrations at 24/07/2016.

The *Ia* event selected has representative conditions for events type *Ia*. This day registered 14 hours of insolation, with a mean temperature of 20.8 ºC (maximum of 31 ºC), a mean relative humidity of 47.7% and very low wind speed (mean of 0.54 m s^{-1}). The ABL at 0900 UTC was 591 m and along the day increased to 1244 m at 1200 UTC, 1808 m at 1500 UTC and 1932 m at 1800 UTC. At 0900 UTC started a clear increase in nucleation mode particles (the NPF probably began in the sizes lower than those recorded by the SMPS long DMA - 15 nm). At 1200 UTC a high concentration of particles was observed in Aitken, due to the newly formed particles grew continuously from nucleation to Aitken mode size. The evolution of hourly PSD from 0900 UTC to 1800 UTC (Figure S6.8) allows to observe the effect of the NPF event, with a shift of the distribution towards larger sizes and an increase of the median (CMGD) from 43.1 nm at 0900 UTC to 58.4 nm at 1800 UTC, while the mean size mode changes from 20.4 nm at 0900 UTC to 57.7 nm at 1800 UTC. In this example, the parameters calculated presented the following mean values; *GR*: 2.58 nm h^{-1}, $J_{15\text{-}30}$: 0.73 cm^{-3} s^{-1}, *CS*: $1.4 \cdot 10^{-3}$ s^{-1}, *Q*: $5.1 \cdot 10^{4}$ cm^{-3} s^{-1}, N_{total}: 12,200 # m^{-3}, N_{nuc}: 9,200 # cm^{-3}, O_3: 76.2 µg m^{-3} and NOx: 3.8 µg m^{-3}.

6.3.5. MODEL FOR THE IDENTIFICATION OF NEW PARTICLE FORMATION EVENTS

The statistical process to identify nucleation events consisted of two stages: first, a *k*-means cluster classification has been applied to find the main air quality situations in the city, and second, a discriminant analysis to identify days with nucleation events has been addressed. The variables used in the two stages were N_{nuc}, N_{Ait}, N_{acc}, N_{total}, NOx, O_3, S_{total}, ABL, T, RH and WS.

This methodology allows to evaluate the relationship between NPF days and the air quality of León city. Four clusters have been obtained based on the mean values of the parameters listed in Table S6.2:

1) Cluster 1 (N=8 events) includes the days with the higher pollution load in the city, caused by high traffic density, Saharan outbreaks and the presence of thermal inversions in the lower layers of the atmosphere.
2) Cluster 2 (N=159 events) groups "clean" days, with low N_{total}, high wind speed conditions and days after precipitation, mainly during weekends of spring and summer.
3) Cluster 3 (N=93 events) includes the days of spring and summer with occurrence of NPF events (56 days, previously identified by the visual-based method) and a few winter days in which a high value N_{nuc} and N_{Ait} was registered (possibly associated with an increase in traffic and heating devices emissions).
4) Cluster 4 (N=139 events) contains a high number of "standard days" corresponding to weekends of winter and autumn, and workdays of spring and summer, without any special pollutant event.

Applying a discriminant analysis in cluster 3 to identify days with NPF events without using the visual method, 55 of the 56 NPF events, regardless of the type, were detected and there were 6 "false positives". The statistically significant variables were N_{total}, N_{nuc}, N_{Ait}, WS, T, ABL, RH, O_3, NOx. The standardised coefficients of the canonical discriminant function for each variable are included in Table S6.3. Hyvönen et al. (2005) in Finland and Mikkonen et al. (2006) in Italy, who applied a discriminant analysis to classify nucleation events and non-events, obtained the best classification with: i) relative humidity and condensation sink; and ii) relative humidity, radiation and ozone concentration, respectively. This fact shows that, depending on the study area, the factors for nucleation occurrence are diverse, as indicated by Kerminen et al. (2018).

The indexes TSS, HSS and CSI, applied to the whole sample of days included in cluster 3, reported a value of 0.887, 0.820 and 0.839, respectively, showing a great performance of discrimination. Contingence table is included in Table S6.4. An error index of 12.7% was determined, very similar to that obtained by Hyvönen et al. (2005) and lower than that found by Mikkonen et al. (2006). The results suggested that the application of this method on a longer sampling campaign may be a good approximation to identify the NPF events and subsequently be classified.

6.4. CONCLUSIONS

The real-time measurement of submicron particles showed that the Aitken (N_{Ait}) and accumulation (N_{acc}) mode particles registered their maximum concentrations in cold months, during rush hours in the morning (0600-0900 UTC) and in the afternoon (1700-2000 UTC). Nevertheless, nucleation (N_{nuc}) mode particles registered their maximum concentrations in warm months, influenced by new particle formation (NPF) processes, being one of the main contributors to submicrometric aerosol. A total of 45 type *Ia* events (very clear and strong NPF events), 36 of type *Ib,* and 15 of type *II* have been identified, which occurred between 1100 and 1500 UTC.

A different relationship between planetary boundary layer (ABL) and N_{nuc} by periods has been observed. In the warm period, a positive significant correlation between ABL and N_{nuc} was registered, while during the cold period the pattern was the opposite. It indicates that, in warm period, a higher ABL caused better conditions (a low pollutant atmosphere) for the occurrence of NPF events.

A statistical method to identify NPF days based on two-steps has been applied. First, using N_{total}, N_{nuc}, N_{Ait}, N_{acc}, wind speed, temperature, ABL, relative humidity, O_3 and NOx, four clusters of days were determined, that include: i) the days with the higher pollution load in the city (high traffic density or Saharan outbreaks); ii) “clean” days, high wind speed conditions and days after precipitation; iii) the days of spring and summer with occurrence of NPF events (56 days) and winter days with a high value N_{nuc} and N_{Ait}; and iv) “standard days” without any special pollutant event. Second, in the third cluster, using a quadratic discriminant analysis with the same variables, 55 of 56 NPF days included were identified. An error index of 12.7% was obtained, so the method is valuable to analyse long-term samplings more precisely.

This study contributes to supplement the information on submicrometric aerosol concentration in NW Iberian Peninsula, an area with scarce data, with special emphasis on particle nucleation

events. Also, the method proposed is a step forward to develop a method to identify NPF events quickly and effectively. Furthermore, this work raises questions about the suitability of the currently used air quality indices, based on mass particle, given the low mass contribution of ultrafine particles and their great health effects.

6.5. REFERENCES

Alam, A., Shi, J.P., Harrison, R.M., 2003. Observations of new particle formation in urban air. J. Geophys. Res. Atmos. 108, n/a--n/a. doi:10.1029/2001jd001417

Alonso-Blanco, E., Gómez-Moreno, F.J., Artíñano, B., Iglesias-Samitier, S., Juncal-Bello, V., Piñeiro-Iglesias, M., López-Mahía, P., Pérez, N., Brines, M., Alastuey, A., García, M.I., Rodríguez, S., Sorribas, M., del Águila, A., Titos, G., Lyamani, H., Alados-Arboledas, L., 2018. Temporal and spatial variability of atmospheric particle number size distributions across Spain. Atmos. Environ. 190, 146–160. doi:10.1016/j.atmosenv.2018.06.046

Alonso-Blanco, E., Gómez-Moreno, F.J., Núñez, L., Pujadas, M., Cusack, M., Artíñano, B., 2017. Aerosol particle shrinkage event phenomenology in a South European suburban area during 2009–2015. Atmos. Environ. 160, 154–164. doi:10.1016/j.atmosenv.2017.04.013

Arnold, F., Pirjola, L., Aufmhoff, H., Schuck, T., Lahde, T., Hameri, K., 2006. First gaseous sulfuric acid measurements in automobile exhaust: Implications for volatile nanoparticle formation. Atmos. Environ. 40, 7097–7105. doi:10.1016/j.atmosenv.2006.06.038

Bianchi, F., Tröstl, J., Junninen, H., Frege, C., Henne, S., Hoyle, C.R., Molteni, U., Herrmann, E., Adamov, A., Bukowiecki, N., Chen, X., Duplissy, J., Gysel, M., Hutterli, M., Kangasluoma, J., Kontkanen, J., Kürten, A., Manninen, H.E., Münch, S., Peräkylä, O., Petäjä, T., Rondo, L., Williamson, C., Weingartner, E., Curtius, J., Worsnop, D.R., Kulmala, M., Dommen, J., Baltensperger, U., 2016. New particle formation in the free troposphere: A question of chemistry and timing. Science (80-.). 352, 1109–1112. doi:10.1126/science.aad5456

Blanco-Alegre, C., Calvo, A.I., Coz, E., Castro, A., Oduber, F., Prévôt, A.S.H.H., Močnik, G., Fraile, R., 2019. Quantification of source specific black carbon scavenging using an aethalometer and a disdrometer. Environ. Pollut. 246, 336–345. doi:10.1016/j.envpol.2018.11.102

Blanco-Alegre, C., Castro, A., Calvo, A.I., Oduber, F., Fernández-gonzález, D., Valencia-barrera, R.M., Vega-maray, A.M., Molnár, T., Fraile, R., 2021. Towards a model of wet deposition of bioaerosols : The raindrop size role. Sci. Total Environ. 767, 145426. doi:10.1016/j.scitotenv.2021.145426

Buonanno, G., Marini, S., Morawska, L., Fuoco, F.C., 2012. Individual dose and exposure of Italian children to ultrafine particles. Sci. Total Environ. 438, 271–277. doi:10.1016/j.scitotenv.2012.08.074

Burtscher, H., 2005. Physical characterization of particulate emissions from diesel engines: A review. J. Aerosol Sci. 36, 896–932. doi:10.1016/j.jaerosci.2004.12.001

Carslaw, D., 2015. The openair manual open-source tools for analysing air pollution data. King's Coll. London 1, 287.

Carslaw, D.C., Ropkins, K., 2012. Openair - An r package for air quality data analysis. Environ. Model. Softw. 27–28, 52–61. doi:10.1016/j.envsoft.2011.09.008

Casati, R., Scheer, V., Vogt, R., Benter, T., 2007. Measurement of nucleation and soot mode particle emission from a diesel passenger car in real world and laboratory in situ dilution. Atmos. Environ. 41, 2125–2135. doi:10.1016/j.atmosenv.2006.10.078

Casquero-Vera, J.A., Lyamani, H., Dada, L., Hakala, S., Paasonen, P., Román, R., Fraile, R., Petäjä, T., Olmo-Reyes, F.J., Alados-Arboledas, L., 2020. New particle formation at urban and high-altitude remote sites in the south-eastern Iberian Peninsula. Atmos. Chem. Phys. 20, 14253–14271. doi:10.5194/acp-20-14253-2020

Dal Maso, M., Kulmala, M., Riipinen, I., Wagner, R., Hussein, T., Aalto, P., Lehtinen, K.E.J., 2005. Formation and growth of fresh atmospheric aerosols: Eight years of aerosol size distribution data from SMEAR II, Hyytiälä, Finland. Boreal Environ. Res. 10, 323–336.

de Jesus, A.L., Rahman, M.M., Mazaheri, M., Thompson, H., Knibbs, L.D., Jeong, C., Evans, G., Nei, W., Ding, A., Qiao, L., Li, L., Portin, H., Niemi, J. V., Timonen, H., Luoma, K., Petäjä, T., Kulmala, M., Kowalski, M., Peters, A., Cyrys, J., Ferrero, L., Manigrasso, M., Avino, P., Buonano, G., Reche, C., Querol, X., Beddows, D., Harrison, R.M., Sowlat, M.H., Sioutas, C., Morawska, L., 2019. Ultrafine particles and PM2.5 in the air of cities around the world: Are they representative of each other? Environ. Int. 129, 118–135. doi:10.1016/j.envint.2019.05.021

Doswell, C.A., Davies-Jones, R., Keller, D.L., 1990. On Summary Measures of Skill in Rare Event Forecasting Based on Contingency Tables. Weather Forecast. 5, 576–585. doi:10.1175/1520-0434(1990)005<0576:OSMOSI>2.0.CO;2

Dusek, U., Frank, G.P., Hildebrandt, L., Curtius, J., Schneider, J., Walter, S., Chand, D., Drewnick, F., Hings, S., Jung, D., Borrmann, S., Andreae, M.O., 2006. Size matters more than chemistry for cloud-nucleating ability of aerosol particles. Science (80-.). 312, 1375–1378. doi:10.1126/science.1125261

EEA, 2016. Air quality in Europe - 2016 Report. Copenhagen, Denmark. doi:10.2800/413142

Ehn, M., Thornton, J.A., Kleist, E., Sipilä, M., Junninen, H., Pullinen, I., Springer, M., Rubach, F., Tillmann, R., Lee, B., Lopez-Hilfiker, F., Andres, S., Acir, I.-H., Rissanen, M., Jokinen, T., Schobesberger, S., Kangasluoma, J., Kontkanen, J., Nieminen, T., Kurtén, T., Nielsen, L.B., Jørgensen, S., Kjaergaard, H.G., Canagaratna, M., Maso, M.D., Berndt, T., Petäjä, T., Wahner, A., Kerminen, V.-M., Kulmala, M., Worsnop, D.R., Wildt, J., Mentel, T.F., 2014. A large source of low-volatility secondary organic aerosol. Nature 506, 476–479. doi:10.1038/nature13032

Feichter, J., Stier, P., 2012. Assessment of black carbon radiative effects in climate models. Wiley Interdiscip. Rev. Clim. Chang. 3, 359–370. doi:10.1002/wcc.180

Fuchs, N., Sutugin, A., 1971. High-dispersed aerosols, topics in current aerosol research GM Hidy, JR Brock. ed. Pergamon, New York.

Fuzzi, S., Baltensperger, U., Carslaw, K., Decesari, S., Denier van der Gon, H., Facchini, M.C., Fowler, D., Koren, I., Langford, B., Lohmann, U., Nemitz, E., Pandis, S., Riipinen, I., Rudich, Y., Schaap, M., Slowik, J.G., Spracklen, D. V, Vignati, E., Wild, M., Williams, M., Gilardoni, S., 2015. Particulate matter, air quality and climate: lessons learned and future needs. Atmos. Chem. Phys. 15, 8217–8299. doi:10.5194/acp-15-8217-2015

Hakola, H., Tarvainen, V., Laurila, T., Hiltunen, V., Hellén, H., Keronen, P., 2003. Seasonal variation of VOC concentrations above a boreal coniferous forest. Atmos. Environ. 37, 1623–1634. doi:10.1016/S1352-2310(03)00014-1

Hama, S.M.L., Cordell, R.L., Kos, G.P.A., Weijers, E.P., Monks, P.S., 2017. Sub-micron particle number size distribution characteristics at two urban locations in Leicester. Atmos. Res. 194, 1–16. doi:10.1016/j.atmosres.2017.04.021

Hamed, A., Korhonen, H., Sihto, S.L., Joutsensaari, J., Jrvinen, H., Petäjä, T., Arnold, F., Nieminen, T., Kulmala, M., Smith, J.N., Lehtinen, K.E.J., Laaksonen, A., 2011. The role of relative humidity in continental new particle formation. J. Geophys. Res. Atmos. 116, 1–12. doi:10.1029/2010JD014186

He, J., Gong, S., Yu, Y., Yu, L., Wu, L., Mao, H., Song, C., Zhao, S., Liu, H., Li, X., Li, R., 2017. Air pollution characteristics and their relation to meteorological conditions during 2014–2015 in major Chinese cities. Environ. Pollut. 223, 484–496. doi:10.1016/j.envpol.2017.01.050

HEI Review Panel, 2013. Understanding the Health Effects of Ambient Ultrafine Particles. Heal. Eff. Inst. 122.

Hussein, T., Karppinen, A., Kukkonen, J., Härkönen, J., Aalto, P., Hämeri, K., Kerminen, V.M., Kulmala, M., 2006. Meteorological dependence of size-fractionated number concentrations of urban aerosol particles. Atmos. Environ. 40, 1427–1440. doi:10.1016/j.atmosenv.2005.10.061

Hussein, T., Martikainen, J., Junninen, H., Sogacheva, L., Wagner, R., Dal Maso, M., Riipinen, I., Aalto, P., Kulmala, M., 2008. Observation of regional new particle formation in the urban atmosphere. Tellus, Ser. B Chem. Phys. Meteorol. 60, 509–521. doi:10.1111/j.1600-0889.2008.00365.x

Hussein, T., Puustinen, A., Aalto, P., Mäkelä, J.M., Hämeri, K., Kulmala, M., 2004. Urban aerosol number size distributions. Atmos. Chem. Phys. 4, 391–411. doi:10.5194/acp-4-391-2004

Hyvönen, S., Junninen, H., Laakso, L., Dal Maso, M., Grönholm, T., Bonn, B., Keronen, P., Aalto, P., Hiltunen, V., Pohja, T., Launiainen, S., Hari, P., Mannila, H., Kulmala, M., 2005. A look at aerosol formation using data mining techniques. Atmos. Chem. Phys. 5, 3345–3356. doi:10.5194/acp-5-3345-2005

Iglesias-Samitier, S., Juncal-Bello, V., Piñeiro-Iglesias, M., López-Mahía, P. Muniategui-Lorenzo, S. Prada-Rodríguez, D., 2014. Levels and evolution of atmospheric nanoparticles in a suburban area with Atlantic influence, in: 2nd Iberian Meeting on Aerosol Science and Technology. Publicacions Universitat Rovira I Virgili, p. 79.

Jones, A.M., Harrison, R.M., 2006. Estimation of the emission factors of particle number and mass fractions from traffic at a site where mean vehicle speeds vary over short distances. Atmos. Environ. 40, 7125–7137. doi:10.1016/j.apcatb.2007.04.020

Joutsensaari, J., Ozon, M., Nieminen, T., Mikkonen, S., Lähivaara, T., Decesari, S., Facchini, M.C., Laaksonen, A., Lehtinen, K., 2018. Identification of new particle formation events with deep learning. Identif. new Part. Form. events with Deep Learn. 18, 1–28. doi:10.5194/acp-2017-1189

Kerminen, V.-M., Petäjä, T., Yan, C., Bianchi, F., Chu, B., Kulmala, M., 2019. Atmospheric new particle formation in China. Atmos. Chem. Phys. 19, 115–138. doi:10.5194/acp-19-115-2019

Kerminen, V.M., Chen, X., Vakkari, V., Petäjä, T., Kulmala, M., Bianchi, F., 2018. Atmospheric new particle formation and growth: Review of field observations. Environ. Res. Lett. 13. doi:10.1088/1748-9326/aadf3c

Kinney, P.L., 2008. Climate change, air quality, and human health. Am. J. Prev. Med. 35, 459–467. doi:10.1016/j.amepre.2008.08.025

Kirkby, J., Curtius, J., Almeida, J., Dunne, E., Duplissy, J., Ehrhart, S., Franchin, A., Gagné, S., Ickes, L., Kürten, A., Kupc, A., Metzger, A., Riccobono, F., Rondo, L., Schobesberger, S., Tsagkogeorgas, G., Wimmer, D., Amorim, A., Bianchi, F., Breitenlechner, M., David, A., Dommen, J., Downard, A., Ehn, M., Flagan, R.C., Haider, S., Hansel, A., Hauser, D., Jud, W., Junninen, H., Kreissl, F., Kvashin, A., Laaksonen, A., Lehtipalo, K., Lima, J., Lovejoy, E.R., Makhmutov, V., Mathot, S., Mikkilä, J., Minginette, P., Mogo, S., Nieminen, T., Onnela, A., Pereira, P., Petäjä, T., Schnitzhofer, R., Seinfeld, J.H., Sipilä, M., Stozhkov, Y., Stratmann, F., Tomé, A., Vanhanen, J., Viisanen, Y., Vrtala, A., Wagner, P.E., Walther, H., Weingartner, E., Wex, H., Winkler, P.M., Carslaw, K.S., Worsnop, D.R.,

Baltensperger, U., Kulmala, M., 2011. Role of sulphuric acid, ammonia and galactic cosmic rays in atmospheric aerosol nucleation. Nature 476, 429–435. doi:10.1038/nature10343

Kulmala, M., Kerminen, V.M., Petäjä, T., Ding, A.J., Wang, L., 2017. Atmospheric gas-to-particle conversion: Why NPF events are observed in megacities? Faraday Discuss. 200, 271–288. doi:10.1039/c6fd00257a

Kulmala, M., Lehtinen, K.E.J., Laaksonen, A., 2006. Cluster activation theory as an explanation of the linear dependence between formation rate of 3 nm particles and sulphuric acid concentration. Atmos. Chem. Phys. 6, 787–793. doi:10.5194/acp-6-787-2006

Kulmala, M., Petäjä, T., Mönkkönen, P., Koponen, I.K., Dal Maso, M., Aalto, P., Lehtinen, K.E.J., Kerminen, V.-M., 2005. On the growth of nucleation mode particles: source rates of condensable vapor in polluted and clean environments. Atmos. Chem. Phys. 5, 409–416. doi:10.5194/acp-5-409-2005

Lehtinen, K.E.J., Korhonen, H., Dal Maso, M., Kulmala, M., 2008. On the concept of condensation sink diameter. Boreal Environ. Res. 8, 405–412.

Lohmann, U., Feichter, J., 2005. Global indirect aerosol effects: a review. Atmos. Chem. Phys. 5, 715–737. doi:10.5194/acp-5-715-2005

Lyman, W.J., Reehl, W.F., Rosenblatt, D.H., 1990. Handbook of chemical property estimation methods: environmental behavior of organic compounds.

Ma, N., Birmili, W., 2015. Estimating the contribution of photochemical particle formation to ultrafine particle number averages in an urban atmosphere. Sci. Total Environ. 512–513, 154–166. doi:10.1016/j.scitotenv.2015.01.009

Mikkonen, S., Lehtinen, K.E.J., Hamed, A., Joutsensaari, J., Facchini, M.C., Laaksonen, A., 2006. Using discriminant analysis as a nucleation event classification method. Atmos. Chem. Phys. 6, 5549–5557. doi:10.5194/acp-6-5549-2006

Morawska, L., Jayaratne, E.R., Mengersen, K., Jamriska, M., Thomas, S., 2002. Differences in airborne particle and gaseous concentrations in urban air between weekdays and weekends. Atmos. Environ. 36, 4375–4383. doi:10.1016/S1352-2310(02)00337-0

Morawska, L., Ristovski, Z., Jayaratne, E.R., Keogh, D.U., Ling, X., 2008. Ambient nano and ultrafine particles from motor vehicle emissions: Characteristics, ambient processing and implications on human exposure. Atmos. Environ. 42, 8113–8138. doi:10.1016/j.atmosenv.2008.07.050

Nel, A., 2005. Atmosphere: Enhanced: air pollution-related illness: effects of particles. Science (80-.). 308, 804–806. doi:10.1126/science.1108752

Oduber, F., Calvo, A.I., Blanco-Alegre, C., Castro, A., Vega-Maray, A.M., Valencia-Barrera, R.M., Fernández-González, D., Fraile, R., 2019. Links between recent trends in airborne pollen concentration, meteorological parameters and air pollutants. Agric. For. Meteorol. 264, 16–26. doi:10.1016/j.agrformet.2018.09.023

Oduber, F., Calvo, A.I., Castro, A., Blanco-Alegre, C., Alves, C., Calzolai, G., Nava, S., Lucarelli, F., Nunes, T., Barata, J., Fraile, R., 2021. Characterization of aerosol sources in León (Spain) using Positive Matrix Factorization and weather types. Sci. Total Environ. 754, 142045. doi:10.1016/j.scitotenv.2020.142045

Olofson, K.F.G., Andersson, P.U., Hallquist, M., Ljungström, E., Tang, L., Chen, D., Pettersson, J.B.C., 2009. Urban aerosol evolution and particle formation during wintertime temperature inversions. Atmos. Environ. 43, 340–346. doi:10.1016/j.atmosenv.2008.09.080

Pekkanen, J., Penttinen, P., Timonen, K.L., Tiittanen, P., Mirme, A., Ruuskanen, J., 2007. Number concentration and size of particles in urban air: effects on spirometric lung function in adult asthmatic subjects. Environ. Health Perspect. 109, 319. doi:10.2307/3454889

Pope, C.A., 2000. Review: Epidemiological basis for particulate air pollution health standards. Aerosol Sci. Technol. 32, 4–14. doi:10.1080/027868200303885

Pope, C.A., Dockery, D.W., 2006. Health effects of fine particulate air pollution: Lines that connect. J. Air Waste Manag. Assoc. 56, 709–742. doi:10.1080/10473289.2006.10464485

Rahman, M.M., Mazaheri, M., Clifford, S., Morawska, L., 2017. Estimate of main local sources to ambient ultrafine particle number concentrations in an urban area. Atmos. Res. 194, 178–189. doi:10.1016/j.atmosres.2017.04.036

Riipinen, I., Sihto, S.L., Kulmala, M., Arnold, F., Dal Maso, M., Birmili, W., Saarnio, K., Teinilä, K., Kerminen, V.M., Laaksonen, A., Lehtinen, K.E.J.J., 2007. Connections between atmospheric sulphuric acid and new particle formation during QUEST III-IV campaigns in Heidelberg and Hyytiälä. Atmos. Chem. Phys. 7, 1899–1914. doi:10.5194/acp-7-1899-2007

Rose, D., Wehner, B., Ketzel, M., Engler, C., Voigtländer, J., Tuch, T., Wiedensohler, A., 2006. Atmospheric number size distributions of soot particles and estimation of emission factors. Atmos. Chem. Phys. 6, 1021–1031. doi:10.5194/acp-6-1021-2006

Salma, I., Borsòs, T., Weidinger, T., Aalto, P., Hussein, T., Dal Maso, M., Kulmala, M., 2011. Production, growth and properties of ultrafine atmospheric aerosol particles in an urban environment. Atmos. Chem. Phys. 11, 1339–1353. doi:10.5194/acp-11-1339-2011

Seminara, G., Carli, B., Forni, G., Fuzzi, S., Mazzino, A., Rinaldo, A., 2020. Biological fluid dynamics of airborne COVID-19 infection. Rend. Lincei 31, 505–537. doi:10.1007/s12210-020-00938-2

Tong, Z., Chen, Y., Malkawi, A., Adamkiewicz, G., Spengler, J.D., 2016. Quantifying the impact of traffic-related air pollution on the indoor air quality of a naturally ventilated building. Environ. Int. 89–90, 138–146. doi:10.1016/j.envint.2016.01.016

Tong, Z., Yang, B., Hopke, P.K., Zhang, K.M., 2017. Microenvironmental air quality impact of a commercial-scale biomass heating system. Environ. Pollut. 220, 1112–1120. doi:10.1016/j.envpol.2016.11.025

Tröstl, J., Chuang, W.K., Gordon, H., Heinritzi, M., Yan, C., Molteni, U., Ahlm, L., Frege, C., Bianchi, F., Wagner, R., Simon, M., Lehtipalo, K., Williamson, C., Craven, J.S., Duplissy, J., Adamov, A., Almeida, J., Bernhammer, A.K., Breitenlechner, M., Brilke, S., Dias, A., Ehrhart, S., Flagan, R.C., Franchin, A., Fuchs, C., Guida, R., Gysel, M., Hansel, A., Hoyle, C.R., Jokinen, T., Junninen, H., Kangasluoma, J., Keskinen, H., Kim, J., Krapf, M., Kürten, A., Laaksonen, A., Lawler, M., Leiminger, M., Mathot, S., Möhler, O., Nieminen, T., Onnela, A., Petäjä, T., Piel, F.M., Miettinen, P., Rissanen, M.P., Rondo, L., Sarnela, N., Schobesberger, S., Sengupta, K., Sipilä, M., Smith, J.N., Steiner, G., Tomè, A., Virtanen, A., Wagner, A.C., Weingartner, E., Wimmer, D., Winkler, P.M., Ye, P., Carslaw, K.S., Curtius, J., Dommen, J., Kirkby, J., Kulmala, M., Riipinen, I., Worsnop, D.R., Donahue, N.M., Baltensperger, U., 2016. The role of low-volatility organic compounds in initial particle growth in the atmosphere. Nature 533, 527–531. doi:10.1038/nature18271

Tuch, T.M., Wehner, B., Pitz, M., Cyrys, J., Heinrich, J., Kreyling, W.G., Wichmann, H.E., Wiedensohler, A., 2003. Long-term measurements of size-segregated ambient aerosol in two German cities located 100 km apart. Atmos. Environ. 37, 4687–4700. doi:10.1016/j.atmosenv.2003.07.010

Uria-Tellaetxe, I., Carslaw, D.C., 2014. Conditional bivariate probability function for source identification. Environ. Model. Softw. 59, 1–9. doi:10.1016/j.envsoft.2014.05.002

Viard, V.B., Fu, S., 2015. The effect of Beijing's driving restrictions on pollution and economic activity. J. Public Econ. 125, 98–115. doi:10.1016/j.jpubeco.2015.02.003

Wang, X., Li, X., Ma, R., Li, Y., Wang, W., Huang, H., Xu, C., An, Y., 2018. Quadratic discriminant analysis model for assessing the risk of cadmium pollution for paddy fields in a county in China. Environ. Pollut. 236, 366–372. doi:10.1016/j.envpol.2018.01.088

Wang, Z.B., Hu, M., Sun, J.Y., Wu, Z.J., Yue, D.L., Shen, X.J., Zhang, Y.M., Pei, X.Y., Cheng, Y.F., Wiedensohler, A., 2013. Characteristics of regional new particle formation in urban and regional background environments in the North China Plain. Atmos. Chem. Phys. 13, 12495–12506. doi:10.5194/acp-13-12495-2013

Wehner, B., Wiedensohler, A., 2003. Long term measurements of submicrometer urban aerosols: Statistical analysis for correlations with meteorological conditions and trace gases. Atmos. Chem. Phys. 3, 867–879. doi:10.5194/acp-3-867-2003

Wu, Z., Hu, M., Lin, P., Liu, S., Wehner, B., Wiedensohler, A., 2008. Particle number size distribution in the urban atmosphere of Beijing, China. Atmos. Environ. 42, 7967–7980. doi:10.1016/j.atmosenv.2008.06.022

Yli-Juuti, T., Nieminen, T., Hirsikko, A., Aalto, P.P., Asmi, E., Hõrrak, U., Manninen, H.E., Patokoski, J., Dal Maso, M., Petäjä, T., Rinne, J., Kulmala, M., Riipinen, I., 2011. Growth rates of nucleation mode particles in Hyytiälä during 2003-2009: Variation with particle size, season, data analysis method and ambient conditions. Atmos. Chem. Phys. 11, 12865–12886. doi:10.5194/acp-11-12865-2011

SUPPLEMENTARY MATERIAL

S.6.1. NEW PARTICLE FORMATION PARAMETERS

The following parameters to evaluate NPF events were calculated as in Dal Maso et al. (2005) and compiled below to assist in the search for expressions and for easier reading.

$$J_{15-30} = \frac{dN_{15-30}}{dt} + F_{COAG} + F_{GROWTH}$$

where N_{15-30} is the number of particles in nucleation mode; F_{coag} is the loss of particles due to coagulation; F_{growth} is the flow of particles that grow outside the nucleation range.

$$F_{growth} = \frac{1}{\Delta D_p} \; x \; GR_{15-30} \; x \; N_{15-30}$$

where GR_{15-30} is the rate of change in diameter; N_{15-30} is the number of particles in nucleation mode; ΔD_p is 30-15 =15 nm.

$$GR_{15-30} = \frac{\Delta D_p}{dt} = \frac{Dp_2 - Dp_1}{t_2 - t_1} = \text{nm h}^{-1}$$

$Dp_2 - Dp_1$ is the geometric mean of the nucleation mode in the moments t_1 and t_2.

$$F_{coag} = N_{15-30}\, x \sum_j K_{ij}\, xN_j$$

where $\sum_j K_{ij}\, xN_j$ is the coagulation sink; K_{ij} e is the coagulation sink between sizes *i* and *j*; N_j is the particle concentration in the size *j*.

$$K_{ij} = 2\mu\left(d_i + d_j\right)x\,\left(D_i + D_j\right)x\,\beta_{Fij}$$

$d_i + d_j$ are the mean diameter of channels; $D_i + D_j$ are the diffusion coefficients depending on size ($m^2\ s^{-1}$); β_{Fij} is the correction Fuchs factor.

$$CS = 2\pi\, x\, D\, x \sum_i B_{Mi}\, xdp_i\, x\, N_i$$

where *D* is the diffusion coefficient of the condensing vapor in the gas phase (in this study *D* is the H_2SO_4 diffusion coefficient, 0.104 $cm^2\ s^{-1}$) (Lyman et al., 1990), β_{Mi} is the transitional correction factor using an accommodation coefficient of 1 (Fuchs and Sutugin, 1971), d_{pi} (nm) is the particle diameter and *N*i (# cm^{-3}) is the PNC for each particle size discrete interval *i*.

$$B_{Mi} = \frac{1 + K_n}{1 + 0.337K_n + \frac{4K_n}{3\alpha} + \frac{4K_n{}^2}{3\alpha}}$$

where K_n is the Knudsen number; α is the accommodation coefficient ($\alpha = 1$)

$$K_n = 2\frac{\gamma_v}{D_p}$$

where γ_r is mean free path; D_p is the geometric mean of the mode of nucleation

$$Q = CS\, x\, C$$

Q ($cm^{-3}\ s^{-1}$) is the condensable vapour ratio; CS is the condensation sink; C is the condensable vapour concentration.

$$C = A\, x\, \frac{dD_p}{dt}$$

A is a constant = $1.37 \cdot 10^7$ h $cm^{-3}nm^{-1}$: D_p is the geometric mean of the mode of nucleation

S.6.2. VERIFICATION INDEXES

To verify the discriminant model, three indexes used for common events were used: True Skill Statistic (TSS), Heidke Skill Score (HSS) and Critical Success Index (CSI) (Doswell et al., 1990). Also, to compare with other studies that used a discriminant analysis to determinate NPF days, we evaluate the performance of the classification as Hyvönen et al. (2005), with "error" index. These indexes were given by:

$$TSS = \frac{(XW - YZ)}{(X + Y) \cdot (Z + W)}$$

$$HSS = \frac{2(XW - YZ)}{(X + Y) \cdot (Y + W) + (X + Z) \cdot (Z + W)}$$

$$CSI = \frac{X}{X + Y + Z}$$

$$error = \left(\frac{Y + Z}{X + Y + W + Z}\right) \cdot 100$$

where *X*, *Y*, *W* and *Z* are the numbers of days included in the categories of the following Table:

		Prediction	
		Yes NPF	No NPF
Observation	Yes NPF	*X*	*Y*
	No NPF	*Z*	*W*

S.6.3. FIGURES

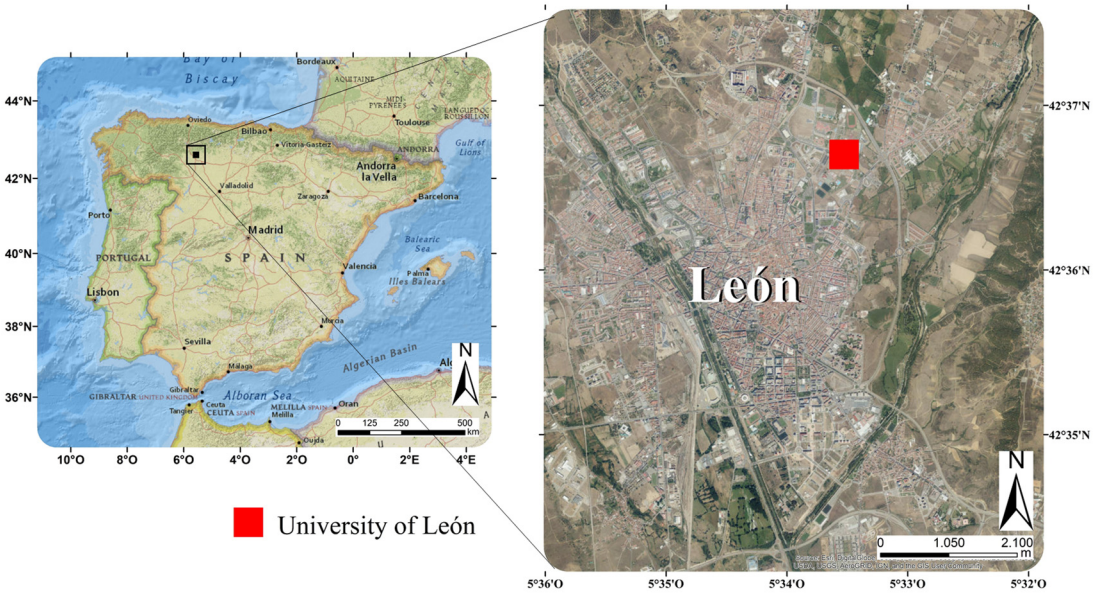

Figure S6.1. Geographic location of the city of León and sampling site.

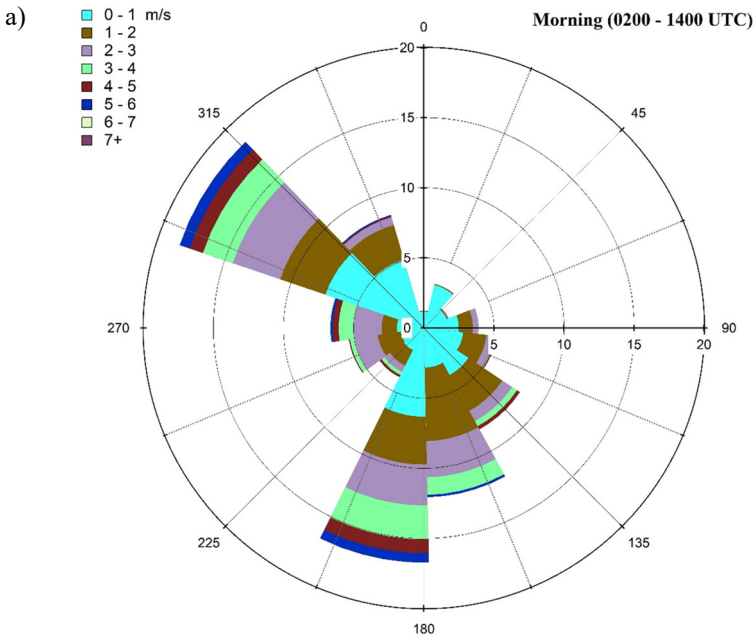

b)

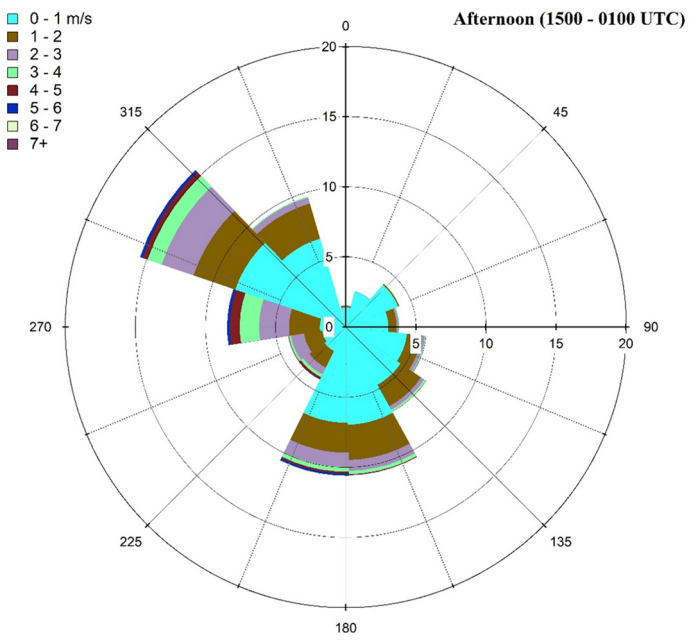

Figure S6.2. Wind rose displaying the distribution of wind speed and wind direction at León during morning (a) and afternoon (b).

a)

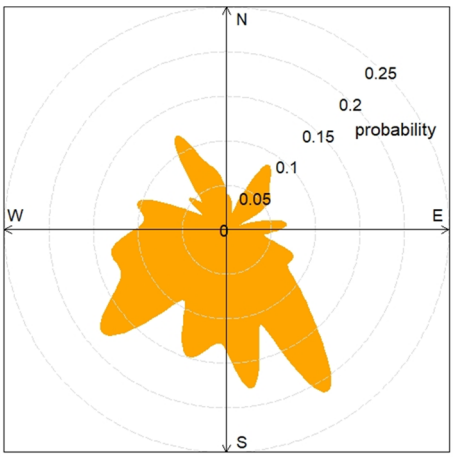

CPF at the 90th percentile (=8806.2)

b)

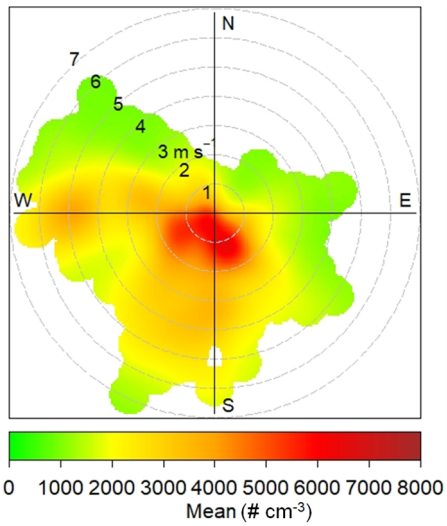

Figure S6.3. a) Conditional Probability Function (CPF) plot of total particle number concentration (N_{total}) for concentrations > 90th percentile (8806.2 # cm^{-3}). The radial axis is the probability. b) Bivariate polar plot of N_{total}. The radial axis is wind speed in m s^{-1}.

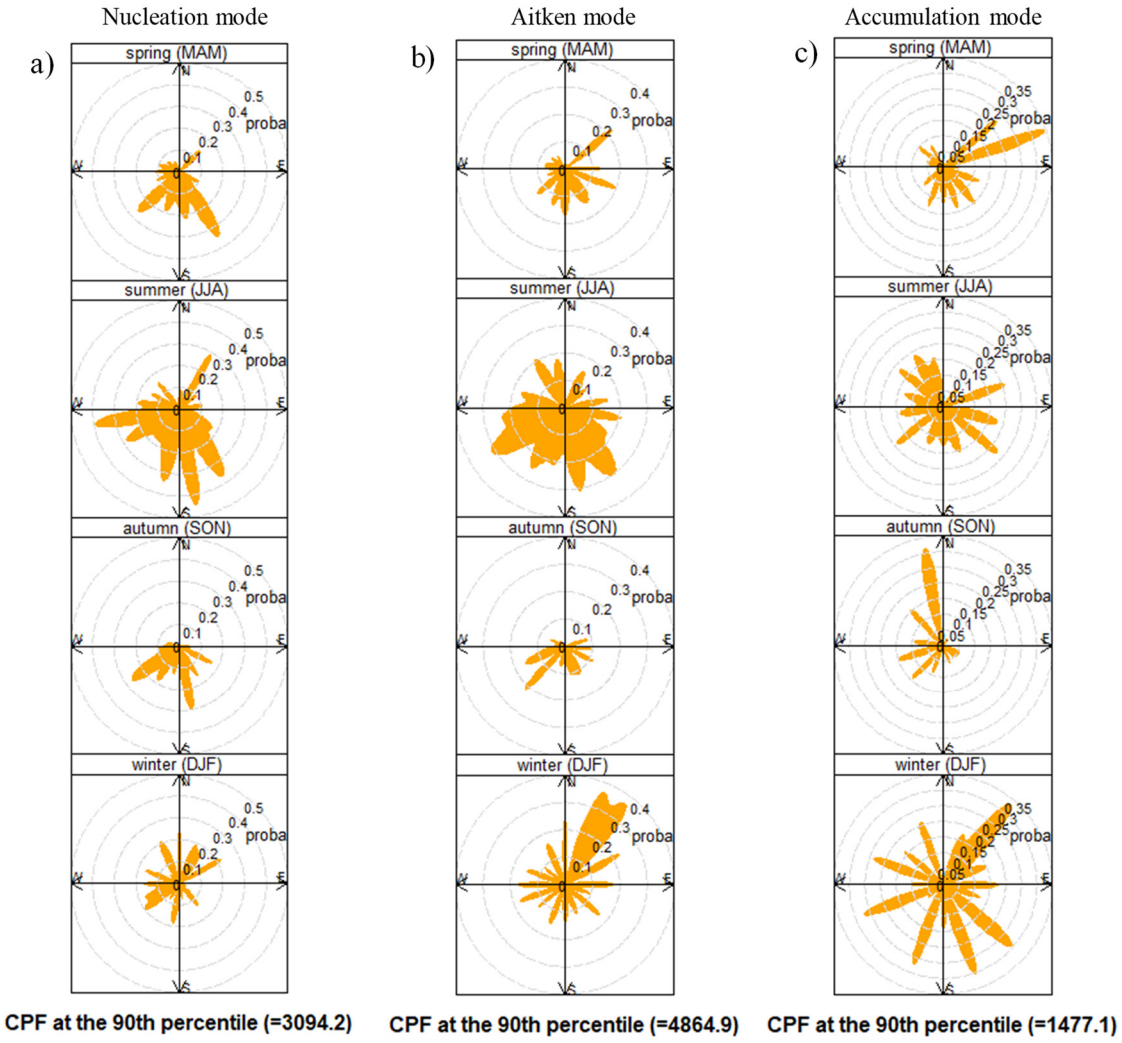

Figure S6.4. Conditional Probability Function (CPF) plot of modal concentrations for concentrations > 90th percentile in each season of the measurement period: a) nucleation-mode particles, b) Aitken-mode particles and c) accumulation-mode particles. The radial axis is the probability.

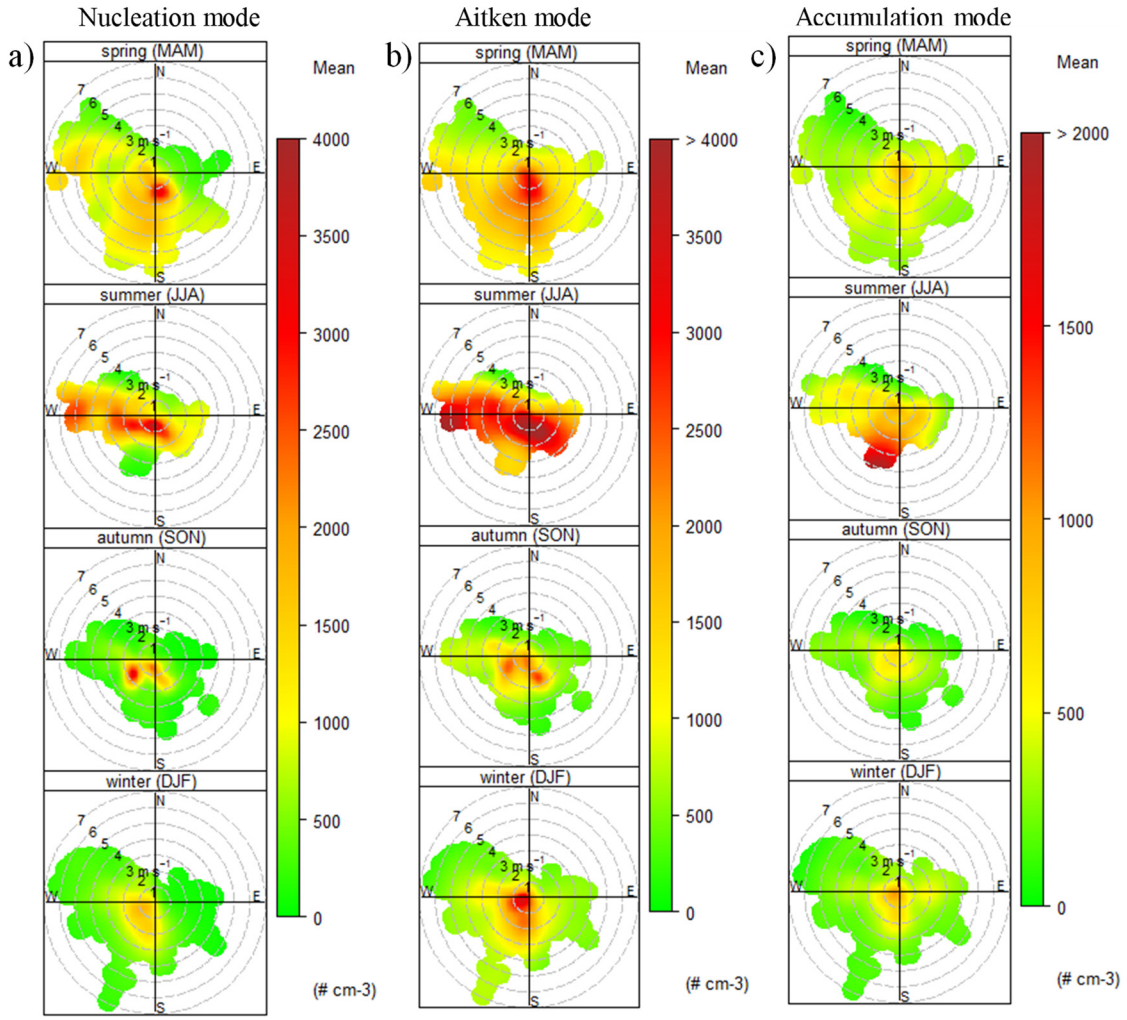

Figure S6.5. Bivariate polar plot of modal concentrations in each season of the measurement period: a) nucleation-mode particles; b) Aitken-mode particles; c) accumulation-mode particles. The radial axis is wind speed in m s^{-1}.

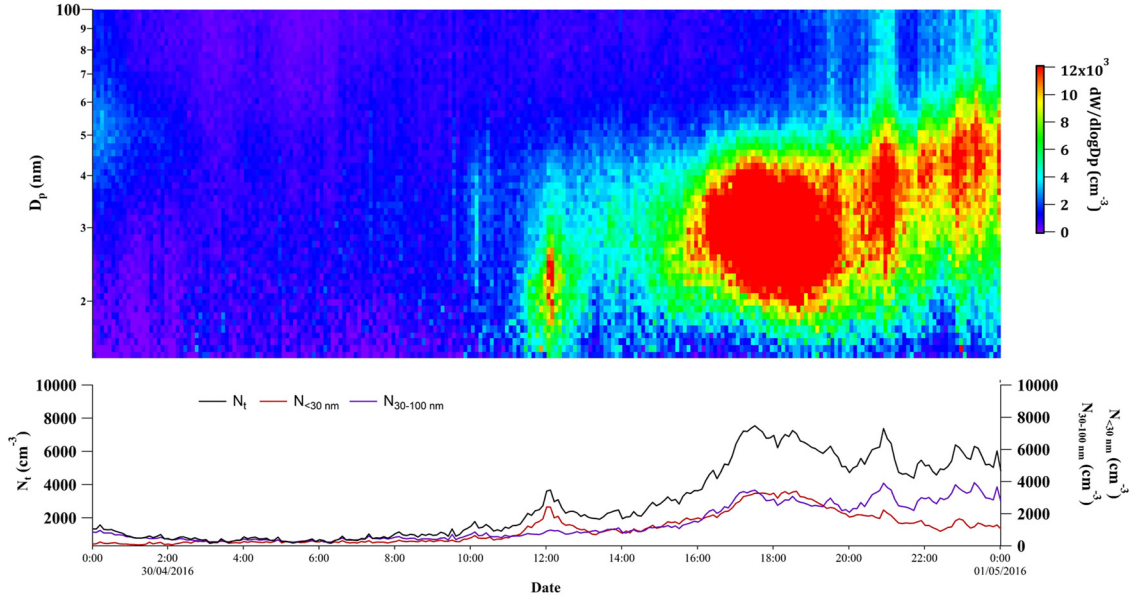

Figure S6.6. Example of a NPF event of type *Ib*. Evolution of the aerosol size distributions (surface plot) and total (N_{total}), nucleation (N_{nuc}) and Aitken (N_{Ait}) particle number concentrations at 30/04/2016.

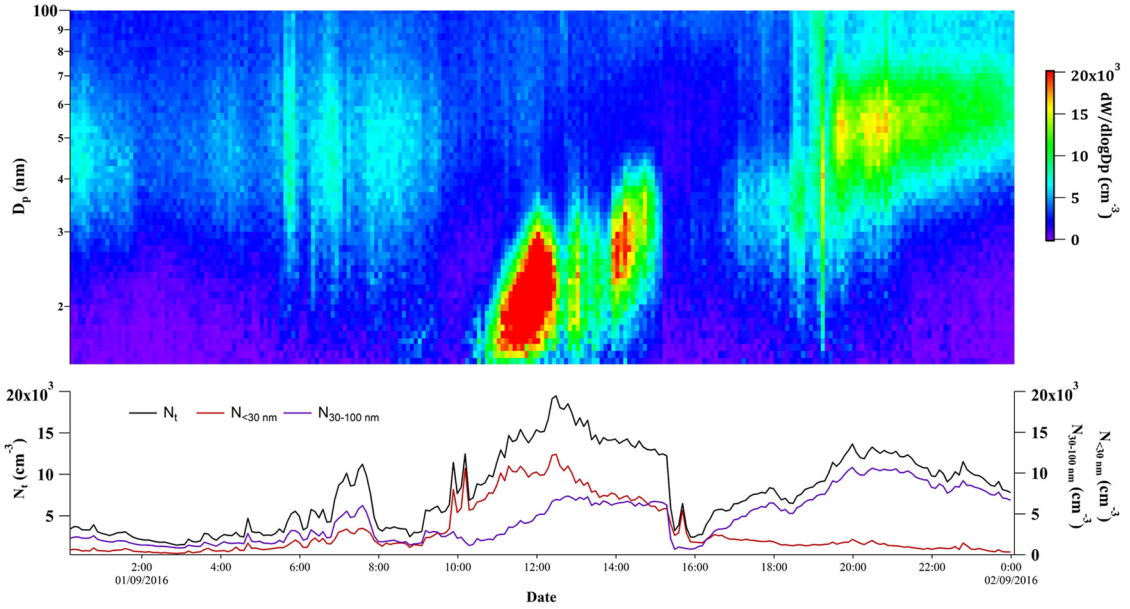

Figure S6.7. Example of a NPF event of type *II*. Evolution of the aerosol size distributions (surface plot) and total (N_{total}), nucleation (N_{nuc}) and Aitken (N_{Ait}) particle number concentrations at 01/09/2016.

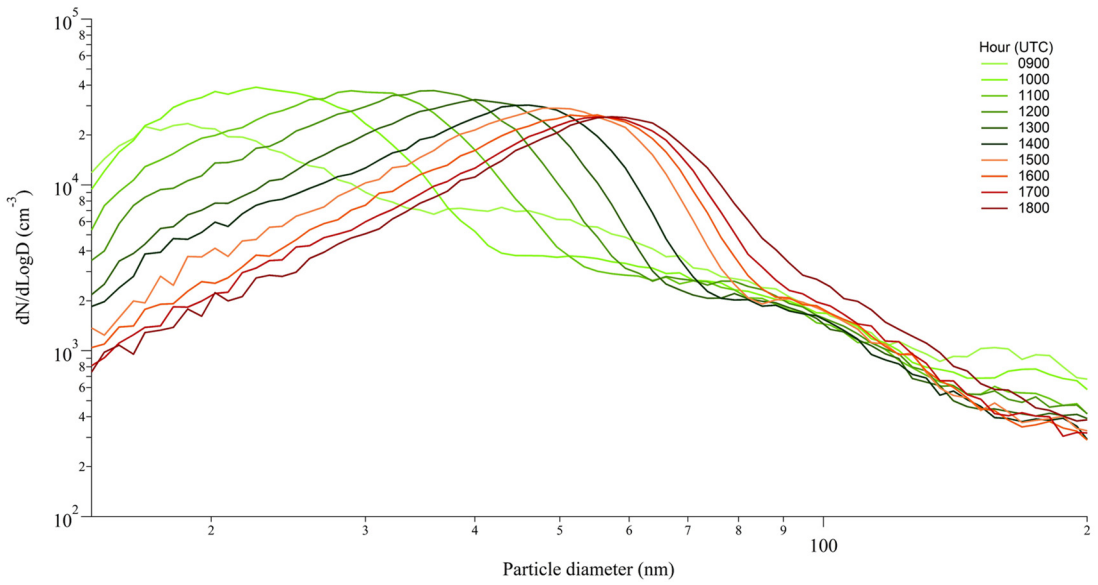

Figure S6.8. Evolution of hourly PSD during NPF event registered at 24/07/2016.

S.6.4. TABLES

Table S6.1. Summary of 45 NPF events of type *Ia*: Growth Ratio (*GR*, nm h^{-1}), nucleation rate formation (J_{15-30}, cm^{-3} s^{-1}), Condensation Sink (*CS*, 10^{-3} s^{-1}), condensable vapour source rate (*Q*, 10^4 cm^{-3} s^{-1}), O_3 (µg m^{-3}), NO_X (µg m^{-3}), N_{total} (# cm^{-3}) and N_{nuc} (# cm^{-3}).

Date	Start (UTC)	End (UTC)	*GR*	J_{15-30}	*CS*	*Q*	O_3	NO_X	N_{total}	N_{nuc}
01/04/2016	1212	1335	1.06	2.86	1.75	0.09	85.0	4.5	15,700	12,700
06/04/2016	1117	1234	0.87	2.90	1.48	2.14	86.5	2.0	14,700	11,100
01/05/2016	1119	1306	0.71	1.16	0.98	1.07	90.3	7.7	10,100	7300
02/05/2016	1143	1254	0.81	0.40	0.96	0.91	86.0	10.0	10,000	6300
03/05/2016	1243	1318	4.87	1.39	0.40	2.66	103.0	7.0	9000	3500
23/05/2016	1004	1121	2.57	2.33	0.94	3.51	71.5	7.5	9800	6700
01/06/2016	1012	1111	2.23	1.93	1.05	3.34	102.0	12.0	9600	7500
02/06/2016	1224	1317	3.06	0.95	0.52	2.13	110.5	8.0	7700	3700
10/06/2016	0925	1042	1.26	1.40	0.31	0.27	81.0	5.5	3500	2500
11/06/2016	0937	1036	3.53	2.10	1.00	3.03	73.0	8.5	10,600	6700
13/06/2016	0913	1024	2.74	0.70	0.33	1.68	58.0	4.5	4000	2300
19/06/2016	0931	1106	2.58	2.14	1.38	4.39	65.3	9.7	12,700	9800
22/06/2016	1013	1112	2.10	2.44	0.80	2.47	92.0	6.0	9700	6100
27/06/2016	0949	1054	0.80	0.52	0.29	0.41	87.0	2.0	4100	2000
30/06/2016	0847	952	3.38	5.34	1.92	10.42	63.0	10.0	27,400	21,200
02/07/2016	0935	1046	2.14	1.07	0.50	1.70	62.5	5.0	5600	3300
03/07/2016	0841	1016	2.17	1.27	1.33	3.40	56.7	6.7	13,300	8700
05/07/2016	0828	1021	1.11	1.73	0.68	1.60	76.0	8.7	7700	5400
09/07/2016	1104	1239	2.47	1.53	0.77	3.30	124.0	5.0	9500	5400
12/07/2016	1225	1330	3.37	0.81	0.61	2.72	96.0	3.5	5700	4800
14/07/2016	1101	1312	1.03	0.87	0.79	1.16	91.0	3.7	8000	4900
15/07/2016	1025	1154	1.89	1.24	0.63	1.94	84.0	8.5	6500	4300
16/07/2016	1155	1406	1.96	1.13	0.68	1.61	125.0	2.3	6300	4600
23/07/2016	0907	1124	1.68	0.64	0.34	0.58	73.0	2.0	3000	2300
24/07/2016	0943	1100	2.58	0.73	1.42	5.12	66.0	4.5	12,200	9200
28/07/2016	0750	0943	1.01	2.11	0.80	0.83	67.0	11.0	7700	5200
31/07/2016	0750	0925	2.89	3.27	2.08	8.32	45.5	7.0	16,500	14,000
02/08/2016	0908	1031	1.84	0.97	0.41	0.96	79.0	10.0	6500	3600
05/08/2016	0908	1031	2.22	3.88	1.32	1.75	68.0	2.5	12,000	8800
06/08/2016	1020	1125	2.30	2.88	1.20	4.92	77.0	5.5	11,800	7900
08/08/2016	1032	1125	2.64	2.02	0.98	3.31	98.5	14.0	9000	6300
11/08/2016	1002	1137	1.41	1.62	0.74	1.86	69.5	5.5	7400	5900
18/08/2016	1038	1119	1.51	3.39	0.58	1.60	74.0	10.6	6800	3400
20/08/2016	1032	1213	3.45	2.50	1.12	3.68	101.7	2.7	8600	6700

26/08/2016	1356	1513	1.65	1.43	0.96	1.83	115.0	7.0	9600	6300
30/08/2016	1005	1158	2.04	1.39	1.19	3.27	74.5	10.5	10,000	2600
04/09/2016	1041	1246	1.46	1.58	1.09	2.39	121.7	9.3	11,300	7000
05/09/2016	0947	1116	2.91	2.88	1.23	5.02	105.5	11.0	10,700	8300
17/09/2016	1103	1238	1.35	1.83	1.11	2.37	62.0	8.0	9900	7900
18/09/2016	1057	1214	2.03	2.09	0.89	2.37	76.5	2.0	7800	6500
26/09/2016	1347	1446	1.71	2.03	1.22	2.78	80.0	4.0	12,000	7700
28/09/2016	1049	1206	1.64	1.88	0.73	2.09	50.5	2.5	6300	5000
01/10/2016	1031	1154	2.76	2.68	0.56	2.23	77.5	2.0	5200	4600
26/10/2016	1046	1151	1.03	1.26	0.52	1.00	62.5	12.0	5000	4000
27/10/2016	1052	1151	2.95	1.52	0.48	2.09	79.5	2.0	4500	3400
Mean values	1026	1149	2.08	1.84	0.91	2.58	82.1	3.0	9200	6400

Table S6.2. Summary of clusters days' characteristics.

	1	2	3	4
N_{total} (cm^{-3})	9400	1900	5600	3700
N_{nuc} (cm^{-3})	3200	400	1500	800
N_{Ait} (cm^{-3})	4900	1000	3200	2000
N_{acc} (cm^{-3})	1400	460	910	870
WS ($m\ s^{-1}$)	0.6	1.2	0.6	0.8
T (ºC)	8.7	8.4	13.7	12.2
RH (%)	58.2	71.3	57.7	60.1
ABL (m)	397	475	428	429
Number of days	8	159	93	139
Number of NPF *Ia*	2	2	39	2
Number of NPF (*Ia*, *Ib* or *II*)	4	15	56	21

Table S6.3. Standardised coefficients of the canonical discriminant function for each variable used. The function in the centroid of groups is -1.789 for non NPF days and 1.182 for NPF days.

Variable	Coefficients
N_{total} (cm^{-3})	-1.266
N_{nuc} (cm^{-3})	0.766
N_{Ait} (cm^{-3})	0.997
WS ($m\ s^{-1}$)	-0.758
T (ºC)	0.581
ABL (m)	-0.092
RH (%)	-0.123
O_3	0.329
NOx	-0.158

Table S6.4. Contingence table obtained from quadratic discriminant analysis applied to days included in cluster 3.

		Prediction	
		Yes NPF	No NPF
Observation	Yes NPF	55	1
	No NPF	6	31

CHAPTER 7. Searching the contribution of coal combustion to black carbon

Full title: *Searching the contribution of coal combustion to black carbon: coupling tracers with the aethalometer model*

Submitted for publication

7.1. INTRODUCTION

One of the main risks to human health and climate change is air pollution. According to the World Health Organisation (WHO) estimates, approximately 90% of the population breathes polluted air. The places with the highest burden of pollution, caused by gases and particulate matter, are the Eastern Mediterranean Region and South-East Asia (WHO, 2013).

Black carbon (BC) is one of the most important components of atmospheric particulate matter, a short-lived climate pollutant emitted from incomplete combustion of fossil fuel and biomass. It has some distinctive physical properties: strongly absorbs visible light, is refractory and insoluble in water and many organic solvents and exists as an aggregate of small spherules (Bond et al., 2013). The main sources of BC are: i) diesel engines used for transport, ii) residential solid fuels (wood and coal), iii) forest fires and iv) industrial processes (Bond et al., 2013). The BC concentration depends on the source contributions and the atmospheric conditions. An important factor is the atmospheric boundary layer (ABL) height, which controls the BC concentration at surface level (Joshi et al., 2016) along whole year, due to the greater or lesser dispersion of pollutants. The atmospheric lifetime of BC ranges from days to weeks and its main sinks are wet

and dry deposition (Begam et al., 2016). Blanco-Alegre et al. (2019) have found a decrease of 40% in the BC concentration after rain events in León (Spain).

Recent studies on BC health risks indicate that the ensemble of BC-organic carbon may contribute to around 3 million premature deaths every year (Apte et al., 2015; Bond et al., 2013a; Lelieveld et al., 2015; WHO, 2012). The other great impact of BC is its effect on climate inasmuch as BC strongly absorbs solar radiation and can acts as cloud and ice nuclei. BC is the second strongest contributor to current global warming, after CO_2, with a global mean radiative forcing estimated from 0.4 to 1.2 W m^{-2} (ICCP, 2014). Other effects are the reduction of atmospheric visibility and plant growth stunting (Auffhammer et al., 2006; Chameides et al., 1999). Therefore, studying BC is critical due to its multiple effects on climate, public health and air quality (EEA, 2016; Kinney, 2008; Tong et al., 2017, 2016).

The aethalometer (Hansen et al., 1984) has become an instrument widely used to quantify BC. It measures the aerosol light attenuation (at wavelengths from near-ultraviolet to near-infrared) and determines the equivalent BC (eBC) (Andreae and Gelencsér, 2006; Petzold et al., 2013) by using the specific mass attenuation cross-section reported in the manufacturer manual, for the working wavelengths. The wavelength dependence of the determined absorption coefficient was used to estimate the contribution of the main sources to eBC, fossil fuel (eBC_{ff}) and biomass burning (eBC_{bb}) using the so-called Aethalometer model (Sandradewi et al., 2008a) approach. This approach can be applied whenever the presence of iron oxides is not foreseen (iron oxides are also responsible for the enhancement in the UV and visible wavelengths (Fialho et al., 2014) and result in wrong estimations given by the Sandradewi et al. (2008a) approach).

The Aethalometer model, developed in an area not influenced with coal sources, only assumes the presence of two major sources of BC, biomass burning and fossil fuel (associated with traffic), although, considering (Harrison et al., 2013), this approach needs improvement for areas where the presence of other sources, such as coal combustion, cannot be neglected. Information on the contribution of coal combustion to eBC is still scarce. The fact that coal smoke absorbs at the shortest wavelengths as biomass smoke (Bond et al., 2002; Harrison et al., 2013) constitutes a major problem in estimating the contribution of each source to the eBC, by using only the aethalometer measurements. Thus, in regions where coal combustion is a common practice, the Sandradewi et al. (2008a) approach can be improved by adding other type of measurements as Herich et al. (2011) have previously shown.

It has to be emphasised that Absorption Ångström Exponent (AAE) values for coal combustion can be very variable, from close to 1 to nearly 3 (Bond, 2001), depending on the type of coal and combustion technology (Harrison et al., 2013). In some studies, the values for biomass are also variables related with biomass type and combustion condition (Garg et al., 2016; Pokhrel et al.,

2016; Xie et al., 2018). However, in other studies the values for traffic, around 1.0 and for biomass, around 1.5-2, are much more delimited (Kirchstetter et al., 2004; Tobler et al., 2020; Zotter et al., 2017).

The importance of BC source apportionment studies lies in the fact that coal and residential biomass burning are the main emission sources (between 60-80%) of this carbonaceous component, not only in Africa and Asia (Bond et al., 2013), but also in European cities with coal power plants (Kucbel et al., 2017). In 2010, in Europe, residential combustion of solid fuels (biomass and coal) for heating accounted for 13-21% of the total ambient $PM_{2.5}$ emissions (WHO/United Nations, 2018). Thus, the methodology to estimate the contribution of coal combustion to eBC would be very useful in areas such as the city of León (Spain), where the use of coal in domestic heating devices is still very widespread. China or southern Poland are other examples where this practice has become one of the most polluting activities. Along with other contaminants, high emissions of elements such as fluorine, arsenic, selenium, mercury and lead may have significant global repercussions and be particularly harmful to human health (WHO/United Nations, 2018). Evidence of this is that some authors have already found a relation between coal combustion and mortality in Beijing (Tang et al., 2017).

The main aim of this paper is to characterise the eBC sources during a 14-month sampling campaign in León, a city located in a coal-mining region, in the NW of the Iberian Peninsula. The annual and seasonal evolution of this pollutant was studied and the contribution for its three main sources (traffic, coal combustion and biomass burning) was quantified. To achieve this purpose, a methodology to decouple the eBC contribution of coal combustion and biomass burning is established during the cold period. This work represents a step forward in the quantification of eBC from different sources and the method developed can be very useful in regions where coal combustion, biomass burning and traffic are the main BC sources. Furthermore, it can provide new information for air quality models, which need new metrics in Europe to implement actions that reduce BC concentrations.

7.2. MATERIAL AND METHODS

7.2.1. SAMPLING SITE

Sampling was conducted between 2 January 2016 and 31 March 2017 at the campus of the University of León (León, Spain) (Figure S7.1). In total 346 days were covered, but only 327 were fully studied due to sampling problems. León is a city located in the NW of the Iberian

Peninsula (42° 36′ N, 05° 35′ W at 838 m a.s.l.) with a population of about 200,000 inhabitants (population density close to 3300 dwellers km^{-2}) (INE, 2017). According to the Spanish Meteorological Office (http://www.aemet.es/en/), in the last 35 years, an annual mean precipitation of 515 mm and a temperature of 11.1 °C were registered. In the city, along the whole year, the main sources of particulate emissions identified by Positive Matrix Factorization six-factor solution, were: traffic (29%), aged sea salt (26%), secondary aerosols (16%), dust (13%), marine aerosol (7%) and biomass burning (3%) (Oduber et al., 2021). The traffic density can be considered medium compared with other Spanish cities, concentrated mainly on the ring road that surrounds the city (~250 m northeast from the sampling point), with an average daily vehicle intensity of 25,000 vehicles day^{-1}. The vehicular fleet is composed by 44% vehicles powered by gasoline and 56% by diesel (DGT, 2016). Furthermore, biomass (mainly oak and beech) and coal burning for residential heating are common in the cold months. Oduber et al. (2019) recorded a decrease of 2.35 µg m^{-3} $year^{-1}$ in PM_{10} levels in the last 19 years in this city, mainly due to the environmental policies adopted. In the last 10 years, the city presented an average PM_{10} concentration of 20.0±5.0 µg m^{-3} (Junta de Castilla y León, 2018b).

In 2016, 476 tonnes of BC were emitted in the province of León (IDAE, 2017). The sectors with the highest BC emission were non-industrial combustion plants (55%), waste treatment and disposal (15%), road transport (14%), other types of transport and road-mobile machinery (10%), industrial combustion (4%) and combustion in production and transformation of energy (2%) (Spanish Ministry for the Ecological Transition, 2018). In León, the total heat demand is 1.6×10^{6} MW h $year^{-1}$ (IDAE, 2017). Regarding heating devices, the main energy sources are gas-oil (29%), gas (28%) and electrical (11%), followed by biomass burning (6%) and coal combustion (6%) (Junta de Castilla y León, 2008). The León mining basin is constituted by anthracite and hard coal deposits, with a high carbon content (>75%) (Junta de Castilla y León, 2009), but a significant fraction of the coal used is imported (~85%), mainly anthracite from Russia.

7.2.2. METHODOLOGY

7.2.2.1. Black carbon

Aerosol light-attenuation at seven wavelengths (370, 470, 520, 590, 660, 880 and 950 nm) was continuously measured with an aethalometer, model AE-31 (Magee Scientific, USA) equipped with an Extended Range chamber and a PM_{10} inlet without pre-drying the sample. The sampling

flow rate was set at 4 L min^{-1}, and measurements were taken every 2-minutes. To reduce data noise 10-minutes and 1-hour averages were calculated. A detailed description of the instrument can be found in Fialho et al. (2005) and Hansen (2005).

The eBC data recorded during the sampling period were corrected following WMO/GAW Aerosol Measurement Procedures, Guidelines and Recommendations (WMO, 2016). Aethalometer data were also corrected for loading effect (Figure S7.2) by using the Weingartner et al. (2003) algorithm with the winter campaign parameters for cold months and with the summer campaign parameters for warm months (Table S7.1) proposed by Sandradewi et al. (2008b). The 470 nm (α_1) and 950 nm (α_2) wavelengths were used to estimate hourly eBC, eBC_{ff}, eBC_{bb} concentrations and AAE (Sandradewi et al., 2008a). The AAE specific values used to discriminate between fossil fuel and biomass burning contributions were AAE_{ff} =1.0 and AAE_{bb}=1.68 (Zotter et al., 2017). The anomalous AAE data recorded every 2-minutes (those below 0.7 and above 5) were eliminated since these measurements are not indicative of the real eBC. These values were selected based on the pdf (probability density function) of the AAE values (Figure S7.3). The deleted data constitute less than 1% throughout the sampling period.

As mentioned above, coal combustion can become an important contributor to eBC during the cold period in León. It is expected that eBC attributed to biomass burning also includes eBC from coal combustion (eBC_{bb+cc}) (Bond et al., 2002; Harrison et al., 2013) and use the same AAE of 1.68 for them since it is the combustion efficiency which controls the optical properties rather than fuel. To achieve the aim of estimating the coal combustion (eBC_{cc}) fraction from eBC_{bb+cc}, a model was developed by considering the linear regression between the eBC_{bb+cc} with biomass and coal combustion tracers.

7.2.2.2. Carbonaceous aerosols

A high-volume air sampler (CAV-A/Mb model) equipped with a PM_{10} inlet head and 150 mm diameter quartz filters were used to collect the aerosol in the air flow, for later carbon analysis. Each filter sampled for a period of 23.5 h (≈ 1 day, from 1200 UTC to 1130 UTC of the day after) and the mass content was determined by gravimetric methods. Total carbon (TC) mass was obtained by the Thermal Optical Transmittance method (TOT). The method for the determination of the split of TC mass into organic carbon (OC) and elemental carbon (EC) and the technique and equipment used were previously described by, respectively, Pio et al. (2011) and Castro et al. (1999).

7.2.2.3. Major tracers

A low volume sampler (TECORA ECHOPM) equipped with a PM_{10} inlet head collected aerosol on teflon filters (47 mm diameter) for 23.5 h periods (≈ 1 day), later used in PIXE (Particle-Induced X-ray Emission) for major and trace element analysis, following the methodology described by Lucarelli et al. (2014). These daily samples were also analyse by ionic chromatography coupled with pulsed amperometric detection (Gonçalves et al., 2021) to obtain levoglucosan concentrations. The estimated uncertainties for the ion chromatography and PIXE measurements depends on the analysed element and its detection limit. These uncertainties ranged from 2% to 14% during the sampling campaign.

7.2.2.4. Meteorological parameters

A weather station was used to record temperature (T), relative humidity (RH), pressure (P) and wind speed (WS) and direction. The latter two variables have been used as input data for *polar plots* (Carslaw, 2015; Carslaw and Ropkins, 2012). Furthermore, ABL height, which controls the eBC concentration at ground level (Heintzenberg et al., 2016), was obtained from National Oceanic and Atmospheric Administration (NOAA) data every 3 hours. Consistent with meteorological variables and the use of heating devices, the year was divided into two periods: cold period, from September 15 to April 14, and warm period, from April 15 to September 14.

7.2.3. STATISTICAL ANALYSES

A univariate analysis (i.e. mean, minimum, maximum and standard deviation) and bivariate Pearson correlations with 95% confidence intervals have been used to characterise eBC in León. Through the Pearson correlations, the linear association, direction, and strength of the relationships between eBC, air pollutants and meteorological variables have been determined. The strength of correlation (significant over 0.1 for 10455 hours of sampling) was classified according to the following positive or negative correlation ranges: <0.1 no correlation, 0.1-0.3 weak, 0.3-0.5 moderate, 0.5-0.7 strong, and >0.7 very strong correlation.

To characterise the days according to their pollutant concentration, a two-stage cluster classification was performed. Details will be presented in section 7.3.2.2.

7.3. RESULTS AND DISCUSSION

7.3.1. AETHALOMETER MODEL APPLICATION

In the following subsections, after the application of the Aethalometer model (Sandradewi et al., 2008a), an analysis of the evolution of eBC and AAE, the relation of eBC with meteorological conditions and the results of the thermal optical transmittance method are included.

7.3.1.1. Evolution of eBC

After applying the Aethalometer model, and once the contribution of each source to the eBC (eBC_{ff} and eBC_{bb+cc}) was known, a seasonal analysis was carried out.

a) A mean hourly eBC mass concentration of 0.9±0.9 μg m^{-3} was obtained for the sampling campaign. León is characterised by the absence of manufacturing activities compared to other industrialised cities, but with a regular use of coal combustion in domestic heating devices (Junta de Castilla y León, 2009). As can be seen in Table S7.2, the locations with eBC concentrations similar to León like Rotterdam (0.8±0.5 μg m^{-3}), Amsterdam (1.4±0.6 μg m^{-3}) (Klompmaker et al., 2015), Montreal (1.1±1.3 μg m^{-3}) (Weichenthal et al., 2014) and Valparaiso (0.8-0.9 μg m^{-3}) (Marín et al., 2017) present more population and industry than León.

b) In Figure 7.1, eBC concentrations are plotted throughout the sampling period, with a time resolution of 10 minutes. In winter, high values are reached, probably due to residential biomass burning and coal combustion. It is worth noting the higher eBC values registered in January 2017 compared to January 2016. This was probably a consequence of the lower mean temperature recorded in January 2017 (on average, 2 °C less than in January 2016). The dynamics of the atmospheric boundary layer height may also have played an important role. In autumn and winter, the ABL height is lower, preventing the dispersion of pollutants (Joshi et al., 2016), particularly in October, November and December 2016. The correlation between ABL height (at 0000, 0300,

0600, 0900, 1200, 1500, 1800 and 2100) and daily eBC concentrations has been determined. A significant statistical negative correlation all year round has been obtained (Table S7.3), but the link was especially strong in autumn and winter, when the ABL height was lower. The time frame with a major influence of the ABL on the eBC concentrations was between 0900 and 1800 (highest values of Pearson correlations), with a maximum influence at 0900. Besides, these time periods coincide with rush hours. The lowest ABL heights at 0900 were registered in winter and autumn (424±356 and 229±219 m, respectively), while in spring and summer values of 695±223 and 573±164 m, respectively, were recorded.

It should be noted that the sporadic points observed in Figure 7.1 with high concentrations in summer months are probably due to the occurrence of stubble burnings, activity still very common in the area near the sampling point (Lucas-Borja et al., 2016). These activities contributed for the high concentrations of eBC in the atmosphere of León, corroborated by the increase in the levels of potassium (as will be seen in section 3.2.1), a biomass burning tracer (Herich et al., 2011).

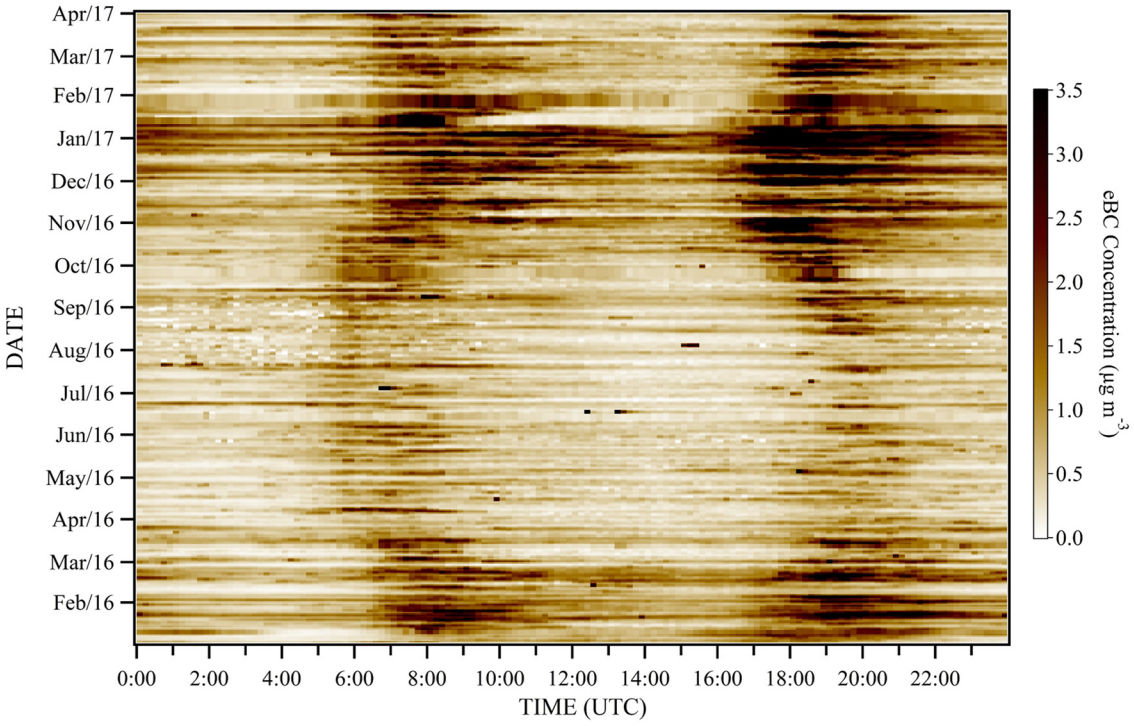

Figure 7.1. Temporal variations of eBC concentration (colour code) measured at León between January 2016 and March 2017.

c) The month with the highest eBC mean concentration was December 2016 with 1.6±0.6 μg m^{-3}, value about 3 times higher than the lowest (0.5±0.1 μg m^{-3}), registered in April 2016 (Table 7.1). The monthly maximum AAE (1.43±0.37) was reached in January 2017, corresponding to the maximum eBC_{bb+cc} concentration (0.67±0.41 μg m^{-3}). In contrast, the monthly minimum AAE (1.23±0.46) was recorded in June 2016 when the minimum eBC_{bb+cc} concentration (0.12±0.24 μg m^{-3}) was observed. AAE and eBC values were mainly associated with road traffic emissions (the low eBC values in the summer months result from the decrease in the number of vehicles in circulation due to the vacation period), the contribution of biomass and coal combustion in the cold period and the meteorological conditions (Table S7.3) such as thermal inversions (Gramsch et al., 2014; Lyamani et al., 2012).

As previously mentioned, AAE values for coal combustion can be very variable, ranging from values close to 1 to nearly 3 (Bond, 2001). Nevertheless, Sun et al. (2017) documented an AAE_{cc} of 1.30±0.32 for anthracite chunks coal, typically used in León, in stoves for raw-coal chunks. Thus, the emission from coal combustion can contribute to an increase in the AAE in the cold period. Months with high biomass burning correspond to an AAE increase due to the emission of bigger particles from this source (Russell et al., 2009; Alonso-Blanco et al., 2018).

Table 7.1. Monthly mean values (± standard deviation) calculated for eBC, eBC_{ff} and eBC_{bb+cc}, interpolated Absorption Ångström Exponent obtained from 470 nm and 950 nm (AAE) and percentage of biomass burning plus coal combustion (BB+CC (%)).

Year	Season	Month	eBC (μg m^{-3})	eBC_{ff} (μg m^{-3})	eBC_{bb+cc} (μg m^{-3})	AAE	BB+CC (%)
2016	Winter	January	1.00±0.41	0.69±0.3	0.31±0.14	1.29±0.33	32±9
	Winter	February	0.94±0.47	0.62±0.29	0.31±0.20	1.30±0.36	32±7
	Spring	March	0.72±0.30	0.50±0.20	0.22±0.12	1.27±0.41	29±8
	Spring	April	0.49±0.13	0.35±0.11	0.14±0.04	1.31±0.47	29±7
	Spring	May	0.56±0.14	0.43±0.11	0.13±0.04	1.25±0.48	23±6
	Summer	June	0.53±0.20	0.41±0.14	0.12±0.11	1.23±0.46	22±8
	Summer	July	0.54±0.19	0.41±0.14	0.12±0.10	1.24±0.49	22±8
	Summer	August	0.61±0.20	0.48±0.16	0.12±0.05	1.26±0.54	20±3
	Autumn	September	0.80±0.33	0.58±0.21	0.22±0.15	1.3±0.5	27±8
	Autumn	October	0.98±0.31	0.73±0.24	0.24±0.11	1.25±0.36	25±6
	Autumn	November	1.10±0.52	0.72±0.34	0.38±0.19	1.31±0.33	34±7
	Winter	December	1.62±0.59	1.02±0.36	0.6±0.28	1.31±0.27	36±8
2017	Winter	January	1.50±0.81	0.83±0.54	0.67±0.41	1.43±0.37	44±14
	Winter	February	0.82±0.34	0.50±0.19	0.32±0.20	1.37±0.44	37±10
	Spring	March	0.79±0.34	0.46±0.18	0.33±0.22	1.37±0.42	39±12

7.3.1.2. Relationship between eBC and meteorological conditions

Pearson correlations (Table S7.4) indicated a significant negative correlation between eBC_{bb+cc} and temperature due to the use of heating devices, mainly in autumn and winter. Although moderate in the winter months, as for AAE, a weak negative correlation with temperature throughout the year was observed. Temperature explained 17% of the variance of AAE in December 2016. eBC_{ff} did not show a clear relationship with temperature because its main source was traffic, non-dependent directly on weather conditions. Thus, throughout the year, a significant weak negative correlation was registered.

A significant moderate negative correlation between wind speed and eBC has been observed throughout the year, as observed in other studies (Kucbel et al., 2017). Thus, under high wind speed conditions, eBC concentration decreases, due to the higher pollutant dispersion. Wind speed explained 21% of the variance of eBC_{ff} in March 2017.

For relative humidity, the probability was less than 1% in all months, contrary to other studies (Kucbel et al., 2017). The study of the relationship between eBC and rainfall has been conducted by Blanco-Alegre et al. (2018), who showed a different rain scavenging effect according to the eBC source.

eBC_{bb+cc} and eBC_{ff} concentrations showed dependence on wind direction and speed, as depicted in the polar plots (Figure 7.2). In the cold period (autumn and winter), the eBC_{ff} mostly originated in quadrant III (between S and W), which coincides with the geographical location of the city centre. The contribution from I and II quadrants was mainly due to the León ring road. Likewise, the values of eBC_{bb+cc} were higher in the cold period, but in spring and summer there was greater variability due to nearby wildfires and stubble burning. In winter 2017, the highest concentrations were associated with quadrant III, where a dense residential area with houses using gas-oil, gas and coal for heating devices is located.

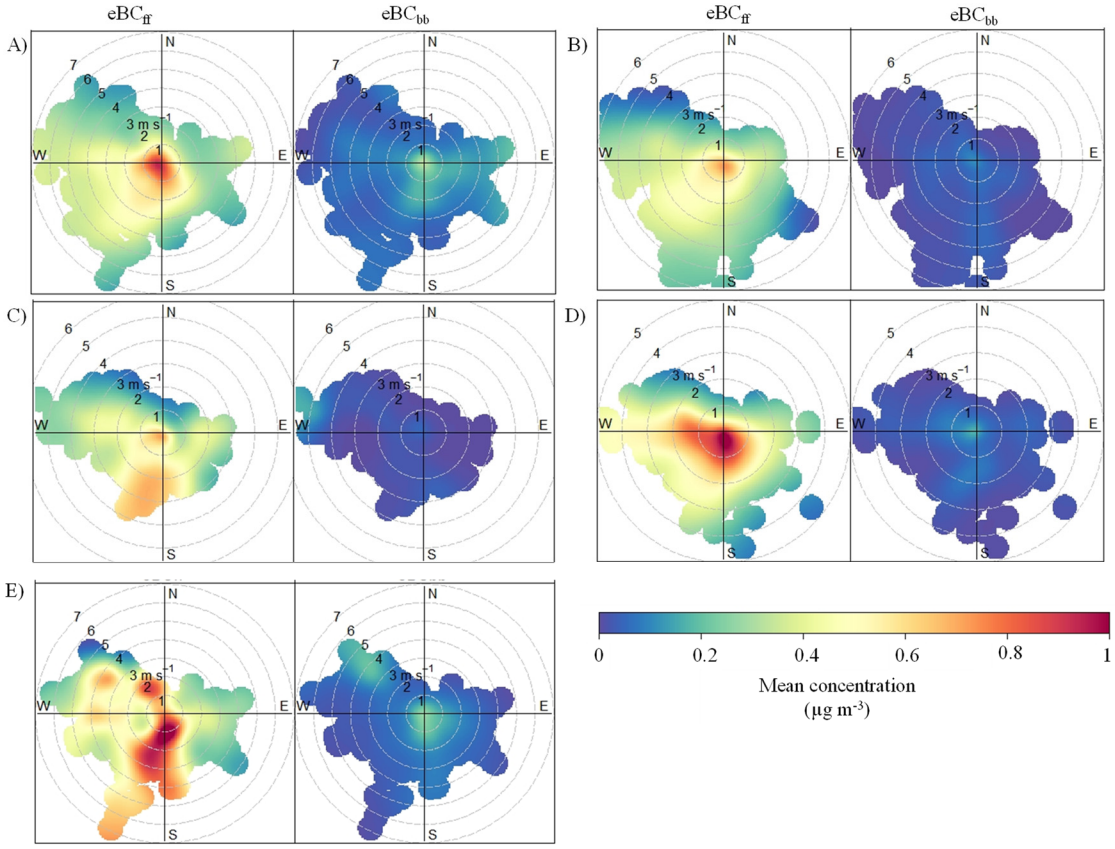

Figure 7.2. Seasonal polar plot of eBC_{ff} (left) and eBC_{bb+cc} (right) measured at León during the sampling campaign. A) Winter 2016; B) Spring 2016; C) Summer 2016; D) Autumn 2016; E) Winter 2017. The graphs were generated using Openair in R programming (Carslaw, 2015; Carslaw and Ropkins, 2012).

7.3.1.3. Comparison aethalometer- Thermal optical transmittance methods

PM_{10} concentrations were higher in the cold period than in the warm period (17.0±8.7 vs 12.6±8.3 µg m^{-3}). The summer values could be explained by the occurrence of forest fires and Saharan dust intrusions (Díaz et al., 2017) and the winter values by the occurrence of thermal inversions (see ABL in Table S7.3) and an increase in the use of heating devices.

The daily (24 h samples) eBC/PM_{10} ratio ranged between 0.01 and 0.29, averaging 0.071±0.036 in the cold period and 0.050±0.029 in the warm period. Similar values were obtained in Beijing, also with traffic and coal combustion as important sources of BC during cold period (Liu et al., 2016b; Yu et al., 2015), whilst lower ratios were registered in Delnice (Croatia) (Godec et al., 2016).

The eBC obtained from the aethalometer and the EC-OC estimated through the thermo-optical method have been correlated. The eBC/OC daily ratio showed higher values in the cold period (0.45±0.17) than in the warm period (0.31±0.13) (Table S7.5). Similar values were obtained in cities of developing countries such as Dakar and Bamako (Val et al., 2013) and European regions as London (United Kingdom) or Melpitz (Germany) (Kendall et al., 2001; Müller, 1999). The ratio estimated for the cold period is typical of fossil fuel and coal combustion (Massling et al., 2015). However, the lower ratio registered during the warm period is due to biomass burning, that causes an emission of ammonia gas and potassium (Yao et al., 2016). The evolution of these ratios along the sampling period is presented in Figure A4.

The EC/eBC daily ratios (Table S7.5) for the cold (0.86±0.45) and the warm 1.09±0.31) periods are lower than those reported by Liu et al. (2016a) in Tianjin (China) (higher differences between EC and eBC in polluted days were observed), but in the range of values compiled by Salako et al. (2012) in nine cities of Asia and Oceania. Thus, the relationship EC-eBC showed a strong positive correlation throughout the sampling period ($r=0.84$; $p<0.01$). However, during the cold period, a difference of 8% was observed (Figure 7.3), mainly on days with EC concentrations higher than 1 $\mu g\ m^{-3}$, similar to what was observed by Liu et al. (2016a). Nevertheless, the fit was better during the cold period ($r^2=0.77$) than during the warm period ($r^2=0.67$). Besides, the slope between ligth absortion at 880 nm, assuming the parameters mentioned in paragraph 2.2.1, and EC concentration by TOT method (Figure S7.5) has been obtained (4.46±0.16 $m^2\ g^{-1}$). This slope is the mass absorption cross-section (MAC) and it is in the range of values reported by Karanasiou et al. (2015).

Higher correlations between EC-eBC was reported in other studies, but many of them were based on a lower number of samples and presented lower concentrations than those of the current research (Ahmed et al., 2009; Hitzenberger et al., 2006; Jeong et al., 2004; Lavanchy et al., 1999; Liu et al., 2016a; Safai et al., 2014). The differences can be due to intersite variability of physical and chemical characteristics of BC, inasmuch as BC particles sometimes are primarily EC but in other cases they are a complex mixture of carbon and non-carbon species (Jeong et al., 2004; Long et al., 2013). Also, filter photometers are cross-sensitive to scattering and overestimate eBC at SSA above 0.85 (Yus-Díez et al., 2021) and other factor may be the lensing effect that can increase the eBC/EC ratio (Zhang et al., 2018).

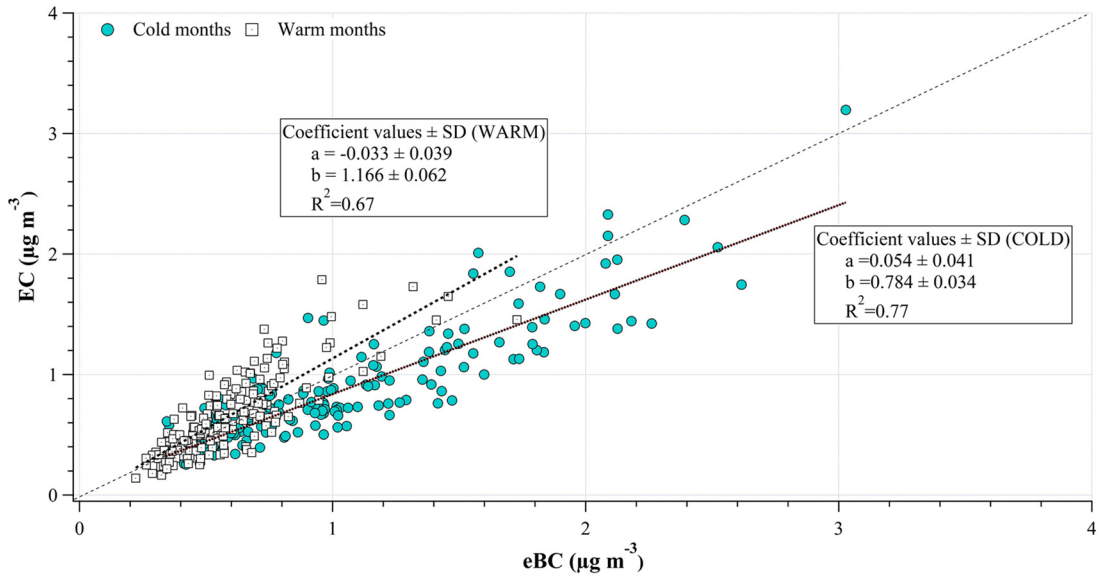

Figure 7.3. Comparison between EC and eBC throughout the sampling period, discriminating between cold (circles) and warm (boxes) period. Dashed line is the 1:1 relation.

7.3.2. COAL COMBUSTION CONTRIBUTION

An analysis of the contribution of coal combustion to the total eBC concentration is shown below assuming the biomass burning fraction, eBC_{bb+cc}, estimated from the aethalometer data after applying the Sandradewi et al. (2008a) approach, and using biomass and coal combustion tracers.

7.3.2.1. Model variables analysis

Several tracers of biomass burning (levoglucosan, K and Se) and coal combustion (As and SO_2) were evaluated to be used in the construction of the model (Puig et al., 2008; Vejahati et al., 2010; C. Wang et al., 2018). The tracers with the best fit to the eBC_{bb+cc} data were K (r^2=0.75) and As (r^2=0.56), so they were selected. Other tracers like levoglucosan (r^2=0.13), SO_2 (r^2=0.04) or Se (r^2=0.31) presented a worse fit with eBC_{bb+cc}.

The annual evolution of PM_{10}, As, K and meteorological variables is depicted in Figure 7.4.

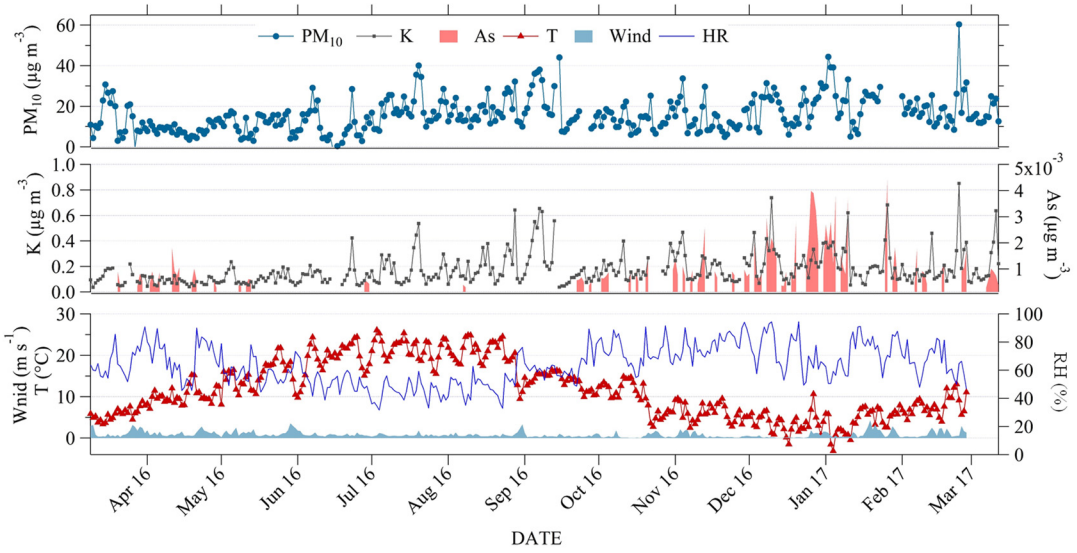

Figure 7.4. Annual evolution of PM_{10}, As, K and meteorological variables during the sampling campaign.

The mean concentrations in the cold period were PM_{10} (17.0±8.7 µg m^{-3}), As (0.66±0.86 ng m^{-3}) and K (0.183±0.127 µg m^{-3}), whereas values in the warm period were PM_{10} (12.6±8.3 µg m^{-3}), As (0.11±0.24 ng m^{-3}) and K (0.162±0.126 µg m^{-3}). The mean values for the meteorological variables (T, RH and WS) in the cold period were 7.3±4.1 °C, 69.8±11.4% and 0.86±0.85 m s^{-1}, while the corresponding values in the warm period were 16.2±5.9 °C, 56.1±12.9% and 0.97±0.62 m s^{-1}. The analysis of the remaining variables of the model (eBC_{bb+cc}, percentage of biomass burning (BB(%)) and AAE) was already presented in section 3.1. Although three sources of eBC (eBC_{ff} (traffic), eBC_{bb}, eBC_{cc}) were identified in the cold period, some periods of Saharan dust intrusions were identified. However, these data were not considered in this study due to the non-negligible interference that results from the presence of iron oxides associated with this type of events. The contribution of coal combustion to eBC_{bb+cc} for the rest of the year was considered negligible, so in the warm period only two sources dominated (eBC_{ff}, eBC_{bb}).

The selected variables to build the model were temperature, BB (%), AAE, eBC_{bb+cc}, As and K concentration.

7.3.2.2. Model of coal combustion contribution

To select the days to develop the model, a two-stage cluster classification was performed for the cold period (from 15 September to 14 April). From the 6 aforementioned variables

(temperature, BB (%), AAE, eBC_{bb+cc}, As and K concentration), three clusters were established by grouping the data according to the variables that provided further information (mean values):

- *Cluster 1* corresponds to 49% of the days with an average temperature of 6.1±3.3 °C, PM_{10} concentration of 18.1±8.5 μg m^{-3} and:
  - eBC_{bb+cc} concentration of 0.50±0.29 μg m^{-3};
  - K concentration C_K as biomass burning tracer of 0.200±0.105 μg m^{-3};
  - As concentration C_{As} as coal combustion tracer of 1.24±0. 86 ng m^{-3}.
- *Cluster 2* corresponds to 16% of the days with an average temperature of 5.2±3.7 °C, PM_{10} concentration of 20.7±9.7 μg m^{-3} and:
  - eBC_{bb+cc} concentration of 0.59±0.31 μg m^{-3};
  - K concentration C_K of 0. 260±0.111 μg m^{-3};
  - As concentration C_{As} of 1.26±0. 61 ng m^{-3}.
- *Cluster 3* includes 35% of the days, with an average temperature of 8.5±3.9 °C, PM_{10} concentration of 13.5±6.2 μg m^{-3} and:
  - eBC_{bb+cc} concentration of 0.22±0.11 μg m^{-3};
  - K concentration C_K of 0.149±0.060 μg m^{-3};
  - As concentration C_{As} of 0.75±0.54 ng m^{-3}.

In cluster 1 and 2, the low temperatures could explain the increase in the concentration of biomass burning and coal combustions tracers, while the opposite happens in cluster 3.

Considering that Cluster 3 integrates days in which coal combustion emissions could be neglected, the multi-linear regression analysis only considered data from days included in Cluster 1 (N=51) and Cluster 2 (N=16). The estimated eBC_{bb+cc} concentration for biomass burning and coal combustion is expressed as:

$$\mathrm{eBC_{bb+cc}}(\mu g\, m^{-3}) = \overbrace{(0.045 \pm 0.032)}^{\approx zero} + \overbrace{(1.92 \pm 0.15) \times C_K}^{eBC_{bb}} + \overbrace{(119 \pm 20) \times C_{As}}^{eBC_{cc}} \qquad \textit{Eq. 7.1}$$

with a model standard error of 0.11 μg m^{-3}, and correlation coefficient of r=0.92 (Figure 7.5). Figure S7.6 shows the time series of eBC_{bb+cc} concentration estimated by the model and eBC_{bb+cc} measured.

The application of this model allows to discriminate between eBC_{cc} (mean value of 26% of eBC_{bb+cc}) and eBC_{bb} (mean value of 74% of eBC_{bb+cc}) for the cold period (for days included in clusters 1 and 2). A strong correlation between eBC_{bb} and K (r=0.93) and between eBC_{cc} and As (r=0.94) has been registered (Figure S7.7).

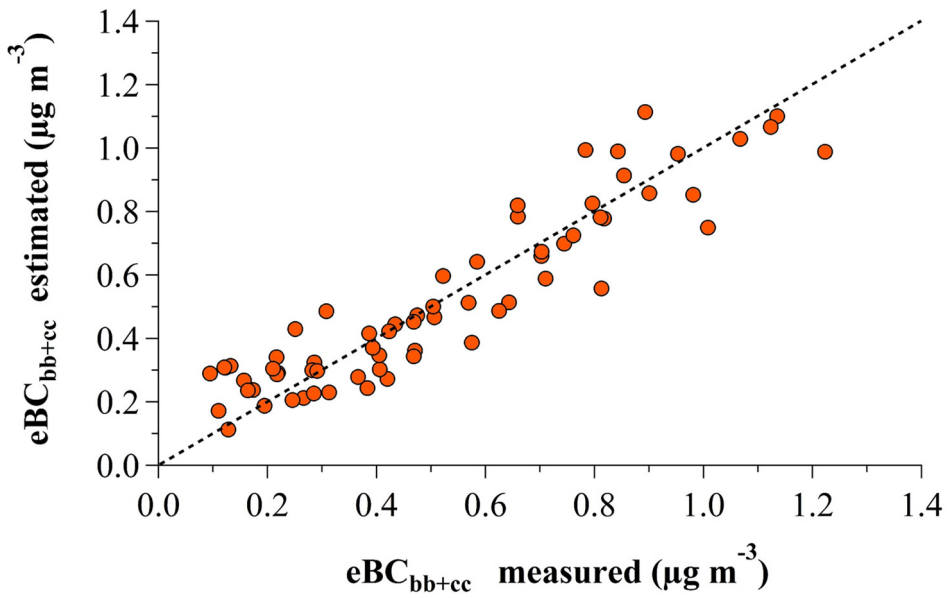

Figure 7.5. eBC$_{bb+cc}$ concentration estimated by the model vs eBC$_{bb+cc}$ measured. Dashed line is the 1:1 relation.

To analyse the robustness of the model, the same procedure was carried out but considering only the days of the cold period with As concentrations higher than the median (0.00082 μg m^{-3}). Similar results were obtained (see Supplementary material).

The mean annual concentrations of eBC$_{ff}$ and eBC$_{bb+cc}$ were 0.58±0.18 and 0.28±0.16 μg m^{-3} respectively. The model allowed estimating mean winter concentrations for eBC$_{ff}$, eBC$_{bb}$ and eBC$_{cc}$ of 0.65±0.34, 0.27±0.19 and 0.09±0.08 μg m^{-3} respectively (Table 7.2). eBC$_{bb}$ concentration was found to be higher in January 2017 (0.49±0.30 μg m^{-3}), more than double that estimated for January of the previous year (0.23±0.11 μg m^{-3}), and four times higher than the concentrations during summer 2016 (0.12±0.11 μg m^{-3}) and spring (0.15±0.07 μg m^{-3}) months. The highest eBC$_{cc}$ levels were estimated for December 2016 and January 2017 (0.18 μg m^{-3}). The low temperatures in winter months promote the use of biomass and coal in heating devices, resulting in the highest levels of eBC$_{bb}$ and eBC$_{cc}$. The coal combustion percentage CC(%) was almost double in winter (10±2%) when compared to autumn (6±1%), lower percentages than those observed by Liu et al. (2016b) in Beijing (China), an area with a higher use of coal than in León.

Table 7.2. Monthly mean values (± standard deviation) calculated for eBC_{ff}, eBC_{bb}, eBC_{cc}, percentage of biomass burning (BB(%)) and coal combustion (CC(%)) from eBC after the application of the model proposed.

Year	Season	Month	eBC_{bb} ($\mu g\ m^{-3}$)	eBC_{cc} ($\mu g\ m^{-3}$)	BB (%)	CC (%)
2016	Winter	January	0.23±0.11	0.08±0.04	23±7	8±2
	Winter	February	0.20±0.13	0.11±0.07	21±5	11±3
	Spring	March	0.18±0.11	0.08±0.04	25±8	10±3
	Spring	April	0.11±0.04	0.03±0.03	29±7	12±4
	Spring	May	0.13±0.04	-	23±6	-
	Summer	June	0.12±0.11	-	22±8	-
	Summer	July	0.12±0.10	-	22±8	-
	Summer	August	0.12±0.05	-	20±3	-
	Autumn	September	0.21±0.16	0.05±0.03	24±9	6±2
	Autumn	October	0.19±0.08	0.05±0.02	20±5	5±1
	Autumn	November	0.30±0.16	0.08±0.05	27±6	7±2
	Winter	December	0.42±0.20	0.18±0.10	25±6	11±4
2017	Winter	January	0.49±0.30	0.18±0.12	33±11	12±4
	Winter	February	0.25±0.16	0.07±0.04	29±9	9±2
	Spring	March	0.30±0.21	0.06±0.04	36±13	7±2

7.4. CONCLUSIONS

The temporal evolution of black carbon concentrations in an urban background area located in a coal-mining region, where the use of this fuel is widespread, was studied. A model was developed to separate the contribution of BC from biomass burning from that resulting from coal combustion based on the aethalometer data and tracer concentrations. The annual mean eBC concentration was 0.9±0.9 $\mu g\ m^{-3}$. When correlating eBC with EC, a difference of 12% was observed between the thermo-optical and aethalometer method, especially for eBC concentrations higher than 1 $\mu g\ m^{-3}$.

The combination of coal combustion and biomass burning tracers (As and K, respectively) and the Aethalometer model is shown to be a useful tool for the determination of the three main sources of eBC. For this purpose, the cold days (characterised by a wide use of coal in domestic heating devices) were selected to build a new model.

The Aethalometer model estimates the concentration of biomass burning and traffic based on the assumption that only these two sources are present. In cities where coal remains widely used, the model results should be taken with care, since the smoke from biomass and coal absorbs at the same wavelength. Thus, this study has tried to address a method to differentiate between the concentration from biomass burning (eBC_{bb}) and that from coal combustion (eBC_{cc}) by a multi-linear regression model (r^2=0.85) using the tracers K and As. These contributions in the cold period were, on average, 74% from biomass burning and 26% from coal combustion, resulting in a mean winter concentration for traffic (eBC_{ff}), eBC_{bb} and eBC_{cc} of, respectively, 0.65±0.34, 0.27±0.19 and 0.09±0.08 μg m^{-3}.

The methodology to estimate the contribution of coal combustion to eBC will constitute a useful tool in areas where the use of coal is still very widespread. The findings will be crucial in the adoption of mitigation measures to prevent environmental impacts related to coal combustion emissions. Furthermore, the predictive model can be regarded as a first approach to estimate the contribution of coal combustion to black carbon concentrations.

7.5. REFERENCES

Ahmed, T., Dutkiewicz, V.A., Shareef, A., Tuncel, G., Tuncel, S., Husain, L., 2009. Measurement of black carbon (BC) by an optical method and a thermal-optical method: Intercomparison for four sites. Atmos. Environ. 43, 6305–6311. doi:10.1016/j.atmosenv.2009.09.031

Alonso-Blanco, E., Castro, A., Calvo, A.I., Pont, V., Mallet, M., Fraile, R., 2018. Wildfire smoke plumes transport under a subsidence inversion: Climate and health implications in a distant urban area. Sci. Total Environ. 619–620, 988–1002. doi:10.1016/j.scitotenv.2017.11.142

Andreae, M.O., Gelencsér, A., 2006. Black carbon or brown carbon? the nature of light-absorbing carbonaceous aerosols. Atmos. Chem. Phys. 6, 3131–3148. doi:10.5194/acp-6-3131-2006

Apte, J.S., Marshall, J.D., Cohen, A.J., Brauer, M., 2015. Addressing Global Mortality from Ambient PM2.5. Environ. Sci. Technol. 49, 8057–8066. doi:10.1021/acs.est.5b01236

Auffhammer, M., Ramanathan, V., Vincent, J.R., 2006. Integrated model shows that atmospheric brown clouds and greenhouse gases have reduced rice harvests in India. Proc. Natl. Acad. Sci. 103, 19668–19672. doi:10.1073/pnas.0609584104

Barros, V.R., C.B. Field, D.J. Dokken, M.D. Mastrandrea, K.J. Mach, T.E. Bilir, M. Chatterjee, K.L. Ebi, Y.O. Estrada, R.C. Genova, B. Girma, E.S. Kissel, A.N. Levy, S. MacCracken, P.R.M., (eds.), L.L.W., ICCP, 2014. Climate Change 2014 Impacts, Adaptation, and Vulnerability Part B: Regional Aspects, Igarss 2014. doi:10.1007/s13398-014-0173-7.2

Begam, G.R., Vachaspati, C.V., Ahammed, Y.N., Kumar, K.R., Babu, S.S., Reddy, R.R., 2016. Measurement and analysis of black carbon aerosols over a tropical semi-arid station in Kadapa, India. Atmos. Res. 171, 77–91. doi:10.1016/j.atmosres.2015.12.014

Blanco-Alegre, C., Calvo, A.I., Coz, E., Castro, A., Oduber, F., Prévôt, A.S.H.H., Močnik, G., Fraile, R., 2019. Quantification of source specific black carbon scavenging using an aethalometer and a disdrometer. Environ. Pollut. 246, 336–345. doi:10.1016/j.envpol.2018.11.102

Bond, T.C., 2001. Spectral dependence of visible light absorption by carbonaceous particles emitted from coal combustion. Geophys. Res. Lett. 28, 4075–4078. doi:10.1029/2001GL013652

Bond, T.C., Covert, D.S., Kramlich, J.C., Larson, T. V, Charlson, R.J., 2002. Primary particle emissions from residential coal burning: Optical properties and size distributions. J. Geophys. Res. Atmos. 107. doi:10.1029/2001JD000571

Bond, T.C., Doherty, S.J., Fahey, D.W., Forster, P.M., Berntsen, T., Deangelo, B.J., Flanner, M.G., Ghan, S., Kärcher, B., Koch, D., Kinne, S., Kondo, Y., Quinn, P.K., Sarofim, M.C., Schultz, M.G., Schulz, M., Venkataraman, C., Zhang, H., Zhang, S., Bellouin, N., Guttikunda, S.K., Hopke, P.K., Jacobson, M.Z., Kaiser, J.W., Klimont, Z., Lohmann, U., Schwarz, J.P., Shindell, D., Storelvmo, T., Warren, S.G., Zender, C.S., 2013. Bounding the role of black carbon in the climate system: A scientific assessment. J. Geophys. Res. Atmos. 118, 5380–5552. doi:10.1002/jgrd.50171

Carslaw, D., 2015. The openair manual open-source tools for analysing air pollution data. King's Coll. London 1, 287.

Carslaw, D.C., Ropkins, K., 2012. Openair - An r package for air quality data analysis. Environ. Model. Softw. 27–28, 52–61. doi:10.1016/j.envsoft.2011.09.008

Castro, L.M., Pio, C.A., Harrison, R.M., Smith, D.J.T., 1999. Carbonaceous aerosol in urban and rural European atmospheres: estimation of secondary organic carbon concentrations. Atmos. Environ. 33, 2771–2781. doi:10.1016/S1352-2310(98)00331-8

Chameides, W., Yu, H., Liu, S., Bergin, M., Xhou, X., Mearns, L., Wang, G., Kiang, C., Saylor, R.D., Luo, C., Huang, Y., Steiner, A., Giorgi, F., 1999. Study of the effects of atmospheric regional haze on agriculture: enhance crop yields in China through emission controls? Proc. Natl. Acad. Sci. 96, 13626–13633.

DGT, 2016. Informe anual-Parque vehicular por provincias en España.

Díaz, J., Linares, C., Carmona, R., Russo, A., Ortiz, C., Salvador, P., Machado, R., 2017. Saharan dust intrusions in Spain : Health impacts and associated synoptic conditions. Environ. Res. 156, 455–467. doi:10.1016/j.envres.2017.03.047

EEA, 2016. Air quality in Europe - 2016 Report. Copenhagen, Denmark. doi:10.2800/413142

Fialho, P., Cerqueira, M., Pio, C., Cardoso, J., Nunes, T., Custódio, D., Alves, C., Almeida, S.M., Almeida-Silva, M., Reis, M., Rocha, F., 2014. The application of a multi-wavelength aethalometer to estimate iron dust and black carbon concentrations in the marine boundary layer of Cape Verde. Atmos. Environ. 97, 136–143. doi:10.1016/j.atmosenv.2014.08.008

Fialho, P., Hansen, A.D.A., Honrath, R.E., 2005. Absorption coefficients by aerosols in remote areas: A new approach to decouple dust and black carbon absorption coefficients using seven-wavelength Aethalometer data. J. Aerosol Sci. 36, 267–282. doi:10.1016/j.jaerosci.2004.09.004

Garg, S., Chandra, B.P., Sinha, V., Sarda-Esteve, R., Gros, V., Sinha, B., 2016. Limitation of the use of the absorption angstrom exponent for source apportionment of equivalent black carbon: a case study from the North West Indo-Gangetic plain. Environ. Sci. Technol. 50, 814–824. doi:10.1021/acs.est.5b03868

Godec, R., Jakovljević, I., Šega, K., Čačković, M., Bešlić, I., Davila, S., Pehnec, G., 2016. Carbon species in PM10 particle fraction at different monitoring sites. Environ. Pollut. 216, 700–710. doi:10.1016/j.envpol.2016.06.034

Gonçalves, C., Rienda, I.C., Pina, N., Gama, C., Nunes, T., Tchepel, O., Alves, C., 2021. PM10-Bound Sugars: Chemical Composition, Sources and Seasonal Variations. Atmosphere (Basel). 12, 194. doi:10.3390/atmos12020194

Gramsch, E., Cáceres, D., Oyola, P., Reyes, F., Vásquez, Y., Rubio, M.A., Sánchez, G., 2014. Influence of surface and subsidence thermal inversion on PM2.5 and black carbon concentration. Atmos. Environ. 98, 290–298. doi:10.1016/j.atmosenv.2014.08.066

Hansen, A.D.A., 2005. The Aethalometer, Magee Scientific Corporation. Magee Scientific, Berkeley, CA, USA.

Hansen, A.D.A., Rosen, H., Novakov, T., 1984. The aethalometer - An instrument for the real-time measurement of optical absorption by aerosol particles. Sci. Total Environ. 36, 191–196. doi:10.1016/0048-9697(84)90265-1

Harrison, R.M., Beddows, D.C.S., Jones, A.M., Calvo, A., Alves, C., Pio, C., 2013. An evaluation of some issues regarding the use of aethalometers to measure woodsmoke concentrations. Atmos. Environ. 80, 540–548. doi:10.1016/j.atmosenv.2013.08.026

Heintzenberg, J., Cereceda-Balic, F., Vidal, V., Leck, C., 2016. Scavenging of black carbon in Chilean coastal fogs. Sci. Total Environ. 541, 341–347. doi:10.1016/j.scitotenv.2015.09.057

Herich, H., Hueglin, C., Buchmann, B., 2011. A 2.5 year's source apportionment study of black carbon from wood burning and fossil fuel combustion at urban and rural sites in Switzerland. Atmos. Meas. Tech. 4, 1409–1420. doi:10.5194/amt-4-1409-2011

Hitzenberger, R., Petzold, A., Bauer, H., Ctyroky, P., Pouresmaeil, P., Laskus, L., Puxbaum, H., 2006. Intercomparison of Thermal and Optical Measurement Methods for Elemental Carbon and Black Carbon at an Urban Location. Environ. Sci. Technol. 40, 6377–6383. doi:10.1021/es051228v

IDAE, 2017. Spanish Institute for Energy Diversification and Saving.

INE, 2017. Cifras oficiales de población resultantes de la revisión del Padrón municipal a 1 de enero de 2016.

Jeong, C.H., Hopke, P.K., Kim, E., Lee, D.W., 2004. The comparison between thermal-optical transmittance elemental carbon and Aethalometer black carbon measured at multiple monitoring sites. Atmos. Environ. 38, 5193–5204. doi:10.1016/j.atmosenv.2004.02.065

Joshi, H., Naja, M., Singh, K.P., Kumar, R., Bhardwaj, P., Babu, S.S., Satheesh, S.K., Moorthy, K.K., Chandola, H.C., 2016. Investigations of aerosol black carbon from a semi-urban site in the Indo-Gangetic Plain region. Atmos. Environ. 125, 346–359. doi:10.1016/j.atmosenv.2015.04.007

Junta de Castilla y León, 2018. Datos de la Red de Control de la Calidad del Aire. URL: http://servicios.jcyl.es/esco/index.action.

Junta de Castilla y León, 2009. El carbón en Castilla y León. Junta de Castilla y León. Consejería de Economía y Empleo - Dirección General de Energía y Minas.

Junta de Castilla y León, 2008. Encuesta de hogares y medio ambiente. Castilla y León 2008. URL: http://www.jcyl.es/estadistica.

Karanasiou, A., Minguillón, M. C., Viana, M., Alastuey, A., Putaud, J.-P., Maenhaut, W., Panteliadis, P., Močnik, G., Favez, O., and Kuhlbusch, T.A.J., 2015. Thermal-optical analysis for the measurement of elemental carbon (EC) and organic carbon (OC) in ambient air a literature review. Atmos. Meas. Tech. 8, 9649–9712. doi:10.5194/amtd-8-9649-2015

Kendall, M., Hamilton, R.S., Watt, J., Williams, I.D., 2001. Characterisation of selected speciated organic compounds associated with particulate matter in London. Atmos. Environ. 35, 2483–2495. doi:10.1016/S1352-2310(00)00431-3

Kinney, P.L., 2008. Climate change, air quality, and human health. Am. J. Prev. Med. 35, 459–467. doi:10.1016/j.amepre.2008.08.025

Kirchstetter, T.W., Novakov, T., Hobbs, P. V., 2004. Evidence that the spectral dependence of light absorption by aerosols is affected by organic carbon. J. Geophys. Res. D Atmos. 109, 1–12. doi:10.1029/2004JD004999

Klompmaker, J.O., Montagne, D.R., Meliefste, K., Hoek, G., Brunekreef, B., 2015. Spatial variation of ultrafine particles and black carbon in two cities: Results from a short-term measurement campaign. Sci. Total Environ. 508, 266–275. doi:10.1016/j.scitotenv.2014.11.088

Kucbel, M., Corsaro, A., Švédová, B., Raclavská, H., Raclavský, K., Juchelková, D., 2017. Temporal and seasonal variations of black carbon in a highly polluted European city: Apportionment of potential sources and the effect of meteorological conditions. J. Environ. Manage. 203, 1178–1189. doi:10.1016/j.jenvman.2017.05.038

Lavanchy, V.M.H., Gäggeler, H.W., Nyeki, S., Baltensperger, U., 1999. Elemental carbon (EC) and black carbon (BC) measurements with a thermal method and an aethalometer at the high-alpine research station Jungfraujoch. Atmos. Environ. 33, 2759–2769. doi:10.1016/S1352-2310(98)00328-8

Lelieveld, J., Evans, J.S., Fnais, M., Giannadaki, D., Pozzer, A., 2015. The contribution of outdoor air pollution sources to premature mortality on a global scale. Nature 525, 367–371. doi:10.1038/nature15371

Liu, B., Bi, X., Feng, Y., Dai, Q., Xiao, Z., Li, L., Wu, J., 2016. Fine carbonaceous aerosol characteristics at a megacity during the Chinese Spring Festival as given by OC / EC online measurements. Atmos. Res. 181, 20–28. doi:10.1016/j.atmosres.2016.06.007

Liu, Q., Ma, T., Olson, M.R., Liu, Y., Zhang, T., Wu, Y., Schauer, J.J., 2016. Temporal variations of black carbon during haze and non-haze days in Beijing. Sci. Rep. 6, 1–10. doi:10.1038/srep33331

Long, C.M., Nascarella, M.A., Valberg, P.A., 2013. Carbon black vs. black carbon and other airborne materials containing elemental carbon: Physical and chemical distinctions. Environ. Pollut. 181, 271–286. doi:10.1016/j.envpol.2013.06.009

Lucarelli, F., Calzolai, G., Chiari, M., Giannoni, M., Mochi, D., Nava, S., Carraresi, L., 2014. The upgraded external-beam PIXE/PIGE set-up at LABEC for very fast measurements on aerosol samples. Nucl. Instruments Methods Phys. Res. Sect. B Beam Interact. with Mater. Atoms 318, 55–59. doi:10.1016/j.nimb.2013.05.099

Lucas-Borja, M.E., Madrigal, J., Candel-Pérez, D., Jiménez, E., Moya, D., Heras, J. de las, Guijarro, M., Vega, J.A., Fernández, C., Hernando, C., 2016. Effects of prescribed burning, vegetation treatment and seed predation on natural regeneration of Spanish black pine (Pinus nigra Arn. ssp. salzmannii) in pure and mixed forest stands. For. Ecol. Manage. 378, 24–30. doi:10.1016/j.foreco.2016.07.019

Lyamani, H., Fernández-Gálvez, J., Pérez-Ramírez, D., Valenzuela, A., Antón, M., Alados, I., Titos, G., Olmo, F.J., Alados-Arboledas, L., 2012. Aerosol properties over two urban sites in South Spain during an extended stagnation episode in winter season. Atmos. Environ. 62, 424–432. doi:10.1016/j.atmosenv.2012.08.050

Marín, J.C., Raga, G.B., Arévalo, J., Baumgardner, D., Córdova, A.M., Pozo, D., Calvo, A., Castro, A., Fraile, R., Sorribas, M., 2017. Properties of particulate pollution in the port city of Valparaiso, Chile. Atmos. Environ. 171, 301–316. doi:10.1016/j.atmosenv.2017.09.044

Massling, A., Nielsen, I.E., Kristensen, D., Christensen, J.H., Sorensen, L.L., Jensen, B., Nguyen, Q.T., Nøjgaard, J.K., Glasius, M., Skov, H., 2015. Atmospheric black carbon and sulfate concentrations in Northeast Greenland. Atmos. Chem. Phys. 15, 9681–9692. doi:10.5194/acp-15-9681-2015

Müller, K., 1999. A 3 year study of the aerosol in northwest Saxony (Germany). Atmos. Environ. 33, 1679–1685. doi:10.1016/S1352-2310(98)00333-1

NOAA, 2017. National Oceanic and Atmospheric Administration.

Oduber, F., Calvo, A.I., Blanco-Alegre, C., Castro, A., Vega-Maray, A.M., Valencia-Barrera, R.M., Fernández-González, D., Fraile, R., 2019. Links between recent trends in airborne pollen concentration, meteorological parameters and air pollutants. Agric. For. Meteorol. 264, 16–26. doi:10.1016/j.agrformet.2018.09.023

Oduber, F., Calvo, A.I., Castro, A., Blanco-Alegre, C., Alves, C., Calzolai, G., Nava, S., Lucarelli, F., Nunes, T., Barata, J., Fraile, R., 2021. Characterization of aerosol sources in León (Spain) using Positive Matrix Factorization and weather types. Sci. Total Environ. 754, 142045. doi:10.1016/j.scitotenv.2020.142045

Petzold, A., Ogren, J.A., Fiebig, M., Laj, P., Li, S.M., Baltensperger, U., Holzer-Popp, T., Kinne, S., Pappalardo, G., Sugimoto, N., Wehrli, C., Wiedensohler, A., Zhang, X.Y., 2013. Recommendations for reporting black carbon measurements. Atmos. Chem. Phys. 13, 8365–8379. doi:10.5194/acp-13-8365-2013

Pio, C., Cerqueira, M., Harrison, R.M., Nunes, T., Mirante, F., Alves, C., Oliveira, C., Sanchez, A., Campa, D., Artíñano, B., Matos, M., 2011. OC / EC ratio observations in Europe : Re-thinking the approach for apportionment between primary and secondary organic carbon. Atmos. Environ. 45, 6121–6132. doi:10.1016/j.atmosenv.2011.08.045

Pokhrel, R.P., Wagner, N.L., Langridge, J.M., Lack, D.A., Jayarathne, T., Stone, E.A., Stockwell, C.E., Yokelson, R.J., Murphy, S.M., 2016. Parameterization of single-scattering albedo (SSA) and absorption Ångström exponent (AAE) with EC/OC for aerosol emissions from biomass burning. Atmos. Chem. Phys. 16, 9549–9561. doi:10.5194/acp-16-9549-2016

Puig, R., Àvila, A., Soler, A., 2008. Sulphur isotopes as tracers of the influence of a coal-fired power plant on a Scots pine forest in Catalonia (NE Spain). Atmos. Environ. 42, 733–745. doi:10.1016/j.atmosenv.2007.09.059

Russell, P.B., Bergstrom, R.W., Shinozuka, Y., Clarke, D., DeCarlo, P.F., Jimenez, J.L., Livingston, J.M., Redemann, J., Holben, B., Dubovik, O., Strawa, A., 2009. Absorption Angstrom Exponent in AERONET and related data as an indicator of aerosol composition. Atmos. Chem. Phys. Discuss. 9, 21785–21817. doi:10.5194/acpd-9-21785-2009

Safai, P.D., Raju, M.P., Rao, P.S.P., Pandithurai, G., 2014. Characterization of carbonaceous aerosols over the urban tropical location and a new approach to evaluate their climatic importance. Atmos. Environ. 92, 493–500. doi:10.1016/j.atmosenv.2014.04.055

Salako, G.O., Hopke, P.K., Cohen, D.D., Begum, B.A., Biswas, S.K., Pandit, G.G., Chung, Y.S., Rahman, S.A., Hamzah, M.S., Davy, P., Markwitz, A., Shagjjamba, D., Lodoysamba, S., Wimolwattanapun, W., Bunprapob, S., 2012. Exploring the variation between EC and BC in a variety of locations. Aerosol Air Qual. Res. 12, 1–7. doi:10.4209/aaqr.2011.09.0150

Sandradewi, J., Prévôt, A.S.H., Szidat, S., Perron, N., Alfarra, M.R., Lanz, V.A., Weingartner, E., Baltensperger, U.R.S., 2008a. Using aerosol light absorption measurements for the quantitative determination of wood burning and traffic emission contribution to particulate matter. Environ. Sci. Technol. 42, 3316–3323. doi:10.1021/es702253m

Sandradewi, J., Prévôt, A.S.H., Weingartner, E., Schmidhauser, R., Gysel, M., Baltensperger, U., 2008b. A study of wood burning and traffic aerosols in an Alpine valley using a multi-wavelength Aethalometer. Atmos. Environ. 42, 101–112. doi:10.1016/j.atmosenv.2007.09.034

Spanish Ministry for the Ecological Transition, 2018. Spanish Ministry for the Ecological Transition.

Sun, J., Zhi, G., Hitzenberger, R., Chen, Y., Tian, C., Zhang, Yayun, Feng, Y., Cheng, M., Zhang, Yuzhe, Cai, J., Chen, F., Qiu, Y., Jiang, Z., Li, J., Zhang, G., Mo, Y., 2017. Emission factors and light absorption properties of brown carbon from household coal combustion in China. Atmos. Chem. Phys. 17, 4769–4780. doi:10.5194/acp-17-4769-2017

Tang, G., Zhao, P., Wang, Yinghong, Gao, W., Cheng, M., Xin, J., Li, X., Wang, Yuesi, 2017. Mortality and air pollution in Beijing: The long-term relationship. Atmos. Environ. 150, 238–243. doi:10.1016/j.atmosenv.2016.11.045

Tobler, A., Bhattu, D., Canonaco, F., Lalchandani, V., Shukla, A., Thamban, N.M., Mishra, S., Srivastava, A.K., Bisht, D.S., Tiwari, S., Singh, S., Močnik, G., Baltensperger, U., Tripathi, S.N., Slowik, J.G., Prévôt, A.S.H., 2020. Chemical characterization of PM2.5 and source apportionment of organic aerosol in New Delhi, India. Sci. Total Environ. 745, 1–12. doi:10.1016/j.scitotenv.2020.140924

Tong, Z., Chen, Y., Malkawi, A., Adamkiewicz, G., Spengler, J.D., 2016. Quantifying the impact of traffic-related air pollution on the indoor air quality of a naturally ventilated building. Environ. Int. 89–90, 138–146. doi:10.1016/j.envint.2016.01.016

Tong, Z., Yang, B., Hopke, P.K., Zhang, K.M., 2017. Microenvironmental air quality impact of a commercial-scale biomass heating system. Environ. Pollut. 220, 1112–1120. doi:10.1016/j.envpol.2016.11.025

Val, S., Liousse, C., Doumbia, E.H.T., Galy-Lacaux, C., Cachier, H., Marchand, N., Badel, A., Gardrat, E., Sylvestre, A., Baeza-Squiban, A., 2013. Physico-chemical characterization of African urban aerosols (Bamako in Mali and Dakar in Senegal) and their toxic effects in human bronchial epithelial cells: Description of a worrying situation. Part. Fibre Toxicol. 10. doi:10.1186/1743-8977-10-10

Vejahati, F., Xu, Z., Gupta, R., 2010. Trace elements in coal: Associations with coal and minerals and their behavior during coal utilization - A review. Fuel 89, 904–911. doi:10.1016/j.fuel.2009.06.013

Wang, C., Liu, H., Zhang, Y., Zou, C., Anthony, E.J., 2018. Review of arsenic behavior during coal combustion : Volatilization , transformation , emission and removal technologies. Prog. Energy Combust. Sci. 68, 1–28. doi:10.1016/j.pecs.2018.04.001

Weichenthal, S., Farrell, W., Goldberg, M., Joseph, L., Hatzopoulou, M., 2014. Characterizing the impact of traffic and the built environment on near-road ultrafine particle and black carbon concentrations. Environ. Res. 132, 305–310. doi:10.1016/j.envres.2014.04.007

Weingartner, E., Saathoff, H., Schnaiter, M., Streit, N., Bitnar, B., Baltensperger, U., 2003. Absorption of light by soot particles: Determination of the absorption coefficient by means of aethalometers. J. Aerosol Sci. 34, 1445–1463. doi:10.1016/S0021-8502(03)00359-8

WHO/United Nations, 2018. Residential heating with wood and coal: health impacts and policy options in Europe and North America.

WHO, 2013. Review of evidence on health aspects of air pollution – REVIHAAP Project, World Health Organization. Copenhagen, Denmark.

WHO, 2012. Health effects of Black carbon. Copenhagen, Denmark.

WMO, 2016. WMO/GAW Aerosol Measurement procedures guidelines and recommendations, GAW Report. Geneva, Switzerland.

Xie, M., Shen, G., Holder, A.L., Hays, M.D., Jetter, J.J., 2018. Light absorption of organic carbon emitted from burning wood, charcoal, and kerosene in household cookstoves. Environ. Pollut. 240, 60–67. doi:10.1016/j.envpol.2018.04.085

Yao, L., Yang, L., Chen, J., Wang, X., Xue, L., Li, W., Sui, X., Wen, L., Chi, J., Zhu, Y., Zhang, J., Xu, C., Zhu, T., Wang, W., 2016. Characteristics of carbonaceous aerosols: Impact of biomass burning and secondary formation in summertime in a rural area of the North China Plain. Sci. Total Environ. 557–558, 520–530. doi:10.1016/j.scitotenv.2016.03.111

Yu, N., Zhu, Y., Xie, X., Yan, C., Zhu, T., Zheng, M., 2015. Characterization of ultrafine particles and other traffic related pollutants near roadways in Beijing. Aerosol Air Qual. Res. 15, 1261–1269. doi:10.4209/aaqr.2014.11.0295

Yus-Díez, J., Bernardoni, V., Močnik, G., Alastuey, A., Ciniglia, D., Ivančič, M., Querol, X., Perez, N., Reche, C., Rigler, M., Vecchi, R., Valentini, S., Pandolfi, M., 2021. Determination of the multiple-scattering correction factor and its cross-sensitivity to scattering and wavelength dependence for different AE33 Aethalometer filter tapes: A multi-instrumental approach. Atmos. Meas. Tech. Discuss. 2021, 1–30.

Zhang, Y., Favez, O., Canonaco, F., Liu, D., Močnik, G., Amodeo, T., Sciare, J., Prévôt, A.S.H., Gros, V., Albinet, A., 2018. Evidence of major secondary organic aerosol contribution to lensing effect black carbon absorption enhancement. npj Clim. Atmos. Sci. 1, 47. doi:10.1038/s41612-018-0056-2

Zotter, P., Herich, H., Gysel, M., El-Haddad, I., Zhang, Y., Močnik, G., Hüglin, C., Baltensperger, U., Szidat, S., Prévôt, A.S.H., 2017. Evaluation of the absorption Ångström exponents for traffic and wood burning in the Aethalometer based source apportionment using radiocarbon measurements of ambient aerosol. Atmos. Chem. Phys. 17, 4229–4249. doi:10.5194/acp-17-4229-2017

SUPPLEMENTARY MATERIAL

S.7.1. FIGURES

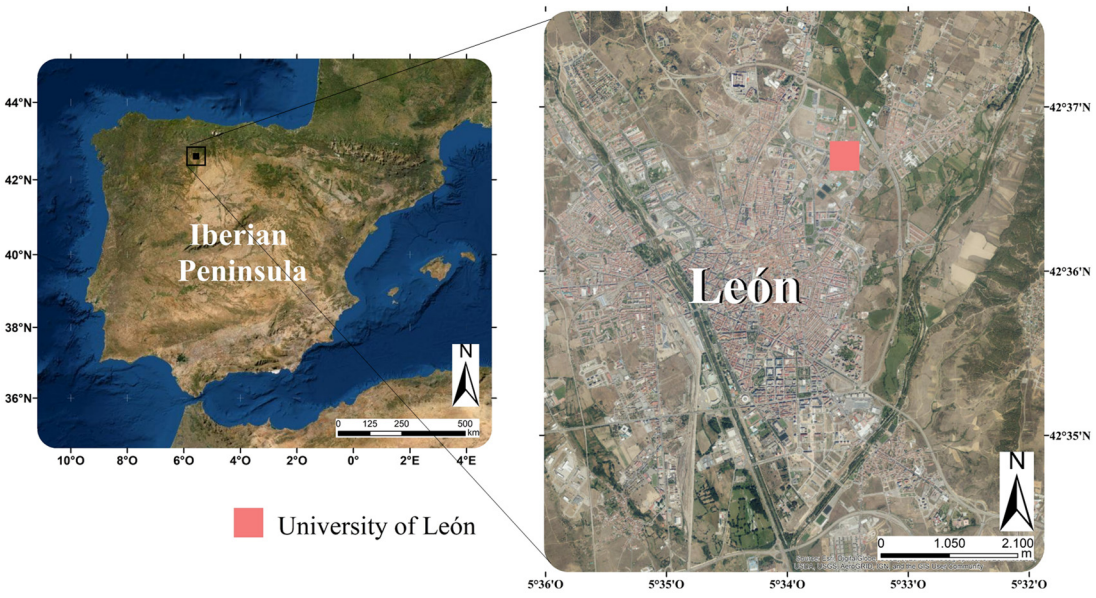

Figure S7.1. Geographic location of the city of León, Spain (left) and sampling site. Source: Earthstar Geographics, ESRI.

a)

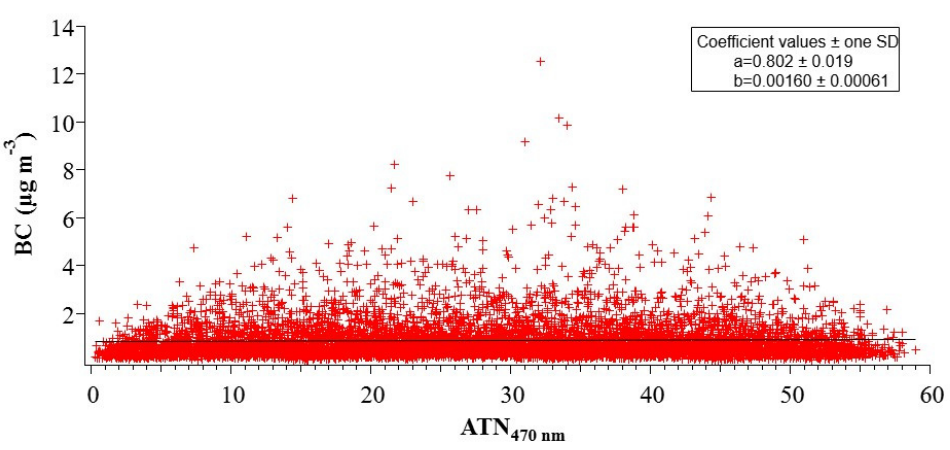

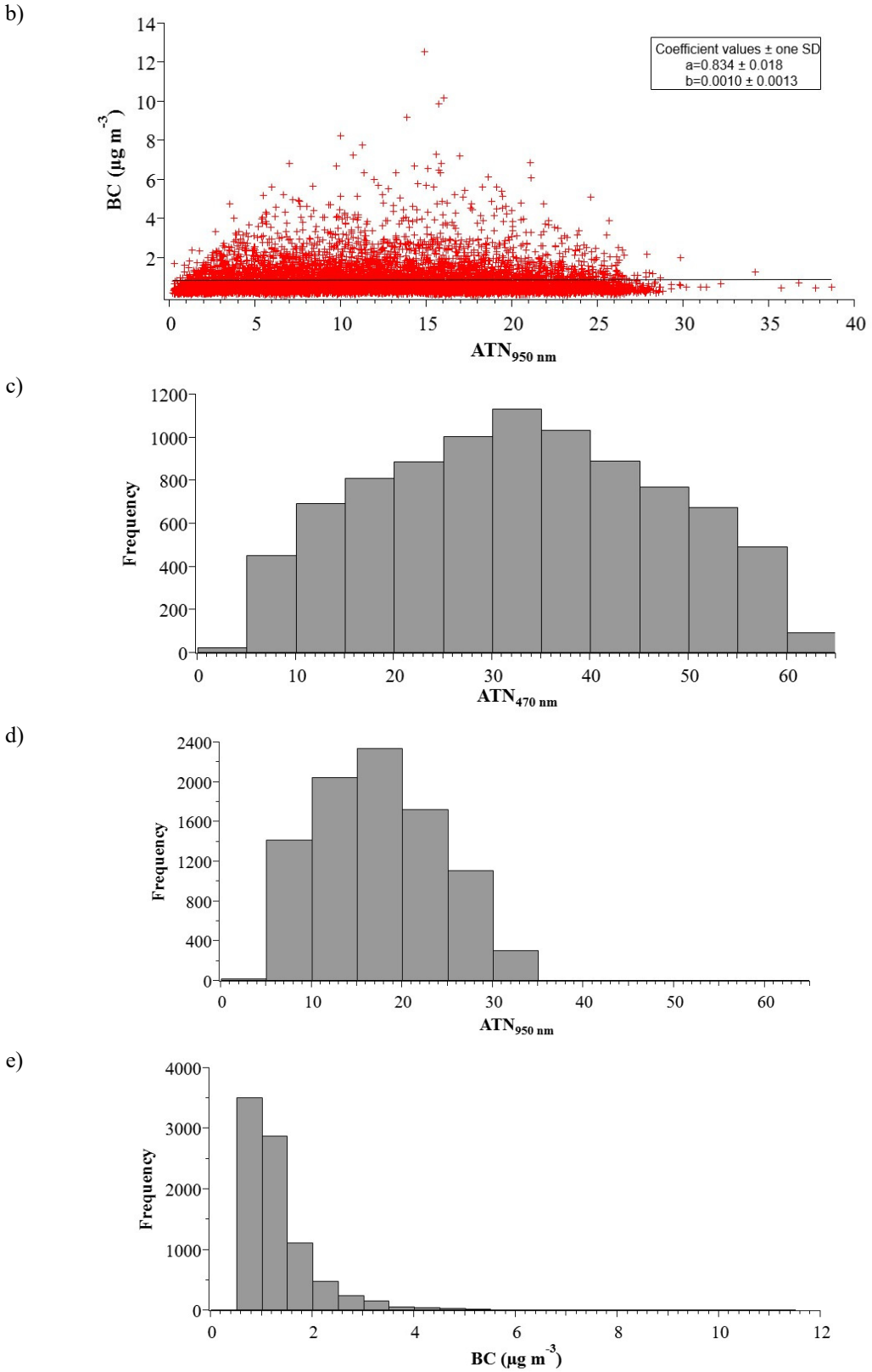

Figure S7.2. BC as a function of a) $ATN_{470\ nm}$ and b) $ATN_{950\ nm}$ plot; c) Frequency distribution of the number of measurements per $ATN_{470\ nm}$; d) Frequency distribution of the number of measurements per $ATN_{950\ nm}$; e) The BC frequency in the ATN range of 10-75.

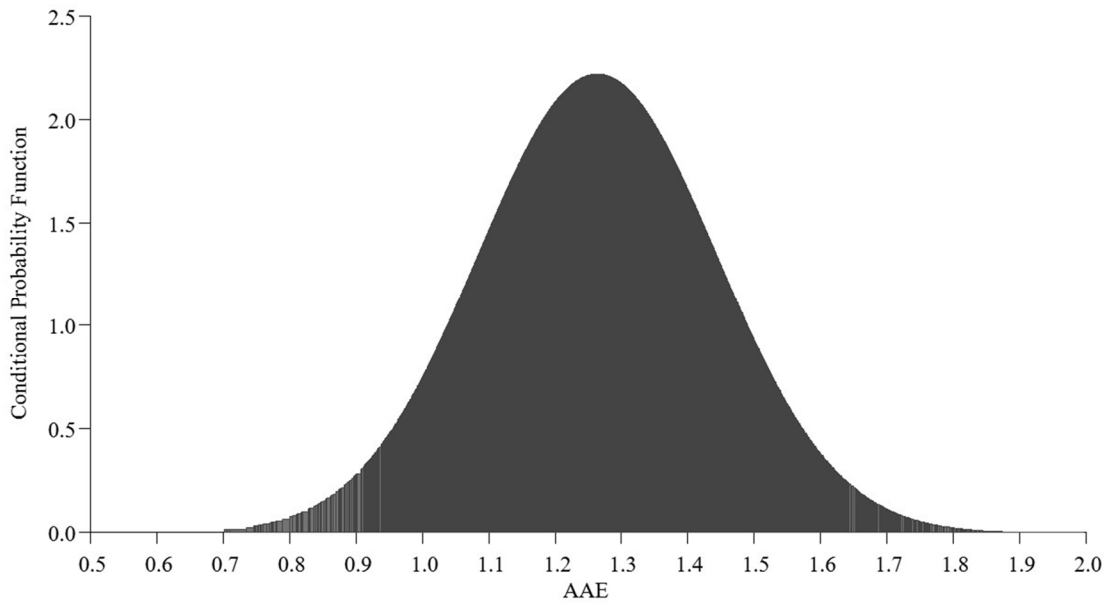

Figure S7.3. Probability distribution function of the AAE (470/950) over the full campaign.

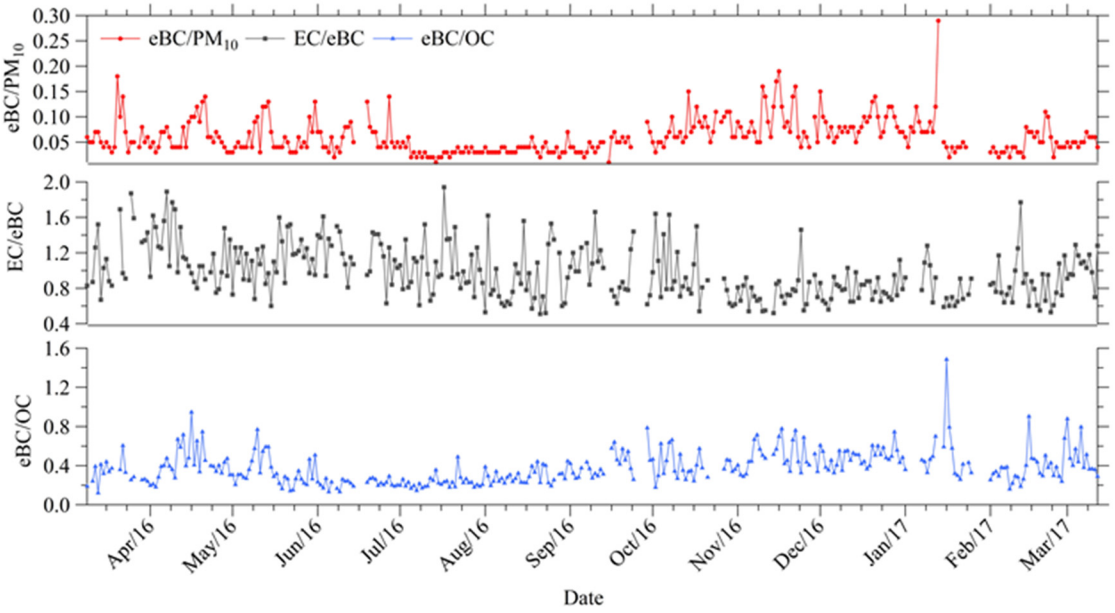

Figure S7.4. Temporal variations of ratios: eBC /PM_{10} (above), EC/eBC (middle) and eBC/OC (below) at León from January 2016 to March 2017.

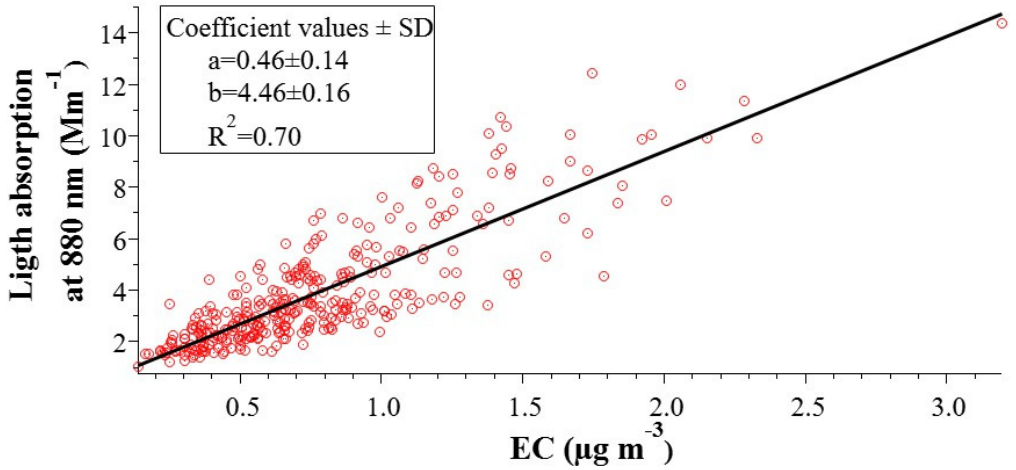

Figure S7.5. Regression between light absorption at 880 nm estimated from Aethalometer measurements and elemental carbon (EC) measured by TOT method.

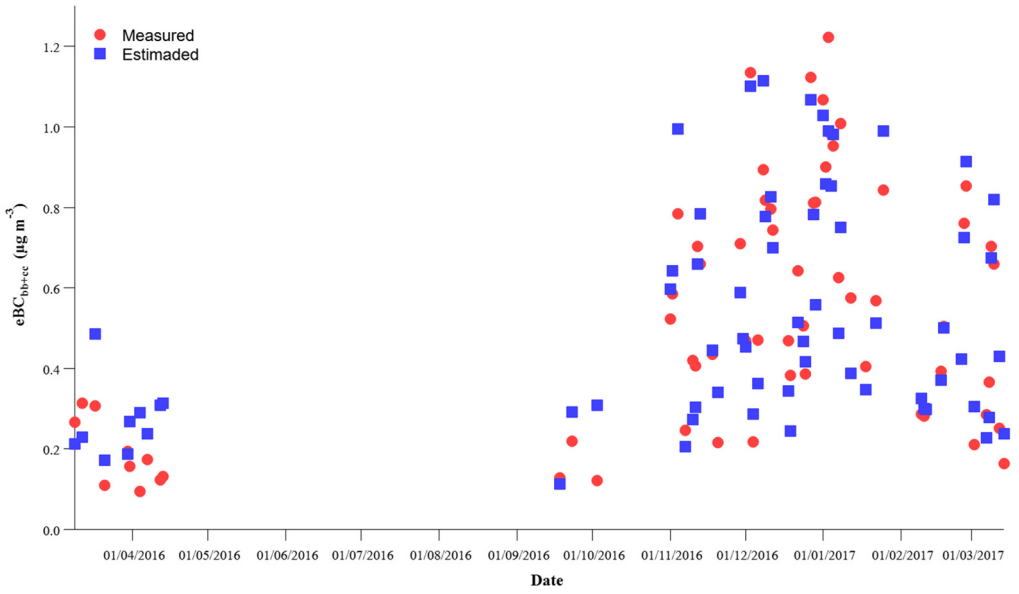

Figure S7.6. Time series of eBC_{bb+cc} concentration estimated by the model and eBC_{bb+cc} measured at León along sampling campaign.

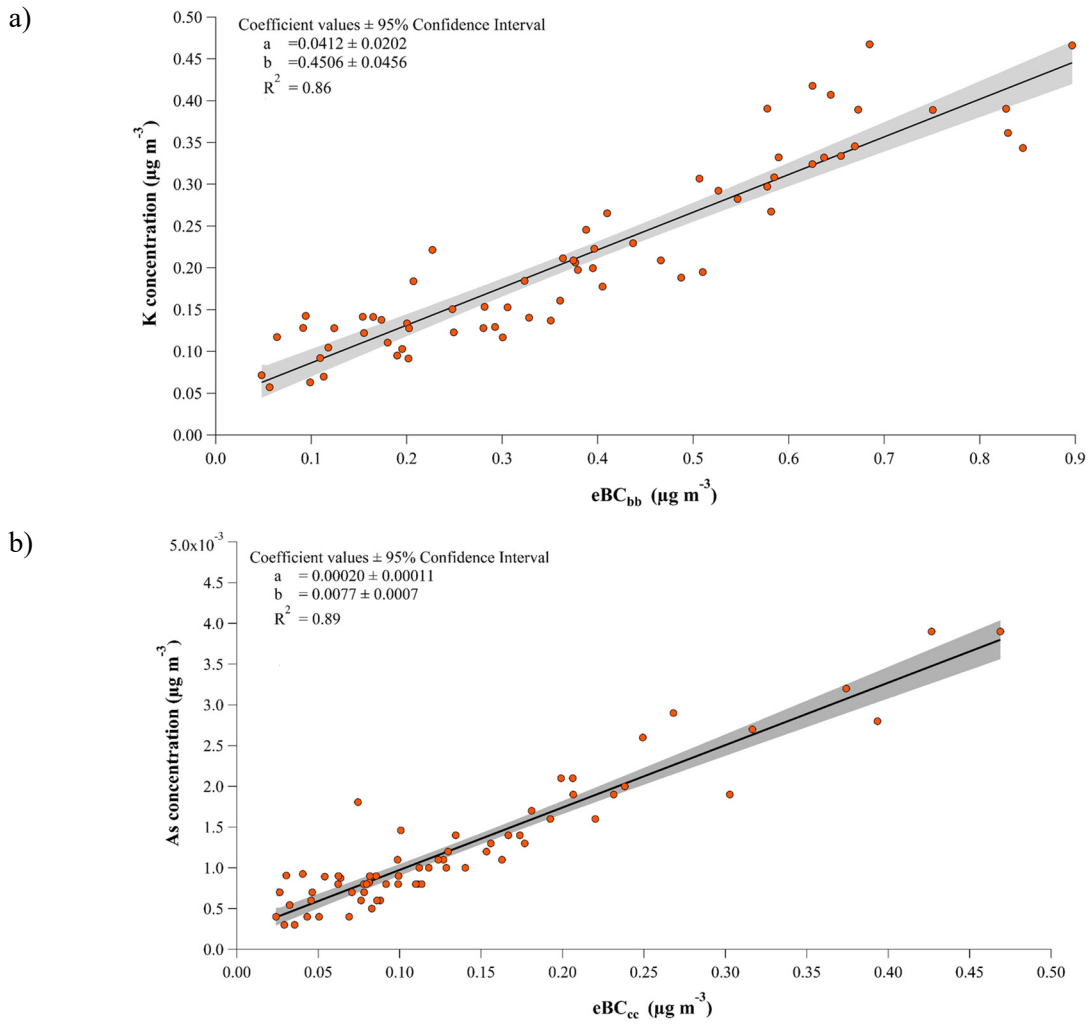

Figure S7.7. Regression between (a) eBC_{bb}-K and (b) eBC_{cc} –As in the cold period.

S.7.2. TABLES

Table S7.1. Parameters $f(\lambda_w)$ or the compensation of the "load effect" of each αw as a function of the cold or warm period of the year.

α_w (nm)	370	470	520	590	660	880	950
$f(\alpha_w)$ Cold period	1.155	1.137	1.128	1.116	1.103	1.064	1.051
$f(\alpha_w)$ Warm period	1.141	1.132	1.127	1.120	1.114	1.093	1.086

Table S7.2. Comparison of eBC concentrations measured in this study and values reported in the literature.

Station	Location	Environment type	Period	eBC ($\mu g\ m^{-3}$)	Reference
León (Spain)	42°36′N, 05°35′W, 838 m	Urban background	Jan.2016-Mar. 2017	0.9±0.9	Present study
Valparaiso (Chile)	33º01′S, 71º37′W, 80 m	Urban	Dec.2014-Jan. 2015	0.8-0.9	(Marín et al., 2017)
Pantnagar (India)	29°00′N, 79°30′W, 231 m	Urban background	2009-2012	5.5±4.7	(Joshi et al., 2016)
Rome (Italy)	44°25'N,12°12'E, 20 m	Urban background	May-Jun. 2012	1.7±1.2	(Costabile et al., 2015)
Beijing (China)	40°03′N, 116°25′E, 535 m	Urban-rural fringe	2014	4.4±3.7	(Ji et al., 2017)
New York (USA)	40°48'N, 73°54''W, 20 m	Urban	2003-2011	1.4-2	(Rattigan et al., 2013)
Ostrava (Czech Republic)	49°47′N, 18°13′E, 230 m	Urban	2012-2014	3.5±4.1	(Kucbel et al., 2017)
London (UK)	51°30′N, 0°07′E, 25m	Urban	Jan.-Aug. 2012	1.3±1.1	(Liu et al., 2014)
Amsterdam (Netherlands)	52°23′N, 4°54′E, 0 m	Urban background	Jan.-Jul.2013	0.8±0.5	(Klompmaker et al., 2015)
Rotterdam (Netherlands)	51°55′N 4°28′E, 0 m	Urban background		1.4±0.6	
Montreal (Canada)	45°30′N, 73°35′O, 216 m	Urban	Jun.- Jul. 2012	1.1±1.3	(Weichenthal et al., 2014)

Table S7.3. Mean annual ABL heights at different hours of the day and by season (Wi: winter; Sp: spring; Su: summer; Au: autumn; An: annual). Pearson correlations between eBC and ABL heights.

	Mean ABL altitude (m)					eBC concentration (µg m-3)					Pearson correlations				
ABL time (UTC)	Wi	Sp	Su	Au	An	Wi	Sp	Su	Au	An	Wi	Sp	Su	Au	An
0000	192	131	84	102	127	0.66	0.34	0.57	0.56	0.53	-0.49	-0.31	-0.26	-0.42	-0.29
0300	202	121	56	103	120	0.57	0.49	0.71	0.62	0.60	-0.49	-0.25	-0.25	-0.37	-0.25
0600	183	216	81	84	140	1.45	0.85	0.87	1.40	1.14	-0.48	0.03	-0.19	-0.46	-0.20
0900	424	695	573	229	480	1.27	0.54	0.55	1.09	0.85	-0.66	-0.32	-0.41	-0.65	-0.70
1200	923	1213	1287	675	1024	0.80	0.43	0.39	0.77	0.59	-0.52	-0.21	0.24	-0.59	-0.58
1500	958	1458	1915	741	1268	1.19	0.48	0.41	1.41	0.86	-0.44	0.06	0.29	-0.57	-0.51
1800	262	424	504	101	322	2.10	0.82	0.85	2.03	1.43	-0.56	-0.34	-0.43	-0.51	-0.51
2100	227	151	154	103	158	1.15	0.54	0.62	0.91	0.80	-0.50	-0.21	-0.17	-0.52	-0.35

Bold font indicates that the correlation is significant at 95% level.

Table S7.4. Pearson correlations between eBC, eBC_{ff}, eBC_{bb+cc} concentrations, AAE and meteorological parameters (temperature, relative humidity and wind speed) for monthly and annual analysis.

Parameter	RH (%)				Wind speed (m s^{-1})				T (°C)			
	AAE	eBC_{bb+c}	eBC_{ff}	eBC	AAE	eBC_{bb+}	eBC_{ff}	eBC	AAE	eBC_{bb+cc}	eBC_{ff}	eBC
Jan. 16	0.052	**0.231**	**0.178**	**0.216**	-0.075	**-0.413**	**-0.295**	**-0.367**	**-0.231**	-0.067	**0.086**	0.048
Feb. 16	**0.125**	0.057	-0.020	0.010	**-0.137**	**-0.421**	**-0.313**	**-0.411**	**-0.261**	**-0.171**	0.047	-0.039
Mar. 16	0.056	0.010	-0.033	-0.023	-0.073	**-0.414**	**-0.289**	**-0.392**	**-0.211**	**-0.165**	-0.007	-0.068
Apr. 16	**-0.089**	**0.109**	**0.123**	**0.135**	-0.018	**-0.357**	**-0.207**	**-0.274**	**-0.152**	**-0.175**	0.015	-0.036
May. 16	**-0.276**	**-0.096**	0.035	0.007	**0.089**	**-0.278**	**-0.211**	**-0.253**	**0.094**	**0.090**	**0.090**	**0.101**
Jun. 16	-0.030	**0.094**	0.045	**0.083**	-0.014	**-0.144**	**-0.142**	**-0.188**	0.009	0.026	0.046	0.052
Jul. 16	**0.080**	**0.126**	**0.164**	**0.194**	-0.047	**-0.148**	**-0.213**	**-0.245**	**-0.116**	**-0.081**	-0.069	**-0.093**
Aug. 16	**0.103**	**0.078**	**0.254**	**0.237**	**-0.139**	**-0.219**	**-0.324**	**-0.328**	**-0.156**	-0.015	**-0.145**	**-0.128**
Sep. 16	0.063	**-0.103**	**-0.106**	**-0.123**	**-0.120**	**-0.158**	**-0.220**	**-0.237**	-0.033	**0.164**	**0.131**	**0.166**
Oct. 16	-0.019	-0.064	**-0.150**	**-0.145**	0.044	**-0.300**	**-0.221**	**-0.261**	-0.042	-0.005	**0.155**	**0.134**
Nov. 16	**0.233**	**0.108**	**-0.079**	-0.021	**-0.288**	**-0.398**	**-0.213**	**-0.321**	**-0.319**	0.008	**0.259**	**0.208**
Dec. 16	**0.103**	-0.043	**-0.189**	**-0.161**	**-0.301**	**-0.346**	**-0.130**	**-0.244**	**-0.417**	**-0.160**	**0.175**	0.066
Jan. 17	**0.128**	**0.255**	**0.150**	**0.224**	**-0.293**	**-0.440**	**-0.205**	**-0.346**	**-0.409**	**-0.182**	**0.115**	0.009
Feb. 17	0.036	**-0.120**	**-0.138**	**-0.153**	**-0.088**	**-0.450**	**-0.228**	**-0.359**	**-0.130**	-0.003	**0.176**	**0.130**
Mar. 17	-0.018	**-0.119**	**-0.118**	**-0.147**	**-0.350**	**-0.459**	**-0.206**	**-0.382**	**-0.114**	0.065	**0.225**	**0.198**
Annual	**-0.08**	**0.15**	**0.07**	**0.11**	**-0.10**	**-0.31**	**-0.24**	**-0.31**	**-0.22**	**-0.27**	**-0.04**	**-0.14**

Bold font indicates that the correlation is significant at 95% level

Table S7.5. PM_{10} and BC/PM_{10}, OC/EC, EC/BC and BC/OC ratios in León by season for January 2016–March 2017.

Season	PM_{10} ($\mu g\ m^{-3}$)	eBC/PM_{10}	OC/EC	EC/eBC	eBC/OC
Cold period	17.0±8.7	0.071±0.036	3.08±1.12	0.86±0.45	0.45±0.17
Warm period	12.6±8.3	0.050±0.029	3.62±1.50	1.09±0.31	0.31±013
Annual	15.6±8.6	0.061±0.034	3.35±1.35	0.98±0.38	0.38±0.17

S.7.3. METHOD USING THE MEDIAN VALUE TO ESTIMATE THE COAL COMBUSTION CONTRIBUTION

The days of the cold period (from 15 September to 14 April) with higher As concentration than the median (0.00082 $\mu g\ m^{-3}$) were selected to develop the model. Similar values were obtained than using the method presented in the manuscript, showing the robustness of the model.

The multilinear regression analysis only used these days (N=80) to estimate the model parameters. The estimated eBC_{bb+cc} concentration for biomass burning and coal combustion is expressed as:

$$eBC_{bb+cc}(\mu g\ m^{-3}) = \overbrace{(0.147 \pm 0.047)}^{\approx zero} + \overbrace{(2.02 \pm 0.18) \times C_K}^{eBC_{bb}} + \overbrace{(118 \pm 26) \times C_{As}}^{eBC_{cc}} \qquad Eq.\ S7.1$$

with a model standard error of 0.11 $\mu g\ m^{-3}$, and correlation coefficient of r=0.90.

The application of the model (Eq. S7.1) allowed the eBC_{cc} and eBC_{bb} to be estimated separately for the cold period. For the days included in the model, the contributions to the eBC_{bb+cc} were broken down into 75% from biomass burning and 25% from coal combustion. After the extraction of eBC_{cc} from eBC_{bb+cc} very strong correlations between eBC_{bb} and K (biomass burning tracer) (r=0.91) and eBC_{cc} and As (coal tracer) (r=0.88) were registered.

The concentrations of EC, segregated by source after application of the model throughout the sampling period, are shown in Table S7.6 (equivalent to Table 7.2).

Table S7.6. Monthly mean values (± standard deviation) calculated for eBC_{ff}, eBC_{bb}, eBC_{cc}, percentage of biomass burning (BB(%)) and coal combustion (CC(%)) from eBC after the application of model.

Year	Season	Month	eBC_{ff} ($\mu g\ m^{-3}$)	eBC_{bb} ($\mu g\ m^{-3}$)	eBC_{cc} ($\mu g\ m^{-3}$)	BB (%)	CC (%)
2016	Winter	January	0.69±0.30	0.31±0.14	0.11±0.05	32±9	11±3
	Winter	February	0.62±0.29	0.31±0.20	0.11±0.07	32±7	11±3
	Spring	March	0.50±0.20	0.20±0.12	0.08±0.04	26±9	11±3
	Spring	April	0.35±0.11	0.12±0.04	0.05±0.02	26±8	12±4
	Spring	May	0.43±0.11	0.13±0.04	-	23±6	-
	Summer	June	0.41±0.14	0.12±0.11	-	22±8	-
	Summer	July	0.41±0.14	0.12±0.10	-	22±8	-
	Summer	August	0.48±0.16	0.12±0.05	-	20±3	-
	Autumn	September	0.58±0.21	0.21±0.15	0.05±0.01	25±8	4±4
	Autumn	October	0.73±0.24	0.23±0.11	0.05±0.02	23±7	6±1
	Autumn	November	0.72±0.34	0.32±0.17	0.09±0.04	29±8	9±2
	Winter	December	1.02±0.36	0.47±0.24	0.17±0.09	28±8	10±3
2017	Winter	January	0.83±0.54	0.55±0.29	0.17±0.11	37±12	11±4
	Winter	February	0.50±0.19	0.28±0.17	0.07±0.04	33±10	9±2
	Spring	March	0.46±0.18	0.31±0.21	0.07±0.04	37±13	8±3

References of Supplementary Material

Costabile, F., Angelini, F., Barnaba, F., Gobbi, G.P., 2015. Partitioning of Black Carbon between ultrafine and fine particle modes in an urban airport vs. urban background environment. Atmos. Environ. 102, 136–144. doi:10.1016/j.atmosenv.2014.11.064

Ji, D., Li, L., Pang, B., Xue, P., Wang, L., Wu, Y., Zhang, H., Wang, Y., 2017. Characterization of black carbon in an urban-rural fringe area of Beijing. Environ. Pollut. 223, 1–11. doi:10.1016/j.envpol.2017.01.055

Joshi, H., Naja, M., Singh, K.P., Kumar, R., Bhardwaj, P., Babu, S.S., Satheesh, S.K., Moorthy, K.K., Chandola, H.C., 2016. Investigations of aerosol black carbon from a semi-urban site in the Indo-Gangetic Plain region. Atmos. Environ. 125, 346–359. doi:10.1016/j.atmosenv.2015.04.007

Klompmaker, J.O., Montagne, D.R., Meliefste, K., Hoek, G., Brunekreef, B., 2015. Spatial variation of ultrafine particles and black carbon in two cities: Results from a short-term measurement campaign. Sci. Total Environ. 508, 266–275. doi:10.1016/j.scitotenv.2014.11.088

Kucbel, M., Corsaro, A., Švédová, B., Raclavská, H., Raclavský, K., Juchelková, D., 2017. Temporal and seasonal variations of black carbon in a highly polluted European city: Apportionment of potential sources and the effect of meteorological conditions. J. Environ. Manage. 203, 1178–1189. doi:10.1016/j.jenvman.2017.05.038

Liu, D., Allan, J.D., Young, D.E., Coe, H., Beddows, D., Fleming, Z.L., Flynn, M.J., Gallagher, M.W., Harrison, R.M., Lee, J., Prevot, A.S.H., Taylor, J.W., Yin, J., Williams, P.I., Zotter, P., 2014. Size distribution, mixing state and source apportionment of black carbon aerosol in London during winter time. Atmos. Chem. Phys. 14, 10061–10084. doi:10.5194/acp-14-10061-2014

Marín, J.C., Raga, G.B., Arévalo, J., Baumgardner, D., Córdova, A.M., Pozo, D., Calvo, A., Castro, A., Fraile, R., Sorribas, M., 2017. Properties of particulate pollution in the port city of Valparaiso, Chile. Atmos. Environ. 171, 301–316. doi:10.1016/j.atmosenv.2017.09.044

Rattigan, O. V, Civerolo, K., Doraiswamy, P., Felton, H.D., Hopke, P.K., 2013. Long term black carbon measurements at two urban locations in New York. Aerosol Air Qual. Res. 13, 1181–1196. doi:10.4209/aaqr.2013.02.0060

Weichenthal, S., Farrell, W., Goldberg, M., Joseph, L., Hatzopoulou, M., 2014. Characterizing the impact of traffic and the built environment on near-road ultrafine particle and black carbon concentrations. Environ. Res. 132, 305–310. doi:10.1016/j.envres.2014.04.007

CHAPTER 8. Aethalometer measurements in a road tunnel

Full title: Aethalometer measurements in a road tunnel: A step forward in the characterization of black carbon emissions from traffic

Published in: Science of The Total Environment, 2020, 703, 135483.
DOI: 10.1016/j.scitotenv.2019.135483

8.1. INTRODUCTION

Nowadays, airborne particulate matter with diameters below 10 µm (PM_{10}) has major effects on climatic change while airborne particulate matter with diameters below 2.5 µm ($PM_{2.5}$) poses a major risk to human health (WHO, 2013). In Europe, more than 90% of urban dwellers are exposed to $PM_{2.5}$ levels that exceed the reference value set by the WHO (EEA, 2013).

Traffic exhaust emissions of motorised vehicles are one of the main sources of $PM_{2.5}$ in many urban areas (Bycenkiene et al., 2014; Sun et al., 2013). Besides, traffic non-exhaust emissions, such as particles from tyre wear, brakes, road surface abrasion and dust resuspension, are one of the principal contributors to airborne particulate matter, especially in semi-enclosed places like tunnels (Querol et al., 2004; Thorpe and Harrison, 2008). While strict policies have led to significant reductions in exhaust emissions, currently non-exhaust emissions from road vehicles, are unabated (Padoan and Amato, 2018; Thorpe and Harrison, 2008). Data from European cities showed that exhaust and non-exhaust sources contribute, at least, equal amounts to total traffic-related emissions (Amato et al., 2016, 2014; Denier van der Gon et al., 2013). One of main

constituents of $PM_{2.5}$ is black carbon (BC). It is emitted from incomplete combustion of fossil fuel or biomass and it is a carbonaceous material that is formed primarily in flames and directly emitted to the atmosphere. BC presents particular physical properties: it strongly absorbs visible light and is refractory with a vaporization temperature of around 3700 °C (Bond et al., 2013). BC pollution has been linked to respiratory infections (such as adverse effects on lung function and increased cancer risks) and cardiovascular diseases, as well as to increased morbidity and mortality among different age groups (Silverman et al., 2012; Suglia et al., 2008). Globally, BC is considered a major short-lived climate forcer through direct radiative forcing and cloud, sea-ice and snow effects. The global mean radiative forcing caused by BC was estimated to be from 0.4 to 1.2 W m^{-2}, becoming the second man-made strongest contributor after CO_2 (Bond et al., 2013; Ramanathan and Carmichael, 2008). Hence, the study of BC concentration is crucial due to its effects on multiple essential policy objectives (e.g., climate, energy, air quality, public health, etc.) (EEA, 2016; Kinney, 2008; Tong et al., 2016).

The aethalometer (Hansen et al., 1984) has become extensively used over the last years, and especially the seven wavelength (from near-ultraviolet to near-infrared) model, to measure the aerosol light absorption. The use of the mass absorption cross-section, proposed by the manufacture, allows the calculation of the equivalent black carbon (eBC) concentration, defined as the light absorbing constituent considered BC (Sandradewi et al., 2008b).

Aiming at determining vehicle emissions, studies should be carried out in areas where traffic is the main pollution source. In the last years, different methods have been used to analyse vehicle emissions. The chassis dynamometer methods enable to test vehicles under controlled laboratory conditions. This procedure ensures a high repeatability of results, but is very costly (Alves et al., 2015a; Traver et al., 2002). In addition, it does not allow reproducing the real-world conditions (Franco et al., 2013). However, studies carried out in tunnels describe the real-world emission behaviour of on-road vehicles, capturing both exhaust and non-exhaust emissions (Alves et al., 2016b, 2016a; Handler et al., 2008; Kristensson et al., 2004; McGaughey et al., 2004; Pio et al., 2013). Hitherto, most of the studies in tunnels focused on PM_{10}, $PM_{2.5}$ and emissions factors of gaseous pollutants, but current information on black carbon concentration in tunnels is still scarce.

In this paper, black carbon emissions are analysed from a sampling campaign carried out in an urban roadway tunnel in Braga (Portugal). Furthermore, correlations between eBC and gaseous emissions and number of vehicles are discussed. This study, together with the ones already published about this campaign (Alves et al., 2015b, 2016b), provide a complete characterization of the particulate material emitted by vehicles. Aethalometer measurements in road tunnels can supply a valuable information regarding Absorption Ångström Exponent (AAE) and black carbon emission factors for application in models and for updating emission inventories.

8.2. EXPERIMENTAL

8.2.1. SAMPLING SITE AND MEASUREMENTS

The study site is a road tunnel in Braga (Portugal), a city located in the west of the Iberian Peninsula (41°33′N, 08°25′W and 215 m above sea level). Braga is the third most populated city in Portugal, with about 200,000 residents in 2011 and a population density of 1000 inhabitants km^{-2}. The tunnel connects two main avenues to Liberdade Avenue in the centre of the city, and habitually has large traffic intensity (~ 15,000 vehicles per day) (Alves et al., 2015a,b). Sampling of BC and gaseous pollutants (CO, CO_2 and NO_x) has been carried out continuously for 7 days from 1 to 8 February 2013 (Friday to Thursday), at two sampling points, one outside (urban background site) and other inside the tunnel (Figure 8.1). Except for the aethalometer, which was installed only in the tunnel, the other sampling devices were mounted at both locations.

The tunnel consists of a single parallelepiped shaped reinforced concrete bore that is 1040 m long, carrying two lanes in most of its extension of one-way traffic. Traffic volume by vehicle type through the tunnel was manually counted at 15-minute intervals throughout each of the sampling days (8:00–20:00 h, local time). Traffic count data was grouped as follows: light vehicles (a), trucks (b), heavy diesel vehicles (c) and total number of vehicles (d). The ventilation system (smoke extraction fans) was cut off during the sampling campaign.

An automatic CO and CO_2 infrared monitor from Gray Wolf (WolfSense IQ-610) was installed inside the tunnel after calibration and intercomparison with an air quality meter from TSI, model 7525, which was used outdoors. The continuous monitoring of NO and NO_2 was done by using chemiluminescence analysers from Environment S.A., France (model 31M). The campaign included parallel high-volume PM_{10} sampling on quartz filters, from 8:30–12:00 h, 12:00–16:00 h and 16:00–18:00 h, in the tunnel and at the urban background station. The filters were then analysed for organic and elemental carbon (OC and EC) by a thermal-optical system (Pio et al., 2011). A more detailed description of the sampling campaign can be found in Alves et al. (2015b).

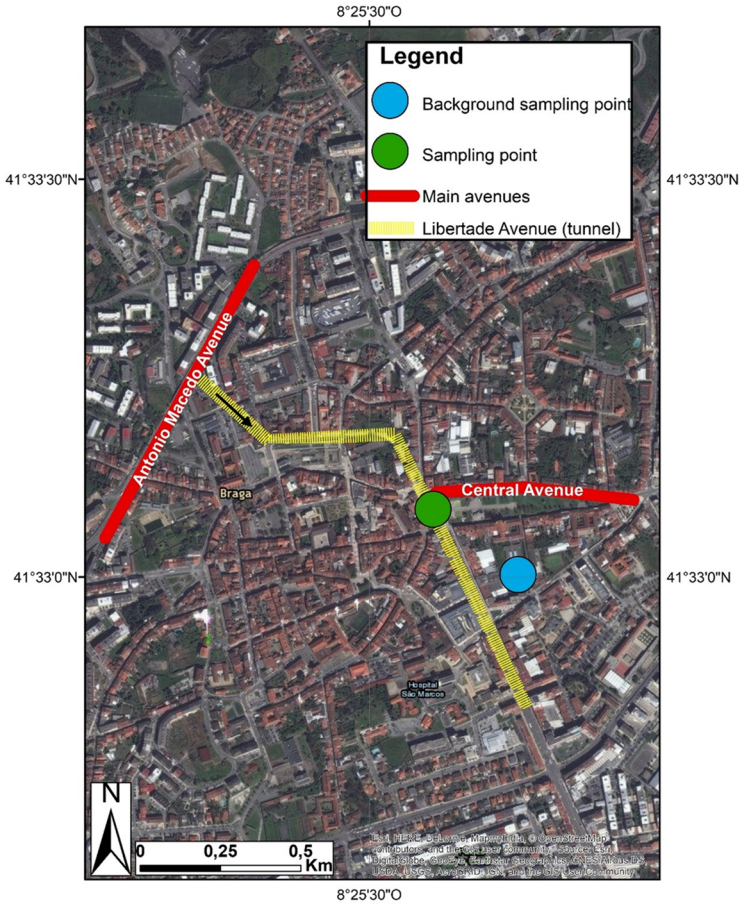

Figure 8.1. Geographic location of the sampling site in Braga (Portugal). Yellow fractional line indicates the tunnel, the arrow the traffic direction, the blue dot represents the background sampling point and the green dot the sampling point inside the tunnel. The main avenues of Braga were represented with continuous red lines.

8.2.2. BLACK CARBON DATA

Aerosol light-absorption at seven wavelengths (370, 470, 520, 590, 660, 880 and 950 nm) was continuously measured during the sampling campaign with an aethalometer Model AE-31 (Magee Scientific, USA). The instrument operated at a flow rate between 2.3 and 3.2 STP L min^{-1} with a time resolution of 5 minutes. The aethalometer uses a differential-radiometric optical transmission technique to determine the eBC aerosol particles suspended in the sampled air (Hansen et al., 1984). It is equipped with a quartz filter tape (Pallflex, type Q250F) to collect the aerosol particles. The concentration of eBC was determined by measuring the change in the transmittance through the filter. A detailed description of the instrument can be found in Hansen et al. (1984), Weingartner et al. (2003) and Virkkula et al. (2007). Although the measurements were made every 5-minutes, the data were averaged at a resolution of 1 h to reduce the

uncertainties derived from instrumental noise, flow rate, filter spot area and detector response (Corrigan et al., 2006).

The contribution from fossil fuel (eBC_{ff}) and biomass burning (eBC_{bb}) was estimated through the aethalometer model (Sandradewi et al., 2008a). For this purpose, the absorption Ångström exponent between 470 and 950 nm ($AAE_{470-950}$) was estimated (Becerril-Valle et al., 2017; Harrison et al., 2013; Sandradewi et al., 2008a). The wavelength at 470 nm has been used rather than the 370 nm one, because results using the latter could be distorted by the presence of secondary organic aerosol (Zotter et al., 2017). The limits used for the aethalometer model in this case are $AAE_{ff} = 0.97$ (corresponding to AAE values during rush-hour traffic) and $AAE_{bb} = 1.68$ (Zotter et al., 2017).

The eBC data recorded during the sampling period were corrected following WMO/GAW Aerosol Measurement Procedures, Guidelines and Recommendations (WMO, 2016). Aethalometer data were also corrected for loading effect by using the Weingartner et al. (2003) model with the winter campaign parameters proposed by Sandradewi et al. (2008b).

8.2.3. STATISTICAL ANALYSES

A univariate analysis (i.e. mean, median, minimum, maximum, quartiles and standard deviation) and a bivariate correlation (Pearson correlations with 95% confidence intervals around the point estimates) were performed to characterize eBC in the tunnel. Pearson correlations were computed to determine the relationships between eBC parameters, gaseous emission factors (CO, CO_2, NOx) and number of vehicles.

8.2.4. EMISSION FACTORS

Emission factors (EFs) were estimated from measurements of eBC, CO_2 and CO concentrations using the following equation (McGaughey et al., 2004):

$$EF_{eBC} = \frac{\Delta[eBC]}{\Delta[CO_2] + \Delta[CO]} \times \omega_c \qquad \textit{Eq. 8.1}$$

where EF is the emission factor defined as mass of pollutant emitted per kilogram of fuel burned; $\Delta[eBC]$ is the black carbon concentration inside the tunnel subtracted from the background levels

(μg m^{-3}); $\Delta[CO_2]$ and $\Delta[CO]$ are the background-subtracted concentrations of CO_2 and CO given in μgC m^{-3} (i.e., when converting concentrations of CO_2 and CO from mol fractions to mass units, a molecular weight of 12 g mol^{-1}, rather than 44 g mol^{-1} and 28 g mol^{-1} for CO_2 and CO, respectively, was used), and ω_c is the carbon weight fraction of the fuel, 0.87 for diesel and gasoline (EPA, 2015). Organic compounds can be ignored in the denominator because their contribution to total carbon concentrations in the tunnels is negligible compared to those made by CO_2 and CO (Kirchstetter et al., 1999; McGaughey et al., 2004). It should be noted that, since no aethalometer was available outside the tunnel, the eBC concentrations in the urban background atmosphere were estimated from a ratio EC_{in}/EC_{out} of 16.3 (Alves et al., 2015b) obtained in the same sampling campaign.

These emission factors are commonly normalised to vehicle distance travelled. For this, a typical fuel consumption per unit of distance travelled by vehicle class (mass emitted per kilometre) is assumed. A composite fuel consumption value (g km^{-1}) was estimated after weighting typical consumption values by the percentage of vehicles in each category obtained through the traffic counts in the tunnel. Fuel consumptions of 4.84 L fuel / 100 km for the diesel fleet and 8.78 L fuel / 100 km for gasoline vehicles were taken from Brimblecombe et al. (2015).

8.3. RESULTS AND DISCUSSION

The eBC results complement those compiled in previous publications (Alves et al., 2015b, 2016b) from the same sampling campaign, which provide information on gaseous pollutants, and carbonaceous and elemental composition of size-segregated particles.

8.3.1. EQUIVALENT BLACK CARBON VALUES

Based on traffic counts, around 56,000 vehicles circulated in the tunnel during daytime hours (8:00–20:00 h, local time). The total number of vehicles for all week was estimated to be 105,000. The percentage of heavy-duty traffic in the tunnel was very low. In fact, 96% of the circulating fleet was composed of passenger cars and light-duty vehicles. Motorbikes represented 1% of the fleet, while the remaining 3% were composed of heavy-duty vehicles, from which 30% was

compressed natural gas buses (Alves et al., 2016b). The daily mean of total vehicles during weekdays was around 10,000 vehicles, while during weekend a decreased in the traffic density of around 40% was registered (Table 8.1). The traffic of light-duty vehicles in the tunnel can be considered representative of the fleet in Portugal. At the time of the campaign, and according to data provided by the Portuguese Institute of Statistics, the percentages of passenger cars for different European emission norms were as follows: 15.0 (Euro 5), 22.8 (Euro 4), 18.4 (Euro 3), 22.9 (Euro 2), 13.2 (Euro 1) and 7.0 (pre-Euro).

In the tunnel, the daily mean eBC mass concentration was 21±10 μg m^{-3} (Figure 8.2), close to the limit proposed by the World Health Organization (WHO) for daily $PM_{2.5}$ concentrations (25 μg m^{-3}). The eBC concentrations reached a maximum value of 49.0 μg m^{-3} (Tuesday, 05 February 2013 at 1800 UTC) lower than that reported by Miguel et al. (1998) in Oakland, and a minimum of 0.14 μg m^{-3} (Table 8.1). Regarding eBC sources, eBC_{ff} was 20.7±10.3 μg m^{-3}, representing 98% of total eBC, while eBC_{bb} was 0.4±0.8 μg m^{-3}, showing a residual penetration of eBC into the tunnel from residential biomass combustion emissions in the city. Thus, exhaust emissions from traffic are clearly the main BC source in the tunnel. Hourly mean eBC/OC and EC/eBC ratios of 0.60 and 1.38 were obtained, respectively (Table 8.2). The PM_{10}/EC ratio (4.40) presented a similar value than those reported in other studies (Handler et al., 2008). The maximum values occurred between 1400 and 1900 UTC, during the rush hours, when traffic density is greater because of commuting from work. However, during the weekend, a peak was observed between 0900 and 1200 UTC, probably due to leisure and shopping activities (Figure 8.3). Based on Mann-Whitney U-test, no statistically significant differences between eBC concentration during workdays and weekend, were observed ($p>0.05$).

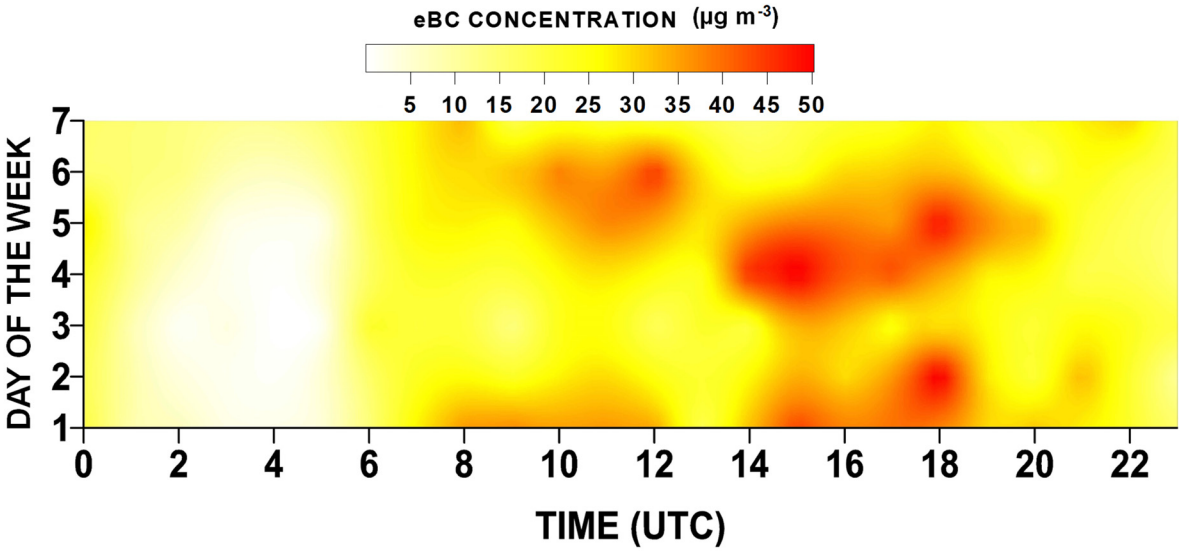

Figure 8.2. Evolution of the eBC concentration (μg m^{-3}) throughout the week. The first day of the week is Monday.

Table 8.1. Daily eBC (μg m^{-3}), $AAE_{470\text{-}950}$ (mean, minimum and maximum), number of vehicles registered and percentage of data available during the sampling campaign.

Date	eBC			$AAE_{470\text{-}950}$			Sum of veh.	Veh. h^{-1}
	Mean	Max.	Min.	Mean	Max.	Min.		Mean
01 February	20±12	45.0	1.4	0.95±0.09	1.22	0.84	7319	477
02 February	23±8	41.7	12.6	0.92±0.07	1.09	0.83	6705	339
03 February	20±4	27.8	13.4	1.00±0.06	1.24	0.92	3738	196
04 February	23±12	40.0	2.0	1.00±0.13	1.27	0.84	9376	426
05 February	24±9	49.0	9.7	0.95±0.04	1.03	0.87	8865	454
06 February	17±8	30.1	0.14	0.98±0.13	1.47	0.81	10,119	426
07 February	19±9	30.7	1.9	1.00±0.10	1.26	0.89	9844	447
Whole campaign	21±10	49.0	0.14	0.97±0.10	1.47	0.81	55,966	395

During weekdays, after rapid traffic intensification at 0700 UTC, eBC values were consistently higher than 25 μg m^{-3}. During nighttime (0000 to 0700 UTC), values were between 0 and 15 μg m^{-3} along all the week. However, the daily maximum reached during weekdays (49.0 μg m^{-3}) was greater than that attained during the weekend (41.7 μg m^{-3}). On weekdays, between 0600 and 2300 UTC a mean eBC concentration of 25.0 μg m^{-3} was registered, while during the weekend a mean value of 22.6 μg m^{-3} was obtained (10% decrease compared with weekdays). A similar pattern was observed for other pollutants (CO or NO_x) in tunnels (Kristensson et al., 2004; Martins et al., 2006) or in ambient measurements like León (Spain), although with much lower eBC values (Blanco-Alegre et al., 2019), due to the dependence on traffic intensity and dispersion.

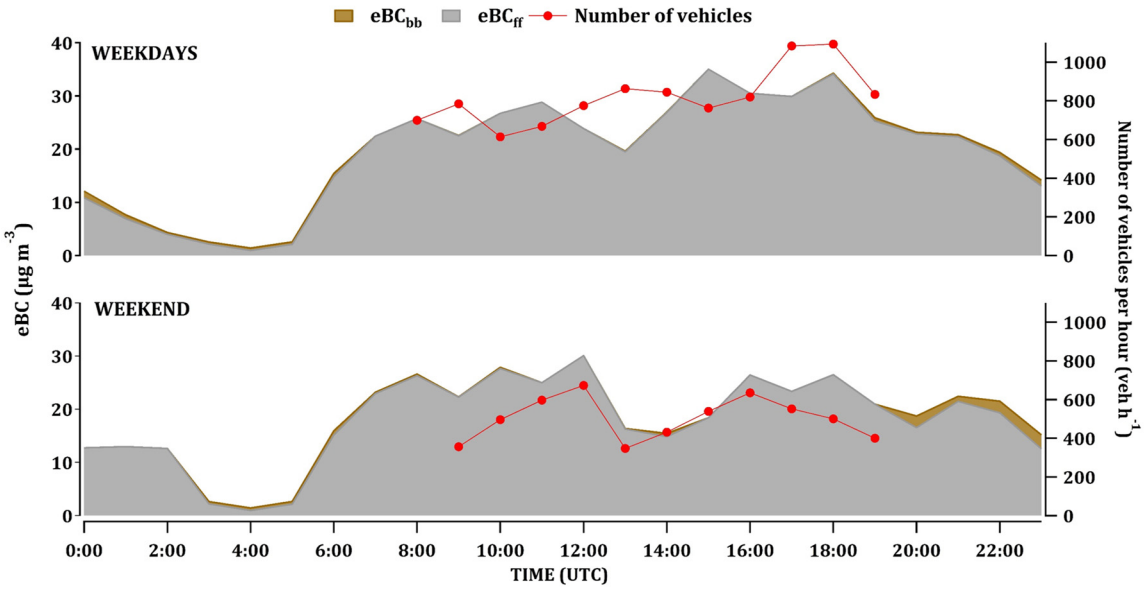

Figure 8.3. Evolution of eBC_{ff}, eBC_{bb} concentration (μg m^{-3}) and number of vehicles per hour throughout the day along weekdays and weekend.

Table 8.2. EC, OC, PM_{10} mean values in the tunnel and ratios between PM_{10}, carbonaceous constituents and percentage of data available during the sampling campaign.

Day	Weekday	EC	OC	PM_{10}	PM_{10}/EC	EC/eBC	eBC/OC	eBC/PM_{10}	Time (%)
		($\mu g\ m^{-3}$)							
01 February	Friday	21.9	32.4	143.9	6.56	1.08	0.62	0.14	44%
02 February	Saturday	28.0	28.2	127.3	4.54	1.20	0.83	0.18	42%
03 February	Sunday	26.2	31.2	94.6	3.61	1.33	0.63	0.21	44%
04 February	Monday	26.2	51.6	134.3	5.12	1.16	0.44	0.17	44%
05 February	Tuesday	34.5	37.6	150.9	4.37	1.44	0.64	0.16	43%
06 February	Wednesday	30.5	25.0	106.3	3.49	1.85	0.66	0.16	45%
07 February	Thursday	32.5	36.5	133.3	4.10	1.71	0.52	0.14	44%
Mean		29.1	35.3	128.1	4.40	1.38	0.60	0.16	44%

8.3.2. ABSORPTION ÅNGSTRÖM EXPONENT

During daytime hours (8:00–20:00 h, local time), a mean Absorption Ångström Exponent ($AAE_{470\text{-}950}$) value of 0.93±0.04 was obtained, ranging from a minimum of 0.81 and a maximum of 1.07 (Figure 8.4). At night, when the traffic density was low, a maximum AAE of 1.47 was recorded. Taking into account nocturnal data (without traffic counts), the mean value of $AAE_{470\text{-}950}$ was 0.97±0.10 (Table 8.1). The highest concentrations of eBC corresponded to $AAE_{470\text{-}950}$ values between 0.85 and 0.95. In general, values greater than 1.0 occurred at night-time, with eBC values less than 20 $\mu g\ m^{-3}$. These low values may be due to the low dispersion of pollutants inside the tunnel, a semi-enclosed place. AAE values estimated in the tunnel, where practically pure traffic emissions are overwhelming, are similar to those documented in other studies, such as Zotter et al. (2016), who obtained an AAE_{ff} of 0.9 from ^{14}C measurements of EC fractions on filter samples in Switzerland. Likewise, values in the tunnel are similar to those measured for outdoor traffic in León (Spain) (Blanco-Alegre et al., 2019) and in the range of values (0.6-0.9) reported for traffic events in New Delhi (India) (Garg et al., 2016). It has to be emphasised that because of the low AAE values obtained, the mineral dust interference in results is minimal (Petzold et al., 2013). Furthermore, $AAE_{370\text{-}950}$ and $AAE_{470\text{-}950}$ values did not present statistically significant differences each other (r^2=0.94; $p<0.001$). In Figure S8.1, BC has been plotted as a function of attenuation BC(ATN) for the wavelengths of 470 and 950 nm) with slope values close to 0, indicating no dependence on ATN (Drinovec et al., 2015). Figure S8.2 provides complementary information to Figure 8.4, showing the great variability of AAE values at night, when the traffic volume is much lower.

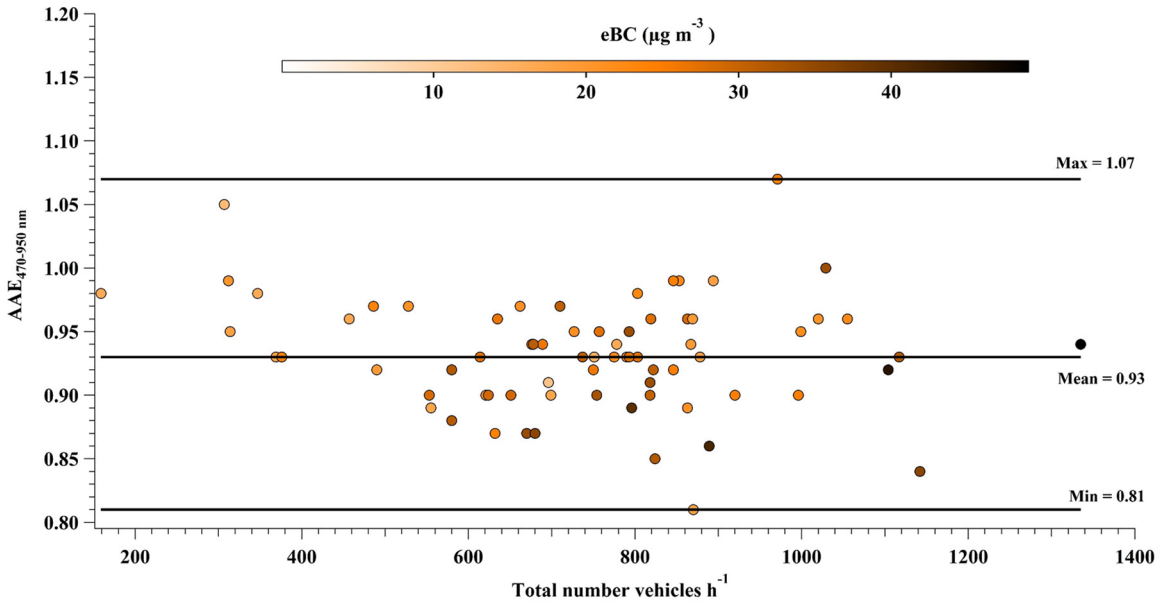

Figure 8.4. Absorption Ångström exponent ($AAE_{470\text{-}950}$) vs total vehicles per hour in the tunnel during daytime hours (8:00–20:00 h, local time).

8.3.3. VEHICLES-BC RELATIONSHIP

Figure 8.5 shows the linear regression between eBC concentration and the number of different types of vehicles inside the tunnel: light vehicles (a), trucks (b), heavy diesel vehicles (c) and total number of vehicles (d). Almost all the fleet in circulation (94%) consisted of light-duty vehicles. The contribution of light automobiles was higher than that of heavy diesel vehicles and trucks, thus, results of (a) and (d) were similar. There was a positive correlation, statistically significant, between eBC and light vehicles (r^2=0.23; $p<0.001$) and between eBC and the total number of vehicles (r^2=0.22; $p<0.001$). Thus, these results highlight the clear relationship between a high traffic density and eBC concentration. However, there were not statistically significant correlations between trucks and heavy diesel vehicles and eBC, probably due to their low number. Besides, another factor that can affect the dispersion of values can be the turbulence of the air promoted by the number of vehicles in circulation and high speeds (Kristensson et al., 2004).

In Figure 8.5, the slope was higher for trucks and heavy diesel vehicles (0.169 and 0.153 µg m^{-3} $vehicle^{-1}$, respectively) than for light vehicles (0.016 µg m^{-3} $vehicle^{-1}$). Thus, a small number of trucks and heavy diesel vehicles cause a high concentration of BC. From the intercept values, it can be seen that trucks and heavy vehicles contribute to a higher concentration of BC than light vehicles (23.42 vs. 13.68 µg m^{-3}).

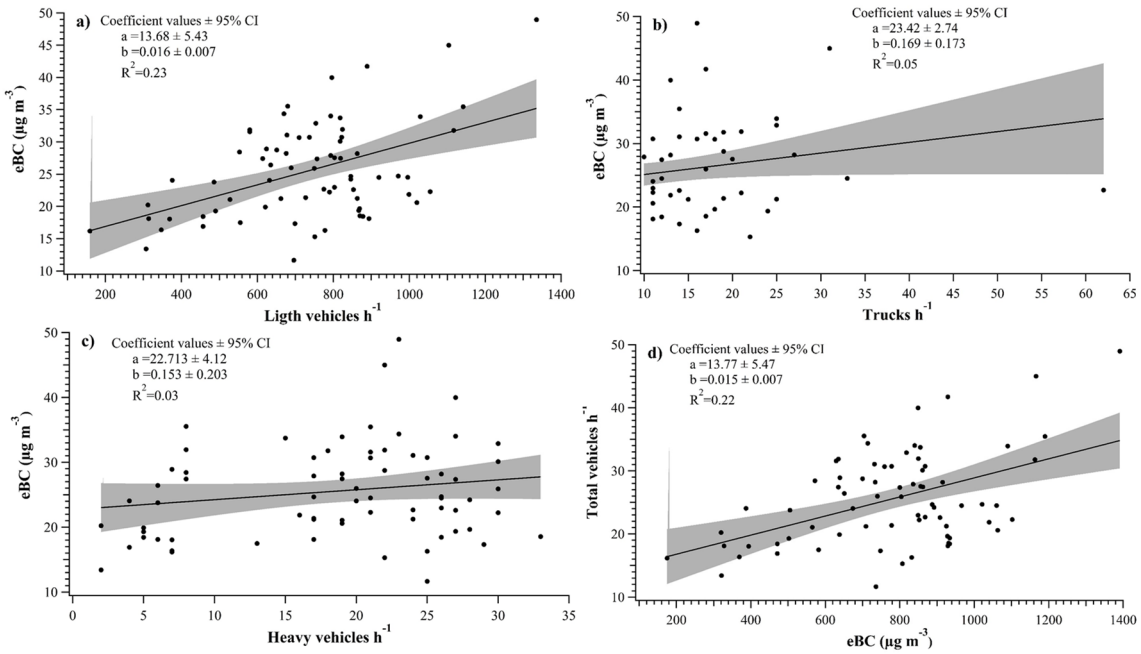

Figure 8.5. Linear regression and confidence bands (shaded) with 95% significance level between eBC (µg m^{-3}) and a) number of light vehicles per hour; b) number of trucks per hour; c) number of heavy diesel vehicles per hour; d) total number of vehicles per hour. The parameter *a* is the intercept and *b* is the slope.

8.3.4. GASEOUS EMISSIONS-BC RELATIONSHIP

Correlations between eBC concentrations and gaseous compounds are depicted in Figure 8.6. According to Alves et al. (2015b), the mean emission factors (g veh^{-1} km^{-1}) of these gaseous pollutants were: EF_{CO2} (212±18.2), EF_{CO} (4.09±2.52), EF_{NO} (0.61±0.14) and EF_{NO2} (0.29±0.07), similar to other studies in tunnels in Brazil (Martins et al., 2006) and Sweden (Kristensson et al., 2004). On average, the concentrations of CO, CO_2, NO and NO_2 were 20, 1.6, 53 and 43 higher in the tunnel than at the urban background, respectively (Alves et al., 2015b). Statistically significant positive correlations between eBC and all gaseous pollutants were found: CO (r^2=0.45; p<0.001), CO_2 (r^2=0.50; p<0.001), NO (r^2=0.40; p<0.001) and NO_2 (r^2=0.49; p<0.001). The sum of NOx, which reflects the primary emission more than the individual oxides, presented a significant positive correlation with eBC concentration (r^2=0.44; p<0.001). Similar CO-eBC results were obtained by Latha and Badarinath (2004) at an urban site. However, the eBC-NO_2 relationship does not follow the one described by Wang et al. (2012), who determined on-road diesel vehicle emission factors for nitrogen oxides and black carbon in two Chinese cities, observing that high eBC emission trucks are usually not high NOx emission sources and vice-versa. Their results suggested that, while a small number of high BC emission trucks contribute disproportionally to the total BC emissions, high NOx emission trucks do not dominate the total NOx emissions.

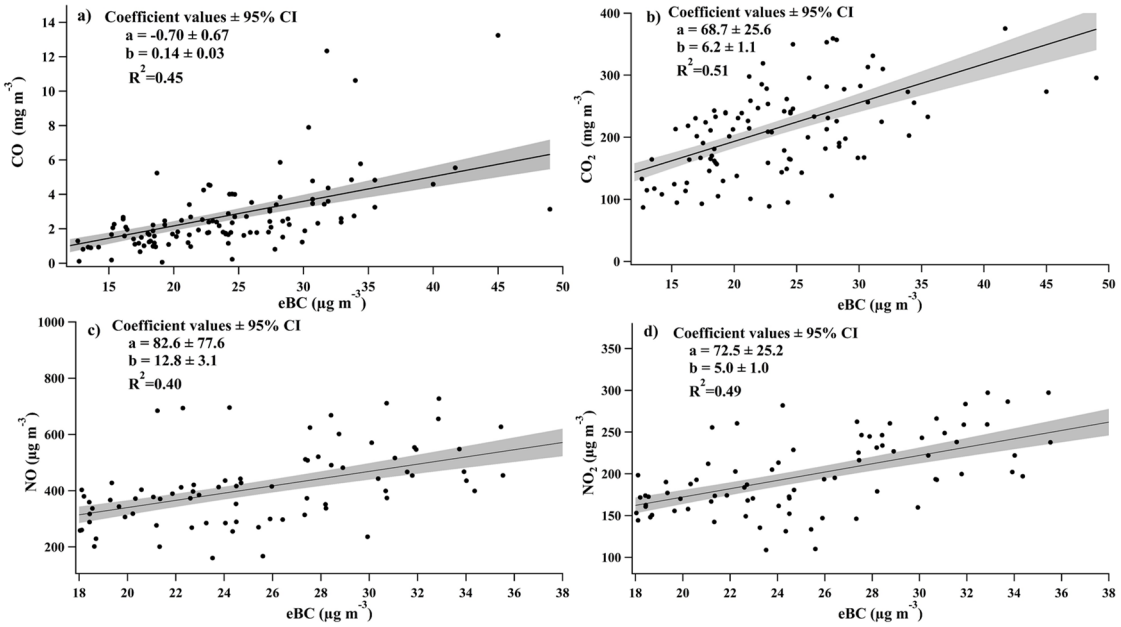

Figure 8.6. Linear regression and confidence bands (shaded) with 95% significance level between eBC concentrations and levels of: a) CO b) CO_2 c) NO and d) NO_2.

8.3.5. EMISSION FACTORS

The mean EF_{BC} estimated inside the tunnel was 0.31±0.08 g (kg fuel)$^{-1}$. The EFs obtained in the present work are in the range of values reported by other studies (Ban-Weiss et al., 2009; Dallmann et al., 2013, 2012; Gëller et al., 2005; Grieshop et al., 2006; Jezek et al., 2015; Miguel et al., 1998; Strawa et al., 2010) (Table 8.3). Emission factors depend on traffic intensity, emission category (Euro standards), driving modes (idle, low- and high-speed acceleration, low- and high-speed cruise), vehicle age, load, fuel type, installed emission control technologies, as well as on external factors, such as local mixing and meteorology (Grieshop et al., 2006; Park et al., 2011; Wang et al., 2018). In the morning (0800-1300 UTC), a mean value of 0.32±0.07 g (kg fuel)$^{-1}$ has been estimated, while in the afternoon (1400-2100 UTC) the EF_{BC} was 0.30±0.08 g (kg fuel)$^{-1}$. During the sampling campaign, a maximum EF_{BC} of 0.48 g (kg fuel)$^{-1}$ (on Tuesday at 1800 UTC) and a minimum of 0.20 g (kg fuel)$^{-1}$ (on Wednesday at 0900 UTC) were registered. When these EFs were converted into mass emitted per km and vehicle, EF_{BC} presented a mean value of 0.11±0.08 mg veh^{-1} km^{-1}, ranging from 0.05 mg veh^{-1} km^{-1} to 0.52 mg veh^{-1} km^{-1}. These values are lower than those reported for road tunnels in São Paulo, Brazil (Sánchez-Coyllo et al., 2009). However, it should be borne in mind that, in this latter work, BC was estimated thought reflectance analysis of filters.

During the mornings, a mean value of 0.13±0.10 mg veh^{-1} km^{-1} has been estimated in our study, while during the afternoons the value was 0.10±0.05 mg veh^{-1} km^{-1}. For weekdays, a mean value

of 0.08±0.02 mg veh^{-1} km^{-1} has been estimated, whilst weekend days presented a higher value of 0.19±0.10 mg veh^{-1} km^{-1}.

Table 8.3. Mean BC emission factors measured in this study compared with other field measurements.

Study	City	Study type	EF_{BC} (g $(kg\ fuel)^{-1}$)	Vehicle type
Grieshop et al. (2006)	Pittsburgh (USA)	Tunnel	0.03	Light duty gasoline and diesel vehicles
Strawa et al. (2010)	Oakland (USA)	Tunnel	0.022	Light duty gasoline and diesel vehicles
Miguel et al. (1998)	Oakland (USA)	Tunnel	0.03	Light duty gasoline and diesel vehicles
Miguel et al. (1998)	Oakland (USA)	Tunnel	1.44	Heavy duty diesel
Ban-Weiss et al. (2009)	Oakland (USA)	Tunnel	1.7	Light duty gasoline and diesel vehicles
Gëller et al. (2005)	California (USA)	Tunnel	0.02	Light duty gasoline and diesel vehicles
Park et al. (2011)	Wilmington (USA)	Mobile platform in a tunnel	0.09	Light duty gasoline vehicle
Dallmann et al. (2012)	Oakland (USA)	Tunnel	0.54	Heavy-duty diesel trucks
Dallmann et al. (2013)	Oakland (USA)	Tunnel	0.10	Roadside measurement
Jezek et al. (2015)	Slovenia	Chasing	0.28	Petrol cars
Jezek et al. (2015)	Slovenia	Chasing	0.64	Light duty gasoline and diesel vehicles
Brimblecombe et al. (2015)	Hong Kong	Mobile platform in a tunnel	1.28	Diesel fleet
This study	Braga (Portugal)	Tunnel	0.31±0.08	Light and heavy-duty gasoline and diesel vehicles

8.4. CONCLUSIONS

The following main conclusions could be extracted from this sampling campaign, carried out continuously for 7 days in a road tunnel in Braga (Portugal) with an aethalometer:

- Inside the tunnel, the mean eBC mass concentration was 21±10 μg m^{-3}, close to the limit proposed by the WHO for daily $PM_{2.5}$ concentrations (25 μg m^{-3}). eBC concentrations reached an hourly maximum of 49.0 μg m^{-3}.
- The maximum values reached during weekdays occurred between 1400 and 1900 UTC, during the rush hours, when traffic density is greater due to commuting. However, during the weekend days, a peak between 0900 and 1200 UTC was observed, probably due to leisure and shopping activities.
- A mean Absorption Ångström Exponent ($AAE_{470\text{-}950}$) of 0.97±0.10 was obtained, with a maximum of 1.07 during daytime hours, for a source of practically pure traffic.
- There was a positive correlation, statistically significant, between eBC and light vehicles (r^2=0.23; $p<0.001$) and between eBC and total number of vehicles (r^2=0.22; $p<0.001$).
- There was a statistically significant positive correlation between eBC and gaseous emissions (CO, CO_2, NO and NO_2).
- The mean eBC emission factor, EF_{BC} inside the tunnel was 0.31±0.08 g $(kg\ fuel)^{-1}$. When this EF was converted into mass emitted per km, EF_{BC} presented a mean value of 0.11±0.08 mg veh^{-1} km^{-1}.

The study of black carbon in a road tunnel contributes to better characterize emissions of this pollutant from traffic in real circulation conditions and without influence from other sources providing valuable information on BC emission factors, which are useful as input data to climate and air quality models, as well as to updated emission inventories. Furthermore, the quantification of BC is essential to assess air quality in road tunnels and, thus, improve ventilation systems.

8.5. REFERENCES

Alves, C.A., Barbosa, C., Rocha, S., Calvo, A., Nunes, T., Cerqueira, M., Pio, C., Karanasiou, A., Querol, X., 2015a. Elements and polycyclic aromatic hydrocarbons in exhaust particles emitted by light-duty vehicles. Environ. Sci. Pollut. Res. 22, 11526–11542. doi:10.1007/s11356-015-4394-x

Alves, C.A., Gomes, J., Nunes, T., Duarte, M., Calvo, A., Custódio, D., Pio, C., Karanasiou, A., Querol, X., 2015b. Size-segregated particulate matter and gaseous emissions from motor vehicles in a road tunnel. Atmos. Res. 153, 134–144. doi:10.1016/j.atmosres.2014.08.002

Alves, C.A., Oliveira, C., Martins, N., Mirante, F., Caseiro, A., Pio, C., Matos, M., Silva, H.F., Oliveira, C., Camões, F., 2016a. Road tunnel, roadside, and urban background measurements of aliphatic compounds in size-segregated particulate matter. Atmos. Res. 168, 139–148. doi:10.1016/j.atmosres.2015.09.007

Alves, C.A., Vicente, A.M.P., Gomes, J., Nunes, T., Duarte, M., Bandowe, B.A.M., 2016b. Polycyclic aromatic hydrocarbons (PAHs) and their derivatives (oxygenated-PAHs, nitrated-PAHs and azaarenes) in size-fractionated particles emitted in an urban road tunnel. Atmos. Res. 180, 128–137. doi:10.1016/j.atmosres.2016.05.013

Amato, F., Alastuey, A., Karanasiou, A., Lucarelli, F., Nava, S., Calzolai, G., Severi, M., Becagli, S., Gianelle, V.L., Colombi, C., Alves, C., Custódio, D., Nunes, T., Cerqueira, M., Pio, C., Eleftheriadis, K., Diapouli, E., Reche, C., Minguillón, M.C., Manousakas, M.I., Maggos, T., Vratolis, S., Harrison, R.M., Querol, X., 2016. AIRUSE-LIFE+: A harmonized PM speciation and source apportionment in five southern European cities. Atmos. Chem. Phys. 16, 3289–3309. doi:10.5194/acp-16-3289-2016

Amato, F., Cassee, F.R., Denier van der Gon, H.A.C., Gehrig, R., Gustafsson, M., Hafner, W., Harrison, R.M., Jozwicka, M., Kelly, F.J., Moreno, T., Prevot, A.S.H., Schaap, M., Sunyer, J., Querol, X., 2014. Urban air quality: The challenge of traffic non-exhaust emissions. J. Hazard. Mater. 275, 31–36. doi:10.1016/j.jhazmat.2014.04.053

Ban-Weiss, G.A., Lunden, M.M., Kirchstetter, T.W., Harley, R.A., 2009. Measurement of black carbon and particle number emission factors from individual heavy-duty trucks. Environ. Sci. Technol. 43, 1419–1424. doi:10.1021/es8021039

Becerril-Valle, M., Coz, E., Prévôt, A.S.H., Močnik, G., Pandis, S.N., Sánchez de la Campa, A.M., Alastuey, A., Díaz, E., Pérez, R.M., Artíñano, B., 2017. Characterization of atmospheric black carbon and co-pollutants in urban and rural areas of Spain. Atmos. Environ. 169, 36–53. doi:10.1016/j.atmosenv.2017.09.014

Blanco-Alegre, C., Calvo, A.I., Coz, E., Castro, A., Oduber, F., Prévôt, A.S.H., Močnik, G., Fraile, R., 2018. Quantification of source specific black carbon scavenging using an aethalometer and a disdrometer. Environ. Pollut. 246, 336–345. doi:10.1016/j.envpol.2018.11.102

Bond, T.C., Doherty, S.J., Fahey, D.W., Forster, P.M., Berntsen, T., Deangelo, B.J., Flanner, M.G., Ghan, S., Kürcher, B., Koch, D., Kinne, S., Kondo, Y., Quinn, P.K., Sarofim, M.C., Schultz, M.G., Schulz, M., Venkataraman, C., Zhang, H., Zhang, S., Bellouin, N., Guttikunda, S.K., Hopke, P.K., Jacobson, M.Z., Kaiser, J.W., Klimont, Z., Lohmann, U., Schwarz, J.P., Shindell, D., Storelvmo, T., Warren, S.G., Zender, C.S., 2013. Bounding the role of black carbon in the climate system: A scientific assessment. J. Geophys. Res. Atmos. 118, 5380–5552. doi:10.1002/jgrd.50171

Brimblecombe, P., Townsend, T., Lau, C.F., Rakowska, A., Chan, T.L., Močnik, G., Ning, Z., 2015. Through-tunnel estimates of vehicle fleet emission factors. Atmos. Environ. 123, 180–189. doi:10.1016/j.atmosenv.2015.10.086

Bycenkiene, S., Plauskaite, K., Dudoitis, V., Ulevicius, V., 2014. Urban background levels of particle number concentration and sources in Vilnius, Lithuania. Atmos. Res. 143, 279–292. doi:10.1016/j.atmosres.2014.02.019

Corrigan, C.E., Ramanathan, V., Schauer, J.J., 2006. Impact of monsoon transitions on the physical and optical properties of aerosols. J. Geophys. Res. Atmos. 111, 1–15. doi:10.1029/2005JD006370

Dallmann, T.R., DeMartini, S.J., Kirchstetter, T.W., Herndon, S.C., Onasch, T.B., Wood, E.C., Harley, R.A., 2012. On-road measurement of gas and particle phase pollutant emission factors for individual heavy-duty diesel trucks. Environ. Sci. Technol. 46, 8511–8518. doi:10.1021/es301936c

Dallmann, T.R., Kirchstetter, T.W., Demartini, S.J., Harley, R.A., 2013. Quantifying on-road emissions from gasoline-powered motor vehicles: accounting for the presence of medium- and heavy-duty diesel trucks. Environ. Sci. Technol. 47, 13873–13881.

Denier van der Gon, H.A.C., Gerlofs-Nijland, M.E., Gehrig, R., Gustafsson, M., Janssen, N., Harrison, R.M., Hulskotte, J., Johansson, C., Jozwicka, M., Keuken, M., Krijgsheld, K., Ntziachristos, L., Riediker, M., Cassee, F.R., 2013. The policy relevance of wear emissions from road transport, now and in the future - An international workshop report and consensus statement. J. Air Waste Manag. Assoc. 63, 136–149. doi:10.1080/10962247.2012.741055

Drinovec, L., Močnik, G., Zotter, P., Prévôt, A.S.H., Ruckstuhl, C., Coz, E., Rupakheti, M., Sciare, J., Müller, T., Wiedensohler, A., Hansen, A.D.A., 2015. The "dual-spot" Aethalometer: An improved measurement of aerosol black carbon with real-time loading compensation. Atmos. Meas. Tech. 8, 1965–1979. doi:10.5194/amt-8-1965-2015

EEA, 2016. Air quality in Europe - 2016 Report. Copenhagen, Denmark. doi:10.2800/413142

EEA, 2013. Air Quality in Europe - 2013 Report. Copenhagen, Denmark. doi:10.2800/92843

EPA, 2015. Annexes to the Inventory of U.S. GHG Emissions and Sinks: 1990 e 2013, Annex 2 Methodology and Data for Estimating CO2 Emissions from Fossil Fuel Combustion.

Franco, V., Kousoulidou, M., Muntean, M., Ntziachristos, L., Hausberger, S., Dilara, P., 2013. Road vehicle emission factors development: A review. Atmos. Environ. 70, 84–97. doi:10.1016/j.atmosenv.2013.01.006

Garg, S., Chandra, B.P., Sinha, V., Sarda-Esteve, R., Gros, V., Sinha, B., 2016. Limitation of the use of the absorption angstrom exponent for source apportionment of equivalent black carbon: a case study from the North West Indo-Gangetic plain. Environ. Sci. Technol. 50, 814–824. doi:10.1021/acs.est.5b03868

Gëller, M.D., Sardar, S.B., Phuleria, H., Fine, P.M., Sioutas, C., 2005. Measurements of particle number and mass concentrations and size distributions in a tunnel environment. Environ. Sci. Technol. 39, 8653–8663. doi:10.1021/es050360s

Grieshop, A.P., Lipsky, E.M., Pekney, N.J., Takahama, S., Robinson, A.L., 2006. Fine particle emission factors from vehicles in a highway tunnel: Effects of fleet composition and season. Atmos. Environ. 40, 287–298. doi:10.1016/j.atmosenv.2006.03.064

Handler, M., Puls, C., Zbiral, J., Marr, I., Puxbaum, H., Limbeck, A., 2008. Size and composition of particulate emissions from motor vehicles in the Kaisermühlen-Tunnel, Vienna. Atmos. Environ. 42, 2173–2186. doi:10.1016/j.atmosenv.2007.11.054

Hansen, A.D.A., Rosen, H., Novakov, T., 1984. The aethalometer - An instrument for the real-time measurement of optical absorption by aerosol particles. Sci. Total Environ. 36, 191–196. doi:10.1016/0048-9697(84)90265-1

Harrison, R.M., Beddows, D.C.S., Jones, A.M., Calvo, A., Alves, C., Pio, C., 2013. An evaluation of some issues regarding the use of aethalometers to measure woodsmoke concentrations. Atmos. Environ. 80, 540–548. doi:10.1016/j.atmosenv.2013.08.026

Jezek, I., Katrasnik, T., Westerdahl, D., Mocnik, G., 2015. Black carbon, particle number concentration and nitrogen oxide emission factors of random in-use vehicles measured with the on-road chasing method. Atmos. Chem. Phys. 15, 11011–11026. doi:10.5194/acp-15-11011-2015

Kinney, P.L., 2008. Climate change, air quality, and human health. Am. J. Prev. Med. 35, 459–467. doi:10.1016/j.amepre.2008.08.025

Kirchstetter, T., Harley, R.A., Kreisberg, N.M., Stolzenburg, M.R., Hering, S. V., 1999. On-road measurement of fine particle and nitrogen oxide emissions from light- and heavy-duty motor vehicles. Atmos. Environ. 33, 2955–2968. doi:10.1016/S1352-2310(99)00089-8

Kristensson, A., Johansson, C., Westerholm, R., Swietlicki, E., Gidhagen, L., Wideqvist, U., Vesely, V., 2004. Real-world traffic emission factors of gases and particles measured in a road tunnel in Stockholm, Sweden. Atmos. Environ. 38, 657–673. doi:10.1016/j.atmosenv.2003.10.030

Latha, K.M., Badarinath, K.V.S., 2004. Correlation between black carbon aerosols, carbon monoxide and tropospheric ozone over a tropical urban site. Atmos. Res. 71, 265–274. doi:10.1016/j.atmosres.2004.06.004

Martins, L.D., Andrade, M.F., Freitas, E.D., Pretto, A., Gatti, L. V., Albuquerque, É.L., Tomaz, E., Guardani, M.L., Martins, M.H.R.B., Junior, O.M.A., 2006. Emission factors for gas-powered vehicles traveling through road tunnels in São Paulo, Brazil. Environ. Sci. Technol. 40, 6722–6729. doi:10.1021/es052441u

McGaughey, G.R., Desai, N.R., Allen, D.T., Seila, R.L., Lonneman, W.A., Fraser, M.P., Harley, R.A., Pollack, A.K., Ivy, J.M., Price, J.H., 2004. Analysis of motor vehicle emissions in a Houston tunnel during the Texas Air Quality Study 2000. Atmos. Environ. 38, 3363–3372. doi:10.1016/j.atmosenv.2004.03.006

Miguel, A.H., Kirchstetter, T.W., Harley, R.A., Hering, S. V., 1998. On-road emissions of particulate polycyclic aromatic hydrocarbons and black carbon from gasoline and diesel vehicles. Environ. Sci. Technol. 32, 450–455. doi:10.1021/es970566w

Padoan, E., Amato, Fulvio, 2018. Vehicle Non-Exhaust Emissions: Impact on Air Quality, in: Amato, F. (Ed.), An Urban Air Quality Problem for Public Health; Impact and Mitigation Measures. Elsevier, London, pp. 21–65. doi:10.1016/B978-0-12-811770-5.00002-9

Park, S.S., Kozawa, K., Fruin, S., Mara, S., Hsu, Y.K., Jakober, C., Winer, A., Herner, J., 2011. Emission factors for high-emitting vehicles based on on-road measurements of individual vehicle exhaust with a mobile measurement platform. J. Air Waste Manag. Assoc. 61, 1046–1056. doi:10.1080/10473289.2011.595981

Petzold, A., Ogren, J.A., Fiebig, M., Laj, P., Li, S.M., Baltensperger, U., Holzer-Popp, T., Kinne, S., Pappalardo, G., Sugimoto, N., Wehrli, C., Wiedensohler, A., Zhang, X.Y., 2013. Recommendations for reporting black carbon measurements. Atmos. Chem. Phys. 13, 8365–8379. doi:10.5194/acp-13-8365-2013

Pio, C., Cerqueira, M., Harrison, R.M., Nunes, T., Mirante, F., Alves, C., Oliveira, C., Sanchez, A., Campa, D., Artíñano, B., Matos, M., 2011. OC / EC ratio observations in Europe : Re-thinking the approach for apportionment between primary and secondary organic carbon. Atmos. Environ. 45, 6121–6132. doi:10.1016/j.atmosenv.2011.08.045

Pio, C., Mirante, F., Oliveira, César, Matos, M., Caseiro, A., Oliveira, Cristina, Querol, X., Alves, C., Martins, N., Cerqueira, M., Camões, F., Silva, H., Plana, F., 2013. Size-segregated chemical composition of aerosol emissions in an urban road tunnel in Portugal. Atmos. Environ. 71, 15–25. doi:10.1016/j.atmosenv.2013.01.037

Querol, X., Alastuey, A., Ruiz, C.R., Artiñano, B., Hansson, H.C., Harrison, R.M., Buringh, E., Ten Brink, H.M., Lutz, M., Bruckmann, P., Straehl, P., Schneider, J., 2004. Speciation and origin of PM10 and PM2.5 in selected European cities. Atmos. Environ. 38, 6547–6555. doi:10.1016/j.atmosenv.2004.08.037

Ramanathan, V., Carmichael, G., 2008. Global and regional climate changes due to black carbon. Nat. Geosci. 1, 221–227. doi:10.1038/ngeo156

Sánchez-Coyllo, O.R., Ynoue, R.Y., Martins, L.D., Astolfo, R., Miranda, R.M., Freitas, E.D., Borges, A.S., Fornaro, A., Freitas, H., Moreira, A., Andrade, M.F., 2009. Vehicular particulate matter emissions in road tunnels in Sao Paulo, Brazil. Environ. Monit. Assess. 149, 241–249. doi:10.1007/s10661-008-0198-5

Sandradewi, J., Prévôt, A.S.H., Szidat, S., Perron, N., Alfarra, M.R., Lanz, V.A., Weingartner, E., Baltensperger, U.R.S., 2008a. Using aerosol light absorption measurements for the quantitative determination of wood burning and traffic emission contribution to particulate matter. Environ. Sci. Technol. 42, 3316–3323. doi:10.1021/es702253m

Sandradewi, J., Prévôt, A.S.H., Weingartner, E., Schmidhauser, R., Gysel, M., Baltensperger, U., 2008b. A study of wood burning and traffic aerosols in an Alpine valley using a multi-wavelength Aethalometer. Atmos. Environ. 42, 101–112. doi:10.1016/j.atmosenv.2007.09.034

Silverman, D.T., Samanic, C.M., Lubin, J.H., Blair, A.E., Stewart, P.A., Vermeulen, R., Coble, J.B., Rothman, N., Schleiff, P.L., Travis, W.D., Ziegler, R.G., Wacholder, S., Attfield, M.D., 2012. The diesel exhaust in miners study: a nested case-control study of lung cancer and diesel exhaust. JNCI J. Natl. Cancer Inst. 104, 855–868. doi:10.1093/jnci/djs034

Strawa, A.W., Kirchstetter, T.W., Hallar, A.G., Ban-Weiss, G.A., McLaughlin, J.P., Harley, R.A., Lunden, M.M., 2010. Optical and physical properties of primary on-road vehicle particle emissions and their implications for climate change. J. Aerosol Sci. 41, 36–50. doi:10.1016/j.jaerosci.2009.08.010

Suglia, S.F., Gryparis, A., Schwartz, J., Wright, R.J., 2008. Association between traffic-related black carbon exposure and lung function among urban women. Environ. Health Perspect. 116, 1333–1337. doi:10.1289/ehp.11223

Sun, Y., Zhou, X., Wai, K., Yuan, Q., Xu, Z., Zhou, S., Qi, Q., Wang, W., 2013. Simultaneous measurement of particulate and gaseous pollutants in an urban city in north china plain during the heating period: Implication of source contribution. Atmos. Res. 134, 24–34. doi:10.1016/j.atmosres.2013.07.011

Thorpe, A., Harrison, R.M., 2008. Sources and properties of non-exhaust particulate matter from road traffic: A review. Sci. Total Environ. 400, 270–282. doi:10.1016/j.scitotenv.2008.06.007

Tong, Z., Chen, Y., Malkawi, A., Adamkiewicz, G., Spengler, J.D., 2016. Quantifying the impact of traffic-related air pollution on the indoor air quality of a naturally ventilated building. Environ. Int. 89–90, 138–146. doi:10.1016/j.envint.2016.01.016

Traver, M.L., Tennant, C.J., Mcdaniel, T.I., Mcconnell, S.S., Bailey, B.K., Maldonado, H., 2002. Interlaboratory cross-check of heavy-duty vehicle chassis dynamometers, in: SAE Powertrain & Fluid Systems Conference & Exhibition. SAE International, p. 11. doi:10.4271/2002-01-2879

Virkkula, A., Mäkelä, T., Hillamo, R., Yli-Tuomi, T., Hirsikko, A., Hämeri, K., Koponen, I.K., 2007. A simple procedure for correcting loading effects of Aethalometer data. J. Air Waste Manage. Assoc. 57, 1214–1222. doi:10.3155/1047-3289.57.10.1214

Wang, J.M., Jeong, C.H., Zimmerman, N., Healy, R.M., Evans, G.J., 2018. Real world vehicle fleet emission factors: Seasonal and diurnal variations in traffic related air pollutants. Atmos. Environ. 184, 77–86. doi:10.1016/j.atmosenv.2018.04.015

Wang, X., Westerdahl, D., Hu, J., Wu, Y., Yin, H., Pan, X., Max Zhang, K., 2012. On-road diesel vehicle emission factors for nitrogen oxides and black carbon in two Chinese cities. Atmos. Environ. 46, 45–55. doi:10.1016/j.atmosenv.2011.10.033

Weingartner, E., Saathoff, H., Schnaiter, M., Streit, N., Bitnar, B., Baltensperger, U., 2003. Absorption of light by soot particles: Determination of the absorption coefficient by means of aethalometers. J. Aerosol Sci. 34, 1445–1463. doi:10.1016/S0021-8502(03)00359-8

WHO, 2013. Review of evidence on health aspects of air pollution – REVIHAAP Project, World Health Organization. Copenhagen, Denmark.

WMO, 2016. WMO/GAW Aerosol Measurement procedures guidelines and recommendations, GAW Report.

Zotter, P., Herich, H., Gysel, M., El-Haddad, I., Zhang, Y., Močnik, G., Hüglin, C., Baltensperger, U., Szidat, S., Prévôt, A.S.H., 2017. Evaluation of the absorption Ångström exponents for traffic and wood burning in the Aethalometer based source apportionment using radiocarbon measurements of ambient aerosol. Atmos. Chem. Phys. 17, 4229–4249. doi:10.5194/acp-17-4229-2017

SUPPLEMENTARY MATERIAL

a)

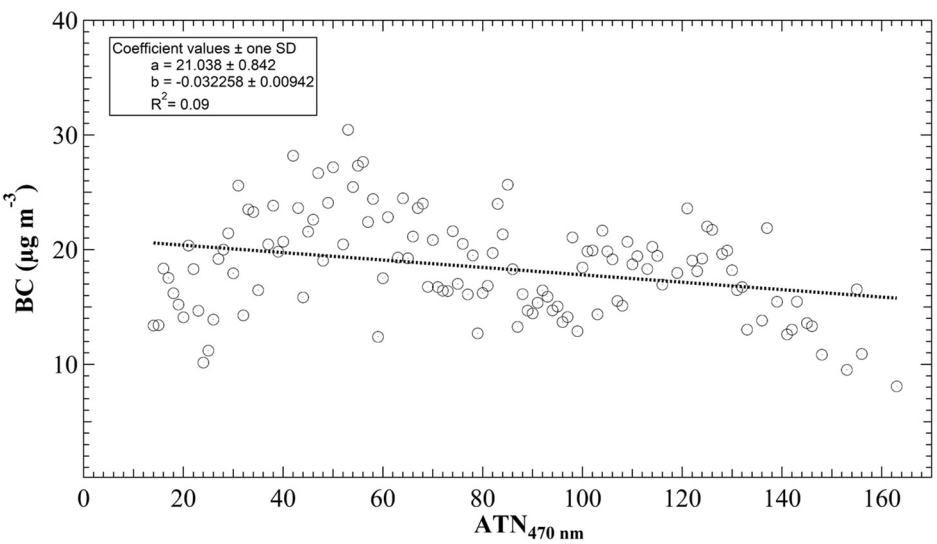

b)

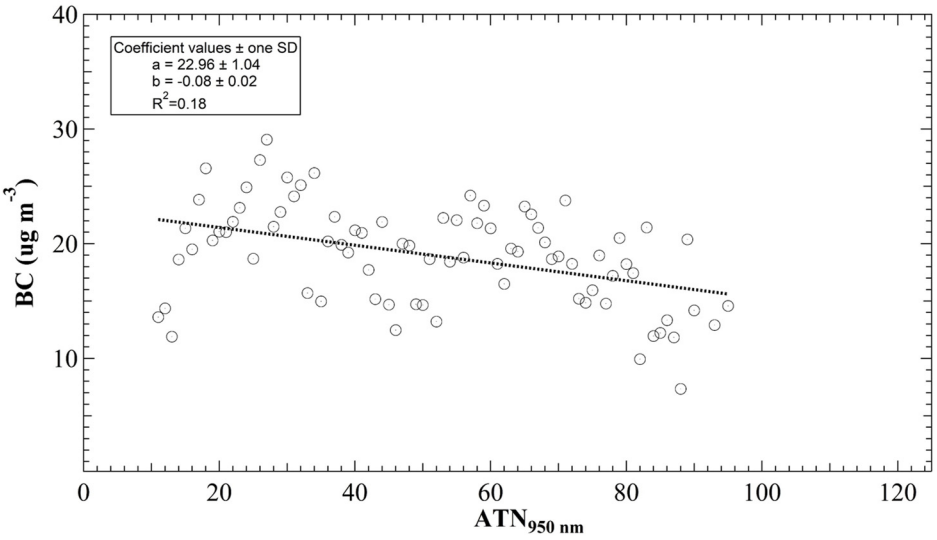
Coefficient values ± one SD
a = 22.96 ± 1.04
b = -0.08 ± 0.02
R2=0.18
BC (ug m-3)
ATN950 nm

c)

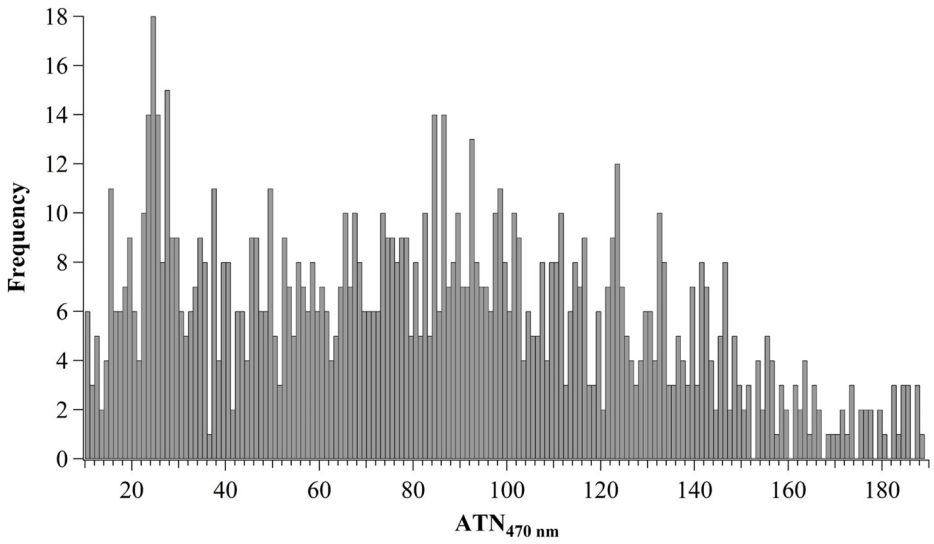
Frequency
ATN470 nm

d)

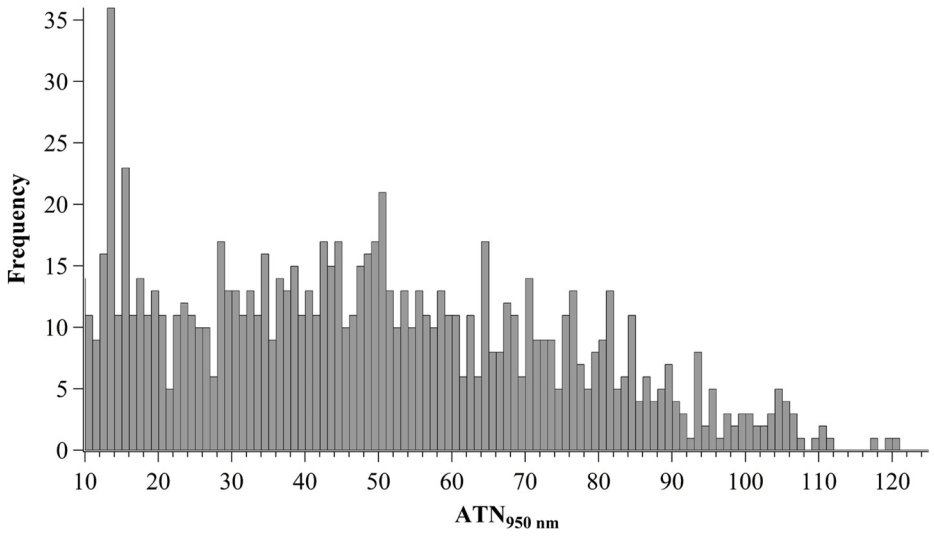
Frequency
ATN950 nm

e)

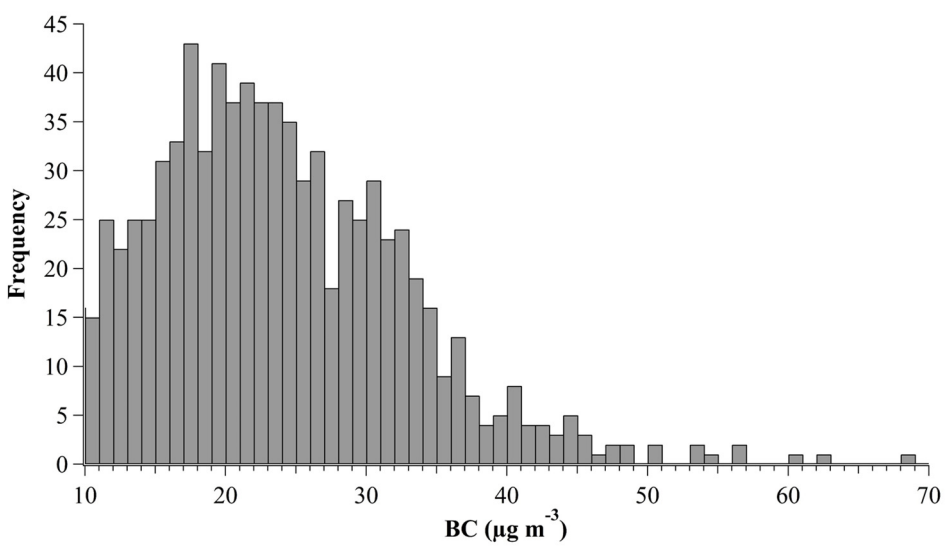

Figure S8.1. BC as a function of a) $ATN_{470\ nm}$ and b) $ATN_{950\ nm}$ plot (only considers the average values for the 1 ATN bin with at least 4 values to average); c) Frequency distribution of the number of measurements per $ATN_{470\ nm}$; c) Frequency distribution of the number of measurements per $ATN_{950\ nm}$; e) The BC frequency in the ATN range of 10-125.

a)

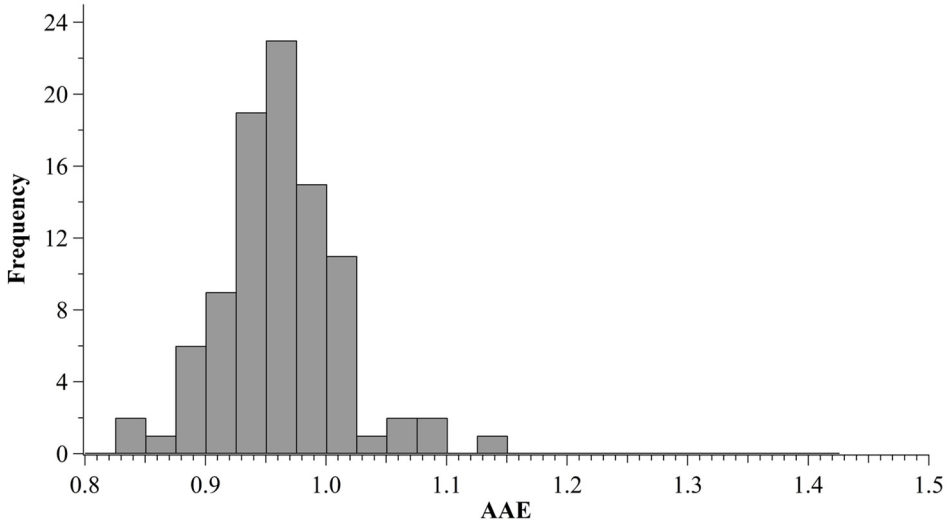

b)

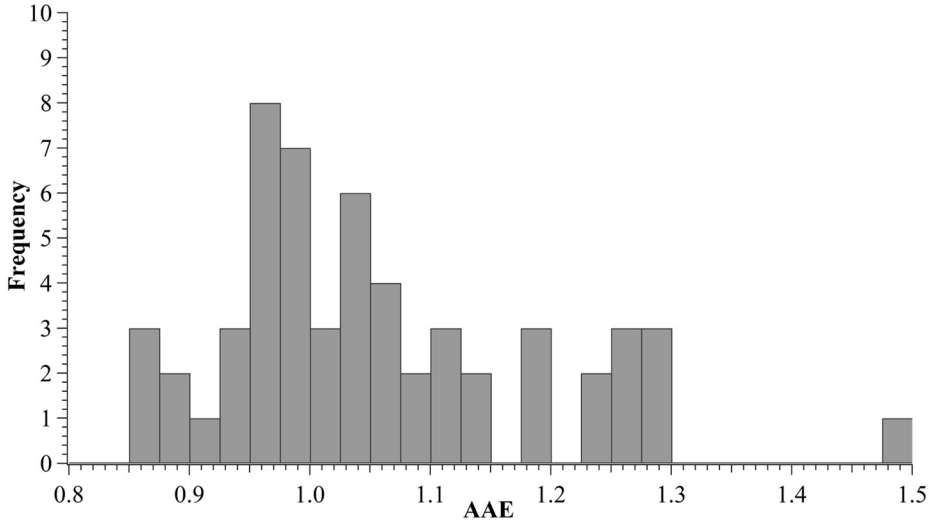

c)

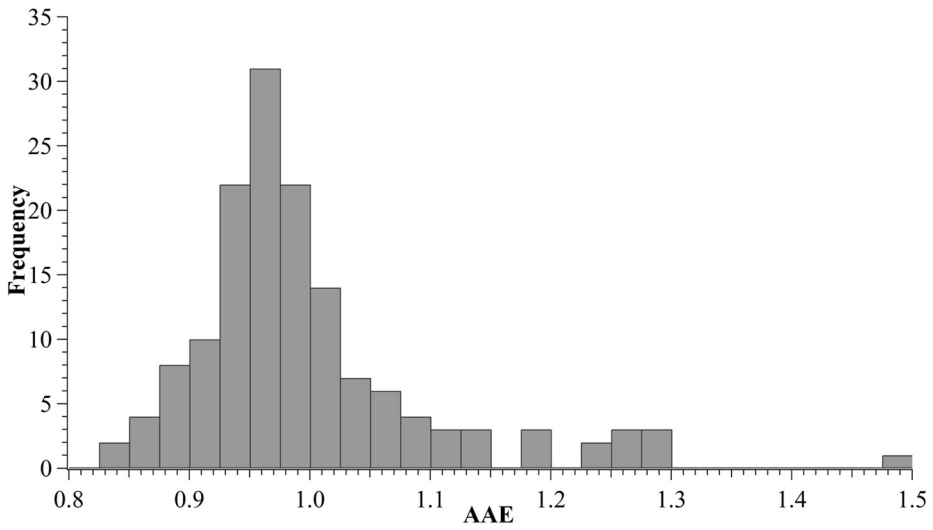

Figure S8.2. Frequency distribution of hourly AAE for daytime (a), nighttime (b) and the whole campaign (c).

CHAPTER 9. Quantification of source specific black carbon scavenging

Full title: Quantification of source specific black carbon scavenging using an aethalometer and a disdrometer

Published in: Environmental Pollution, 2019, 336–345.
DOI: 10.1016/j.envpol.2018.11.102

9.1. INTRODUCTION

Atmospheric aerosols, both natural and anthropogenic, affect human health (Apte et al., 2015; Fröhlich-Nowoisky et al., 2016; HEI Review Panel, 2013; Pöschl, 2005; WHO, 2007) and climatic change because of the significant contribution to the Earth's radiation budget either directly and indirectly (Andreae and Ramanathan, 2013; ICCP, 2014b; Menon et al., 2002; Pöschl, 2005). In Europe, more than 90% of city dwellers are exposed to $PM_{2.5}$ levels that exceed the reference value set by WHO (EEA, 2013).

One of the major atmospheric aerosol pollutants is black carbon (BC) which is emitted during incomplete combustion of fossil fuel or biomass. It is a carbonaceous material formed primarily in flames and directly emitted to the atmosphere, with some particular physical properties: it strongly absorbs visible light and is refractory with a vaporization temperature of around 3700 °C (Bond et al., 2013a). It is noteworthy that BC particles are insoluble in water and organic solvents and, therefore, they are not scavenged directly from the atmosphere due to wet deposition (Quinn, 2011). Some studies (e.g. Granat et al., 2010) indicate that BC keeps its hydrophobic property

even after being in the atmosphere for several days. However, the BC morphology (organised as fractal-like aggregates) facilitates sorption of other species (Petzold et al., 2013) and it becomes hydrophilic and accessible for wet deposition. The BC cycle is controlled by emissions, transport and deposition. Among these factors, wet deposition is the most complex (Mori et al., 2014).

According to Bond et al., (2013), the main sources of BC are: i) diesel engines used for transport, ii) residential solid fuels (wood and coal), iii) forest fires, and iv) industrial processes. In these burning processes, small carbon spherules are formed, with diameters between 10 and 50 nm and, subsequently, accumulated in aggregates. This aggregates formation starts at or shortly after emission and the aggregates get internally or externally mixed. Their size distribution depends on the formation mechanism and atmospheric processes during transport, while they grow via coagulation. Regarding to aggregate sizes, these particles belong to the Aitken mode (30-100 nm) but due to subsequent coagulation and condensation of inorganic and organic secondary molecules, they can grow to sizes in the accumulation mode (100-1000 nm) (Conrady et al., 2013).

BC also plays an important role in the environment, for example in the formation of acid precipitation through the catalytic oxidation of sulphur dioxide to sulphate (Novakov, 1984; Singh et al., 2016). The main BC aerosol effect on climate is due to the strong ability to absorb solar radiation. The impact of BC on climate change remains largely uncertain (Hienola et al., 2013). Nevertheless, the global mean radiative forcing caused by BC was estimated to be from 0.4 to 1.2 W m^{-2}, becoming the second strongest contributor to global warming, after CO_2 (Bond et al., 2013a; ICCP, 2014b). Several studies (AMAP, 2011; Righi et al., 2011) have found that BC affects the Earth's radiation budget in three different ways: i) aerosol direct effect (absorption or scattering of shortwave radiation), ii) aerosol indirect effect (interaction with clouds) and iii) semi-direct effects (BC deposition to ice/snow enhances the absorption of shortwave radiation inducing melting process).

BC may be a pollutant toxic to human health, linked to many illnesses: respiratory (such as adverse effects on lung function and increase cancer risks) and cardiovascular diseases (Janssen et al., 2011; WHO, 2012), and it causes an increase in population morbidity and mortality (Silverman et al., 2012; Suglia et al., 2008), mainly affecting the children's health (UNICEF, 2016) (due to the immature host defence system) and people with chronic respiratory diseases (Jansen et al., 2005). The set of BC and organic carbon is estimated that producing annually around 3 million premature deaths (Apte et al., 2015; Bond et al., 2013a; Lelieveld et al., 2015; WHO, 2012). Hence, the study of black carbon concentration is crucial due to its effects on multiple essential policy objectives like climate, air quality or public health (EEA, 2016; Font and Fuller, 2016; Kinney, 2008; Tong et al., 2017, 2016).

To measure BC, the use of aethalometer (Hansen et al., 1984) has been common in last years. The aethalometer provides the concentration of equivalent black carbon (eBC) (carbon mass derived from the light attenuation coefficient). The multi-wavelength aethalometer data may be used to separate the fossil fuel (eBC_{ff}) and the biomass burning (eBC_{bb}) contributions to eBC through the "aethalometer model" (Becerril-Valle et al., 2017; Harrison et al., 2013; Sandradewi et al., 2008b; Zotter et al., 2017).

Wet and dry deposition is the only important sink of BC, due to its stability. The atmospheric lifetime of BC aerosols ranges from days to weeks depending on the local meteorology (Begam et al., 2016). Dry deposition is able to eliminate larger particles in several days, and sub-micron fraction in several weeks, hence this is a slow process. However, observations have shown that wet deposition represents 70–85% of the tropospheric sink for the carbonaceous aerosols (Pöschl, 2005). Therefore, wet deposition is the main process to mitigate the effects of BC on the climate, human health and ecosystems (Cerqueira et al., 2010) in a brief lapse of time, but this process is not yet well explored. Wet deposition is considered one of the most uncertain processes in models (Textor et al., 2006).

Below-cloud scavenging (BCS) linked to wet deposition, constitutes an important sink of aerosol particles, including BC (Chate, 2005; Latha et al., 2005; Sportisse, 2007; Tost et al., 2006; Zhao et al., 2015). However, the study of BC aerosol-precipitation interaction does not constitute an easy task. The complexity in the characterization of BCS lies in the dependence on several parameters, for example concentration, chemical composition or electric charges (Ladino et al., 2011). Many researchers have tried to quantify the wet scavenging effect on aerosols and gases (Chate et al., 2003; Laakso et al., 2003; Maria and Russell, 2005; Olszowski, 2015b), but there are few studies on BC scavenging by rainfall to date. Furthermore, most of them are based on the determination of elemental carbon (EC) concentration by thermo-optical methods (Armalis, 1999; Budhavant et al., 2016; Cerqueira et al., 2010; Custódio et al., 2014; Granat et al., 2010). These studies are carried out in time intervals (sampling period of one day or several hours) that are long compared to the rain event duration. A simultaneous and continuous study of BC concentration and raindrop sizes would provide a deeper knowledge about the BC-precipitation interaction.

A 15 months sampling campaign for measuring BC concentration (with an aethalometer) and raindrop physical characteristics (with a disdrometer) has been carried out in León (NW Spain). An estimation of below-cloud scavenging on BC according to rainfall characteristics and origin of air masses has also been accomplished. As far as we know, this type of studies is unprecedented.

9.2. MATERIAL AND METHODS

9.2.1. SAMPLING SITE AND MEASUREMENTS

The sampling site is located in the campus of the University of León (Figure S9.1), a city situated in the NW of the Iberian Peninsula (42° 36′ N, 05° 35′ W) at 838 m above sea level and with a population of about 200,000 including the metropolitan area. According to Oduber et al. (2018) the main source of particulate emissions is traffic and domestic heating, due to the absence of large emitting industries. It is worth noting that, nowadays, the use of coal combustion in heating devices is still usual in León. León features a Mediterranean climate with continental features and tempered by the proximity of the Cantabrian Mountain Range with an annual mean precipitation of 515 mm (Castro et al., 2010).

The sampling was carried out between 12 February 2016 and 31 August 2017 (except spring 2017, due to technical issues). The instruments were located on the terrace of the Faculty of Veterinary Medicine of the University of Léon.

The following season distribution along the year was considered: winter from 15 December to 14 March, spring from 15 March to 14 June, summer from 15 June to 14 September and autumn from 15 September to 14 December.

9.2.2. BLACK CARBON DATA

An aethalometer model AE-31 (Magee Scientific, USA) with a time resolution of 2 minutes and a precision of 10^{-3} µg m^{-3} was used for BC concentration determination. It continuously measures attenuation of light due to the deposition of ambient aerosol on the instrument's filter tape at seven wavelengths: 370, 470, 520, 590, 660, 880 and 950 nm. The sample flow rate was set to be 4 L min^{-1} and verified with Gilian Gilibrator 2 measurements. To determine the eBC concentration in the sampled air, the aethalometer uses a differential radiometric optical transmission technique. The instrument operation was described in detail by Hansen (2005) and Virkkula et al. (2007).

In order to avoid possible bias in measurements due to the fast changes in relative humidity, the aethalometer data recorded during rain was not considered: only data before and after rain were considered. To decrease uncertainties derived from detector response, instrumental noise, flow rate and filter spot area (Corrigan et al., 2006), the 2-min eBC data has been averaged at a resolution of 1 h, comparable to the rain events duration.

The contribution from fossil fuel (eBC_{ff}) and biomass burning (eBC_{bb}) was estimated through the application of the aethalometer model (Sandradewi et al., 2008a). Likewise, hourly eBC, eBC_{ff}, eBC_{bb} concentrations and Absorption Ångström Exponent (AAE) were determined. Light absorption measurements at λ_1=470 nm and λ_2=950 nm (Becerril-Valle et al., 2017; Harrison et al., 2013; Sandradewi et al., 2008b) have been used in this work ($AAE(\lambda_1, \lambda_2) = -\frac{\ln[b_{abs}(\lambda_1)/b_{abs}(\lambda_2)]}{\ln(\lambda_1/\lambda_2)}$). To obtain the AAE values, the shorter wavelength of 470 nm has been used rather than the 370 nm one, because the latter is influenced by the varying presence of secondary organic aerosol (SOA) with highly variable optical properties (Zotter et al., 2017). The source specific AAE values used in the aethalometer model to estimate the biomass burning and fossil fuel contributions are AAE_{bb}=1.68, according to Zotter et al. (2017) and AAE_{ff}=0.95 derived from measurements in a traffic hotspot in the León centre in May during morning rush hours. The mean temperatures were high, so traffic can be considered like the only source at this point. In Supplementary material, the aethalometer model equations are shown.

The AAE values below 0.7 and above 4 (less than 2% along the sampling) were eliminated from the database because these measurements could be affected by instrumental noise, detector response or meteorological conditions (Corrigan et al., 2006).

The eBC data recorded during the sampling period were corrected following Aerosol, Clouds, and Trace gases Research InfraStructure Network (ACTRIS) guidelines using the Weingartner et al. (2003) algorithm.

9.2.3. DISDROMETER AND METEOROLOGICAL DATA

The raindrop size spectrum has been obtained using a disdrometer, Laser Precipitation Monitor (LPM) of *Thies Clima*, which registered drops between 0.125 and 8 mm in 22 drop size ranges. A detailed description can be found in Fernández-Raga et al. (2009). From the data provided by the LPM, the following rainfall variables were obtained every minute: precipitation intensity, accumulated precipitation, number of drops in 21 channels, volume swept by falling drops

(mm^3 m^{-3}), mean and standard deviation of raindrop sizes. The 1-min data have been averaged at a resolution of 1 h, like eBC data.

Next to disdrometer, a weather station was installed for continuously registering the temperature, humidity, wind intensity and direction. Univariate analysis (i.e. mean, median, minimum, maximum, quartiles and standard deviation) was used to calculate hourly BC concentration, rainfall variables and meteorological data.

9.2.4. AIR MASS TRAJECTORIES

Through the application of HYSPLIT4 (Hybrid Single Particle Lagrangian Integrated Trajectory) (Draxler and Rolph, 2012) the air masses trajectories were analysed in order to determine sources and origin of the air masses present in León during rain events. This model was used to compute four-days back trajectories at every rain event, at arrival altitudes of 500 and 1000 m a.g.l. over León (Custódio et al., 2014). The average altitude of 1000 m is representative of the diurnal mixing layer thickness at León (Calles et al., 2018). The model was run with meteorological data from the Global Data Assimilation System (GDAS) archives (http://ready.arl.noaa.gov/HYSPLIT_traj.php). Based on back trajectories at 1000 m a.g.l. over sampling point, a six groups classification of the prevailing air mass origin and transport pathway have been made. The group assigned coincides with the sector on which the air mass spent most of the time. The regions (Figure S9.2) are:

- Group I: Arctic
- Group II: Atlantic
- Group III: Continental
- Group IV: North America
- Group V: North Atlantic
- Group VI: Saharan

Besides, a Circulation Weather Types (CWTs) classification was carried out based on Lamb (1972), to identify the type of weather related with a specific synoptic situation. This method has been previously used in the Iberian Peninsula (Calvo et al., 2012; Russo et al., 2014). The direction and vorticity of the geostrophic flow, obtained for 16 grid points distributed over the Iberian Peninsula (Trigo and DaCamara, 2000), have been used to establish each of the 26 different CWTs. Eight weather types are identified as “pure” and are characterised by a specific predominant wind component, regardless of their intensity: N, S, E, W, NW, SW, SE and NE.

Other two of them are the so-called "non-directional": anticyclonic (A) and cyclonic (C). As a result of the combination of "non-directional" with "pure" types, other 16 CWTs, so-called "hybrid" types, are obtained. A detailed explication of this classification may be found in Trigo and DaCamara (2000).

9.2.5. SELECTING DATA CRITERIA

The rain events considered in this study are those that fulfil the following conditions:

- an accumulated precipitation greater than 0.2 mm was registered in one hour (minimum rain amount considered significant),
- there was a minimum of 2 h without rain between events,
- there were eBC and eBC_{ff} concentrations greater than 0.5 µg m^{-3} and greater than 0.1 µg m^{-3} for eBC_{bb},
- rain duration was shorter than 24 h.
- a maximum difference of 2 m s^{-1} in wind speed and 50° in wind direction during rain event has been registered (Kyrö et al., 2009; Paramonov et al., 2011) to avoid changes in eBC concentration due to advection (Laakso et al., 2003).

Furthermore, in order to minimize the eventual interference of coal combustion in the eBC_{bb} estimated by the aethalometer model, the events in which coal combustion tracers (As and Se) (Vejahati et al., 2010; C. Wang et al., 2018) were registered, have been removed from eBC_{bb} analysis. Levoglucosan [biomass burning tracer (Gonçalves et al., 2011)] or ^{14}C measurements (as in Zotter et al. 2017) were not available.

For each rain event, the eBC, eBC_{ff} and eBC_{bb} concentration one hour before and one hour after precipitation have been analysed. In order to determine the eBC concentration change between time intervals t_1 and t_2, with eBC concentrations c_1 and c_2, respectively, the following parameter was calculated:

$$\Delta eBC_{rel} = -100\frac{\Delta eBC}{c_1} \qquad \textit{Eq. 9.1}$$

where $\Delta eBC = c_2 - c_1$ and the minus sign before 100 has been introduced in order to get a positive value of ΔeBC_{rel} when the eBC concentration decreases (effective scavenging).

Furthermore, for a group of events, a new parameter has been defined as the concentration-weighted average $\left(\Delta eBC\% = \frac{\sum(\Delta eBC_{rel} \cdot c_1)}{\sum c_1}\right)$.

A global analysis of all the events that meet the previously cited requirements was carried out. The average length of rain events in León was 3:28 h with a standard deviation of 4:07 h. The episodes of extreme duration could be referred to as "long events". A possible quantification may be the 10% of the total events or the average plus one standard deviation. Both criteria conducted to the same threshold of about 8 hours. Consequently, events exceeding 8 h were called long events, and the rest short events.

The equation used to estimate eBC scavenging coefficient, was the same often used to calculate scavenging coefficient (λ) from the concentration change c of aerosol particles and other elements like sulphates (Chate et al., 2003; Laakso et al., 2003; Maria and Russell, 2005; Olszowski, 2015b). In this study, C is the eBC concentration. The scavenging coefficient λ (s^{-1}) is defined as a rate of aerosols washout by precipitation.

$$\lambda = -1 \cdot \frac{dC}{dt} \qquad \textit{Eq. 9.2}$$

The integration of this equation between t_1 and t_2 with concentrations C_1 and C_2 gives:

$$\lambda = -\frac{1}{t_1 - t_2} \cdot ln\frac{C_2}{C_1} \qquad \textit{Eq. 9.3}$$

The scavenging coefficient λ varies with collection efficiency, particles and raindrop size distributions and their terminal velocities, for different particle sizes (Seinfeld and Pandis, 2016).

When speaking about an effective scavenging, we will refer to the positive values of $\Delta eBC\%$ and λ. This decrease of the BC concentration can also be influenced by vertical mixing changes or even by advection.

9.2.6. DIURNAL PATTERN NORMALIZATION

We eliminated the important effect of the diurnal cycle on the eBC, eBC_{ff} and eBC_{bb} concentrations by normalizing the daily concentrations to the daily average. For no-rain days during the sampling period, daily patterns of eBC, eBC_{ff} and eBC_{bb} hourly concentration were obtained. The eBC concentration of all days without rain between March 2016 and August 2017 were used and the seasonal daily patterns were calculated in the following way: first of all, for

each day, the ratio between the hourly eBC concentration and the mean eBC concentration of that day was calculated. With the daily normalised values, the average diurnal pattern was determined. In other words, we have calculated the hourly ratio ($R_{i,j}$) of the diurnal pattern for the hour *i* of the day *j* through the following formula:

$$R_{i,j} = \frac{c_{i,j}}{\bar{c}_j} \qquad \textit{Eq. 9.4}$$

where $\bar{c}_j = \frac{\sum_i c_{i,j}}{n}$, *n* being the number of hours in one day (24). We have subsequently determined the average R_i mean for each season:

$$R_i = \frac{\sum_j R_{i,j}}{d} \qquad \textit{Eq. 9.5}$$

d being the number of complete sampling days without rain for each season (22, 52, 81, 70, 81 and 62 days for winter 2016, spring 2016, summer 2016, autumn 2016, winter 2017 and summer 2017, respectively).

9.3. RESULTS AND DISCUSSION

The seasonal eBC values in León, during sampling are presented in Table S9.1. eBC_{ff} values registered during autumn 2016 and winter 2017 are higher probably due to the increase in road traffic and the use of heating devices. In all seasons, there were two peaks throughout the day (0600-0800 and 1600-2000 UTC), mainly during rush hours' traffic (Figure S9.3). In the afternoons, heating emissions add to the afternoon peak. Likewise, eBC_{bb} values in winter and autumn were higher, because of the use of biomass for heating. Other cities like Beijing, Leicester, Hefei or Kadapa, have shown the same pattern (Begam et al., 2016; Cheng et al., 2014; S. M. L. Hama et al., 2017; X. Zhang et al., 2015; Y. Zhang et al., 2017) caused by traffic and domestic heating.

9.3.1. RAIN EFFECT ON EBC CONCENTRATION

Seventy-five rain events were observed during the sampling period. The rain events are concentrated in winter and spring, showing a clear decrease in summer (Figure S9.4).

9.3.1.1. Rain events characteristics

The main characteristics of short and long events are shown in Table 9.1. Seven long events were observed during the sampling period. There was an effective eBC scavenging in 6 events (86% of total), with a mean decrease of 48±37%. Long events featured the mean raindrop diameter of 0.34±0.19 mm, with a mean swept volume per event of $1.9 \cdot 10^{10}$ mm^3 m^{-3} and a mean number of drops of $8.8 \cdot 10^7$ m^{-2}. Of the 75 events registered, 68 rain events were short. There was an effective eBC scavenging in 49 of the short events (73% of total), with a mean decrease of 39±38%. The mean raindrop diameter for short events was 0.34±0.20 mm, with a mean swept volume per event of $2.5 \cdot 10^9$ mm^3 m^{-3} and a mean number of drops of $9.0 \cdot 10^6$ m^{-2}.

The decrease in eBC_{bb} concentration in both short and long events is significantly higher compared to eBC_{ff}. This fact is probably due to the higher fraction of organics from biomass burning, and also a higher degree of oxygenation (O:C) of biomass burning organic aerosol compared to traffic organic aerosol, thus increasing its hydrophilic property (Cerully et al., 2011; Safai et al., 2014; Zheng et al., 2017). In addition, the size including the organics for wood burning being larger than for traffic emissions may play a role. Following the criteria given in section 2.5 (more specifically, the criterium c), the events considered to determine the eBC, eBC_{ff} and eBC_{bb} values were different. Therefore, the eBC value may not lie between the eBC_{ff} and eBC_{bb} specific ones.

Table 9.1. Number of rain events (*N*), percentage of rain events with effective scavenging (% of events) and mean decrease (and standard deviation) in BC concentration (*ΔeBC%*).

	Short events (<8 h)			Long events (>8 h)		
	N	% of events	*ΔeBC%*	*N*	% of events	*ΔeBC%*
eBC	68	73	39±38	7	86	48±37
eBC_{ff}	60	75	40±33	7	71	46±30
eBC_{bb}	27	85	75±46	3	67	96±5

9.3.1.2. Extreme scavenging events

According to the scavenging efficiency, a classification of rain events in three groups has been carried out: type I (ΔeBC_{rel} higher than 50%), type II (ΔeBC_{rel} between 0-50%) and type III (non-effective scavenging) (Table 9.2). It can be seen that events with more effective scavenging were characterised by: i) a longer duration of events, ii) a greater precipitation accumulated and iii) a higher wind intensity. The events with no scavenging effect featured somewhat lower eBC concentration before rain. However, there were no major differences in the rainfall parameters analysed between types II and III.

The event with the highest scavenging efficiency occurred on 21st March 2017 with an accumulated rainfall of 3.05 mm and a mean rainfall intensity of 0.57 mm h^{-1}. The maximum intensity was 0.05 mm min^{-1}. The rain started at 0800 UTC and lasted 228 min. The eBC concentration was 2.62 μg m^{-3} and 0.22 μg m^{-3} two hours before and two hours after rain, respectively (ΔeBC_{rel} = 88%). The mean raindrop size was 0.44±0.22 mm and the mode of raindrop size was 0.31 mm. The swept volume was $6.2 \cdot 10^{9}$ mm^{3} m^{-3}.

On the other hand, the event with the highest eBC percentage increase occurred on 24th February 2016 with an accumulated rainfall of 1.92 mm and a mean rainfall intensity of 3.96 mm h^{-1}. The maximum intensity was 0.06 mm min^{-1}. An eBC increase was registered, with 1.33 μg m^{-3} and 1.98 μg m^{-3} two hours before and two hours after rain, respectively (ΔeBC_{rel} = -34%). The rain started at 1149 UTC and lasted 173 min. The mean raindrop size was 0.32±0.19 mm and the mode of raindrop sizes was 0.27 mm. The swept volume was $2.8 \cdot 10^{9}$ mm^{-3} m^{-3}. An explanation could be the change from a deep mixing layer to a shallow one, as proposed by Talukdar et al. (2015) for Calcutta. Thus, the change in surface and air temperature reduced the mixing layer height and the eBC concentration increased.

Besides, another contribution to the differences in scavenging efficiency may be the higher swept volume recorded in the event with effective scavenging, caused by a longer event duration and a higher raindrop diameter.

Table 9.2. Mean and standard deviation values of rain parameters for the three types of events stablished according to the scavenging efficiencies.

	N	Duration (h:min)	Rain (mm)	Rainfall intensity (mm h^{-1})	Wind speed (m s^{-1})	Raindrop diameter (mm)	eBC before rain (μg m^{-3})	Swept volume (mm^3 m^{-3})
Type I (ΔeBC_{rel} >50%)	18	4:24±3:30	8.2±12.5	1.2±1.3	1.9±1.3	0.31±0.09	1.1±0.7	$9.6 \cdot 10^9$
Type II (ΔeBC_{rel} 0-50%)	39	2:47±2:32	2.4±3.4	0.7±0.8	1.1±1.3	0.36±0.09	1.1±0.5	$3.0 \cdot 10^9$
Type III (ΔeBC_{rel} <0%)	15	2:36±2:08	1.8±3.0	0.5±0.4	1.2±1.0	0.35±0.06	0.9±0.4	$2.9 \cdot 10^9$

9.3.2. AIR MASSES ORIGIN AND WEATHER TYPES

The four-days back trajectories of air masses arriving in León at 1000 m a.g.l. were obtained from HYSPLIT model. In Figure S9.5 the seasonal back trajectories for rain events are shown.

The main origins of air masses during rain events were Atlantic (33%), Continental (20%) and North Atlantic (19%) (Table S9.2). In winter 2017, there was a prevalence of air mass coming from North Atlantic (56%), and in summer 2017 there was a high frequency of air masses with Saharan origin (56%). The highest values of eBC concentrations were recorded in air masses coming from North America (during winter 2017) and in intrusions from Sahara (during summer 2017). No significant statistical differences were observed in eBC concentration between air masses during rainy days.

The air masses presented the following effective ($eBC_{initial} > eBC_{final}$) scavenging values: Arctic (29±21%), North Atlantic (35±31%) and Saharan (18±21%). However, Continental (6±39%), North America (6±7%) and Atlantic (4±39%) masses present a lower mean eBC decrease (Table S9.3), maybe due to the high eBC load transported by these air masses.

The most frequent weather types during rain events were C (23 cases) and NW (9 cases). There was a decrease in eBC concentration in all the weather types except for NE and AS. NE type is noteworthy, since it comprises many events. The two AS events were characterised by a stagnation of the air mass coming from Sahara. On the other hand, during NW rain events (9 cases), a *ΔeBC%* of 45% was registered. Other weather types with W component, like W, SW, ANW, CW and AW present a clear decrease (Table S9.3). Figure 9.1 shows the *ΔeBC%* regarding the origin of air (according to Weather Lamb type). There was an effective scavenging in all components except NE, indicative of an eBC source in these directions. This increase coincides with that observed in Continental masses based on HYSPLIT trajectories.

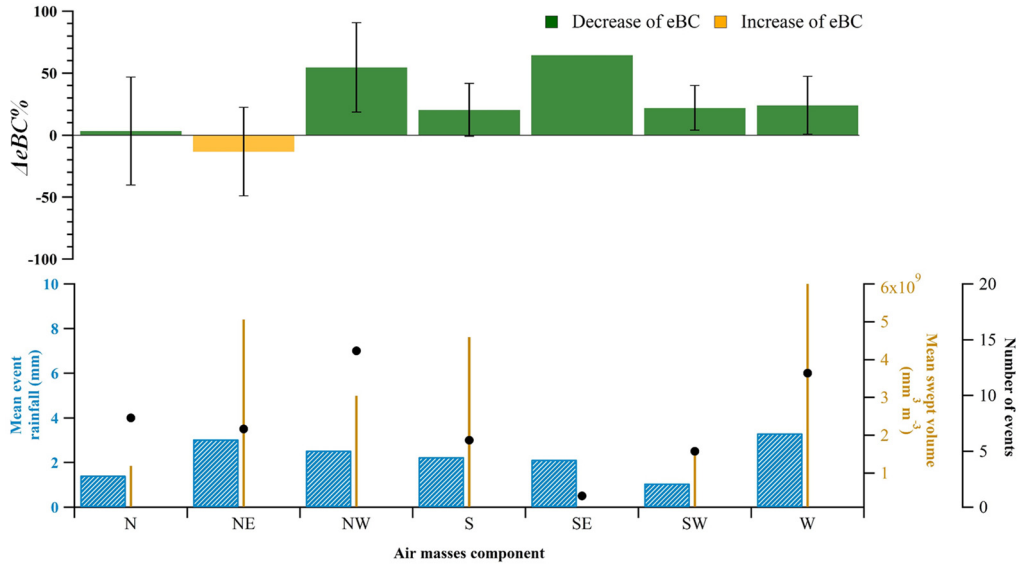

Figure 9.1. *ΔeBC%* between before and after rain according to air mass origin of Circulation Weather Types (CWTs) during rain events. Black dots indicate the number of rain events, striped boxes indicate the mean rainfall (mm) and vertical lines indicate the mean swept (mm^3 m^{-3}) per event.

During rain events of pure anticyclonic type, there was an increase in eBC concentration of 27%, and a mean raindrop diameter of 0.30±0.09 mm. On the contrary, when the type was pure cyclonic, a decrease in eBC concentration of 1% was recorded, with a mean raindrop diameter of 0.36±0.07 mm.

9.3.3. SCAVENGING COEFFICIENTS

During the 68 rain short events (with a mean intensity of 0.82 mm h^{-1}), λ for eBC showed a mean value of $4.7 \cdot 10^{-5}$ s^{-1} (with a standard deviation of $8.4 \cdot 10^{-5}$ s^{-1}) and a median of $4.0 \cdot 10^{-5}$ s^{-1} (interquartile range: $-8.8 \cdot 10^{-6}$ to $7.92 \cdot 10^{-5}$ s^{-1}). Positive values of λ are indicative of effective scavenging (Table 9.3).

In the 7 rain long events (with a mean intensity of 1.42 mm h^{-1}), λ for eBC indicated a mean value of $1.0 \cdot 10^{-5}$ s^{-1} (with a standard deviation of $1.1 \cdot 10^{-5}$ s^{-1}) and a median of $1.1 \cdot 10^{-5}$ s^{-1} (interquartile range: $3.7 \cdot 10^{-6}$ to $1.9 \cdot 10^{-5}$ s^{-1}). It should be noted that λ for eBC_{bb} in short events was around three to four times higher than λ of eBC and eBC_{ff}. The λ for eBC in short events was about four times the value obtained for long events. However, *ΔeBC%* was greater in long events (Table 9.1). Thus, the greater decreased in long events may be caused by the great long duration of events. To estimate the effect of rain duration on the *ΔeBC%*, the correlation between both variables was analysed. A correlation coefficient r^2 of 0.14 was obtained, which means that the rain duration explains a 14% of the total variance of *ΔeBC%*.

Table 9.3. Scavenging coefficients (λ) in s^{-1} of eBC, eBC_{ff} and eBC_{bb} in short and long events. Number of events are in brackets.

	SHORT EVENTS (68)			LONG EVENTS (7)		
	λ (eBC) (68)	λ (eBC_{ff}) (68)	λ (eBC_{bb}) (27)	λ (eBC) (7)	λ (eBC_{ff}) (7)	λ (eBC_{bb}) (3)
Min	$-1.3\cdot10^{-4}$	$-1.0\cdot10^{-4}$	$-8.0\cdot10^{-5}$	$-6.7\cdot10^{-6}$	$-6.6\cdot10^{-6}$	$-9.5\cdot10^{-6}$
Q1	$-8.8\cdot10^{-6}$	$-9.2\cdot10^{-6}$	$2.2\cdot10^{-6}$	$3.7\cdot10^{-6}$	$-3.4\cdot10^{-5}$	$1.1\cdot10^{-5}$
Median	$4.0\cdot10^{-5}$	$3.2\cdot10^{-5}$	$6.6\cdot10^{-5}$	$1.1\cdot10^{-5}$	$1.3\cdot10^{-5}$	$3.1\cdot10^{-5}$
Q3	$7.9\cdot10^{-5}$	$9.4\cdot10^{-5}$	$2.5\cdot10^{-4}$	$1.9\cdot10^{-5}$	$2.9\cdot10^{-5}$	$4.7\cdot10^{-5}$
Max	$2.5\cdot10^{-4}$	$2.8\cdot10^{-4}$	$1.1\cdot10^{-3}$	$2.3\cdot10^{-5}$	$3.4\cdot10^{-5}$	$6.4\cdot10^{-5}$
Mean	$4.7\cdot10^{-5}$	$5.1\cdot10^{-5}$	$1.6\cdot10^{-4}$	$1.0\cdot10^{-5}$	$1.3\cdot10^{-5}$	$2.8\cdot10^{-5}$
Desvest	$8.4\cdot10^{-5}$	$8.5\cdot10^{-5}$	$2.6\cdot10^{-4}$	$1.1\cdot10^{-5}$	$1.8\cdot10^{-5}$	$3.7\cdot10^{-5}$

Current information on BC scavenging ratios available in the literature is still scarce. Nevertheless, the values obtained were similar to those indicated by Latha et al. (2005) ($1.64\cdot10^{-5}$ s^{-1}) in India, although their value was obtained using a different method. The observed differences could be due to the lower BC concentrations in León (8 times lower than in its location, Hyderabad and Secunderabad, India).

A global analysis of rain events gives positive values of λ for eBC (indicative of an effective scavenging), higher for short events. Furthermore, these λ values are in the same order of magnitude that those obtained in other studies about fine and ultrafine aerosols (Laakso et al., 2003; Zikova and Zdimal, 2016).

9.3.4. RELATION BETWEEN LAMBDA AND METEOROLOGICAL PARAMETERS

For each rain event, the λ value has been related to the wind intensity and the rainfall intensity in order to observe the influence of these meteorological variables on eBC concentration. In Figure 9.2, it can be observed that most of the events presented positive values (effective scavenging). The rain events with intensities greater than 2 mm h^{-1} were scarce but they always presented an effective eBC scavenging. Events with rain intensities less than 2 mm h^{-1} caused an effective eBC scavenging in 70% of cases.

It should be noted that there was no clear influence of the wind speed during rain, although in the events with no effective scavenging, low wind speed dominated. Nevertheless, the wind and the eBC concentration two hours before rain presented a statistically significant negative correlation. The wind causes a higher dispersion of eBC, hindering the scavenging by rain.

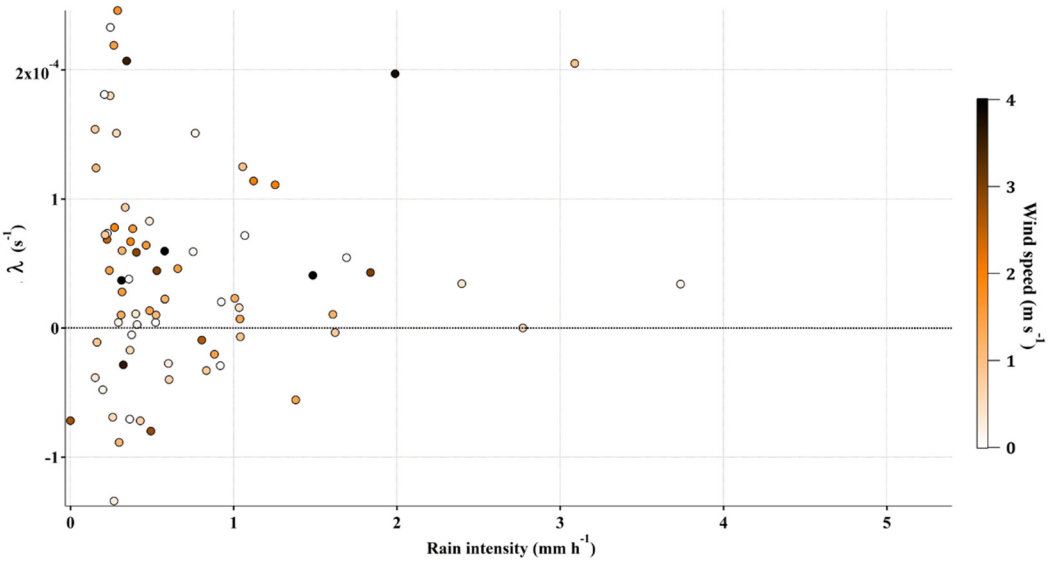

Figure 9.2. Relationship between black carbon scavenging coefficients (λ) and rainfall intensity. Wind speed is indicated by the colour scale inside the dots.

There was a statistically significant negative correlation between event duration and ΔeBC_{rel}. This supports the influence of rain duration over eBC concentration (see Figure S9.6). Other studies have also shown that low intensities and large duration of rain events produce a higher effective scavenging (Chatterjee et al., 2012). Besides, vertical mixing and horizontal advection could also be related with ΔeBC (Joshi et al., 2016), mainly in autumn and winter.

9.3.5. MODEL FOR ΔEBC

To parameterize the ΔeBC, a linear model has been built using aethalometer and disdrometer variables. What variables can be the most appropriate to build this model? Previously, the correlations between ΔeBC and variables like wind speed, eBC concentration before rain, event duration, precipitation accumulated, mean rainfall intensity, mean raindrop diameter and sum of volume swept by falling drops have already been analysed. Furthermore, the raindrop size could also be connected to ΔeBC. In fact, the data obtained from 21 drop size ranges of LPM (between 0.125 and 8 mm) have been used to check the relationship between the number of raindrops in each size channel and the λ in events with efficient scavenging (Table S9.4). As a result, a significant correlation between the λ and the number of drops with diameters between 0.375 and 2.5 mm has been found. The rest of the raindrop diameters did not present significant correlations with λ.

Consequently, the variables tested to build the model have been the following: wind speed, eBC concentration before rain, event duration, precipitation accumulated, mean rainfall intensity, mean raindrop diameter, change in the mixing layer height, sum of volume swept by falling drops and number of drops with diameters between 0.375 and 2.5 mm. Besides, we have included two variables related to the mixing layer height that could affect the rain scavenging: the mean height during rain and the change in height throughout the rain event. The application of an automatic linear modelling (IBM SPSS Statistics 24) by stepwise, with an entry probability of 0.05 and removal probability of 0.10 has been used.

With this methodology, a model has been built from a random sample including the 75% of the total data set. This model has been applied to the remaining 25%. Subsequently, a Kolmogorov-Smirnov statistical test has been carried out in order to check the goodness of fit of the model to the measured data. This process has been repeated ten times and the results are shown in Table S9.5. The significant values obtained ($p>0.05$) shows that null hypothesis is confirmed, measured and predicted data are related and, consequently, the model created may be enforceable.

All ten repetitions of the model include the following variables: eBC concentration before rain, swept volume and precipitation accumulated. Besides, two models also include the mean raindrop diameter. This last variable shows the greater variability.

Finally, a multi-linear regression model has been established ($r^2=0.72$) based on the whole data set. As expected, the model includes the three aforementioned variables, as follows:

$$\Delta eBC = (k_1 \cdot eBC_{\text{before rain}}) + (k_2 \cdot \text{Precipitation accumulated}) + (k_3 \cdot V_{\text{swept}}) + k_4 \quad \textit{Eq. 9.6}$$

The coefficients presented the following values (± standard deviations): $k_1 = -0.557$ (±0.063), $k_2 = -0.0741$ (±0.007) μg m^{-3} mm^{-1}, $k_3 = -3.37 \cdot 10^{-11}$ ($\pm 8.12 \cdot 10^{-12}$) μg mm^{-3} and $k_4 = 0.210$ (±0.083) μg m^{-3}.

Furthermore, a multi-linear regression model has been established for ΔeBC_{ff} ($r^2=0.81$) and ΔeBC_{bb} ($r^2=0.88$).

$$\Delta eBC_{ff} = (k_{1f} \cdot eBC_{\text{before rain}}) + (k_{2f} \cdot \text{Precipitation accumulated}) + (k_{3f} \cdot V_{\text{swept}}) + (k_{4f} \cdot \text{duration}) + k_{5f} \quad \textit{Eq. 9.7}$$

$$\Delta eBC_{bb} = (k_{1b} \cdot eBC_{\text{before rain}}) + (k_{2b} \cdot \emptyset_{raindrop}) + k_{3b} \quad \textit{Eq. 9.8}$$

The coefficients presented the following values for ΔeBC_{ff} (± standard deviations): $k_{1f} = -0.598$ (±0.052), $k_{2f} = 0.044$ (±0.007) μg m^{-3} mm^{-1}, $k_{3f} = -6.44 \cdot 10^{-11}$ ($\pm 1.59 \cdot 10^{-11}$) μg mm^{-3}, $k_{4f} = 0.056$

(±0.02) µg h^{-1} m^{-3} and k_{5f} = 0.153 (±0.068) µg m^{-3}. For ΔeBC_{bb} the values were: k_{1b} = -0.980 (±0.070), k_{2b} = 0.924 (±0.379) µg m^{-3} mm^{-1} and k_{3b} = -0.194 (±0.145) µg m^{-3}. The ΔeBC_{bb} depends more on eBC concentration before rain than ΔeBC. The ΔeBC_{ff} model includes similar variables to ΔeBC model, also incorporating the duration variable.

The model estimates the reduction in eBC well compared to the measured data (Figure 9.3) becoming a valuable tool to predict the eBC behaviour during rain events. Analogous representations for eBC_{ff} (Figure S9.7) and eBC_{bb} (Figure S9.8) are shown in Supplementary material.

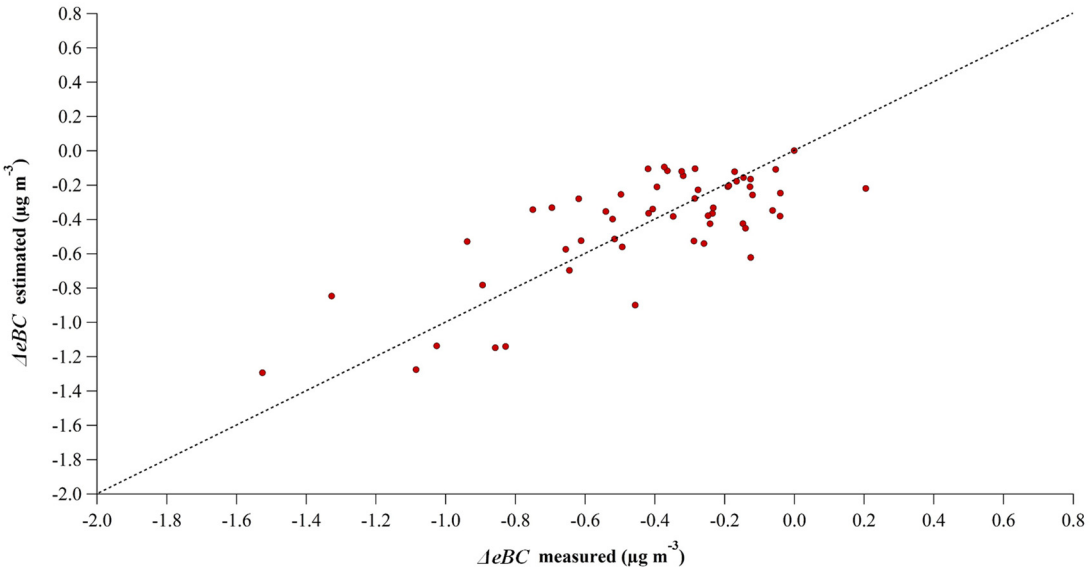

Figure 9.3. ΔeBC estimated by the model vs ΔeBC measured. The dashed line (y=x) shows the perfect estimation.

9.4. CONCLUSIONS

We investigated BC scavenging during rain events in an urban background environment, with these main conclusions:

- In 73% of rain events there was an effective scavenging, with a mean eBC decrease 48±37% in long rain events (>8 h) and 39±38% in short rain events.
- Rain scavenging was analysed depending on air mass origin. The air masses with a clear efficient scavenging came from Arctic ($\Delta eBC\%$=29±21%), North Atlantic (35±31%) and Saharan (18±21%) areas.
- Concerning the BC sources, the scavenging of eBC_{bb} is significantly higher compared to eBC_{ff}, probably due to the increase of its hydrophilicity because of the higher fraction

of organics and a higher degree of oxygenation of biomass burning organic aerosol compared to traffic organic aerosol. Concretely, the scavenging coefficient (λ) mean value of eBC_{ff} for short and long rain events was $5.1 \cdot 10^{-5}$ and $1.3 \cdot 10^{-5}$ s^{-1}, respectively. For eBC_{bb}, the λ values were $1.6 \cdot 10^{-4}$ and $2.8 \cdot 10^{-5}$ s^{-1} in short and long events, respectively.

- Events with intensities higher than 2 mm h^{-1} (the maximum intensity registered in the sampling campaign was 7 mm h^{-1}) always presented an effective scavenging on eBC. However, the highest values of λ were recorded for rain events characterised by a low rainfall intensity and long duration. Furthermore, there was a significant positive correlation between the λ and the number of drops with diameters between 0.375 and 2.5 mm.
- A linear model (r^2=0.72) was built to estimate the *ΔeBC* values with variables from weather station, aethalometer and disdrometer: eBC concentration before rain, swept volume and precipitation accumulated. A Kolmogorov-Smirnov statistical test has confirmed the goodness of fit of the model to the measured data. Finally, two other models have also been proposed to estimate the *ΔeBC* values from biomass burning and fossil fuel combustion.

One of the most important outcomes of the project is the finding that the scavenging of BC depends on the BC source (biomass burning and fossil fuel combustion). This fact could be a key factor to include in the climate models to account both the aerosol-cloud interaction and the radiative forcing caused by clouds and BC.

The combination of aethalometer-disdrometer measurements has proved to be a valuable tool for the quantification of the eBC scavenging, allowing identifying the raindrop variables that contribute to an effective scavenging of this pollutant.

9.5. REFERENCES

Andreae, M., Ramanathan, V., 2013. Climate's dark forcings. Science (80-.). 340, 280–281.

Apte, J.S., Marshall, J.D., Cohen, A.J., Brauer, M., 2015. Addressing Global Mortality from Ambient PM2.5. Environ. Sci. Technol. 49, 8057–8066. doi:10.1021/acs.est.5b01236

Armalis, S., 1999. Wet deposition of elemental carbon in Lithuania. Sci. Total Environ. 239, 89–93. doi:10.1016/S0048-9697(99)00288-0

Becerril-Valle, M., Coz, E., Prévôt, A.S.H., Močnik, G., Pandis, S.N., Sánchez de la Campa, A.M., Alastuey, A., Díaz, E., Pérez, R.M., Artíñano, B., 2017. Characterization of atmospheric black carbon

and co-pollutants in urban and rural areas of Spain. Atmos. Environ. 169, 36-53. doi:10.1016/j.atmosenv.2017.09.014

Begam, G.R., Vachaspati, C.V., Ahammed, Y.N., Kumar, K.R., Babu, S.S., Reddy, R.R., 2016. Measurement and analysis of black carbon aerosols over a tropical semi-arid station in Kadapa, India. Atmos. Res. 171, 77–91. doi:10.1016/j.atmosres.2015.12.014

Bond, T.C., Doherty, S.J., Fahey, D.W., Forster, P.M., Berntsen, T., Deangelo, B.J., Flanner, M.G., Ghan, S., Kürcher, B., Koch, D., Kinne, S., Kondo, Y., Quinn, P.K., Sarofim, M.C., Schultz, M.G., Schulz, M., Venkataraman, C., Zhang, H., Zhang, S., Bellouin, N., Guttikunda, S.K., Hopke, P.K., Jacobson, M.Z., Kaiser, J.W., Klimont, Z., Lohmann, U., Schwarz, J.P., Shindell, D., Storelvmo, T., Warren, S.G., Zender, C.S., 2013. Bounding the role of black carbon in the climate system: A scientific assessment. J. Geophys. Res. Atmos. 118, 5380–5552. doi:10.1002/jgrd.50171

Budhavant, K.B., Rao, P.S.P., Safai, P.D., Leck, C., Rodhe, H., 2016. Black carbon in cloud-water and rain water during monsoon season at a high altitude station in India. Atmos. Environ. 129, 256–264. doi:10.1016/j.atmosenv.2016.01.028

Calvo, A.I., Pont, V., Olmo, F.J., Castro, A., Alados-Arboledas, L., Vicente, A.M., Fernández-Raga, M., Fraile, R., 2012. Air masses and weather types: A useful tool for characterizing precipitation chemistry and wet deposition. Aerosol Air Qual. Res. 12, 856–878. doi:10.4209/aaqr.2012.03.0068

Castro, A., Alonso-Blanco, E., González-Colino, M., Calvo, A.I., Fernández-Raga, M., Fraile, R., 2010. Aerosol size distribution in precipitation events in León, Spain. Atmos. Res. 96, 421–435. doi:10.1016/j.atmosres.2010.01.014

Cerqueira, M., Pio, C., Legrand, M., Puxbaum, H., Kasper-Giebl, A., Afonso, J., Preunkert, S., Gelencsér, A., Fialho, P., 2010. Particulate carbon in precipitation at European background sites. J. Aerosol Sci. 41, 51–61. doi:10.1016/j.jaerosci.2009.08.002

Cerully, K.M., Raatikainen, T., Lance, S., Tkacik, D., Tiitta, P., Petäjä, T., Ehn, M., Kulmala, M., Worsnop, D.R., Laaksonen, A., Smith, J.N., Nenes, A., 2011. Aerosol hygroscopicity and CCN activation kinetics in a boreal forest environment during the 2007 EUCAARI campaign. Atmos. Chem. Phys. 11, 12369–12386. doi:10.5194/acp-11-12369-2011

Chate, D.M., 2005. Study of scavenging of submicron-sized aerosol particles by thunderstorm rain events. Atmos. Environ. 39, 6608–6619. doi:10.1016/j.atmosenv.2005.07.063

Chate, D.M., Rao, P.S.P., Naik, M.S., Momin, G.A., Safai, P.D., Ali, K., 2003. Scavenging of aerosols and their chemical species by rain. Atmos. Environ. 37, 2477–2484. doi:10.1016/S1352-2310(03)00162-6

Chatterjee, A., Das, S., Ghosh, S., Raha, S., 2012. Wet scavenging of black carbon and sulphate depends on the nature of the rain; effect on the climate and global change, in: EGU General Assembly Conference Abstracts. p. 8392.

Cheng, Y.H., Liao, C.W., Liu, Z.S., Tsai, C.J., Hsi, H.C., 2014. A size-segregation method for monitoring the diurnal characteristics of atmospheric black carbon size distribution at urban traffic sites. Atmos. Environ. 90, 78–86. doi:10.1016/j.atmosenv.2014.03.023

Conrady, K., Heinke Schlünzen, K., Herber, A., 2013. Atmospheric concentration of black carbon in the western Arctic. Universität Hamburg.

Corrigan, C.E., Ramanathan, V., Schauer, J.J., 2006. Impact of monsoon transitions on the physical and optical properties of aerosols. J. Geophys. Res. Atmos. 111, 1–15. doi:10.1029/2005JD006370

Custódio, D., Cerqueira, M., Fialho, P., Nunes, T., Pio, C., Henriques, D., 2014. Wet deposition of particulate carbon to the Central North Atlantic Ocean. Sci. Total Environ. 496, 92–99. doi:10.1016/j.scitotenv.2014.06.103

Draxler, R., Rolph, G., 2012. HYSPLIT (Hybrid Single-Particle Lagrangian Integrated Trajectory). Silver Spring, MD NOAA Air Resour. Lab.

EEA, 2016. Air quality in Europe - 2016 Report. Copenhagen, Denmark. doi:10.2800/413142

EEA, 2013. Air Quality in Europe - 2013 Report. Copenhagen, Denmark. doi:10.2800/92843

Fernández-Raga, M., Castro, A., Palencia, C., Calvo, A.I., Fraile, R., 2009. Rain events on 22 October 2006 in León (Spain): Drop size spectra. Atmos. Res. 93, 619–635. doi:10.1016/j.atmosres.2008.09.035

Font, A., Fuller, G.W., 2016. Did policies to abate atmospheric emissions from traffic have a positive effect in London? Environ. Pollut. 218, 463–474. doi:10.1016/j.envpol.2016.07.026

Fröhlich-Nowoisky, J., Kampf, C.J., Weber, B., Huffman, J.A., Pöhlker, C., Andreae, M.O., Lang-Yona, N., Burrows, S.M., Gunthe, S.S., Elbert, W., Su, H., Hoor, P., Thines, E., Hoffmann, T., Després, V.R., Pöschl, U., 2016. Bioaerosols in the Earth system: Climate, health, and ecosystem interactions. Atmos. Res. 182, 346–376. doi:10.1016/j.atmosres.2016.07.018

Gonçalves, C., Alves, C., Fernandes, A.P., Monteiro, C., Tarelho, L., Evtyugina, M., Pio, C., 2011. Organic compounds in PM2.5 emitted from fireplace and woodstove combustion of typical Portuguese wood species. Atmos. Environ. 45, 4533–4545. doi:10.1016/j.atmosenv.2011.05.071

Granat, L., Engström, J.E., Praveen, S., Rodhe, H., 2010. Light absorbing material (soot) in rainwater and in aerosol particles in the Maldives. J. Geophys. Res. Atmos. 115, 1–12. doi:10.1029/2009JD013768

Hama, S.M.L., Cordell, R.L., Kos, G.P.A., Weijers, E.P., Monks, P.S., 2017. Sub-micron particle number size distribution characteristics at two urban locations in Leicester. Atmos. Res. 194, 1–16. doi:10.1016/j.atmosres.2017.04.021

Hansen, A.D.A., 2005. The Aethalometer, Magee Scientific Corporation.

Hansen, A.D.A., Rosen, H., Novakov, T., 1984. The aethalometer - An instrument for the real-time measurement of optical absorption by aerosol particles. Sci. Total Environ. 36, 191–196. doi:10.1016/0048-9697(84)90265-1

Harrison, R.M., Beddows, D.C.S., Jones, A.M., Calvo, A., Alves, C., Pio, C., 2013. An evaluation of some issues regarding the use of aethalometers to measure woodsmoke concentrations. Atmos. Environ. 80, 540–548. doi:10.1016/j.atmosenv.2013.08.026

HEI Review Panel, 2013. Understanding the Health Effects of Ambient Ultrafine Particles. Heal. Eff. Inst. 122.

Hienola, A.I., Pietikäinen, J.P., Jacob, D., Pozdun, R., Petäjä, T., Hyvärinen, A.P., Sogacheva, L., Kerminen, V.M., Kulmala, M., Laaksonen, A., 2013. Black carbon concentration and deposition estimations in Finland by the regional aerosol-climate model REMO-HAM. Atmos. Chem. Phys. 13, 4033–4055. doi:10.5194/acp-13-4033-2013

ICCP, 2014. Climate Change 2014 Impacts, Adaptation, and Vulnerability Part B: Regional Aspects, Igarss 2014. doi:10.1007/s13398-014-0173-7.2

Jansen, K.L., Larson, T. V., Koenig, J.Q., Mar, T.F., Fields, C., Stewart, J., Lippmann, M., 2005. Associations between health effects and particulate matter and black carbon in subjects with respiratory disease. Environ. Health Perspect. 113, 1741–1746. doi:10.1289/ehp.8153

Janssen, N.A.H., Hoek, G., Simic-Lawson, M., Fischer, P., van Bree, L., ten Brink, H., Keuken, M., Atkinson, R.W., Anderson, H.R., Brunekreef, B., Cassee, F.R., 2011. Black Carbon as an Additional Indicator of the Adverse Health Effects of Airborne Particles Compared with PM10 and PM2.5. Environ. Health Perspect. 119, 1691–1699. doi:10.1289/ehp.1003369

Kinney, P.L., 2008. Climate Change, Air Quality, and Human Health. Am. J. Prev. Med. 35, 459–467. doi:10.1016/j.amepre.2008.08.025

Kyrö, E.M., Grönholm, T., Vuollekoski, H., Virkkula, A., Kulmala, M., Laakso, L., 2009. Snow scavenging of ultrafine particles: Field measurements and parameterization. Boreal Environ. Res. 14, 527–538.

Laakso, L., Grönholm, T., Rannik, Ü., Kosmale, M., Fiedler, V., Vehkamäki, H., Kulmala, M., 2003. Ultrafine particle scavenging coefficients calculated from 6 years field measurements. Atmos. Environ. 37, 3605–3613. doi:10.1016/S1352-2310(03)00326-1

Ladino, L., Stetzer, O., Hattendorf, B., Günther, D., Croft, B., Lohmann, U., 2011. Experimental Study of Collection Efficiencies between Submicron Aerosols and Cloud Droplets. J. Atmos. Sci. 68, 1853–1864. doi:10.1175/JAS-D-11-012.1

Lamb, H.H., 1972. British Isles Weather Types and a Register of the Daily Sequence of Circulation Patterns 1861-1971, Geophysical memoirs. H.M. Stationery Office.

Latha, K., Badarinath, K.V.S., Manikya Reddy, P., 2005. Scavenging efficiency of rainfall on black carbon aerosols over an urban environment. Atmos. Sci. Lett. 6, 148–151. doi:10.1002/asl.108

Lelieveld, J., Evans, J.S., Fnais, M., Giannadaki, D., Pozzer, A., 2015. The contribution of outdoor air pollution sources to premature mortality on a global scale. Nature 525, 367–371. doi:10.1038/nature15371

Maria, S.F., Russell, L.M., 2005. Organic and inorganic aerosol below-cloud scavenging by suburban New Jersey precipitation. Environ. Sci. Technol. 39, 4793–4800. doi:10.1021/es0491679

Menon, S., Hansen, J., Nazarenko, L., Luo, U., 2002. Climate Effects of Black Carbon Aerosols in China and India. Science (80-.). 297, 2250–2253. doi:10.1126/science.1075159

Mori, T., Kondo, Y., Ohata, S., Moteki, N., Matsui, H., Oshima, N., Iwasaki, A., 2014. Wet deposition of black carbon at a remote site in the East China Sea 1–25. doi:10.1002/2013JD020968.Received

Novakov, T., 1984. The role of soot and primary oxidants in atmospheric chemistry. Sci. Total Environ. 36, 1–10. doi:10.1016/0048-9697(84)90241-9

Oduber, F., Castro, A., Calvo, A.I., Blanco-Alegre, C., Alonso-Blanco, E., Belmonte, P., Fraile, R., 2018. Summer-autumn air pollution in León, Spain: changes in aerosol size distribution and expected effects on the respiratory tract. Air Qual. Atmos. Heal. 11, 505-520. doi:10.1007/s11869-018-0556-6

Olszowski, T., 2015. Concentration Changes Of PM10 Under Liquid Precipitation Conditions. Ecol. Chem. Eng. S 22, 363–378. doi:10.1515/eces-2015-0019

Paramonov, M., Grönholm, T., Virkkula, A., 2011. Below-cloud scavenging of aerosol particles by snow at an urban site in Finland. Boreal Environ. Res. 16, 304–320. doi:10.1017/CBO9781107415324.004

Petzold, A., Ogren, J.A., Fiebig, M., Laj, P., Li, S.M., Baltensperger, U., Holzer-Popp, T., Kinne, S., Pappalardo, G., Sugimoto, N., Wehrli, C., Wiedensohler, A., Zhang, X.Y., 2013. Recommendations for reporting black carbon measurements. Atmos. Chem. Phys. 13, 8365–8379. doi:10.5194/acp-13-8365-2013

Pöschl, U., 2005. Atmospheric aerosols: Composition, transformation, climate and health effects. Angew. Chemie - Int. Ed. 44, 7520–7540. doi:10.1002/anie.200501122

Quinn, P., Stohl, A., Arneth, A., Berntsen, T., 2011. AMAP, 2011. The impact of black carbon on Arctic climate., Arctic Monitoring and Assessment Programme (AMAP), Oslo.

Righi, M., Klinger, C., Eyring, V., Hendricks, J., Lauer, A., Petzold, A., 2011. Climate impact of biofuels in shipping: Global model studies of the aerosol indirect effect. Environ. Sci. Technol. 45, 3519–3525. doi:10.1021/es1036157

Russo, A., Trigo, R.M., Martins, H., Mendes, M.T., 2014. NO2, PM10 and O3 urban concentrations and its association with circulation weather types in Portugal. Atmos. Environ. 89, 768–785. doi:10.1016/j.atmosenv.2014.02.010

Safai, P.D., Raju, M.P., Rao, P.S.P., Pandithurai, G., 2014. Characterization of carbonaceous aerosols over the urban tropical location and a new approach to evaluate their climatic importance. Atmos. Environ. 92, 493–500. doi:10.1016/j.atmosenv.2014.04.055

Sandradewi, J., Prévôt, A.S.H., Szidat, S., Perron, N., Alfarra, M.R., Lanz, V.A., Weingartner, E., Baltensperger, U.R.S., 2008a. Using aerosol light abosrption measurements for the quantitative determination of wood burning and traffic emission contribution to particulate matter. Environ. Sci. Technol. 42, 3316–3323. doi:10.1021/es702253m

Sandradewi, J., Prévôt, A.S.H., Weingartner, E., Schmidhauser, R., Gysel, M., Baltensperger, U., 2008b. A study of wood burning and traffic aerosols in an Alpine valley using a multi-wavelength Aethalometer. Atmos. Environ. 42, 101–112. doi:10.1016/j.atmosenv.2007.09.034

Seinfeld, J.H., Pandis, S., 2016. Atmospheric from Air Pollution to Climate Change. Atmos. Chem. Phys. 51, 1248. doi:10.1016/0016-7037(87)90252-3

Silverman, D.T., Samanic, C.M., Lubin, J.H., Blair, A.E., Stewart, P.A., Vermeulen, R., Coble, J.B., Rothman, N., Schleiff, P.L., Travis, W.D., Ziegler, R.G., Wacholder, S., Attfield, M.D., 2012. The Diesel Exhaust in Miners Study: A Nested Case-Control Study of Lung Cancer and Diesel Exhaust. JNCI J. Natl. Cancer Inst. 104, 855–868. doi:10.1093/jnci/djs034

Singh, S., Elumalai, S.P., Pal, A.K., 2016. Rain pH estimation based on the particulate matter pollutants and wet deposition study. Sci. Total Environ. 563–564, 293–301. doi:10.1016/j.scitotenv.2016.04.066

Sportisse, B., 2007. A review of parameterizations for modelling dry deposition and scavenging of radionuclides. Atmos. Environ. 41, 2683–2698. doi:10.1016/j.atmosenv.2006.11.057

Suglia, S.F., Gryparis, A., Schwartz, J., Wright, R.J., 2008. Association between traffic-related black carbon exposure and lung function among urban women. Environ. Health Perspect. 116, 1333–1337. doi:10.1289/ehp.11223

Talukdar, S., Jana, S., Maitra, A., Gogoi, M.M., 2015. Characteristics of black carbon concentration at a metropolitan city located near land-ocean boundary in Eastern India. Atmos. Res. 153, 526–534. doi:10.1016/j.atmosres.2014.10.014

Textor, C., Schulz, M., Guibert, S., Kinne, S., Balkanski, Y., Bauer, S., Berntsen, T., Berglen, T., Boucher, O., Chin, M., Dentener, F., Diehl, T., Easter, R., Feichter, H., Fillmore, D., Ghan, S., Ginoux, P., Gong, S., Grini, Hendricks, J., Horowitz, L., Huang, P., Isaksen, I., Iversen, T., Kloster, S., Koch, D., Kirkevåg, A., Kristjansson, J.E., Krol, M., Lauer, A., Lamarque, J.F., Liu, X., Montanaro, V., Myhre, G., Penner, J., Pitari, G., Lamarque, J.F., Liu, X., Montanaro, V., Myhre, G., Penner, J., Pitari, G., Reddy, S., Seland, Ø., Stier, P., Takemura, T., Tie, X., 2006. Analysis and quantification of the diversities of aerosol life cycles within AeroCom. Atmos. Chem. Phys. 6, 1777–1813. doi:10.5194/acpd-5-8331-2005

Tong, Z., Chen, Y., Malkawi, A., Adamkiewicz, G., Spengler, J.D., 2016. Quantifying the impact of traffic-related air pollution on the indoor air quality of a naturally ventilated building. Environ. Int. 89–90, 138–146. doi:10.1016/j.envint.2016.01.016

Tong, Z., Yang, B., Hopke, P.K., Zhang, K.M., 2017. Microenvironmental air quality impact of a commercial-scale biomass heating system. Environ. Pollut. 220, 1112–1120. doi:10.1016/j.envpol.2016.11.025

Tost, H., Jöckel, P., Kerkweg, A., Sander, R., Lelieveld, J., 2006. Technical note: A new comprehensive scavenging submodel for global atmospheric chemistry modelling. Atmos. Chem. Phys. Discuss. 5, 11157–11181. doi:10.5194/acpd-5-11157-2005

Trigo, R.M., DaCamara, C.C., 2000. Circulation weather types y their influence on the precipitation regime in Portugal. Int. J. Clim. 20, 1559–1581. doi:10.1002/1097-0088(20001115)20

UNICEF, 2016. Clear the air for children. The impact of air pollution on children. [WWW Document]. URL https://www.unicef.org/publications/index_92957.html (accessed 11.11.16).

Vejahati, F., Xu, Z., Gupta, R., 2010. Trace elements in coal: Associations with coal and minerals and their behavior during coal utilization - A review. Fuel 89, 904–911. doi:10.1016/j.fuel.2009.06.013

Virkkula, A., Mäkelä, T., Hillamo, R., Yli-Tuomi, T., Hirsikko, A., Hämeri, K., Koponen, I.K., 2007. A Simple Procedure for Correcting Loading Effects of Aethalometer Data. J. Air Waste Manage. Assoc. 57, 1214–1222. doi:10.3155/1047-3289.57.10.1214

Wang, C., Liu, H., Zhang, Y., Zou, C., Anthony, E.J., 2018. Review of arsenic behavior during coal combustion : Volatilization , transformation , emission and removal technologies. Prog. Energy Combust. Sci. 68, 1–28. doi:10.1016/j.pecs.2018.04.001

Weingartner, E., Saathoff, H., Schnaiter, M., Streit, N., Bitnar, B., Baltensperger, U., 2003. Absorption of light by soot particles: Determination of the absorption coefficient by means of aethalometers. J. Aerosol Sci. 34, 1445–1463. doi:10.1016/S0021-8502(03)00359-8

WHO, 2012. Health effects of Black carbon. Copenhagen, Denmark.

Zhang, X., Rao, R., Huang, Y., Mao, M., Berg, M.J., Sun, W., 2015. Black carbon aerosols in urban central China. J. Quant. Spectrosc. Radiat. Transf. 150, 3–11. doi:10.1016/j.jqsrt.2014.03.006

Zhang, Y., Chen, J., Yang, H., Li, R., Yu, Q., 2017. Seasonal variation and potential source regions of PM2.5-bound PAHs in the megacity Beijing, China: Impact of regional transport. Environ. Pollut. 231, 329–338. doi:10.1016/j.envpol.2017.08.025

Zhao, S., Yu, Y., He, J., Yin, D., Wang, B., 2015. Below-cloud scavenging of aerosol particles by precipitation in a typical valley city, northwestern China. Atmos. Environ. 102, 70–78. doi:10.1016/j.atmosenv.2014.11.051

Zheng, X., Zhang, S., Wu, Y., Zhang, K.M., Wu, X., Li, Z., Hao, J., 2017. Characteristics of black carbon emissions from in-use light-duty passenger vehicles. Environ. Pollut. 231, 348–356. doi:10.1016/j.envpol.2017.08.002

Zikova, N., Zdimal, V., 2016. Precipitation scavenging of aerosol particles at a rural site in the Czech Republic. Tellus B 68, 1–14. doi:10.3402/tellusb.v68.27343

Zotter, P., Herich, H., Gysel, M., El-Haddad, I., Zhang, Y., Močnik, G., Hüglin, C., Baltensperger, U., Szidat, S., Prévôt, A.S.H., 2017. Evaluation of the absorption Ångström exponents for traffic and wood burning in the Aethalometer based source apportionment using radiocarbon measurements of ambient aerosol. Atmos. Chem. Phys., 17, 4229-4249. https://doi.org/10.5194/acp-17-4229-2017.

SUPPLEMENTARY MATERIAL

S.9.1. AETHALOMETER MODEL

Assuming that only these two sources exist, the total absorption coefficient $b_{abs,total}\ (\lambda_w)$ at wavelength λ_w is:

$$b_{abs,total}\ (\lambda_w) = b_{abs,ff}\ (\lambda_w) + b_{abs,bb}\ (\lambda_w)$$

where $b_{abs,ff}\ (\lambda_w)$, $b_{abs,bb}\ (\lambda_w)$ are the absorption coefficients of fossil fuel combustion and biomass burning, respectively.

Source apportionment of fossil fuel has been estimated through the following equations:

$$\frac{b_{abs,ff(\lambda_1)}}{b_{abs,ff(\lambda_2)}} = \left(\frac{\lambda_{w1}}{\lambda_{w2}}\right)^{-\mathrm{AAE_{ff}}}$$

$$\mathrm{eBC_{ff}} = \frac{b_{abs,ff(\lambda_2)}}{b_{abs,total(\lambda_2)}} \cdot \mathrm{eBC_{total}}(\lambda_{w2})$$

where $\mathrm{AAE_{ff}}$ is the absorption Ångström exponent for eBC fossil fuel.

S.9.2. TABLES

Table S9.1. Seasonal mean values of eBC (μg m^{-3}), $\mathrm{eBC_{ff}}$ (μg m-3) and $\mathrm{eBC_{bb}}$ (μg m^{-3}) measured at León during sampling (January 2016–August 2017). The values next to the mean correspond to the standard deviation.

SEASON	eBC (μg m^{-3})	$\mathrm{eBC_{ff}}$ (μg m^{-3})	$\mathrm{eBC_{bb}}$ (μg m^{-3})
Winter 2016	1.0±0.9	0.8±0.8	0.2±0.3
Spring 2016	0.6±0.5	0.5±0.4	0.1±0.2
Summer 2016	0.6±0.5	0.6±0.4	0.1±0.2
Autumn 2016	1.2±1.1	1.0±1.0	0.2±0.4
Winter 2017	1.3±1.3	1.0±1.2	0.4±0.5
Summer 2017	0.6±0.5	0.5±0.3	0.1±0.2

Table S9.2. Seasonal percentage of air masses origin (four-days before rain events).

Origin	Winter 2016	Spring 2016	Summer 2016	Autumn 2016	Winter 2017	Summer 2017	Total
Arctic	17	11	13	8	0	0	7
Atlantic	17	44	25	50	13	22	35
Continental	0	22	25	21	19	22	19
North America	0	0	0	8	6	0	3
North Atlantic	67	11	0	0	56	0	19
Saharan	0	11	38	13	6	56	17

Table S9.3. Rainfall characteristics and eBC variation based on Circulation Weather Types (CWTs) and air mass origin with HYSPLIT during rain events measured at León during sampling campaign. The values next to the mean correspond to the standard deviation.

		N	Duration (min)	Rain (mm)	Rainfall intensity (mm h^{-1})	Wind speed (m s^{-1})	Raindrop diameter (mm)	eBC before rain (µg m^{-3})	Swept volume (mm^3 m^{-3})	*ΔeBC%*
Lamb Weather type	C	23	313	5±6.8	1.52	0.9±0.7	0.4±0.1	0.9±0.4	$7.2 \cdot 10^9$	-1
	NW	9	173	3.4±4.6	1.07	2.1±1	0.3±0.1	1.1±0.6	$3.7 \cdot 10^9$	-45
	N	8	98	1.4±1.2	0.9	1.2±0.8	0.4±0.1	1.3±0.6	$1.4 \cdot 10^9$	-3
	NE	6	180	3.5±4.4	1.36	0.9±0.7	0.3±0.2	0.9±0.3	$3.4 \cdot 10^9$	22
	W	7	266	3.6±5.3	0.59	2.1±1.4	0.3±0.1	1.1±0.4	$6.5 \cdot 10^9$	-27
	A	5	72	0.3±0.2	0.25	0.4±0.3	0.3±0.1	1.2±0.7	$5.6 \cdot 10^8$	27
	SW	4	120	1.2±1.7	0.47	1.4±0.5	0.3±0.1	0.9±0.4	$1.5 \cdot 10^9$	-29
	ANW	5	108	0.9±1.2	0.45	1.5±1.9	0.4±0.1	1.5±1	$1.7 \cdot 10^9$	-71
	CS	3	140	1.5±0.2	0.92	0.5±0.7	0.4±0.1	1.4±0.9	$1.7 \cdot 10^9$	-38
	CW	3	240	3.4±4.3	1.07	2.2±2.1	0.3±0.1	0.8±0.2	$4.7 \cdot 10^9$	-26
	AS	2	90	0.8±0.3	0.68	1±0	0.4±0.1	0.6±0.2	$1.4 \cdot 10^9$	10
	AW	2	270	2.2±2.6	0.38	0.8±0.3	0.3±0	0.9±0.4	$5.2 \cdot 10^9$	-9
	S	1	480	7.4	0.92	0.1	0.3	0.6	$1.3 \cdot 10^{10}$	-29
	ANE	1	120	0.5	0.23	0	0.3	1	$7.4 \cdot 10^8$	-42
	CSE	1	120	2.1	1.07	0	0.4	1.6	$3.1 \cdot 10^9$	-65
	CSW	1	60	0.6	0.6	0.7	0.4	0.5	$7.5 \cdot 10^8$	8
	A component	13	120	0.9±1.2	0.37	0.7±1.0	0.35±0.08	1.2±0.8	$1.8 \cdot 10^9$	-20
	C component	30	282	4.4±6.2	1.38	0.9±1.0	0.36±0.08	1±0.5	$6.3 \cdot 10^9$	-8
HYSPLIT model	Arctic	6	110	2.8±5.9	0.86	1±1.4	0.4±0.1	1.1±0.6	$2.2 \cdot 10^9$	-29
	Atlantic	27	180	2.8±3.5	1.18	1.3±1.2	0.3±0.1	1±0.5	$4.1 \cdot 10^9$	-4
	Continental	16	281	4±7.5	1.16	0.9±0.6	0.4±0.1	1±0.4	$5.8 \cdot 10^9$	-6
	North America	3	120	1.3±0.4	0.94	0.7±0.6	0.4±0	0.9±0.2	$1.4 \cdot 10^9$	-6
	North Atlantic	15	212	2.5±3.8	0.55	1.7±1.4	0.3±0.1	1±0.5	$3.8 \cdot 10^9$	-35
	Saharan	14	210	3.4±3.9	0.97	0.9±0.8	0.3±0.1	1.3±0.8	$4.6 \cdot 10^9$	-18

Table S9.4. Pearson correlation values between ΔeBC% and rain event characteristics.

	Variable	*ΔeBC%*
Rain event characteristics	Wind intensity (2 hours before rain)	**-0.348**
	Accumulated rain	**-0.225**
	Rain intensity	**-0.227**
	Event duration	**-0.242**
	Swept volume	**-0.230**
Raindrop diameter (mm)	0.125	-0.251
	0.25	-0.223
	0.375	**-0.257**
	0.5	**-0.287**
	0.75	**-0.284**
	1	**-0.281**
	1.25	**-0.278**
	1.5	**-0.276**
	1.75	**-0.269**
	2	**-0.278**
	2.5	**-0.255**
	3	-0.209
	3.5	-0.162
	4	-0.124

***Bold font indicates that the correlation is significant at 95% level.**

Table S9.5. Verification of the model performed (N=10), variables obtained in each N model and Kolmogorov-Smirnov (K-S) statistical test carried out between the predicted and the measured values. In N=0 was represented the model obtained with 100% of data.

N	$eBC_{before\ rain}$	V_{swept}	Precipitation accumulated	$D_{raindrop}$	Intercept	K-S (p)
1	-0.559	$-3.072 \cdot 10^{-11}$	0.040	-	0.217	0.490
2	-0.559	$-3.802 \cdot 10^{-11}$	0.044	1.126	-0.142	0.538
3	-0.636	$-2.979 \cdot 10^{-11}$	0.036	-	0.244	0.456
4	-0.587	$-3.443 \cdot 10^{-11}$	0.041	-	0.249	0.417
5	-0.639	$-2.913 \cdot 10^{-11}$	0.039	-	0.261	0.522
6	-0.559	$-3.072 \cdot 10^{-11}$	0.040	-	0.217	0.490
7	-0.594	$-4.228 \cdot 10^{-11}$	0.045	-	0.276	0.569
8	-0.481	$-3.198 \cdot 10^{-11}$	0.041	0.844	-0.112	0.621
9	-0.587	$-3.443 \cdot 10^{-11}$	0.041	-	0.249	0.373
10	-0.577	$-3.381 \cdot 10^{-11}$	0.041	-	0.246	0.500
0	**-0.557**	$\mathbf{-3.370 \cdot 10^{-11}}$	**0.041**	-	**0.210**	**0.468**

S.9.3. FIGURES

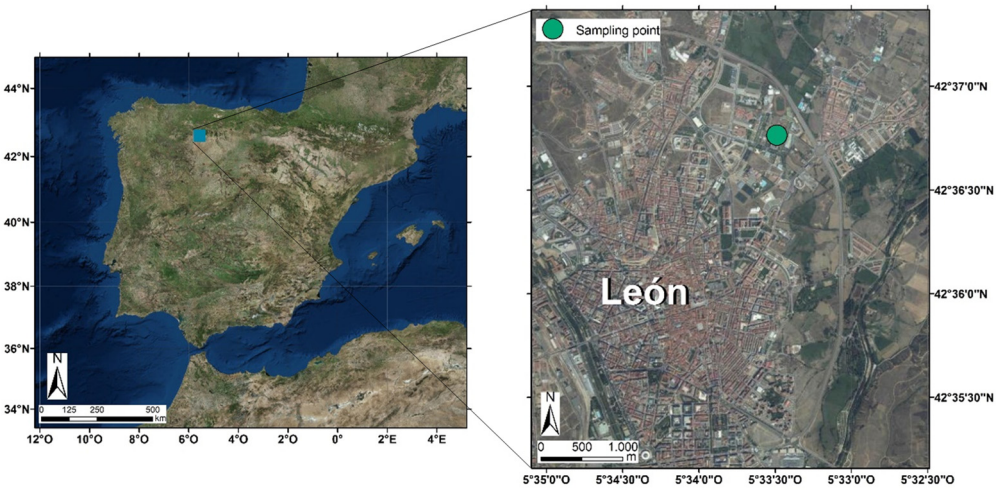

Figure S9.1. León city in the NW Iberian Peninsula and the surroundings of the sampling site. Source: Earthstar Geographics, ESRI.

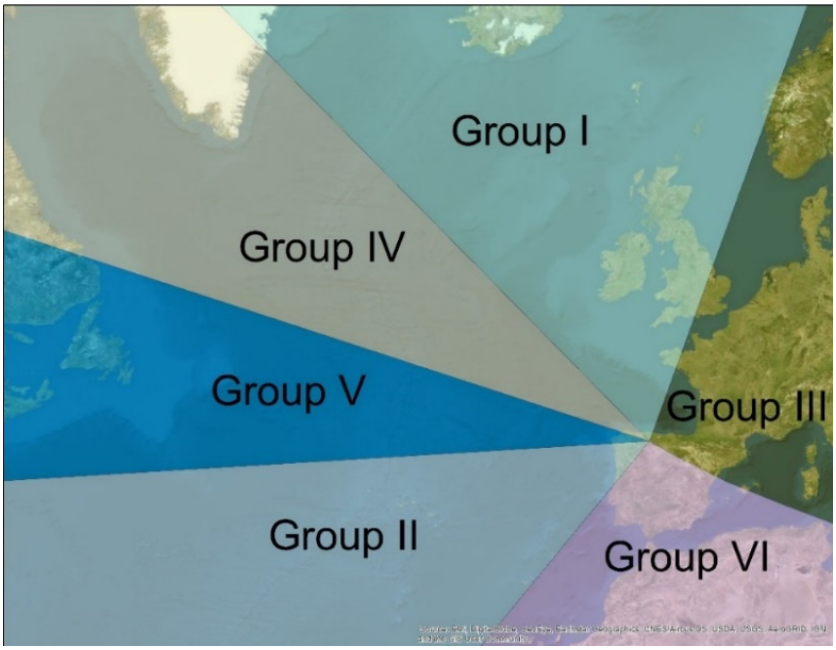

Figure S9.2. Delimitation of regions for the determination of the air masses origin: I: Arctic; II: Atlantic; III: Continental; IV: North America; V: North Atlantic, and VI: Saharan.

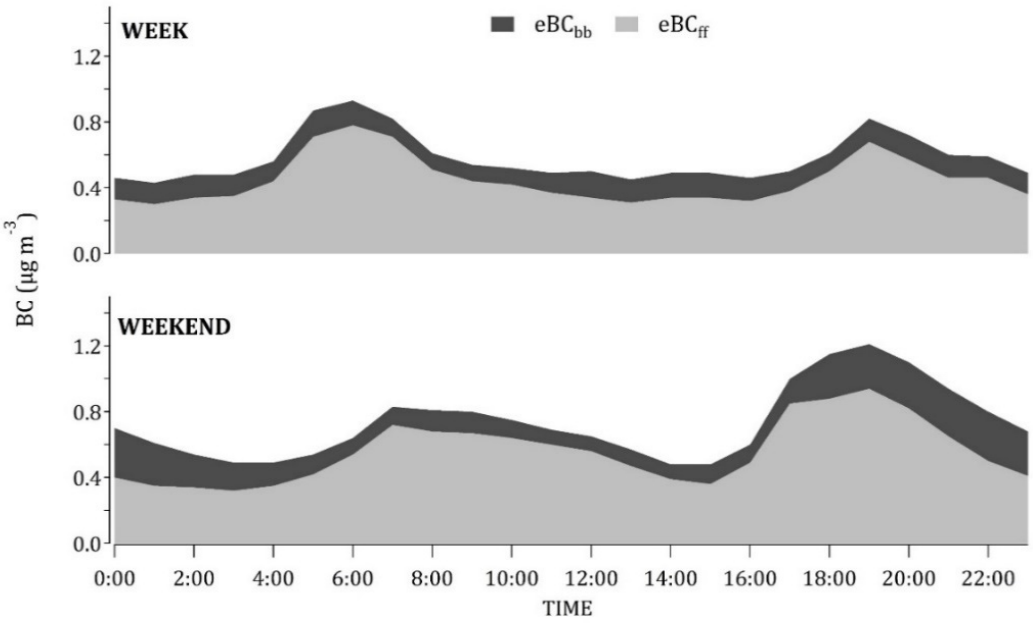

Figure S9.3. Diurnal pattern of eBC_{ff} and eBC_{bb} during summer 2017.

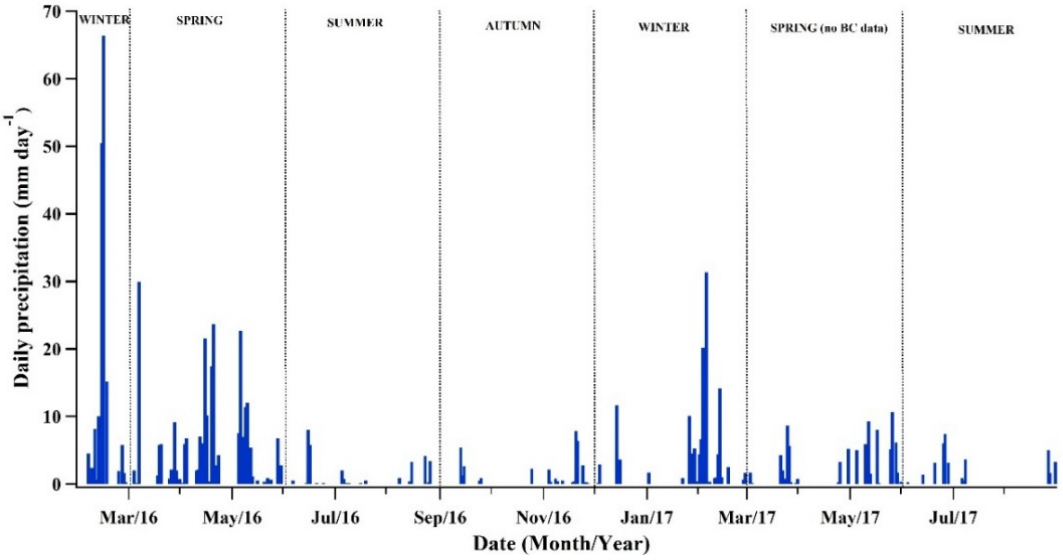

Figure S9.4. Time series of rain events at León during the sampling period.

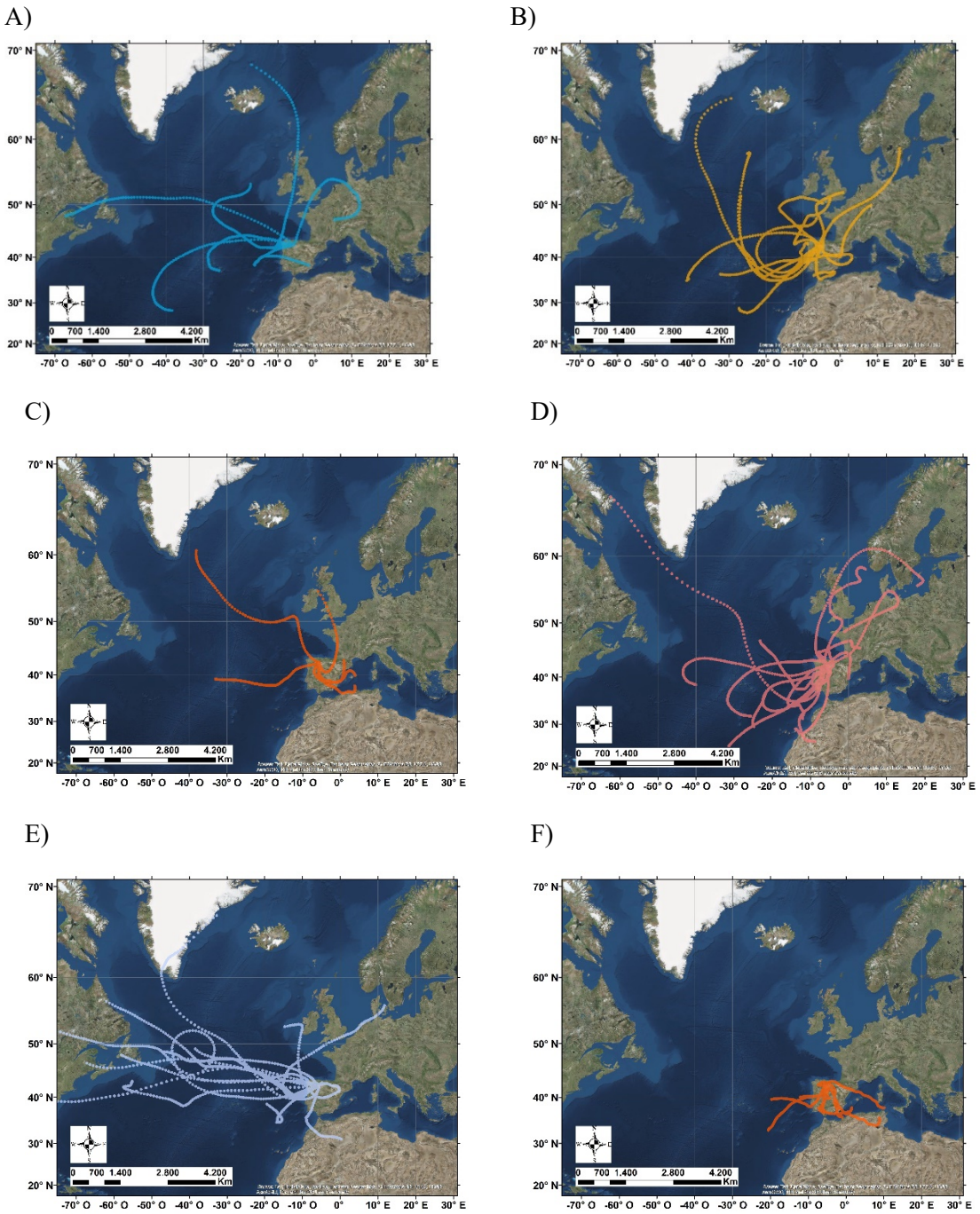

Figure S9.5. Four-days back trajectories arriving at 1000 m a.g.l during rain events in León. A) Winter 2016; B) Spring 2016; C) Summer 2016; D) Autumn 2016; E) Winter 2017; F) Summer 2017.

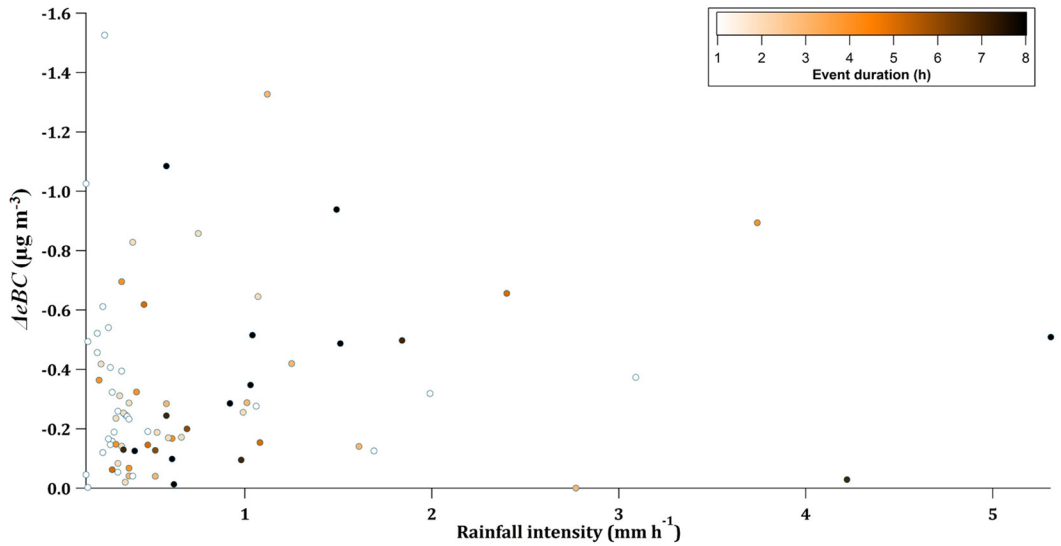

Figure S9.6. *ΔeBC* as a function of rainfall intensity in events with effective scavenging. Colour dots indicate event duration (h).

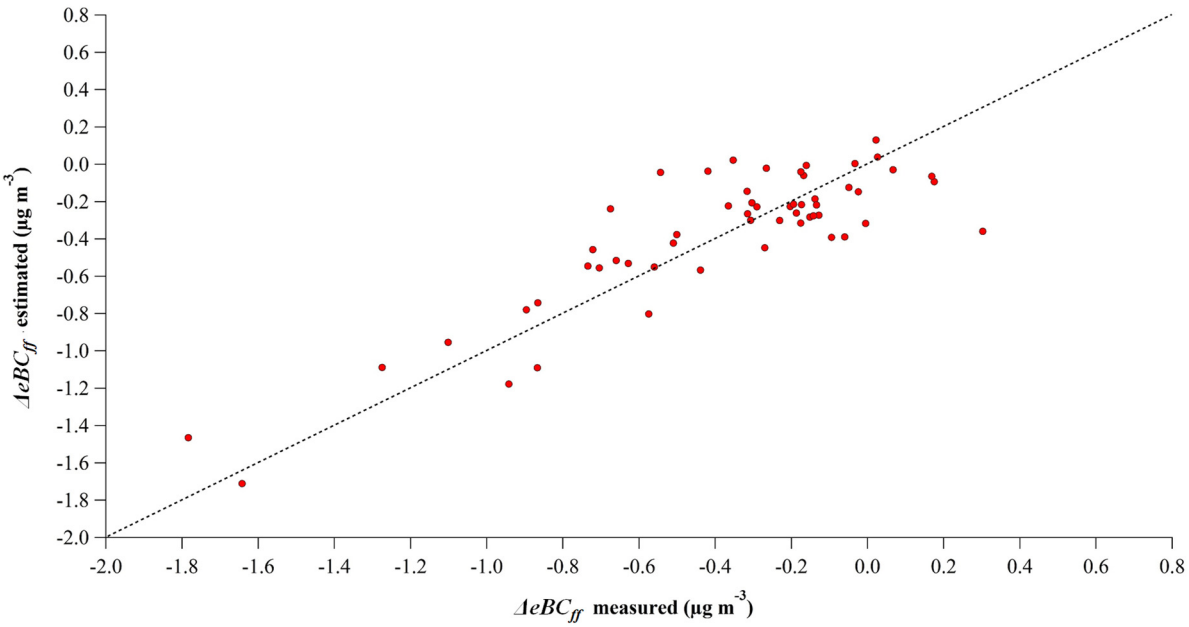

Figure S9.7. ΔeBC_{ff} estimated by the model vs ΔeBC_{ff} measured. The dashed line ($y=x$) shows the perfect estimation.

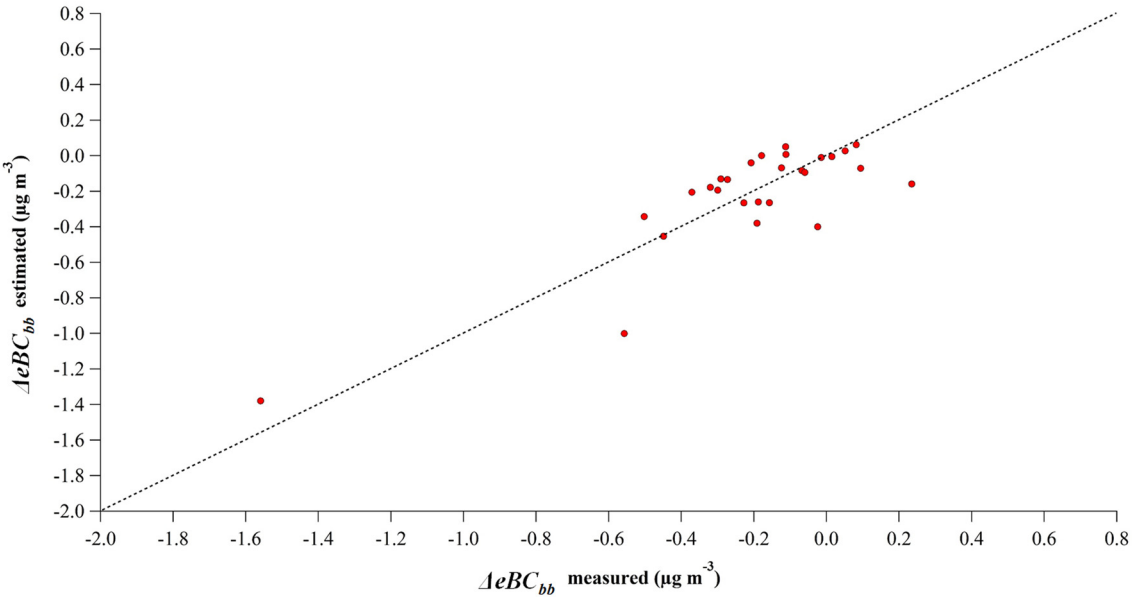

Figure S9.8. ΔeBC_{bb} estimated by the model vs ΔeBC_{bb} measured. The dashed line ($y=x$) shows the perfect estimation.

CHAPTER 10. Towards a model of wet deposition of bioaerosols

Full title: Towards a model of wet deposition of bioaerosols: the raindrop size role

Published in: Science of The Total Environment, 2021, 767, 145426.
DOI: 10.1016/j.scitotenv.2021.145426

10.1. INTRODUCTION

Poor air quality causes a negative impact on human health (Apte et al., 2015; HEI Review Panel, 2013; WHO, 2013) and on the environment (Fröhlich-Nowoisky et al., 2016; Menon et al., 2002; Pöschl, 2005). Air pollutants include the aerosols or particulate matter (PM), that may be bioaerosols (pollen, fungal spore, viruses or bacteria) and non-biological particles (Oduber et al., 2019). Focusing on bioaerosols, and more concretely on pollen, it has to be emphasised that its concentration causes a clear impact on human health, such as lung diseases or allergies. It should be borne in mind that, in the past four decades an increase in pollen allergies has been registered, and it is one of the main health problems that concerns population in urban and industrialised areas (D'Amato et al., 2010, 2002). In Spain, pollen allergies concern about 15% of the total population and 30% of the young population (Caillaud et al., 2014; Subiza Garrido-Lestache, 2004), being a topic of study in recent years (Aguilera and Ruiz-Valenzuela, 2019; Recio et al., 2018). Furthermore, air pollutants can act as adjuvants and alter the immunogenicity of allergenic proteins of pollen while climate change affects the atmospheric abundance of bioaerosols and aeroallergens (Reinmuth-Selzle et al., 2017) and hence, the human exposure to them.

Wet deposition is the main process to remove bioaerosol from the atmosphere (Fröhlich-Nowoisky et al., 2016; Textor et al., 2006). Depending on the height of aerosol particles in the atmosphere, there are two types of processes: In-Cloud Scavenging (ICS), when aerosol particles serve as nuclei for cloud droplets or ice crystals, and Below-Cloud Scavenging (BCS), when aerosol particles are collected by falling raindrops (it depends on the collection efficiency between a falling raindrop and aerosol particles). In this work, we will focus on BCS suffered by nine types of pollen.

The processes that produce the collection of aerosol particles by raindrops are various (Brownian diffusion, interception, inertial impaction, etc.) and they have been previously discussed (Chate, 2005; Zhao and Zheng, 2006). These processes are similar to fog scavenging (Collett et al., 2008, 2001; Gilardoni et al., 2014), since rain and fog are a set of water drops with different sizes and velocities. Inasmuch as pollen particle diameters range between 10 to 100 μm, the process of inertial impaction (prevailing for particles with size d_p >1 μm) is the most important one (Rasch et al., 2000). It should be noted that BCS of pollen could depend on several factors such as pollen concentration, composition and the presence of electric charges (Ladino et al., 2011) or raindrop size distribution and rainfall intensity (Blanco-Alegre et al., 2018; Zikova and Zdimal, 2016).

The influence of rainfall on the pollination process is clear (Lawson and Rands, 2019) and climate change drives alterations in the plant-pollinator interaction (Byers, 2017). Consequently, the analysis of the main bioaerosol particle sinks, including rainfall, has become a key objective in recent research. Several studies have related the rainfall seasonality with pollen concentration (El-Moslimany, 2019; Jantz et al., 2013) and other works have found negative correlations between aeroallergens/pollen and rainfall (Fernández-González et al., 2019; F. Oduber et al., 2019c).

Concerning the impact on human health, Idrose et al. (2019) noted that there is no evidence of interaction between rainfall and total pollen counts in the cases of asthma admissions. Nevertheless D'Amato et al. (2016) reported that during the first 30 min of a thunderstorm, patients suffering from pollen allergies may inhale a high concentration of the allergenic material dispersed into the atmosphere, which in turn can induce severe asthmatic reactions. This fact may be caused by the increase in air humidity and the change of pressure which facilitates the rupturing of pollen grains and the release of allergen bearing respirable particles (Kluska et al., 2020). Other studies have revealed that the interaction between air pollutants and pollen grains may aggravate allergic disorders, since air pollutants adhered to pollen grains facilitate the release of allergens. Thus, the pollen grains are not directly responsible for allergic disorders inasmuch as their size

(>10 µm) constrains their penetration into the respiratory tract (Bartra Tomás et al., 2007; D'Amato et al., 2010, 2007, 2001; Sedghy et al., 2018).

In recent years the modelling of the elimination of different biological agents has been the subject of many studies through the use of local conditions and the and the execution of onsite measurements (Fenu and Malloci, 2020; Mirra et al., 2020; Oduber et al., 2021; Wang et al., 2011; Zamani Beidokhti et al., 2019). Although the studies on wet removal of ultrafine and fine aerosol particles and other pollutants are common (Blanco-Alegre et al., 2019, 2018; Chate and Pranesha, 2004; Laakso et al., 2003; Maria and Russell, 2005), the information related to the scavenging of pollen by rain is scarce. Huffman et al. (2013) and Dong et al. (2019) indicated that bioaerosols have been detected in fog, rain and snow, and they may influence the water cycle (acting as cloud condensation and ice nuclei). The dry deposition of pollen and spores was predominant (87%) in the study carried out by Dong et al. (2019) while wet deposition, including BCS, caused the remaining 13%. That study suggested that rain scavenging may be independent of the taxon studied; however, Kluska et al. (2020) observed differences between taxa in the washing by rain.

Therefore, the main aim of this study is the evaluation of below cloud scavenging caused by rain on nine types of airborne pollen in an urban background station. In addition, we have estimated the efficiency of BCS as a function of several rain parameters, including raindrop size. The novelty of this study lies in the BCS evaluation on airborne pollen with a time resolution of one hour, and the study of the wash-off caused by the different raindrop diameters, a type of information scarcely found in the scientific literature. This innovative approach may allow the improvement of pollen forecast in the Mediterranean area, a region with serious concerns related to pollen allergies.

The paper is structured as follows: i) section 2 (material and methods) includes a description of sampling site, instruments and methodology; ii) in section 3 (results), a study of rain scavenging effect on different types of pollen has been conducted to propose a model to estimate the change of pollen concentration during rainfall events taking into account the different raindrop sizes; iii) section 4 (conclusions) includes the main outcomes from the research together with the major impacts.

10.2.MATERIAL AND METHODS

10.2.1. SAMPLING SITE

The sampling campaign was conducted between January 2015 and December 2018 in León, Spain, a city located northwest of the Iberian Peninsula (838 m above sea level) with a population of about 200,000 residents in 2018. León has a Mediterranean climate with continental features, but it is tempered by the Cantabrian range next to the area. The instruments were located at about 15 m above the ground, on the terrace of the Faculty of Veterinary Sciences at the University of León, on the north-eastern border of the city (Figure S10.1). In the study area, the major sources of aerosol particles are traffic, domestic heating devices in winter, and wildfires and Saharan intrusions in summer (Oduber et al., 2021). With regard to bioaerosols, the main source area is the Cantabrian range (about 30 km from the city northbound). The main vegetation characteristics of this area are: i) forest with different types of vegetation, whose pollination contributes to a high pollen concentration; ii) several deciduous forests, like poplars (*Populus L.*) or ash trees (*Fraxinus Tourn. ex L.*) are present in valleys and as ornamental flora; iii) vegetation like grasses (*Poaceae Barnhart*) and other herbaceous plants are also found in grasslands and meadows (Del Río González, 2005). The vegetation of green areas near the sampling point (university campus and parks) is mainly characterised by trees of the families Cupressaceae and Pinaceae, *Platanus hispanica*, *Aesculus hippoacastanum*, *Fraxinus excelsior* and *Fraxinus angustifolia*, *Betula pubescens*, *Acer negundo*, *Tilia platyphylus*, as well as other trees with entomophilous pollination. The lawns are basically constituted by grasses and *Plantago sp.*, which are often cut before flowering.

10.2.2. POLLEN CONCENTRATION CHARACTERIZATION

The atmospheric pollen concentration was measured using a volumetric *Hirst* type spore-trap (Lanzoni VPPS 2000) (Hirst, 1952). The hourly counts by light (optical) microscopy for the visual detection of pollen and spores were carried out following the recommendations of the Spanish Aerobiological Network, fulfilling the European Standard: Ambient air - Sampling and analysis of airborne pollen grains and fungal spores for networks related to allergy - Volumetric *Hirst* method (2018 CEN FprEN 16868:2018 E). The pollen measurement uncertainty was about 10%,

due to the determination of flow rate of Hirst-type pollen trap (Oteros et al., 2017; UNI 11108:2004, 2004). The analyses were done using a 40x optical microscope (400 magnifications). Four longitudinal bands of a Melinex tape of 48 mm x 12 mm area were analysed. The analysis according to the microscope model assumes 12% of that surface, higher than the 10% established by the standard.

The pollen identification included 54 types:

- Families: Apiaceae, Asteraceae, Brassicaceae, Campanulaceae, Cupresaceae, Cyperaceae, Chenopodiaceae, Ericaceae, Fabaceae, Juncaceae, Lamiaceae, Myrtaceae, Poaceae Polygonaceae, Oleaceae, Rosaceae, Scrophulariaceae, Urticaceae.
- Genera*: Acer*, *Aesculus*, *Ailanthus*, *Alnus*, *Artemisia*, *Betula*, *Carpinus*, *Castanea*, *Cedrus*, *Corylus, Echium*, *Fagus*, *Fraxinus*, *Galium*, *Helianthus*, *Juglans*, *Ligustrum*, *Mercurialis*, *Morus*, *Olea*, *Papaver*, *Pinus*, *Plantago*, *Platanus*, *Populus*, *Quercus*, *Rumex*, *Salix*, *Sambucus, Sedum*, *Taraxacum*, *Tilia*, *Ulmus, Typha.*
- Species*: Quercus pyrenaica and Quercus rotundifolia.*

We selected the following types of pollen to analyse: *Betula* (18 to 28 µm), *Castanea* (10 to 16 µm), Cupressaceae (20 to 30 µm), Oleaceae (20 to 32 µm), *Pinus* (45 to 100 µm), *Plantago* (19 to 35 µm), Poaceae (20 to 45 µm), *Quercus* (25 to 30 µm) and *Urticaceae* (12 to 18 µm) (Trigo Pérez et al., 2008). The mean hourly pollen concentrations were expressed as pollen grains per cubic meter of air. These types of pollen, of different allergenic potential, have been selected for several reasons: shape, ornamentation of the exine and dimensions (Trigo Pérez et al., 2008), since these parameters can modify the degree of hydration of the pollen and/or the permanence of water on the surface of the pollen and consequently change its weight. The period of pollination of the vegetation was also considered, so that the different seasons are represented.

10.2.3. RAIN CHARACTERIZATION

In order to characterize raindrops, a disdrometer Laser Precipitation Monitor (*LPM*) of *Thies Clima* has been used to detect drops between 0.125-8 mm in 22 channels, on a one-minute basis, during all the campaign. The LPM was placed beside the *Hirst* type spore-trap. The LPM has been accurately described by Fernández-Raga et al. (2009). Several rainfall variables have been calculated on a one-hour basis (like the pollen concentration data): precipitation intensity, total accumulated precipitation, number of drops by channels, drop concentration, total drop section (cross-sectional area), volume swept by falling drops by channels, and the mean and standard

deviation of raindrop sizes. The basic meteorological variables (temperature, wind speed and direction and relative humidity) have been measured through a weather station placed next to disdrometer, on a one-minute basis.

The volume $S_v(D_r)$ swept ($mm^3\ m^{-3}$) by a raindrop of diameter D_r is defined in Eq. 10.1, where $S(D_r)$ is the section of the raindrop, $U_t(D_r)$ is the terminal velocity of raindrops, calculated by Fernández-Raga et al. (2009), based on studies of Gunn and Kinzer (1949) and t is the sampling time (one minute in this campaign).

$$S_V(D_r) = S(D_r) \cdot U_t(D_r) \cdot t \qquad \textit{Eq. 10.1}$$

10.2.4. RAIN EVENTS SELECTION

The rain event selection has been carried out in five steps:

1) Data elimination when the event data are not complete, due to temporary errors in the data collection of rain or pollen.
2) Rain criteria: events were only considered when
   i. an accumulated precipitation higher than 0.1 mm was registered in one hour, so the precipitation intensity in the event (total rain h^{-1}) exceeded 0.1 mm h^{-1}. This criterion is more restrictive than the ones found in other studies about scavenging of aerosol particles (Laakso et al., 2003);
   ii. there was a minimum of 2 rain-free hours between events (Blanco-Alegre et al., 2019). This interval was selected to eliminate the errors due to overlapping of samples to be examined under the optical microscope.
3) Meteorological conditions could affect the scavenging process (Hussein et al., 2006). Thus, to elude changes in pollen concentration caused by meteorological factors beyond precipitation, we only consider those events with variations in temperature and wind speed below ±3 °C and ±2 m s^{-1}, respectively, between 2 hours before and after rain. Similar meteorological conditions have been used by other authors to avoid the influence of meteorology on rain scavenging (Blanco-Alegre et al., 2019; Kyrö et al., 2009; Zhao et al., 2015).
4) The selected events must present a pollen concentration higher than 1 pollen m^{-3} in the air for 5 days in a row before rain. This indicates that pollination has begun and the presence of pollen is not due to distant transport (Jato et al., 2006).
5) The selected events were classified by rain intensity: low (<1 mm h^{-1}), medium (1-5 mm h^{-1}) and high (>5 mm h^{-1}). Besides, we classified the selected events by total

rainfall recorded: lower than 1 mm, between 1 and 5 mm, between 5 and 20 mm and higher than 20 mm.

In keeping with these criteria, a total of 122 events have been retained to analyse during the sampling campaign.

10.2.5. SCAVENGING EFFICIENCY AND COEFFICIENT

Once the rain events had been selected, the pollen concentration was analysed 2 hours before rain (t_1), during rain, and 2 hours after rain (t_2). To evaluate the BCS we have calculated 2 parameters for each event: the scavenging efficiency ($\%\Delta C_{rel}$) and the scavenging coefficient (λ). $\%\Delta C_{rel}$ was determined by Eq. 10.2, to evaluate the change in pollen concentration in the interval between t_1 and t_2 with concentrations C_1 and C_2. It should be noted that the minus sign has been introduced in order to get a positive value of $\%\Delta C_{rel}$ with effective scavenging (when pollen concentration decreases). To eliminate the influence of daily pattern, the concentration of each type of pollen was corrected, using the approach previously proposed by Blanco-Alegre et al. (2018).

$$\%\Delta C_{rel} = -\left(\frac{C_2 - C_1}{C_1}\right) \cdot 100 \qquad \textit{Eq. 10.2}$$

The λ coefficient, defined as a rate of aerosols washout by precipitation, was calculated following the criteria proposed by Seinfeld and Pandis (2016) through Eq. 10.3, the same used for the concentration change C of aerosol particles (Chate et al., 2003; Laakso et al., 2003).

$$\lambda = -\frac{1}{C} \cdot \frac{dC}{dt} \qquad \textit{Eq. 10.3}$$

From the semi-empirical approach described by other authors (Laakso et al., 2003; Mircea and Stefan, 1998), Eq. 3 was integrated between the instants t_1 and t_2 with concentrations C_1 and C_2, obtaining Eq. 10.4. As with $\%\Delta C_{rel}$, positive values of λ are indicative of effective scavenging.

$$\lambda = -\frac{1}{t_2 - t_1} \cdot ln\left(\frac{C_2}{C_1}\right) \qquad \textit{Eq. 10.4}$$

Besides, for each type of pollen, we calculated two additional global parameters: the percentage of events with effective scavenging ($\%ES$) and the scavenging efficiency with the concentration-weighted average ($\%\Delta C$), calculated from Eq. 10.5 for all events of each type of pollen.

$$\%\Delta C = \frac{\sum(\%\Delta C_{rel} \cdot C_I)}{\sum C_I} \qquad \textit{Eq. 10.5}$$

Subsequently, a statistical analysis with the Kruskal-Wallis (Kruskal and Wallis, 1952) one-way analysis of variance test (at a significance level of 5%) was conducted as a non-parametric method to test $\%\Delta C$ values between pollen types and rainfall groups, and a post-hoc analysis was also conducted to observe between which pairs of rainfall groups there were statistically significant differences.

10.2.6. LINEAR MODEL

The variation of pollen concentration during rain will be model through the application of an automatic stepwise linear model (IBM SPSS) with an entry probability of 0.05 and a removal probability of 0.10. The methodology used involved the construction of a model from a random sample, which consisted of 75% of total data. The model was finally applied to the remaining 25% of data. Subsequently, the Kolmogorov-Smirnov goodness of fit test was conducted to check how well the model fits the measured data.

10.3. RESULTS AND DISCUSSION

10.3.1. METEOROLOGICAL AND PRECIPITATION ANALYSIS

Based on the data obtained from the four years of the sampling campaign, between January 2015 and December 2018 a total of 472 precipitation-days were registered, with 236 possible events to analyse, of which only 122 complied with the selection criteria described in section 2.4 for total pollen concentration. In order to discard extreme events, we only have evaluated the events included between percentiles P_5 and P_{95}.

The rain events presented a mean duration of 214 minutes (median: 120 minutes), a mean rain accumulated of 3.58 mm (median: 0.73 mm) and a mean rainfall intensity of 0.87 mm h^{-1} (median: 0.37 mm h^{-1}). It is noteworthy that the types of pollen had different numbers of events analysed, since there were events with and without concentration of some types of pollen. A summary of rain characteristics for each type of pollen is shown in Table 10.1.

During these events, the mean temperature was 14.0 °C, with a maximum of 34.2 °C and a minimum of -3.2 °C. The wind speed ranged between 0.0 and 5.6 m s^{-1} (mean value of 1.6 m s^{-1}) but without variations higher than 2 m s^{-1} between before and after rain. Thus, the meteorological influence in the scavenging process during rain has been purged with the restrictive selection criteria carried out.

Table 10.1. Mean values of: number of drops, drop concentration, accumulated rain, rain intensity, swept volume (S_v) and mean and standard deviation of raindrop size for each type of pollen and for total pollen concentration classified according to rain intensity groups. *N* is the number of events for each type of pollen.

Type of pollen (*N*)	Rain intensity group (mm h^{-1})	Number of drops (# m^{-2})	Drop concentration (# m^{-3})	Accumulated rain (mm)	Rain intensity (mm h^{-1})	S_v (mm^3 m^{-3})	Raindrop size (mm)
Total pollen (122)	<1	$4.13 \cdot 10^6$	$9.41 \cdot 10^6$	1.85	0.38	$2.99 \cdot 10^9$	0.42±0.25
	1-5	$7.19 \cdot 10^6$	$1.22 \cdot 10^7$	5.85	1.55	$6.70 \cdot 10^9$	0.45±0.28
	>5	$3.50 \cdot 10^6$	$3.88 \cdot 10^7$	34.10	9.09	$2.35 \cdot 10^{10}$	0.36±0.28
Betula (11)	<1	$6.21 \cdot 10^5$	$9.77 \cdot 10^5$	0.49	0.29	$6.03 \cdot 10^8$	0.41±0.19
	1-5	$3.13 \cdot 10^5$	$3.14 \cdot 10^7$	6.84	1.37	$9.92 \cdot 10^9$	0.37±0.22
	>5	$1.55 \cdot 10^7$	$1.96 \cdot 10^5$	5.81	5.81	$4.73 \cdot 10^9$	0.34±0.23
Castanea (5)	<1	$1.51 \cdot 10^3$	$1.65 \cdot 10^5$	0.36	0.26	$1.47 \cdot 10^8$	0.50±0.38
	1-5	-	-	-	-	-	-
	>5	-	-	-	-	-	-
Cupressaceae (47)	<1	$6.85 \cdot 10^6$	$1.20 \cdot 10^7$	2.26	0.37	$3.91 \cdot 10^9$	0.38±0.20
	1-5	$8.01 \cdot 10^6$	$8.55 \cdot 10^6$	4.79	1.84	$5.86 \cdot 10^9$	0.41±0.25
	>5	$4.63 \cdot 10^5$	$3.76 \cdot 10^7$	16.12	5.38	$1.38 \cdot 10^{10}$	0.30±0.26
Oleaceae (24)	<1	$1.11 \cdot 10^7$	$5.75 \cdot 10^6$	1.52	0.33	$2.73 \cdot 10^9$	0.40±0.23
	1-5	$3.00 \cdot 10^7$	$7.76 \cdot 10^6$	10.51	1.26	$1.24 \cdot 10^{10}$	0.38±0.23
	>5	-	-	-	-	-	-
Pinus (31)	<1	$1.25 \cdot 10^6$	$3.66 \cdot 10^6$	1.16	0.37	$1.54 \cdot 10^9$	0.40±0.21
	1-5	$5.62 \cdot 10^6$	$7.98 \cdot 10^6$	5.37	1.08	$5.39 \cdot 10^9$	0.39±0.22
	>5	$1.55 \cdot 10^7$	$1.96 \cdot 10^5$	5.81	5.81	$4.73 \cdot 10^9$	0.34±0.23
Plantago (39)	<1	$9.55 \cdot 10^5$	$8.11 \cdot 10^6$	1.26	0.36	$1.86 \cdot 10^9$	0.48±0.32
	1-5	$1.78 \cdot 10^5$	$1.01 \cdot 10^7$	4.72	1.83	$3.83 \cdot 10^9$	0.62±0.38
	>5	$4.18 \cdot 10^6$	$2.47 \cdot 10^7$	11.26	6.89	$9.10 \cdot 10^9$	0.33±0.25
Poaceae (49)	<1	$7.19 \cdot 10^6$	$4.03 \cdot 10^6$	1.36	0.36	$2.14 \cdot 10^9$	0.48±0.31
	1-5	$8.09 \cdot 10^4$	$7.06 \cdot 10^6$	2.88	1.15	$2.67 \cdot 10^9$	0.53±0.29
	>5	$4.18 \cdot 10^6$	$2.47 \cdot 10^7$	11.26	6.89	$9.10 \cdot 10^9$	0.33±0.25
Quercus (33)	<1	$1.27 \cdot 10^6$	$1.22 \cdot 10^7$	1.96	0.40	$3.03 \cdot 10^9$	0.47±0.29
	1-5	$8.09 \cdot 10^4$	$7.21 \cdot 10^6$	2.95	1.23	$2.84 \cdot 10^9$	0.49±0.28
	>5	$7.90 \cdot 10^6$	$1.20 \cdot 10^7$	7.71	7.71	$6.06 \cdot 10^9$	0.33±0.24
Urticaceae (24)	<1	$1.21 \cdot 10^6$	$1.08 \cdot 10^7$	1.39	0.37	$2.28 \cdot 10^9$	0.48±0.30
	1-5	$2.35 \cdot 10^5$	$2.02 \cdot 10^7$	6.74	2.34	$6.82 \cdot 10^9$	0.40±0.26
	>5	-	-	-	-	-	-

For *Castanea*, whose pollen is typical in summer (the driest season), only five rain events were considered. For Cupressaceae and Poaceae, with typical pollens of autumn-winter and spring-early summer (periods with high precipitation), the highest numbers of events (47 and 49, respectively) were registered. The mean raindrop sizes in the low rain intensity group ranged between 0.38±0.20 mm (Cupressaceae) and 0.48±0.30 mm (Urticaceae), in the medium rain intensity between 0.38±0.23 mm (Oleaceae) and 0.62±0.38 mm (*Plantago*) and in the high rain intensity between 0.30±0.26 mm (Cupressaceae) and 0.34±0.23 mm (*Betula*). There were no statistical differences in raindrop size between the events registered for the different types of pollen (p=0.170), so the results between types of pollen are comparable. With respect to the accumulated rain and rainfall intensity, the averages were similar between the events corresponding to the different types of pollen and rain intensity groups.

10.3.2. POLLEN CONCENTRATION ANALYSIS

The evolution of pollen concentration of the different types analysed is depicted in Figure 10.1 along with the precipitation. During all the sampling campaign, the highest pollen concentrations were reached between March and August. A detailed description about the main pollen seasons by types can be found in Oduber et al. (2019).

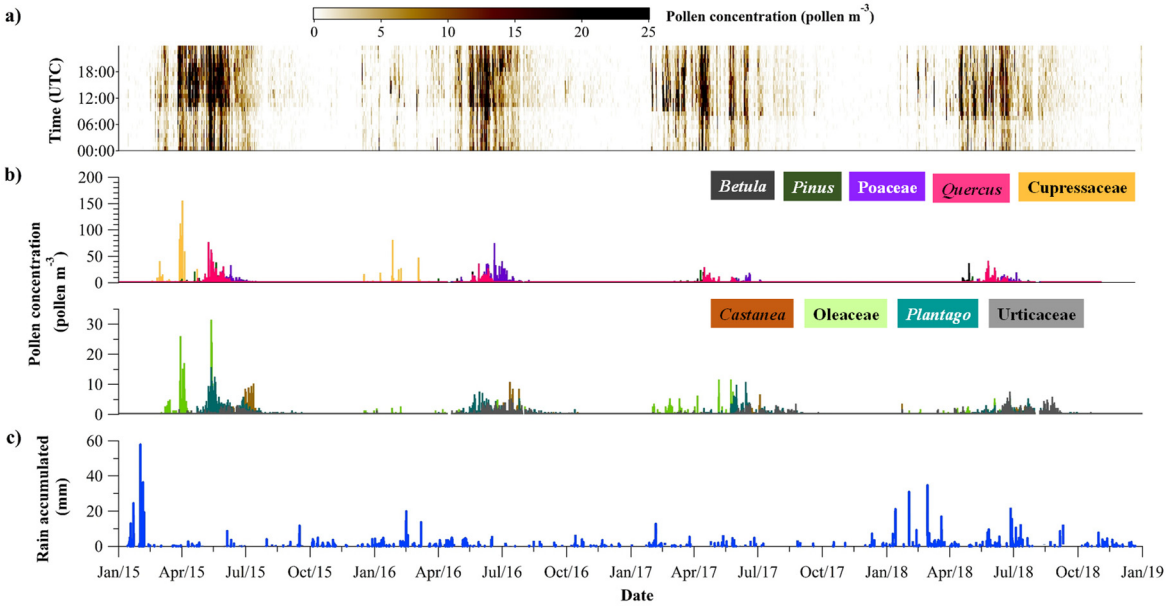

Figure 10.1. a) Total pollen concentration registered each hour; b) concentration of different types of pollen and c) distribution of rain accumulated during the sampling campaign.

The maximum of pollen concentration was observed on 7 March 2017, with 211.5 pollen m^{-3}. By types, the highest daily concentrations were reached by Cupressaceae (7 March 2017 with 205.7 pollen m^{-3} and 31 March 2015 with 156.2 pollen m^{-3}), *Quercus* (7 May 2017 with 77.4 pollen m^{-3}) and Poaceae (18 June 2016 with 75.6 pollen m^{-3}). The highest pollen concentrations occurred on days without rain, with a statistically significant negative correlation (r=-0.068; p=0.01) among pollen concentration and daily precipitation.

10.3.3. STUDY OF THE SCAVENGING EFFECT

Airborne pollen scavenging has been analysed by means of different parameters, as shown in section 2.5.

10.3.3.1. Scavenging efficiency

The *%ΔC* values have been calculated for each pollen type (Table 10.2). Globally, there was a clear effective BCS for all pollen types. The *%ΔC* mean value for total pollen was 24±18% and the types of pollen with higher values were Cupressaceae and *Castanea* (71 and 40%, respectively). On the other hand, the types with lower scavenging were *Betula*, Oleaceae, Poaceae, *Quercus* and Urticaceae (ranging between 14 and 16%). Dong et al. (2019), in a study conducted in Seoul (South Korea), examined plant assemblages collected in atmospheric deposits to evaluate dry and wet deposition. They reported that a small fraction of bioaerosols (~15%) precipitated via ICS or BCS. Only a small number of plant genera presented a higher wet deposition (e.g. *Quercus*), probably due to their role in precipitation, acting as nucleation species in the atmosphere. Also, they said that the different plant taxa did not vary significantly between dry and wet deposition. Thus, contrary to suggested by Dong et al. (2019), our results show clearly differences in the washing parameters depending on the type of pollen, a behaviour previously found by Kluska et al. (2020). The *%ΔC* values obtained were similar to those estimated for aerosols in the coarse mode (19%) in León from July 2015 to January 2016 (Blanco-Alegre et al., 2018) and lower than values (70%) based on models in July 1997 (Loosmore and Cederwall, 2004). It should be borne in mind that in the coarse mode (pollen sizes included), inertial impaction is the most important process (Rasch et al., 2000), while in ultrafine and fine modes, Brownian diffusion and interception mechanisms prevail (Chate, 2005). The inverse relationship between pollen concentration and total rainfall have also been reported by several authors in various climatic regions. Alan et al. (2018), in a study conducted between 2015 and 2016 in

Ankara and Zonguldak (Turkey), two cities with different climatic properties, studied the correlations between Poaceae pollen and Phl p 5 allergen. They found different results according to the climatic characteristics and topography of each city. Also, Bruffaerts et al. (2018) examined the evolution of pollen concentrations in Brussels (Belgium) during 40 years and the effect of meteorological changes on pollen concentration. They found that the annual changes in pollen annual cycles are related with changes in the annual cycles of temperature, radiation, humidity and rainfall. It should be noted that Kluska et al. (2020) reported this inverse relationship but only with rainfall intensities higher than 5 mm h^{-1} in Poland, but this threshold may vary by climatic zones.

Another important parameter to analyse the pollen scavenging is *%ES*, in order to quantify the sensitivity of each pollen type to rain scavenging. The *%ES* mean value of total pollen was 71%, so 71% of events presented an effective scavenging during rain, with *Betula* being the type of pollen with the highest *%ES* value. Huffman et al. (2013), in a study carried out in a montane pine zone in Colorado (USA) between July and August of 2011, found that rain can cause intense bursts of bioaerosol emission during or after rain events, causing an increase of bioaerosol concentration by an order of magnitude. They detected the presence of bioaerosols in rain samples, concluding that atmospheric bioaerosols and rainfall are tightly coupled, at least at midlatitude semi-arid forest ecosystems. The presence of bioaerosols in rain samples may be explained by the effective scavenging on pollen particles. It is noteworthy that pollen types with the highest values of *%ΔC* (*Castanea* and Cupressaceae) presented the lowest values of *%ES*, together with *Pinus* and Urticaceae. There were statistical differences in *%ΔC* between the types of pollen (p=0.043). After a *post hoc* analysis, there were statistical differences between Oleaceae and: Cupressaceae (p=0.003), *Pinus* (p=0.007), *Quercus* (p=0.008) and Urticaceae (p=0.008). The *Castanea* results must be carefully tackled due to the low number of events.

Table 10.2. Mean, percentiles $P_{0.05}$ and $P_{0.95}$ and quartile 2 values of $\%\Delta C_{rel}$ (scavenging efficiency), effective scavenging (*%ES*) and mean and standard deviation of *%ΔC* (scavenging efficiency using the concentration-weighted average) obtained for each type of pollen and for total pollen concentration.

	Total pollen	*Betula*	*Castanea*	Cupressaceae	Oleaceae	*Pinus*	*Plantago*	Poaceae	*Quercus*	Urticaceae
N	122	11	5	47	24	31	39	49	33	24
%ES	71	82	60	66	75	55	77	78	73	63
P_5	-400	-73	0	-486	-50	-400	-105	-93	-100	-134
Q_2	50	100	100	86	100	-67	100	100	75	42
P_{95}	100	100	100	100	100	100	100	100	100	100
%ΔC	24.3	15.1	40.3	70.9	16.7	20.1	24.6	15.3	14.8	14.2
SD	17.9	5.5	4.5	39.0	5.5	15.1	6.3	7.7	7.5	9.4

For the study of scavenging depending on rain characteristics, the *%ΔC* values have been obtained per pollen type and rain intensity groups, as depicted in Figure 10.2. The medium (1-5 mm h^{-1}) and high rain intensity (>5 mm h^{-1}) presented the highest *%ΔC* values (69.7 and 69.2%, respectively) for total pollen concentration. The low rain intensity (<1 mm h^{-1}) also presented a low value of 40.9%. In addition, *%ES* values were higher in medium and high intensities (92.9 and 100%, respectively) than in low intensity (71.4%). Thus, with rain intensities higher than 5 mm h^{-1}, the total pollen concentration always decreased.

In regards to accumulated rain, all groups presented effective scavenging: lower than 1 mm (40.3%), between 1 and 5 mm (58.6%) and between 5 and 20 mm (39.2%). Particularly striking is the high value obtained for events with an accumulated rain higher than 20 mm (99.8%), with a practically total scavenging of airborne pollen. There were no statistical differences in *%ΔC* between the three groups of rain intensity (p=0.243). On the contrary, there were statistical differences in *%ΔC* between the groups of accumulated rain lower than 1 mm and higher than 20 mm (p=0.029). Therefore, contrary to reported by Kluska et al. (2020), there is an effective washing of pollen with precipitation intensities below 5 mm h^{-1}. This fact may be related with the different spatial characteristics among regions (Rzeszów in Poland and León in Spain), such as altitude (210 vs 838 m) or climate (polar maritime vs Mediterranean climate with continental features) and the different number of pollen types analysed (four vs nine).

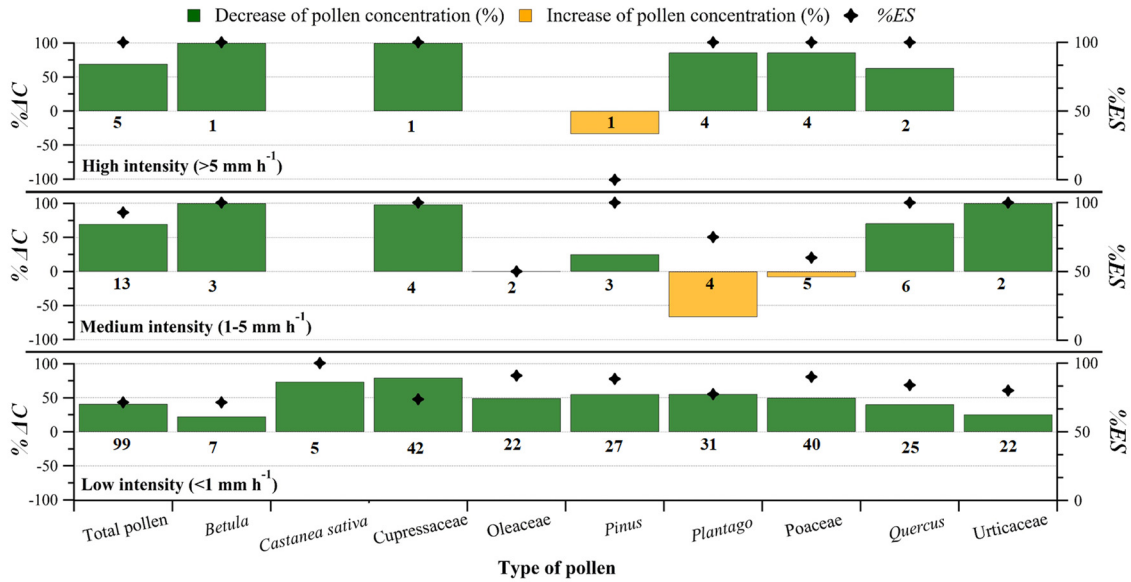

Figure 10.2. Scavenging efficiency using the concentration-weighted average (*%ΔC*) and effective scavenging (*%ES*) averages obtained for each type of pollen by rain intensity groups. The number indicates the number of events.

By pollen types, it is worth noting that with low rain intensities, all types presented an effective scavenging, with values ranging between 22.4% (*Betula*) and 79.5% (Cupressaceae). Besides, all *%ES* values were higher than 70%, showing effective scavenging with rain intensities lower than 1 mm h^{-1} on pollen. However, in medium rain intensity there was divergence according to the pollen type. Only *Betula*, Cupressaceae, *Pinus*, *Quercus* and Urticaceae presented an effective scavenging. Oleaceae, *Plantago* and Poaceae presented negative *%ΔC* values and low values of *%ES*. Regarding high rain intensity, all types presented high values of *%ΔC* and *%ES*, except *Pinus*, the pollen type with the highest sizes. The *Pinus* pollen behaviour could be explained by its physics characteristics; although it is the largest type due to its two lateral air sacs (like floaters), these do not present cytoplasmic content and do not participate in the hydration of the pollen; they only serve to float better (Trigo Pérez et al., 2008). Therefore, it would not be heavier despite its size and this fact can explain the lower scavenging suffered.

Also, the minor scavenging effect of rain in *Betula* and *Pinus* may be related to their biology of pollination, since these types shed a large amount of pollen during their short pollen season (around one month) while other types like Poaceae, Cupressaceae or Urticaceae present a longer pollen season. Previous studies report that the high pollen concentration during precipitation may be favored by the transport of pollen by thermal currents (Zhao et al., 2014) and by the impaction and condensation effects (Kasprzyk et al., 2001).

10.3.3.2. Scavenging coefficient

For total pollen concentration, a mean scavenging coefficient (λ) of $2.50 \cdot 10^{-2}$ s^{-1} and a median of $5.30 \cdot 10^{-3}$ s^{-1} have been obtained (Table 10.3). The mean value is three orders of magnitude higher than λ obtained for fine ($2.6 \cdot 10^{-5}$ s^{-1}) and coarse aerosol modes ($5.8 \cdot 10^{-5}$ s^{-1}) (Blanco-Alegre et al., 2018) in a sampling campaign carried out at the same place as this study, showing a high scavenging effect on pollen concentration. One of the pollen types with higher values of λ and *%ΔC* was *Castanea*. Conversely, Cupressaceae presented a higher *%ΔC* but a low value of λ and *%ES*. This may be due to the characteristics of Cupressaceae rain events: they were long or with high rain intensity when the scavenging was effective. Another important fact is that Cupressaceae has a tiny opening and a very fine exine, with much cytoplasmic content (Trigo Pérez et al., 2008). It takes a long time to activate and its mechanisms are not well known at present. Therefore, it takes time to fill up with water and it takes time to sediment. The rest of pollen types with higher values of λ were *Betula*, Oleaceae, Poaceae and *Plantago*, with values ranged between $1.15 \cdot 10^{-1}$ and $1.45 \cdot 10^{-1}$ s^{-1}. There were no statistically significant differences in λ between types of pollen ($p=0.194$).

Table 10.3. Mean, standard deviation, median, P_5 and P_{95} percentile values and of scavenging coefficients (λ), for each type of pollen and for total pollen concentration.

λ (s^{-1})	$\bar{x}$	SD	Median	P_5	P_{95}
Total pollen	$2.50 \cdot 10^{-2}$	$5.95 \cdot 10^{-2}$	$5.30 \cdot 10^{-3}$	$-1.46 \cdot 10^{-2}$	$1.76 \cdot 10^{-1}$
Betula	$1.15 \cdot 10^{-1}$	$1.29 \cdot 10^{-1}$	$5.60 \cdot 10^{-2}$	$-8.94 \cdot 10^{-3}$	$3.35 \cdot 10^{-1}$
Castanea	$2.01 \cdot 10^{-1}$	$1.84 \cdot 10^{-1}$	$3.26 \cdot 10^{-1}$	0	$3.44 \cdot 10^{-1}$
Cupressaceae	$5.82 \cdot 10^{-2}$	$9.74 \cdot 10^{-2}$	$1.16 \cdot 10^{-2}$	$-2.34 \cdot 10^{-2}$	$3.21 \cdot 10^{-1}$
Oleaceae	$1.17 \cdot 10^{-1}$	$1.25 \cdot 10^{-1}$	$8.01 \cdot 10^{-2}$	$-3.04 \cdot 10^{-3}$	$3.30 \cdot 10^{-1}$
Pinus	$7.80 \cdot 10^{-2}$	$1.30 \cdot 10^{-1}$	$6.10 \cdot 10^{-3}$	$-1.86 \cdot 10^{-2}$	$3.21 \cdot 10^{-1}$
Plantago	$1.45 \cdot 10^{-1}$	$1.47 \cdot 10^{-1}$	$1.07 \cdot 10^{-1}$	$-1.16 \cdot 10^{-2}$	$3.45 \cdot 10^{-1}$
Poaceae	$1.23 \cdot 10^{-1}$	$1.39 \cdot 10^{-1}$	$5.53 \cdot 10^{-2}$	$-9.38 \cdot 10^{-3}$	$3.27 \cdot 10^{-1}$
Quercus	$9.77 \cdot 10^{-2}$	$1.39 \cdot 10^{-1}$	$2.31 \cdot 10^{-2}$	$-8.66 \cdot 10^{-3}$	$3.34 \cdot 10^{-1}$
Urticaceae	$9.25 \cdot 10^{-2}$	$1.42 \cdot 10^{-1}$	$4.51 \cdot 10^{-3}$	$-1.16 \cdot 10^{-2}$	$3.39 \cdot 10^{-1}$

By rain intensity groups, λ average was $2.41 \cdot 10^{-2}$ s^{-1} (low intensity), $2.13 \cdot 10^{-2}$ s^{-1} (medium intensity) and $5.12 \cdot 10^{-2}$ s^{-1} (high intensity), so the rain intensity higher than 5 mm h^{-1} was the most efficient. Furthermore, the higher values of λ were registered for an accumulated precipitation higher than 20 mm ($2.94 \cdot 10^{-2}$ s^{-1}). The rest of accumulated precipitation groups presented these values: lower than 1 mm, $2.32 \cdot 10^{-2}$ s^{-1}; between 1-5 mm, $2.65 \cdot 10^{-2}$ s^{-1}; between 5-20 mm, $2.87 \cdot 10^{-2}$ s^{-1} and higher than 20 mm, $2.94 \cdot 10^{-2}$ s^{-1}. There were no statistically significant differences in λ between groups of rain intensity ($p=0.235$) or between groups of accumulated rain ($p=0.338$).

10.3.4. RAINDROP SIZE EFFECT

Kluska et al. (2020) proposed that the raindrop size parameter need to be considered. Several decades ago, Gatz and Dingle (1971) suggested that larger raindrops during high rain intensities were less effective to remove pollen than smaller drops during lower intensity rainfall.

In our study, the scavenging effect of the different raindrop sizes has been evaluated through the swept volume (S_v) caused by each range of raindrop sizes on total pollen concentration (Figure 10.3). In low and medium rain intensities, the S_v on the total pollen concentration was caused by raindrops of sizes between 0.25 and 3 mm. However, for high rain intensity events, S_v was higher in the raindrop sizes between 0.5 and 4 mm. Besides, raindrops larger than 4 mm caused scavenging only in high intensity events (>5 mm h^{-1}). The total S_v in high rain intensity events ($2.4 \cdot 10^{10}$ mm^3 m^{-3}) was eight and three times higher than in low ($3.0 \cdot 10^9$ mm^3 m^{-3}) and

medium ($6.7 \cdot 10^{10}$ mm^3 m^{-3}) rain intensity events. There were statistically significant differences in S_v between the rain intensity groups ($p<0.001$). Thus, these results could explain the highest values of $\%\Delta C$ and λ in events with a high rain intensity, caused by a higher swept volume.

10.3.5. MODELLING THE VARIATION OF POLLEN CONCENTRATION

In order to estimate the variation of the total pollen concentration ($\Delta C=C_1-C_2$) during rain events, a linear model has been built. The variables used are shown in Table 10.4. Although many other studies have related pollen concentration to rainfall (Buters et al., 2015; Ge et al., 2017; Shen et al., 2006; Y. Zhang et al., 2015), here we will focus on the analysis of the likely impact of rain on pollen concentration using the combination of weather and pollen parameters. As indicated in the paragraph 2.6, the methodology process has been repeated ten times and the results are shown in Table S10.1. In all cases significant values ($p>0.05$) have been obtained, so measured and predicted data are related and, consequently, the model created is consistent. It is noted that in all cases pollen concentration before rain (C_1) and temperature before rain (T_1) were included. Other variables as wind speed (ws) and mean raindrop diameter (D_r) were not continuous. The inclusion of raindrop diameter confirm the importance of this parameter in the removal of atmospheric pollen, as other authors suggest (Gatz and Nelson Dingle, 1971; Kluska et al., 2020).

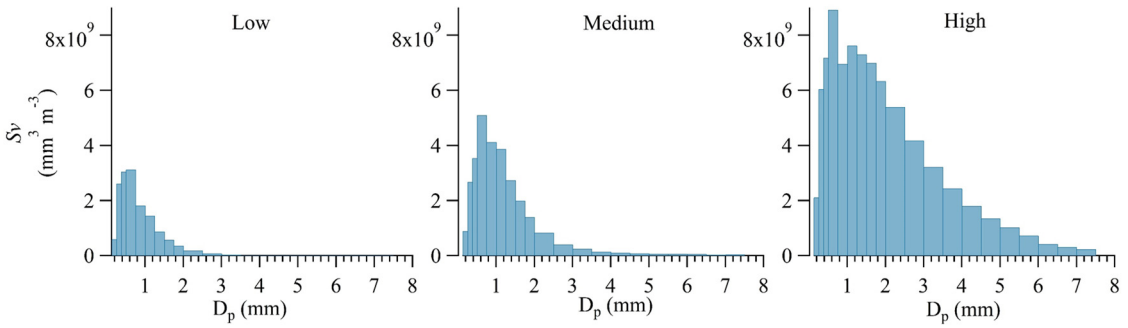

Figure 10.3. Mean swept volume (S_v) caused by different raindrop sizes classified by rain intensities [low (<1 mm h^{-1}), medium (1-5 mm h^{-1}) and high (>5 mm h^{-1})] on rain events considered for total pollen concentration.

Table 10.4. Variables used to build the linear model to estimate the total pollen variation during rain events.

Symbol	Variable	Units
C_1	Pollen concentration before rain	pollen m^{-3}
ws	Wind speed	m s^{-1}
T	Temperature	°C
P	Pressure	hPa
RH	Relative humidity	%
t	Event duration	h
R	Accumulated precipitation	mm
I	Mean rainfall intensity	mm h^{-1}
D_r	Mean raindrop diameter	mm
Swept	Sum of volume swept by falling drops	mm^3 m^{-3}
$Ndrops_x$	Number of drops per m^2 in the size channel of *x* mm	# m^{-2}
$Ndrops_{total}$	Total drops per m^3	# m^{-3}

Therefore, using the whole data set, a multi-linear regression model has been established (r^2=0.94), which includes the aforementioned variables. The coefficient values are shown under each term.

$$\Delta C = \underbrace{(k_1 \cdot C_1)}_{0.770\ (\pm 0.022) C_1} + \underbrace{(k_2 \cdot T_1)}_{-0.125\ (\pm 0.038) T_1} + \underbrace{(k_3 \cdot ws)}_{0.512\ (\pm 0.255) ws} + \underbrace{(k_4 \cdot D_r)}_{2.785\ (\pm 1.169) D_r} + \underbrace{k_5}_{-0.912\ (\pm 0.333)}$$

The variation of the measured concentration and the results obtained applying the model are similar (Figure 10.4); thus, the use of the model is a valuable tool to predict the total pollen concentration after rain.

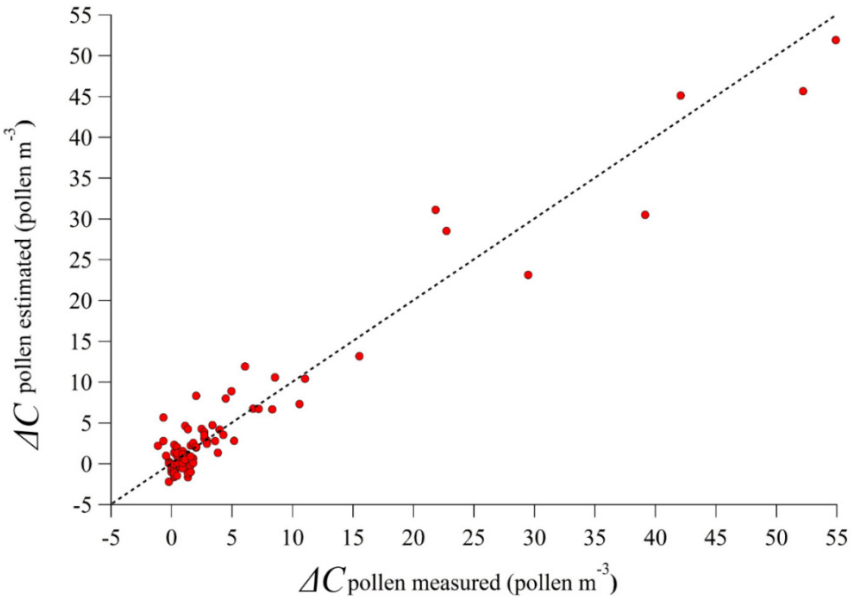

Figure 10.4. Variation ΔC of pollen concentration estimated by the model vs variation ΔC of pollen concentration measured after each rain event.

For each pollen type, the same analysis was performed, in order to obtain individual model variations of each pollen concentration. Nevertheless, the low number of rain events recorded for several types of pollen caused that only one type of pollen presented high values of r^2: Cupressaceae (0.98). Hereafter, we show the model obtained with 100% of data. The coefficient values for Cupressaceae variation are presented under each term:

$$\Delta C_{\text{Cupressaceae}} = \underbrace{(k_1 \cdot C_1)}_{0.918\ (\pm 0.022) C_1} + \underbrace{(k_2 \cdot Ndrops_{0.25})}_{-2.135 \cdot 10^{-5}\ (\pm 0.038) Ndrops_{0.25}} + \underbrace{(k_3 \cdot Ndrops_{0.5})}_{2.895 \cdot 10^{-5}\ (\pm 6.0 \cdot 10^{-6}) Ndrops_{0.5}} + \underbrace{k_4}_{-0.517\ (\pm 0.392)}$$

where C_1 is the Cupressaceae concentration before rain, $Ndrops_{0.25}$ is the number of raindrops between 0.25 and 0.375 mm and $Ndrops_{0.5}$ is the number of raindrops between 0.5 and 0.75 mm. It is worth highlighting that the main scavenging effect was caused by 0.5-0.75 mm size raindrops, the channel with the highest values of swept volume.

A detailed analysis of each type of pollen requires more years of sampling and is one of the next challenges.

10.4. CONCLUSIONS

The evaluation of wet deposition of bioaerosols have been carried out through the study of below cloud scavenging on nine types of pollen under different rainfall conditions during a sampling period of four years in an urban background environment. As a result, a clear effective scavenging in all types of pollen analysed was observed with a concentration-weighted average (*%ΔC*) of 24±18%. The types of pollen with the highest values were *Castanea* and Cupressaceae (70.9 and 40.3%, respectively). The rain scavenging for pollen was very different from that of coarse aerosol particles: the mean λ coefficient for pollen scavenging was $2.50 \cdot 10^{-2}$ s^{-1} (median of $5.30 \cdot 10^{-3}$ s^{-1}), three orders of magnitude higher than the value obtained for coarse aerosol in a sampling campaign conducted at the same place. Rain intensity over 5 mm h^{-1} was the most efficient. All types presented high values of *%ΔC* and *%ES,* except *Pinus*, the larger pollen, probably related with its physics characteristics. This scavenging occurred in the swept volume (S_v) mainly produced by raindrop sizes between 0.25 and 3 mm. The swept volume could explain the highest scavenging with high rain intensities, inasmuch as the average value of S_v in high rain intensity events ($2.4 \cdot 10^{10}$ mm^3 m^{-3}) was eight and three times higher than in low and medium rain intensity events, respectively. Finally, a linear model (r^2=0.94) was built to estimate the pollen

concentration after rain with input variables from a weather station, a disdrometer and the pollen concentration before rain. Thus, this kind of studies constitutes a valuable tool for the bioaerosol forecast in the Mediterranean area, a region with severe problems with pollen allergies. Future studies will focus on the research of the root causes of the different scavenging efficiency values obtained for the different types of pollen and the mechanism of scavenging on pollen.

10.5. REFERENCES

Aguilera, F., Ruiz-Valenzuela, L., 2019. A new aerobiological indicator to optimize the prediction of the olive crop yield in intensive farming areas of southern Spain. Agric. For. Meteorol. 271, 207–213. doi:10.1016/j.agrformet.2019.03.004

Alan, Ş., Şahin, A.A., Sarışahin, T., Şahin, S., Kaplan, A., Pınar, N.M., 2018. The effect of geographical and climatic properties on grass pollen and Phl p 5 allergen release. Int. J. Biometeorol. 62, 1325–1337. doi:10.1007/s00484-018-1536-0

Apte, J.S., Marshall, J.D., Cohen, A.J., Brauer, M., 2015. Addressing Global Mortality from Ambient PM2.5. Environ. Sci. Technol. 49, 8057–8066. doi:10.1021/acs.est.5b01236

Bartra Tomás, J., Mullol, J., Del Cuvillo, A., Dávila, I., Ferrer, M., Jáuregui, I., Montoro, J., Sastre, J., Valero, A., 2007. Air pollution and allergens. J. Investig. Allergol. Clin. Immunol. 17, 3–8.

Blanco-Alegre, C., Calvo, A.I., Coz, E., Castro, A., Oduber, F., Prévôt, A.S.H.H., Močnik, G., Fraile, R., 2019. Quantification of source specific black carbon scavenging using an aethalometer and a disdrometer. Environ. Pollut. 246, 336–345. doi:10.1016/j.envpol.2018.11.102

Blanco-Alegre, C., Castro, A., Calvo, A.I., Oduber, F., Alonso-Blanco, E., Fernández-González, D., Valencia-Barrera, R.M., Vega-Maray, A.M., Fraile, R., 2018. Below-cloud scavenging of fine and coarse aerosol particles by rain: The role of raindrop size. Q. J. R. Meteorol. Soc. 144, 2715–2726. doi:10.1002/qj.3399

Bruffaerts, N., De Smedt, T., Delcloo, A., Simons, K., Hoebeke, L., Verstraeten, C., Van Nieuwenhuyse, A., Packeu, A., Hendrickx, M., 2018. Comparative long-term trend analysis of daily weather conditions with daily pollen concentrations in Brussels, Belgium. Int. J. Biometeorol. 62, 483–491. doi:10.1007/s00484-017-1457-3

Buters, J., Prank, M., Sofiev, M., Pusch, G., Albertini, R., Annesi-Maesano, I., Antunes, C., Behrendt, H., Berger, U., Brandao, R., Celenk, S., Galan, C., Grewling, Ł., Jackowiak, B., Kennedy, R., Rantio-Lehtimäki, A., Reese, G., Sauliene, I., Smith, M., Thibaudon, M., Weber, B., Cecchi, L., 2015. Variation of the group 5 grass pollen allergen content of airborne pollen in relation to geographic location and time in season. J. Allergy Clin. Immunol. 136, 87-95.e6. doi:10.1016/j.jaci.2015.01.049

Byers, D.L., 2017. Studying Plant–Pollinator Interactions in a Changing Climate: A Review of Approaches. Appl. Plant Sci. 5, 1700012. doi:10.3732/apps.1700012

Caillaud, D., Toloba, Y., Raobison, R., Besancenot, J.P., Thibaudon, M., Martin, S., Segala, C., 2014. Impact sanitaire des pollens: revue des études épidé miologiques. Rev. Mal. Respir. 31, 142–149. doi:10.1016/j.rmr.2013.09.017

Chate, D.M., 2005. Study of scavenging of submicron-sized aerosol particles by thunderstorm rain events. Atmos. Environ. 39, 6608–6619. doi:10.1016/j.atmosenv.2005.07.063

Chate, D.M., Pranesha, T.S., 2004. Field studies of scavenging of aerosols by rain events. J. Aerosol Sci. 35, 695–706. doi:10.1016/j.jaerosci.2003.09.007

Chate, D.M., Rao, P.S.P., Naik, M.S., Momin, G.A., Safai, P.D., Ali, K., 2003. Scavenging of aerosols and their chemical species by rain. Atmos. Environ. 37, 2477–2484. doi:10.1016/S1352-2310(03)00162-6

Collett, J.L., Herckes, P., Youngster, S., Lee, T., 2008. Processing of atmospheric organic matter by California radiation fogs. Atmos. Res. 87, 232–241. doi:10.1016/j.atmosres.2007.11.005

Collett, J.L., Sherman, D.E., Moore, K.F., Hannigan, M.P., Lee, T., 2001. Aerosol Particle Processing and Removal by Fogs: Observations in Chemically Heterogeneous Central California Radiation Fogs. Water, Air Soil Pollut. Focus 1, 303–312. doi:10.1023/A:1013175709931

D'Amato, G., Cecchi, L., Bonini, S., Nunes, C., Annesi-Maesano, I., Behrendt, H., Liccardi, G., Popov, T., Van Cauwenberge, P., 2007. Allergenic pollen and pollen allergy in Europe. Allergy Eur. J. Allergy Clin. Immunol. 62, 976–990. doi:10.1111/j.1398-9995.2007.01393.x

D'Amato, G., Cecchi, L., D'Amato, M., Liccardi, G., 2010. Urban Air Pollution and Climate Change as Environmental Risk Factors of Respiratory Allergy: An Update. J Investig Allergol Clin Immunol 20(2), 95–102. doi:10.1016/j.anai.2016.08.015

D'Amato, G., Liccardi, G., D'Amato, M., Cazzola, M., 2002. Outdoor air pollution, climatic changes and allergic bronchial asthma. Eur. Respir. J. 20, 763–776. doi:10.1183/09031936.02.00401402

D'Amato, G., Liccardi, G., D'Amato, M., Cazzola, M., 2001. The role of outdoor air pollution and climatic changes on the rising trends in respiratory allergy. Respir. Med. 95, 606–611. doi:10.1053/rmed.2001.1112

D'Amato, G., Vitale, C., D'Amato, M., Cecchi, L., Liccardi, G., Molino, A., Vatrella, A., Sanduzzi, A., Maesano, C., Annesi-Maesano, I., 2016. Thunderstorm-related asthma: What happens and why. Clin. Exp. Allergy 46, 390–396. doi:10.1111/cea.12709

Del Río González, S., 2005. El cambio climático y su influencia en la vegetación de Castilla y León (España). Itinera Geobot. 16, 5–534.

Dong, K., Woo, C., Yamamoto, N., 2019. Plant assemblages in atmospheric deposition. Atmos. Chem. Phys. 19, 11969–11983. doi:10.5194/acp-19-11969-2019

El-Moslimany, A., 2019. Reduced Poaceae pollen under conditions of severe summer drought in the Middle East: Implications for rainfall seasonality in pollen diagrams. Rev. Palaeobot. Palynol. 271, 104068. doi:10.1016/j.revpalbo.2019.04.007

Fenu, G., Malloci, F.M., 2020. DSS LANDS: A Decision Support System for Agriculture in Sardinia. HighTech Innov. J. 1, 129–135. doi:10.28991/hij-2020-01-03-05

Fernández-González, M., Ribeiro, H., Pereira, J.R.S., Rodríguez-Rajo, F.J., Abreu, I., 2019. Assessment of the potential real pollen related allergenic load on the atmosphere of Porto city. Sci. Total Environ. 668, 333–341. doi:10.1016/j.scitotenv.2019.02.345

Fernández-Raga, M., Castro, A., Palencia, C., Calvo, A.I., Fraile, R., 2009. Rain events on 22 October 2006 in León (Spain): Drop size spectra. Atmos. Res. 93, 619–635. doi:10.1016/j.atmosres.2008.09.035

Fröhlich-Nowoisky, J., Kampf, C.J., Weber, B., Huffman, J.A., Pöhlker, C., Andreae, M.O., Lang-Yona, N., Burrows, S.M., Gunthe, S.S., Elbert, W., Su, H., Hoor, P., Thines, E., Hoffmann, T., Després, V.R., Pöschl, U., 2016. Bioaerosols in the Earth system: Climate, health, and ecosystem interactions. Atmos. Res. 182, 346–376. doi:10.1016/j.atmosres.2016.07.018

Gatz, D.F., Nelson Dingle, A., 1971. Trace substances in rain water: concentration variations during convective rains, and their interpretation. Tellus 23, 14–27. doi:10.3402/tellusa.v23i1.10286

Ge, Y., Li, Y., Bunting, M.J., Li, B., Li, Z., Wang, J., 2017. Relation between modern pollen rain, vegetation and climate in northern China: Implications for quantitative vegetation reconstruction in a steppe environment. Sci. Total Environ. 586, 25–41. doi:10.1016/j.scitotenv.2017.02.027

Gilardoni, S., Massoli, P., Giulianelli, L., Rinaldi, M., Paglione, M., Pollini, F., Lanconelli, C., Poluzzi, V., Carbone, S., Hillamo, R., Russell, L.M., Facchini, M.C., Fuzzi, S., 2014. Fog scavenging of organic and inorganic aerosol in the po valley. Atmos. Chem. Phys. 14, 6967–6981. doi:10.5194/acp-14-6967-2014

Gunn, R., Kinzer, G.D., 1949. The terminal velocity of fall for water droplets in stagnant Air. J. Meteorol. doi:10.1175/1520-0469(1949)006<0243:TTVOFF>2.0.CO;2

HEI Review Panel, 2013. Understanding the Health Effects of Ambient Ultrafine Particles. Heal. Eff. Inst. 122.

Hirst, J.M., 1952. An automatic volumetric spore trap. Ann. Appl. Biol. 39, 257–265. doi:10.1111/j.1744-7348.1952.tb00904.x

Huffman, J.A., Prenni, A.J., Demott, P.J., Pöhlker, C., Mason, R.H., Robinson, N.H., Fröhlich-Nowoisky, J., Tobo, Y., Després, V.R., Garcia, E., Gochis, D.J., Harris, E., Müller-Germann, I., Ruzene, C., Schmer, B., Sinha, B., Day, D.A., Andreae, M.O., Jimenez, J.L., Gallagher, M., Kreidenweis, S.M., Bertram, A.K., Pöschl, U., 2013. High concentrations of biological aerosol particles and ice nuclei during and after rain. Atmos. Chem. Phys. 13, 6151–6164. doi:10.5194/acp-13-6151-2013

Hussein, T., Karppinen, A., Kukkonen, J., Härkönen, J., Aalto, P., Hämeri, K., Kerminen, V.M., Kulmala, M., 2006. Meteorological dependence of size-fractionated number concentrations of urban aerosol particles. Atmos. Environ. 40, 1427–1440. doi:10.1016/j.atmosenv.2005.10.061

Idrose, N.S., Dharmage, S.C., Lowe, A.J., Lambert, K.A., Lodge, C.J., Abramson, M.J., Douglass, J.A., Newbigin, E.J., Erbas, B., 2019. A systematic review of the role of grass pollen and fungi in thunderstorm asthma. Environ. Res. 181, 108911. doi:10.1016/j.envres.2019.108911

Jantz, N., Homeier, J., León-Yánez, S., Moscoso, A., Behling, H., 2013. Trapping pollen in the tropics - Comparing modern pollen rain spectra of different pollen traps and surface samples across Andean vegetation zones. Rev. Palaeobot. Palynol. 193, 57–69. doi:10.1016/j.revpalbo.2013.01.011

Jato, V., Rodríguez-Rajo, F.J., Alcázar, P., De Nuntiis, P., Galán, C., Mandrioli, P., 2006. May the definition of pollen season influence aerobiological results? Aerobiologia (Bologna). 22, 13–25. doi:10.1007/s10453-005-9011-x

Kasprzyk, I., Harmata, K., Myszkowska, D., Stach, A., Stpalska, D., 2001. Diurnal variation of chosen airborne pollen at five sites in Poland. Aerobiologia (Bologna). 17, 327–345. doi:10.1023/A:1013078627196

Kluska, K., Piotrowicz, K., Kasprzyk, I., 2020. The impact of rainfall on the diurnal patterns of atmospheric pollen concentrations. Agric. For. Meteorol. 291, 108042. doi:10.1016/j.agrformet.2020.108042

Kruskal, W.H., Wallis, W.A., 1952. Use of ranks in one-criterion variance analysis. J. Am. Stat. Assoc. 47, 583–621.

Kyrö, E.M., Grönholm, T., Vuollekoski, H., Virkkula, A., Kulmala, M., Laakso, L., 2009. Snow scavenging of ultrafine particles: Field measurements and parameterization. Boreal Environ. Res. 14, 527–538.

Laakso, L., Grönholm, T., Rannik, Ü., Kosmale, M., Fiedler, V., Vehkamäki, H., Kulmala, M., 2003. Ultrafine particle scavenging coefficients calculated from 6 years field measurements. Atmos. Environ. 37, 3605–3613. doi:10.1016/S1352-2310(03)00326-1

Ladino, L., Stetzer, O., Hattendorf, B., Günther, D., Croft, B., Lohmann, U., 2011. Experimental study of collection efficiencies between submicron aerosols and cloud droplets. J. Atmos. Sci. 68, 1853–1864. doi:10.1175/JAS-D-11-012.1

Lawson, D.A., Rands, S.A., 2019. The effects of rainfall on plant–pollinator interactions. Arthropod. Plant. Interact. 13, 561–569. doi:10.1007/s11829-019-09686-z

Loosmore, G.A., Cederwall, R.T., 2004. Precipitation scavenging of atmospheric aerosols for emergency response applications: Testing an updated model with new real-time data. Atmos. Environ. 38, 993–1003. doi:10.1016/j.atmosenv.2003.10.055

Maria, S.F., Russell, L.M., 2005. Organic and inorganic aerosol below-cloud scavenging by suburban New Jersey precipitation. Environ. Sci. Technol. 39, 4793–4800. doi:10.1021/es0491679

Menon, S., Hansen, J., Nazarenko, L., Luo, U., 2002. Climate effects of black carbon aerosols in China and India. Science (80-.). 297, 2250–2253. doi:10.1126/science.1075159

Mircea, M., Stefan, S., 1998. A theoretical study of the microphysical parameterization of the scavenging coefficient as a function of precipitation type and rate. Atmos. Environ. 32, 2931–2938. doi:10.1016/S1352-2310(98)00018-1

Mirra, R., Ribarov, C., Valchev, D., Ribarova, I., 2020. Towards Energy Efficient Onsite Wastewater Treatment. Civ. Eng. J. 6, 1218–1226. doi:10.28991/cej-2020-03091542

Oduber, F., Calvo, A.I., Blanco-Alegre, C., Castro, A., Vega-Maray, A.M., Valencia-Barrera, R.M., Fernández-González, D., Fraile, R., 2019. Links between recent trends in airborne pollen concentration, meteorological parameters and air pollutants. Agric. For. Meteorol. 264, 16–26. doi:10.1016/j.agrformet.2018.09.023

Oduber, F., Calvo, A.I., Castro, A., Alves, C., Blanco-Alegre, C., Fernández-González, D., Barata, J., Calzolai, G., Nava, S., Lucarelli, F., Nunes, T., Rodríguez, A., Vega-Maray, A.M., Valencia-Barrera, R.M., Fraile, R., 2021. One-year study of airborne sugar compounds: Cross-interpretation with other chemical species and meteorological conditions. Atmos. Res. 251. doi:10.1016/j.atmosres.2020.105417

Oduber, F., Isabel, A., Castro, A., Blanco-alegre, C., Alves, C., Calzolai, G., Nava, S., Lucarelli, F., Nunes, T., Barata, J., Fraile, R., 2021. Characterization of aerosol sources in León (Spain) using Positive Matrix Factorization and weather types. Sci. Total Environ. 754, 142045. doi:10.1016/j.scitotenv.2020.142045

Oteros, J., Buters, J., Laven, G., Röseler, S., Wachter, R., Schmidt-Weber, C., Hofmann, F., 2017. Errors in determining the flow rate of Hirst-type pollen traps. Aerobiologia (Bologna). 33, 201–210. doi:10.1007/s10453-016-9467-x

Pöschl, U., 2005. Atmospheric aerosols: Composition, transformation, climate and health effects. Angew. Chemie - Int. Ed. 44, 7520–7540. doi:10.1002/anie.200501122

Rasch, P.J., Feichter, J., Law, K., Mahowald, N., Penner, J., Benkovitz, C., Genthon, C., Giannakopoulos, C., Kasibhatla, P., Koch, D., Levy, H., Maki, T., Prather, M., Roberts, D.L., Roelofs, G.J., Stevenson, D., Stockwell, Z., Taguchi, S., Kritz, M., Chipperfield, M., Baldocchi, D., McMurry, P., Barrie, L., Balkanski, Y., Chatfield, R., Kjellstrom, E., Lawrence, M., Lee, H.N., Lelieveld, J., Noone, K.J., Seinfeld, J., Stenchikov, G., Schwartz, S., Walcek, C., Williamson, D., 2000. A comparison of scavenging and deposition processes in global models: Results from the WCRP Cambridge workshop of 1995, Tellus, Series B: Chemical and Physical Meteorology. doi:10.3402/tellusb.v52i4.17091

Recio, M., Picornell, A., Trigo, M.M., Gharbi, D., García-Sánchez, J., Cabezudo, B., 2018. Intensity and temporality of airborne Quercus pollen in the southwest Mediterranean area: Correlation with meteorological and phenoclimatic variables, trends and possible adaptation to climate change. Agric. For. Meteorol. 250–251, 308–318. doi:10.1016/j.agrformet.2017.11.028

Reinmuth-Selzle, K., Kampf, C.J., Lucas, K., Lang-Yona, N., Fröhlich-Nowoisky, J., Shiraiwa, M., Lakey, P.S.J., Lai, S., Liu, F., Kunert, A.T., Ziegler, K., Shen, F., Sgarbanti, R., Weber, B., Bellinghausen, I., Saloga, J., Weller, M.G., Duschl, A., Schuppan, D., Pöschl, U., 2017. Air Pollution and Climate Change Effects on Allergies in the Anthropocene: Abundance, Interaction, and Modification of Allergens and Adjuvants. Environ. Sci. Technol. 51, 4119–4141. doi:10.1021/acs.est.6b04908

Sedghy, F., Varasteh, A.R., Sankian, M., Moghadam, M., 2018. Interaction between air pollutants and pollen grains: The role on the rising trend in allergy. Reports Biochem. Mol. Biol. 6, 219–224.

Seinfeld, J.H., Pandis, S.N., 2016. Atmospheric Chemistry and Physics: From Air Pollution to Climate Change, Atmospheric Chemistry and Physics. Wiley. doi:10.1016/0016-7037(87)90252-3

Shen, C., Liu, K. biu, Tang, L., Overpeck, J.T., 2006. Quantitative relationships between modern pollen rain and climate in the Tibetan Plateau. Rev. Palaeobot. Palynol. 140, 61–77. doi:10.1016/j.revpalbo.2006.03.001

Subiza Garrido-Lestache, J., 2004. Allergenic pollens in Spain. Allergol. Immunopathol. (Madrid). 32, 97–182.

Textor, C., Schulz, M., Guibert, S., Kinne, S., Balkanski, Y., Bauer, S., Berntsen, T., Berglen, T., Boucher, O., Chin, M., Dentener, F., Diehl, T., Easter, R., Feichter, H., Fillmore, D., Ghan, S., Ginoux, P., Gong, S., Grini, A., Hendricks, J., Horowitz, L., Huang, P., Isaksen, I., Iversen, T., Kloster, S., Koch, D., Kirkevåg, A., Kristjansson, J.E., Krol, M., Lauer, A., Lamarque, J.F., Liu, X., Montanaro, V., Myhre, G., Penner, J., Pitari, G., Lamarque, J.F., Liu, X., Montanaro, V., Myhre, G., Penner, J., Pitari, G., Reddy, S., Seland, Ø., Stier, P., Takemura, T., Tie, X., 2006. Analysis and quantification of the diversities of aerosol life cycles within AeroCom. Atmos. Chem. Phys. 6, 1777–1813. doi:10.5194/acpd-5-8331-2005

Trigo Pérez, M. del M., Jato Rodríguez, V., González, Fernández, D., Galán Soldevilla, C., 2008. Atlas aeropalinológico de España. León.

UNI 11108:2004, 2004. Air quality: Method for sampling and counting of airborne pollen grains and fungal spores.

Wang, X., Zhang, L., Moran, M.D., 2011. On the discrepancies between theoretical and measured below-cloud particle scavenging coefficients for rain-a numerical investigation using a detailed one-dimensional cloud microphysics model. Atmos. Chem. Phys. 11, 11859–11866. doi:10.5194/acp-11-11859-2011

WHO, 2013. Review of evidence on health aspects of air pollution – REVIHAAP Project, World Health Organization. Copenhagen, Denmark.

Zamani Beidokhti, M., (Omid) Naeeni, S.T., AbdiGhahroudi, M.S., 2019. Biosorption of Nickel (II) from Aqueous Solutions onto Pistachio Hull Waste as a Low-Cost Biosorbent. Civ. Eng. J. 5, 447. doi:10.28991/cej-2019-03091259

Zhang, Y., Bielory, L., Mi, Z., Cai, T., Robock, A., Georgopoulos, P., 2015. Allergenic pollen season variations in the past two decades under changing climate in the United States. Glob. Chang. Biol. 21, 1581–1589. doi:10.1111/gcb.12755

Zhao, H., Zheng, C., 2006. Monte Carlo solution of wet removal of aerosols by precipitation. Atmos. Environ. 40, 1510–1525. doi:10.1016/j.atmosenv.2005.10.043

Zhao, L., Lee, X., Smith, R.B., Oleson, K., 2014. Strong contributions of local background climate to urban heat islands. Nature 511, 216–219. doi:10.1038/nature13462

Zhao, S., Yu, Y., He, J., Yin, D., Wang, B., 2015. Below-cloud scavenging of aerosol particles by precipitation in a typical valley city, northwestern China. Atmos. Environ. 102, 70–78. doi:10.1016/j.atmosenv.2014.11.051

Zikova, N., Zdimal, V., 2016. Precipitation scavenging of aerosol particles at a rural site in the Czech Republic. Tellus B 68, 1–14. doi:10.3402/tellusb.v68.27343

SUPPLEMENTARY MATERIAL

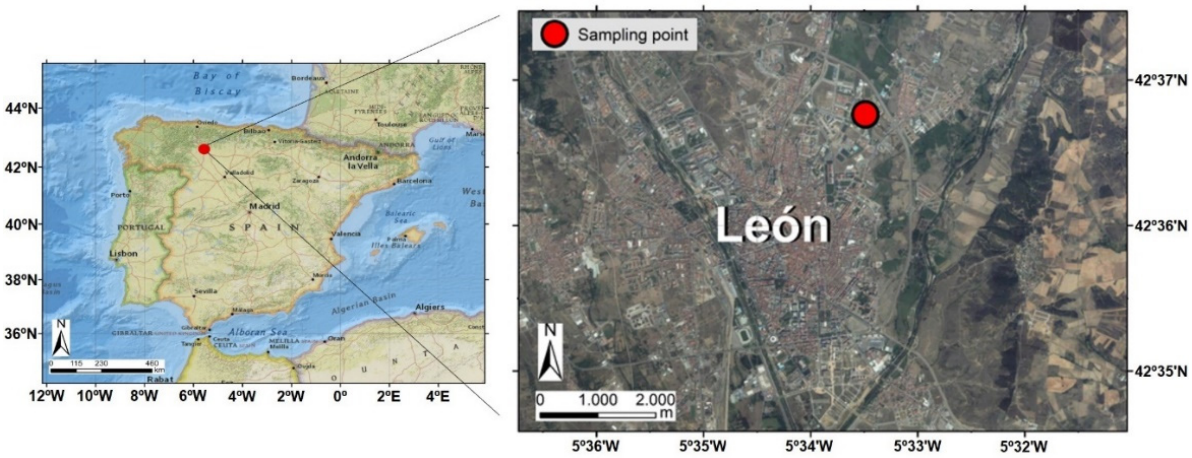

Figure S10.1. Sampling point and surroundings in the NW Iberian Peninsula. Source: Earthstar Geographics, ESRI.

Table S10.1. Coefficients obtained to verify the model performed for each of the 10 models, and Kolmogorov-Smirnov (K-S) statistical test carried out between the predicted and the measured values. The last row (*N*=0) includes the model obtained with the whole data set was represented.

N	k_1	k_2 (m^{-3} °C^{-1})	k_3 (s m^{-4})	k_4 (m^{-3} mm^{-1})	k_5 (m^{-3})	K-S (statistic)	r^2
1	0.774	-0.101	0.488	-	-0.126	0.429	0.978
2	0.736	-0.121	-	3.019	-0.316	0.353	0.979
3	0.792	-0.139	-	-	0.983	0.360	0.738
4	0.738	-0.123	-	2.988	-0.333	0.261	0.754
5	0.783	-0.121	-	-	1.193	0.545	0.602
6	0.743	-0.138	-	2.985	-0.013	0.259	0.940
7	0.795	-0.127	0.512	-	0.184	0.250	0.926
8	0.790	-0.107	0.599	-	-0.084	0.214	0.968
9	0.736	-0.121	-	3.019	-0.316	0.421	0.962
10	0.776	-0.150	0.556	3.239	-1.084	0.186	0.798
0	**0.770**	**-0.125**	**0.512**	**2.785**	**-0.912**	**0.165**	**0.938**

CHAPTER 11. Links between aerosol radiative forcing and rainwater

Full title: *Links between aerosol radiative forcing and rainwater: stratiform and convective precipitation*

Submitted for publication

11.1. INTRODUCTION

In recent years, atmospheric aerosols are one of the main areas of study because of their importance in current and future global climate (ICCP, 2014a). The action of aerosols on climate is mainly evaluated by radiative forcing: i) aerosol direct radiative forcing (ADRF), via scattering and absorption of solar and terrestrial radiation (Charlson et al., 1992), which depends on their chemical and physical properties; ii) aerosol indirect radiative forcing (AIRF), caused by the radiation behaviour regarding the modulation of cloud properties by aerosols serving as ice or cloud condensation nuclei (CCN) (Matsui and Pielke, 2006); iii) semi-direct effect, that is the quantification of the impact of the direct effect on the thermodynamics of the atmosphere (heating or cooling), inflecting the bounty of CCN, the raindrop size distribution and the cloud properties (albedo, lifetime, reflectivity, etc.) (Bond et al., 2013; Rosenfeld et al., 2014). Radiative forcing further modifies the rain characteristics and temperature at ground level (Bollasina et al., 2011; Menon et al., 2002). The change of aerosol radiative forcing depending on aerosol particle concentration is clearly noticeable during Saharan intrusions (Oduber et al., 2019a) or haze conditions (Rupakheti et al., 2020). It is noted that aerosol particles are one of the largest causes of uncertainty in the assessment of climate forcing due to their short residence time in the atmosphere and their spatial heterogeneity (Höller et al., 2003; Schultze and Rockel, 2018).

There is great uncertainty in the aerosol radiative forcing estimations because of different reasons: the existence of many aerosol sources, the varied aerosol chemical composition with different properties and its vertical distribution and the surface albedo (Patel et al., 2017; Reddy et al., 2013). Further, the optical properties of aerosols depend on their concentration, the chemical composition and their mixing state (Panicker et al., 2013). The physicochemical and optical properties aerosols of have been largely studied (Ayash et al., 2008; Calvo, 2009; Kaskaoutis et al., 2013; Paulot et al., 2018; Perrone and Bergamo, 2011; Rama Gopal et al., 2017). However, there is still a deficiency of information concerning the effect of the presence of higher or lower aerosol atmospheric forcing in the atmosphere, related with aerosol burden and with rain parameters measured at ground level.

One of the main sinks of aerosols in the atmosphere is rain. Rain causes two types of wet scavenging depending on how high the aerosols are in the atmosphere: In-Cloud Scavenging (ICS) and Below-Cloud Scavenging (BCS) (Ladino et al., 2011). For ICS, aerosol particles serve as CCN, while for BCS (also called impaction scavenging or washout) they are captured by hydrometeors. Besides, the effect of rain on aerosol particles can be different if rain is convective or stratiform (Textor et al., 2006), since there are differences in hydrometeor size distribution and in the total of precipitation according to the type of rain (Huang et al., 2019). The differences in microphysics between convective and stratiform events, already reported in several studies (Thurai et al., 2016; Wu et al., 2013), are due to the different formation of both types of precipitation. Convective precipitation rates (related with an intense ascending motion throughout the troposphere) are often more considerable than stratiform rain rates (related with a weak ascending or descending velocity throughout the troposphere) (Houze, 2014; Wu et al., 2013). The relationship between rainfall intensity R (in mm h^{-1}) and radar reflectivity Z (in mm^6 m^{-3}) is often described as $Z=a \cdot R^b$ (Fraile and Fernández-Raga, 2009), and has been used to discern between convective and stratiform precipitation. Different results have been obtained using disdrometer data depending on the criterion used (Fernández-Raga et al., 2009; Lee et al., 2004; Lee and Zawadzki, 2005).

The relationship between aerosols, clouds and rain characteristics is very complex. An example is that models at various scales relate aerosols with clouds and their amount of precipitation (Da Silva et al., 2019; López-Romero et al., 2021; Sarangi et al., 2017; Teller and Levin, 2005), but do not include characteristics of rainfall (raindrop diameter or rain intensity). Regarding cloud–radiation interactions, a higher energy on the Earth's surface can influence the development of convection (Machado et al., 2004). Consequently, the complete aerosol-cloud radiation interaction may affect the rain scavenging effect. Studies about the relation between aerosol radiative forcing effects and any type of precipitation are scarce. An example is the analysis of radiative forcing effect of two heavy haze events in southern Nepal, included in Rupakheti et al.

(2020). The authors reported that during haze, aerosol optical thickness (AOT) levels were 230-300% higher than the annual mean value.

To our knowledge, few studies are concerned with documenting the aerosol radiative forcing of the atmosphere before rain events and the characterization of the microphysical properties of the scavenging event. The statistical study of this relationship for stratiform and convective events is the focus of this study. The main aims of this paper, with data gathered in Léon, Spain, over one year, are: i) to quantify the effect of scavenging on the aerosol content in order to analyze the evolution of aerosol radiative forcing before and after stratiform rain, and ii) to identify any relationship between direct aerosol radiative forcing before rain and the characteristics of rainfall.

11.2. METHODS

11.2.1. SAMPLING SITE

Between the 12th of February 2016 and the 14th of March 2017, the measurement campaign instruments were installed in the Faculty of Veterinary Science of the University of Léon. Around the sampling site, the main sources of particulate emissions are traffic, domestic heating devices, wildfires and Saharan intrusions (Blanco-Alegre et al., 2019; Oduber et al., 2021).

León (42°36′N, 05°35′W), a city located in the NW of the Iberian Peninsula (838 m), presented a population of 200,000 inhabitants. León presents an annual average temperature of 11.1 °C with 13 snowy days and 75 rainy days, with a total mean precipitation of 515 mm concentrated in winter and spring, based on the past 35 years (data provided by Spanish Meteorological Office, http://www.aemet.es/en/portada).

11.2.2. AEROSOL PARTICLE SIZE DISTRIBUTION

A continuous monitoring of particle size distributions of ultrafine (UFP) and accumulation mode particles has been carried out using a high-resolution nanoparticle sizer (TSI-SMPS Model 3938). The range analyzed was between 14.3 and 1000 nm in 110 channels. The set flow ratio has been 0.3 and 3 L min^{-1} for aerosol and sheath flow, respectively. A complete scan was obtained every 6 minutes. The TSI-SMPS system consists in a long differential mobility classifier (DMA 3081) connected to a condensation particle counter (CPC 3772), with an inlet air dryer (RH <40%). Particle losses in SMPS measurements, based on an equivalent pipe length (Wiedensohler et al., 2012), have been taken into account. A detailed description of this device can be found in Blanco-Alegre et al. (2021).

An optical spectrometer, a Passive Cavity Aerosol Spectrometer Probe (PCASP-X) has been used to obtain the particle size distributions for coarse aerosol between 803 nm and 17.42 µm after Mie theory correction (Castro et al., (2015), on a one-minute basis. Later, the aerosol optical diameters measured with PCASP-X were converted into aerodynamic diameters using the fundamental equation relating optical (d_o) and aerodynamic diameter ($d_a = d_o(\rho)^{-0.5}$) (Chien et al., 2016), with an assumed particle density (ρ) of 1.93 g cm^{-3}. This value corresponds to the mean annual density obtained from the analysis of all daily quartz filters during the study period. Then the PCASP-X particle diameters were shifted from the aerodynamic diameter obtained to equivalent mobility diameters, assuming a dynamic shape factor of 1.0 (Bullard et al., 2017; Khlystov et al., 2004). After that, the new particle sizes were binned in 126 channels, choosing the SMPS over the PCASP-X (110 of SMPS and 16 of PCASP-X) when there is overlap between channels, from 0.017 to 17.42 µm recalculating the mean concentration of PCASP-X channels in 6 minutes.

The particle number size distribution (PNSD) has been obtained in every rain event for three intervals: before, during and after rainfall. The PNSD was fitted to a multi-lognormal distribution through the sum of two or three lognormal distributions formulae.

11.2.3. DENSITY AND REFRACTIVE INDEX

The density (ρ) and the refractive index (m) of aerosols were estimated keeping the methodology described by Levin et al. (2010) or Calvo et al. (2013), using equations 1 and 2, respectively (Hasan and Dzubay, 1983).

$$\rho^{-1} = \sum_j \frac{X_j}{\rho_j} \qquad \textit{Eq. 11.1}$$

$$m = \rho \sum_j \frac{X_j n_{j,i}}{\rho_j} - \rho \sum_j \frac{X_j k_j}{\rho_j} i \qquad \textit{Eq. 11.2}$$

where, for each component, X_j is the mass, ρ_j is the density, n_j and k_j are the real and imaginary parts of refractive index, respectively, and i is the imaginary unit ($i^2 = -1$).

The aerosol chemical composition needed for estimating ρ and m was obtained from the analysis of 24 h PM_{10} filter samples collected during the sampling campaign (AERORAIN project):

- Quartz filters (150 mm diameter) were used to determine PM_{10} by gravimetry (±0.00001 g) on an electronic semi-microbalance (Mettler Toledo, XPE105DR). An analysis of organic and elemental carbon was also performed (Alves et al., 2015; Pio et al., 2011).
- Teflon filters (47 mm diameter) were analysed to determine the main trace elements using the Particle-Induced X-ray Emission (PIXE) technique (Lucarelli et al., 2015). In addition, an analysis of water-soluble inorganic ions by ion chromatography (IC) was carried out on a Thermo Scientific Dionex™ ICS-5000 equipment.

A detailed description of the sampling and the chemical analyses is included in Oduber et al. (2021).

11.2.4. RAINDROP CHARACTERIZATION AND METEOROLOGICAL DATA

A Laser Precipitation Monitor (LPM) from *Thies Clima* has been used to register hydrometeors between 0.125-8 mm in 22 channels during the study period. A detailed description of this equipment has been presented by Fernández-Raga et al. (2009). We obtained the following rainfall variables, on a one-minute basis: precipitation intensity, precipitation amount (mm), drops by channels, drop concentration (# m^{-3}), mean swept volume by falling drops by channel (mm^3 m^{-3}) calculated based on Gunn and Kinzer (1949) measurements and mean of raindrop sizes. On top of the disdrometer, a weather station was used for registering the temperature, relative humidity, pressure, wind speed and direction.

The gamma distribution that depends on two parameters, α (shape) and β (scale), defined in Eq. 11.3, is often used to characterize the raindrop size distribution (Fernandez-Raga et al., 2017). The falling velocity of the curve to zero is described by the scale parameter. Concerning the shape

parameter, if α>1, the mode (α-1)/β (i.e., the most frequent raindrop size) can be calculated. The path chosen to calculate α and β was the moment method (Marques et al., 2014a).

$$f(x) = \frac{\beta^{\alpha} x^{\alpha-1} e^{-\beta x}}{\Gamma(\alpha)} \qquad \textit{Eq. 11.3}$$

where Γ is the gamma or factorial function, defined as Eq. 11.4:

$$\Gamma(\alpha) = \int_0^{\infty} t^{\alpha-1} e^{-t} dt \qquad \textit{Eq. 11.4}$$

11.2.5. RADIATIVE FORCING MODEL

The aerosol optical properties together with vertical profiles of temperature, ozone and relative humidity have been used as inputs in the Radiative Transfer Model Global Atmospheric ModEl (RTM GAME) (Dubuisson et al., 2004, 1996). This model estimates the instantaneous shortwave clear-sky aerosol direct radiative forcing. Besides, radiative transfer computations depend on optical aerosol parameters such as aerosol optical thickness (AOT), single scattering albedo (SSA) and asymmetry parameter (g). The surface albedo is a crucial parameter, since highly absorbing carbonaceous aerosols above highly-reflecting surfaces can change the sign of forcing heating more the lower atmosphere (Satheesh et al., 2010). In this study, the optical parameters were based on the Mie theory taken into account the aerosol size distribution and the refractive index. As a result, SSA, g and extinction coefficient profiles were calculated at the seven wavelengths (0.48, 0.55, 0.65, 0.87, 1.24, 1.65 and 2.13 µm) used in the GAME radiative transfer model.

The vertical profiles of atmospheric properties (temperature, relative humidity and pressure) and Atmospheric Boundary Layer (ABL) have been obtained of National Oceanic and Atmospheric Administration (NOAA) (www.ready.noaa.gov/READYamet.php) every 3 hours.

To obtain the optical properties, a monthly refractive index was estimated. The aerosol optical thickness and surface albedo were obtained from two AErosol RObotic NETwork (AERONET) photometers, located in Palencia (41°9'N, 4°7'W) and Valladolid (41°7'N, 4°7'W) at about 120 km from León. To determine whether the data registered in Valladolid and Palencia could be extrapolated to León, a comparison of AOT was carried out during the period from July 2017 to May 2019 (AOT data were available at the three sites). The AOT retrieved by ESR.PACK, used in León, is comparable to the one retrieved by AERONET with mean deviation values between

−0.0030 and +0.0041 (Estellés et al., 2012). During, before (3 hours) and after (3 hours) precipitation in León, a determination coefficient (r^2) of 0.78 was found between AOT values registered in León and Valladolid, and of 0.73 in León and Palencia (Figure S11.1). So, the AOT data are consistent in the area around the sampling point.

The upward and downward net radiative fluxes were calculated in Calvo et al. (2010) over the entire shortwave region. The fluxes were performed every 3 h (0600, 0900, 1200, 1500 and 1800 UTC), concurring with before and after rain events along the whole study. Then, the aerosol direct forcing at the bottom (ΔF_{BOA}) and at the top (ΔF_{TOA})of the atmosphere were computed by Eq. 11.5 and 11.6.

$$\Delta F_{BOA} = F_{BOA}(w)\downarrow - F_{BOA}(o)\downarrow \qquad \textit{Eq. 11.5}$$

$$\Delta F_{TOA} = -(F_{TOA}(w)\uparrow - F_{TOA}(o)\uparrow) \qquad \textit{Eq. 11.6}$$

where $F_{BOA}(w)_{\downarrow}$ and $F_{BOA}(o)_{\downarrow}$ are the downward net radiative fluxes at the bottom of the atmosphere with (w) and without (o) aerosol particles, respectively. Likewise, $F_{TOA}(w)_{\uparrow}$ and $F_{TOA}(o)_{\uparrow}$ are the upward net radiative fluxes simulated at the top of atmosphere with (w) and without (o) aerosols, respectively. Thus, a positive value of ΔF infers an aerosol warming effect. The atmospheric forcing, ΔF_{ATM}, was calculated using Eq. 11.7, and represents the absorption of solar radiation due to absorbing properties of particles from ground level to 20 km.

$$\Delta F_{ATM} = \Delta F_{TOA} - \Delta F_{BOA} \qquad \textit{Eq. 11.7}$$

Besides, we have calculated the associated heating rate (K day^{-1}) of these aerosols, computed with GAME, to compute the potential heating for the whole atmospheric column, before and after rain. Likewise, to analyze the rain scavenging effect on ΔF_{ATM} during stratiform events, the parameter $\Delta F\%$ has been obtained following Eq. 11.8, during the period between the times t_1 (1 hour before rain) and t_2 (1 hour after rain).

$$\Delta F\% = \left(\frac{\Delta F_{ATM_2} - \Delta F_{ATM_1}}{\Delta F_{ATM_1}}\right) \cdot 100 \qquad \textit{Eq. 11.8}$$

For a given aerosol optical thickness, radiative forcing results depend on the variability of the SSA, g parameter, surface albedo, the size distribution and refractive index. Error budgets have to be taken into account when interpreting results, but several studies have already shown the GAME model to be reliable (Calvo et al., 2010; Granados-Muñoz et al., 2019; Roger et al., 2006). The uncertainties reported in these papers indicate that the radiative impacts of aerosols presented an accuracy of 12% at *BOA*, 20% at *TOA*, and 16% in the *ATM*. As AOT values in this paper

(from 0.03 to 0.54) are of the same order as these studies, these sensitivities are consistent and addressed.

11.2.6. CRITERIA FOR RAIN EVENT SELECTION

The selection criteria of rain events are conditioned by the availability of AERONET data needed to run the GAME radiative transfer model. Data are only available during hours with solar radiation (between 0600 and 1800 UTC). The rain event selection was carried out taking into account the following considerations:

1) Rain events should occur during daytime hours.
2) Accumulated precipitation should be higher than 0.1 mm, more restrictive than the one proposed by Blanco-Alegre et al. (2019) or Laakso et al. (2003).
3) Snow events and days with Saharan dust outbreaks have not been considered.
4) Only events with a duration of less than 10 hours were considered. A higher duration will obstruct the analysis before-after rainfall on a single day due to the lack of availability of AERONET data.
5) Only events with AOT data available before and after the rain event were considered. It is remarkable that the presence of clouds before and after rain caused that many events did not have AOT data and, therefore, these events were excluded.
6) To run the GAME model the following parameters must be available:
    a. Aerosol particle size distribution. It was obtained in rainy days 1 hour before the beginning of the rain event (always between 0600 and 1800 UTC).
    b. AOT. The closest AOT data to the beginning of the rain event were selected, always within three hours before a rainfall begins.
    c. The vertical profiles of temperature, relative humidity and pressure. The closest radiosounding available was used.

Based on lightning maps (Blitzortung.org, 2020), convective events have been identified, as lightning strikes are the result of the development of convective processes (Choudhury et al., 2021; Wang et al., 2020). Next, this classification was verified by means of the height of the clouds (higher in convective events) through satellite imagery, the Convective Available Potential Energy (*CAPE*) (positive values), meteorological data, and Z-R relationship obtained from disdrometer data. For these convective events, the radiative forcing was only calculated before the start of the rain, since this type of event usually occurs at the end of the afternoon, preventing the estimation of the direct radiative forcing fluxes.

After a detailed analysis of all data from 13 months of the study period, with 103 precipitation-days recorded, only 16 stratiform (non-convective) and 15 convective rain events met the previously cited requirements. Subsequently, all rain events were classified into 2 groups according to ΔF_{ATM} values before rain: "low" (lower than 30 W m^{-2}) and "high" (higher than 30 W m^{-2}). The 30 W m^{-2} value has been selected as threshold since it is the mean ΔF_{ATM} value of all the selected events before rain.

11.2.7. AIR MASS ORIGIN

The air mass origin during rain events was obtained using the model NOAA HYSPLIT4 (Hybrid Single Particle Lagrangian Integrated Trajectory) (R Draxler and Rolph, 2012) based on four-days back trajectories at 1000 m over León. The methodology was the same as in Blanco-Alegre et al. (2019), with a classification into six categories: Arctic, Atlantic Ocean, European continental, North America, North Atlantic Ocean and Saharan desert. The model was run with meteorological data from the Global Data Assimilation System (GDAS) archives (http://ready.arl.noaa.gov/HYSPLIT_traj.php).

11.3. RESULTS AND DISCUSSION

11.3.1. RAINDROP ANALYSIS

As mentioned above, 16 stratiform rain events fulfilled the selection criteria (Figure 11.1). Among them, 5 occurred in winter, 8 in spring and 2 in autumn, with only one event in summer. Rainfall events have been grouped according to the ΔF_{ATM} value before rain. There were 11 "low" events and 5 "high" events. With regard to convective rain events, only 15 met the selection criteria (7 "low" and 8 "high"), concentrated in summer (9) and spring (6).

The stratiform rain events exhibited a mean duration of 188±132 minutes (median: 190 minutes), a mean rainfall amount of 2.61±2.36 mm (median: 1.97 mm) and a mean rainfall intensity of 1.20±1.76 mm h^{-1} (median: 0.58 mm h^{-1}). The convective rain events showed a lower mean duration (68±56 minutes) and a higher mean rainfall amount of 3.5±2.8 mm (median: 3.4 mm h^{-1}) and rainfall intensity, with 5.11±6.53 mm h^{-1} (median: 2.53 mm h^{-1}), than stratiform events. Table 11.1 shows a summary of rain and meteorological parameters during the selected

stratiform and convective events (classified by ΔF_{ATM} groups). The mean raindrop diameter was similar between the "low" and "high" groups of stratiform events (0.51±0.10 vs 0.48±0.12 mm). However, convective events showed a higher mean raindrop diameter (0.96±0.98 vs 0.83±0.63 mm). In order to know if there were differences between mean raindrop diameters of stratiform and convective events, the Mann Whitney U test was applied, revealing statistical differences (p=0.002). Within each group of stratiform and convective events, there were no significant statistical differences between ΔF_{ATM} groups (p=0.721 and p=0.955, respectively).

With regard to temperature, the differences found are linked to seasonal effects. Thus, for example, convective events occurred during spring and summer and presented higher temperatures (18.1±8.9 °C) than stratiform events (14.0±7.9 °C), which occurred mainly in winter, with a higher value of AOT and a lower Atmospheric Boundary Layer (ABL) height (Table 11.2). Within stratiform events, the surface temperature was lower in "high" than in "low" events (16.3±8.3 °C vs 8.9±4.2 °C), also due to the seasonal effect, since "low" events occurred in winter.

Regarding the Z-R relationship, it is remarkable that the selected convective events, using lightning maps, showed higher values of *a* and *b* than the stratiform events, with no statistically significant differences between "low" and "high" groups (p>0.05). Although the Z-R relationship did not often allow a clear separation between types of precipitation (Fernández-Raga et al., 2009; Nzeukou et al., 2004), significant differences were found in *a* (p=0.003) and *b* (p=0.023) between convective and stratiform events.

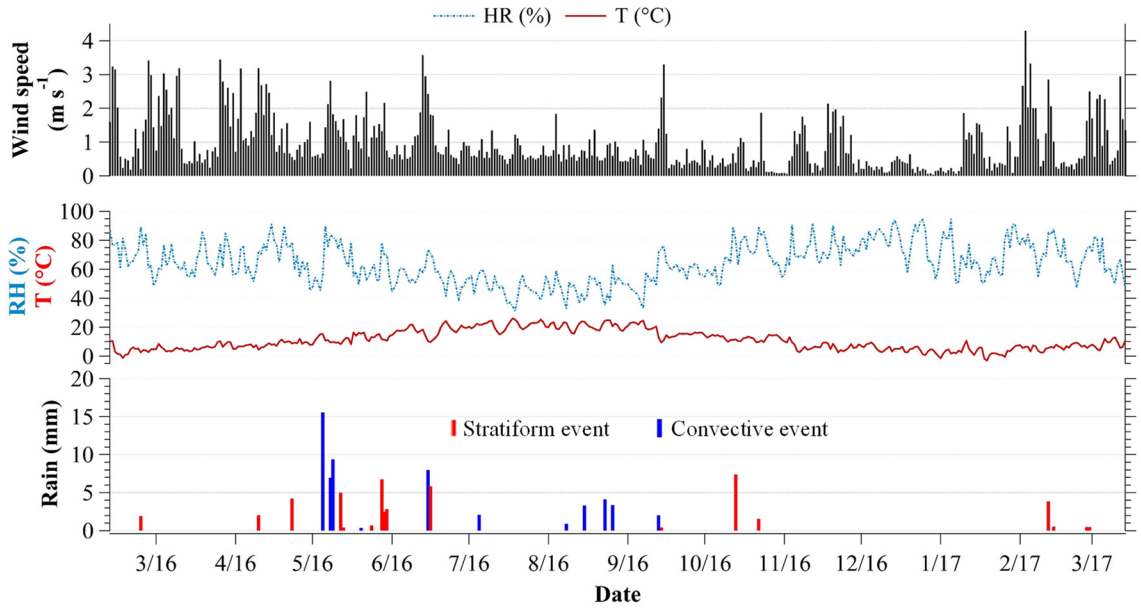

Figure 11.1. Evolution of daily wind speed, relative humidity and temperature along the study period. Distribution of stratiform rain events (in red bars) and convective rain events (in blue bars) that meet the criteria selection.

Table 11.1. Mean values and standard deviation of stratiform and convective rain events classified by ΔF_{ATM}. *N* is the number of events. Median values are in brackets.

	Event classification	Rain amount (mm)	Duration (min)	Rain intensity (mm h^{-1})	Swept volume (mm^3 m^{-3})	Raindrop diameter (mm)	Z-R ($Z=a \cdot R^b$)
Stratiform	Low *N*=11	1.8±1.8 (0.7)	144±130 (91)	1.30±2.11 (0.50)	$2.6 \cdot 10^9 \pm 2.0 \cdot 10^9$ ($1.4 \cdot 10^9$)	0.51±0.08 (0.51)	*a*=157±65 *b*=1.33±0.09
	High *N*=5	4.3±2.7 (3.8)	283±81 (245)	0.96±0.61 (1.10)	$5.9 \cdot 10^9 \pm 2.1 \cdot 10^9$ ($5.8 \cdot 10^9$)	0.48±0.12 (0.48)	*a*=155±68 *b*=1.35±0.08
Convective	Low *N*=7	3.1±3.4 (2.0)	59±71 (27)	7.61±9.14 (2.53)	$3.1 \cdot 10^9 \pm 3.2 \cdot 10^9$ ($3.6 \cdot 10^9$)	0.96±0.98 (0.61)	*a*=251±96 *b*=1.43±0.07
	High *N*=8	3.8±2.3 (3.8)	76±44 (58)	2.93±1.45 (2.62)	$3.8 \cdot 10^9 \pm 2.6 \cdot 10^9$ ($4.0 \cdot 10^9$)	0.83±0.63 (0.62)	*a*=266±99 *b*=1.40±0.08

The air mass origin during stratiform and convective events can be observed in Figure S11.2. In stratiform events, Atlantic and North Atlantic Ocean origins are the most common classes (with 3 events each) in the "low" group, while Atlantic Ocean (3 events) and Saharan desert (2 events) are the most common class in the "high" group. In convective events, the main origin in the "low" group is Saharan desert (3 events) followed by European continental (2 events); in the "high" group the main origins are European continental and Atlantic Ocean with 3 events each.

11.3.2. STRATIFORM RAIN EVENTS

The analysis of optical properties and size distributions of aerosols in stratiform events is detailed below, together with the values of the radiative forcings and the influence of scavenging on them.

11.3.2.1. Particle size distributions and optical parameters

The aerosol size distribution presented three modes before and after rain (Table 11.3). In general, the first mode (~30 nm) was located within nucleation mode, the second one (~100 nm) in Aitken mode and the third one (located between 133 and 1542 nm) in accumulation mode and, occasionally, in coarse mode. The nucleation mode particles undergo a clear scavenging, verified by comparing their concentrations before and after rain: a decrease in the concentration of such particles is recorded, although with similar values of the modal radii. Also, the Aitken and

accumulation modes show a shift towards smaller sizes and a decrease in the number of particles, presumably due to the rain scavenging effect (Blanco Alegre et al., 2021). By groups based on ΔF_{ATM}, the following evidences were observed for stratiform rain events:

- "Low" group: there is a decrease in the particle sizes of the Aitken modal peak (from 88.9 to 79.9 nm) and in the accumulation mode one (from 690.5 to 648.5 nm). The slight increase in the diameter of particles in nucleation mode (from 25.4 to 29.6 nm) could be caused by condensation and coagulation processes during rain (Zikova and Zdimal, 2016). Regarding the particle number concentration, a decrease in all modes is observed.
- "High" group: there is a peak shift to smaller diameters in the three modes (from 40.8 to 25.5, from 121.2 to 74.4 and from 1542.8 to 362.4 nm). In Aitken and accumulation modes, there is an increase in particle concentration and amplitude (peak width or dispersion of sizes around the most frequent size), because of the shift of the peak to smaller diameters, so these peaks are not comparable. The reasons for this increase could be the resuspension of soil particles as a result of wind during rain events, and the energetic collision between raindrops and soil (Rathnayake et al., 2017).

The optical aerosol parameters, together with ABL, allow the analysis of the variations of ΔF_{ATM} (Table 11.2). Before rain, the "low" group presented low AOT values (0.07±0.03) when compared with the "high" group (0.27±0.11). The decrease after rain of this parameter was only clear in the "high" group with a decrease of 2.8 times. Thus, the AOT is a parameter that signs the washout efficiency of the rain in the "high" group between before and after rain. The influence of ABL was also clear, with a pattern opposite to AOT. A different height of ABL caused a different redistribution of AOT (and consequently of radiative effects of aerosols) along the vertical profile. There were statistical differences between before and after rainfall in AOT values and ABL ($p<0.05$). However, the optical parameters SSA and g, which mainly depend on the refractive index, did not show statistical differences between before and after rainfall. This fact can be due to the constant refractive index used along the events. As previously mentioned, the calculation of this parameter is based on the aerosol chemical composition provided by filter analysis, and each filter corresponds to a 24 h sampling.

The high SSA values (above 0.92 for all wavelengths) indicate the presence of aerosol with high scattering and low absorption ability. According to several authors (Soni et al., 2010; Yang et al., 2009), these values at 550 nm are characteristic of mixed aerosols. The positive values of g show that the scattering had the same direction as the incident wave, with values between 0.67 and 0.68 at 400 nm.

Table 11.4 shows the monthly evolution of surface albedo values at seven wavelengths, aerosol density and refractive index during the study period. These values were used as input data for the

GAME model. Regarding the refractive index, the imaginary part is indicative of aerosol absorption, so higher values cause a lower SSA (Moffet and Prather, 2009). The highest values of the imaginary part (0.011-0.015) were registered during the colder months, probably due to the increase in the concentration of black carbon particles from coal combustion in domestic heating devices (Blanco-Alegre et al., 2019). However, during summer, when Saharan dust intrusions (characterized by a high contribution of coarse particles and high concentration of elements associated with crustal source as Al, Ca, Si or Fe (F. Oduber et al., 2019b)) are frequent in León, a lower imaginary part (0.006-0.008) of the refractive index was registered. The surface albedo presented high values during winter months, mainly for wavelengths higher than 1000 nm, with values about double the values registered in summer months.

Table 11.2. Mean values and standard deviation of optical properties of stratiform and convective events classified by ΔF_{ATM} groups, between before and after rain: ABL, AOT, SSA and g at 400, 550 and 850 nm. B=Before rain, A=After rain.

Rain type	Convective		Stratiform			
Event classification	High	Low	High		Low	
Stage	B	B	A	B	A	B
ABL (m)	1333±925	1147±648	536±436	166±41	813±360	623±370
AOT	0.29±0.11	0.13±0.06	0.10±0.06	0.27±0.11	0.11±0.14	0.07±0.03
SSA_{400}	0.91±0.11	0.94±0.03	0.92±0.02	0.93±0.02	0.93±0.02	0.93±0.03
SSA_{550}	0.91±0.10	0.95±0.02	0.93±0.02	0.94±0.01	0.94±0.02	0.93±0.04
SSA_{850}	0.92±0.08	0.95±0.02	0.93±0.02	0.94±0.02	0.94±0.02	0.93±0.04
g_{400}	0.70±0.06	0.67±0.01	0.67±0.01	0.68±0.01	0.67±0.01	0.67±0.01
g_{550}	0.68±0.07	0.65±0.01	0.66±0.01	0.66±0.01	0.65±0.01	0.66±0.01
g_{850}	0.63±0.08	0.60±0.04	0.62±0.01	0.62±0.02	0.61±0.03	0.62±0.03

Table 11.3. Mean values and standard deviation of multi log-normal aerosol particle size distributions classified by ΔF_{ATM} groups, in stratiform and convective events before and after rain. B=Before rain, A=After rain. D is the diameter, σ is the amplitude and N is the number of particles.

Rain type	Convective				Stratiform			
Event classification	High		Low		High		Low	
Stage	B		B		A		B	
D_1 (nm)	35.4±19		29.8±23.6		25.5±18.3		40.8±13.1	
σ_1 (# m^{-3})	1.8±0.5		1.8±0.6		2.3±1.7		1.9±0.2	
N_1 (# particles)	132±169		121±163		2202±4143		2704±1887	
D_2 (nm)	97.5±50.8		73.2±50.5		74.4±54.8		121.2±49	
σ_2 (# m^{-3})	1.7±0.6		1.6±0.4		1.7±0.4		1.7±0.2	
N_2 (# particles)	52±51		50±46		1009±1522		931±1204	
D_3 (nm)	332±450.1		133.6±23.9		362.4±216.5		1542.8±2918	
σ_3 (# m^{-3})	1.6±0.3		1.5±0.2		1.9±1.1		1.4±0.3	
N_3(# particles)	14±19		18±6		626±1232		50±95	
	A		A		A		A	
D_1 (nm)	29.6±11.8		25.4±11.6					
σ_1 (# m^{-3})	1.7±0.4		1.8±0.5					
N_1 (# particles)	2117±3793		2958±2962					
D_2 (nm)	79.9±40.8		88.9±52.9					
σ_2 (# m^{-3})	1.8±0.4		1.7±0.3					
N_2 (# particles)	983±1153		1293±1182					
D_3 (nm)	648.5±804		690.5±1118.9					
σ_3 (# m^{-3})	1.4±0.3		1.5±0.4					
N_3(# particles)	68±146		217±421					

11.3.2.2. Radiative forcing fluxes and scavenging

The radiative forcing fluxes ΔF_{BOA}, ΔF_{TOA} and ΔF_{ATM} have been obtained in all rain stratiform events in one-hour interval. Before rain, the maximum ΔF_{ATM} value was 74.5 W m^{-2} with an associated heating rate of 12.4 K day^{-1} obtained on 24/02/2016 and the minimum was 20.1 W m^{-2}, with 3.5 K day^{-1} on 10/04/2016 (Figure 11.2). The above mentioned ΔF_{ATM} maximum occurred one day after a winter Saharan dust intrusion (Oduber et al., 2019b). As a consequence, an important concentration of coarser particles remained in the atmosphere. Furthermore, a low ABL (124 m) was recorded and the low temperature registered (3.4 °C) may have encouraged an increased use of heating devices. In addition, there is a decrease in ΔF_{ATM} and associated heating rate in the "high" group between before and after the rain (Figure 11.2). The deviation between full or empty ΔF symbols is ΔF_{ATM}, so it includes the "low" (ΔF_{ATM} lower than 30 W m^{-2}) and "high" (ΔF_{ATM} higher than 30 W m^{-2}) groups.

Table 11.4. Monthly surface albedo (at seven wavelengths), refractive index and density used as inputs in the GAME model, throughout the entire study period.

Month/Year	Surface albedo (λ in µm)							Refractive index	Aerosol density (g cm^{-3})
	0.48	0.55	0.65	0.87	1.24	1.65	2.13		
02/2016	0.261	0.051	0.241	0.234	0.228	0.185	0.000	1.557-0.012i	1.83
03/2016	0.099	0.019	0.055	0.043	0.038	0.021	0.000	1.561-0.013i	1.96
04/2016	0.066	0.013	0.034	0.029	0.026	0.015	0.000	1.557-0.011i	1.90
05/2016	0.124	0.024	0.064	0.052	0.036	0.026	0.000	1.564-0.015i	1.74
06/2016	0.115	0.023	0.054	0.050	0.027	0.030	0.000	1.545-0.006i	2.03
07/2016	0.150	0.029	0.073	0.065	0.040	0.039	0.000	1.547-0.006i	2.05
08/2016	0.131	0.026	0.067	0.063	0.039	0.041	0.000	1.552-0.008i	2.15
09/2016	0.149	0.029	0.078	0.070	0.049	0.048	0.000	1.560-0.013i	1.82
10/2016	0.102	0.020	0.053	0.047	0.036	0.032	0.000	1.556-0.012i	1.84
11/2016	0.079	0.015	0.047	0.042	0.040	0.034	0.000	1.559-0.013i	1.79
12/2016	0.123	0.024	0.079	0.069	0.065	0.059	0.000	1.550-0.009i	1.95
01/2017	0.073	0.014	0.042	0.036	0.035	0.026	0.000	1.544-0.007i	2.02
02/2017	0.231	0.045	0.191	0.179	0.173	0.145	0.000	1.552-0.011i	2.02
03/2017	0.099	0.019	0.053	0.045	0.038	0.027	0.000	1.557-0.012i	1.83

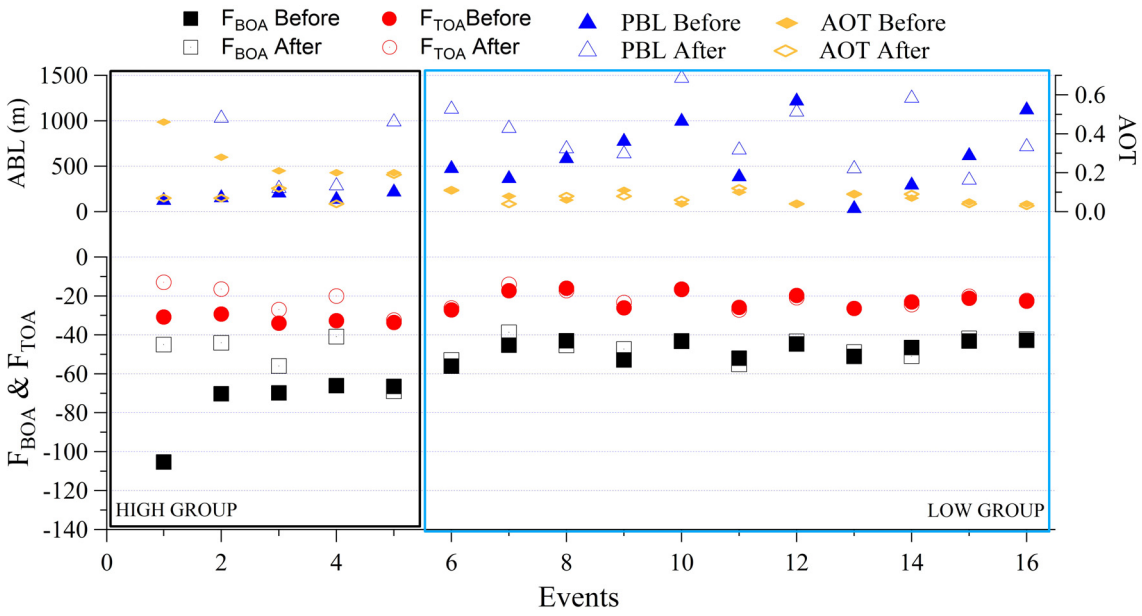

Figure 11.2. Atmospheric forcing at the top (ΔF_{TOA}) (circles) and at the bottom (ΔF_{BOA}) (squares) of the atmosphere, ABL height (triangles) and AOT (diamonds) before (fill) and after (no fill) rain in each stratiform event. Events are presented in descending order of ΔF_{ATM}.

In order to quantify how the scavenging caused by rain on aerosol particles (Blanco-Alegre et al., 2019) could affect radiative forcing fluxes, the GAME model has been applied. Values before and after rain have been compared, using ΔF_{ATM} as a scavenging efficiency tracer linked to AOT, height of ABL and aerosol optical properties.

Regarding $\Delta F\%$ for ΔF_{ATM} by groups, a slight mean decrease (-2.5±8.3%, median: -8.2%) for the "low" group was registered. The "high" group showed a clear decrease (-27.0±25.3%, median: -32.7%). Similar values were registered for ΔF_{BOA}, with -2.0±7.2% for the "low" group and -29.7±23% for the "high" group. At the top of the atmosphere, $\Delta F\%$ for ΔF_{TOA} showed also comparable values, -1.4±8.0% and -32.9±21.2% for "low" and "high" groups, respectively.

The scavenging effect is clearly observed in the $\Delta F\%$ values in the "high" group related with low ABL heights and high AOT values (Figure 11.2), and to a lesser extent, in the "low" group, probably caused by the lower aerosol load in the atmosphere (Figure 11.3), with a good correlation between ΔF_{ATM} before rain with $\Delta F\%$ values (r^2=0.64). Evidence of this is that Pearson correlations among $\Delta F\%$, ΔF_{ATM} before rain and rain variables (rain intensity, accumulated rain, mean drop diameter, mode, α and β) only showed a significant correlation between ΔF_{ATM} before rain and $\Delta F\%$ ($p<0.01$). Consequently, the specific characteristics of rainfall do not appear to influence the greater or lesser $\Delta F\%$.

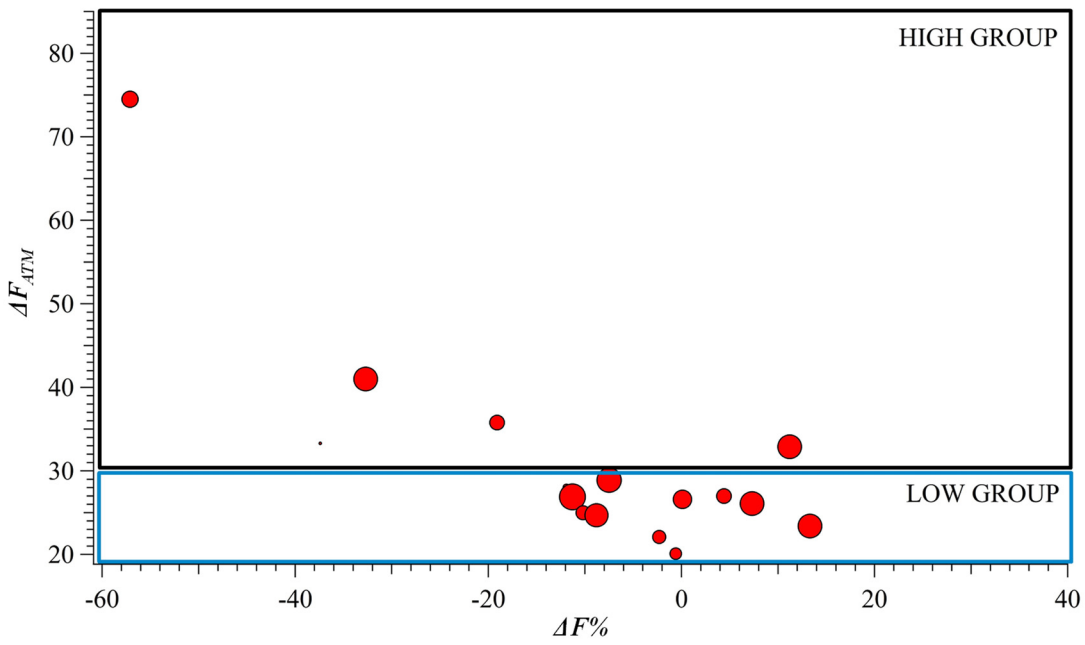

Figure 11.3. Atmospheric forcing before rain (ΔF_{ATM}) vs variation of radiative forcing between before and after rain ($\Delta F\%$) in stratiform events. The size of points is proportional to the mean raindrop size in each event, ranging from 0.30 to 0.61 mm.

When comparing the raindrop size distribution parameters (α and β) and characteristics of rain (Table 11.1) according to the radiative forcing groups ("low" and "high"), we obtain Figure S11.3. The mean of shape parameter α in "low" and "high" groups was 3.32±1.26 and 2.61±1.27, respectively. Regarding the scale parameter β, mean values of 6.90±3.48 and 6.26±5.23 mm^{-1} were registered in "low" and "high" groups, respectively. The high standard deviation values are consequence of the great variability of the number of raindrops with diameters larger than 2 mm. It should be remembered that α and β parameters are not dependent on the size of the sample, only on the shape of the distribution (Fernandez-Raga et al., 2017). α and β did not show significant differences between "low" and "high" groups. However, the mode of the gamma distribution through $(\alpha-1)/\beta$, presented statistical differences ($p<0.05$) between "low" (0.25±0.13 mm) and "high" (0.35±0.05 mm) groups. High atmospheric forcing in the atmosphere before rain is related to a larger raindrop size mode. Therefore, the groups of stratiform events based on radiative forcing before rain show differences in a parameter of the raindrop size distribution measured at ground level.

11.3.2.3. Associated heating rate

Regarding the variation of the associated heating rate caused by aerosols in the atmosphere, the "low" group presented a mean heating rate before and after rain of 3.9±0.7 and 3.7±0.4 K day^{-1}, respectively. A slight decrease of 0.2±0.6 K day^{-1} (median: 0.02 K day^{-1}) was registered. However, a more pronounced decrease is observed in the "high" group between before and after rain (1.9±4.0 K day^{-1}, median: 0.91 K day^{-1}), with a heating rate of 6.8±3.3 K day^{-1} before rain and 4.9±1.4 K day^{-1} after rain. The analysis of the heating rate of aerosol particles and gases along the atmospheric vertical profile provides information about the variations before and after rain (Figure 11.4). The scavenging was observed in the "low" and "high" groups at altitudes below 1 km, the zone with the maximum associated heating rate caused by aerosols before rain.

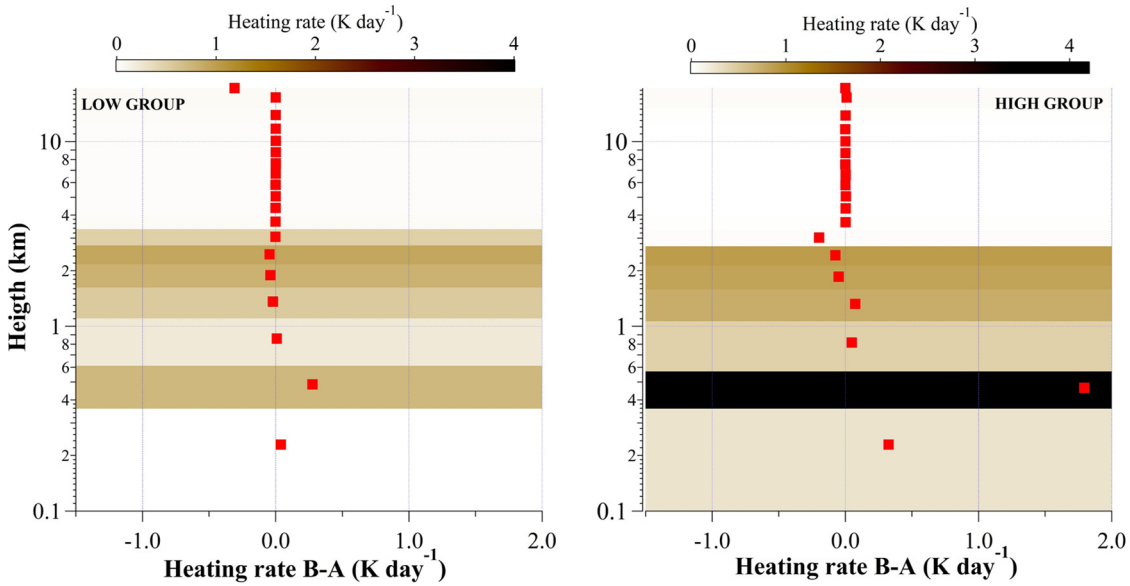

Figure 11.4. Mean variation of heating rate (K day^{-1}) caused by atmospheric aerosols between before and after rain, for each layer defined according to radiosounding data, in the atmospheric vertical column (red markers). In color code the mean heating rate (K day^{-1}) caused by aerosols before the stratiform rain. Events classified into two groups according to the ΔF_{ATM} before rain. B=Before rain, A=After rain.

11.3.3. CONVECTIVE RAIN EVENTS

In the following paragraphs, an analysis of optical properties and particle size distributions before convective events will be shown, and then the values of the radiative forcing and the possible semi-direct effect of aerosol on precipitation characteristics will be explored.

11.3.3.1. Particle size distributions and optical parameters

The particle size distributions before convective rain events evidenced a pattern different from the one observed in stratiform events. The aerosol size distribution presented two or three peaks before and after rain. Similarly to the results found in stratiform events, the first peak (~30 nm) in convective events was located within the nucleation mode, the second one (~100 nm) in Aitken and, at times, the third peak in the accumulation mode. The particle concentration was noticeably lower in all the modes because of the highly seasonal nature of events, occurred in summer, a season with a lower use of vehicles and heating devices and a more intense pollutant dispersion related with high ABL.

The optical aerosol parameters and ABL also showed clear differences with regard to stratiform events (Table 11.2). In the "low" group, AOT presented low values (0.13±0.06) before rain, while AOT in the "high" group was 0.29±0.11, both higher than the respective groups in stratiform events. The seasonal influence (convective events occurred mainly in spring and summer) on ABL height was also clear, with values higher than 1000 m. This fact caused a different redistribution of AOT along the vertical profile. The optical parameters SSA and g did not show statistical differences between groups or with regard to stratiform events. The SSA and g values at 550 nm were very similar to those in stratiform events, characteristic of mixed aerosols (Soni et al., 2010; Yang et al., 2009). All SSA values are in the range of 0.85-0.95 for northern hemisphere reported by Dubovik et al. (2002).

11.3.3.2. Radiative forcing fluxes

The radiative forcing fluxes ΔF_{BOA}, ΔF_{TOA} and ΔF_{ATM} have been obtained before rain convective events on an hourly basis. The maximum ΔF_{ATM} value before rain was 64.5 W m^{-2} with an associated heating rate of 12.3 K day^{-1} obtained on 08/05/2016 and the minimum was 25.0 W m^{-2} with 4.4 K day^{-1} on 09/05/2016. In the "low" group, the ΔF_{ATM}, ΔF_{BOA} and ΔF_{TOA} presented a mean value of 27.0±1.6, -55.1±5.5 and -28.1±5.3 W m^{-2}, respectively. In the "high" group, the ΔF_{ATM},

ΔF_{BOA} and ΔF_{TOA} presented the highest mean values: 44.6±11, -86.8±11.1 and -42.2±11.2 W m^{-2}, respectively. In the "high" group the values were higher than those obtained in the same stratiform group.

As seen in Table 11.1, the convective events showed a higher mean raindrop diameter 0.96±0.98 mm significantly different from the one found in stratiform events (0.83±0.63 mm). This fact could be related to the incorporation in cloud of aerosol that act as CCN when an aerosol laden air mass is incorporated into the updraft during convective events (Hirtl et al., 2019; Maalick et al., 2016) favoring raindrop formation and growth. Figure 11.5 shows how the highest raindrop diameters were related to the highest ABL before rain. However, AOT and ΔF_{ATM} before rain values did not present a clear relation with mean raindrop diameter or mean rain amount.

As in stratiform events, in convective rain events the raindrop size distribution parameters (α, β and mode) and characteristics of rain were analyzed (Figure S11.3). Lower values of shape parameter α were registered in convective than in stratiform events, 1.70±0.98 and 2.03±1.02 in "low" and "high" groups, respectively. The β value showed higher differences between stratiform and convective events, with 2.77±2.38 and 3.08±1.74 in "low" and "high" groups, respectively. Contrary to stratiform events, there are no statistical differences ($p>0.05$) for gamma distribution mode values between "low" (0.37±0.23 mm) and "high" (0.49±0.48 mm) groups. Therefore, "low" and "high" groups in convective events based on radiative forcing before rain do not show clear differences in raindrop size distribution measured at ground level, but there are clear differences between convective and stratiform events.

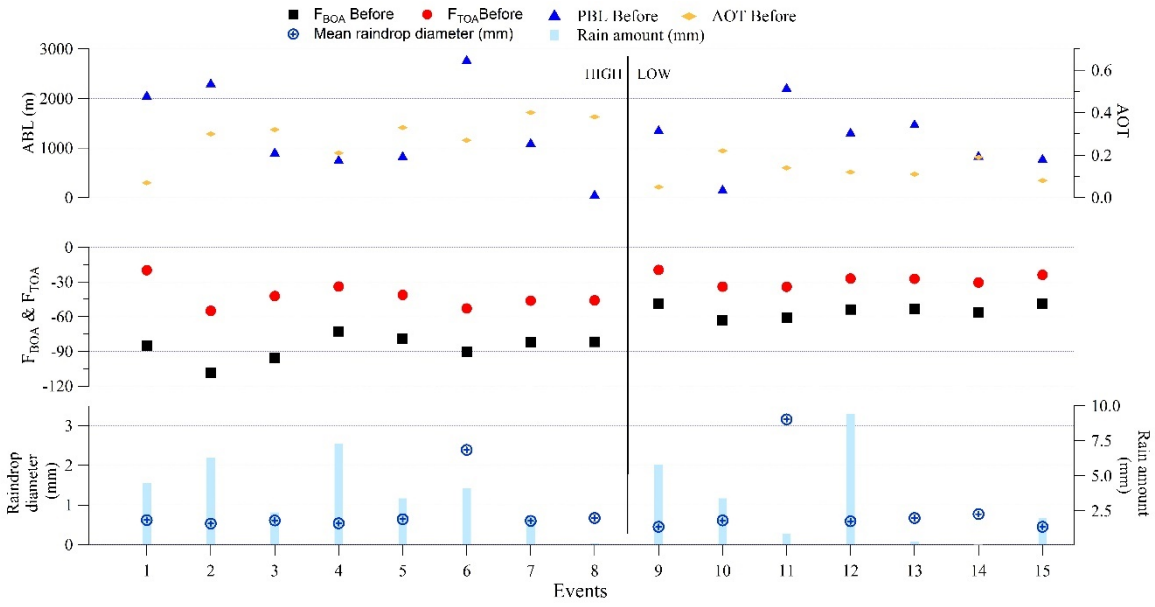

Figure 11.5. Atmospheric forcing at the top (ΔF_{TOA}) (circles) and at the bottom (ΔF_{BOA}) (squares) of atmosphere, ABL height (triangles) and AOT (diamonds) before rain in each convective event. It includes the "low" (ΔF_{ATM} lower than 30 W m^{-2}) and "high" (ΔF_{ATM} higher than 30 W m^{-2}) groups. Bars are the rain amount (mm) and circles plus are the mean raindrop diameter in each event. Events are presented in descending order of ΔF_{ATM}.

The lowest β values in convective events are consequence of the highest number of raindrops with diameters larger than 2 mm (the curve of the gamma distribution falls to zero very slowly), according to the mean raindrop diameter for stratiform and convective events (Table 11.1). This may be due to the mainly horizontal transport of the aerosol during stratiform rain, while in the convective events the aerosols are carried by the updraft towards the cloud, being able to act as CCN, and therefore affecting the characteristics of the precipitation (López-Romero et al., 2021).

Several studies about models at various scales relate the radiative forcing caused by aerosols and the amount of precipitation in clouds (Da Silva et al., 2019; López-Romero et al., 2021; Sarangi et al., 2017; Teller and Levin, 2005). The GAME sensitivity of Aerosol Radiative Effect in shortwave is mainly caused by the differences in the aerosol vertical distribution, load and SSA (Granados-Muñoz et al., 2019). However, at ground level our results did not show a clear relationship between radiative forcing caused by aerosols before rain and the specific characteristics of rainfalls, except for the gamma mode value in stratiform events. The differences observed are the result of the complexity of the semi-direct effect and an important source of uncertainty: to what extent does direct forcing of aerosols modify the thermodynamic profile and cause different rain characteristics? Future studies should analyze indirect aerosol effects under other conditions since they probably influence the degree of direct and semi-direct aerosol effects (and vice versa) by varying the properties of clouds (Schultze and Rockel, 2018).

11.4. CONCLUSIONS

The radiative forcing of aerosols before and after rain events was estimated during a study period of 13 months. For this purpose, the radiative transfer GAME model was applied. After the application of a set of selection criteria, 16 stratiform and 15 convective rain events were selected and grouped according to the atmospheric forcing (ΔF_{ATM}) value before rain: “low” group (>30 W m^{-2}) and “high” group (<30 W m^{-2}).

There were statistically significant differences between stratiform and convective events in rain duration, mean raindrop diameter and parameters a and b of radar reflectivity Z and rainfall intensity R relationship. The raindrop diameter was similar between “low” and “high” groups in stratiform events (0.51±0.08 vs 0.48±0.12 mm). However, the convective events showed a higher mean raindrop diameter (0.96±0.98 vs 0.83±0.63 mm).

In stratiform events, the scavenging effect is clearly observed in the “high” group ($\Delta F\%$=-27.0±25.3%) with a decrease of the associated heating rate caused by aerosols below 1

km of 1.9±4.0 K day^{-1}. To a lesser extent, this is observed in the "low" group too, probably caused by the lower aerosol burden in the atmosphere. The aerosol optical thickness (AOT) in stratiform events, presented low values before rain in the "low" group (0.07±0.03) while AOT in the "high" group was 0.27±0.11. AOT is a parameter that signs the washout efficiency of the rain in the "high" group between before and after rain, with a decrease of 2.7 times. However, other optical parameters like single scattering albedo (SSA) and the asymmetry parameter (g) did not present statistical differences between before and after rain. This fact can be due to the constant refractive index used in the events. There is a relationship between radiative forcing before rain and the specific rain characteristics measured at ground level in stratiform events, since the mode of the gamma distribution presented statistical differences between "low" (0.25±0.13 mm) and "high" (0.35±0.05 mm) groups. High atmospheric forcing (ΔF_{ATM}) values before rain are connected to a large raindrop size mode.

In convective events, the optical aerosol parameters and ABL showed clear differences when compared to stratiform events. The seasonal influence on ABL was also clear, with values higher than 1000 m, causing a different redistribution of AOT along the vertical profile. Contrary to stratiform events, in convective events the groups based on radiative forcing before rain did not show clear differences in their raindrop size distribution measured at ground level. In our study, the low resolution of the vertical aerosol distribution could explain the lack of striking links between aerosol forcings and rainfall characteristics. The height of ABL, as a dynamical tracer of the atmosphere, seems to be a relevant parameter in relation to the size of the raindrops.

This work is a step forward in the study of the relationship between radiative forcing caused by aerosols and precipitation, analyzing not only the amount of precipitation but also the specific characteristics of rainfall (e.g. raindrop size, swept volume) at ground level. Future studies should analyze the evolution of optical parameters using a high resolution of chemical composition, density and refractive index, between before and after rain.

11.5. REFERENCES

Alves, C.A., Lopes, D.J., Calvo, A.I., Evtyugina, M., Rocha, S., Nunes, T., 2015. Emissions from Light-Duty Diesel and Gasoline in-use Vehicles Measured on Chassis Dynamometer Test Cycles. Aerosol Air Qual. Res. 15, 99–116. doi:10.4209/aaqr.2014.01.0006

Ayash, T., Gong, S., Jia, C.Q., 2008. Direct and indirect shortware radiative effects of sea salt aerosols. J. Clim. 21, 3207–3220. doi:10.1175/2007JCLI2063.1

Blanco-Alegre, C., Calvo, A.I., Coz, E., Castro, A., Oduber, F., Prévôt, A.S.H.H., Močnik, G., Fraile, R., 2019. Quantification of source specific black carbon scavenging using an aethalometer and a disdrometer. Environ. Pollut. 246, 336–345. doi:10.1016/j.envpol.2018.11.102

Blitzortung.org, 2020. Lightning maps. BY-SA 4.0 / Light. data by Blitzortung.org Contrib.

Bollasina, M.A., Ming, Y., Ramaswamy, V., 2011. Anthropogenic aerosols and the weakening of the south asian summer monsoon. Science (80-.). 334, 502–505. doi:10.1126/science.1204994

Bond, T.C., Doherty, S.J., Fahey, D.W., Forster, P.M., Berntsen, T., Deangelo, B.J., Flanner, M.G., Ghan, S., Kürcher, B., Koch, D., Kinne, S., Kondo, Y., Quinn, P.K., Sarofim, M.C., Schultz, M.G., Schulz, M., Venkataraman, C., Zhang, H., Zhang, S., Bellouin, N., Guttikunda, S.K., Hopke, P.K., Jacobson, M.Z., Kaiser, J.W., Klimont, Z., Lohmann, U., Schwarz, J.P., Shindell, D., Storelvmo, T., Warren, S.G., Zender, C.S., 2013. Bounding the role of black carbon in the climate system: A scientific assessment. J. Geophys. Res. Atmos. 118, 5380–5552. doi:10.1002/jgrd.50171

Bullard, R.L., Singh, A., Anderson, S.M., Lehmann, C.M.B., Stanier, C.O., 2017. 10-Month characterization of the aerosol number size distribution and related air quality and meteorology at the Bondville, IL Midwestern background site. Atmos. Environ. 154, 348–361. doi:10.1016/j.atmosenv.2016.12.055

Calvo, A.I., 2009. Caracterización y transporte del aerosol atmosférico: medio urbano, rural y quema de biomasa 137–177.

Calvo, A.I., Pont, V., Castro, A., Mallet, M., Palencia, C., Roger, J.C., Dubuisson, P., Fraile, R., 2010. Radiative forcing of haze during a forest fire in Spain. J. Geophys. Res. Atmos. 115, 1–10. doi:10.1029/2009JD012172

Calvo, A.I., Tarelho, L.A.C., Teixeira, E.R., Alves, C., Nunes, T., Duarte, M., Coz, E., Custodio, D., Castro, A., Artiñano, B., Fraile, R., 2013. Particulate emissions from the co-combustion of forest biomass and sewage sludge in a bubbling fluidised bed reactor. Fuel Process. Technol. 114, 58–68. doi:10.1016/j.fuproc.2013.03.021

Castro, A., Calvo, A.I., Alves, C., Alonso-Blanco, E., Coz, E., Marques, L., Nunes, T., Fernández-Guisuraga, J.M., Fraile, R., 2015. Indoor aerosol size distributions in a gymnasium. Sci. Total Environ. 524–525, 178–186. doi:10.1016/j.scitotenv.2015.03.118

Charlson, R.J., Schwartz, S.E., Hales, J.M., Cess, R.D., Coakley, J.A., Hansen, J.E., Hofmann, D.J., 1992. Climate forcing by anthropogenic aerosols. Science (80-.). 255, 423–430. doi:10.1126/science.255.5043.423

Chien, C.H., Theodore, A., Wu, C.Y., Hsu, Y.M., Birky, B., 2016. Upon correlating diameters measured by optical particle counters and aerodynamic particle sizers. J. Aerosol Sci. 101, 77–85. doi:10.1016/j.jaerosci.2016.05.011

Choudhury, B.A., Goswami, B.N., Zahan, Y., Rajesh, P. V., 2021. Seasonality in power law scaling of convective and stratiform rainfall with lightning intensity over Indian Monsoon regions. Atmos. Res. 248, 105265. doi:10.1016/j.atmosres.2020.105265

Da Silva, N., Mailler, S., Drobinski, P., 2019. Aerosol indirect effects on the temperature-precipitation scaling. Atmos. Chem. Phys. Discuss. 1–25. doi:10.5194/acp-2018-1334

Draxler, R., Rolph, G., 2012. Hysplit (Hybrid Single-Particle Lagrangian Integrated Trajectory). Silver Spring. NOAA Air Resour. Lab.

Dubovik, O., Holben, B., Eck, T.F., Smirnov, A., Kaufman, Y.J., King, M.D., Tanré, D., Slutsker, I., 2002. Variability of absorption and optical properties of key aerosol types observed in worldwide locations. J. Atmos. Sci. 59, 590–608. doi:10.1175/1520-0469(2002)059<0590:voaaop>2.0.co;2

Dubuisson, P., Buriez, J.C., Fouquart, Y., 1996. High spectral resolution solar radiative transfer in absorbing and scattering media: Application to the satellite simulation. J. Quant. Spectrosc. Radiat. Transf. 55, 103–126. doi:10.1016/0022-4073(95)00134-4

Dubuisson, P., Dessailly, D., Vesperini, M., Frouin, R., 2004. Water vapor retrieval over ocean using near-infrared radiometry. J. Geophys. Res. D Atmos. 109, 1–14. doi:10.1029/2004JD004516

Estellés, V., Campanelli, M., Smyth, T.J., Utrillas, M.P., Martínez-Lozano, J.A., 2012. Evaluation of the new ESR network software for the retrieval of direct sun products from CIMEL CE318 and PREDE POM01 sun-sky radiometers. Atmos. Chem. Phys. 12, 11619–11630. doi:10.5194/acp-12-11619-2012

Fernandez-Raga, M., Castro, A., Marcos, E., Palencia, C., Fraile, R., 2017. Weather types and rainfall microstructure in Leon, Spain. Int. J. Climatol. 37, 1834–1842. doi:10.1002/joc.4816

Fernández-Raga, M., Castro, A., Palencia, C., Calvo, A.I., Fraile, R., 2009. Rain events on 22 October 2006 in León (Spain): Drop size spectra. Atmos. Res. 93, 619–635. doi:10.1016/j.atmosres.2008.09.035

Fraile, R., Fernández-Raga, M., 2009. On a more consistent definition of radar reflectivity. Atmosfera 22, 375–385.

Granados-Muñoz, M.J., Sicard, M., Papagiannopoulos, N., Barragán, R., Bravo-Aranda, J.A., Nicolae, D., 2019. Two-dimensional mineral dust radiative effect calculations from CALIPSO observations over Europe. Atmos. Chem. Phys. 19, 13157–13173. doi:10.5194/acp-19-13157-2019

Gunn, R., Kinzer, G.D., 1949. The terminal velocity of fall for water droplets in stagnant Air. J. Meteorol. doi:10.1175/1520-0469(1949)006<0243:TTVOFF>2.0.CO;2

Hasan, H., Dzubay, T.G., 1983. Apportioning light extinction coefficients to chemical species in atmospheric aerosol. Atmos. Environ. 17, 1573–1581. doi:10.1016/0004-6981(83)90310-4

Hirtl, M., Stuefer, M., Arnold, D., Grell, G., Maurer, C., Natali, S., Scherllin-Pirscher, B., Webley, P., 2019. The effects of simulating volcanic aerosol radiative feedbacks with WRF-Chem during the EyjafjallajÖkull eruption, April and May 2010. Atmos. Environ. 198, 194–206. doi:10.1016/j.atmosenv.2018.10.058

Höller, R., Ito, K., Tohno, S., Kasahara, M., 2003. Wavelength-dependent aerosol single-scattering albedo: Measurements and model calculations for a coastal site near the Sea of Japan during ACE-Asia. J. Geophys. Res. D Atmos. 108, 1–15. doi:10.1029/2002jd003250

Houze, R. A., J., 2014. Cloud Dynamics. Academic Press.

Huang, Y., Wang, Y., Cui, X., 2019. Differences between Convective and Stratiform Precipitation Budgets in a Torrential Rainfall Event. Adv. Atmos. Sci. 36, 495–509. doi:10.1007/s00376-019-8159-1

ICCP, 2014. Climate change 2014: Impacts, adaptation, and vulnerability. Part A: Global and sectoral aspects. Contribution of working group II to the fifth assessment report of the intergovernmental panel on climate change.

Kaskaoutis, D.G., Sinha, P.R., Vinoj, V., Kosmopoulos, P.G., Tripathi, S.N., Misra, A., Sharma, M., Singh, R.P., 2013. Aerosol properties and radiative forcing over Kanpur during severe aerosol loading conditions. Atmos. Environ. 79, 7–19. doi:10.1016/j.atmosenv.2013.06.020

Khlystov, A., Stanier, C., Pandis, S.N., 2004. An algorithm for combining electrical mobility and aerodynamic size distributions data when measuring ambient aerosol. Aerosol Sci. Technol. 38, 229–238. doi:10.1080/02786820390229543

Laakso, L., Grönholm, T., Rannik, Ü., Kosmale, M., Fiedler, V., Vehkamäki, H., Kulmala, M., 2003. Ultrafine particle scavenging coefficients calculated from 6 years field measurements. Atmos. Environ. 37, 3605–3613. doi:10.1016/S1352-2310(03)00326-1

Ladino, L., Stetzer, O., Hattendorf, B., Günther, D., Croft, B., Lohmann, U., 2011. Experimental study of collection efficiencies between submicron aerosols and cloud droplets. J. Atmos. Sci. 68, 1853–1864. doi:10.1175/JAS-D-11-012.1

Lee, G.W., Zawadzki, I., 2005. Variability of drop size distributions: Time-scale dependence of the variability and its effects on rain estimation. J. Appl. Meteorol. 44, 241–255. doi:10.1175/JAM2183.1

Lee, G.W., Zawadzki, I., Szyrmer, W., Sempere-Torres, D., Uijlenhoet, R., 2004. A general approach to double-moment normalization of drop size distributions. J. Appl. Meteorol. 43, 264–281. doi:10.1175/1520-0450(2004)043<0264:AGATDN>2.0.CO;2

Levin, E.J.T.T., McMeeking, G.R., Carrico, C.M., Mack, L.E., Kreidenweis, S.M., Wold, C.E., Moosmüller, H., Arnott, W.P., Hao, W.M., Collett, J.L., Malm, W.C., Moosmöller, H., Arnott, W.P., Hao, W.M., Collett, J.L., Malm, W.C., 2010. Biomass burning smoke aerosol properties measured during Fire Laboratory at Missoula Experiments (FLAME). J. Geophys. Res. Atmos. 115, 1–15. doi:10.1029/2009JD013601

López-Romero, J.M., Montávez, J.P., Jerez, S., Lorente-Plazas, R., Palacios-Peña, L., Jiménez-Guerrero, P., 2021. Precipitation response to aerosol–radiation and aerosol–cloud interactions in regional climate simulations over Europe. Atmos. Chem. Phys. 21, 415–430. doi:10.5194/acp-21-415-2021

Lucarelli, F., Chiari, M., Calzolai, G., Giannoni, M., Nava, S., Udisti, R., Severi, M., Querol, X., Amato, F., Alves, C., Eleftheriadis, K., 2015. The role of PIXE in the AIRUSE project “testing and development of air quality mitigation measures in Southern Europe.” Nucl. Instruments Methods Phys. Res. Sect. B Beam Interact. with Mater. Atoms 363, 92–98. doi:10.1016/j.nimb.2015.08.023

Maalick, Z., Kühn, T., Korhonen, H., Kokkola, H., Laaksonen, A., Romakkaniemi, S., 2016. Effect of aerosol concentration and absorbing aerosol on the radiation fog life cycle. Atmos. Environ. 133, 26–33. doi:10.1016/j.atmosenv.2016.03.018

Machado, L.A.T., Laurent, H., Dessay, N., Miranda, I., 2004. Seasonal and diurnal variability of convection over the Amazonia: A comparison of different vegetation types and large scale forcing. Theor. Appl. Climatol. 78, 61–77. doi:10.1007/s00704-004-0044-9

Marques, R.F. de P.V., de Mello, C.R., da Silva, A.M., Franco, C.S., de Oliveira, A.S., 2014. Performance of the probability distribution models applied to heavy rainfall daily events. Ciência e Agrotecnologia 38, 335–342. doi:10.1590/s1413-70542014000400003

Matsui, T., Pielke, R.A., 2006. Measurement-based estimation of the spatial gradient of aerosol radiative forcing. Geophys. Res. Lett. 33. doi:10.1029/2006GL025974

Menon, S., Hansen, J., Nazarenko, L., Luo, U., 2002. Climate effects of black carbon aerosols in China and India. Science (80-.). 297, 2250–2253. doi:10.1126/science.1075159

Moffet, R.C., Prather, K.A., 2009. In-situ measurements of the mixing state and optical properties of soot with implications for radiative forcing estimates. Proc. Natl. Acad. Sci. U. S. A. 106, 11872–11877. doi:10.1073/pnas.0900040106

Nzeukou, A., Sauvageot, H., Ochou, A.D., Kebe, C.M.F., 2004. Raindrop size distribution and radar parameters at Cape Verde. J. Appl. Meteorol. 43, 90–105. doi:10.1175/1520-0450(2004)043<0090:RSDARP>2.0.CO;2

Oduber, F., Calvo, A.I., Blanco-Alegre, C., Castro, A., Nunes, T., Alves, C., Sorribas, M., Fernández-González, D., Vega-Maray, A.M., Valencia-Barrera, R.M., Lucarelli, F., Nava, S., Calzolai, G., Alonso-Blanco, E., Fraile, B., Fialho, P., Coz, E., Prevot, A.S.H., Pont, V., Fraile, R., 2019a. Unusual winter Saharan dust intrusions at Northwest Spain: Air quality, radiative and health impacts. Sci. Total Environ. 669, 213–228. doi:10.1016/j.scitotenv.2019.02.305

Oduber, F., Calvo, A.I., Blanco-Alegre, C., Castro, A., Nunes, T., Alves, C., Sorribas, M., Fernández-González, D., Vega-Maray, A.M., Valencia-Barrera, R.M., Lucarelli, F., Nava, S., Calzolai, G., Alonso-Blanco, E., Fraile, B., Fialho, P., Coz, E., Prevot, A.S.H.H., Pont, V., Fraile, R., 2019b. Unusual winter Saharan dust intrusions at Northwest Spain: Air quality, radiative and health impacts. Sci. Total Environ. 669, 213–228. doi:10.1016/j.scitotenv.2019.02.305

Oduber, F., Calvo, A.I., Castro, A., Blanco-Alegre, C., Alves, C., Calzolai, G., Nava, S., Lucarelli, F., Nunes, T., Barata, J., Fraile, R., 2021. Characterization of aerosol sources in León (Spain) using Positive Matrix Factorization and weather types. Sci. Total Environ. 754, 142045. doi:10.1016/j.scitotenv.2020.142045

Panicker, A.S., Park, S.H., Lee, D.I., Kim, D.C., Jung, W.S., Jang, S.M., Jeong, J.H., Kim, D.S., Yu, J., Jeong, H., 2013. Observations of Black Carbon characteristics and radiative forcing over a Global Atmosphere Watch supersite in Korea. Atmos. Environ. 77, 98–104. doi:10.1016/j.atmosenv.2013.04.020

Patel, P.N., Dumka, U.C., Kaskaoutis, D.G., Babu, K.N., Mathur, A.K., 2017. Optical and radiative properties of aerosols over Desalpar, a remote site in western India: Source identification, modification processes and aerosol type discrimination. Sci. Total Environ. 575, 612–627. doi:10.1016/j.scitotenv.2016.09.023

Paulot, F., Paynter, D., Ginoux, P., Naik, V., Horowitz, L.W., 2018. Changes in the aerosol direct radiative forcing from 2001 to 2015: Observational constraints and regional mechanisms. Atmos. Chem. Phys. 18, 13265–13281. doi:10.5194/acp-18-13265-2018

Perrone, M.R., Bergamo, A., 2011. Direct radiative forcing during Sahara dust intrusions at a site in the Central Mediterranean: Anthropogenic particle contribution. Atmos. Res. 101, 783–798. doi:10.1016/j.atmosres.2011.05.011

Pio, C., Cerqueira, M., Harrison, R.M., Nunes, T., Mirante, F., Alves, C., Oliveira, C., Sanchez, A., Campa, D., Artíñano, B., Matos, M., 2011. OC / EC ratio observations in Europe : Re-thinking the approach for apportionment between primary and secondary organic carbon. Atmos. Environ. 45, 6121–6132. doi:10.1016/j.atmosenv.2011.08.045

Rama Gopal, K., Balakrishnaiah, G., Arafath, S.M., Raja Obul Reddy, K., Siva Kumar Reddy, N., Pavan Kumari, S., Raghavendra Kumar, K., Chakradhar Rao, T., Lokeswara Reddy, T., Reddy, R.R., Nazeer Hussain, S., Vasudeva Reddy, M., Suresh Babu, S., Mallikarjuna Reddy, P., 2017. Measurements of

scattering and absorption properties of surface aerosols at a semi-arid site, Anantapur. Atmos. Res. 183, 84–93. doi:10.1016/j.atmosres.2016.08.016

Rathnayake, C.M., Metwali, N., Jayarathne, T., Kettler, J., Huang, Y., Thorne, P.S., O'Shaughnessy, P.T., Stone, E.A., 2017. Influence of rain on the abundance of bioaerosols in fine and coarse particles. Atmos. Chem. Phys. 17, 2459–2475. doi:10.5194/acp-17-2459-2017

Reddy, K., Kumar, D.V.P., Ahammed, Y.N., Naja, M., 2013. Aerosol vertical profiles strongly affect their radiative forcing uncertainties: study by using ground-based lidar and other measurements. Remote Sens. Lett. 4, 1018–1027. doi:10.1080/2150704X.2013.828182

Roger, J.C., Mallet, M., Dubuisson, P., Cachier, H., Vermote, E., Dubovik, O., Despiau, S., 2006. A synergetic approach for estimating the local direct aerosol forcing: Application to an urban zone during the Expérience sur Site pour Contraindre les Modèles de Pollution et de Transport d'Emission (ESCOMPTE) experiment. J. Geophys. Res. Atmos. 111. doi:10.1029/2005JD006361

Rosenfeld, D., Andreae, M.O., Asmi, A., Chin, M., de Leeuw, G., Donovan, D.P., Kahn, R., Kinne, S., Kivekäs, N., Kulmala, M., Lau, W., Schmidt, K.S., Suni, T., Wagner, T., Wild, M., Quaas, J., 2014. Global observations of aerosol-cloud-precipitation-climate interactions. Rev. Geophys. 52, 750–808. doi:10.1002/2013RG000441

Rupakheti, D., Kang, S., Rupakheti, M., 2020. Two heavy haze events over Lumbini in southern Nepal: Enhanced aerosol radiative forcing and heating rates. Atmos. Environ. 236, 117658. doi:10.1016/j.atmosenv.2020.117658

Sarangi, C., Tripathi, S.N., Kanawade, V.P., Koren, I., Sivanand Pai, D., 2017. Investigation of the aerosol-cloud-rainfall association over the Indian summer monsoon region. Atmos. Chem. Phys. 17, 5185–5204. doi:10.5194/acp-17-5185-2017

Satheesh, S.K., Vinoj, V., Krishna Moorthy, K., 2010. Radiative effects of aerosols at an urban location in southern India: Observations versus model. Atmos. Environ. 44, 5295–5304. doi:10.1016/j.atmosenv.2010.07.020

Schultze, M., Rockel, B., 2018. Direct and semi-direct effects of aerosol climatologies on long-term climate simulations over Europe. Clim. Dyn. 50, 3331–3354. doi:10.1007/s00382-017-3808-5

Soni, K., Singh, S., Bano, T., Tanwar, R.S., Nath, S., Arya, B.C., 2010. Variations in single scattering albedo and Angstrom absorption exponent during different seasons at Delhi, India. Atmos. Environ. 44, 4355–4363. doi:10.1016/j.atmosenv.2010.07.058

Teller, A., Levin, Z., 2005. The effects of aerosols on precipitation and dimensions of subtropical clouds; a sensitivity study using a numerical cloud model. Atmos. Chem. Phys. Discuss. 5, 7211–7245. doi:10.5194/acpd-5-7211-2005

Textor, C., Schulz, M., Guibert, S., Kinne, S., Balkanski, Y., Bauer, S., Berntsen, T., Berglen, T., Boucher, O., Chin, M., Dentener, F., Diehl, T., Easter, R., Feichter, H., Fillmore, D., Ghan, S., Ginoux, P., Gong, S., Grini, A., Hendricks, J., Horowitz, L., Huang, P., Isaksen, I., Iversen, T., Kloster, S., Koch, D., Kirkevåg, A., Kristjansson, J.E., Krol, M., Lauer, A., Lamarque, J.F., Liu, X., Montanaro, V., Myhre, G., Penner, J., Pitari, G., Lamarque, J.F., Liu, X., Montanaro, V., Myhre, G., Penner, J., Pitari, G., Reddy, S., Seland, Ø., Stier, P., Takemura, T., Tie, X., 2006. Analysis and quantification of the diversities of aerosol life cycles within AeroCom. Atmos. Chem. Phys. 6, 1777–1813. doi:10.5194/acpd-5-8331-2005

Thurai, M., Gatlin, P.N., Bringi, V.N., 2016. Separating stratiform and convective rain types based on the drop size distribution characteristics using 2D video disdrometer data. Atmos. Res. 169, 416–423. doi:10.1016/j.atmosres.2015.04.011

Wang, H., Chen, D., Yin, J., Xu, D., Dai, G., Chen, L., 2020. An improvement of convective precipitation nowcasting through lightning data dynamic nudging in a cloud-resolving scale forecasting system. Atmos. Res. 242, 104994. doi:10.1016/j.atmosres.2020.104994

Wiedensohler, A., Birmili, W., Nowak, A., Sonntag, A., Weinhold, K., Merkel, M., Wehner, B., Tuch, T., Pfeifer, S., Fiebig, M., Fjäraa, A.M., Asmi, E., Sellegri, K., Depuy, R., Venzac, H., Villani, P., Laj, P., Aalto, P., Ogren, J.A., Swietlicki, E., Williams, P., Roldin, P., Quincey, P., Hüglin, C., Fierz-Schmidhauser, R., Gysel, M., Weingartner, E., Riccobono, F., Santos, S., Grüning, C., Faloon, K., Beddows, D., Harrison, R., Monahan, C., Jennings, S.G., O'Dowd, C.D., Marinoni, A., Horn, H.G., Keck, L., Jiang, J., Scheckman, J., McMurry, P.H., Deng, Z., Zhao, C.S., Moerman, M., Henzing, B., De Leeuw, G., Löschau, G., Bastian, S., 2012. Mobility particle size spectrometers: Harmonization of technical standards and data structure to facilitate high quality long-term observations of atmospheric particle number size distributions. Atmos. Meas. Tech. 5, 657–685. doi:10.5194/amt-5-657-2012

Wu, D., Dong, X., Xi, B., Feng, Z., Kennedy, A., Mullendore, G., Gilmore, M., Tao, W.K., 2013. Impacts of microphysical scheme on convective and stratiform characteristics in two high precipitation squall line events. J. Geophys. Res. Atmos. 118, 11,119-11,135. doi:10.1002/jgrd.50798

Yang, M., Howell, S.G., Zhuang, J., Huebert, B.J., 2009. Attribution of aerosol light absorption to black carbon, brown carbon, and dust in China - Interpretations of atmospheric measurements during EAST-AIRE. Atmos. Chem. Phys. 9, 2035–2050. doi:10.5194/acp-9-2035-2009

Zikova, N., Zdimal, V., 2016. Precipitation scavenging of aerosol particles at a rural site in the Czech Republic. Tellus B 68, 1–14. doi:10.3402/tellusb.v68.27343

SUPPLEMENTARY MATERIAL

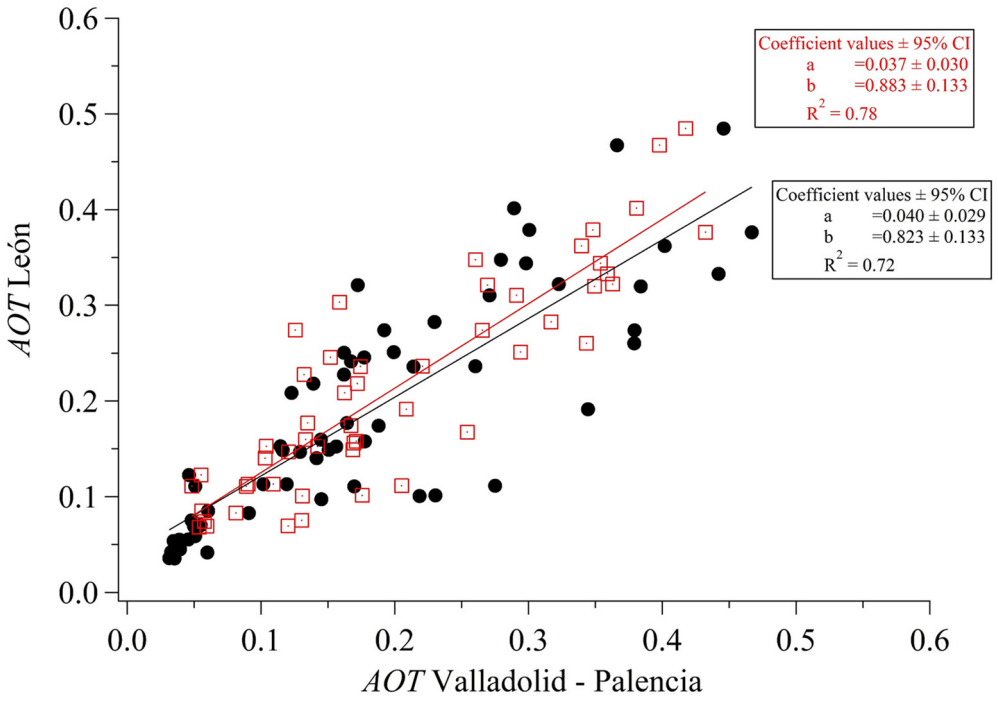

Figure S11.1. Comparison of Aerosol Optical Thickness (AOT) values between León and Valladolid (circles) and Palencia (boxes) during July 2017 and May 2019 three hours before and after rain events.

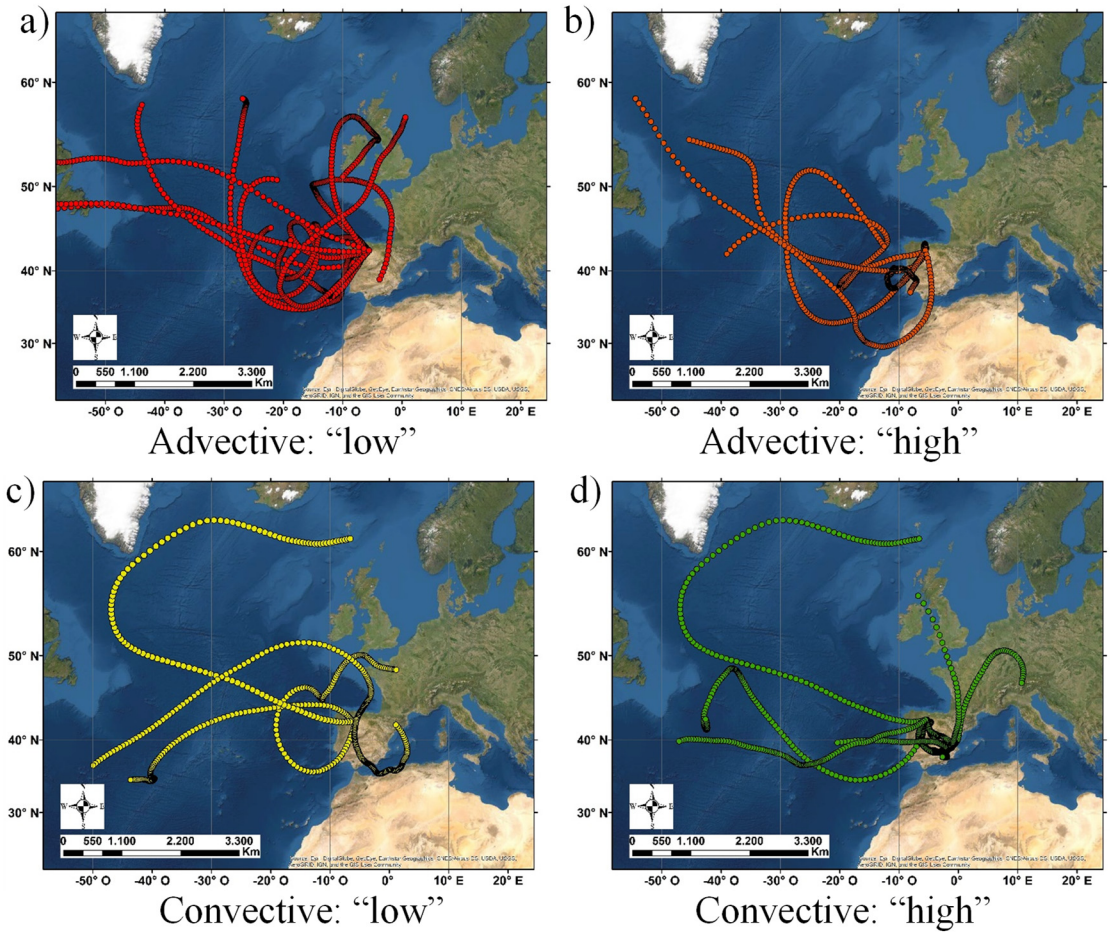

Figure S11.2. Four-days back trajectories arriving at 1000 m a.g.l during: a) stratiform "low" events (red); b) stratiform "high" events (orange); c) convective "low" events (yellow) and d) convective "high" events (green) in León.

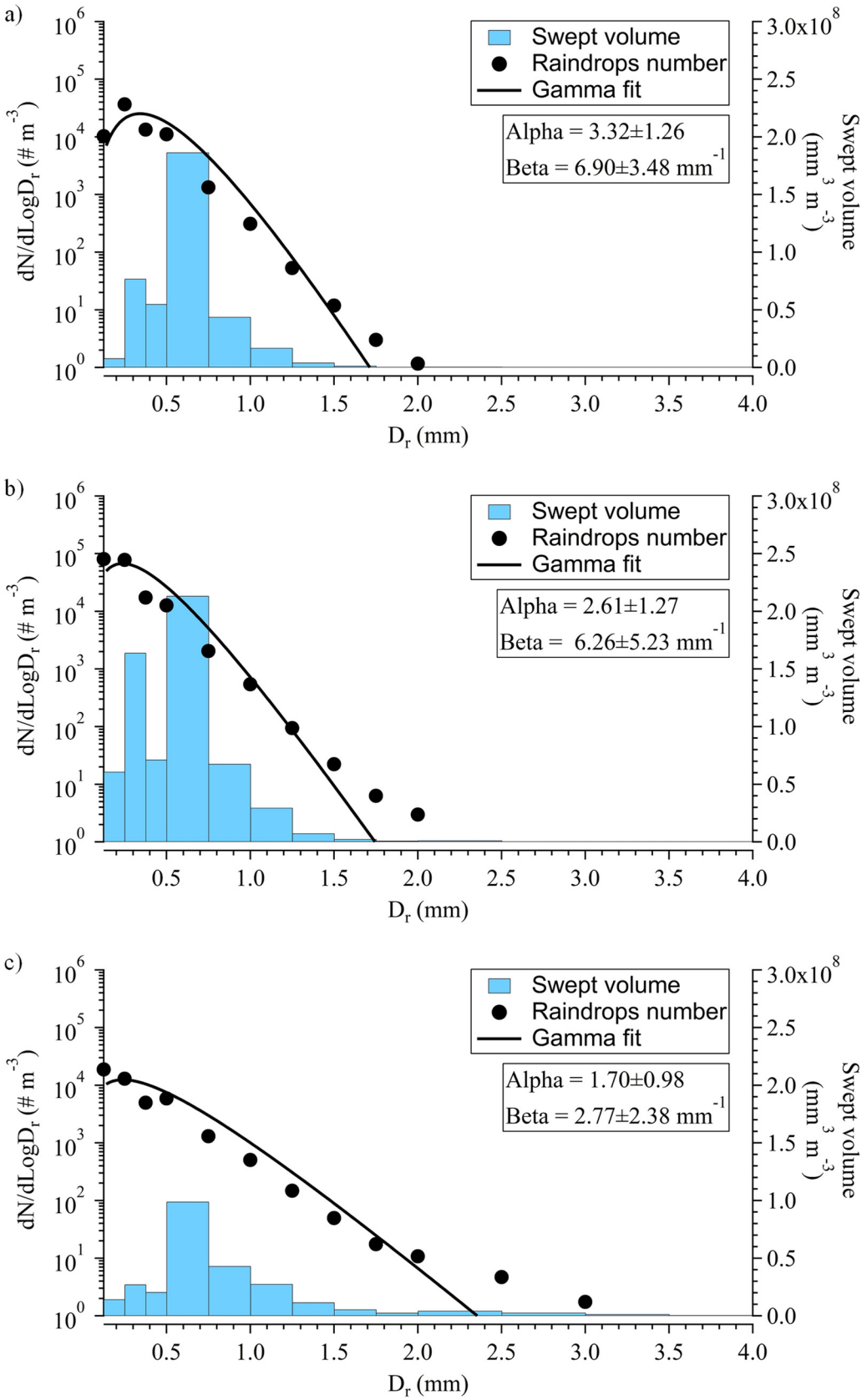
a)
Swept volume
Raindrops number
Gamma fit
Alpha = 3.32±1.26
Beta = 6.90±3.48 mm-1
dN/dLogDr (# m-3)
Swept volume (mm3 m-3)
Dr (mm)
b)
Swept volume
Raindrops number
Gamma fit
Alpha = 2.61±1.27
Beta = 6.26±5.23 mm-1
dN/dLogDr (# m-3)
Swept volume (mm3 m-3)
Dr (mm)
c)
Swept volume
Raindrops number
Gamma fit
Alpha = 1.70±0.98
Beta = 2.77±2.38 mm-1
dN/dLogDr (# m-3)
Swept volume (mm3 m-3)
Dr (mm)

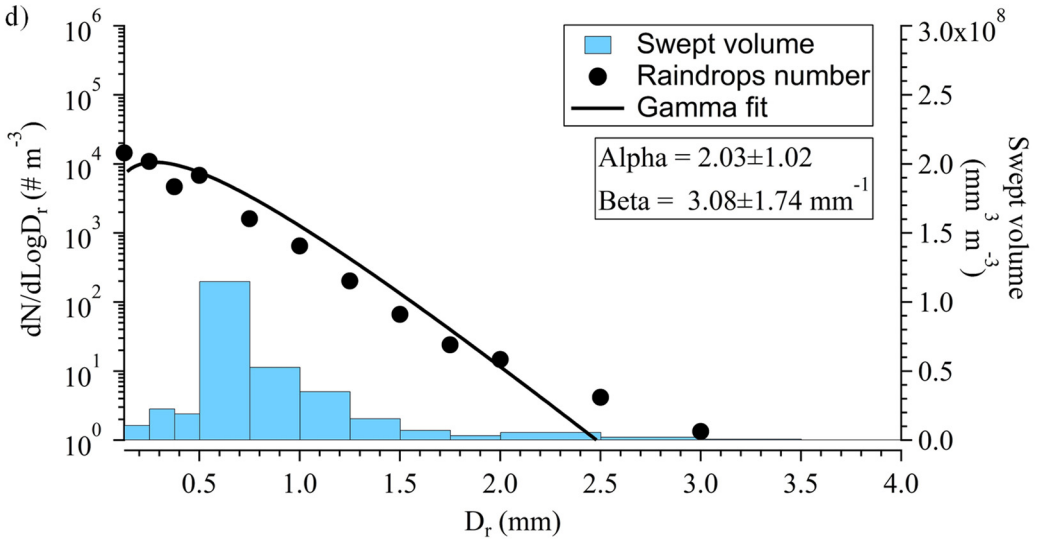

Figure S11.3. Mean raindrop size distribution of: a) stratiform "low" events; b) stratiform "high" events; c) convective "low" events and d) convective "high" events. The mean values of α and β are shown. The number of raindrops is the average percentage of each channel multiplied by the sum of the total number of raindrops of all events.

CAPÍTULO 12. CONCLUSIONES Y PERSPECTIVAS

12.1. CONCLUSIONES

Este último capítulo incluye las principales conclusiones derivadas de la presente tesis doctoral, de acuerdo con los objetivos planteados en el ***Capítulo 2***.

El primer objetivo abordaba el estudio de las características físicas del aerosol y la cuantificación del efecto lavado que tiene la precipitación sobre el aerosol atmosférico en función del espectro de tamaños de las gotas de lluvia. Este objetivo se ha tratado en los ***Capítulos 4, 5 y 6.*** Las conclusiones generales sobre este objetivo son:

- La moda de nucleación se correlaciona positivamente con una mayor altura de la capa límite atmosférica en el periodo cálido que, a su vez, provoca mejores condiciones para la presencia de eventos de eventos de formación de nuevas partículas. Partiendo de una clasificación subjetiva, se identificaron 45 eventos de tipo *Ia* (con un buen nivel de confianza y sin partículas pre-existentes), entre las 1100 y las 1500 UTC, en primavera y verano.

- El lavado ejercido por la lluvia sobre el aerosol atmosférico depende del tamaño y la composición de la partícula y del tamaño de la gota. Se ha observado un lavado efectivo, aunque en diferente grado, en todos los rangos de tamaño de partículas, tanto para partículas biogénicas como no biogénicas.

- El estudio del lavado de la moda fina y gruesa de los aerosoles mostró un coeficiente de lavado λ medio de $2.6 \cdot 10^{-5}$ y $5.8 \cdot 10^{-5}$ s^{-1}, respectivamente, y una disminución de la concentración total de partículas de un 18% tras la lluvia. El lavado menos eficaz se observó en el rango de tamaño entre 0.6 y 1 µm.

- Las partículas incluidas en la moda Aitken mostraron el menor valor del coeficiente de lavado λ de $3.1 \cdot 10^{-5}$ s^{-1}, con una eficiencia de lavado de tan solo el 4%. Las modas de nucleación y acumulación presentaron valores más altos (15% y $3.9 \cdot 10^{-5}$ s^{-1}; 22% y $5.0 \cdot 10^{-5}$ s^{-1}, respectivamente). El lavado de aerosoles más efectivo, se registró con intensidades de precipitación inferiores a 1 mm h^{-1} y superiores a 3 mm h^{-1}, con una clara disminución de los picos modales en la distribución multi-lognormal de tamaños de aerosol. Además, los tamaños de gota de lluvia entre 1.25 y 3.5 mm lavaron eficientemente los tamaños de aerosol entre 70 y 300 nm.

El segundo objetivo trataba de discernir entre la contribución de carbono negro por procesos de quema de combustibles fósiles y de biomasa y de evaluar el efecto de la precipitación sobre la concentración de carbono negro emitido por diferentes fuentes. Este objetivo ha sido tratado en los ***Capítulos 7, 8 y 9***, y las conclusiones generales obtenidas son:

- La concentración de carbono negro (BC) procedente del tráfico en el interior de un túnel, con el paso de 56,000 vehículos durante el periodo de muestreo (8 días), fue 21±10 µg m^{-3}, con un máximo horario de 49 µg m^{-3}. El Exponente Ångström de Absorción (AAE) medio fue 0.97±0.10. El factor de emisión de BC (EF_{BC}) dentro del túnel fue 0.31±0.08 g $(kg\ fuel)^{-1}$ y al ser convertido a masa por km, el EF_{BC} presentó un valor medio de 0.11±0.08 mg veh^{-1} km^{-1}.

- A partir del modelo del etalómetro para discernir entre el BC procedente de la quema de biomasa y de combustibles fósiles, se observó que la concentración media anual de BC en León fue 0.9 µg m^{-3}, aportando la quema de biomasa y carbón 0.3 µg m^{-3} y la quema de combustibles fósiles 0.6 µg m^{-3}. La mayor quema de biomasa y combustión de carbón en los periodos más fríos provocó que el Exponente Ångström de Absorción alcanzara un máximo de 1.43 en enero de 2017 y la mayor concentración de BC en diciembre de 2016 con 1.6 µg m^{-3}, triplicando los valores del mes de abril de 2016.

- Se construyó un nuevo modelo a partir del modelo de etalómetro clásico y el uso de trazadores de biomasa y carbón (K y As, respectivamente), para discriminar entre la concentración de BC emitido por la quema de ambos combustibles. La aplicación de dicho modelo en León concluyó que durante el periodo más frío la contribución al BC

por la quema de biomasa y carbón fue de 74% y 26%, respectivamente, con unas concentraciones medias de invierno para el BC procedente de la quema de combustibles fósiles, quema de biomasa y quema de carbón, de 0.65, 0.27 y 0.09 $\mu g\ m^{-3}$, respectivamente.

- En el 73% de los eventos de lluvia de León hubo un barrido efectivo del BC, con una disminución media de la concentración del 48% en eventos de lluvia largos (>8 h) y del 39% en eventos cortos. Se observó un lavado diferente en función de la fuente de BC: el valor medio del coeficiente de barrido (λ) del BC procedente de la quema de combustibles fósiles para eventos de lluvia cortos y largos fue de $5.1 \cdot 10^{-5}$ y $1.3 \cdot 10^{-5}\ s^{-1}$, respectivamente, mientras que para el BC de la quema de biomasa los valores fueron $1.6 \cdot 10^{-4}$ y $2.8 \cdot 10^{-5}\ s^{-1}$ en eventos cortos y largos, respectivamente. En relación al tamaño de gota de lluvia, hubo una correlación positiva significativa entre λ y el número de gotas con diámetros entre 0.375 y 2.5 mm.

Las conclusiones del tercer objetivo, desarrollado en los ***Capítulos 10 y 11*** y centrado en el impacto de la precipitación en dos variables con consecuencias importantes para la vida humana, la concentración de bioaerosoles y el forzamiento radiativo, son:

- El material polínico estudiado en León durante 4 años presentó un lavado efectivo por la lluvia en el 71% de los casos, con una disminución media del 24% en la concentración total de polen, destacando los tipos de polen *Castanea* (71%) y Cupressaceae (40%). El lavado del polen por lluvia fue muy diferente al de las partículas de aerosol en la moda gruesa: el coeficiente medio de barrido del polen fue de $2.50 \cdot 10^{-2}\ s^{-1}$ (mediana de $5.30 \cdot 10^{-3}\ s^{-1}$), tres órdenes de magnitud superior al valor obtenido para la moda gruesa. La intensidad de lluvia más eficaz fue la superior a $5\ mm\ h^{-1}$.

- Se construyó un modelo lineal (r^2=0.94) para estimar la concentración de polen total después de la lluvia con variables como la concentración de polen antes de la lluvia y otras variables procedentes de una estación meteorológica y un disdrómetro láser. Además, se construyó otro modelo para un tipo concreto de polen (Cupressaceae) que estimaba su concentración tras la lluvia a partir de la concentración inicial de polen y de tres parámetros físicos de la lluvia: el tamaño de la gota, la intensidad de la lluvia y el volumen barrido por las gotas en su caída.

- Se realizó un estudio de 16 eventos de precipitación estratiformes y 15 convectivos, que se agruparon según el valor del forzamiento radiativo atmosférico antes de la lluvia

("bajo" <30 W m^{-2} y "alto" >30 W m^{-2}). Se observaron diferencias significativas entre el grupo de lluvia estratiforme y convectiva en la duración de la lluvia, en los parámetros *a* y *b* de la relación *Z-R* y en el diámetro medio de las gotas de lluvia. El diámetro de la gota de lluvia fue similar entre el grupo de eventos estratiformes "bajo" y "alto" (0.51 vs 0.48 mm). Sin embargo, los eventos convectivos mostraron un diámetro medio de gota mayor (0.96 vs 0.83 mm).

- El espesor óptico del aerosol fue el parámetro que en mayor medida se vio afectado por el lavado de la lluvia en el grupo "alto", con una reducción de 2.7 veces. Sin embargo, otros parámetros ópticos como el albedo de dispersión simple y el parámetro de asimetría no mostraron diferencias significativas entre antes y después de la lluvia. Este hecho pudo deberse al índice de refracción constante utilizado a lo largo de los eventos.

- En eventos de precipitación estratiforme, el efecto lavado se observó claramente en el grupo "alto" con una disminución del forzamiento radiativo del 27.0% y una disminución de la tasa de calentamiento causada por aerosoles por debajo de 1 km de 1.9±4.0 K $día^{-1}$. Además, se registró una clara relación entre el forzamiento radiativo antes de la lluvia y la distribución de tamaño de las gotas medidas a nivel del suelo, ya que la moda de la distribución gamma presentó diferencias entre el grupo "bajo" (0.25 mm) y "alto" (0.35 mm). Por lo tanto, en la precipitación estratiforme, una mayor energía en la atmósfera antes de la lluvia se relaciona con un tamaño de gota de lluvia mayor.

12.2. PERSPECTIVAS DE FUTURO

Como cierre a la presente tesis doctoral, a partir de los resultados, conocimientos y experiencia obtenidos, proponemos una serie de líneas de investigación futuras relacionadas con la tesis, divididas en cuatro bloques principales: i) carbono negro; ii) bioaerosoles; iii) lavado provocado por la precipitación; iv) aplicaciones directas.

i. Debido a la importancia climática y a su efecto en la salud humana, el estudio del carbono negro en los próximos años será fundamental. Estará centrado en mediciones con el equipo AE-33, el cual presenta ya implementado el modelo del etalómetro para discernir entre quema de biomasa y de combustibles fósiles. Tal y como se ha observado

en los resultados de la presente tesis, uno de los retos será la elaboración de un modelo capaz de estimar la contribución del carbono negro procedente de tres o más fuentes (incluyendo, por ejemplo, la quema de carbón). Asimismo, la combinación del equipo AE-33 junto con el equipo SP2-XR, que aporta información sobre el tamaño del BC, puede ser clave para discernir fuentes a través de largos periodos de muestreo.

Por otra parte, una vez conocida la concentración y distribución de tamaño del BC, será posible introducirlo en modelos de deposición en el sistema respiratorio humano, mediante la aplicación de la Norma ISO 7708 o el ExDoM2 (Exposure Dose Model 2).

Asimismo, mediante la medida en continuo de las partículas inferiores a 6 nm (SMPS acoplado a una nano-DMA que mide rangos de partícula entre 2 y 165 nm) se podría evaluar la posible influencia negativa de la presencia de BC en los eventos de nucleación, aún con bajas concentraciones de partículas totales antes de los eventos.

ii. En los últimos años, los bioaerosoles o partículas biogénicas han pasado a ser uno de los temas de estudio centrales dentro del campo del aerosol atmosférico, debido a su efecto en la salud humana (principalmente alergias). Por ello, en la próxima década el estudio de la concentración de polen, esporas de hongos y bacterias se focalizará en el análisis en continuo y con una mayor resolución temporal mediante equipos basados en la medida de la fluorescencia del aerosol atmosférico, tales como el WIBS (*Wideband Integrated Bioaerosol Spectrometer*) o el *SwisensPoleno*. Además, la predicción de la concentración de los bioaerosoles utilizando parámetros meteorológicos permitirá una mejora sustancial en la previsión de alergias. Para ello, es primordial la creación previa de una librería con patrones de fluorescencia característicos de los distintos tipos de polen, esporas de hongos y bacterias.

El desarrollo de esta línea de investigación será de gran ayuda para el estudio del efecto de los bioaerosoles sobre la salud, tanto a escala individual como colectiva, especialmente en lo relativo a las instituciones sanitarias.

iii. El estudio del lavado provocado por la lluvia sobre diferentes aerosoles atmosféricos ha permitido observar diferencias en función del tamaño de la gota de lluvia, del aerosol y de la intensidad de precipitación. Por lo tanto, ya que la combinación de medidas de disdrómetro y SMPS constituye una valiosa herramienta, se propone ampliar el estudio para un espectro más amplio, tanto de intensidades de precipitación como de tamaños de gota de lluvia. Actualmente se está trabajando en el estudio del lavado durante

episodios especiales de alta concentración de contaminantes como incendios forestales o intrusiones de polvo sahariano. Otra posible línea de investigación podría ser orientar el estudio hacia el lavado en ciudades más contaminadas.

Además, dada la importancia de los eventos de nucleación en la ciudad de León, sería clave el estudio de la interacción lluvia-aerosol para tamaños de partícula inferior a 6 nm (podría muestrearse este rango de tamaños acoplando una nano-DMA al SMPS). Por otro lado, consideramos que el análisis de eventos de niebla, con gotas inferiores a 0.1 mm, permitiría completar el estudio de la interacción gota-aerosol, ampliando el espectro de tamaños de la gota. Para ello, podría utilizarse un monitor de niebla del tipo FM-120 (*Fog Monitor*), que proporciona la distribución de tamaño de gotas desde 2 µm. La combinación del disdrómetro utilizado en esta tesis y el FM-120 ofrecería datos del tamaño de gota desde 2 µm hasta más de 8 mm. Aparte del lavado por lluvia y niebla, hemos comenzado otra línea de investigación consistente en el estudio sobre el lavado de los aerosoles por otro hidrometeoro, como es la nieve, en función de su tamaño.

iv. La utilidad en la vida real de los resultados obtenidos debe ser uno de los pilares de cualquier investigación científica. Por lo tanto, la aplicación de los resultados de la presente tesis a la modelización climática y al lavado artificial de aerosoles (en interiores y/o exteriores) puede ser viable a corto o medio plazo.

Desde el punto de vista climático, la combinación de los datos del etalómetro AE-33 con los de un nefelómetro Aurora 3000 y un fotómetro CIMEL permitiría la evaluación en continuo del forzamiento radiativo provocado por el carbono negro y por otros aerosoles atmosféricos. La información obtenida puede ser valiosa en la modelización climática a través de la influencia del BC en el forzamiento radiativo.

En cuanto al lavado de aerosoles atmosféricos, algunos estudios han sugerido la creación de nubes mediante la siembra de núcleos de condensación, otros han apuntado hacia la utilización de esprays desde edificios altos en las ciudades con el fin de disminuir la carga de material particulado atmosférico. Por lo tanto, parece clara la necesidad de establecer una metodología consistente en la aplicación directa de gotas sobre aerosoles para solucionar graves episodios de alta contaminación atmosférica en las ciudades. Sin embargo, pensamos que no se trata solamente de un aspecto físico, sino que también es necesario considerar la composición química de las gotas y de las partículas a eliminar para obtener una alta eficiencia de eliminación. Por ello, el estudio

de nuevos rangos de tamaño de gota y la viabilidad de su aplicación sobre grandes volúmenes debe ser centro de investigación científica, toda vez que la emisión de contaminantes antrópicos se reduce muy lentamente.

El lavado artificial de los aerosoles no solo se restringe a ambientes exteriores, sino que podría tener importantes repercusiones en interiores (locales públicos y privados). Esta necesidad se ha visto reforzada en los últimos tiempos por la urgencia en conseguir ambientes "limpios" tras la aparición de la COVID-19 y la constatación de su transmisión mediante aerosoles.

12.3. CONCLUSIONS

This last chapter includes the main conclusions derived from this dissertation, in accordance with the aims set out in ***Chapter 2***.

The first aim addressed the study of the physical characteristics of aerosol and the quantification of the scavenging of precipitation on atmospheric aerosol as a function of the raindrop size spectrum. This goal has been discussed in ***Chapters 4, 5 and 6.*** The general conclusions on this objective are:

- The nucleation mode is positively correlated with a higher atmospheric boundary layer height in the warm period, which in turn leads to better conditions for the occurrence of new particle formation events. Based on a subjective classification, 45 type *Ia* events (with a good confidence level and no pre-existing particles) were identified between 1100 and 1500 UTC in spring and summer.

- The scavenging caused by rain on atmospheric aerosol depends on particle size and on the composition and size of the raindrop. Effective scavenging has been observed, although to a different extent, in all particle size ranges, for both biogenic and non-biogenic particles.

- The study of the scavenging of the fine and coarse modes of the aerosols showed a mean scavenging coefficient of $2.6 \cdot 10^{-5} \pm 6.0 \cdot 10^{-5}$ and $5.8 \cdot 10^{-5} \pm 9.6 \cdot 10^{-5}$ s^{-1}, respectively,

and a decrease in total particle concentration of 18% after rainfall. The least effective washout was observed in the size range between 0.6 and 1 µm.

- Particles included in the Aitken mode showed the lowest scavenging coefficient λ of $3.1 \cdot 10^{-5}$ s^{-1}, with a washout efficiency of only 4%. The nucleation and accumulation modes showed higher values (15% and $3.9 \cdot 10^{-5}$ s^{-1}; 22% and $5.0 \cdot 10^{-5}$ s^{-1}, respectively). The most effective aerosol scavenging was recorded at precipitation intensities below 1 mm h^{-1} and above 3 mm h^{-1}, with a clear decrease of the modal peaks in the multi-lognormal aerosol size distribution. Furthermore, raindrop sizes between 1.25 and 3.5 mm efficiently scavenged aerosol sizes between 70 and 300 nm.

The second aim was to distinguish between the contribution of black carbon from fossil fuel and biomass burning processes and to assess the effect of precipitation on the concentration of black carbon released by different sources. This goal has been developed in ***Chapters 7, 8 and 9***, and the general conclusions are as follows:

- The concentration of black carbon (BC) from traffic inside a tunnel, with 56,000 vehicles passing through during the sampling period (8 days), was 21±10 µg m^{-3}, with an hourly maximum of 49 µg m^{-3}. The mean Ångström Absorption Exponent (AAE) was 0.97±0.10. The BC emission factor (EF_{BC}) inside the tunnel was 0.31±0.08 g $(kg\ fuel)^{-1}$ and when converted to mass per km, the EF_{BC} had a mean value of 0.11±0.08 mg veh^{-1} km^{-1}.

- To distinguish between BC concentration from biomass burning and fossil fuel, it was observed that the mean annual value in León was 0.9 µg m^{-3}, with biomass and coal combustion contributing 0.3 µg m^{-3} and fossil fuel burning 0.6 µg m^{-3}. The higher biomass burning and coal combustion in the colder periods caused the Ångström Absorption Exponent to reach a maximum of 1.43 in January 2017 and the highest BC concentration in December 2016 with 1.6 µg m^{-3}, three times higher than the values registered in April 2016.

- A new model was built from the classical aethalometer model and the use of biomass and coal tracers (K and As, respectively) to discriminate between the BC concentration emitted by the burning of both fuels. The application of the model in León concluded that during the coldest period the contribution to BC from biomass and coal burning was 74% and 26%, respectively, with mean winter concentrations for BC from fossil

fuel burning, biomass burning and coal burning of 0.65, 0.27 and 0.09 μg m^{-3}, respectively.

- In 73% of the rain events there was an effective scavenging of BC, with a mean decrease in eBC concentration of 48% in long rain events (>8 h) and 39% in short rain events. A different washout was observed as a function of the black carbon source: the mean value of the scavenging coefficient (λ) of BC from fossil fuel burning for short and long rainfall events was $5.1 \cdot 10^{-5}$ and $1.3 \cdot 10^{-5}$ s^{-1}, respectively, while for BC from biomass burning the values were $1.6 \cdot 10^{-4}$ and $2.8 \cdot 10^{-5}$ s^{-1} in short and long events, respectively. In relation to raindrop size, there was a significant positive correlation between λ and the number of raindrops with diameters between 0.375 and 2.5 mm.

The conclusions of the third aim, developed in ***Chapters 10 and 11,*** focused on studying the impact of precipitation on two variables with important consequences for human health, bioaerosol concentration and radiative forcing:

- The pollen material studied in León over 4 years showed effective rain scavenging in 71% of the cases, with a mean decrease of 24% in total pollen concentration; *Castanea* (71%) and Cupressaceae (40%) pollen types are particularly noteworthy. Rain scavenging of pollen was very different from that of aerosol particles in the coarse mode: the mean pollen scavenging coefficient was $2.50 \cdot 10^{-2}$ s^{-1} (median of $5.30 \cdot 10^{-3}$ s^{-1}), three orders of magnitude higher than the value obtained for the coarse mode. The most effective rainfall intensity was the one over 5 mm h^{-1}.

- A linear model (r^2=0.94) to estimate pollen concentration after rain was built with variables such as pollen concentration before rain and other variables from a weather station and a disdrometer. In addition, for a specific type of pollen (Cupressaceae), we were able to model its concentration from the initial pollen concentration and three physical parameters of the rain: the drop size, the rain intensity and the volume swept by the raindrops.

- After a study of 16 stratiform and 15 convective precipitation events, grouped according to the value of atmospheric forcing before rainfall ("low" <30 W m^{-2} and "high" >30 W m^{-2}), significant differences between stratiform and convective events were observed in rain duration, mean raindrop diameter and *Z-R* ratio parameters *a* and *b*. The raindrop diameter was similar between the "low" and "high" stratiform events

group (0.51 vs. 0.48 mm). However, convective events showed a higher mean raindrop diameter (0.96 vs. 0.83 mm).

- Aerosol optical thickness was the parameter that showed most clearly the rain washout in the "high" group, with a decrease of 2.7 times. However, other optical parameters such as single scattering albedo and the asymmetry parameter did not show statistical differences between before and after rain. This could be due to the constant refractive index used throughout the events.

- In stratiform rain events, the scavenging effect was clearly observed in the "high" group with a decrease in ΔF_{ATM} of 27.0% and a decrease in the aerosol heating rate below 1 km of 1.9±4.0 K day^{-1}. Furthermore, there was a clear relationship between the radiative forcing before rainfall and the specific rain characteristics measured at ground level, as the mode of the gamma distribution differed between the "low" (0.25 mm) and "high" (0.35 mm) groups. Therefore, in stratiform events, a higher energy in the atmosphere before rain is related to a larger raindrop size.

12.4. FUTURE PROSPECTS

At the end of this dissertation, based on the results, knowledge and experience gained in the past few years years, the main lines of future research related to the dissertation are discussed, divided into four thematic areas: i) black carbon; ii) bioaerosols; iii) scavenging of aerosols; iv) direct applications.

i. Due to the climatic importance and its effect on human health, the study of black carbon in the coming years will be crucial. It will be focused on measurements with the AE-33 aethalometer, which has already implemented the aethalometer model to discern between biomass and fossil fuel burning. As observed in the results of this dissertation, one of the challenges will be the modelling of the origin of black carbon from three or more sources (including, for example, coal burning). Also, the combination of the AE-33 together with the SP2-XR equipment, which provides information about BC size, may be key to discern sources using long sampling periods.

In addition, once the concentration and size distribution of BC is known, it will be possible to include these data into some models of deposition in the human respiratory system such as the application of the International Standard ISO 7708 or ExDoM2 (Exposure Dose Model 2).

Moreover, by means of a continuous measurement of particles smaller than 6 nm (SMPS coupled to a nano-DMA measuring particle ranges between 2 and 165 nm), the possible negative influence of the presence of BC on the occurrence of nucleation events could be assessed, even with low concentrations of total particles before the events.

ii. In recent years, bioaerosols or biogenic particles have become one of the main topics of study within the field of atmospheric aerosols, due to their effect on human health (mainly allergies). Therefore, in the next decade, the study of the concentration of pollen, fungal spores and bacteria will focus on continuous analysis with a higher temporal resolution using equipment based on the measurement of atmospheric aerosol fluorescence, such as the WIBS (*Wideband Integrated Bioaerosol Spectrometer*) or the *SwisensPoleno*. In addition, prediction of bioaerosol concentration using meteorological parameters will allow a substantial improvement in allergy forecasting. For this purpose, the prior creation of a library with fluorescence patterns characteristic of different types of pollen, fungal spores and bacteria is essential.

The development of this research line will certainly be helpful in the study of the effect of bioaerosols on health, both at the individual and collective level, especially in relation to health institutions.

iii. The study of the rain scavenging on different atmospheric aerosols has allowed to observe some differences related to raindrop size, aerosol size and precipitation intensity. Therefore, as the combination of disdrometer and SMPS measurements is a valuable tool, we propose to extend the study to a broader spectrum of both precipitation intensities and raindrop sizes. Currently, work is being carried out on scavenging during special events of high pollutant concentration, such as wildfires or dust intrusions. Another possible line of research could be to focus on scavenging in more polluted cities.

Furthermore, given the importance of nucleation events in the city of León, the study of rain-aerosol interaction for particle sizes below 6 nm (this size range could be sampled by coupling a nano-DMA to the SMPS) would be key. On the other hand, we consider that the analysis of fog events, with droplets smaller than 0.1 mm, would allow us to complete the

study of droplet-aerosol interaction, broadening the spectrum of droplet sizes. For this purpose, a fog monitor of type FM-120, which provides drop size distribution from 2 µm, could be used. The combination of the disdrometer used in this dissertation and the FM-120 would provide drop size data from 2 µm to more than 8 mm. Apart from washout by rain and fog, we have started another line of research consisting of the study of the scavenging of aerosols by another hydrometeor, such as snow, depending on its size.

iv. The usefulness in real life of the results obtained must be one of the pillars of any scientific research. Therefore, the application of the results of this dissertation to climate modelling and artificial aerosol scavenging (indoor and/or outdoor) may be feasible in the short to medium term.

From a climatic point of view, the combination of data from the AE-33 aethalometer with data from an Aurora 3000 nephelometer and a CIMEL photometer would allow the continuous assessment of radiative forcing by black carbon and other atmospheric aerosols. The information thus obtained can be valuable in climate modelling through BC influence on radiative forcing.

Regarding the scavenging of atmospheric aerosols, some studies have suggested the creation of clouds by seeding condensation nuclei; others have pointed towards the use of sprays from high buildings in cities in order to decrease the burden of particulate matter in the atmosphere. Therefore, it seems clear that there is a need to establish a methodology consisting of direct application of raindrops on aerosols to solve severe episodes of high air pollution in cities. However, we believe that this is not only a physical aspect, but it is also necessary to consider the chemical composition of the raindrops and of the particles to be removed in order to obtain a high removal efficiency. Therefore, the study of new raindrop size ranges and the feasibility of their application over large volumes should be the focus of scientific research, since the emission of anthropogenic pollutants is decreasing at a very slow pace today.

Artificial washout of aerosols is not only restricted to outdoor environments but could have important repercussions indoors (public and private places). This need has recently been reinforced by the urgency to achieve "clean" environments following the emergence of COVID-19 and the discovery of its transmission by aerosols.

ANEXO A

A1. EFICIENCIA DE COLISIÓN

La *eficiencia de colisión* se define como la fracción de las partículas de aerosol con diámetro d_p, contenidas en el volumen de colisión, que se recogen por la caída de gotas de lluvia de diámetro D_r. El volumen de colisión V se define como:

$$V = \frac{\pi}{4} {D_r}^2 v_t(D) t \qquad \textit{Eq. A1}$$

siendo D_r el diámetro de las gotas de lluvia, v_t la velocidad terminal y t el tiempo.

Existen múltiples estudios experimentales sobre la eficiencia de colisión entre la gota de lluvia y las partículas bajo condiciones controladas. Así, Quérel et al. (2014) y Wang and Pruppacher (1977) encontraron un aumento de la eficiencia de colisión al aumentar el tamaño de las partículas y la carga (Figura A1). El lavado sobre diferentes tamaños de aerosol será diferente en función del tamaño de gota. Para evaluarlo, se estima la eficiencia de colisión $E\ (d_p, D_r)$ y, a partir de ella, se puede obtener un valor teórico del *coeficiente de scavenging* $\lambda\ (d_p, D_r)$, visto en el apartado 1.3.2.

La Eq. A2 se muestra la eficiencia de colisión $E\ (d_p, D_r)$ entre gotas de lluvia y partículas de aerosol, propuesta por Seinfeld and Pandis (2016; ver Eq. 20.53), basada en Slinn (1983) y Andronache et al. (2006). La expresión y su desarrollo ha sido utilizada por numerosos autores como Andronache et al. (2006), Chate (2005), Loosmore and Cederwall (2004), Mircea et al.

(2000), Tost et al. (2006) o Wang et al. (2010). Todos los símbolos de la Eq. A2 se incluyen en la Tabla A2.

$$E(d_p, D_r) = \overbrace{\frac{4}{R_e S_c}\left[1 + 0.4{R_e}^{1/2}{S_c}^{1/3} + 0.16{R_e}^{1/2}{S_c}^{1/2}\right]}^{Difusión\ browniana} + \overbrace{4\frac{d_p}{D_r}\left[\frac{\eta_a}{\eta_w} + \left(1 + 2{R_e}^{1/2}\right)\frac{d_p}{D_r}\right]}^{Interceptación}$$
$$+ \overbrace{\left[\left(\frac{St - St_t}{St - St_t + \frac{2}{3}}\right)^{3/2}\left(\frac{\rho_p}{\rho_w}\right)^{1/2}\right]}^{Impacto\ inercial} + \overbrace{\left[\frac{4\alpha_{th}\left(2 + 0.6{R_e}^{1/2}{P_r}^{1/3}\right)(T_a - T_s)}{U_t\,(D_r)\,D_r}\right]}^{Termoforesis}$$
$$+ \overbrace{\left[\frac{4\gamma_{dph}\left(2 + 0.6{R_e}^{1/2}{S_{cw}}^{1/3}\right)\left(\frac{{P_s}^0}{T_s} - \frac{{P_a}^0 RH}{T_a}\right)}{U_t\,(D_r)\,D_r}\right]}^{Difusioforesis}$$
$$+ \overbrace{\left[\frac{16kC_cQ_rq_p}{3\pi\eta_a U_t\,(D_p)\,{D_r}^2 d_p}\right]}^{Efecto\ electroestático}$$

Eq. A2

donde

$$S_c = \frac{\eta_a}{\rho_a D_{diff}} \quad ; \quad D_{diff} = \frac{k_b T_a C_c}{3\pi\,\eta_a\,d_p} \quad ; \quad R_e = \frac{D_p\,U_t\,(D_r)\,\rho_a}{2\,\eta_a} \quad ; \quad St = \frac{2\tau\left[U_t\,(D_p) - u_t\,(d_p)\right]}{D_r};$$

$$\tau = \frac{(\rho_p - \rho_a){d_p}^2 C_c}{18\,\eta_a} \quad ; \quad C_c = 1 + \frac{2\delta}{d_p}\left(1.257 + 0.4e^{\left(-0.55\frac{d_p}{\delta}\right)}\right) \quad ; \quad St_t = \frac{1.2 + \frac{1}{12}ln(1+R_e)}{1 + ln(1+R_e)} \quad ;$$

$$u_t(d_p) = \frac{\rho_p {d_p}^2 g\,C_c}{18\,\eta_a}\,; \alpha_{th} = \frac{2C_c\left(k_a + \frac{5\delta}{D_p k_p}\right)k_a}{5P\left(1 + \frac{5\delta}{D_r}\right)\left(2k_a + k_p + \frac{10\delta}{D_r k_p}\right)}\,; P_r = \frac{c_p\eta_a}{k_a} \;;\; \gamma_{dph} = \frac{T_a D_{diffw}}{P}\sqrt{\frac{M_w}{M_a}}\,;$$

$$Sc_w = \frac{\eta_a}{\rho_a D_{diffw}} \;;\; Q_r = a\xi {D_r}^2 \;;\; q_p = a\xi {d_p}^2$$

El término correspondiente al impacto inercial solo es válido cuando *St* es mayor que St_t, y depende del exponente $(\rho_p/\rho_w)^{1/2}$, debido a que la densidad de la partícula ρ_p es diferente de 1 g cm^{-3} (Seinfeld and Pandis, 2016; Slinn, 1983).

Tabla 1.2. Significado de las variables implicadas en el cálculo de la eficiencia de colisión (Eq. 1.10).

Símbolo	Significado
τ	Tiempo de relajación de las partículas *(s)*
a	cte.= $0.83 \cdot 10^{-6}$
C_c	Factor de corrección *Cunningham slip*
D_{diff}	Coeficiente de difusividad *Browniano* de las partículas $(m^2\ s^{-1})$
K	cte. = $9 \cdot 10^9\ N\ m^2\ C^{-2}$
k_a	Conductividad térmica del aire $(J\ m^{-1}\ s^{-1}\ K^{-1})$
k_b	Constante de *Boltzmann* $(J\ K^{-1})$
k_p	Conductividad térmica de una partícula $(J\ m^{-1}\ s^{-1}\ K^{-1})$
η_a	Viscosidad del aire $(kg\ m^{-1}\ s^{-1})$
η_w	Viscosidad del agua $(kg\ m^{-1}\ s^{-1})$
P_a^0	Presión de vapor del agua a una temperatura T_a *(Pa)*
P_r	Número *Prandtl* del aire
Ps^0	Presión de vapor del agua a una temperatura T_s *(Pa)*
q_p	Carga media de una partícula *(C)*
Q_r	Carga media de una gota *(C)*
R_e	Número de *Reynolds* de una gota
S_c	Número de *Schmid*t de una partícula
S_{cw}	Número de *Schmidt* del agua en el aire
S_t	Número de *Stokes* de una partícula
St_t	Número crítico de *Stokes* de una partícula
T_a	Temperatura del aire *(K)*
T_s	Temperatura de la superficie de la gota *(K)*
δ	Camino libre medio de las moléculas de aire *(m)*
ρ_a	Densidad del aire $(kg\ m^{-3})$
ξ	Parámetro de electrificación entre 0 y 7 $(C\ m^{-2})$

En la Figura A1 hemos realizado una simulación de la eficiencia de colisión total para diferentes tamaños de gota de lluvia y de partículas de aerosol. Se observa cómo un aumento del tamaño de las partículas (principalmente superiores a 0.2 µm) provoca un aumento de la eficiencia de colisión, sobre todo en tamaños de gota de lluvia inferiores a 0.8 mm. A mayor diámetro de gota de lluvia se requiere un mayor tamaño de partícula para que su interacción presente valores similares de eficiencia de colisión.

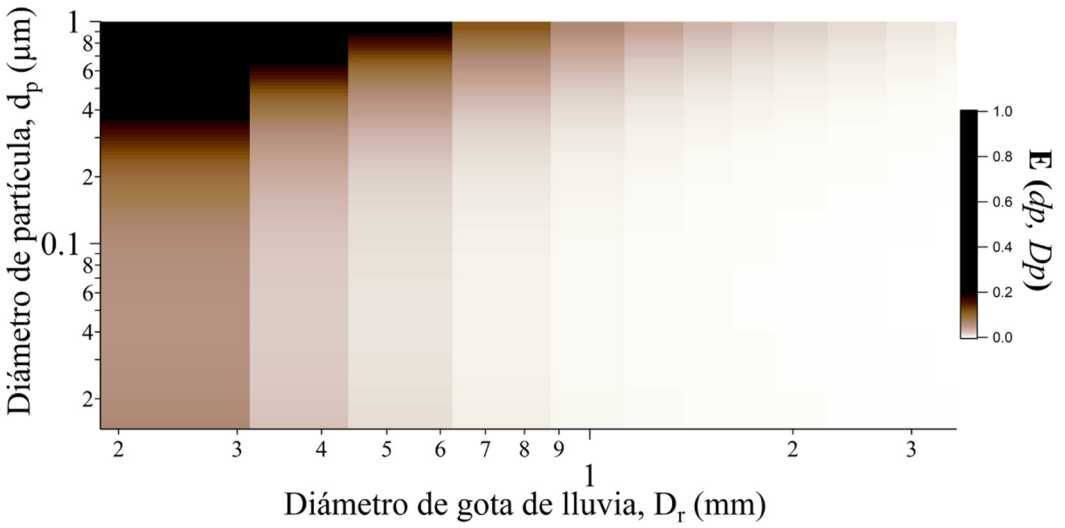

Figura A1. Eficiencia de colisión total por diferentes mecanismos entre diferentes tamaños de gota de lluvia y partículas de aerosol.

En la Figura A2 mostramos un ejemplo de la eficiencia de colisión teórica entre partículas de aerosol con diámetro entre 14 y 1000 nm y gotas de lluvia con diámetros de 0.31, 1.13 y 1.88 mm, para una distribución de tamaño de gota gamma con parámetros α=3 y β=6.3 mm^{-1}, teniendo en cuenta los diferentes mecanismos de barrido debajo de la nube. Estos rangos de tamaño son aplicables a los rangos incluidos en la presente tesis. Puede observarse que:

- La contribución de cada mecanismo difiere en función del tamaño de gota y partícula de aerosol, mostrando menor eficiencia de colisión en todos los mecanismos de lavado a mayor tamaño de gota de lluvia.
- La difusioforesis es el segundo mecanismo de lavado en orden de importancia, a lo largo del rango analizado.
- El efecto electrostático y la termoforesis se podrían considerar insignificantes.
- Para gotas de lluvia de diámetro 0.31 mm, la difusión browniana es el principal mecanismo de lavado de partículas con diámetros inferiores a 50 nm (Figura A2a), mientras que la interceptación es el principal mecanismo de lavado en los aerosoles entre 50 y 1000 nm.
- Para gotas de lluvia de diámetro 1.13 mm, igualmente los principales mecanismos de lavado para partículas de aerosol con diámetros inferiores a 65 nm son la difusión browniana y difusioforesis (Figura A2b). Para partículas de aerosol entre 65 y 1000 nm la interceptación es el principal mecanismo.
- Para gotas de lluvia de diámetro 1.88 mm, el patrón es prácticamente idéntico al observado para el tamaño de gota de 1.13 mm, pero presenta menores eficiencias de colisión (Figura A2c).

a)

b)

c)

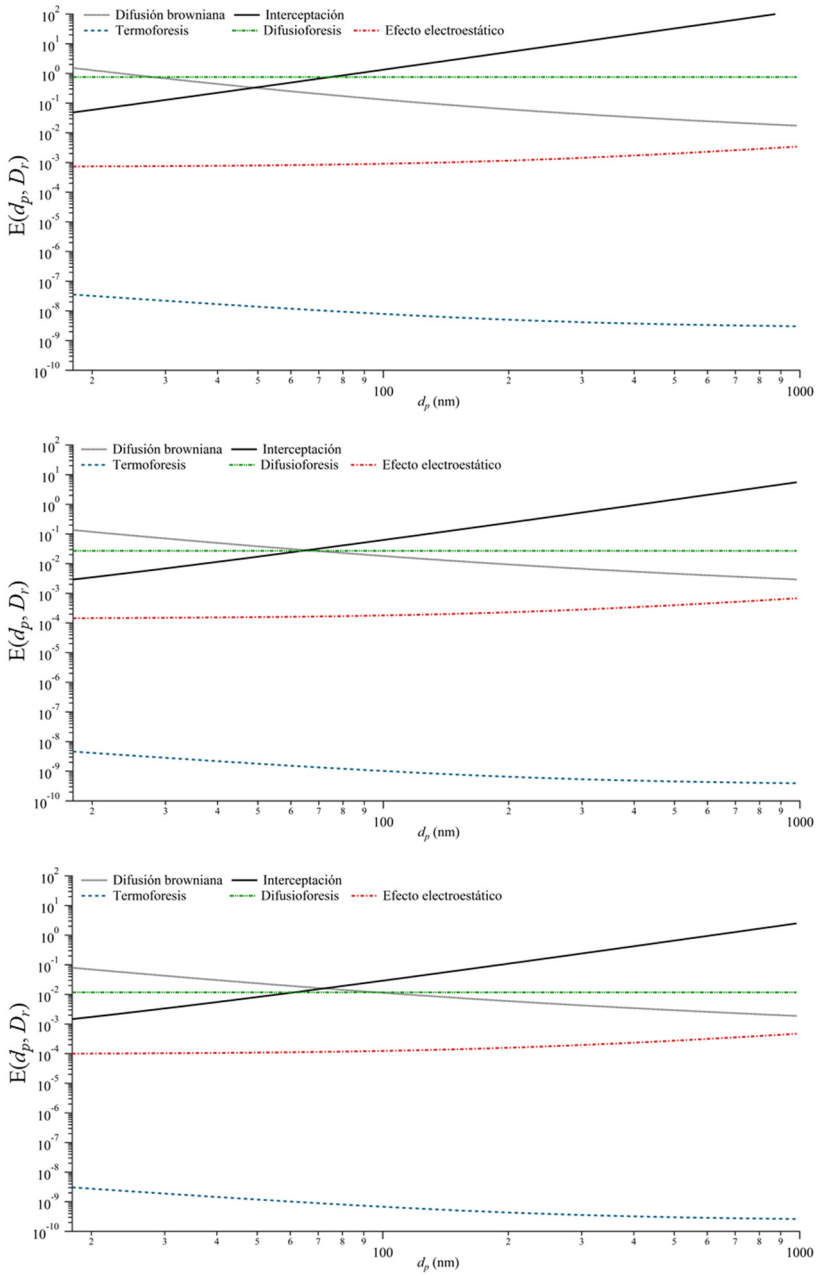

Figura A2. Eficiencia de colisión por diferentes mecanismos provocado por gotas de lluvia de a) 0.31 mm, b) 1.13 mm y c) 1.88 mm en partículas de aerosol de tamaños entre 14 y 1000 nm en una precipitación cuyos parámetros de ajuste a una DSD gamma son α=3 y β=6.3 mm^{-1}.

A2. REFERENCIAS

Andronache, C., Grönholm, T., Laakso, L., Phillips, V., Venalainen, A., Phillips, Y., Venäläinen, A., 2006. Scavenging of ultrafine particles by rainfall at a boreal site: observations and model estimations. Atmos. Chem. Phys. 6, 4739–4754. doi:10.5194/acp-6-4739-2006

Chate, D.M., 2005. Study of scavenging of submicron-sized aerosol particles by thunderstorm rain events. Atmos. Environ. 39, 6608–6619. doi:10.1016/j.atmosenv.2005.07.063

Loosmore, G.A., Cederwall, R.T., 2004. Precipitation scavenging of atmospheric aerosols for emergency response applications: Testing an updated model with new real-time data. Atmos. Environ. 38, 993–1003. doi:10.1016/j.atmosenv.2003.10.055

Mircea, M., Stefan, S., Fuzzi, S., 2000. Precipitation scavenging coefficient: Influence of measured aerosol and raindrop size distributions. Atmos. Environ. 34, 5161–5167. doi:10.1016/S1352-2310(00)00349-6

Quérel, A., Lemaitre, P., Monier, M., Porcheron, E., Flossmann, A.I., Hervo, M., 2014. An experiment to measure raindrop collection efficiencies: Influence of rear capture. Atmos. Meas. Tech. 7, 1321–1330. doi:10.5194/amt-7-1321-2014

Seinfeld, J.H., Pandis, S., 2006. Atmospheric from air pollution to climate change, Atmospheric Chemistry and Physics. Wiley. doi:10.1016/0016-7037(87)90252-3

Seinfeld, J.H., Pandis, S.N., 2016. Atmospheric Chemistry and Physics: From Air Pollution to Climate Change, Atmospheric Chemistry and Physics. Wiley. doi:10.1016/0016-7037(87)90252-3

Slinn, W.G.N., 1983. Precipitation scavenging. Division of Biomedical Environmental Research, US Department of Energy, Washington DC.

Tost, H., Jöckel, P., Kerkweg, A., Sander, R., Lelieveld, J., 2006. Technical note: A new comprehensive scavenging submodel for global atmospheric chemistry modelling. Atmos. Chem. Phys. Discuss. 5, 11157–11181. doi:10.5194/acpd-5-11157-2005

Wang, P.K., Pruppacher, H.R., 1977. An experimental determination of the efficiency with which aerosol particles are collected by water drops in subsaturated air. J. Atmos. Sci. 34, 1664–1669. doi:10.1175/1520-0469(1977)034<1664:AEDOTE>2.0.CO;2

Wang, X., Zhang, L., Moran, M.D., 2010. Uncertainty assessment of current size-resolved parameterizations for below-cloud particle scavenging by rain. Atmos. Chem. Phys. 10, 5685–5705. doi:10.5194/acp-10-5685-2010

ANEXO B

B1. PREPARACIÓN PRE-MUESTREO

Un periodo de estudio superior a un año requiere una importante preparación del material y puesta a punto de los equipos que intervendrán en el mismo. Por lo tanto, previamente a la campaña de muestreo se preparó el material: filtros de muestreo de material particulado, limpieza de botes de lluvia y placas Petri, así como la realización de pruebas previas de los equipos descritos en el apartado 3.3. A continuación se describe brevemente el pre-muestreo.

B1.1. EQUIPOS DE MEDIDA

Los equipos de muestreo se probaron con diferentes parámetros de funcionamiento para encontrar aquella configuración más óptima al inicio del muestreo. Para ello se llevó a cabo un pre-muestreo entre julio de 2015 y enero de 2016. Los instrumentos involucrados en el pre-muestreo de forma continua fueron: un contador óptico de partículas (PCASP-X), un disdrómetro láser y una estación meteorológica, descritos detalladamente junto al resto de instrumentos de medida en el apartado 3.3. Cabe destacar que, como resultado de este periodo de muestreo previo al estudio en sí, se desarrolló y publicó un artículo contenido en esta tesis doctoral (***Capítulo 5***: "*Below-cloud scavenging of fine and coarse aerosol particles by rain: The role of raindrop size*").

B1.2. FILTROS DE MUESTREO

La preparación de los filtros de material particulado utilizados fue diferente en función de la composición de su material: los filtros de cuarzo requieren empaquetado, calcinación, pesaje e identificación, los de teflón requieren pesaje e identificación, y los filtros de policarbonato empaquetado e identificación. Para la recogida de PM_{10} se siguió la metodología señalada en la normativa EN12341:2014. Los filtros de cuarzo fueron colocados en un colector de alto volumen y los filtros de teflón y policarbonato en colectores de bajo volumen. Estos dispositivos son descritos detalladamente en el apartado 3.3.

Pretratamiento de filtros

Los filtros de cuarzo (diámetro de 150 mm y poro de 0.45 µm) se calcinaron, antes del muestreo, en una mufla a 600 ºC durante 5 horas, para eliminar cualquier posible componente orgánico presente. También se muestreó en filtros de teflón (diámetro de 47 mm y poro de 0.2 µm) y policarbonato (diámetro de 47 mm y poro de o.2 µm) para diferentes análisis (Figura B1).

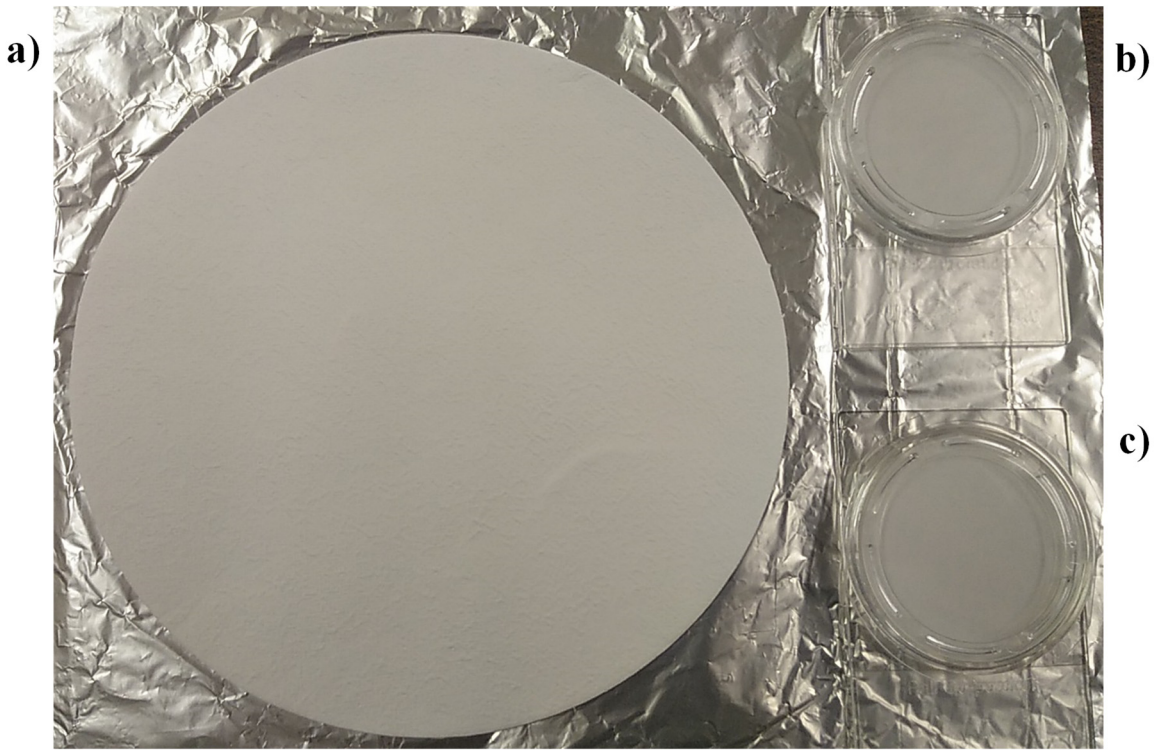

Figura B1. Filtro de: a) cuarzo; b) policarbonato; c) teflón.

La determinación de la concentración de PM_{10} se realizó mediante el método gravimétrico en una sala de pesaje que se mantuvo a una temperatura (20 ºC) y una humedad relativa (40-50%) controladas. Los filtros de cuarzo y teflón se pesaron antes y después del muestreo, siendo colocados en la sala de pesaje 24 h antes para la homogenización de su temperatura y humedad con el aire ambiental. Para el pesaje se utilizó una balanza semi-micro electrónica (Mettler Toledo, modelo XPE105DR) de precisión 0.00001 g (Figura B2).

B1.3. MATERIAL PARA MUESTRAS DE LLUVIA

Los botes para recolectar la lluvia fueron botellas de 3.5 L de cristal que previamente a ser usados se sonicaron dos veces con agua destilada y una vez con agua milli-Q y posteriormente fueron secados al aire para evitar impurezas provocadas por el depósito de restos de cualquier material secante. En la Figura B3 se puede observar una de estas botellas con el agua recolectada en las anteriores 24 h. Las botellas fueron pesadas antes y después del muestreo para determinar el volumen muestreado cada 24 h. Posteriormente, el agua recolectada se separaba para diferentes análisis en dos botes de 150 ml (para el análisis del carbono disuelto e iones) y uno de 25 ml (para la determinación de elementos químicos), también lavados y sonicados previamente con agua destilada y agua milli-Q.

Además, parte de la precipitación recolectada fue filtrada en filtros de cuarzo de 25 mm de diámetro. El procedimiento de manipulación de estos filtros fue igual al mencionado en el apartado B1.2 para los filtros de cuarzo.

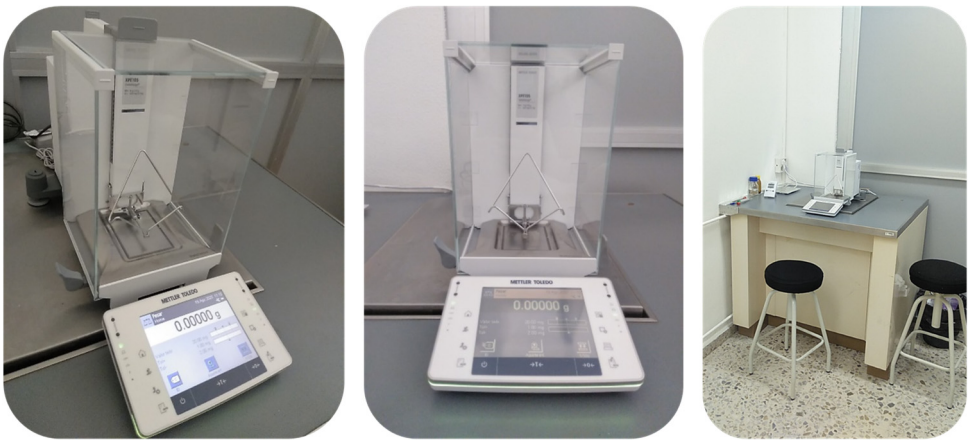

Figura B2. Balanza semi-micro electrónica (Mettler Toledo, modelo XPE105DR) ubicada en la sala de pesaje de filtros de la Facultad de Ciencias Biológicas y Ambientales de la Universidad de León.

Figura B3. Botella para recolectar el agua de lluvia.

B2. MUESTREO: EQUIPOS DE MEDIDA

B2.1. FUNCIONAMIENTO DEL SMPS

A continuación, se describe brevemente el funcionamiento del SMPS y un esquema detallado de cada componente, que incluye un clasificador de partículas con una DMA incorporada y un contador de partículas CPC (Figura B4):

1. Antes de su entrada en el SMPS, la muestra de aerosol polidisperso circula a través de un secador de Nafion colocado en la entrada que seca el aerosol a una humedad relativa del 40% o menos (Wiedensohler et al., 2012) y pasa a través de un ciclón que realiza un primer cribado evitando la entrada de partículas superiores a 1 µm.
2. El flujo de aerosol pasa a través del impactador inercial, el cual separa la muestra en dos rangos de diámetros aerodinámicos de partícula: un aerosol polidisperso de tamaños inferiores a 1 µm y las partículas superiores a 1 µm (segundo cribado).
3. El flujo de aerosol polidisperso en el rango de tamaño seleccionado atraviesa un cargador bipolar (en nuestro caso fue un neutralizador de rayos-X de la marca TSI).
4. Posteriormente, estas partículas cargadas se clasifican en la DMA según su movilidad en un campo eléctrico, propiedad que depende de su tamaño y de su estado de carga. Las partículas con la movilidad eléctrica seleccionada, en un momento dado, constituyen un flujo de aerosol monodisperso que sale de la DMA y entra en el contador CPC.

5. El CPC cuenta las partículas clasificadas en un rango de diámetro determinado, generando una distribución de tamaños al completar el análisis de seis minutos. Para ello el CPC funciona mediante butanol que actúa como líquido condensable sobre las partículas permitiendo su detección óptica. El flujo de aerosol entra en la cámara óptica (láser y fotodetector) provocando la dispersión de la luz lo cual se traduce en un impulso eléctrico.
6. Finalmente, la distribución del tamaño de partícula resultante se obtiene mediante software a través de la integración del tamaño de partícula correspondiente al voltaje seleccionado en la DMA y al número de partículas contadas en el CPC para ese voltaje.

Para una descripción más completa y detallada de los espectrómetros de partículas SMPS se recomiendan dos tesis: Alonso-Blanco (2019) y Sorribas Panero (2007).

a)

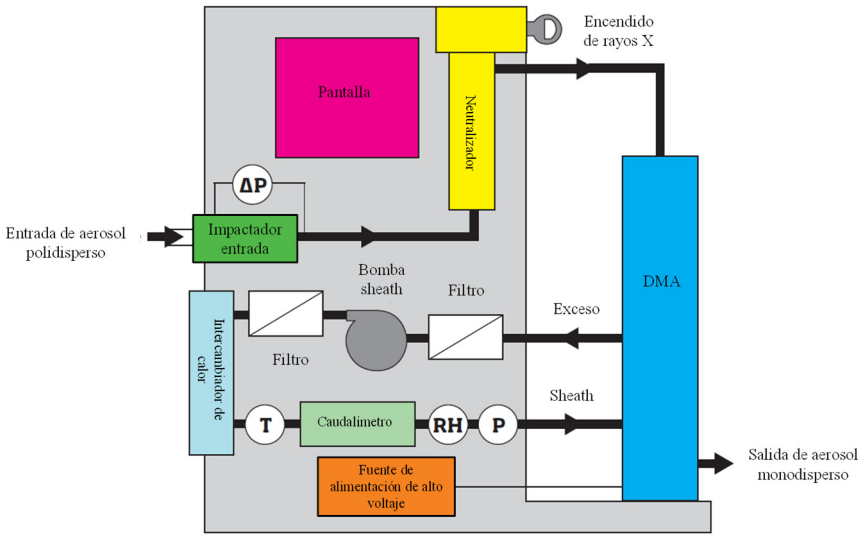

b)

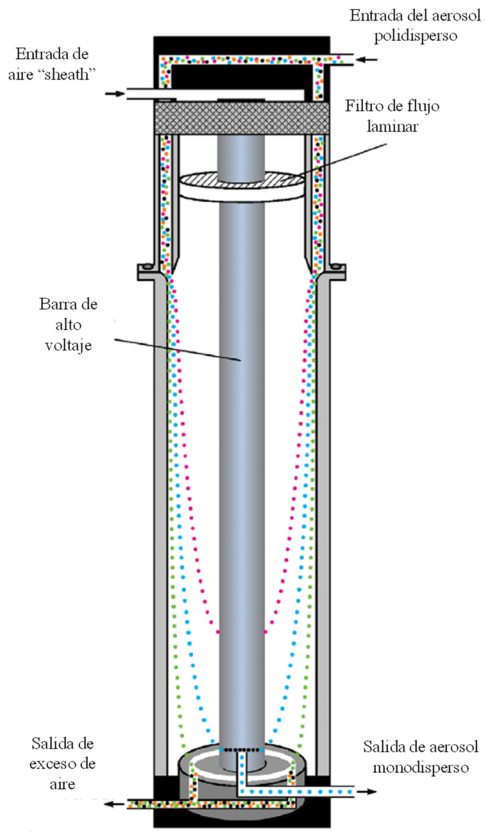

c)

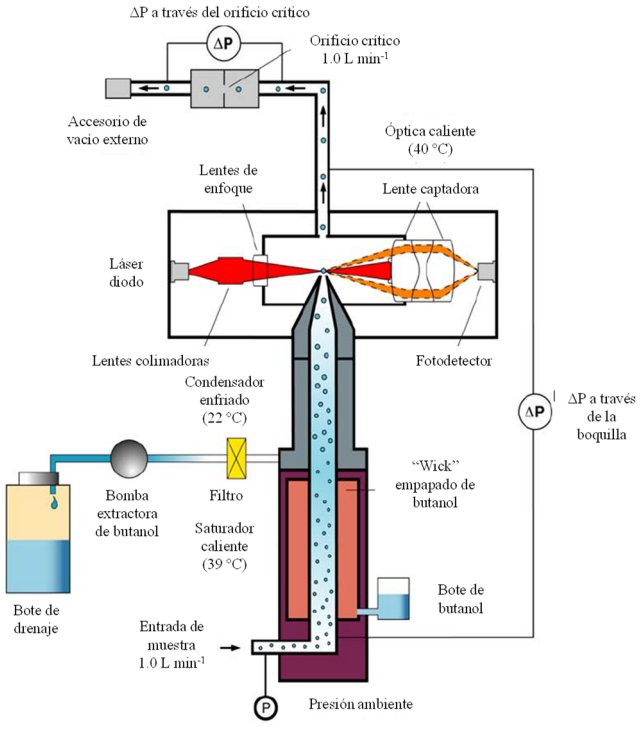

Figura B4. Esquema de: a) clasificador; b) analizador de movilidad diferencial DMA; c) contador de partículas CPC. Imágenes modificadas de los manuales de la empresa TSI (TSI, 2007a, 2007b).

B2.2. CORRECCIONES DEL CONTADOR DE PARTÍCULAS ÓPTICO PCASP-X

Para determinar la concentración de partículas en cada canal se deben realizar diferentes correcciones sobre el número de cuentas que indica el espectrómetro directamente. A continuación, se definen las correcciones realizadas:

- Altitud: se debe ajustar el valor de la medida del volumen muestreado, de acuerdo al fabricante, en función de la altitud del punto de muestreo (837 m).
- Actividad: se define como el porcentaje de tiempo durante el cual la sonda está contabilizando partículas activamente. En función de este valor y a través de un algoritmo se corrige la medida. Existe un tiempo fijo de retardo tras el paso de una partícula a través del láser, durante el cual la información sobre su tamaño se transfiere al sistema de datos, y la electrónica se reajusta para el paso de la siguiente partícula (Baumgardner et al., 1985).
- Índice de refracción: el espectrómetro PCASP-X es calibrado con esferas de látex, fuertemente dispersoras y no absorbentes de la radiación, como muestra el alto valor del componente real y la parte imaginaria cero de su índice de refracción (1.58-0i). Como las partículas ambientales son generalmente menos dispersoras de la radiación y tienen ciertas propiedades absorbentes, el equipo subestima el verdadero diámetro de los aerosoles ambientales, y las distribuciones de tamaño obtenidas deben corregirse en función del índice de refracción de las partículas muestreadas (Guyon et al., 2003). Para ello se estimó un índice de refracción mensual a partir de la composición química de los filtros muestreados, siguiendo la metodología de Hasan and Dzubay (1983) y Levin et al. (2010). En el ***Capítulo 11*** se incluye el artículo "Links between aerosol radiative forcing and rainwater: stratiform and convective Precipitation", donde se muestran los valores de los índices de refracción y densidad estimados mensualmente. La densidad estimada permite transformar la concentración de partículas en masa de aerosoles.

B3. REFERENCIAS

Alonso-Blanco, E., 2019. Caracterización de la distribución de tamaños y propiedades higroscópicas del aerosol atmosférico en España mediante Analizadores de Movilidad Diferencial (DMA). Álcala de Henares.

Baumgardner, D., Strapp, W., Dye, J.E., 1985. Evaluation of the forward scattering spectrometer probe. Part II: Corrections for coincidence and dead-time losses. J. Atmos. Ocean. Technol 2, 626–632.

Guyon, P., Boucher, O., Graham, B., Beck, J., Mayol-Bracero, O.L., Roberts, G.C., Maenhaut, W., Artaxo, P., Andreae, M.O., 2003. Refractive index of aerosol particles over the Amazon tropical forest during LBA-EUSTACH 1999. J. Aerosol Sci. 34, 883–907. doi:10.1016/S0021-8502(03)00052-1

Hasan, H., Dzubay, T.G., 1983. Apportioning light extinction coefficients to chemical species in atmospheric aerosol. Atmos. Environ. 17, 1573–1581. doi:10.1016/0004-6981(83)90310-4

Levin, E.J.T.T., McMeeking, G.R., Carrico, C.M., Mack, L.E., Kreidenweis, S.M., Wold, C.E., Moosmüller, H., Arnott, W.P., Hao, W.M., Collett, J.L., Malm, W.C., Moosmöller, H., Arnott, W.P., Hao, W.M., Collett, J.L., Malm, W.C., 2010. Biomass burning smoke aerosol properties measured during Fire Laboratory at Missoula Experiments (FLAME). J. Geophys. Res. Atmos. 115, 1–15. doi:10.1029/2009JD013601

Sorribas Panero, M. del M., 2007. Medida y caracterización del aerosol atmosférico en un ambiente rural y costero del suroeste de Europa. La distribución numérica de tamaños en el rango sub-micrométrico. Universidad de Valladolid.

TSI, 2007a. Model 3772/3771 Condensation Particle Counter. Operation and Service Manual.

TSI, 2007b. Scanning Mobility Particle Sizer TM Spectrometer (SMPS) Model 3936.